Year : 2012

Characterization of gravitation al rock slope deformations at different spatial sc_ales based on field, rem ote sensing and numerical approaches

Pedrazzini Andrea

UNIL | Université de Lausanne

Institut de géomatique
et d'analyse du risque

Characterization of gravitational rock slope deformations at different spatial scales based on field, remote sensing and numerical approaches

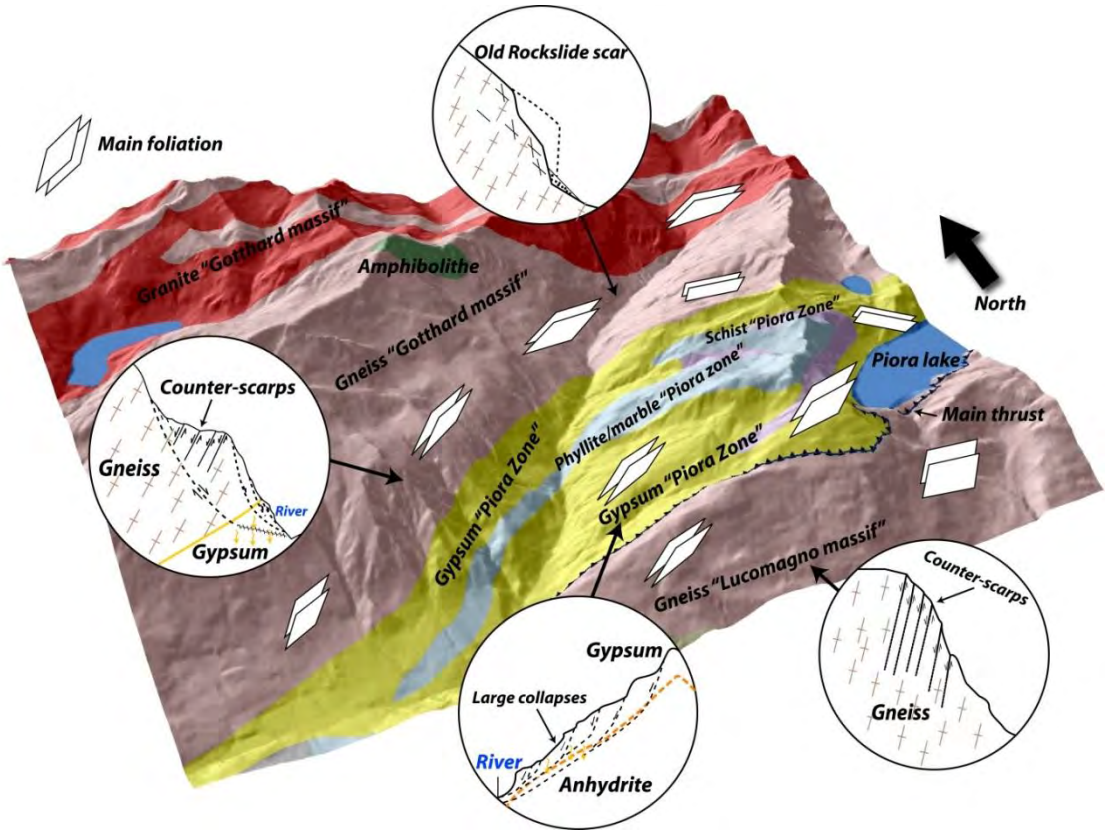

Thèse de doctorat

présentée à la Faculté des Géosciences et de l'Environnement de l'Université de Lausanne

par

Andrea Pedrazzini

Ingénieur-géologue diplomé de l'Université de Lausanne

Devant le Jury composé par:

Prof. Klaus Holliger, président du Jury
Prof. Michel Jaboyedoff, Directeur de thèse
Dr. Marc-Henri Derron, Expert Interne
Dr. Federico Agliardi, Expert Externe
Prof. Masahiro Chigira, Expert Externe
Prof. Giovanni Crosta, Expert Externe

UNIL | Université de Lausanne
Faculté des géosciences et de l'environnement
bâtiment Amphipôle
CH-1015 Lausanne

IMPRIMATUR

Vu le rapport présenté par le jury d'examen, composé de

Président de la séance publique :	M. le Professeur Klaus Holliger
Président du colloque :	M. le Professeur Klaus Holliger
Directeur de thèse :	M. le Professeur Michel Jaboyedoff
Expert interne :	M. le Docteur Marc-Henri Derron
Expert externe :	M. le Professeur Masahiro Chigira
Expert externe :	M. le Docteur Federico Agliardi
Expert externe :	M. le Professeur Giovanni B. Crosta

Le Doyen de la Faculté des géosciences et de l'environnement autorise l'impression de la thèse de

Monsieur Andrea PEDRAZZINI

Maîtrise universitaire ès Sciences d'ingénieur géologue
Université de Lausanne

intitulée

CHARACTERIZATION OF GRAVITATIONAL ROCK SLOPE DEFORMATIONS AT DIFFERENT SPATIAL SCALES BASED ON FIELD, REMOTE SENSING AND NUMERICAL APPROACHES

Lausanne, le 25 mai 2012

Pour le Doyen de la Faculté des géosciences et de l'environnement

Professeur Klaus Holliger

Summary

Characterization of gravitational rock slope deformations at different spatial scales based on field, remote sensing and numerical approaches

Andrea Pedrazzini, March2012, Institute of Geomatics and Analysis of Risk, University of Lausanne

Rock slope instabilities such as rock slides, rock avalanche or deep-seated gravitational slope deformations are widespread in Alpine valleys. These phenomena represent at the same time a main factor that control the mountain belts erosion and also a significant natural hazard that creates important losses to the mountain communities. However, the potential geometrical and dynamic connections linking outcrop and slope-scale instabilities are often unknown. A more detailed definition of the potential links will be essential to improve the comprehension of the destabilization processes and to dispose of a more complete hazard characterization of the rock instabilities at different spatial scales.

In order to propose an integrated approach in the study of the rock slope instabilities, ***three main themes*** were analysed in this PhD thesis: (1) ***the inventory and the spatial distribution*** of rock slope deformations at regional scale and their influence on the landscape evolution, (2) ***the influence of brittle and ductile tectonic structures*** on rock slope instabilities development and (3) ***the characterization of hazard*** posed by potential rock slope instabilities through the development of conceptual instability models.

To prose and integrated approach for the analyses of these topics, several techniques were adopted. In particular, high resolution digital elevation models revealed to be fundamental tools that were employed during the different stages of the rock slope instability assessment. A special attention was spent in the application of digital elevation model for detailed geometrical modelling of past and potential instabilities and for the rock slope monitoring at different spatial scales. Detailed field analyses and numerical models were performed to complete and verify the remote sensing approach.

In the first part of this thesis, large slope instabilities in Rhone valley (Switzerland) were mapped in order to dispose of a first overview of tectonic and climatic factors influencing their distribution and their characteristics. Our analyses demonstrate the key influence of neotectonic activity and the glacial conditioning on the spatial distribution of the rock slope deformations. Besides, the volumes of rock instabilities identified along the main Rhone valley, were then used to propose the first estimate of the postglacial denudation and filling of the Rhone valley associated to large gravitational movements.

In the second part of the thesis, detailed structural analyses of the Frank slide and the Sierre rock avalanche were performed to characterize the influence of brittle and ductile tectonic structures on the geometry and on the failure mechanism of large instabilities. Our observations indicated that the geometric characteristics and the variation of the rock mass quality associated to ductile tectonic structures, that are often ignored landslide study, represent important factors that can drastically influence the extension and the failure mechanism of rock slope instabilities.

In the last part of the thesis, the failure mechanisms and the hazard associated to five potential instabilities were analysed in detail. These case studies clearly highlighted the importance to incorporate different analyses and monitoring techniques to dispose of reliable and hazard scenarios. This information associated to the development of a conceptual instability model represents the primary data for an integrated risk management of rock slope instabilities.

Résumé

Caractérisation multi-échelle des mouvements de versants rocheux à l'aide de techniques numériques et d'analyses de terrain

Andrea Pedrazzini, Mars 2012, Institut de géomatique et d'analyse du risque, Université de Lausanne.

Les mouvements de versant tels que les chutes de blocs, les éboulements ou encore les phénomènes plus lents comme les déformations gravitaires profondes de versant représentent des manifestations courantes en régions montagneuses. Les mouvements de versant sont à la fois un des facteurs principaux contrôlant la destruction progressive des chaines orogéniques mais aussi un danger naturel concret qui peut provoquer des dommages importants. Pourtant, les phénomènes gravitaires sont rarement analysés dans leur globalité et les rapports géométriques et mécaniques qui lient les instabilités à l'échelle du versant aux instabilités locales restent encore mal définis. Une meilleure caractérisation de ces liens pourrait pourtant représenter un apport substantiel dans la compréhension des processus de déstabilisation des versants et améliorer la caractérisation des dangers gravitaires à toutes les échelles spatiales.

Dans le but de proposer un approche plus globale à la problématique des mouvements gravitaires, ce travail de thèse propose ***trois axes de recherche principaux***: (*1)* ***l'inventaire et l'analyse*** **de la** ***distribution spatiale des grandes instabilités rocheuses*** **à l'échelle régionale**, (2) ***l'analyse des structures tectoniques cassantes et ductiles en relation avec les mécanismes de rupture des grandes instabilités rocheuses*** et (3) ***la caractérisation des aléas rocheux par une approche multidisciplinaire*** visant à développer un modèle conceptuel de l'instabilité et une meilleure appréciation du danger . Pour analyser les différentes problématiques traitées dans cette thèse, différentes techniques ont été utilisées. En particulier, le modèle numérique de terrain s'est révélé être un outil indispensable pour la majorité des analyses effectuées, en partant de l'identification de l'instabilité jusqu'au suivi des mouvements. Les analyses de terrain et des modélisations numériques ont ensuite permis de compléter les informations issues du modèle numérique de terrain.

Dans la première partie de cette thèse, les mouvements gravitaires rocheux dans la vallée du Rhône (Suisse) ont été cartographiés pour étudier leur répartition en fonction des variables géologiques et morphologiques régionales. En particulier, les analyses ont mis en évidence l'influence de l'activité néotectonique et des phases glaciaires sur la distribution des zones à forte densité d'instabilités rocheuses. Les volumes des instabilités rocheuses identifiées le long de la vallée principale ont été ensuite utilisés pour estimer le taux de dénudations postglaciaire et le remplissage de la vallée du Rhône lié aux grands mouvements gravitaires.

Dans la deuxième partie, l'étude de l'agencement structural des avalanches rocheuses de Sierre (Suisse) et de Frank (Canada) a permis de mieux caractériser l'influence passive des structures tectoniques sur la géométrie des instabilités. En particulier, les structures issues d'une tectonique ductile, souvent ignorées dans l'étude des instabilités gravitaires, ont été identifiées comme des structures très importantes qui contrôlent les mécanismes de rupture des instabilités à différentes échelles.

Dans la dernière partie de la thèse, cinq instabilités rocheuses différentes ont été étudiées par une approche multidisciplinaire visant à mieux caractériser l'aléa et à développer un modèle conceptuel trois dimensionnel de ces instabilités. A l'aide de ces analyses on a pu mettre en évidence la nécessité d'incorporer différentes techniques d'analyses et de surveillance pour une gestion plus objective du risque associée aux grandes instabilités rocheuses.

Acknowledgments

I am very grateful to Prof. Michel Jaboyedoff who has been my mentor over last 7 years of my master and my doctoral studies and offered to me the opportunity to continue my researches at the Institute of Geomatics and Analysis of Risk (IGAR). During these seven years I was glad to be involved in a multitude of different projects that allowed me to improve my knowledge in the field of natural hazards, and slope stability. I would like to address special thanks to Dr. Marc-Henri Derron and to Alexandre Loye for their support and patience in improving my writing.

All my gratitude goes to the Turtle Mountain project and especially to his leader Corey Froese to offer me the opportunity to participate to the stimulating researches on Turtle Mountain and to contribute to fund part of this PhD thesis.

I would like to thank the external members of my examining committee Federico Agliardi and Giovanni Crosta from the University of Milano-Biccocca and Mashairo Chigira from the Kyoto University for reviewing my thesis and for their insightful comments and stimulating discussions during the field work and conferences.

I am also tankful to David Jarman to the days spent in the field together and for his critical review of some chapters of the PhD manuscript.

I definitely appreciated the 7 years spent at the IGAR with many gratifying exchanges with colleagues of different countries. In particular it was extremely appreciable that there was always someone to help you when you have some problem with the computer or with the interpretation of numerical analysis. Many thanks to Pascal Horton, Céline Longchamp, Alexandre Loye, Florian Humair, Lucien Schreiber, Clément Michoud, Daro Carrea and Marc Choffet. Several colleagues and friends were actively involved in this PhD thesis, either for field work or for numerical analyses: Battista Matasci, Marc-André Brideau, Martina Böhme, Marie Charrière, Corey Froese, Florian Humair, Richard Metzger, Willem Langemberg, Céline Longchamp, Alexandre Loye, Mary Tonini and Laura Superchi. Thank you very much for your help, your company and your advice. I would like to thanks also the colleagues of the Geomatics groups for the stimulating discussions during the coffee breaks

Finally, thank for my family and friends, which supported and encouraged me during my studies. I am especially grateful to my parents, Pia and Ennio and to my future wife Laure for the comprehension and moral support during the difficult moments in finalizing this PhD manuscript.

This PhD would not have been possible without financial support of the Swiss National Fund project (200021-118105), the University of Lausanne and of several private companies thought their projects and mandates contributed to finance this PhD thesis.

Table of Contents

1. INTRODUCTION

1.1 GENERALITIES

1.1.1 SLOPE MOVEMENTS AS LANDSCAPE EVOLUTION PROCESSES

Mass transfer from denudation to accumulation areas represents the most important geomorphological expression of landscape evolution (Cendrero and Dramis 1996). In mountain belts this transfer is controlled by a complex interaction between gravity, tectonic and climatic factors (Willet 2010). Slope movements have been identified to have an important influence on the erosion rate of both active and less active mountain belts (Cendrero and Dramis 1996; Densmore et al., 1997; Hovius et al., 1997). In particular, large rock slope deformations, characterized by a high magnitude and a low frequency, are one of the major contributors to the denudation rate (Hewitt et al., 1998; Jarman 2002; Korup et al., 2007).

Recent studies (Korup et al., 2007; Antinao and Gosse 2009) suggest that the contribution of large rock slope deformations could represent between 1% and 10% of the Late Quaternary denudation rate. However, owing to the lack of extensive mapping and absolute chronology, the spatial distribution and the effective contribution of rock slope deformations on landscape evolution are still unclear and represent nowadays an important research topic (Figure 1.1-1).

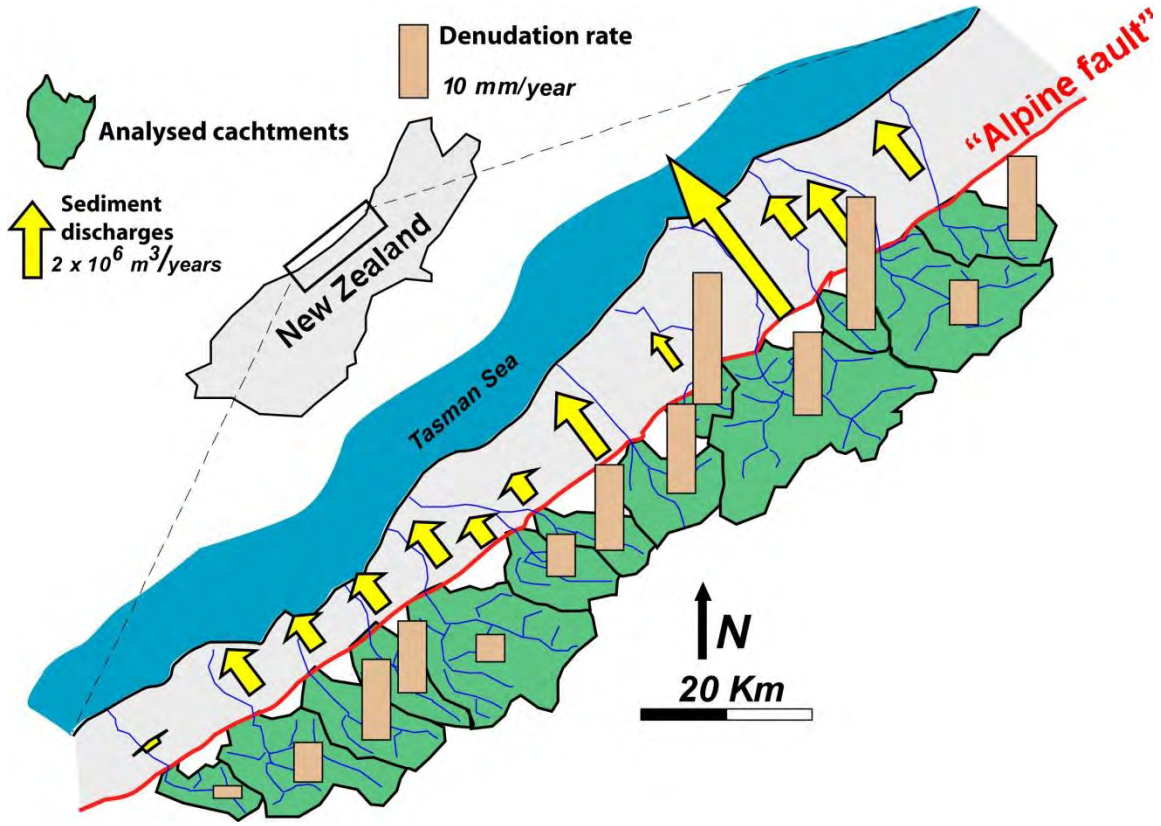

Figure 1.1-1: Example of the influence on the denudation rates and sediment discharges of landslide from 13 catchments draining western side of Southern Alps (New Zealand), calculated from 60 years of landslide record (adapted from Hovius et al., 1997).

1.1.2 SLOPE MOVEMENTS AS NATURAL HAZARDS

At human scale, slope movements represent a major natural hazard in particular in mountainous environment. From 1975 to 2000 almost 17'000 people were killed by landslides and avalanches worldwide (UNEP 2005 and Figure 1.1-2). In the United States, slope movements cause 25 to 50 fatalities and create damage of approximately 1 to 3 billion dollars per year (NRC 2004). In the small Switzerland, between 1972 and 2002, slope movements and flooding killed 88 people and caused economic damages for approximately 8.6 Billon of CHF (Schmidt 2004). In the last decades, the losses related to slope movement processes are increasing worldwide in relations with the growing of the population and the expansion of humans' settlement within potential unstable areas (NRC 2004). Researches in slope movements disciplines are complex because they required the comprehension of the physical processes defining the landslides dynamic but need also to integrate the socio-economics aspects related to the preventions and the consequences of catastrophic failures. This implies that scientists of many fields of study need to be actively implicated to provide an integrated approach on the slope processes problems and to improve the risk management strategies. According to NRC (2004), research priorities concerning slope movements processes can be summarized in three main tasks:

- The improvement on the understanding of landslide processes, thresholds, and triggers.
- The development of improved models of slope deformation and failure processes that could be efficiently implemented to predict the landslide hazards.
- The expanding and the improvement of predictive systems capable of interactively displaying changing landslide hazards in both space and time in areas prone to different types of hazard-triggering mechanisms.

The progressive and continuous improvement of these aspects will provide a more robust and objective description of the slope processes that represent the base for integrated approach of the hazard mitigation and the risk management.

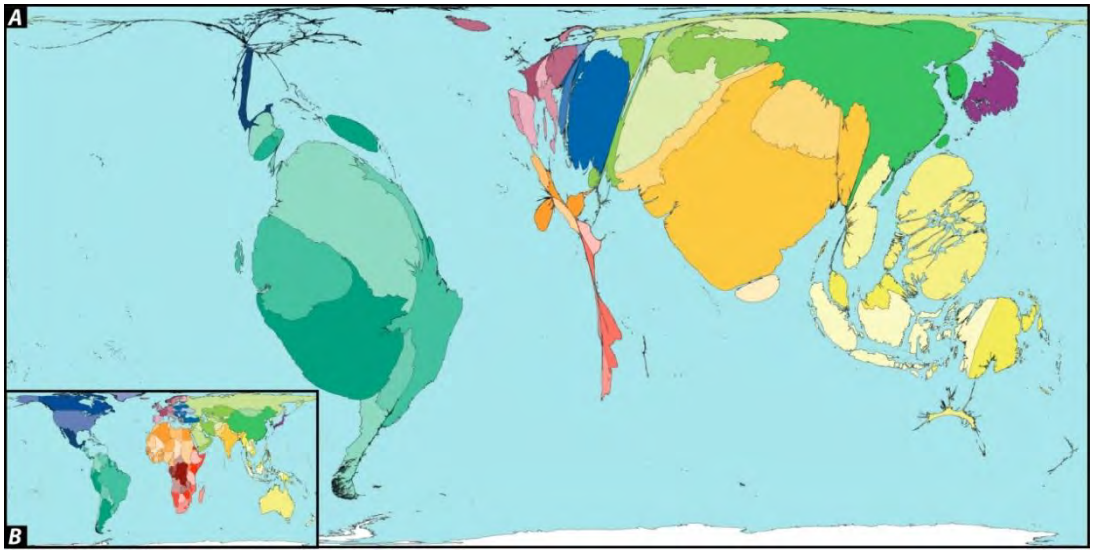

Figure 1.1-2: a) World map of people killed by avalanches and landslides between 1975 and 2000 (adapted from www.worldmapper.org). The size of the territory is proportional to the number of deaths. The number of deaths in rich country is relatively low compared to those in some of the countries under development. However, if economic losses are considered only, this relationship will be inversed. B) Not deformed map of the world.

1.1.3 PARAMETERS GOVERNING THE SLOPE MOVEMENTS DEVELOPMENT

The progressive development and the ultimate failure of a slope are influenced by complex interaction between different factors. To dispose of a first objective assessment of the slope system, Jaboyedoff and Derron (2005) proposed the sub-division of these parameters in two main categories (Figure 1.1-3):

1. The internal parameters.
2. The external factors.

Internal parameters (such as lithology, intact rock proprieties, morphological setting, joint sets geometry, permeability, etc.) are specific for a given slope in a given location and are essentially linked to the geological history of the studied area. External factors (such as gravitational effects, precipitations, glacial unloading, seismicity, etc.) influence the behavior of all slopes independently and are often connected to the recent environments of the slope. External factors continuously transform the internal parameters leading to a progressive degradation of the slope. The final failure is frequently associated to external factors acting as ultimate trigger or to the progressive degradation of the internal parameters through time.

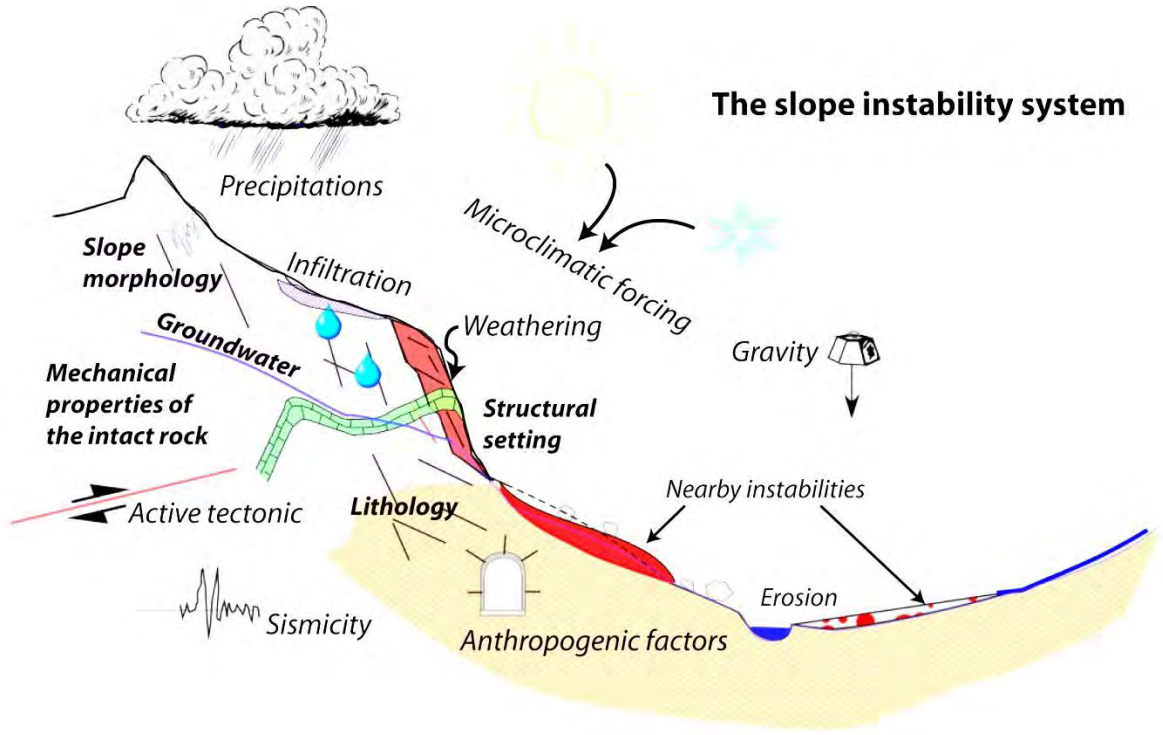

Figure 1.1-3: Representation of slope system and the main internal parameters (bold italic font) and the extern factors (italic font) influencing his stability (modified from Jaboyedoff and Derron 2005).

1.1.4 TERMINOLOGY AND CLASSIFICATIONS

In the literatures, the terms of "slope movements", "landslide" or "mass wasting" are used as generic term to describe the various types of movements in both soil and rock slopes. Several classifications have been proposed to categorize and describe in an objective way the different type of slope movements (Heim 1932; Varnes 1978; Hutchinson, 1988; Flageolet, 1989; Cruden and Varnes 1996). Each classification describes the slope processes based on different criterions such as the type of movements, the involved material, the failure mechanism or the amplitude and the direction of the observed displacements.

Nowadays, a general agreement has been found around the classification proposed by Cruden and Varnes (1997). These latest is primarily based on the characterization of the type of movement (Falls, Topples, Slides, Lateral spread, Flow and Complex/Compound) and on the typology of the involved material (rock, coarse or fine engineering soils). However, the Crunden and Varnes (1997) classification does not allow a precise and concise description of the phenomenon concerning large (slope scale) rock instabilities. For instance, the Frank slide (Cruden and Krahn 1973; Jaboyedoff et al., 2009) started as complex wedge slide/toppling and then propagate as a flow creating an ambiguity in the Cruden and Varnes (1978) classification. Hungr and Evans (2004) proposed a specific classification for large (slope scale) rock deformations based on the role of the rock structure (failure mechanism) and the mechanical proprieties of the rock mass (Table 1.1-1). In this manuscript, the term "rock slope deformation" is used as an "umbrella" term to describe large rock slide, rock avalanches or Deep Seated Gravitational Slope Deformations (DSGSD). When a specific definition is needed, the terminologies suggested by Hutchinson (1988) and by Hungr and Evans (2004) will be adopted.

Table 1.1-1: Classification of large rock slope instabilities proposed by Hungr and Evans (2004) based on rock structures and mechanical properties rock mass.

Structural control	***No systematic structural control***	***Systematic structural control***					
Dominant mechanism		***Sliding***				***Toppling***	
Kinematics		***Translational***	***Compound***			***Flexural***	***Block***
Constraint		***Unconstrained***		***Constrained***			
				At Toe	***At scarp***		
Mechanism Type	***A*** *Rock slump* ***B*** *Rock collapse*	***C*** *Block slide Wedge slide*	***D*** *Structurally defined compound slide*	***E*** *Block slide with toe breakout*	***F*** *Compound slide*	***G*** *Flexural topping*	***H*** *Block Topple*
Typical behaviour in weak rock	*Slow rotational movement*	*Catastrophic*		*Slow*	*Slow*	*Slow*	
Typical behaviour in weak rock	*Catastrophic collapse*	*Catastrophic, limited pre-failure deformation*	*Catastrophic, large pre-failure deformation*	*Catastrophic*			*Catastrophic*

1.2 RESEARCH PROJECT

1.2.1 PROJECT HISTORY

In the beginning, this PhD thesis was principally linked to a research project concerning the study of large rock slope instabilities in the Rhone Valley and funded by the Swiss national science foundation (grant number 200021-118105). Thus, the slope instability system was analysed from landscape evolution perspective with emphasis on the relation between rock slope instabilities distribution and tectonic or postglacial processes.

Then, with the start of the collaboration with the Alberta Geological survey, concerning the potential instabilities mapping of Turtle Mountain (S-W Alberta, Canada), researches on hazard assessment based

on digital elevation model and structural characterization became also an important topic of this PhD. Furthermore, the opportunity to analyse several active rock instabilities allowed developing a multidisciplinary approach, to assess the present and the potential evolution of the instabilities based on the integration of different investigation and monitoring techniques. In this context, the collaboration with private companies allowed the transfer of the developed approaches to practical instability problems concerning both natural and engineered slopes.

Finally, the activities performed during this PhD provided a coherent approach to study the slope system from a landscape evolution perspective but also from a more applied viewpoint.

1.2.2 GOALS

The main goal of this PhD thesis is to propose a multidisciplinary approach based on the integration of field investigations, remote sensing and numerical analyses to study rock slope instabilities at different spatial scales. The main objectives of this PhD thesis can be divided in three different themes that will be analysed and discussed within the manuscript:

a) ***Investigate the characteristics and the distribution of rock slope deformations at regional scale in term of landscape evolution.***

The distribution and the characterization of large slope instabilities in relation with tectonic and climatic factors is the first important step toward a better understanding of the slope system and landscape evolution. The analysis of regional slope instabilities inventories allow disposing a first overview of predisposing factors influencing their distribution within a given area. Moreover, statistical information derived from landslide inventories allows evaluating the influence of rock slope instabilities on erosion rate of mountain belt. This PhD aims to investigate the characteristics of the rock slope instabilities at regional scale in a complex geological/geomorphological environment with emphasis on their relations with present-day tectonic characterized. In this context, the development and the adaptation GIS and statistical tools will be proposed.

b) ***Determine the influence of inherited brittle and ductile tectonic structures on rock slope instability development.***

Old rockslides and rock-avalanches scars provide a preferential view on the internal structure of the instabilities, in particular of the failure surface. Detailed analyses of the structural setting and of the pre-failure slope morphology are crucial to understand the failure mechanism and pre-failure conditions. In this PhD, a special attention is paid to the role played by inherited ductile and brittle tectonic structures in defining the failure mechanism and in delimiting the extent of the unstable rock slopes. Besides, objective and reproducible techniques based on high resolution digital elevation model are tested to obtain an accurate estimation of the pre-failure topography.

c) ***Characterize the hazard posed by potential rock slope instabilities through the development of conceptual instability model and by integrating different modelling techniques.***

The methodological approaches adopted for the study of the past rockslide scars and main finding in term failure mechanism need to be included in the study of the potential rock slope instabilities. This allows disposing of more comprehensive view of the unstable slope system in term of present-day kinematic and potential evolution. This PhD aims to improve the understanding of the slope instability system in term of

failure kinematic and hazard assessment by integrating field investigations, monitoring data and numerical analyses.

1.3 THESIS OUTLINE

This manuscript is divided into 6 chapters. After this general introduction, *Chapter 2* proposes a literature overview focused on the topics and the methodological approaches detailed during PhD project. In *Chapters 3 to 5* are developed the three principal themes of the PhD thesis. These three chapters have been written in a journal format. Each chapter contains two or more journal-like papers including their own introduction (specific literature overview), methodology, results and discussions.

Chapter 3 refers to regional scale analyses of rock slope instabilities in Rhone valley (S-W Switzerland). In this chapter, two distinct articles (sub-chapters) are presented. In the first article (*Chapter 3.1*), an inventory of the large rock slope instabilities mapped on the entire Rhone catchment is presented. The spatial correlational between the instabilities and the geological, glacial and active tectonic constraints are quantitatively evaluated. The second article (*Chapter 3.2*) focuses on the characterization of rockslide and rock avalanche scars along the main Rhone valley in term of spatial distribution, failure mechanisms and volume. Based on these analyses, the influence of large rockslide on the Lateglacial erosion history of the Rhone catchment is estimated.

The influence of inherited brittle and tectonics structures on the stability and the failure mechanisms of large slope instabilities is analysed in *Chapter 4*. The first part of this chapter (*Chapter 4.1*) examines the influence of pre-existing tectonic discontinuities on the 3D kinematic release and on the local reduction of the rock mass strength of Frank slide and adjacent areas (S-W Alberta, Canada). Based on these results, a conceptual model for potential failure mechanism related to the anticline setting is proposed.

The second part of the chapter (*Chapter 4.2*) is dedicated to the analysis of the influence of both ductile and brittle tectonics structures on the failure mechanism and on the failure surface geometry characterizing the Sierre rock-avalanche (S-W Switzerland). Here, the formation of gravity-induced structures and the influence of both ductile and brittle tectonic on the failure mechanism and the run-out of the rock-avalanche are presented.

Chapter 5 focuses on the multidisciplinary characterization of present and potential rocks slopes instabilities in a hazard assessment perspective. Five different case studies are presented. The first case studies (*Chapter 5.1*) discuss the application of high resolution digital elevation model analyses and run-out modelling to characterize hazard posed by a potentially unstable rock slopes at Turtle Mountain (S-W Alberta, Canada). According to displacement datasets and structural observations and DEM modelling, potential failure mechanisms affecting different portions of the mountain as well as the potential unstable volumes are assessed and used for predictive run-out analyses.

The second case study (*Chapter 5.2*), focus on the detailed monitoring and failure mechanism modelling of the slow rockslide activated in July 2006 on the eastern flank of the Eiger Mountain (Central Switzerland). Here, the influence on the instability development of the progressive rock mass strength degradation and the preferential paraglacial relaxation are highlighted. In the third case study (*Chapter 5.3*), the displacements of upper unstable portion of the Randa rockslide are investigated by combining data obtained by PSInSAR™ and classical geodetic sensors. Simple geometrical and geomechanical models are

used to test the validity of the calculated displacements and to understand the role of the pre-existing discontinuities on the displacement directions.

Chapter 5.4 presents the application of terrestrial laser scanning (TLS) to the monitoring of an active landslide area. An unstable slope located in Val Canaria (Ticino, Southern Switzerland) has been monitored using TLS techniques during three years. Decimetric pre-failure deformations, preceding a collapse of 365'000 m^3, have been clearly detected for two years before the collapse. Detailed treatment of TLS data acquired the day just before the collapse allows detecting centimetric pre-failure displacements that were confirmed by ground-based radar measurements.

In case study five (*Chapter 5.5*), TLS technique is combined with field investigation and stability analysis to analyse the predisposing and the triggering factor of past rockslides and to assess the present-day stability in the Arvel quarry (S-W Switzerland). Based on continuous ground-based radar monitoring and periodic TLS acquisitions, a preliminary early warning system and an emergency response procedure were proposed.

Specific discussions and conclusions are presented at the end of each sub-chapter. A general summary of the main outcomes obtained in the PhD as well as the perspective for future works are discussed in *Chapter 6.* Appendixes are integrated in a separate volume containing *5 journal articles* and *2 book chapters* written as co-authors. Additionally, five technical reports produced during the PhD period are also added.

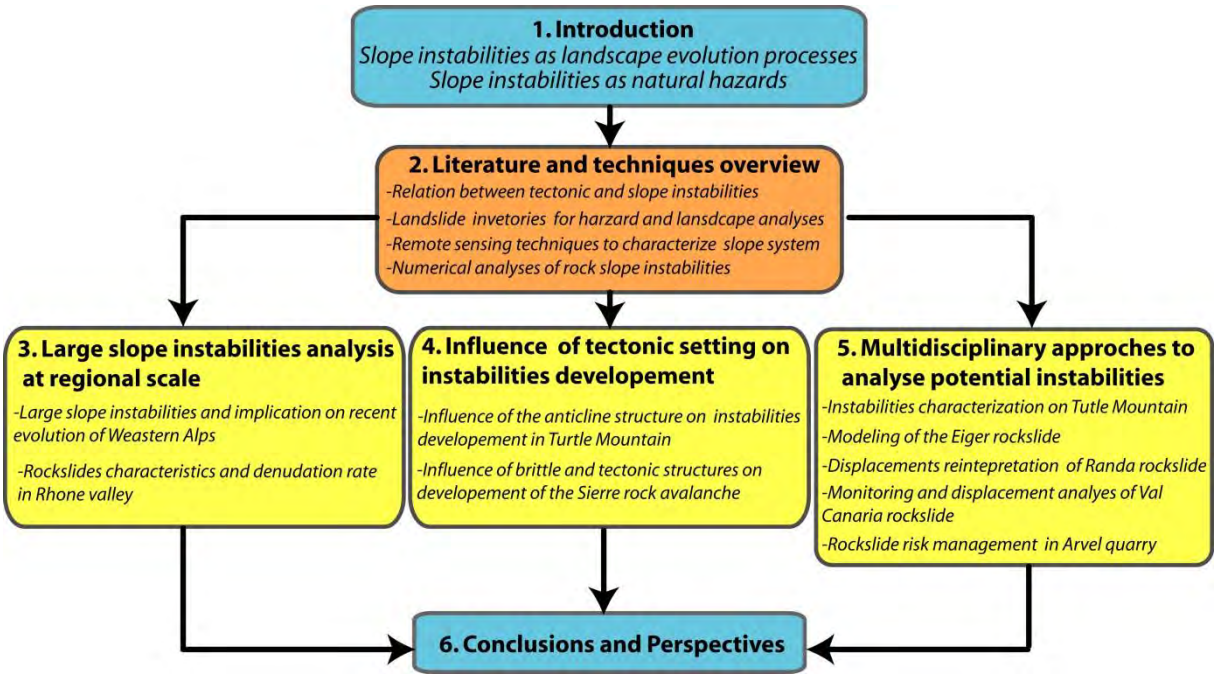

Figure 1.3-1: Flow-chart displaying the manuscript structure.

1.4 REFERENCES

Antinao, J.L., Gosse, J. 2009. Large rockslides in the Southern Central Andres of Chile (32-34.5°S): Tectonic control and significance for quaternary landscape evolution, *Geomorphology*, 104, 117-133.

Cendrero, A., Dramis, F. 1996. The contribution of landslides to landscape evolution in Europe, *Geomorphology*, 15, 191-211.

Cruden, D.M., Krahn, J. 1973. A reexamination of the geology of the Frank Slide, *Canadian geotechnical journal*, 10, 581-591.

Cruden, D.M., Varnes, D.J. 1996 Landslide types and processes. In: Turner A.K.; Shuster R.L. (eds.) *Landslides: Investigation and Mitigation*, Transp. Res. Board, Spec. Rep. 247, 36–75.

Flageolet, J. C., 1989, *Les mouvements de terrain et leur prévention*, Paris, Masson, 520 p.

Densmore, A. L., Anderson, R. S., McAdoo, B. G., Ellis, M. A. 1997. Hillslope evolution by bedrock landslides, *Science*, 75, 369-372.

Jaboyedoff, M., Derron, M-H. 2005. Integrated risk assessment process for landslides, in: *Landslide risk management*, edited by Hungr, O., Fell, R., Couture, R. R., and Eberhardt, E., Taylor and Francis, 776 p.

Jaboyedoff, M., Couture, R., Locat, P. 2009. Structural analysis of Turtle Mountain (Alberta) using Digital Elevation Model: Toward a progressive failure, *Geomorphology*, 103, 5-16.

Heim, A., 1932, *Der Bergsturz und Menschenleben,* Zürich, Fretz und Wasmuth, 218 p.

Hewitt, K. 1998. Catastrophic landslides and their effects on the upper Indus streams, Karakoram Himalaya, northern Pakistan, *Geomorphology*, 26, 47–80.

Hovius, N., Stark, C. P., and Allen, P. A. 1997. Sediment flux from a mountain belt derived by landslide mapping, *Geology*, 25, 231-234.

Hutchinson, D. J. 1988. *General report: morphological and geotechnical parameters of landslides in relation to geology and hydrogeology*: Proc. 5th Int. Symp. on Landslides, 3-35.

Hungr, O., Evans, S.G. 2004. The Occurrence and Classification of Massive Rock Slope Failure, *Felsbau,* No.2.

http://www.worldmapper.org/display.php?selected=252.

Korup, O., Clague, J.J., Hermanns, R.L., Hewitt, K., Strom, A.L., Weidinger, J.T. 2007. Giant landslides, topography, and erosion, *Earth and Planetary Science Letters*, 261, 578-589.

Jarman, D. 2002. Rock slope failure and landscape evolution in the Caledonian Mountains, as exemplified in the Abisko area, Northern Sweden, *Geografiska Annaler,* 84, 213–224.

NRC 2004. Partnership for reducing landslide Risk: assessment of National Landslide Hazards Mitigation Strategies, 144 pp.

Schmidt, F., 2004. Unwetterschäden in der Schweiz 1972-2002: Verteilung, Ursachen, Entwicklung, *Wasser, Energie, Luft*, 1, 21-28.

UNEP. 2005, United Nations Environment Programme-Annual report, 80p.

Willet, S.D. 2010. Late Neogene Erosion at the Alps: A climate Driver? *Annual Review of earth and planetary science*, 38, 411-437.

2. LITERATURE AND TECHNIQUES OVERVIEW

2.1 RELATION BETWEEN TECTONIC AND ROCK SLOPE DEFORMATIONS

Tectonic and tectonic-related structures have been identified in different mountain belts to be one of the key parameters influencing the development and the distribution of large slope movements (Keefer 1984, Ballantyne 2002; Korup et al. 2007; Hermanns et al., 2001). Tectonic can play both an active and a passive role on rock slope deformation development (Agliardi et al., 2009a, b; Jaboyedoff et al., 2011). Tectonic movements play an active role by triggering the initiation or the final collapse of rock slope deformations (Beck, 1968; Radbruch-Hall, 1978; Keefer 1984; McCalpin, 1999) or by prompting the decrease the rock mass strength through the development of a pervasive tectonic fracturing (Molnar et al., 2007; Clarke and Burbank 2010). Frequently, pre-existing tectonic structures play an important passive role by controlling spatial variations of the rock mass strength, thus constraining the development and the localization of rock slope deformations (Kellogg, 2001; Agliardi et al., 2009a; Agliardi et al., 2009b; Brideau et al., 2009). At all spatial scale, both ductile and brittle tectonic structures have been recognized, to be potentially reactivated by gravitational movements (Kellog 2001; Jackson 2002; Ambrosi and Crosta 2006; Saintot et al., 2011; Coe and Harp, 2007). In this chapter, the potential relationships between tectonic and rock slope deformations are briefly presented. Figure 2.1-1 resumes the main relations existing between tectonic and rock slope deformations.

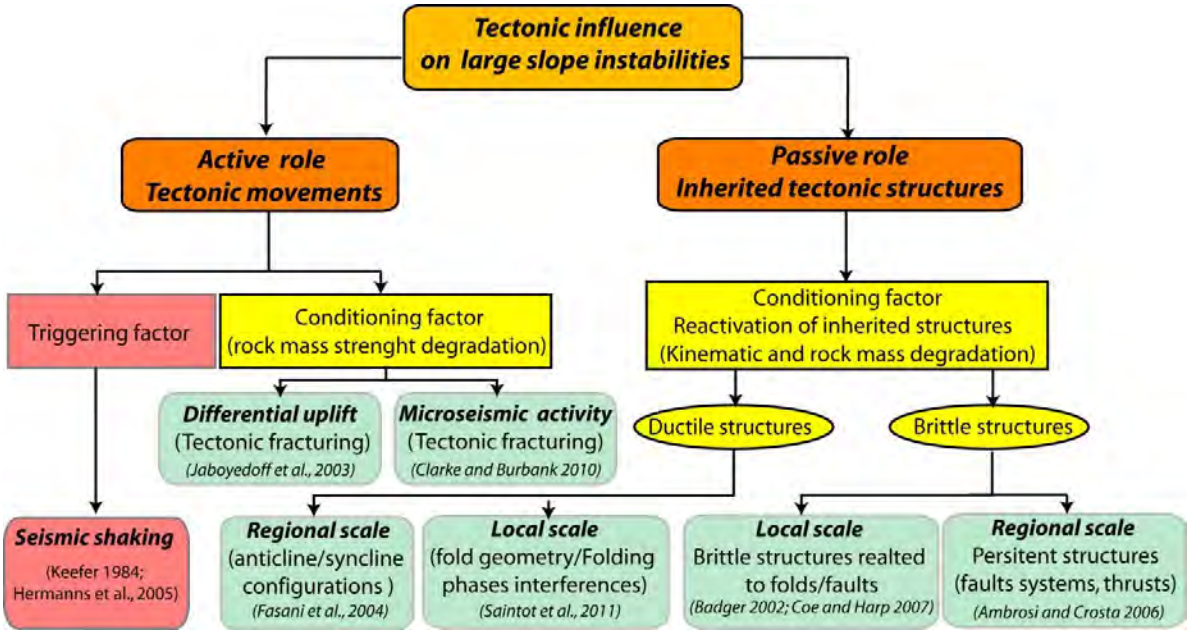

Figure 2.1-1: Flow-chart resuming the potential relations between rock slope deformations, inherited tectonic structures and active tectonic movements.

2.1.1 SEISMICITY AND TECTONIC ACTIVITY

2.1.1.1 Seismicity as triggering factor for rock slope deformation

Recent examples as the Chi–Chi earthquake (Chen et al., 2005; Chigira et al. 2003), the Kahsmir earthquake (Owen et al., 2008) or the Wenchuan earthquake (Xu et al., 2009; Yin et al., 2011) demonstrate a causal relationship between active tectonic and large rock deformations development (Figure 2.1-2). In this context, ground shaking and/or co-seismic slip along active faults is primary triggering factor leading to the development of large rock slope deformations (McCalpin and Hart, 1999; Jibson et al., 2006). Keefer (1984) based on the study of 40 landslide events triggered by earthquakes (Magnitude ≥ 4) suggested the presence of a potential link between the earthquakes magnitude and total surface affected by landslide. In the same way, the author suggested also a correlation linking the maximal landslide distances and the earthquake epicentre for different earthquake magnitudes (Keefer 1984).

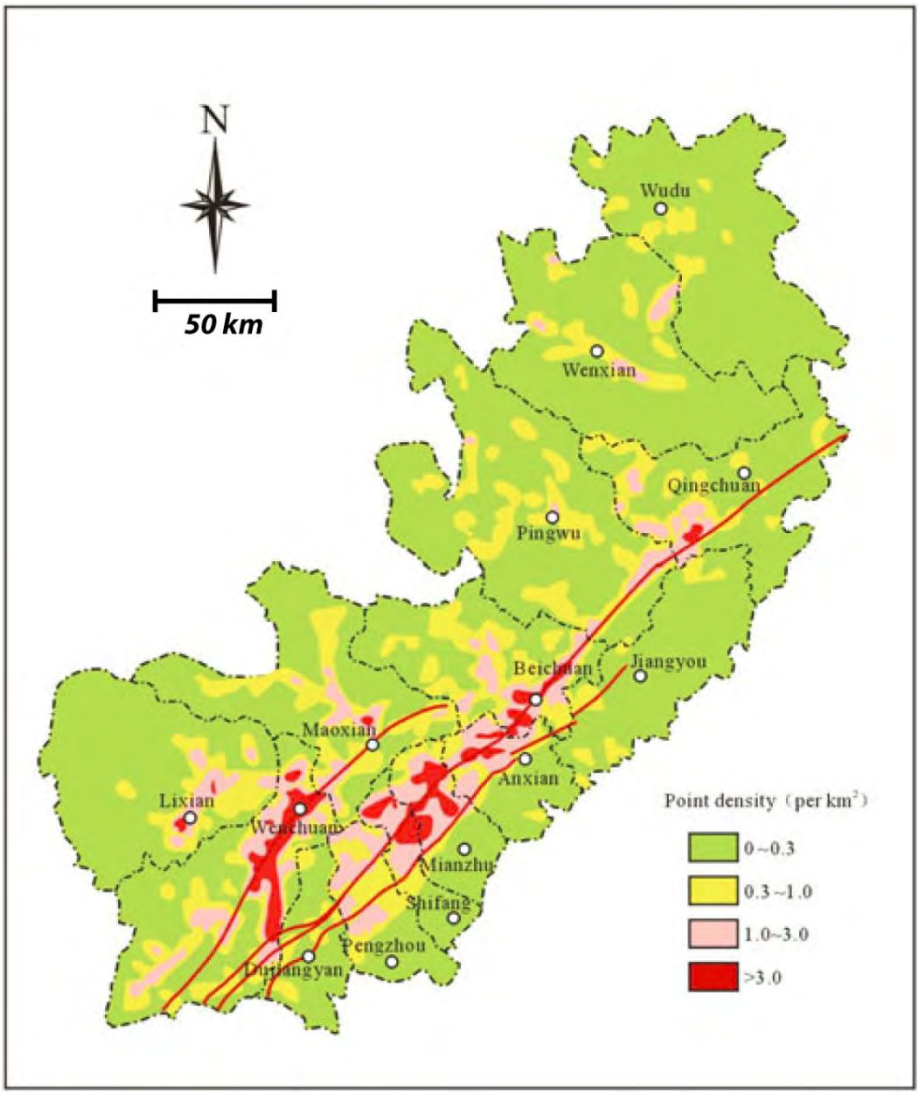

Figure 2.1-2: Density map showing the landslides distribution triggered by the Wenchuan earthquake. Note the high landslide density close to the active faults (from Yin et al., 2011)

Even if frequently mentioned, the connection between earthquakes triggering and postglacial rock slope deformations is often difficult to demonstrate quantitatively. The correlation is often proposed based on

the paleoseismic analyses (Dramis and Sorriso-Valvo 1994; McCalpin 1999; McCalpin and Hart, 1999) or suggested indirectly by the comparison between the spatial distribution of the rock slope deformations and the present-day earthquake activity (Hermanns et al., 2000; Hermanns et al., 2001; Wieczorek and Jäger 1996). In NW Argentina, Hermanns et al. (2006) showed that rock-avalanche deposits are located along a tectonically active mountain front and are most likely related to seismic shaking. In southern-central Andes, Antinao and Gosse (2009) based on variographic techniques, proposes a spatial relation between shallow seismicity and rockslide clusters (Figure 2.1-3). Seismic triggering have also be proposed in different mountain belts to explain the development of late quaternary Deep-Seated Gravitational Slope Deformations (Beck, 1968; Radbruch-Hall, 1978; Forcella and Orombelli, 1984; McCalpin, 1999). In particular, along San Andreas Fault (California, Usa), McCalpin and Hart (1999), based on detailed in-situ analyses of DSGSD scarps, identified the presence of suddenly ground ruptures of more than 1 meter suggesting a co-seismic origin of large slope movements.

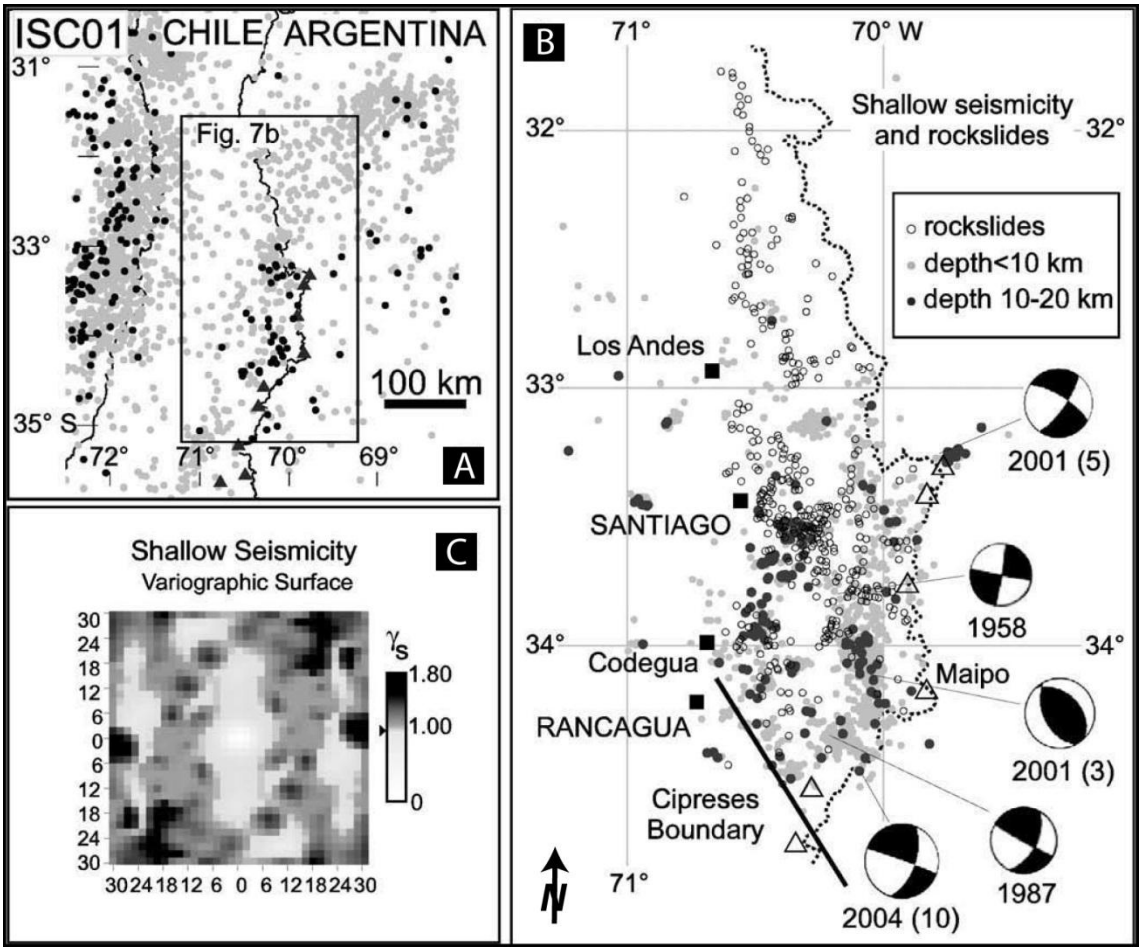

Figure 2.1-3: Relation between seismicity and rockslide clusters in Sothern- central Andes (From Antinao and Gosse 2009). a) Seismicity distribution in the study area (grey dots: all events; black dots: shallow seismicity, <20 km deep). b) Comparison between shallow seismicity (filled dot) and rockslide inventory (open circles). Pleistocene–Holocene volcanic centres are marked by open triangles. c) Variographic surface calculated for shallow seismicity covering the whole study area.

2.1.1.2 Tectonic activity as predisposing factor for rock slope development

Neotectonic activity is also considered as an important predisposing factor on the development of large slope deformations. According to Molnar et al. (2007) active tectonic can influence the rock slope

deformation development by (1) increasing the relief and (2) by fracturing the rock mass. Montgomery and Brandon (2002) indicated that, in tectonic active mountain belt, the landscape adjusts preferentially to the tectonic uplift by increasing the frequency of the bedrock landslide rather than gradual slope steepening. This suggests that rock slope deformations need to be considered as stationary agent to maintain the hillslope at the threshold angle (Selby 1980; Schmidt and Montgomery 1995). Korup et al. (2007) in analysing the worldwide distribution of large catastrophic rock slope failure, showed that about half of the catastrophic failures occurred in small portions of tectonically active mountain belts where mean local relief and erosion rate are relatively high emphasizing the role of rock slope deformations in relief adjustment (Figure 2.1-4).

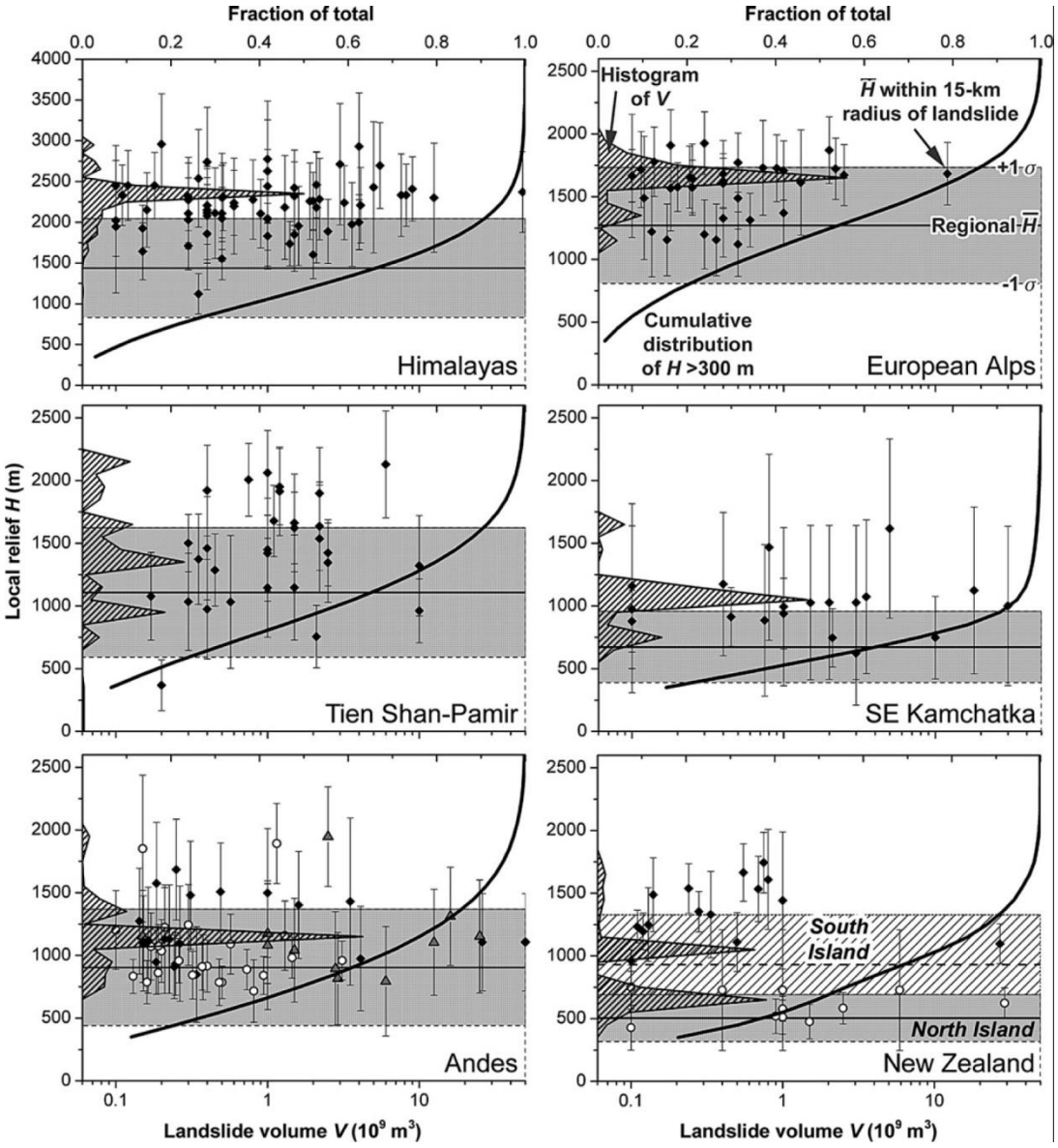

Figure 2.1-4: Relationship between local relief (H) distribution and volumes of catastrophic rock slope deformations in different mountain belts (from Korup et al., 2007). More than half of giant landslides occurred in the steepest 6% of the mountain belt, characterized by H≥ 2km, suggesting the important influence of rock slope deformations for the continuous relief adjustment.

As suggested by Molnar et al. (2007) another important roles played by tectonic activity can be related to the development of pervasive fracturing in the brittle portion of the crust through micro-seismic activity and tectonic strain accommodation along minor faults. Pervasive fracturing induced by tectonic strain have been identified by several authors as an important predisposing factor to explain development and localization of rock slope deformations (Hutchinson, 1995; Cruden and Varnes, 1996; 1998; Hermanns et al., 2001; Kellogg, 2001; Radifeld and Osmunden 2009; Norini et al., 2010). In analysing the anomalous clusters of rockslide between central and Patagonian Andes, Penna et al. (2011) highlighted the absence of a clear structural configuration allowing kinematic predisposition to slope failure. Conversely, they identified an important neotectonic activity and a clear relation between large rockslides and tectonic structures suggesting that pre-fracturing of rock mass related to tectonic movements and to the continuous seismicity represent a main conditioning factor.

Similar interpretations have been proposed by Norini et al. (2010) to explain the distribution of large landslides in Acamby graben (Mexico). These authors identified an important influence of active quaternary faults in decreasing the local relief and in reducing the strength of the rock mass. Recently, Clarke and Burbank (2010) suggested a main control of tectonic fracturing of bedrock to explain the differences in landslide frequency and volume between more active belts like the Southern Alps of New Zealand and less tectonic active areas such as Fiordland (New Zealand). These authors showed that the contrasting fracturing mechanisms and resultant fracture densities observed in the two studied areas strongly influence the bedrock resistance promoting a clear differentiation in the landslide characteristics and in the denudation processes (Figure 2.1-5).

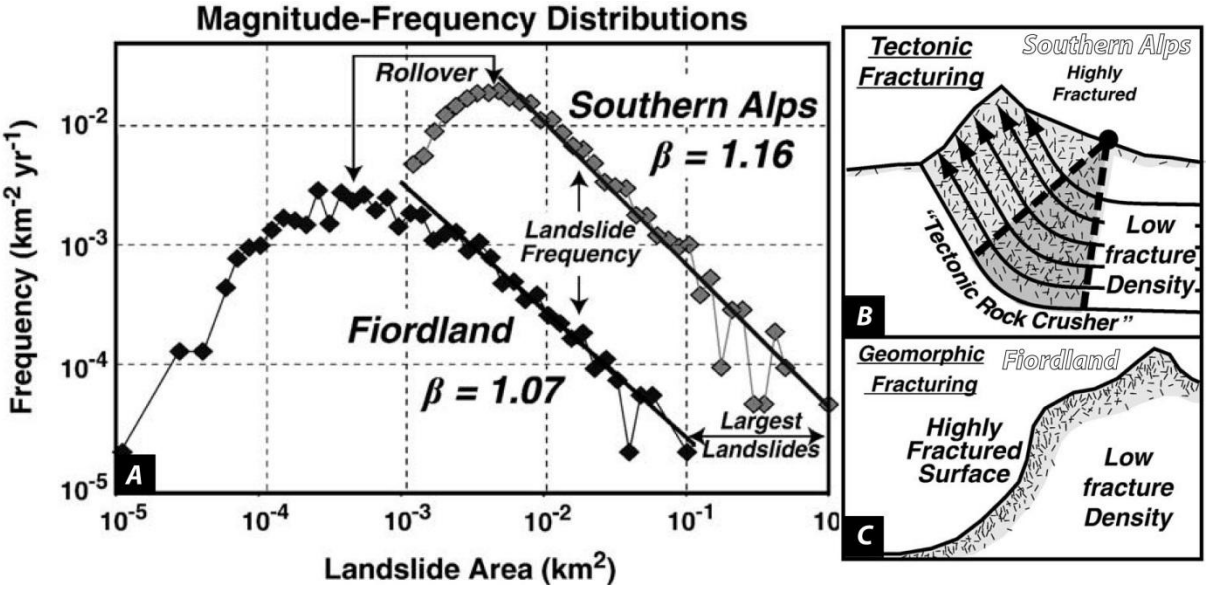

Figure 2.1-5: a) Landslide magnitude–frequency distributions for the western Southern Alps and Fiordland (from Clarke and Burbank 2010) indicating a clear difference between the two landslide inventory in term of landslide frequency and landslide area. b), c) Conceptual models of two modes of bedrock fracturing characterizing the two study areas. b) Tectonic rock crusher model. c) Surface-down geomorphic fracturing (Modified from Molnar et al., 2007).

In moderate active mountain belts such as the European Alps, the influence of seismicity and active tectonic movements as triggering or as predisposing factor for large rock slope deformations is questioned and represent nowadays a main research topic. Based on a detailed rockslide inventory, Abele

(1974) highlighted the significance of tectonic activity as an important predisposing factor to understand the spatial distribution of the rockslides in European Alps. Indeed, the author pointed out the spatial correlation between thrust and large fault systems and the rockslide locational and also the important number of historical rockslide triggering by earthquakes. Forcella and Orombelli (1984) interpreted the DSGSD cluster in Upper Valtellina (Eastern-Central Alps) as the expression of active tectonic movements. However, recent study (Agliardi et al., 2001; Agliardi et al. 2009 a and b) based on detailed geomorphic mapping and numerical modelling, indicated as primary destabilization mechanism the slope debuttressing related to deglaciation. Besides, these authors suggested an important passive role of inherited tectonic structures in driving the movement and limiting the extent of large slope deformations (Agliardi et al., 2001).

In Eastern Swiss Alps, Persuad and Pfiffner (2004), based on morpho-structural mapping, uplift data and fission track ages, indicated that Central Alps are still deforming under active compression in response to on-going collision. Moreover, they suggested a direct influence of tectonic movements on slope deformations development (Persaud and Pfiffner 2004). At the opposite, recent studies performed in the same area by Korup and Schlunegger (2009) indicated that at least 25-40% of the Quaternary uplift can be theoretically accommodated by erosional unloading through river erosion and landsliding of weak rocks. Based on these findings, these authors suggested that in this area, active tectonic plays a minor role on surface processes development.

Several authors (Norton et al., 2010; Champagnac et al., 2007; Vernon et al., 2009) suggested that since Pliocene–Pleistocene rock exhumation and erosion rates of the entire Western Alps are related to isostatic compensation associated to an enhanced erosion or to the glacial rebound (Wittmann et al., 2007; Barletta et al., 2006) without considering the potential tectonic forcing. Inversely, Ustaszewski et al. (2008) through field observation and numerical modeling supported the idea of an important role of tectonic component on the formation of composite gravitational/tectonic faults frequently associated to large rock slope deformations. Besides, Jaboyedoff et al. (2003) identified a clear correlation between uplift gradient and earthquakes location proposing a tectonic origin of the measured uplift rates. The same authors identified also a correlation between historical rockslides and areas with the highest uplift gradient suggesting that new tectonic fracturing and/or movements along pre-existing faults represents potential sources of rock mass weakening and of slopes destabilization.

Hipployte et al. (2006) performed a detailed investigation based on field investigations and cosmogenic dating to determine the origin of recent fault scarp located in Belledonne Outer Crystalline Massif (Western Alps). They proposed a gravitational origin considering these faults to be the geomorphic expression of large DSGSD. Besides, based on geomorphic characteristics and on the location of the detected DSDGD close to faults, the authors suggested that early movements were activated by postglacial earthquake shakings (Hipployte et al., 2006). Recently, Sanchez et al. (2010), through detailed mapping and cosmogenic dating of postglacial large rock slope deformations in the Argentera massif (Western Alps), identified three periods of correlated tectonic and gravitational activity (11-12 Kyr, 7-9 kyr and a last group between 5.5-2.5 kyr). Based on these associations, these authors suggested a spatial and chronological correlation between the tectonic activity and the large rock slope deformations and proposed an active influence of tectonic movements on slope destabilization (Figure 2.1-6). Tectonic

movements was considered to be a potential "triggering" factor but also to control the overall rock mass strength reduction (Sanchez et al., 2010).

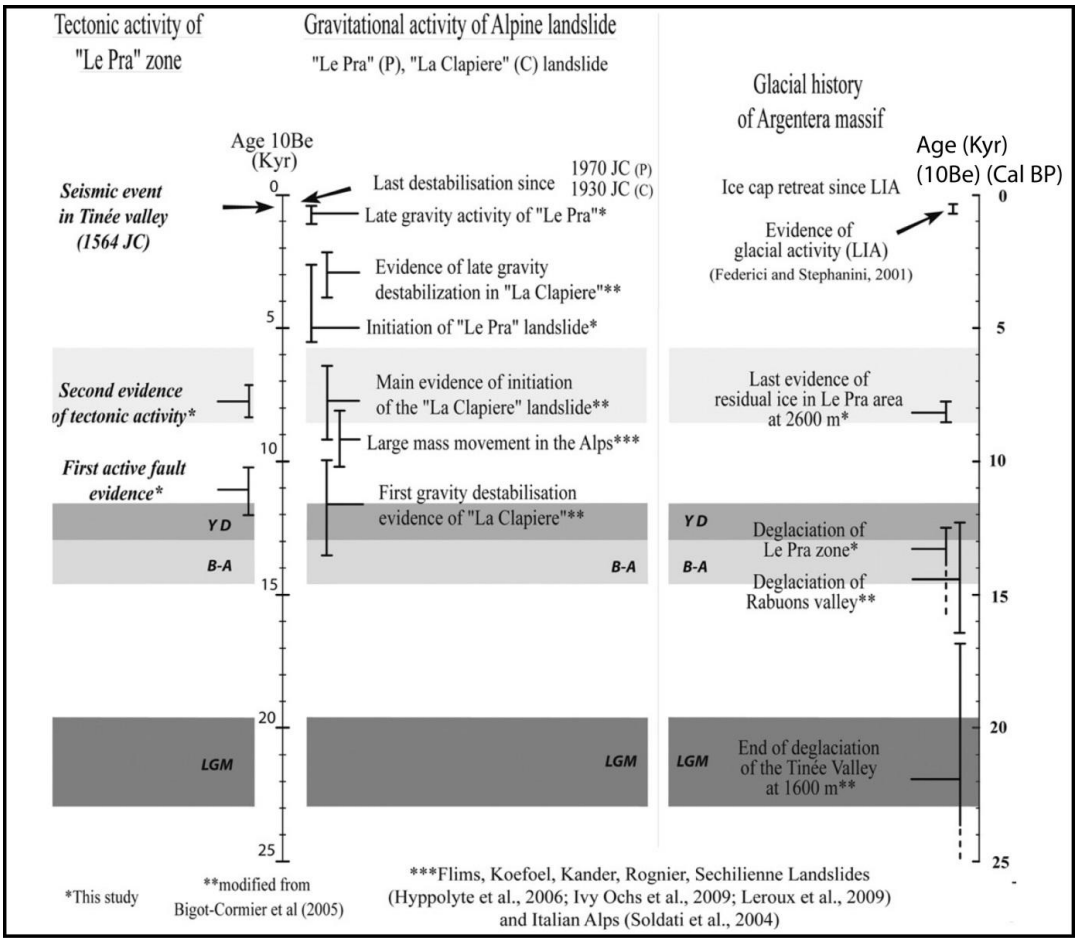

Figure 2.1-6: Comparison between tectonic events, landslide activity and de-glaciation history in the Argentera massif (Western Alps). Note the strong chronological correlation between active tectonic movements and large rock slope deformations (from Sanchez et al., 2010).

2.1.2 PASSIVE REACTIVATION OF TECTONIC STRUCTURES

2.1.2.1 Relations between inherited brittle tectonic structures and rock slope deformations

The geometric and the geomechanical characteristics of inherited brittle structures, in particular, persistent bedding planes (schistosity), faults, or regional joint set are frequently identified as one of the most important predisposing factors influencing the failure mechanism of slope instabilities at all spatial scale (Nemcok et al., 1972; Sauchyn et al., 1998; Agliardi et al., 2001; Sartori et al., 2003; Fasani et al., 2004; Ambrosi and Crosta 2006; Saintot et al., 2011; Bouissou et al., in press). Indeed, it is widely accepted that failure surfaces of rockslides or deep-seated slope deformations are fully or at least partially controlled by pre-existing tectonic fractures. Comparing different case studies, Brideau et al. (2009) highlighted the importance of tectonic structures, not only on the 3D geometry, but also for the reduction of rock mass strength caused by induced damage. At regional scale, joints/faults have a primary influence on the development, the localization and the geometry of large slope failures.

Ambrosi and Crosta (2006) highlighted the influence of large faults systems related to the Insubric line (Northern Italy) in controlling the DSGSD development. According to 3D numerical modelling results,

these authors suggested that regional faults system control the degree of fracturing, strength, and permeability of the rock mass masses. Low rock mass strength and persistent structures related to this fault system promote also the development of a quasi-continuous or continuous failure zone (Ambrosi and Crosta 2006). More recently, similar conclusion was proposed by Agliardi et al., (2009 a and b) based on the detailed analyses of the DSGSDs located in Upper Valtellina Valley (Northern Italy). In particular, numerical models performed by these authors indicated that where ubiquitous joint display a favourable geometric configuration to slope instability, only small internal deformations is necessary to create large gravitational slope deformations (Figure 2.1-7).

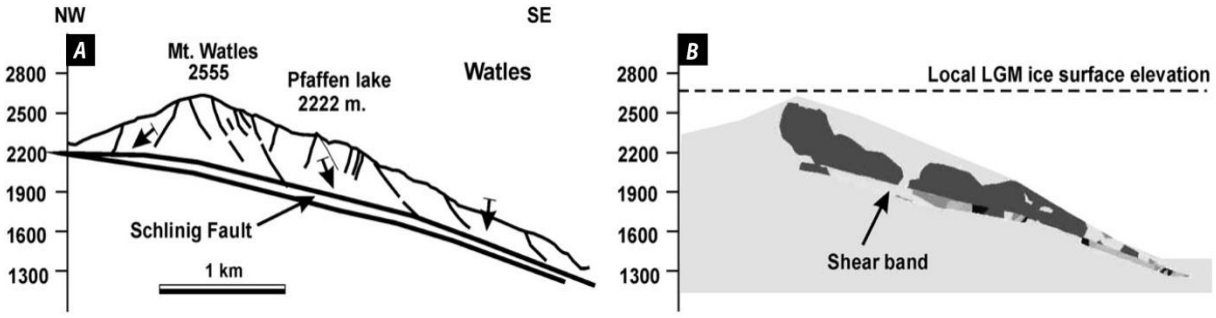

Figure 2.1-7: Comparison between the morpho-structural and the geomechanical model (finite difference model) for the Mt. Watles DSGSD (modified from Agliardi et al., 2009). It is interesting to note the fundamental role of the Schiling fault to drive and to confine the development of the DSGSD.

Jomard (2006) analysed the distribution and the characteristics of DSGSD in the Tinée Valley (Argentera Mercantour massif). According to geometrical model suggested by Bovis (1982) implying a selective reactivation of inherited regional scale tectonic structures, Jomard (2006) suggested that regional tectonic faults can be entirely reactivated (both at surface and in depth) to accommodate the development of large landslides and DSGSD. The consistency of the regional reactivation of pre-existing faults has been also tested through physical modelling by Bachmann et al. (2004, 2006) and Bois et al. (2008).

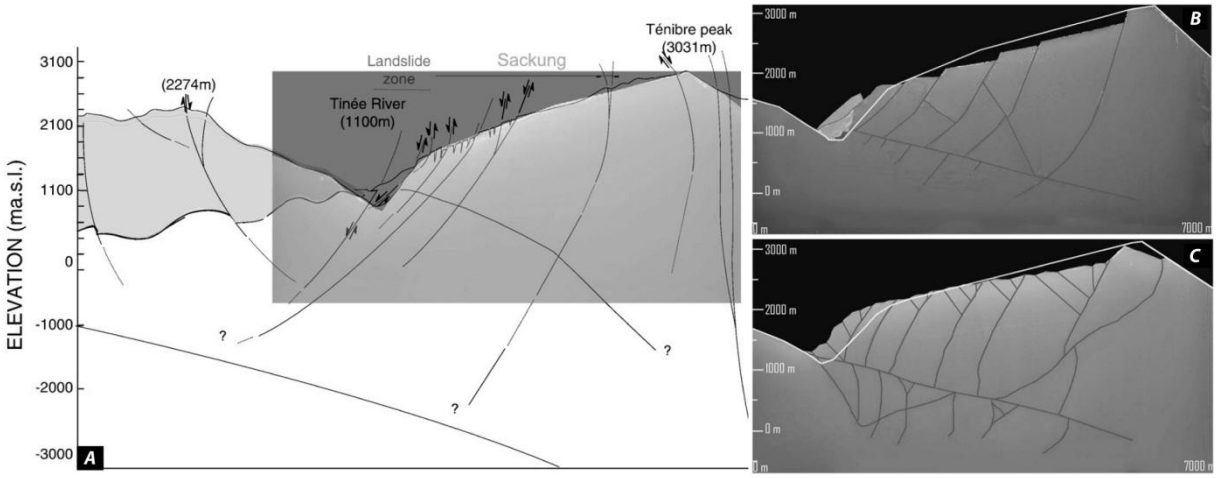

Figure 2.1-8: a) Geological cross-section of the Tinée Valley showing the potential reactivation of inherited tectonic structures by post-glacial gravitational or neotectonic movements (from Bois et al., 2008). b) Results of the physical model obtained by the integration of a series of six sub-vertical listric faults and thrust fault the bottom of the model. c) Same model but with listric faults with a deeper inflexion zone (from Bois et al., 2008).

Martinotti et al. (2011) analyzed the controlling factors the development of the DSGSD in the Aosta Valley (NW Italy) and stressed the important influence of pre-exiting tectonic structure both in term of active and passive role. Indeed, they proposed to classify the DSGSD according to five main controlling factors (Martinotti et al., 2011): deep dissolution (1), neotectonic movement (2), tectono-structural setting (3), plastic flow (4) and mix (5).

In Rocky Mountains (Canada), Jackson (2002) identified that rockslides and rock-avalanches cluster along major thrust faults in the eastern of Rocky Mountains. To explain this clusters, the author suggested a sapping processes associated to glacial deepening and the presence of rocks with different rock mass strength above and below the tectonic thrust. The same mechanism is also proposed to explain the general retreat of the Rocky Mountain front (Jackson 2002). At local scale, inherited tectonic structures such as faults or old shear bands have an important influence in the development of rock slide and rock avalanche. Sartori et al. (2003) analysed the structural setting of the Randa rockslide and they highlighted the main influence of a gently dipping fault located at the base of slope to the lower delimitation and the successive and progressive failure of the Randa rockslide.

Brideau et al. (2005), based on detailed estimation of the Geological Strength Index (Hoek and Brown, 1997) quantified the rock-mass damage related to the tectonic structures and his influence on the development of the Hope slide (British Columbia, Canada). In particular, they highlighted the presence of a shear zone on the north-western sides scarp and of persistent faults in the scarp area, which facilitated the lateral and the rear release of the rock slide (Figure 2.1-9).

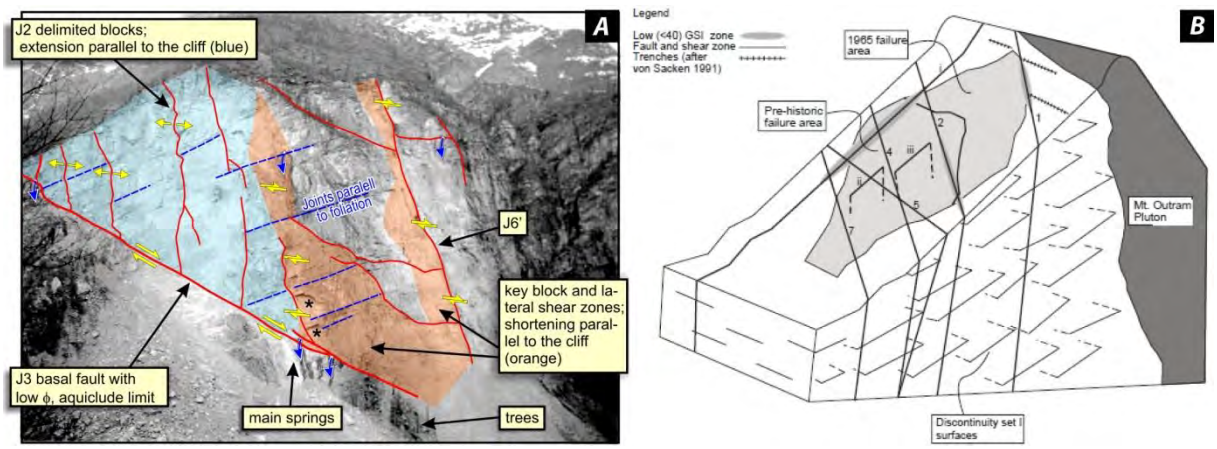

Figure 2.1-9: a) Picture of the lower portion of the Randa rockslide before the rockslide occurred the 18 April 1991, showing the control of the basal fault J3 on the groundwater and the kinematic conditions of the frontal unstable area (from Sartori et al., 2003). b) Schematic 3D cartoon emphasising the presence and the influence of tectonic structures at the Hope Slide (From Brideau et al., 2005).

The influence fold-related fractures on the rock slope instability development represent another important predisposing factor that is frequently observed, particularly in sedimentary, low metamorphic mountain belts. Several studies (Price and Carmichael, 1986; Cooper, 1992; Stearns, 1968; Ramsey and Huber, 1987) showed that different type of fractures can be related to the folding and thrusting. The development of fold-related fractures depends on rheological conditions during the folding phase such as strain rate and temperature (Price and Cosgrove, 1990). Few studies detailed the relation between these structures and the slope instability problems.

Badger (2002) based on field examples of slope instabilities in Washington State (USA) identified two main sets of fractures (one sub-parallel two the bedding and one perpendicular to the bedding planes) originated during the folding phase, which can create different typology of slope instabilities within the anticline slopes. Coe and Harp (2007) suggested an important influence of the folds geometry and fold-related fractures on the rockfall susceptibility in American Fort Canyon (USA). Through detailed analyses of rock mass conditions, these authors identified a variation of the rockfall susceptibility according to the relative position within the fold. Indeed, they suggested a relation between rockfall susceptibility and the geometric characteristics of the fold limbs (curvature and dip). They recognized also that hinge area have the highest rockfall susceptibility because of the increase of tensile tectonic fracturing (Coe and Harp 2007).

Jaboyedoff et al. (2009) in their reinterpretation of the failure mechanism of the Frank Slide highlighted the important role of fold-related fractures in the destabilization of the upper portion of Turtle Mountain (Jaboyedoff et al., 2009). In this area, the wedge J1^J3 that control the overall failure mechanism, is formed by the interaction between a regional scale fracture (J1) and shear fracture related to the formation of the Turtle mountain anticline (J3). Besides, the rear release fracture (J2) is probably associated to a tensile joint originated during the anticline formation. Recently, Humair et al. (2010) suggested a correlation between the rock mass quality and distance to the fold hinge, highlighting that fracturing associate to the folds does not influence the 3D kinematic release only but it has also an important effect on the variation of rock mass strength in Turtle Mountain.

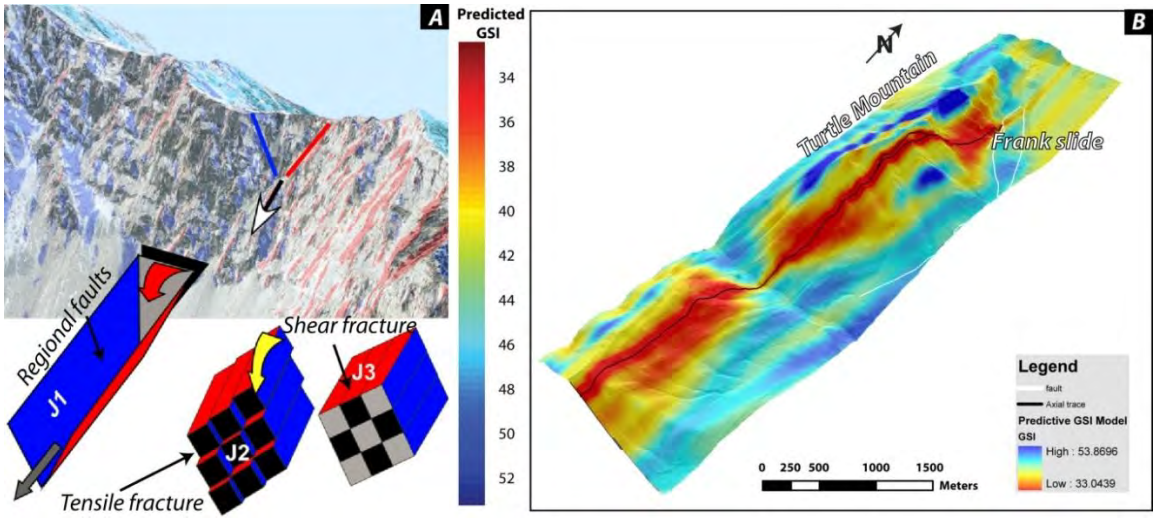

Figure 2.1-10: Influence of fold-related fractures on the development of the instability in Turtle Mountain. a) Failure mechanism interpretation of the upper portion of the Frank slide highlighting the import control of fold-related fractures (from Jaboyedoff et al., 2009) b) Predictive model of the GSI variation through Turtle mountain suggesting the important influence of the hinge area on the spatial distribution rock mass quality (from Humair et al., 2010).

2.1.2.2 Relations between inherited ductile tectonic structures and rock slope deformations

In the literature, few studies have explicitly focused on the influence of inherited tectonic ductile features (i.e. anticline syncline configurations, fold, interference between two distinct folding phases, etc.) in the development of rock slope instabilities. However, this inherited structural configuration can drastically influence the development of large rock slope deformations (Fasani et al., 2004; Scarascia Mungozza et al., 2006; Saintot et al., 2011). Ductile tectonic features can create weakness zones (Brideau et al., 2009), can

influence the shape and morphology of the failure surface (Braathen et al., 2004; Saintot et al., 2011; Oppikofer et al., 2011) or control the displacements observed at the surface (Jaboyedoff et al., 2011). Particularly, large scale antiforms, related to the presence of anticlines, have been identified to be areas where the development of DSGSD (Massironi et al., 2011) and rock avalanches (Scarascia Mungozza et al., 2006) is likely. Fasani et al. (2004) investigated the control of folds and faults on the stability of four rock slopes in the Apennine chain (Central Italy). Their investigation, combining field work and digital elevation models analyses, suggested the important control of folded or inclined bedding in providing continuous failure surface and of persistent joint sets facilitating the development lateral and rear release surface. Scarascia Mungozza et al. (2006) based on field investigations and numerical models analysed the failure mechanisms of the Lettopalena rock avalanches (Central Appenino, Italy). According to the convex dip-slope setting related to the Maiella anticline, they proposed a break-out failure mechanism developed along low angle shear surfaces cutting the bedding planes (Scarascia Mungozza et al., 2006).

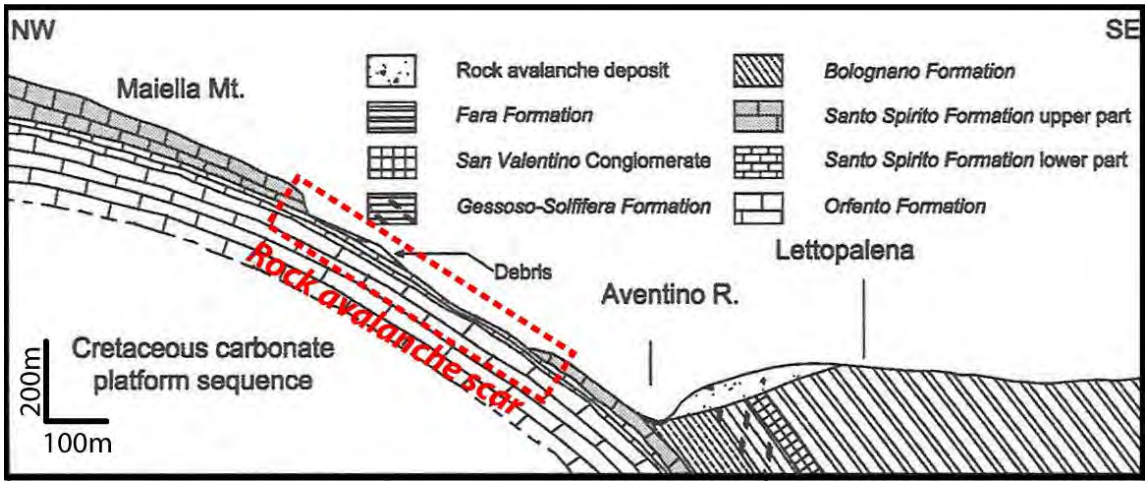

Figure 2.1-11: Geological cross-section showing the convex dips slope configuration the Maiella anticline associated to the Lettopalena rock avalanche (from Scarascia Mugnozza et al., 2006).

Massironi et al. (2010) analysed the geological condition leading to the formation of the Passo Vallaccia DSGSD (eastern Italian Alps). Based on detailed field mapping and distinct elements modelling, they identified a clear control of the Tux cylindrical antiform on the formation of the DSGSD and on the characteristics of the failures mechanisms affecting the different portions of the slope. According to the geometry of the Tux anticline, they subdivided the slope in the three sub-regions with specific deformations behaviours (Figure 2.1-12): (1) the uppermost portion of the slope, corresponding to the hinge of the antiform, is dominated by brittle failure along inherited joint sets, (2) the middle part where the deformation is concentrated along foliation and (3) the lower part, corresponding to the lower antiform flank, where a diffuse shear surface involves deformation of a large portion of the rock mass.

Outcrops-scale ductile structures such as folds or folds interferences have been identified by Saintot et al. (2011) to influence the failure mechanism of several potential rockslides in Norwegian Fjord (Western Norway). Through a detailed inventory, they identified that the interference of different Caledonian folding phases create preferential weakening zones and promoting the development of gravitational fractures (Saintot et al., 2011). This specific configuration was observed to constrain the stability of more than 25% of the potential rockslides.

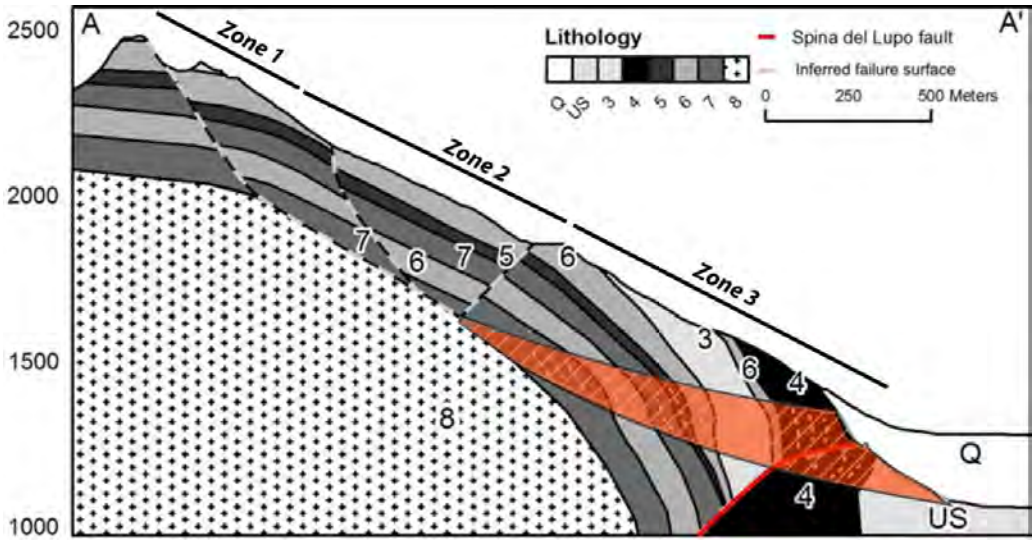

Figure 2.1-12: Cross-section of the Passo Vallaccia DSGSD (from Massironi et al., 2010). It is interesting to note the control of the Tux cylindrical antiform on the three sub-regions characterized by different deformations behaviour. The red area corresponds to the large shear zone where the lower displacements are concentrated.

Oppikofer et al. (2011) performed a detailed study of the failure surface geometry of both old and potential rockslides in fjord region of western Norway. They identified that failure surface of old rockslides display often a stepped basal sliding surface formed by dip slopes of the gneiss foliation linked together by steeply dipping fractures (Oppikofer et al., 2011). Interestingly, the step fractures occur in the hinge zones of the isoclinal folds, where tectonic shear strain is less intense than in the fold limbs. The authors also stressed that the fracturing of the fold hinge area is essential to create continuous sliding surface. In the same way, in their geometrical model of the Åknes rockslide, Jaboyedoff et al. (2011) highlighted that the large open folds and that small scale undulations of the foliation represent the main cause for different displacement patterns observed within the rockslide. They suggested also that slope deformations follow preferentially pre-existing structures (folds, joints and regional faults), but create also new extension fractures along the hinge of metric to decametric folds, defining the back-scarp of the Åknes rockslide (Jaboyedoff et al.,2011).

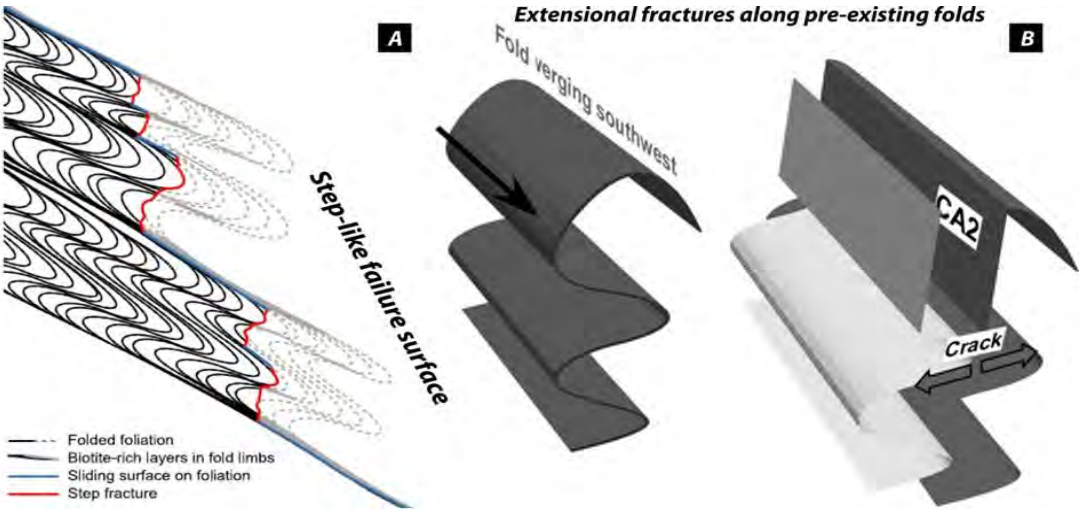

Figure 2.1-13: Influence of metric to hectometric scale folds on the development of rock slope instabilities. a) Stepped–like basal failure surface formed by foliation and tension fracture along developed along the fold hinge (from Oppikofer et al., 2011). b) Scheme of the formation of the back crack observed in the Åkens rockslide (Jaboyedoff et al., 2011).

2.2 STRUCTURES INDUCED BY SLOPE DEFORMATIONS

Stress field in slopes arises from a complex interplay of gravity, topography and geomechanical properties of the rock mass. In some conditions, stress within the slope can lead to the creation of structures comparable to those formed by geodynamic-related deformations (Jaboyedoff et al., 2011). To describe these phenomena, Jaboyedoff et al. (2011) introduce the term of "Slope Tectonics".

At the slope scale, structures induced by slope movements have been identified and described by different authors (Choffat 1929; Lugeon and Oulianoff 1922; Voight 1973; Hutchinson 1988). In particular, brittle structures such as scarp, counterscarps, trenches and doubles ridges have been identified to be the more evident superficial expression of the DSGSD (Radbruch-Hall, 1978; Savage and Varnes, 1987; Bovis 1982; Agliardi et al., 2001). Indeed, Agliardi et al. (2001) highlighted the importance of these structures on the recognition of slope affected by DSGSD. Ductile deformations, such as hectometric scale folds are also frequently observed (Zischinsky, 1969; Mahr and Nemcok, 1977; Zaruba and Mencl 1982).

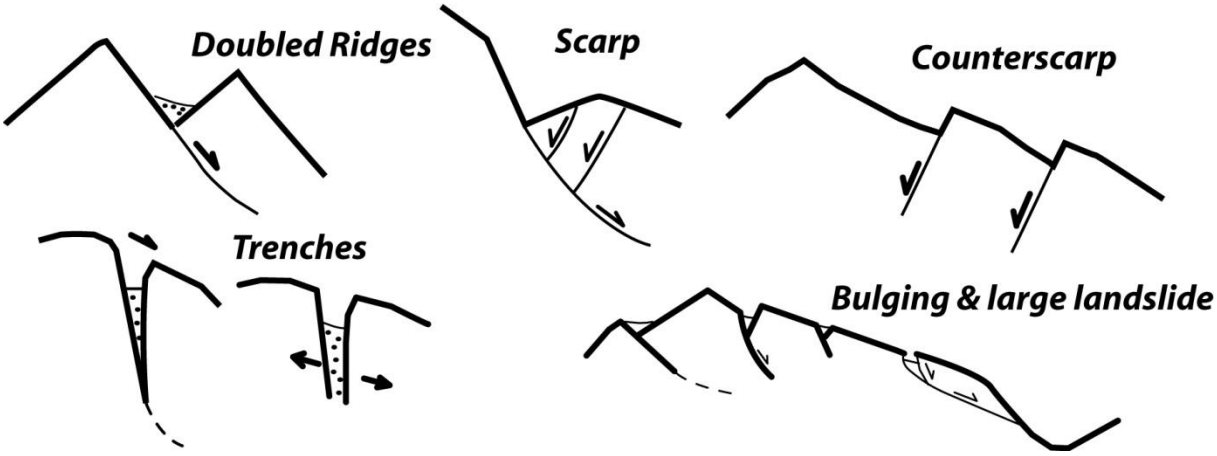

Figure 2.2-1: Large scale brittle slope–induced structures frequently associated to DSGSD (from Agliardi et al., 2001).

However, few studies have been carried out to describe the formative processes and the mesoscopic characteristics of both brittle and ductile slope-induced structures. The most detailed one was proposed by Chigira (1992). In his study, this author presented a detailed description of the mesoscopic and macroscopic characteristics of brittle and ductile slope-related structures associated to different structural and lithological settings.

According to Chigira (1992), at the outcrop scale, the characteristics of slope-induced folds are related to the lithology texture (foliated, massive), the spacing of the main foliation and the overburden depth. The main features can be summarized as follow (Figure 2.2-2):

- Principally flexural-slip folds displaying the presence of radial fracturing particularly developed close to the fold axis.
- Heavily broken and indented axial surfaces (strongly dependent on the overburden thickness and on the lithology type).
- Presence of void formed during folding (the lithostatic stress is not sufficient to close the void created during folding).

Chigira (1992) proposed also an interesting characterisation of brittle structures (faults and shear zone) associated to gravitational movements. In this case, faults characteristics are function of the lithology (massive foliated) and the main foliation attitude and could be summarized as follow (Figure 2.2-2):

- Shear zone characterized by the presence of both unconsolidated and coarse breccia-like material and a more consolidated fault gauge.
- Sharp boundary surface between the surface sliding block (unstable moving block) and the fault gauge.
- Irregular and progressive transition between the breccia-like zone and the underlying (stable) block.

At the slope scale, Chigira (1992) identified that the deformation mode and the morpho-structural features observed at the surface are mainly influenced by the foliation attitude. Based on the relation between foliation and slope attitude, the author proposed the distinction of the various structures induced by slope movements in four different configurations (Figure 2.2-3a). As suggested by different previous authors (Zischinsky, 1969; Radbruch-hall, 1978; Hutschinson 1988), these four configurations influence landscape morphology and the characteristics (shape location, amplitude) of the morpho-structures visible at the slope scale (Figure 2.2-3b). The structures and the morphological presented before are mainly associated to slow rock mass creep.

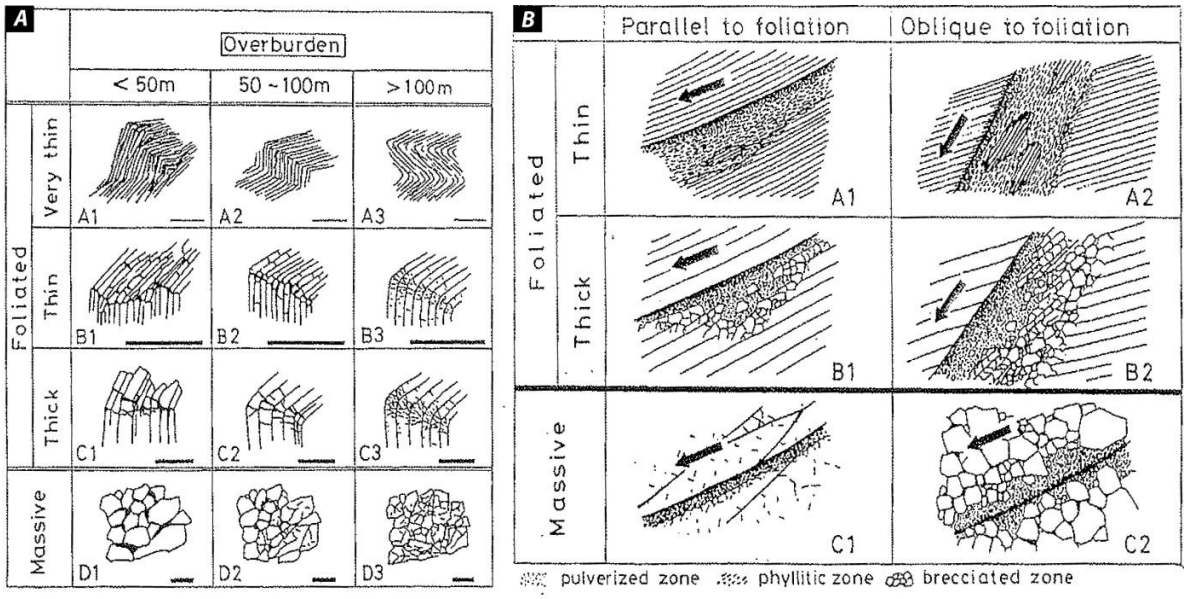

Figure 2.2-2: Characteristics of mesoscale ductile and brittle structures related to slope movements in foliated and massive rock masses (from Chigira 1992). a) Typical features of slope-induced folds as function of the foliation spacing, the overburden thickness and the rock mass typology (massive or foliated). b) Characteristics of faults related to slope movements according to the foliation attitude and rock mass typology.

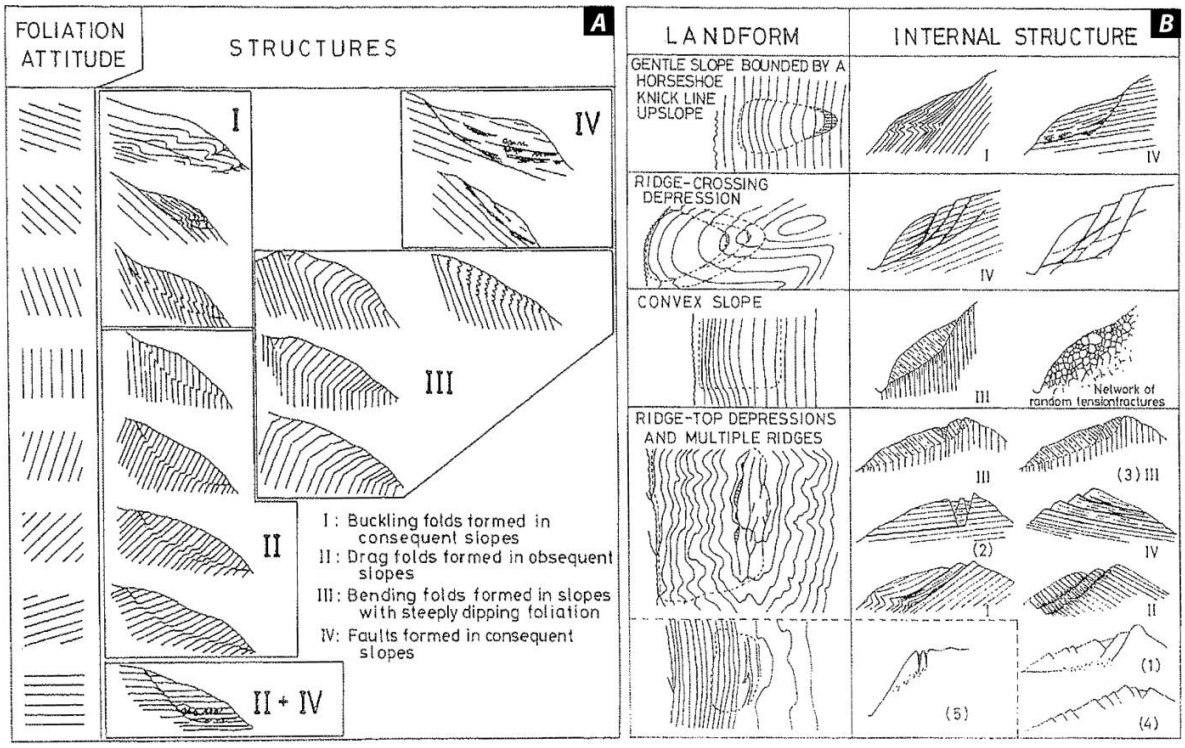

Figure 2.2-3: Macroscopic structures associated to gravitational movements and their influence on the landscape morphology (from Chigira 1992). a) Characteristics of the macroscopic gravitational structures according to the attitude of the main foliation. b) Influence on the landscape morphology of the relation between main foliation attitude and the slope topography.

2.2.1 STRUCTURES CREATED BY RAPID GRAVITATIONAL MOVEMENTS

However, gravity-induced structures can also be formed by rapid and catastrophic rock avalanches both on the failed mass and on the substratum. Heim (1932) already described in detail the structures (such as lobate fan and longitudinal ridges) characterizing the deposits of the Elm rock avalanche and highlighted their significance to understand the propagation mechanism. Choffat (1929) described the formation of folds and thrust within the alluvial sediments of the Rhone valley associated to the rockslide of 650'000 m^3 occurred in March 1929 on the Arvel quarry (Villeneuve, Switzerland). The author observed that the alluvial sediments are folded and thrust by the pushing action of the rock avalanche up to 340 m beyond the front of the rock slide apex. The alluvial deposits were up thrown 7 to 8 m above the pre-failure elevation. More recently, Blair and McPherson (1994) described the typical morphological features of some rock avalanche deposits emphasising the presence of lobate-shape fans and inverse grading.

They suggested that these two characteristics are related to the flow rheology (non-Newtonians fluid) and the presence of differential internal shearing within the rock mass leading to a differential fracturing. Strom (1996) presented a detailed review of the classification criteria and principle of data analysis of the morphology of the rock avalanche deposits. He highlighted that the structures visible on the top of the rock avalanche deposits can be used to identify the mechanical processes occurring during the deposition.

In order to provide a framework to field identification of rock avalanche, Hewitt (2002) described the influence of the local topographic setting on the surface morphology and on the internal structure of several rock avalanche deposits in Karakoram area (Pakistan). This author highlighted the significance of detailed recognition of rock avalanche deposits for the estimation future potential hazards.

Pollet (2004) analysed the granulometry and the depositional structures of three large rock avalanches in the European Alps (Madeleine, Flims and Köfels) that are characterized by a similar initial structural setting (dip-slope configuration). This author observed the presence of several deposits facies characterized by the local preservation of pre-existing structures and the development of faults, concentred shearing zones and metric scale folds (Figure 2.2-4). Based on these observations, Pollet and Schneider (2004) proposed a multi-slab shearing fragmentation model to explain the location of the observed structures and the possible transportation mechanism.

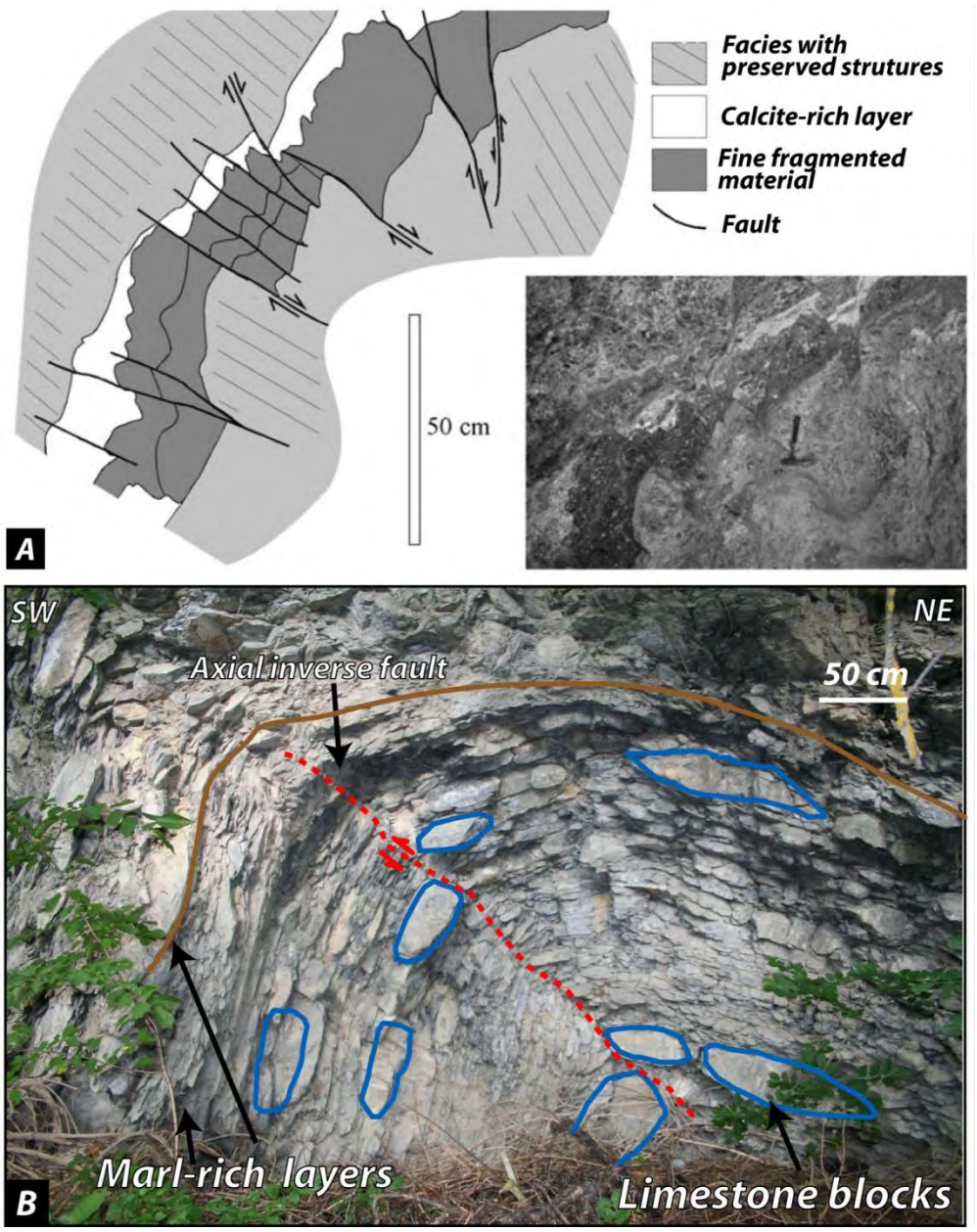

Figure 2.2-4: Examples of structures observed within the rock-avalanche deposit created during the transportation. a) Examples of mesoscale faults observed in the distal part of the Films rockslide deposits (from Pollet, 2004). b) Folds created on marly-limestone layers in the proximal part of the Sierre rock-avalanche deposit.

Shea and van Wyk de Vries (2008) presented a detailed characterization of the brittle structural features (faults, strike-slip faults and thrust) associated to 13 rock-avalanches in North and in South America. Through analogue modelling, they reproduced the brittle structures observed in the field suggesting an

important control of the substratum characteristics (topography, mechanical characteristics) and the friction coefficient of the sliding mass on the development of the different types of brittle structures. Besides, they proposed also a chronological sequence for the creation of the observed structures (Figure 2.2-5).

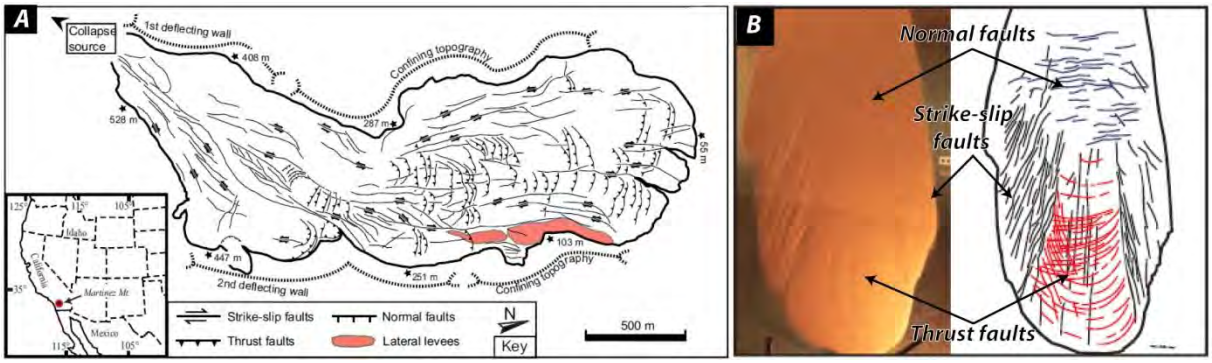

Figure 2.2-5: Example of brittle structures associated to rock-avalanches propagation (from Shea and van Wyk de Vries 2008). a) Map f brittle structures associated to the Martinez Mountain rock avalanche (California, Usa). b) Morphology and structures and associated to rock avalanche of the deposit obtained in a laboratory experiment.

Dufresne and Davies (2009) provided a comprehensive literature overview and a detailed description of the longitudinal ridges and the hummock morphology characterizing several rock avalanche deposits. They suggested that the creation of these structures represents an intrinsic characteristic of granular flows. According to the same authors, the development of longitudinal ridges is largely dependent on (1) the friction behaviour of the involved material, (2) the velocity, direction and geometry of the sliding mass and (3) on the substratum characteristics.

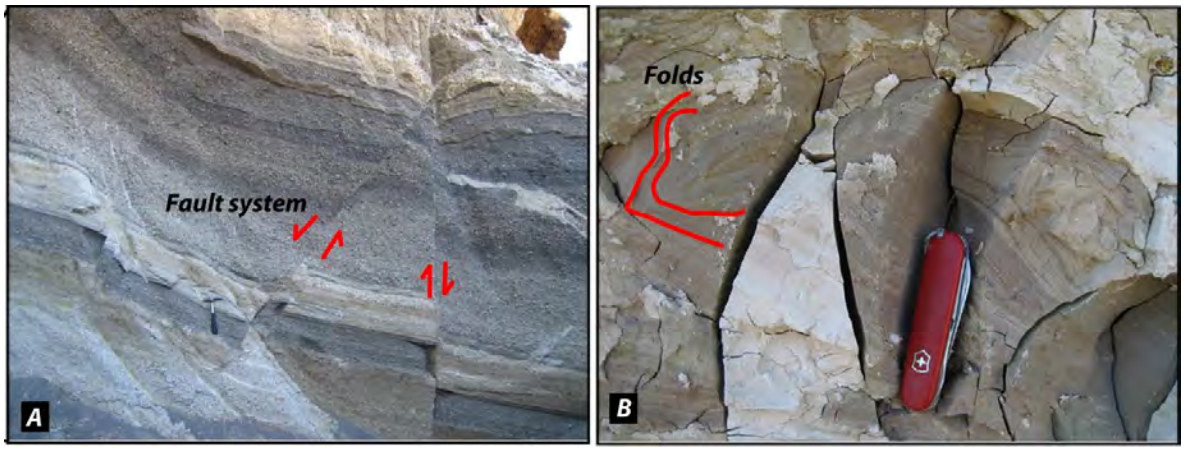

Figure 2.2-6: Examples structures formed within the deformed substratum associated to the debris avalanche of the Jocotitlán volcano (Mexico). a) Conjugate faults within the lacustrine deposits (from Dufresne et al., 2010). b) Complex folds identified within the fine-grained lacustrine deposits (from Dufresne et al., 2010).

Dufrense (2009) proposed also an interesting description of the structures and morphological features created by the interaction between rock avalanche material and the substratum (Figure 2.2-6). This author suggested that the morphological and structural features observed in the field are related to different possible interactions between the substratum and the rock avalanches. According to Dufresne

(2009) and Crosta et al. (2008), the interference between the substratum and the rock avalanche can be subdivided in five main categories:

- Entrainment (mixing between substratum and the rock avalanche body).
- Deformation (depending on the substratum characteristics it can supporting to the formation of folds, faults, shear zones).
- Bulldozing (creation of large scale folding and thrusting in the substratum and important influence on the rock-avalanche mobility).
- Striations and truncation of clasts (the presence of this phenomenon suggests a differential shear movement within the rock mass and the substratum).
- No interaction (frequently observed when the substratum is formed by hard bedrock).

2.3 LANDSLIDE INVENTORIES AS BASIC INFORMATION FOR QUANTITATIVE HAZARD ASSESSMENT AND LANDSCAPE EVOLUTION ANALYSES

Landslide inventories represent an essential source of information for hazard and risk assessment (Soeters and van Westen, 1996; Carrara 1999; Fabbri et al., 2003; Harp et al., 2011) but also for a quantitative analysis of the influence of landslides in landscape evolution (Simonett 1967; Hovius et al., 1997; Densmore et al., 1997; Korup 2005, Guthrie and Evans 2004). In the last decades, the development of the Geographic Information Systems (GIS) and the availability of high resolution digital elevation models (HRDEM) over large areas, allows rapid visualization and detailed characterization of landslides characteristics of a given region (Carrara et al., 1999; McKean and Roering 2004; Chigira et al., 2004; Roering et al., 2005; Van Den Eeckhaut et al., 2006). According to Malamud et al. (2004) landslide inventories can be subdivided in two classes:

- Landslide-event inventories associated with a clear and unique triggering factor (earthquake, rainfall, storm, etc.).
- Historical or geomorphological inventories, representing the sum of many landslide events occurred in a given period within the study area.

Landslide-event inventories can be considered as almost complete if the mapping started just after the triggering event (Malamud et al., 2004; Keefer 1994; Harp et al., 2011). Besides, geomorphological inventories that cover a long time period have a tendency to be incomplete, especially when they concern smaller landsides (Malamud et al., 2004; Van Den Eeckhaut et al., 2006). Depending on the goals and the extent of the area that need to be investigated, landslide inventories can be prepared by different techniques and different details (Soeters and van Westen, 1996; Guzzetti et al., 2005). According to Soeters and van Westen (1996) the following scales of analysis can be differentiated (Figure 2.3-1):

- Small-scale inventories or regional scale inventories (1:100'000 to 1:500'000) are compiled mostly from data obtained in the literature or through inquires to state organisations and private companies. Landslides are frequently represented as points without detailed information concerning their extent and their typology.
- Medium-scale landslide inventories (1:25'000 to 1:50'000) can be compiled through a systematic interpretation of aerial photographs, orthophotos and HRDEM. Local field checks and historical information are also performed (Guzzetti et al., 2005; Jaboyedoff et al., 2008). Landslides are represented by polygons and are classified based on their mechanism (Cruden and Varnes 1996) or based on their activity (Canuti et al., 2004). An attribute table containing generally geometrical and historical information is associated to the landslide map.
- Large-scale inventories (1:5'000 to 1:25'000) are often prepared for limited areas only, based on aerial photographs, orthophotos and HRDEM analyses accompanied by extensive field investigations. At this scale, landslides are frequently represented by precise polygon(s) delineating the different portion of the landslide body. A detailed database containing the geometrical information and available displacements data is often linked to inventories.

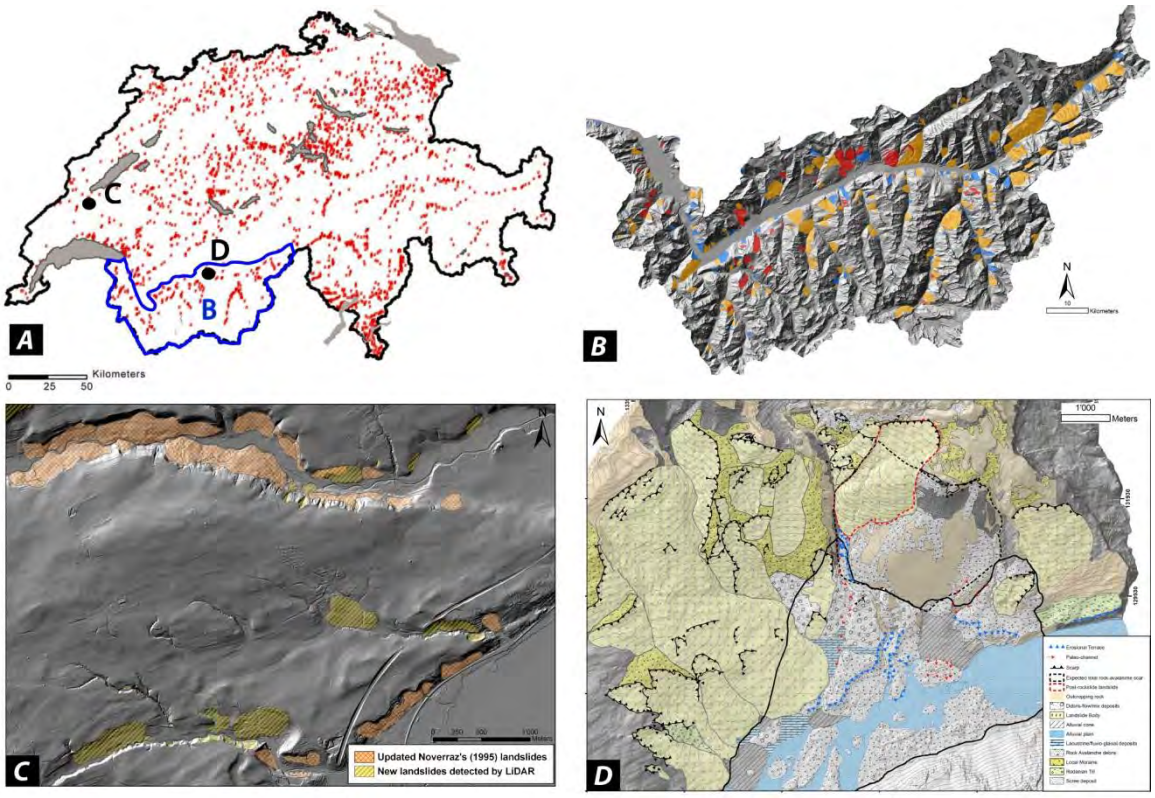

Figure 2.3-1: Examples of landslide maps based on different mapping support and performed at different spatial scale. a) National scale map of the landslides that caused financial damages between 1972 and 2002 obtained by compiling governmental and insurance data (from Schmidt 2004 in Lateltin et al., 2005). b) Regional–scale inventory of rock slope deformations in Rhone valley South-Western Alps based on LiDAR-DEM and orthophoto interpretation. c) Example of a medium-scale landslide map based on field and orthophotos analysis (orange polygons, Noverraz, 1995) and the successive update performed by LiDAR-DEM analysis (Jaboyedoff et al., 2008). d) Local scale map obtained by field survey and HRDEM analyses.

The primary factor defining the reliability of a landslide inventory is related to the availability of different sources of information (literatures data, previous inventory, etc.) and high quality mapping support (topographic maps, orthophotos and high resolution digital elevation model). This point was clearly highlighted by Ardizzone et al. (2007). These authors, emphasized the discrepancy between the two inventories approaches, by comparing the landslides size and distribution based by field mapping and HRDEM interpretation after an important rainfall event in the Collazzone area (central Umbria). They showed that the inventory obtained by HRDEM analysis shows 27% more landslides and 39% less total landslide area, leading to a smaller average landslide size (Ardizzone et al., 2007). All landslide inventory maps, compiled through the interpretation of orthophotos and HRDEM derived maps (shaded relief, slope and azimuth maps) introduce anyway an important part of the subjectivity related to the experience of the interpreter in charge of the inventory. According to Soeters and van Westen (1996) and Guzzetti (2005) the general factors influencing the quality of the landslide inventory can regroup in six main groups:

- Landslide freshness and age (characteristic morphological evidences).
- Persistence of landslide morphology within the landscape (possibility to distinguish the landslide in the morphology).
- Morphological and geological complexity of the study area.
- Degree of experience of the interpreter in charge of the inventory.

- Land use types and surface alterations.
- The type and quality of the mapping supports and the final scale of the map.

The information derived by landslide inventories can be directly analysed using GIS to obtain landslide density maps (Valadão et al., 2002), to compare inventory maps with the same area using different methods (Guzzetti et al., 2000; Galli et al., 2008) and to dispose an overall overview of the relation between landslide distribution and geological and climatic factors (Soeters and van Westen 1996; Grelle et al., 2011; Chau et al., 2004). Moreover, landslide inventories represent the basic information to validate the susceptibility and hazard maps obtained by statistical approaches such as bivariate (Süzen and Doyuran 2004) and multivariate (Carrara et al., 1991) or neural network approaches (Melchiorre et al., 2008).

2.3.1 STATISTICAL PROPRIETIES OF LANDSLIDE INVENTORIES

Geometrical information, such as landslide area or volume that can be extracted from the landslide inventory, can be used to obtain quantitative probabilistic information about the size, frequency and potential spatial distribution future landslide (Guzzetti et al., 2005). Beside, at the catchment or at the mountain range scale, size frequency distribution and volume estimation are of primarily importance to estimate the contribution of landslides to the erosion and the sediment yield (Hovius et al., 1997). In the following sub-chapter, an overview of the most important formulations commonly used to statistically describe the landslide inventories will be proposed.

2.3.1.1 Landslide frequency-area distribution

In the last decades, several studies have been performed to characterize the frequency area distribution of both historical and landslide-event inventories in different geological environment (Simonett 1967; Guthrie and Evans, 2004; Chaytor et al., 2009; Van den Eeckhaut et al., 2007; Korup 2005; ten Brink et al., 2006; Guzzetti et al 2002; Antinao and Gosse 2009; Dussages-Pessier et al., 2003). For most of these, the magnitude–frequency distribution of medium large landslides follows a negative power-law relation. Area-frequency distribution of landslides could be represented in a cumulative way based on the following equation:

$$N_{CL} = cA_L^{-\beta} \qquad \text{Eq. 2.3-1}$$

Where (N_{CL}) is cumulative number of landslide, (A_L) the landslide area with (c) and (β) as constant parameters. However, Stark and Hovius (2001) and successively Guzzetti (2005) highlighted that this data representation is not suitable because the residual in the estimates of cumulative probability are strictly one-sided and asymmetrically distributed biasing any regression fit which assumes normally distributed errors. Moreover, the same authors highlighted that any cross-over from a non-power law to a power law is obscured through the integration smoothing. For these reasons, Stark and Hovius (2001) proposed to represent the landslide frequency distribution in a non-cumulative form:

$$\frac{dN_{CL}}{dA_L} = c' A_L^{-\alpha} \qquad \text{Eq. 2.3-2}$$

Where (N_{CL}) is the non-cumulative number of landslides and (c') and (α) are constant values.

$$N_{CL} = c' A_L^{-(\alpha-1)} \qquad \text{Eq. 2.3-3}$$

Van den Eeckhaut et al. (2007), through a detailed literature overview, showed that for both historical and event-triggered inventories the mean power-law exponent α, expressed in non-cumulative distribution, is 2.3 with a standard deviation of ±0.6 (Van den Eeckhaut et al., 2007).

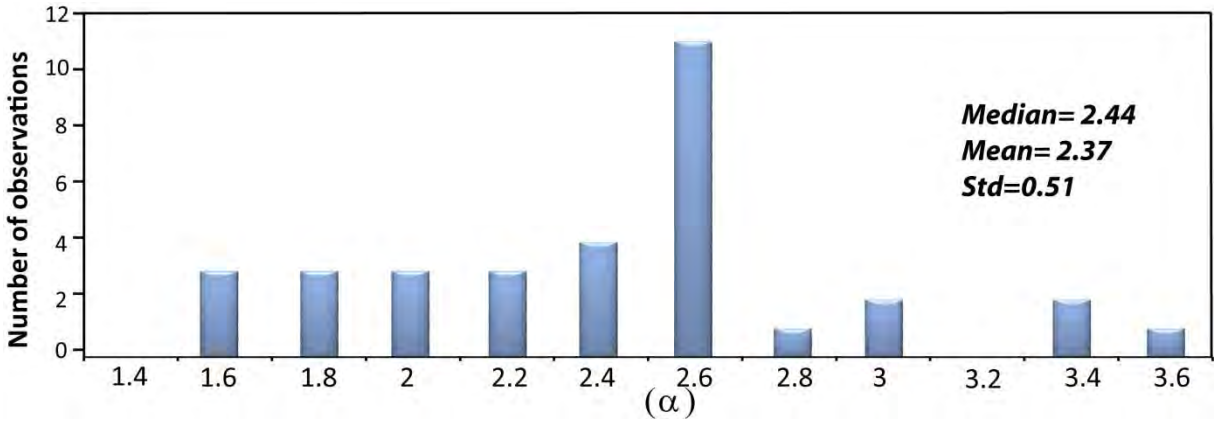

Figure 2.3-2: Histogram of power-law exponents used in the literature to fit the frequency density distribution of landslide inventories (data from Van den Eeckhaut al., 2007; Chaytor et al., 2007; Antinao and Gosse 2009).

A smaller exponent α indicates an important contribution of larger landslide surfaces in the total distribution, inversely, larger exponent suggest more spread distribution and a minor influence of exceptional landslide. Interestingly, the exponent α seems not be affected by the considered range area suggesting that power-law relationship present scale-invariant properties.

According to Guzzetti (2005), the important scatter on α exponent can be related to the natural variability associated to different morphological and lithological conditions but is also unfortunately related to the different methods adopted to obtain the frequency distributions.

Another particular characteristic of magnitude-frequency distribution of landslide inventories is the presence of a "rollover" that corresponds to the point where smaller landslides deviate from power law fitting. Several authors suggested that this singularity is related to an underestimation and the under-sampling of small landslides areas within the landslide inventory (Hungr et al., 1999; Stark and Hovius, 2001; Dussagues et al., 2003). Inversely, others researches (Guthrie and Evans, 2004; Guzzetti et al., 2002; Malamud et al., 2004) suggested that, for complete inventories, the presence of a rollover in not related to an inventory bias but it has a physical meaning. Guzzetti et al. (2002) proposed that the rollover corresponds to the transition between failure mechanisms controlled by friction (larger landslide) and by cohesion (smaller landslides). Besides, based on laboratory experiments, Katz and Aharonov (2006) suggested that the rollover corresponds to the transition between the shallow slumps occurring in unconsolidated and homogeneous materials and larger landslides controlled by local heterogeneities. These authors indicated also that the presence of internal heterogeneities within the rock mass (i.e. joints or shear zones) is the primary cause of the power-law decay observed for larger landslides (Katz and Aharonov 2006).

Stark and Hovius (2001) pointed out that the power-law fit describes the 25% of the entire dataset only highlighting the inadequacy of a pure power-law model for a complete description of the inventory dataset. In order to provide a complete description of the area-frequency distribution (the power-law tail and the rollover), Stark and Hovius (2001) proposed the application of a Double Pareto distribution. In the same way, Guthrie and Evans (2004) analysed the landslide distribution on the Vancouver Island (Canada). They found that frequency distribution of larger landslide can be fitted by a classical power-law distribution (α = 1.55 for cumulative distribution) and that the entire database follow a Double Pareto distribution. Malamud et al. (2004a, b) investigated the frequency-area distribution of three landslide-event inventories (Landslide triggered by the Northridge earthquake, Landslide triggered by snowmelt in Umbria and landslides triggered by rainfall Guatemala) which can be considered to be almost complete. They suggested that the three landslide inventories are well approximated by a three-parameter inverse gamma distribution (Malamud et al., 2004a):

$$p(A_L;\rho,a,s)=\frac{1}{a\Gamma(\rho)}\left[\frac{a}{A_L-s}\right]^{\rho+1}\exp\left[-\frac{a}{A_L-s}\right] \qquad \text{Eq. 2.3-4}$$

Where (A_L) is the landslide area, (ρ) is the parameter controlling the power-law decay for medium to large landslides, (a) is the parameter controlling the location of the maximum probability distribution and (s) is the parameter controlling the rollover for small landslide areas. Based on this landslide probability distribution, the authors proposed the introduction of the landslide-event magnitude scale:

$$m_L = log_{10}\, N_{LT} \qquad \text{Eq. 2.3-5}$$

Where (m_L) is the landslide magnitude and N_{LT} is the total number of landslide within the inventory.
This relation is very useful because it allow estimating the total numbers, area and volume for incomplete historical and landslide-event inventories. Practical applications of this equation was proposed by Van den Eeckhaut et al. (2007) to estimate the total number of landslides and their affected area occurred in Flemish Ardennes (Belgium) and by Antinao and Gosse (2009) to calculate the total volumes of the rockslides in Chilean Andes.
Compared to the landslide inventory presented before, frequency–size distribution obtained for rockfall inventories differs considerably. Dussagues-Pessier et al. (2003) analysed the cumulative frequency distribution of rockfall volume for cliffs in the Grenoble area (Western France), the Yosemite Valley (Usa) and worldwide. They obtained a power-law exponent of 0.45 ± 0.2 (corresponding to 1.4 ±-0.2 for non-cumulative distribution). Oppikofer (2009), using detailed geometrical reconstruction based on HRDEM, analysed the rockslide scar volumes in Tafjord area (Western Norway). The obtained cumulative distribution was fitted by two power-law distribution (0.67 for volumes >1Mm^3 and 0.1 for smaller ones). The author interpreted the low power law exponent for smaller rockslides to be potentially related to a sampling bias or to the possibility that the observed larger rockslide scars occurred in several smaller events which would considerably increase the frequency of smaller rockslides (Oppikofer 2009).

According to Malamud et al. (2004a), the important differences in the power-law exponent between rockfalls and landslides inventories, reveals of a different physical control of the two phenomena. Rockfalls are principally controlled by fragmentation processes. Inversely, others landslide typologies are principally dependent on the geomechanical parameters defining the stability of the slope (Malamud et al. 2004).

Volume-frequency distribution of submarine landslides have also been investigated by several authors (Issler, et al., 2005; ten Brink et al., 2006; Chaytor et al., 2009) especially in relation to tsunami hazard. ten Brink et al. (2006) presented a detailed characterization of the volume of failed slopes along the north shore of Puerto Rico. They determined that cumulative volume distribution of submarine slope failures follow a power-law relation with a power-law exponent of 0.64 similar to what observed for terrestrial rockfall. Differently, Issler et al. (2005) and Chaytor et al. (2009) in analysing the rockslide scars along the northern Atlantic margins observed that the cumulative volume distribution of the failure scars is better described by a log–normal distribution.

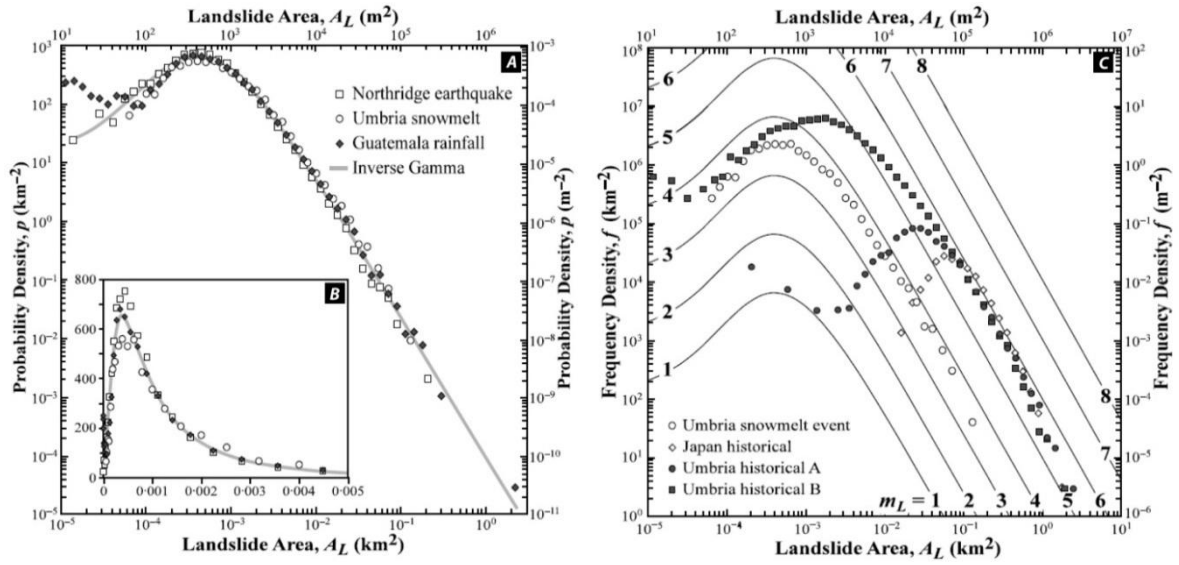

Figure 2.3-3: a) Landslide probability density (on logarithmic axes), as a function of landslide area (A_L), for three "complete" landslide inventories (from Malamud et al., 2004a). b) Same probability density given on linear axes. The grey line corresponds to the inverse-gamma distribution fitting. c) Landslide frequency density (on logarithmic axes), as a function of landslide area (A_L), of historical (Japan, Umbria A and B datasets) and event-triggered (Umbria snow melt) inventories compared to the theoretical landslide probability distribution (landslide magnitude scale) proposed by Malamud et al. (2004a).

2.3.1.2 Landslide area-volume dependency

Determination of landslide volume estimation is important for a correct determination of landslide hazard and to evaluate the long-term evolution of landscapes dominated by mass-wasting processes. Volume estimation is a difficult task requiring information concerning the sub-surface characteristics of the landslide and in particular the detailed location of the depth and the shape of the failure surface. At regional scale, information concerning the subsurface characteristics of landslides is frequently inexistent and consequently not reported in the landslide inventories.

However, field observations suggested by different authors, indicate that for landslide inventories characterized by different sizes and triggered by different mechanisms, the landslide area is commonly linked to landslide volume with the following power-law relation:

$$V = \varepsilon A_L^{\delta} \qquad \text{Eq. 2.3-6}$$

Where (V) is the landslide volume, (A_L) the landslide area (m^2) and ε, δ are constant. Literature is rich of several empirical relationship characterized by their own constant (Simonett 1967; Hovius et al., 1997; Korup 2006; ten Brink et al., 2006, a.o.). Guzzetti et al. (2009) proposed a detailed literature review where they summarized the main representative landslide inventories where ε and δ values was estimated. The same authors, based on 677 landslides (slide type following the Cruden and Varnes, 1996) found a power-law exponent (δ) of 1.45. Korup (2006) based on landslide in New-Zeeland Alps and on literature overview suggested that ε values varies between 0.01 and 0.05 and δ values range between 1.3 and 2.5. Figure 2.3-4 presents the histogram of (δ) values adopted in different landslide inventories in widely diverse location and characterized by different slope failure processes. Based on these data, a mean δ value of 1.41 ± 0.39 is calculated. The similarity between the power-law exponent obtained for inventories of different landslide sizes indicated that the volume-area relationship can be considered scale independent (Figure 2.3-4). However, as suggested by Korup (2006), it is important to remember that power-law relation can be also biased by the common way to calculate the landslide volume based on the multiplication of the landslide area with a mean thickness.

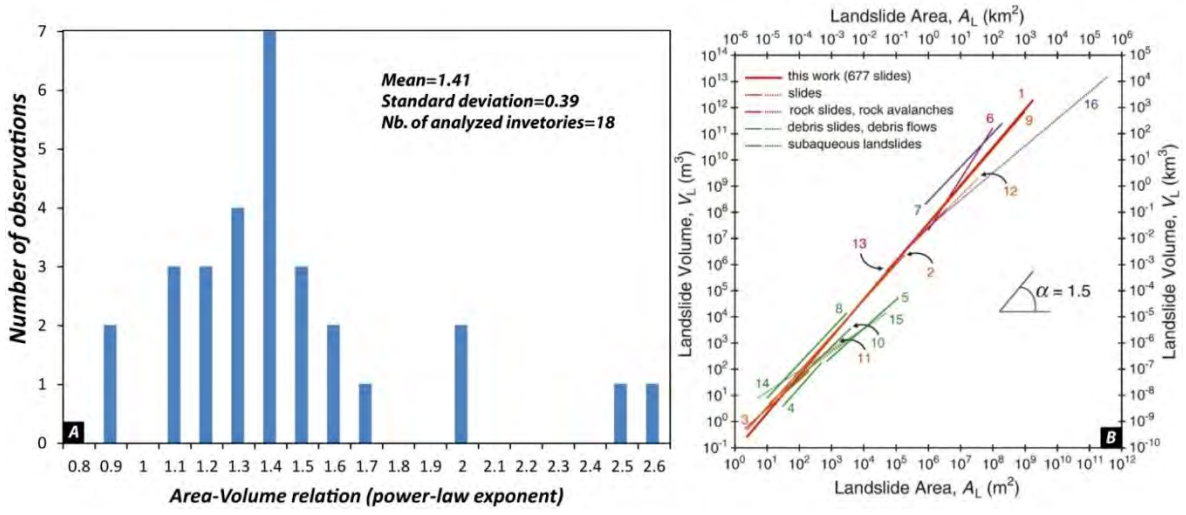

Figure 2.3-4: a) Histogram of empirical power-law exponent proposed in the literature to link the area-volume relation (data based on Guzzetti et al., 2009, Korup 2005 and ten Brink et al., 2006) b) Empirical relationship proposed in the literature to link landslide area A_L to landslide volume V_L (from Guzzetti et al., 2009). Note the similarity, in term of power-law parameters, between landslides of different sizes and origins.

The physical meaning of the area-volume dependency is still poorly understood and almost no detailed studies can be found on this topic. As suggested Guzzetti et al. (2009), the relationship between the volume and the area of landslides of the slide type is essentially geometrical and independent of the geological characteristics of the slope or of the triggering mechanism. A first step in the understanding of the volume-area dependency has been recently proposed by Klar et al. (2011). Based on limit equilibrium

methods, these authors obtained analytical relation between the volume and the surface area of a landslide that agree well with the empirical relations obtained from the field observations. Based on their numerical analyses, they highlighted the insensitivity of the power-law exponent (δ) to the specific mechanical properties of the slope that explain why landslide inventories, developed in different environments, follow the same power-law relation (Klar et al., 2011). Indeed, they suggested that the landslide geometry is not self-similar (landslides tend to be shallower with the increase of the slope and the landslips area) but follows a self-affine behaviour. This means that landslide length and thickness increase simultaneously with the landslide size but following different scaling factors.

2.3.1.3 Landslides and erosion rate

Compared to other geomorphic agents such as river or glacier, the erosion rate related to landslides is more difficult to estimate due to their inhomogeneous distribution and to the irregular occurrence (Burbank and Anderson 2001). Cullman (1875) proposed a first simple approach to estimate the maximal hillslope high (drained conditions):

$$H_c = \frac{4csin\beta cos\varphi}{\gamma_r[1-cos(\beta-\phi)]} \qquad \text{Eq. 2.3-7}$$

Where (c), (β), (φ) are respectively the cohesion, the slope angle and the friction angle and γ_r is the unit weigh of the rock. This formulation provided useful information concerning the maximal slope height that can be encountered in the landscape. However, based on this simple limit equilibrium equation it is not possible to predict directly the denudation rate because no time dependence is present in the formulation. However, based on this equation, Korup and Schlunegger (2007) evaluated the influence of bedrock landsliding in the creation of the Inner gorges. To estimate the theoretical time required for a gorge wall to fail, Korup and Schlunegger (2007) coupled the static equation proposed by Cullmann (1875) to a time-dependent equation describing the progressive loss of cohesion through weathering (Figure 2.3-5):

$$H_c(t) = \frac{2c_0 e^{-\lambda t}}{\gamma_r[cos\beta(sin\beta-cos\beta tan\phi)]} \qquad \text{Eq. 2.3-8}$$

Where (λ) is the mean weathering rate and c_0 is the initial rock cohesion.

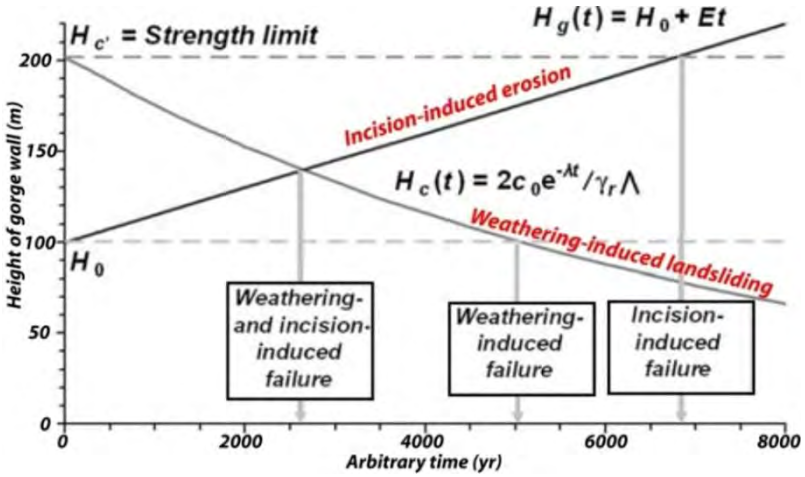

Figure 2.3-5: Schematic competition between weathering-driven rock slope failure and incision-driven failure proposed by Korup and Schlunegger (2007) to explain the possible mechanisms influencing the development of Inner gorges.

With the increase of the availability of detailed landslide inventories a spatial approach to quantify the denudation rate has been developed. This approach is essentially based on the relationship linking landslide size to landslide frequency. A first regional scale study applying this relation has been proposed by Hovius et al. (1997). These authors analysed the impact of landslides in the 13 catchments draining the western side of Southern Alps (New Zealand). In order to estimate the landslide volume, these authors proposed a linear scaling relation between landslide width and landslide thickness (Hovius et al., 1997):

$$t(l) = \varepsilon l \qquad \text{Eq. 2.3-9}$$

Where (*t)* is the landslide thickness, (ε) is a constant scaling factor (0.05±0.02) and (*l)* is the landslide width. Based on this information and according to power–law distribution describing the landslide frequency distribution, the volume for a given landslide can be estimated as (Hovius et al. 1997):

$$v(l) = n(l)A(l)t(l) = \varepsilon l^3 n(l) \qquad \text{Eq. 2.3-10}$$

Where *n (l)* is the number of landslides of length (*l)* derived from the cumulative frequency distribution. The total landslide volumes related to the obtained frequency density distribution is achieved by solving the integral bounded by the minimal and the maximal landslides width defined within the study area (Hovius et al., 1997):

$$V = 2\beta\varepsilon\kappa \int_{L0}^{L1} l^{2-2\beta}\, dl \qquad \textit{Eq. 2.3-11}$$

Where (κ) is the rate of landsliding per unit area per year and β is the exponent of the power-law fitting. (L_1) and (L_0) are respectively the maximal minimal width considered in the inventory. Assuming that the erosion rate is dominated by larger landslide events, (implying $\beta<1.5$ and $L_1>>L_0$) the total landslide volumes could be approximated by (Hovius et al., 1997):

$$V \approx \frac{2\beta\varepsilon\kappa}{(3-2\beta)} {L_1}^{3-2\beta} \qquad \text{Eq. 2.3-12}$$

The landslide discharge volumes obtained for the different catchments of the Western side of Southern Alps ranges between $1x10^6$ and $2x10^6$ m^3/yr corresponding to a denudation rate of 9 mm ±4 mm/yr (Hovius et al., 1997). Malamud et al. (2004a, b) proposed another approach to calculate the total landslide volume and the associated erosion of landslide inventories. Based on inverse-gamma distribution describing the landslide frequency distribution, Malamud et al. (2004a, b) derived the equation to quantify the total landslide volume (V_{LT}) associated with a landslide inventory. According to the empirical scaling relationship between area and volumes proposed by Hovius et al. (1997), the total landslide volumes can be expressed as (Malamud et al. 2004b):

$$V_{LT} = \frac{N_{LT}\varepsilon a^{\rho}}{\Gamma(\rho)} \int_{Amin}^{Amax} A_L^{\delta-\rho-1} exp\left(-\frac{a}{A_L}\right) dA_L \qquad \text{Eq. 2.3-13}$$

Besides, the erosion rate (E_r) of the analyzed inventory is given by:

$$E_r = \frac{V_{LT}}{A_r t_L} \qquad \text{Eq. 2.3-14}$$

where (A_r) is the reference areas where landslides are concentrated and (t_L) is the time interval over which the landslide accumulated.

Malamud et al. (2004b) proposed also a relation to estimate the volume of landslide associated to an earthquake event. According to these authors, if $\dot{N_{CE}}$ is the cumulative number of earthquakes with a moment magnitude greater or equal to M in a given region and time, the Gutenberg–Richter relation can be written as (Malamud et al., 2004b):

$$log\dot{N}_{CE} = -bM + log\dot{a} \qquad \text{Eq. 2.3-15}$$

where b is a constant value specific for a given region and $\dot{a}$ represents the regional level of seismicity and the size of the considered area.

This relation can be successively combined with the empirical relation between the total landslide volume and the earthquake's moment magnitude (Keefer 1994) to obtain the total volumetric rate of the landslides associated to earthquakes (Malamud et al., 2004b):

$$\dot{V_L} = \frac{10^{-11.26\pm0.52}(ln10)b\dot{a}}{1.42-b}\int_{M_{min}}^{M_{max}} 10^{(1.42-b)M}dM \qquad \textit{Eq. 2.3-16}$$

Another approach applied in rockfall inventories was proposed by Hantz et al. (2002, 2003). Based on detailed rockfall inventories in Grenoble area (Eastern France), they showed that the cumulated distribution of rock fall volumes follows a power-law in a volume range covering at least 4 orders of magnitude (Hantz et al., 2002):

$$n(V) = aV^{-b} \qquad \text{Eq. 2.3-17}$$

where n(V) is the mean number of rockslides with a volume greater than (V), which occurred in a given time period, (a) is a positive constant corresponding to the frequency of rockslides with volumes greater than 1 m^3 and (b) is a positive constant characterizing the frequency magnitude.

The total volume of the rockslide inventory (V_{tot}) and its influence on the valley infilling can then be estimated by integrating the following relationship:

$$V_{tot} = \int_{Vmax}^{Vmin} Vdn = \frac{ab}{(1-b)}(V_{max}^{1-b} - V_{min}^{1-b}) \qquad \text{Eq. 2.3-18}$$

where (V_{max}) and (V_{min}) are respectively the maximal expected volume and the minimal volume detected in the inventory. Assuming that the power-law distribution is valid for the whole range of possible volumes, the total rockfall volume for a given time period is:

$$V_{tot} = \int_0^{\infty} Vdn = \frac{ab}{(1-b)}(V_{max}^{1-b}) \qquad \text{Eq. 2.3-19}$$

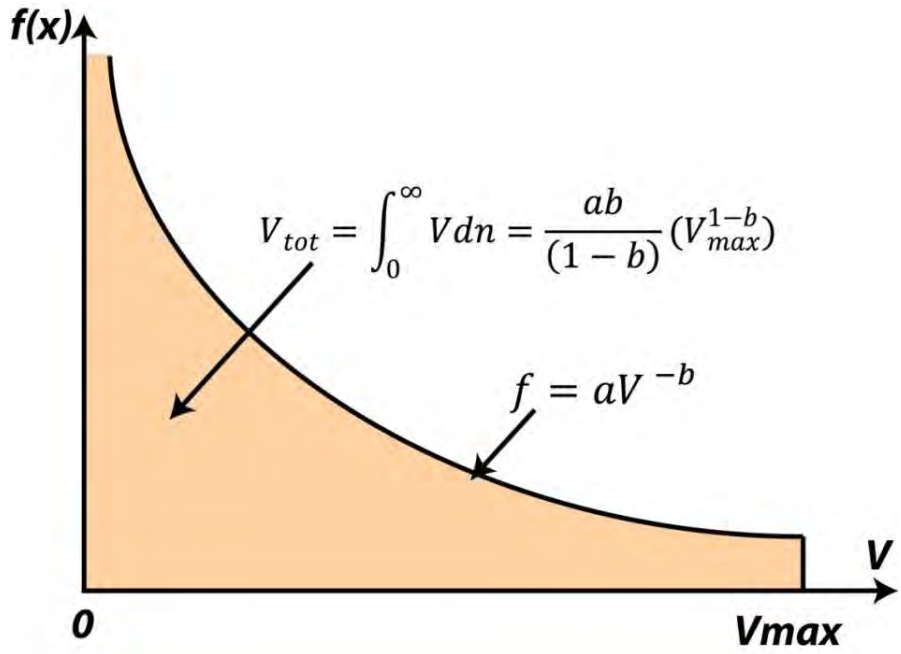

Figure 2.3-6: Cumulated rock fall frequency as a function of the rock fall volume described by a power-law distribution. The volumetric rock fall corresponds to the integration of the power-law between 0 and v_{max} (adapted from Hantz et al., 2003).

2.4 REMOTE SENSING TECHNIQUES FOR ROCK SLOPE CHARACTERIZATION

In the last decades, the application of remote sensing techniques for slope instabilities investigation is experiencing a rapid development (Metternicht et al., 2005). In particular, recent advances in sensor electronic and the ability of personal computer to deal with large datasets consent the use of sensing techniques for a larger scientific community. The possibility to dispose of new accurate data allows a better comprehension of the instability phenomena improving the slope instability characterization at different stage of the investigation (regional scale mapping, detailed local investigation, monitoring and real-time warning).

Remote sensing approaches can be subdivided two main categories (Schowengerdt, 2007):

- Passive remote sensing techniques.
- Active remote sensing techniques.

Passive techniques use natural radiation that is emitted or reflected by and object. Sunlight is the most common source of radiation measured by passive sensors. Examples of passive remote sensors include the different type satellite imagining (RGB, infrared hyper-spectral) and ground–based photography. Instead, active techniques provide their own energy source for the object illumination. Active techniques emit radiation which is oriented toward the target to be investigated. The radiation is then reflected from the target and then measured by the sensor. Examples of active remote sensors include LiDAR (Light Detection And Ranging) or Radar techniques. According to Michoud et al. (2010) remote sensing techniques for landslide investigations can then be subdivided in three main categories depending on the sensor type:

- Passive optical sensor (ground base photography, satellite imaging).
- Active optical sensor (airborne and terrestrial laser scanners, distance-meter).
- Active microwave sensor (InSAR, PsInSAR and GBInSAR).

Table 2.4-1 reports the general characteristics of the remote sensing techniques commonly used to characterize rock instabilities and Table 2.4-2 their principal technical specifications.

Nowadays, a main challenge in slope stability analysis is represented by the integration of different information obtained by the remote sensing techniques to provide focused investigation strategy and reliable monitoring/early warning system (Derron et al., 2011). Because of the high number of remotes sensing techniques, a first important step is the definition of the main advantages and limits of each methodology in order to provide the most appropriate technique(s) for the rock slope that need to be investigated (Derron et al., 2011). The final choice of the technique is based on the balance of different aspects concerning (1) the specificity of the investigated site (goals, site location and specificities), (2) the ability of the investigation technique (accuracy, resolution, and temporal resolution and logistics constraints) and (3) the economic constraints. Moreover, as highlighted by Jaboyedoff and Derron (2005), the risk assessment need to be directly integrated into the initial stage of investigation of the potential rock slope instability through the development of conceptual model and hazard scenarios. The preliminary scenarios need to be successively and continuously updated according to new acquired information concerning the movements and the mechanism of the instability. Moreover, as suggested by Derron et al. (2011) an important issue is to dispose of efficient tools to analyze and interpret the data

obtained by remote sensing techniques. This is in particular the case for new active optical and microwave sensors (such as 3D point clouds or InSAR images) for which specific tools for rock slope analysis are nowadays not sufficiently developed (Derron et al., 2011).

Table 2.4-1: Characteristics and applicability of the main remote sensing techniques to the different stage of investigation rock slope instability (adapted from Derron et al., 2011).

	Instability mapping	***Geometry/Structural analysis***	***Movements detection characterization***	***Movement monitoring***	***Early warning sytem***
Airborne or satellite optical imaging	Excellent for regional scale analysis	Good for contouring	Good when archive are available	----	----
Airborne laser scanning	Excellent for regional/local scale analyses	Good for contouring and persistent structures	Good when archive are available	----	
Advanced InSAR	Good for urban areas	Contouring based on the activity only	Very good when archive are available	A posteriori only	
Terrestrial photogrammetry	Only local characterization	Excellent	Good	Possible, under development	----
Terrestrial laser scanner	Only local characterization	Very good	Good for centimetric movements	Limited to highly risk situation, logistically difficult	----
GBInSAR	----	Poor only low spatial resolution	Very good along the LOS (line of sight direction)	Excellent but movements information in one direction only	Excellent but logistically difficult
Distance meters	----	----	Good	Good (displacement in one direction only)	Good (points only)

In this chapter a short overview of the main remote sensing techniques and their application to rock slope instabilities analysis will be presented. A particular attention is paid to expose the potential applications of LiDAR and InSAR techniques that represent two principal methods used in this PhD. More comprehensive review of the different remote sensing techniques and their potential application for slope movements analysis can be found in Mantovani et al. (1996), Metternicht et al. (2005), Read and Stacey (2009), Michoud et al. (2011) and in Derron et al. (2011).

Table 2.4-2: Specification of common remote sensing techniques applied to rock slope investigations (adapted from Derron et al., 2011).

	Spatial data type	***Range***	***Accuracy***	***Spatial resolution***	***Time resolution***
Airborne or satellite optical imaging	Continuous raster	N.A.	N.A.	~5x pixel size	Days-years
Airborne laser scanning	XYZ point cloud	Meters-Kilometres	Tens of cm in XYZ (~30 cm at 1 km range)	1-100 point/m^2	Days-years
Advanced InSAR	Uneven, discontinuous point	N.A.	~1 mm along the line of sight	Pixel size 1-30 m	Months
Terrestrial photogrammetry	Continuous raster	Meters-Kilometers	½ x pixel size (~5 cm at 500m)	cm (~1 cm at 100m)	Minutes-years
Terrestrial laser scanner	XYZ point clouds	1.5 km Max. on rocks	cm in XYZ size (~1 cm at 100m)	10-10'000 p/m^2	Hours-years
GBInSAR	Continuous raster	4 km max. on rocks	~0.1 mm(along the line of sight)	Pixel size of dm to meters	Minutes-years

2.4.1 HIGH RESOLUTION IMAGING AND PHOTOGRAMMETRY

Aerial photography and imagery obtained by satellites represent primary information for landslides mapping at both regional and local scale (Soeters and Van Westen 1996). Particularly, before the extensive availability of high resolution DEM, aerial stereo-images interpretation represented the most important support to detect and represent the geomorphic features associated to slope instabilities (Nichol et al., 2006). Concerning rock slope instability, this technique has been used since 1930 to delimit and characterize areas occupied by DSGSD (Noverraz 1995; Agliardi et al., 2001; Agliardi et al., 2009), by rockslides and rockslide scars (Jarman 2006) or by potential rockfall sources (Frattini et al., 2007). The increase of the images quality available within Google Earth™ (based on GeoEye-1 satellite and national orthophotos) allows a rapid and precise overview of regional-scale processes. For instance, Crosta et al. (2008) based on Google Earth™ image interpretation, proposed the first inventory of DSGSD and large landslides for the entire European Alps. A total of about 1700 instabilities were mapped and analysed against a variety of factors (geological, geomorphological and neotectonic) in order to assess the favourable conditions leading to the initiation of DSGSDs (Crosta al., 2008).

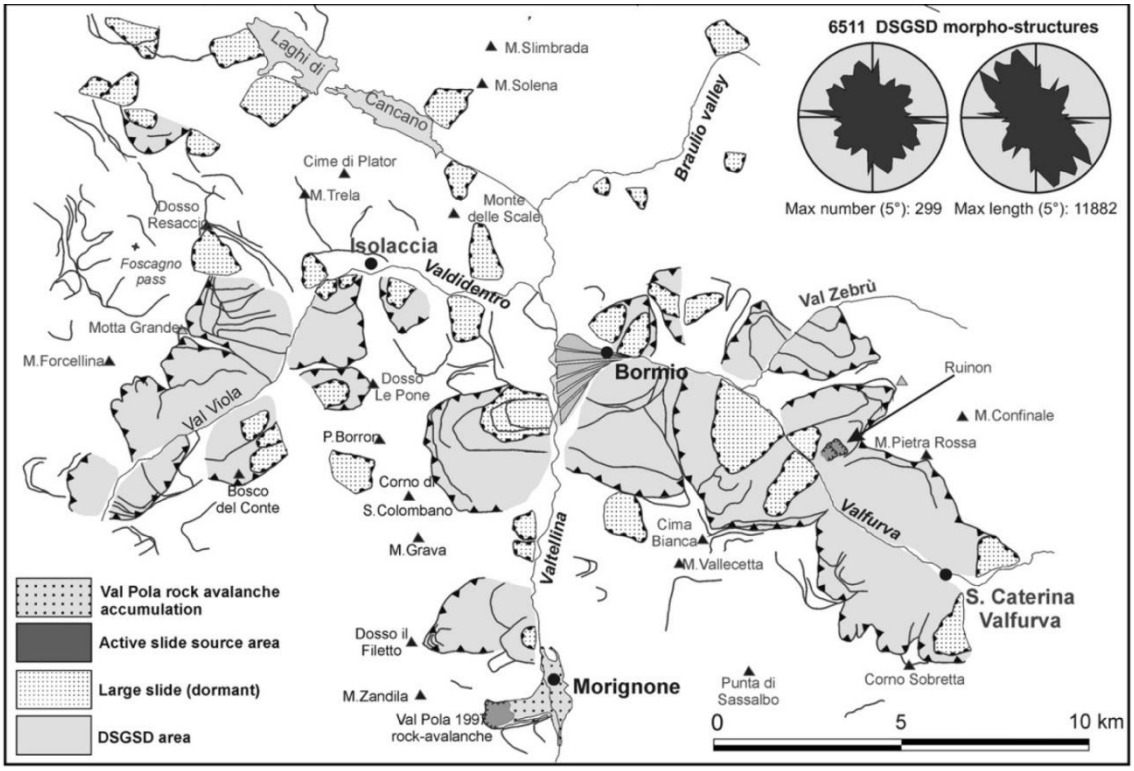

Figure 2.4-1: DSGSD map (from Agliardi et al., 2009) obtained based on stereo image analysis along the upper part of Valtellina valley (Northern Italy).

Digital photogrammetry based on repeated aerial/satellite images represent also a suitable tool for long-term monitoring of low deformation rates (dm-cm/yr) over large areas (Kääb et al., 2005). When multi-temporal aerial photos can be co-registered in the same reference system, rigorous photogrammetric processes allow the extraction of the displacement vectors and the creation of multi-temporal DEMs that can be used for quantitative analyses in most of the geomorphic processes. Even if the photogrammetric approach is less accurate (0.01-1 m depending on the flying height) than other measurement methodologies (GPS or Total Station), it can provide a general view of the on-going processes affecting a

large areas (Brückl et al., 2006). Applications of multi-temporal aerial photos to slope instabilities analyses are numerous, in particular concerning soil-type landslides (Baldi et al., 2008; Prokešová et al., 2010) or paraglacial processes (Huggel et al., 2005; Kääb et al., 1997; Käab et al., 2005 and reference therein). Concerning rock slope instabilities, this technique is adopted principally to assess historic displacements of slow-moving rockslides and DSGSD (Brückl et al., 2006; Strozzi et al., 2010; Malone et al., 2008). Brückl et al. (2006) coupled photogrammetric, GPS measurements and geophysical investigations to propose a possible kinematics of the sagging process in Gradenbach area (Austria). Strozzi et al. (2010) combined photogrammetry, GPS and SAR techniques to describe movements of a rockslide affecting the left side of Great Aletsch glacier between Riederfurka and Bettmerhorn (central Switzerland). These authors highlighted the complementarity of the three methods and in particular the high spatial resolution of the photogrammetric analyses (Strozzi et al., 2010). Malone et al. (2008) employed photogrammetry to analyze the post-failure displacements of a 2 Mm^3 compound rock-slide affecting a main road in northern Peninsular (Malaysia). Based on the analyses of the displacement directions, they suggested the essential control of pre-existing structural setting on the failure mechanism (Malone et al. 2008).

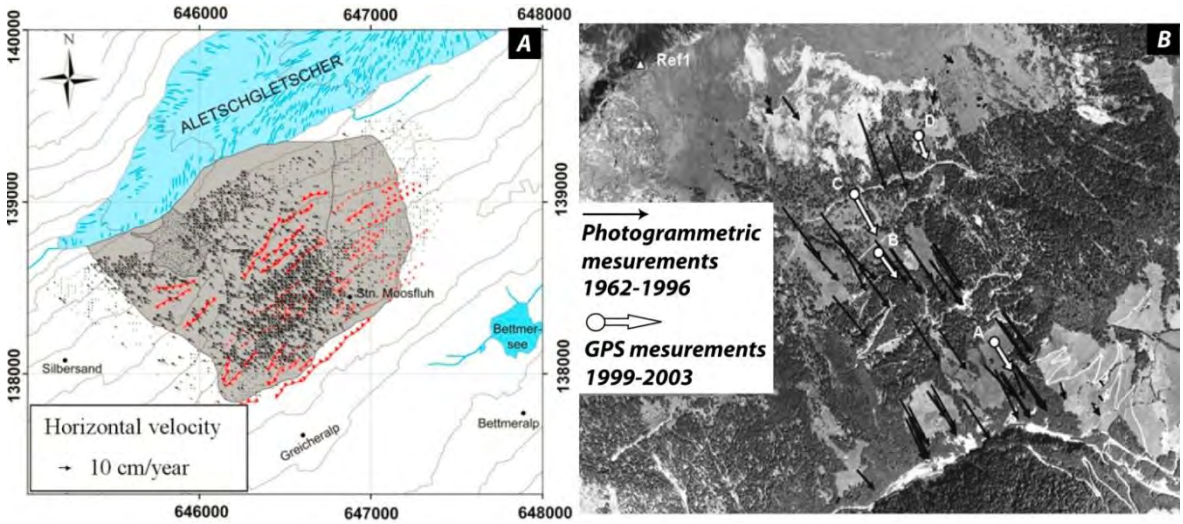

Figure 2.4-2: Displacement vectors obtained through multi-temporal aerial photogrammetry. A) Displacement detected between 1995 and 2006 on a large unstable rock mass located in the NE side of the Aletsch glacier (from Strozzi et al., 2010). b) Comparison between photogrammetric and GPS displacements measured on the Gradenbach DSGSD (from Brückl et al., 2006).

2.4.2 TERRESTRIAL PHOTOGRAMMETRY

Oblique terrestrial photogrammetry, based on pictures taken with common digital cameras has recently become a common method to obtain detailed 3D point clouds of rock slopes (Haneberg 2008; Read and Stacey 2008). In particular, it represents nowadays a routine method in mining engineering to dispose of precise and updated DEMs (Patikova 2000) and to obtained fast and reliable information about the rock mass structures (Poon et al., 2009). In particular, geometrical characteristics of discontinuity sets (orientation, trace length, spacing and primary roughness) can be determined over long distances and in area where classical field measurement are difficult to obtain. A detailed overview of the reliability of the close range photogrammetry technique for quantitative structural mapping has been recently proposed by Sturzenegger and Stead (2009a and b). These authors highlighted the improvement of this technique to

obtain representative structural data in a relative short time and in difficult topographical situations. According to Sturzenegger (2010), main advantages related to the use of remote sensing techniques (both close range photogrammetry and terrestrial laser scanner) for discontinuity characterization are:

- The ability to sample extended windows that provide a more representative statistical analysis.
- The ability to investigate inaccessible steep cliff.
- Drastic reduction of the acquisition time and of the risk for the workers during the field survey.
- The creation of permanent records of the rock slope conditions through time.
- The possibility to measure the orientation of the joint sets close to magnetic ore body where classical measurements are not possible.

Besides, Sturzenegger and Stead (2009 a and b) pointed out some limitations of the remote sensing approaches in particular concerning the problem of occlusion and sampling bias, suggesting that a combination of both field and remote sensing techniques is still needed to provide a comprehensive joint sets analysis.

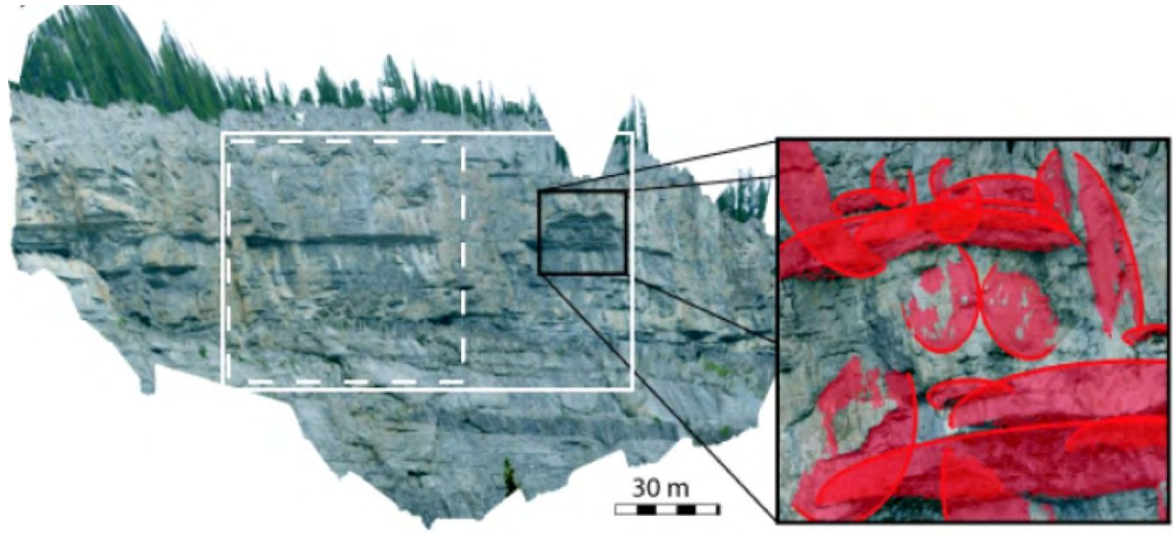

Figure 2.4-3: Photogrammetric digital model, draped on a digital photograph of the Bridal Veil Falls (Alberta, Canada). The black square illustrates how discontinuities are mapped on the rock slope (from Sturzenegger and Stead 2009b).

Repeated oblique terrestrial photogrammetry has been also employed to monitor the evolution of active unstable areas. Chandler and Moore (1989) proposed a first overview of potential application of this technique to characterize the slope instabilities (contour plots, profiles, etc.) and to quantify the activity (volume variation, displacement vectors and strain rate tensors).

Cardenal et al. (2008) combined digital photography and old analogue photographs to follow the evolution of an erosion area above a road cut are near Granada (Spain). These authors highlighted the possibility to obtain a fast and accurate generation of successive DEM using a complete stereoscopic network based on low cost digital photogrammetric workstation (Figure 2.4-4a).

Travelletti et al. (2010) presented a new methodology based on Digital Image Correlation (DIC) technique to analyse the displacement patterns of a translational landslide (Super-Sauze landslide, Southern French Alps). Based on DIC technique, they reached locally a centimetric accuracy, highlighting however, the strong dependence of the DIC on the effective pixel size (Travelletti et al., 2010). The same authors also

exposed the benefits and the limitation of this technique in particular the influence of surface changing and meteorological conditions on the correlation accuracy (Figure 2.4-4b). These limitations suggested that the integration of this methodology in early warning system need to be completed with to other monitoring techniques (Travelletti et al., 2010).

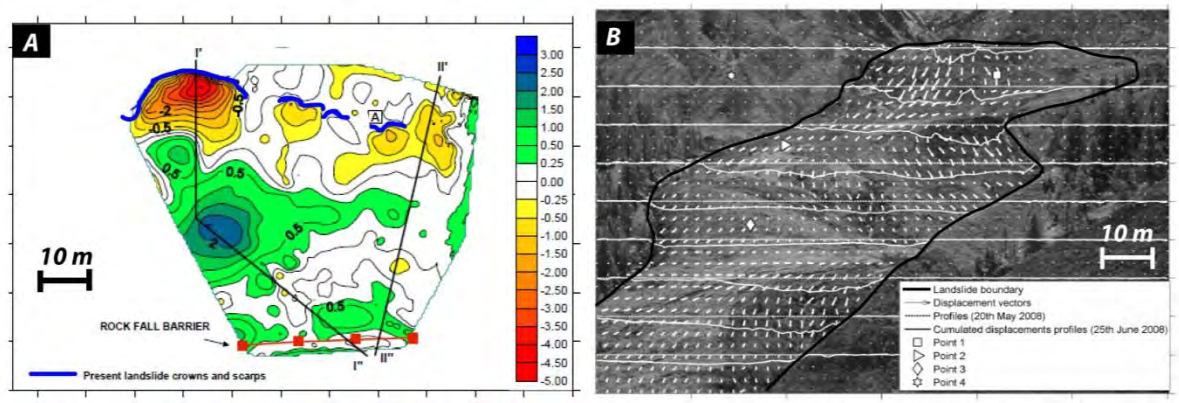

Figure 2.4-4: a) Altitude differences between DEM created by close range digital photogrammetry for a landslide in Spain (from Cardenal et al., 2008). Red-yellow colours indicate denudation, blue-green colours accumulation. B) Displacement field obtained by digital image correlation technique of the central portion of the Super-Sauze landslide (from Travelletti et al., 2010).

2.4.3 AERIAL AND TERRESTRIAL LASER SCANNER TECHNOLOGIES

Laser scanner or LIDAR (Light Detection And Ranging) represents nowadays fundamental tool for geomorphological and geological analyses over large areas but also for detailed investigation of mesoscopic surface processes (Jaboyedoff et al., 2010). Several ranging technologies exist for 3D digitalization of objects (Petrie and Toth 2008). Owing to their longer operational range, only laser scanner that utilize the time-of-flight of the laser pulse are commonly employed in geosciences. Practically, a laser is used to emit a pulse of radiation in a known direction that is successively back scattered by the pointed surface and finally recorded by a detector (Figure 2.4-5). Since the speed of light is known, the travel distance (d) of the light between scanner and the target can be calculated by the following equation (Baltsavias 1999):

$$d = c.\Delta t/2 \qquad \text{Eq. 2.4-1}$$

where (c) is the speed of the light and Δt is the two-way flight time of the laser pulse.

A 3D point clouds is then obtained by continuously changing the shooting direction of the laser beam (Terrestrial Laser Scanner) or by moving the entire scanner device (Aerial Laser Scanner). Laser scanning technique was developed in two distinct ways, depending on the position of the sensor (Jaboyedoff et al., 2010):

- Ground-based LIDAR (TLS).
- Airborne-based LIDAR (ALS).

The ALS system is composed by a measurement device emitting a number of discrete laser beams (up to 100 KHz) and measuring the time taken for the beam to return from the ground back to the aircraft.

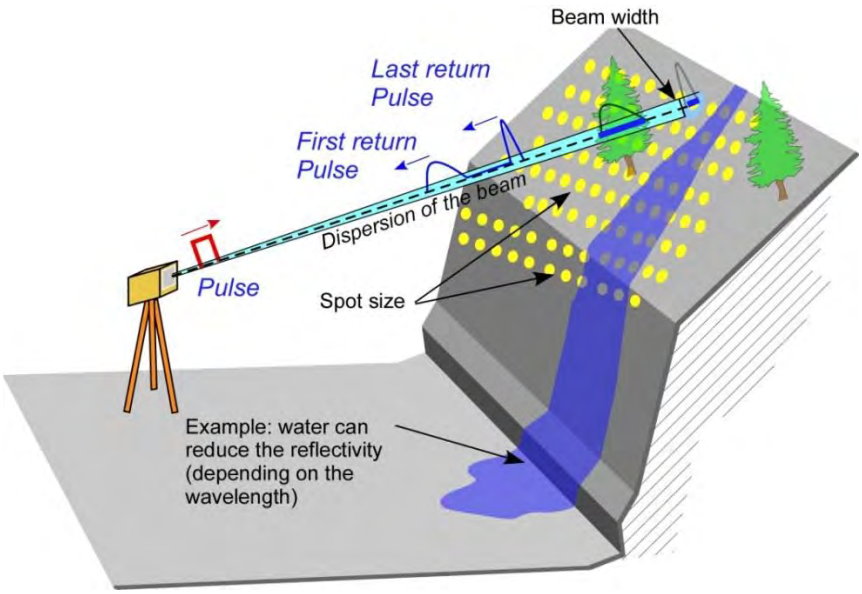

Figure 2.4-5: Example of a Terrestrial Laser scanner acquisition (from Jaboyedoff et al., 2010)

Differential GPS and inertial system provide the continuous monitoring of the attitude and the position of the aircraft permitting the georeferencing of the point cloud. With the present-day technology, the point density varies from 1 pt/m^2 to 100 pts/m^2 (Derron et al., 2011). According to Baltsavias (1999), the accuracy of an ALS point clouds depends essentially on the range, the direction and the position of the laser beam. Other factors influencing the accuracy of the measurement are related to the quality of the DGPS post-processing, the GPS satellite constellation during flight and the accuracy of the inertial sytem (Baltsavias 1999). As stated by Habib (2008), the total accuracy of the ALS measurement can be estimated in 5-15 cm (1σ). More detailed information concerning ALS technique can be found in Baltsavias (1999) and in Wehr and Lohr (1999).

TLS is commonly employed from a fixed position, such as a surveying tripod, to acquire a detailed 3D point cloud of limited area. The static position and the shorter acquisition range allow a better accuracy compared to ALS technique. The point density ranges usually from 50 to 10'000 pts/m^2 depending on the distance of the target and the user-defined resolution. According to Oppikofer et al. (2009), the point accuracy is about 1.5 cm at a distance of 300-400m. The practical operational range depends essentially on the laser wavelength and it is influenced by the reflectivity of the target. The new generation TLS devices can reach more than 3 kilometres (Optech 2011). Detailed information concerning the specificity of the acquisition and treatment can be found in Lichti et al. (2002) and Shan and Toth (2008).

2.4.3.1 Application of ALS and TLS techniques for rock slope analyses

According to Jaboyedoff et al. (2010), four different investigation stages of the can be identified in rock slope stability analysis: (1) Detection and characterization, (2) hazard assessment and susceptibility mapping, (3) modelling and (4) monitoring. The data obtained by TLS and ALS techniques can be very useful to perform and complete the analysis of rock slope instabilities at the different stages of the investigation. Table 2.4-3 resumes the main potential application of TLS and ALS in the four different stages of the investigation.

Table 2.4-3: Possible application of TLS and ALS techniques to rock slope analysis. For each point the main references are also reported (adapted from Jaboyedoff et al., 2010).

	Rockslides /DSGSD	***Rockfall***
Detection and characterization (1)	Mapping of geomorphic features and delimitation of unstable areas. (McKean and Roering 2004; Van Den Eeckhaut et al., 2006).	Rock slope description and geometrical characterization of discontinuity sets (Sturzenegger and Stead 2009a and b; Jaboyedoff et al., 2009).
Hazard assessment and susceptibility mapping (2)	Basic support for representation and topographic-related parameters calculation. Physically and statistically–based susceptibility analyses. (Derron et al., 2005).	Susceptibility mapping based on the intersection with the structural setting and topography. Physically and statistically–based susceptibility analyses (Jaboyedoff et al., 2003; Günther et al. 2003; Loye et al., 2009).
Modelling (3)	Basic information for various types of geomechanical modelling (Humair et al., 2010; Brideau et al., 2010).	2D and 3D trajectory modelling (Dorren et al. 2003; Agliardi et al., 2003).
Monitoring (4)	Surface displacements monitoring and calculation of the evacuated volumes (Oppikofer et al., 2008; Corsini et al., 2009).	Pre-failure movements monitoring, rockfall activity quantification (Abellan et al., 2006; Rosser et al., 2007).

The landslide mapping has been drastically improved by the availability of ALS data. The classical stereo photos analysis is progressively replaced/completed by morphological analyses based on the shaded view of ALS-derived DEM. In particular, the availability of ALS data at regional scale represents a main improvement for the development of detailed landslide inventory (Van Den Eeckhaut et al., 2006; Schulz, 2007). Morphological features associated to landslides such as scarps, counterscarps or trenches are easily detected (Figure 2.4-6).

Haugerud et al. (2003) compared the landslide inventory map of the Puget Lowland (North-western USA) obtained by conventional method (aerial photo interpretation) and ALS-DEM analysis. They highlighted the capability of this latter to detect more than twice as many deep-seated landslides compared to classical stereo-photos techniques (Haugerud et al., 2003).

For rock slope instability analyses the use of ALS laser scanner is commonly adopted as a fundamental support to map and visualize instabilities and main structural features. Henderson and Saintot (2011) used HRDEM-derived maps and aerial photos to map the limits and the structural lineament associated to potential rockslide site in western Norway. Based on this remote sensing data and on fast field verification, they proposed a first rockslide inventory and a preliminary spatial susceptibility ranking to define the areas that are prone to develop larger instabilities (Henderson and Saintot, 2011). Oppikofer (2009) presented a detailed mapping of the rockslide scars and the potential instabilities located in Tafjord area (Western Norway). Based on ALS and TLS data, the author provided also a detailed analysis of the potential unstable volumes and the main failure mechanism.

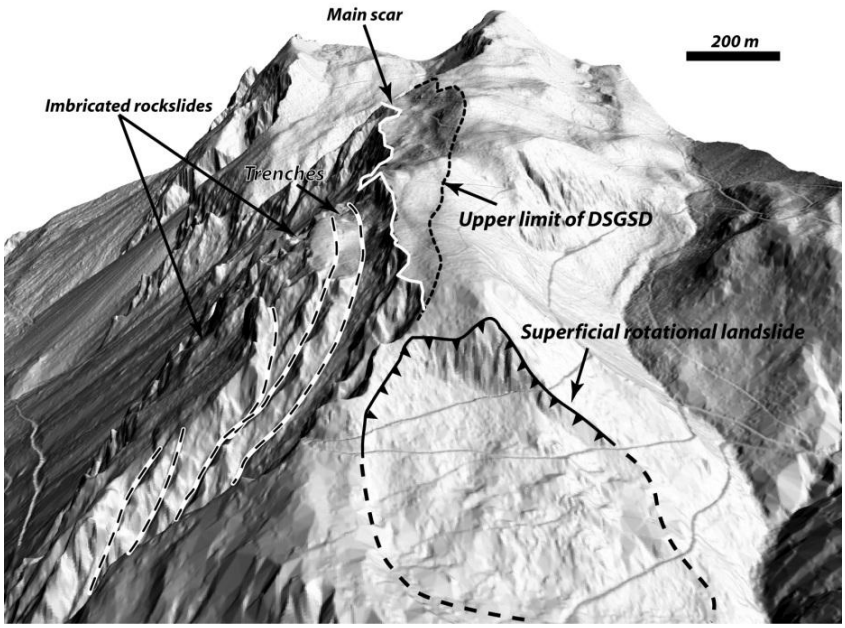

Figure 2.4-6: Hillshade view of the upper part of Les Pics unstable area (Muraz, Western Switzerland) obtained from ALS point clouds (2m cell size). Gravitational features such as scarps, trenches and could be clearly identified. The real instability extend could be better defined using LIDAR-derived DEM than aerial photographs or topographic maps (original DEM from Swisstopo).

The availability of accurate morphometric information (slope, slope aspect, roughness etc.) can be used automatically to detect and map the landslide body. McKean and Roering (2004) proposed an automatic method based on the estimation of the local topographic roughness on ALS-DEM data to identify the landslide boundary. Quantitative morphometric analyses based ALS data have been recently proposed by Loye et al. (2009) to detect potential rock fall sources. These authors suggested that the slope angle distribution characterizing the DEM can be decomposed in several Gaussian distributions that can be considered representative of several morphological units such as rock cliffs, steep slopes, footslopes and plains. Based on in this decomposition, these authors proposed the introduction of a threshold angle that can be used for a preliminary delimitation of potential rockfall sources areas (Loye et al., 2009).

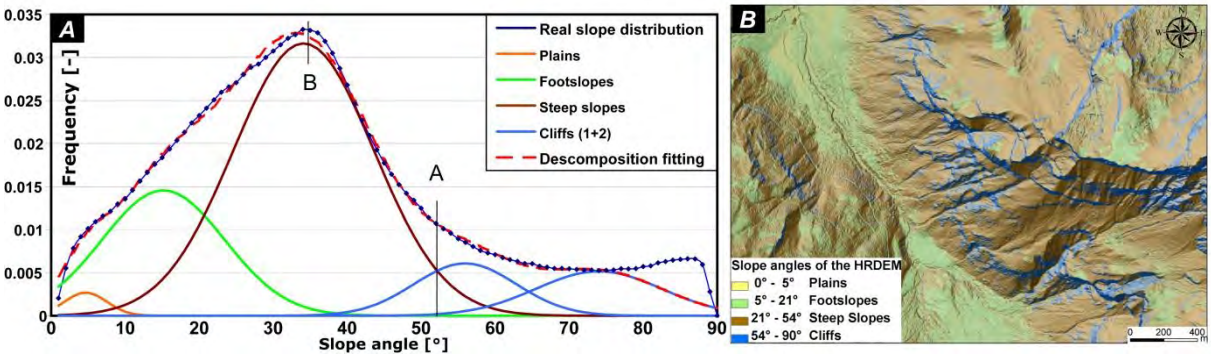

Figure 2.4-7: a) Slope angle distribution (SAD) of 1° bin size for Les Diablerets area (Western Switzerland). The SAD is decomposed in several Gaussian distributions defining different morphological units (modified from Loye et al., 2009). b) Shaded relief view of the same region displaying with distinct colours the dominant morphological unit extracted based on SAD analysis (from Loye et al., 2009).

ALS-DEM is also frequently used to obtain information about the main structural and gravitational features affecting the rock slope at regional scale (Chorowicz et al., 2009; Redfield and Osmundsen 2009).

Jaboyedoff et al. (2004) developed a visualization approach of the ALS data named (COLTOP) that allow the semi-automatic extraction of faults and joint sets orientations at both regional and local scales. This software allows attributing a unique colour code for each topographic orientation that permit the creation of stereonets on the basis of plane orientations measured directly on DEM. Specificity and application and of this principle can be found in Jaboyedoff et al. (2004, 2007, 2009).

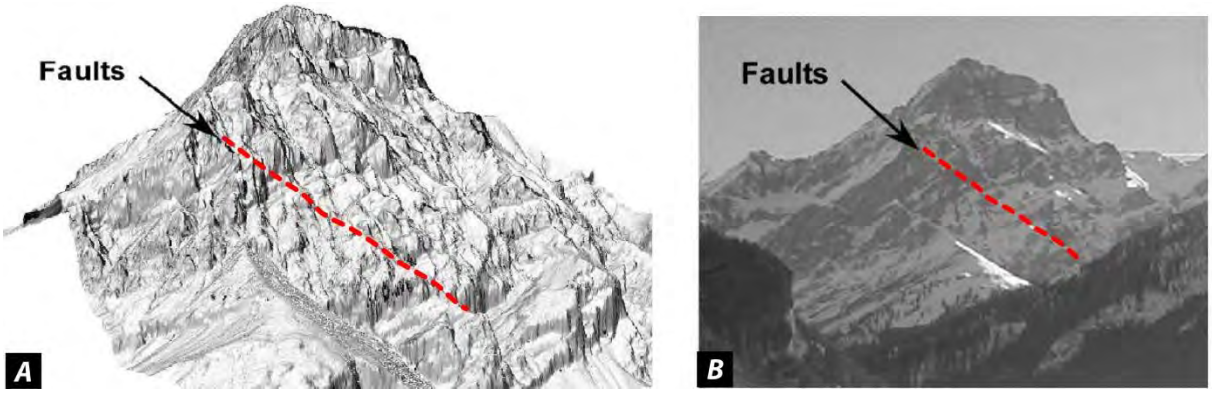

Figure 2.4-8: ALS-DEM 3D view (a) and picture (b) of the west face of the Grand Muveran Mountain (Switzerland). Note the high resolution of the ALS data and the possibility to map faults traces based on DEM view (from Jaboyedoff et al., 2007).

Similarly to terrestrial photogrammetry, TLS technique is nowadays commonly applied to characterize the discontinuity sets at the outcrops in both natural and engineered slopes (Slob et al., 2002; Jaboyedoff et al., 2007; Sturzenegger and Stead 2009 a and b; Lato et al., 2009; Oppikofer et al., 2009). Moreover, the TLS approach has been also recently applied to characterize rock mass parameters in underground environment (Fekete et al., 2010). As shown by Sturzenegger (2009) the joints sets parameters that can be quantitatively estimated using TLS are the geometrical characteristics such as the orientations, the trace length and joint spacing and primary roughness. Inversely, others important parameters such as the joint infilling, alteration and aperture are difficult to acquire using TLS technique (Sturzenegger 2009).
Concerning joint set orientations, at least three different approaches have been developed to extract the discontinuity set orientations from TLS point clouds (Figure 2.4-9):

1. ***The manual approach*** involves the selection of points forming a discontinuity using point clouds analysis software and the fitting of a planar structure across this points (Sturzenegger and Stead 2009 a and b, Oppikofer et al., 2009). This approach gives a complete control to the user on the selection of the more representative plane but it is also time consuming and submitted to a high subjectivity.
2. ***The automatic approach*** is based on the creation of regular triangulated mesh surfaces and the delineation of fracture "patches" from the triangulated surface mesh (Kemeny and Turner 2008; Lato et al., 2009). This approach represents the faster way to extract joint sets orientation from TLS data. However, triangulated meshes suffer from smoothening over corners and edges and create often inaccuracies in plane representation, in particular for complex structural settings. Besides, few possibilities are given, in the available commercial packages to control the parameters defining the automatic joint sets detection (Lato et al., 2009).

3. ***The semi-automatic*** approach is based on the delimitation of neighbourhood points displaying a similar normal vector direction and the successive automatic calculation of mean corresponding plane (Jaboyedoff et al., 2007; Oppikofer et al., 2009; Gigli and Casagli 2011). The representation with a distinct and unique colour allows the easy identification of joint sets by selecting areas with homogeneous colour (Jaboyedoff et al., 2007). In term of operational time and objectivity of the discontinuity set detection, this method can be considered a good compromise between the two precedent approaches.

As for terrestrial photogrammetry technique, TLS suffers theoretically of two types of biases (Sturzenegger and Stead 2009; Lato et al., 2009; Jaboyedoff et al., 2011): (1) scale bias, when discontinuity sets are close to the mean spatial point spacing and (2) orientation bias when joint sets are sub-parallel to the mapping surface or sub-parallel to the scan direction. This latest can commonly be removed adopting the classic trigonometric correction prosed by Terzaghi (1965) or by the scanning the rock outcrops by different positions (Lato et al., 2009).

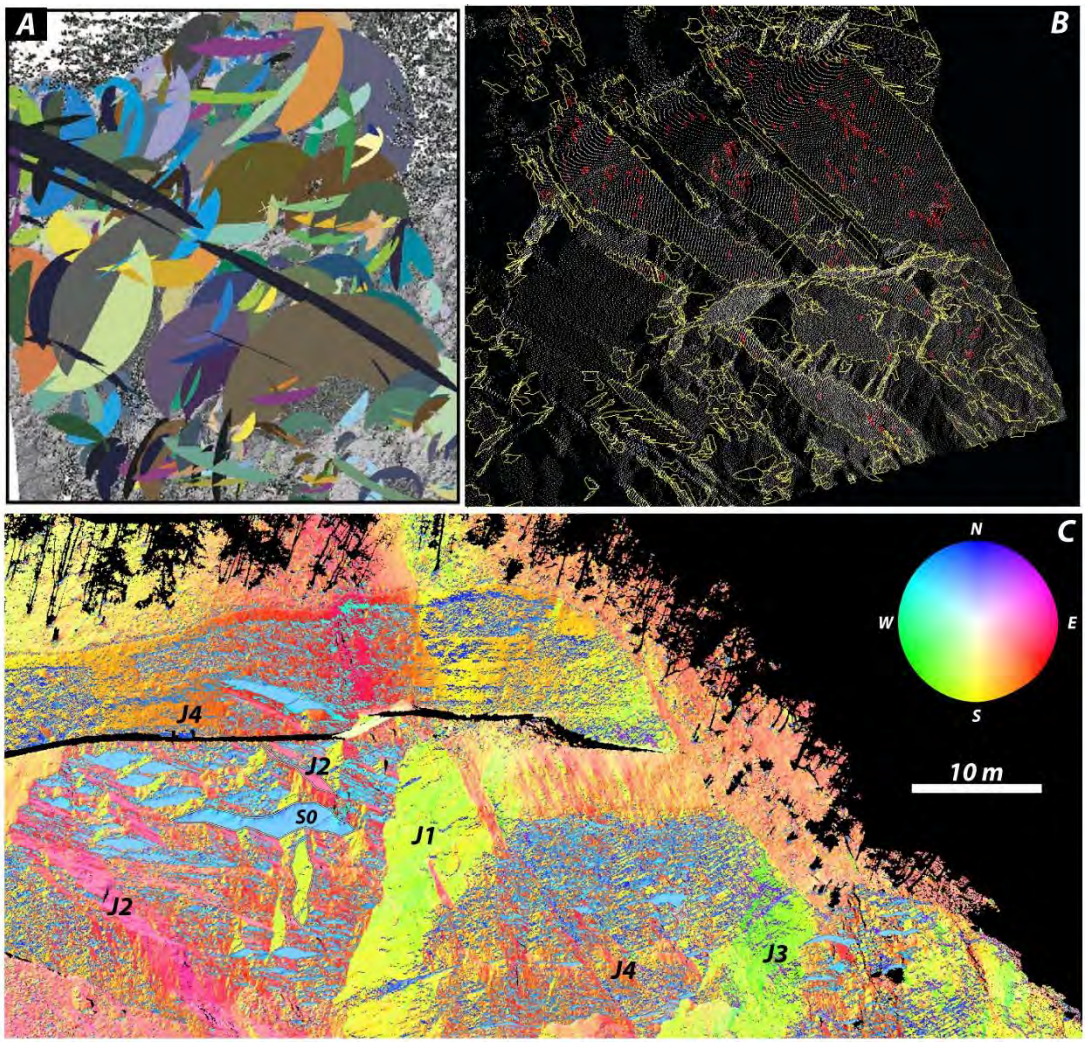

Figure 2.4-9: Example of the three different approaches developed for the extraction discontinuity sets from the TLS point clouds. a) Manual plane fitting of discontinuity sets by the user (from Sturzenegger and Stead 2009a). B) Automatic extraction by creation of triangular mesh (from Kemeny and Turner 2008). C) Semi-automatic extraction (COLTOP 3D approach) based on normal vector calculation and unique colour code representation.

Another important application of LiDAR techniques is the displacements monitoring of soil and rock slopes. Multi-temporal ALS acquisition was recently applied to calculate mass-balance over large areas and to characterize the superficial landslide dynamic of active landslides (Corsini et al., 2009, Burns et al., 2010, Ventura et al., in press).

Corsini et al. (2009) presented a multi-temporal analysis of Ca' Lita and the Valoria earth slide (northern Apennine, Italy) based on repeated ALS acquisition and photogrammetry techniques. These authors highlighted the efficiency of multi temporal ALS images to define the local kinematics and the volumes variation thought the entire landslide area. Ventura et al. (in press) based on four successive ALS acquisitions, analysed the evolution of the Montaguto landslide (Southern Italy). In particular, based on morphometric indicators (roughness and residual topography calculation) they showed the efficacy of repeated ALS acquisitions to recognized the location and the spatial variation of the different morpho-structures (scarps, cracks folds and ridges) that are symptomatic of a specific landslide dynamic (Ventura et al. in press).

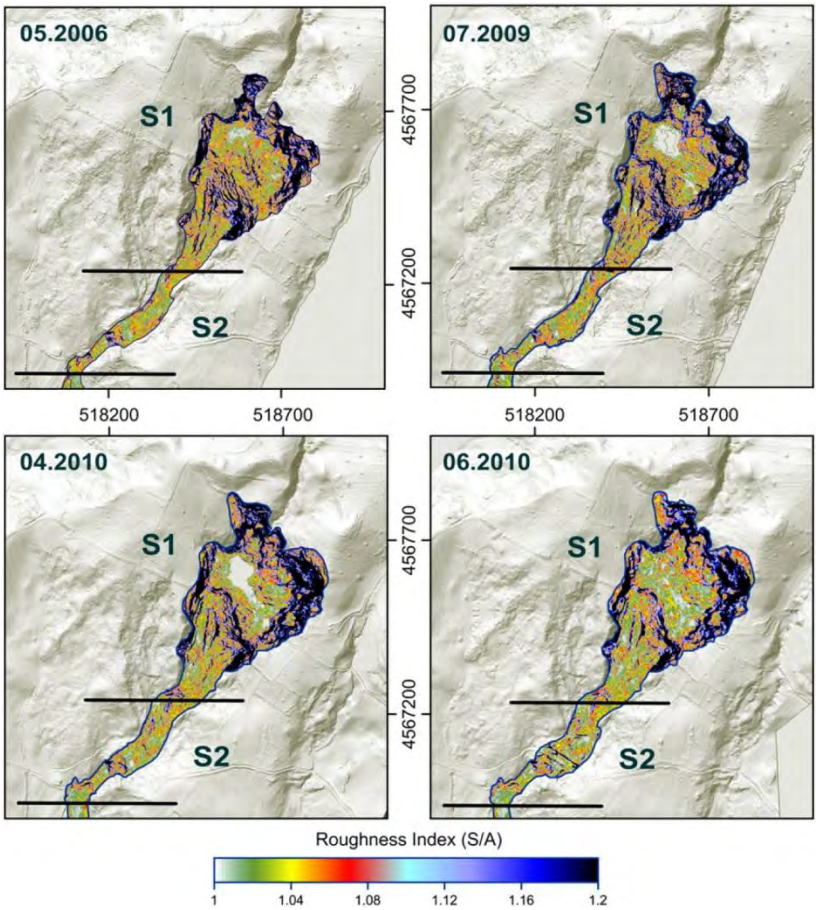

Figure 2.4-10: Spatial and temporal evolution of the surface roughness in the upper area of the Montaguto landslide obtained through repeated ALS acquisition (from Ventura et al., in press).

Successive TLS acquisitions are currently used to map centimetric displacements of soil or rock slopes. Compared to ALS approach, TLS technique is more frequently adopted to monitor the displacements of landslides in particular in rock slopes. Actually, TLS techniques allow a better accuracy and the possibility to obtain complete 3D point clouds of vertical and sub-vertical rock faces. Successive TLS acquisitions

have been successfully applied to detect rockfall activity (Rosser et al., 2007; Abellan et al., 2009; Abellan et al; 2010; Dewez et al., 2009) and to monitor the displacements of active rockslides (Oppikofer et al., 2009; Viero et al., 2010).

As suggested by Jaboyedoff et al. (2010) the characterization of movements using TLS technique is somewhere easier in rock slope than in soil slopes because displacements can be considered as rigid body transformations. Three main approaches are currently used to identify the displacements affecting rock slope (Oppikofer 2009; Michoud et al., 2010):

1. ***Displacement vectors calculation*** based on the identification of identical points or surfaces on the data and the reference point clouds (Travelletti et al., 2008; Oppikofer et al.,2008)
2. ***Point cloud comparison*** by computing of the shortest distance between two adjacent points in the data and the reference point clouds. The comparison is frequently automatically performed using the Iterative Closest Point (ICP) algorithm (Chen and Medioni, 1992; Abellan et al., 2009).
3. Rigid body transformation performed by calculating the ***roto-translation matrix*** between the data and the reference point clouds associated to the displacement of delimited portion of the slope (Teza et al., 2007; Montserrat and Crosetto, 2008; Oppikofer et al., 2009).

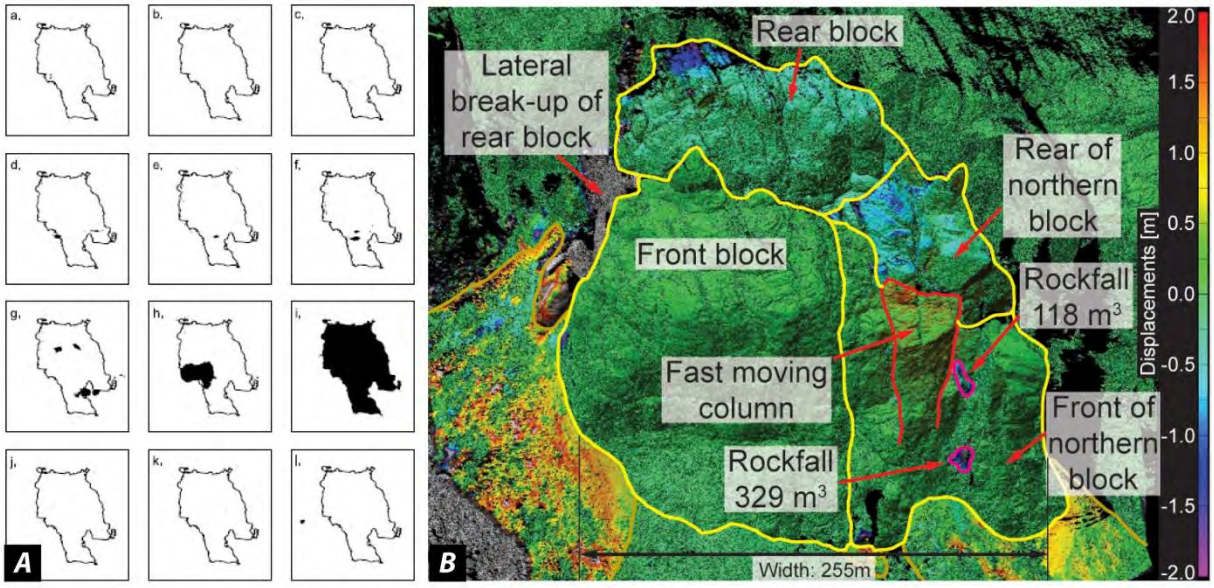

Figure 2.4-11: a) Sequence of rockfalls recorded before and after a larger collapse along the cliffs of the coast of the North York Moors National Park (UK). Black areas correspond to rockfall scars (from Rosser et al., 2007). It is interesting to note the progressive increase of the pre-failure activity before the final collapse. b) Comparison of two successive TLS point clouds acquired showing the differential displacements characterizing the Eiger rockslides (Switzerland). Note that the displacements scale is given in meters (from Oppikofer et al., 2008)

Rosser et al. (2007) based on multi-temporal TLS acquisitions, presented a very interesting study of patterns of precursory rockfall prior to slope failure (Figure 2.4-11a). By monitoring the cliffs of the coast of the North York Moors National Park (UK), they identified a concentration of small scale rockfalls in the area of the final collapses and the absence of rockfall activity in surrounding areas (Rosser et al., 2007). They suggested that magnitude and the time period within which precursory activity is recognizable are directly related to the volume and the geometry of the final collapse (Rosser et al., 2007).

An illustrative application of TLS monitoring of an active rockslide were proposed by Oppikofer et al. (2008). These authors performed a repeated TLS monitoring on the fast moving rockslide (more than 70 cm/day) affecting the eastern flank of the Eiger (Switzerland). Based on this data, the authors quantitatively defined displacement directions and magnitude of the different portions of the rockslide (Figure 2.4-11b). The possibilities to dispose of "real" 3D displacement vectors for a large amount of points allow defining the potential failure mechanisms and to spatially forecast the areas which display the higher predisposition to collapse (Oppikofer et al., 2008).

2.4.4 ADVANCED INSAR AND GB-INSAR

Ground-based (GB-INSAR) and differential satellite radar interferometry (DInSAR) techniques use active microwave sensor to detect millimetric surface movements by analysing the phase difference between successive scenes (Ferretti et al., 2000; Colesanti and Wasowski 2006). Displacements and displacement velocities are then calculated between the two SAR images based on the phase differences and the wavelength of the signal.

Recent improvements in the quality of DInSAR results for deformation mapping and monitoring are provided by the Advanced DInSAR techniques (A-DInSAR). These techniques adopts large multi-temporal stacks of space-borne SAR images acquired over the same area, in order to identify radar targets (coherent reflectors) on which it is possible to detect and measure displacements over time (Wasowski et al., 2007). Displacements are measured along the LOS direction (Line Of Sight) of the satellite (around 23° from the vertical for ENVISAT and ERS satellites). In the last decades, several A-DInSAR techniques have been developed on multi-temporal interferometry data.

According to the processing approach, two different groups of A-DInSAR techniques can be distinguished (Wasowski et al., 2007; Michoud et al., 2010):

- Persistent Scatterers Interferometry such as Permanent Scatterers InSAR (PSInSAR™), Interferometric Point Target Analysis (IPTA), Persistent Scatterers Pair (PSP), Stable Point Network (SPN) of the Standford Method for Persistent Scatterers (StaMPS).
- Interferogram stacking techniques such as Small Baseline Subset (SBAS) or Coherent Pixel Techniques (CPT).

PS-InSAR and related techniques allows the identification of independent radar-bright and radar-phase stable points (Persistent Scatterers, PS) by analysing the pixel amplitude dispersion over time (Ferretti et al., 2000). Differential interferograms are produced with respect to one common master image and advanced phase analyses are then performed in order to maximize the Signal-to-Noise Ratio (Michoud et al., 2010). PS can correspond to buildings, rocky outcrops, and exposed rocks that exhibit a constant "signature" during time. At least 20-30 SAR acquisitions are needed to identify a significant number coherent PS (Michoud et al. 2010). The precision on single measurements is related to PS coherence and varies between 2 to 5 mm (Meisina et al., 2008). Besides, the LOS displacement rates have a precision of 0.1-2 mm/yr. The geocoding accuracy of the PS location is given by the resolution of the SAR system in use. For ESA satellites correspond to ± 7 m in range direction and ± 2 m in azimuth direction with an error in elevation of less than 1.5m (Meisina et al., 2008). The main advantage of Persistent Scatterers approach is the possibility to detect and to monitor the displacements of single isolated objects with a high spatial

resolution, such as building or boulders. For this reason this techniques is particular suitable to follow the displacement rates in urban areas (Raucoules et al., 2008). Besides, the necessity to dispose of high temporal signal stability decrease the possibility to detect coherent PS reflectors in a complex environment such as in mountain regions (Lauknes et al., 2010; Derron et al., 2011).

Different from the PS technique, interferogram stacking techniques such as SBAS are optimized to analyse distributed scattering signals, where several adjacent cells represent the same physical deformation phenomena (Fornaro et al., 2009; Lauknes et al., 2010). In areas with distributed scattering, a complex averaging is applied in order to reduce phase decorrelation noise. This allows obtaining a larger spatial coverage compared to PS techniques. On the other hand, the price of this averaging is an important reduction of the spatial resolution compared to PS techniques (Lauknes et al., 2010). Accuracies of geocoding, displacements and displacement velocities are quite similar to those obtained by PS technique.

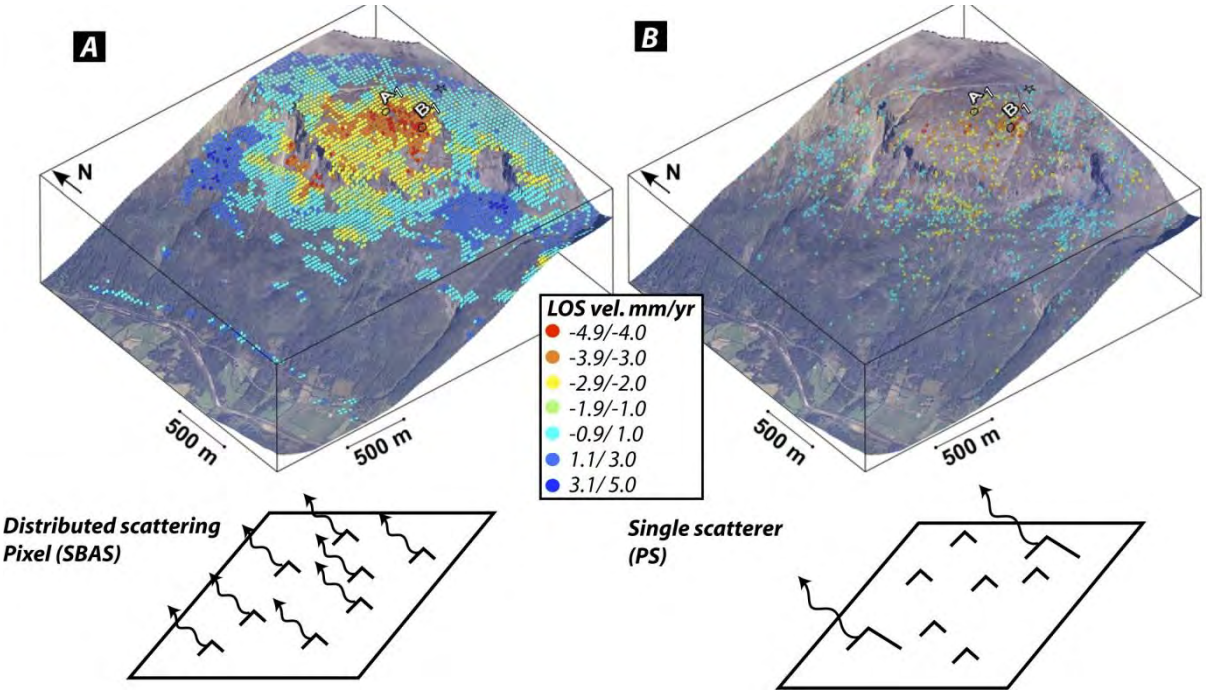

Figure 2.4-12: Mean displacement velocities from the Gámanjunni rock slide estimated using (a) SBAS technique and (b) PS technique (from Lauknes et al., 2010). Points A1, B1 clearly display the difference in the reflector density between the two methods. The images below the maps represent the two different scattering mechanisms.

The availability of displacements data over large areas based on A-DInSAR analyses is used as support for new regional scale landslide inventory and to update pre-existing ones (Catani et al; 2005; Farina et al., 2006; Righini et al., 2011). Classical geomorphological mapping can be coupled with displacements data to obtain information concerning the distribution of the activity within the different landslides and to provide the basis for more detailed local scale studies and for an objective susceptibility and hazard evaluation (Canuti et al., 2004; Catani et al., 2005).

Concerning rock slope stability analyses, A-DInSAR techniques are principally adopted to obtain retroactive displacement maps of active rock slides (Singhroy and Molch 2004; Lauknes et al., 2010; Henderson et al., 2011) or of areas affected by DSGSDs (Ambrosi and Crosta 2006). Information obtained by these techniques allows delimiting the extent and the different displacements patterns characterizing potential rock slope instabilities. Actually, when the presence of ground reflector is enough higher it can

contribute to the interpretation of the potential failure mechanism (Henderson et al., 2011). However, the low spatial resolution, the non-homogenous distribution of the radar reflectors and the possibility to measure displacements along the LOS only, make difficult the extensive application of this technique for detailed failure mechanism analyses or to propose detailed hazard scenarios (Derron et al., 2011).

New processing techniques (Ferretti et al., 2011), the in-situ installation of artificial corner reflectors (Froese et al., 2008) or the integration with other monitoring techniques may increase the applicability and the complementarity of these technologies in complex mountainous environments.

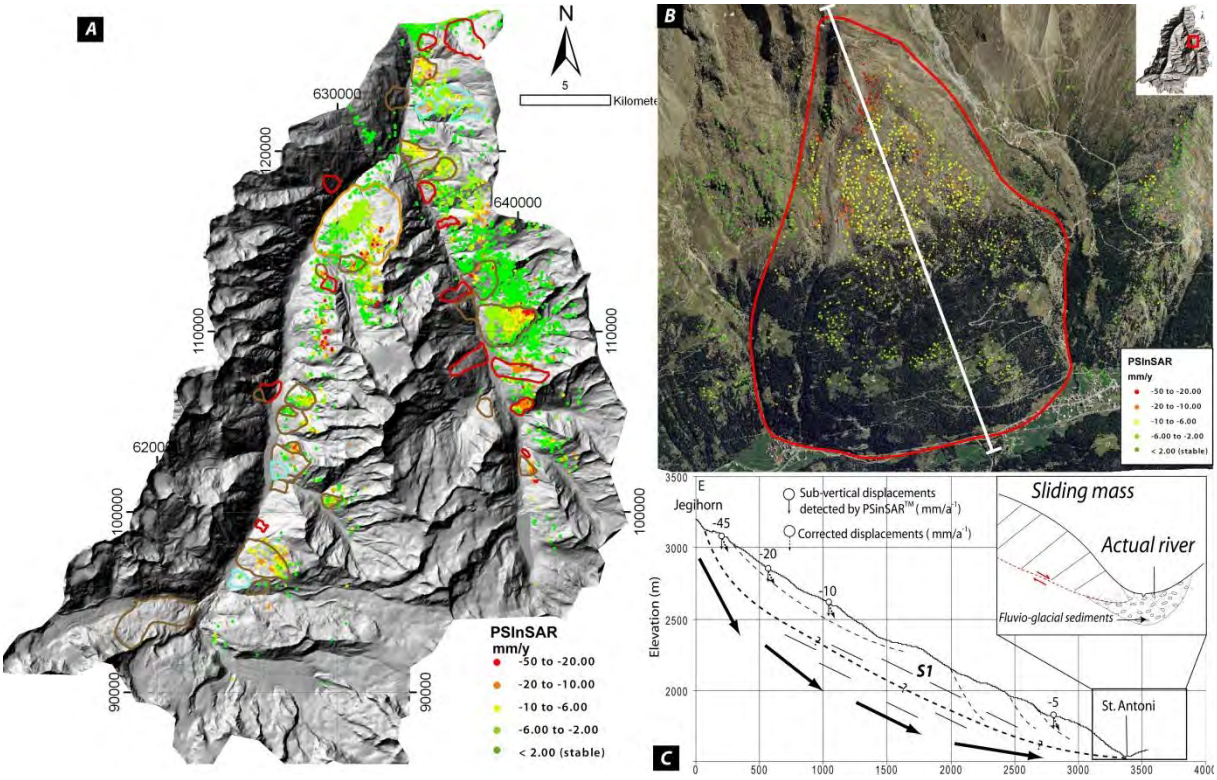

Figure 2.4-13: Application of A-DInSAR techniques (PSInSAR) to detect and characterize rock slope instabilities at regional and local scale (from Pedrazzini et al., 2008). a) Results of the landslide mapping updated using PSInSAR™ data for the Saastal and Mattertal valleys (western Switzerland). Note that the left sides of valleys are not cover by descending satellite orbit. b) PSInSAR™ data of the Tamatten DSGSD (Saastal) showing the activity of the slope. c) Failure mechanism interpretation based on PSInSAR™ results. The progressive decrease of the displacement velocity toward the bottom of the slope suggests a roughly semi-circular failure surface geometry. In the central part of the slope gravitational movements follow the orientation of the main foliation S1.

GB-INSAR technique adopts the same physical principles than the satellite DInSAR but the interferogram is not influenced by the topographic effect, since the position of the antennas remains the same during successive acquisitions (zero baseline condition). The antenna synthetic aperture is obtained by moving the sensor along a straight trajectory and by repeating radar measurements perpendicularly to the expected movements at different spatial intervals (Tarchi et al., 2003; Del Ventisette et al., 2011).

Data treatment consists in the evaluation of the phase difference occurring between the two acquisitions of complex SAR images. The corresponding displacement (Δd) between two successive acquisitions is obtained by:

$$\Delta d = \frac{\Delta \varphi}{4\Pi} \lambda \qquad \text{Eq. 2.4-2}$$

Where (Δφ) represents the phase difference and (λ) is wavelength of the signal. GBInSAR suffers of the typical 2π ambiguity in the interpretation of the phase differences measurement. For this reason, the relative displacements that can be detected between two successive SAR images pixel cannot exceed a quarter of the wave length (λ/4).

The pixel resolution depends on the distance between the device and the monitored area, the length of the rail and the adopted wavelength (Luzi 2010). For commercial GBInSAR devices such as LiSAlab™ sytem (Ellegi™), it is possible to obtain a centimetric pixel resolution at a distance of some tens meters and metric resolution at a distance of few kilometres (Figure 2.4-14). An important advantage compared to satellite approach is represented by the possibility to acquire many SAR images in a very short delay (few minutes) permitting a near-real time monitoring of the instability.

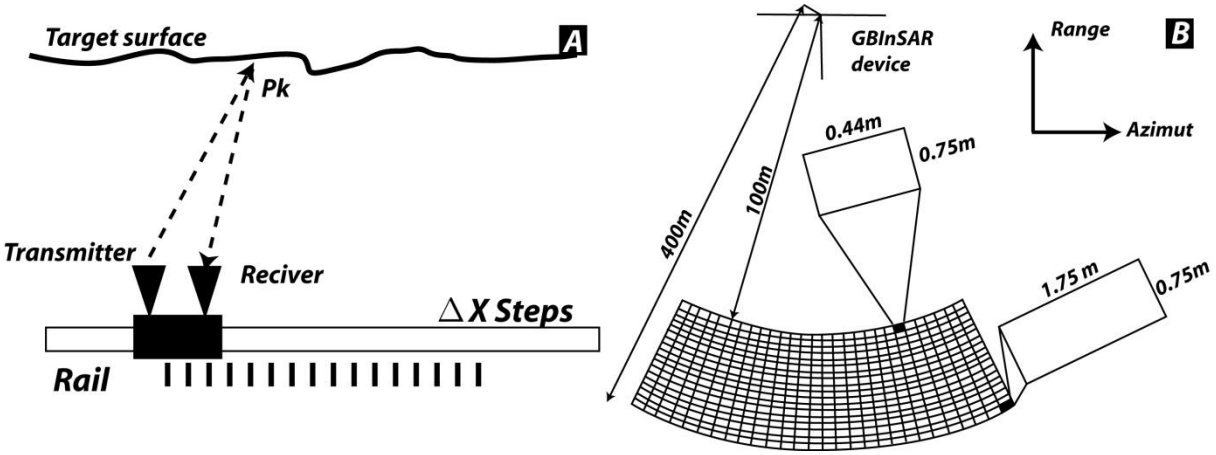

Figure 2.4-14: Illustration of a classical GBInSAR configuration based on a linear motion along a rail (modified from Michoud et al., 2010). b) Distribution of the cell size resolution in a typical GBInSAR configuration (modified from Del Ventisette et al., 2011). Note the important dependency of the distance from the device on the azimuth resolution.

GBInSAR become nowadays an important and widespread techniques for continuous or repeated monitoring of open pit mines and natural cliff around the world (Read and Stacey 2009; Casagli et al., 2010). The capacity of GBInSAR technique to detect millimetric displacements at a range of a couple of km and for large surfaces represents essential information for a detailed hazard assessment and for warning sytem implantation (Blikra et al., 2008; Casagli et al., 2010). Recent studies highlighted the ability of this technique to improve the knowledge of the deformational behaviour of the slope and demonstrated his predictive capability for landslide failure forecast (Gigli et al., 2011; Bozzano et al., 2011).

On the other hand, as the case for the satellite-based A-DInSAR techniques, the three dimensional aspects of the movements cannot be directly analysed, limiting the use of these techniques to define the mode of failure of potential instabilities (Read and Stacey 2009). In order to provide a complete study of the landslide kinematic, Radar technique needs to be used in combination with other monitoring system (Barla et al., 2010). Another limitation of this technique is his low spatial resolution. Gischig et al. (2009) used GBInSAR displacement and LIDAR DEM analysis to propose a conceptual 2-D kinematic model of the upper unstable portion of the Randa rockslide (Switzerland) instability. They highlighted the good correlation between the active fractures and the displacement observed by GBInSAR. However, they also illustrated the limitations related to the spatial resolution and the interpolation smoothing for the interpretation of local displacement patterns.

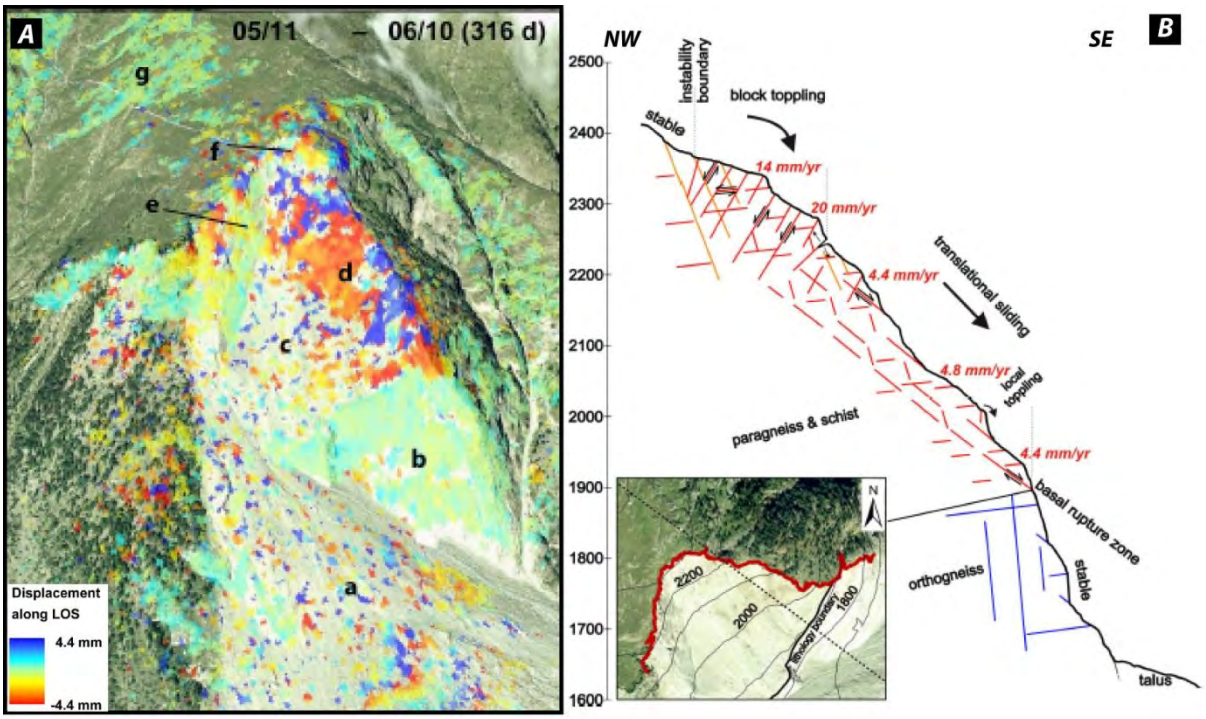

Figure 2.4-15: Example of GBInSAR monitoring and failure mechanism interpretation of the Randa rockslide (Gischig et al., 2009). a) Displacement map obtained by two successive surveys (316 days). It is interesting to note the clear difference in displacements velocity between the upper portion of the slopes ("d", paragneiss lithology) and the lower portion ("b", orthogneiss lithology). b) Conceptual 2-D kinematic model of the instability suggesting block toppling in the upper portion of the slope and planar sliding in the lower part (Gischig et al., 2009).

2.5 NUMERICAL ANALYSES OF ROCK SLOPE INSTABILITIES

Numerical analyses have considerably evolved in the last decades representing nowadays a current technique to investigate the failure mechanisms and, in engineering practice, to propose appropriate slope design (Stead et al., 2006). Recent development in computing software allows faster and extensive application of these techniques within different geometric and geological settings.

On the other hand, classical limit equilibrium analyses, allowing the calculation a static of the factor of safety, still remain a widely used technique in practical rock slope engineering (Wyllie and Mah, 2004). This is mainly related to their simply and rapid applicability and the possibility to perform deterministic and probabilistic analyses in either 2D or 3D. Moreover, the recent development of high-quality commercial codes, allows a rapid treatment of simple failure modes (translational, rotational and toppling failure) and the incorporation of new approaches of groundwater and reinforcement analyses. Table 2.5-2 provides a short summary of the advantages and the limitations of the conventional stereographic and limit equilibrium approaches applied in rock slope engineering. In rock slope analysis, the validity of limit equilibrium approaches is ideally limited to analyse simple structurally-controlled rockslides or rotational landslide. Actually, this technique oversimplifies the rock slopes system by neglecting the progressive deformation (brittle/plastic damage) of the rock mass and the complexity relating the geometry and to the in situ stresses (Varga 2006; Stead et al., 2006). For this reason, limit equilibrium approach cannot provide a comprehensive understanding of the failure mechanism for complex rock slope failures.

Table 2.5-1: Basic methods currently adopted in rock slope engineering to assess the rock slope stability (modified from Stead et al., 2006).

Analysis approach	***Basic input parameters***	***Advantages***	***Limitations***
Stereographic and kinematic (stereographic kinematic analysis/block theory; GIS-based intersection between topography and joint sets).	General slope geometry and discontinuity sets orientations; shear strength of discontinuities	Simple and rapid to conduct. Give a preliminary indication of the potential failure mechanisms and the failure probability; account for the natural variability of joint set orientation and block shape.	Assume rigid blocks, require critical engineering judgment to determine the representative joint sets; impossibility to account for specific joint conditions and potential rock bridges
Limit equilibrium (Factor of safety calculation based on and resisting/mobilizing forces and moment equilibrium for different failure surface geometry)	Representative geometry of the slope, material type and characteristics in particular rock mass and /or joint sets shear strength; ground water conditions, loading/reinforcements characteristics.	Widely used and confirmed approach with several available codes adapted for different failure modes; possibility to perform 2D and 3D analyses in deterministic and probabilistic ways.	Assume rigid blocks; in situ stresses, strains and intact material failure not considered. Progressive shear strength degradation not considered.

This inconsistency can be partially been filled by numerical modelling methods that incorporate intact rock and/or joints deformations and which provide an approximate solution to the complex slope instability processes. The general characteristics of numerical models are the subdivision of the rock mass

into elements or zones (Read and Stacey 2008). For each element, the stress/strain relations are continuously approximated to describe the material behaviour under different internal and external stress conditions. According to Lorig and Varona (2004), the main contributions of numerical models in rock slope stability analyses can be summarized in four main points:

- Numerical models can extrapolate automatically the potential failure mechanism(s) and the most probable failure surface (or shear zone).
- Numerical model can implicitly or/and explicitly incorporate significant geological features (such faults, weathered zones, etc.) and groundwater conditions providing more realistic analysis than classical analytical models in which the conditions are frequently oversimplified leading to conservative solutions.
- Numerical analyses can help to explain in more detailed manner the physical behaviour of the slope instability.
- Numerical method can test in a relative short time, multiple topographical geological and failure mechanism situations and propose different design options.

It is important to remember that in slope stability analysis, mechanical problems are "data-limited" meaning that modelling of the rock slope mechanisms or slope design must be achieved with few site-specific data that are often not representative of the entire slope (Eberhardt 2003; Itasca 2004). The consistency of the results produced by numerical models is strongly dependent on the amount and on the quality of the available data. When quantitative data concerning the rock mass and joint sets characteristics are available, numerical models can be used in fully predictive way. On the other hand, when available data are limited, as it is the case for most large rock slopes analysis, numerical techniques may be used to analyse the dominant failure mechanism and to test various ideas and hypothesis. Table 2.5-2 summarizes the field of potential situations where numerical modelling techniques are applied with respect to the amount of available data.

Table 2.5-2: Spectrum of the different modelling situations (from Itasca 2004).

Typical situation	*Complicated geology; inaccesible; no testing budget*	⟷	*Simply gelogy; large budget; critical hazard problem*
Data	**None**	⟷	**Complete**
Approach/ applicability	*Investigation of the mechanism* ←	*Bracket field behaviour by parameter studies*	→ *Predictive (used in slope design)*

According to Jing (2003) and Stead et al. (2006), there are generally three numerical approaches when analysing a slope stability problem: the rock mass can be treated using a (1) continuum, a (2) discontinuum or a (3) hybrid (continuum/discontinuum) approach. Table 2.5-3 summarizes the main characteristics, advantages and limitations of the three numerical approaches. Detailed review of the mechanical aspects and the applications in rock mechanism and rock engineering can be found in Sharma et al. (2001), Jing (2003) and Bobet (2010).

The choice of the appropriate approach essentially depends on the scale of the analysis and the rock mass characteristics (joint sets density and mechanical properties of the intact rock). Continuum approaches are commonly adopted for analysis of rock slopes where the slope behaviour is determined by the cumulative effect of discontinuity and rock mass proprieties (Coggan et al. 1998; Hoek et al., 1993). This is particularly the case for rock slope characterized by heavy broken and/or weathered rock mass or in weak rocks. On the other hand, rock slopes where the potential failure is controlled by persistent joint sets can be appropriately modelled using discontinuum techniques (Coggan et al., 1998). Hybrid models are particularly suitable to model complex situation involving progressive rock slope failure associated to internal dilatation and fracturing (Stead et al., 2006). These situations are common in rock slopes characterized by blocky rock mass where failure develops through the progressive breaking of rock bridges between non-persistent joint sets.

Table 2.5-3: Characteristics of main numerical models commonly adopted for rock slope analysis (modified from Stead et al., 2006).

Analysis Method	***Critical Parameters***	***Advantages***	***Limitations***
Continuum Modelling (e.g. finite element, finite differences boundary element)	Slope geometry; constitutive criteria, groundwater characteristics; rock mass and contact shear strength; in situ stresses; static and dynamic load; groundwater.	Allow the rock mass deformation; possibility of integration of complex mechanical behaviour; parameter variation thought time.	Input data generally difficult to collect in the field; detailed laboratory test are needed to provide reliable data; limited possibility to perform sensitivity analysis owing to the relative long computational time.
Discontinuum Modelling (e.g. distinct-element, discrete element)	Slope and discontinuity set geometry; intact rock strength, joint set strength and stiffness; in situ stresses; static and dynamic load; groundwater.	Allow movements along block contact and deformation of blocks, can model complex behaviour by integration of different constitutive criteria; integration of dynamic analysis and thermo-hydro mechanical analysis.	High sensibility to scale effect of joint set spacing and persistence; some joint proprieties very difficult to obtain with both field and laboratory test (joint stiffness)
Hybrid Modelling (e.g. FEM/DEM)	Need the integration of both continuum and continuum model parameters; fracture energy release rate; damping factor.	Advantages of both continuous and discontinuous models; can model the progressive fracturing of the intact rock.	Some input data are extremely difficult to obtain; Important calibration phase are need; few application on rock slope analysis.

Brideau et al. (2009) based on detailed field analyses of rock slope instabilities characterized by different rock mass characteristics, proposed a preliminary relationship between rock mass quality (GSI; Hoek and Brown, 1997; Marinos et al., 2005), slope failure mechanisms and appropriate numerical models. They delineated, within the GSI table, five zones where particular failure mechanisms can be expected and they suggested which type of numerical approach is the most appropriate (Brideau et al., 2009). This relationship is particularly suitable for preliminary rock slope analysis because it provides a first overview of the problems based on quantitative field estimations (GSI) and permits to focus further investigations on the key parameters required by the different numerical models.

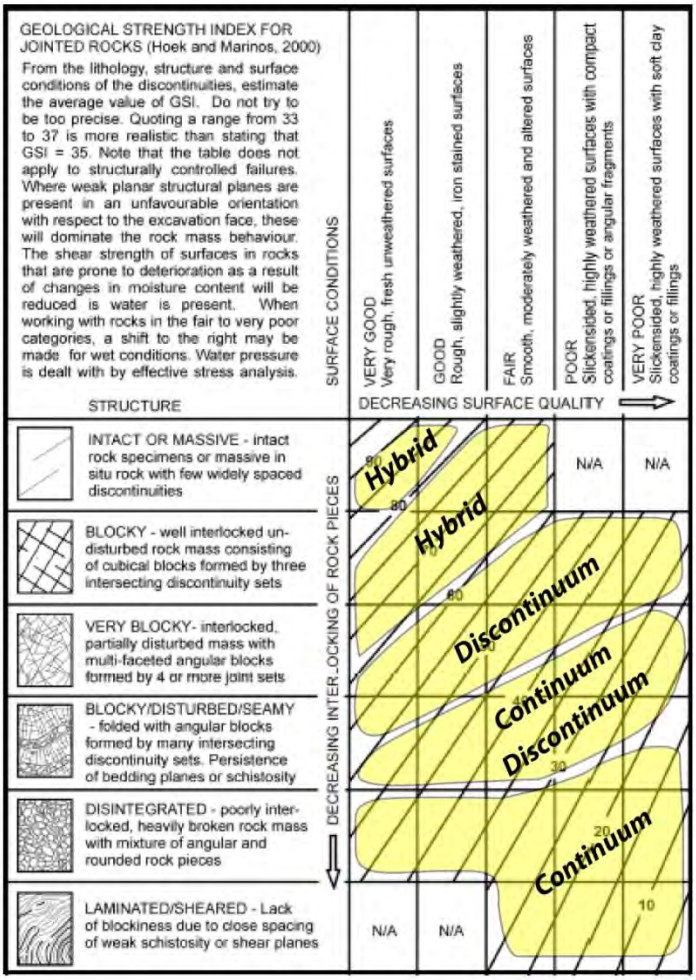

Figure 2.5-1: Representation of suggested numerical model zones within the GSI table (modified from Brideau et al., 2009). It is important to note that the zones delineated into the GSI chart do not have fixed boundaries but can overlay form each other depending on the local slope conditions.

2.5.1 CONTINUUM APPROACHES

Continuum numerical techniques commonly used in slope analyses include finite–element (FEM) and finite difference (FDM) approaches. In both methods, the rock mass is discretised into to a finite number of elements (Jing 2003).

2.5.1.1 Finite difference method (FDM)

FDM technique is based on the postulate that differential equations governing the behaviour of the material can be approximate by finite differences operators. By this approach, the differential equations are reduced to a system of linear equation that can be solved using classical analytical techniques. Single discontinuities such faults or master joints can be explicitly integrated in the system by using grid points as boundary limits and adopting specific frictional laws. Displacements along the discontinuities are then determined by the relative displacement along the corresponding grid points (Bobet 2010). Commercial codes such FLAC (Cundall 1976; Itasca 2004) apply explicit time-marching scheme to approximate the resolution of the problems (Figure 2.5-2). This approach is particularly suitable for modelling non-linear, large strain and dynamic problems where displacements are function of position and time.

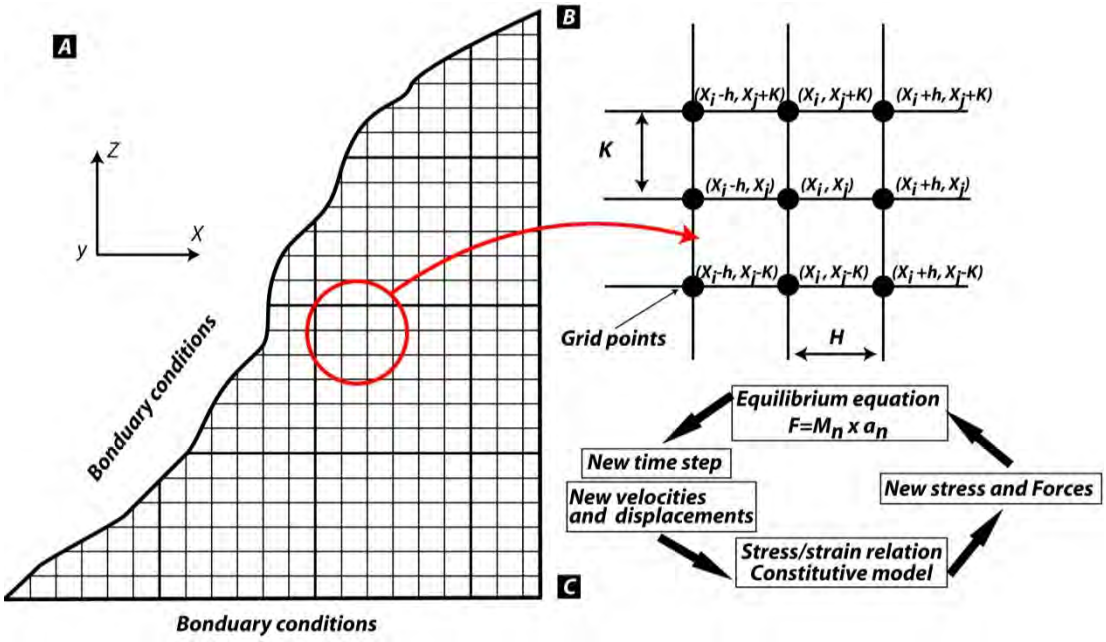

Figure 2.5-2: a) 2D example Finite Difference grid of a slope. b) Detail of the Finite Difference grid with the sub-indices representing the position of the point in the grid. c) Explicit time-marching calculation sequence adopted in FLAC (from Itasca 2004).

In rock slope stability analyses FDM approach is particularly adapted for the analyses of slopes in which failure mechanism is primary controlled by the strength of the whole rock mass such in heavily fractured rock mass or weak lithologies. Several applications of FDM can be found in literature in particular concerning the slope design in open pits or in quarry environment (Carranza-Torres et al., 1997; Bye and Bell 2001; Stacey et al., 2003) or rock cut (Guadagno et al., 2003).

In the last decade, FDM technique was also frequently applied to test the mechanical consistency of the hypotheses concerning the evolution of the large slope instabilities such as large landslides and DSGSD.

Agliardi et al. (2001) adopted an elasto-plastic Mohr–Coulomb yield criterion to analyse the post-glacial development of a DSGSD in central Alps. These authors suggested the application of a ubiquitous-joint constitutive criterion to model the strength anisotropy associated to persistent pre-existing joint sets (Agliardi et al., 2001). Martino et al. (2004) adopted finite-difference analysis to demonstrate the important control of recent tectonics and stratigraphic heterogeneities on the gravitational processes occurred in a built-up area of the central Apennines (Italy). In particular, these authors highlighted the efficacy of FDM techniques to analyse the stress–strain evolution of gravity-induced mass movements in continuum-like rock mass and to evaluate the deformational effects induced by the rigidity contrast between different lithologies (Martino et al. 2004). Brideau et al. (2006 and 2007) based detailed field surveys of rock mass conditions, proposed detailed back-analyses of the failure mechanisms of rock slopes characterized complex rock mass and structural situations emphasizing the importance to adopt appropriate numerical model(s) to capture the key features to understand the potential failure mechanism.

Kinakin and Stead (2005) analysed the distributions of gravitational stress in asymmetric ridges in British Columbia (Canada) to investigate processes leading to the development of sackung features. By adopting elasto-plastic Hoek and Brown constitutive criterion they highlighted the control of rock mass parameters,

in-situ stress and slope geometry on the stresses distribution and on the subsequent location of sackung deformations. Chemenda et al. (2009) used 3D finite-differences technique to analyse gravity-induced destabilization leading to the formation of the la Clapière landslide. By adopting an elasto-plastic Mohr Coulomb constitutive model with a homogeneous reduction of cohesion with time, the authors emphasized the strong influence of the slope topography and the effective mechanical properties of the rock mass on the development of landslides and slope scale deformations. Ambrosi and Crosta (2011) performed parametric analyses of the influence of valley shape, the rock mass anisotropy and the in-situ stresses on the development of DSGSD using 3D FDM. They showed the strong influence of persistent joint set orientations and slope morphology on the final location of the DSGSD and the impact of the tectonic stresses on the final displacements magnitude (Figure 2.5-3).

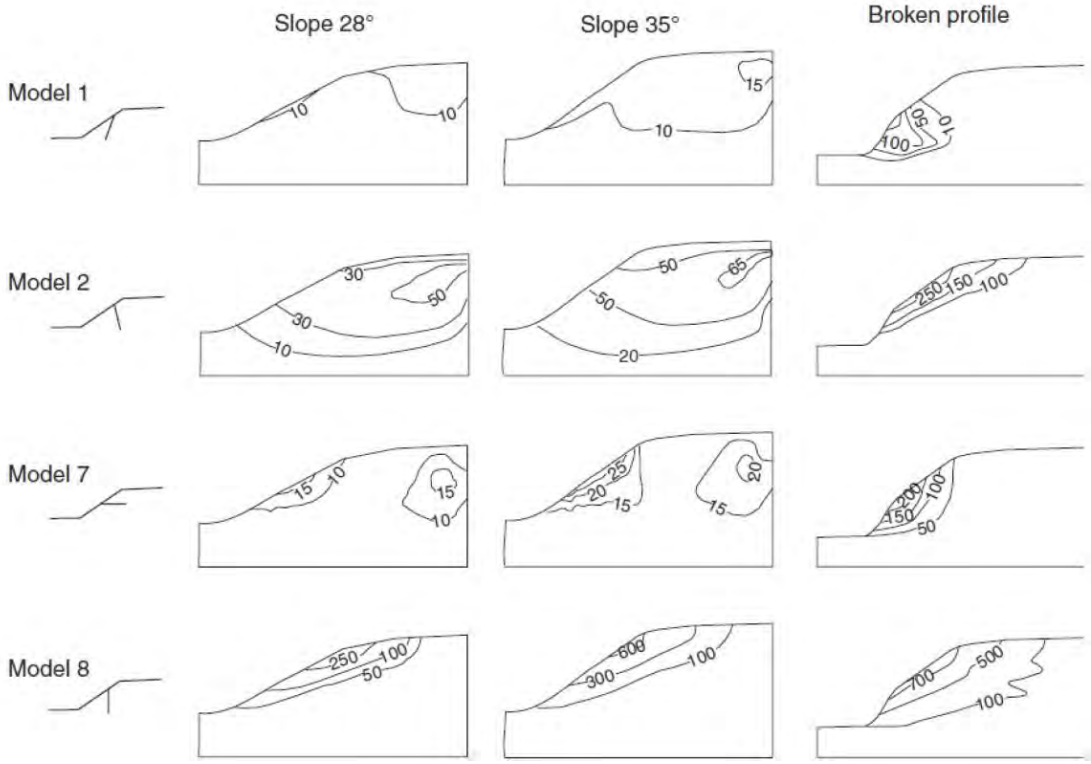

Figure 2.5-3: Distribution of the displacements (in meters) obtained by 3D finite-difference models as a function of the main joint set orientation and the slope profile (from Ambrosi and Crosta 2011).

2.5.1.2 Finite element method (FEM)

FEM is the most popular technique to solve engineering problems involving continuum-like materials (Jing 2003). This numerical method consists in a discretization of the continuum media into small elements displaying a standard shape (triangle, quadrilateral, etc.) and that intersect at their nodes (Figure 2.5-4). The calculation method relies on the assumption that displacements, at any point within the element, can be approximated from the displacements of the nodes (Bodet 2010). At the node level, the behaviour of partial different equations is approximated using standard trial functions techniques (Jing 2003). After defining initial and boundary conditions, the local equations are assembled, into a global system of equations, which approximated the stress and strain within analyzed area (Jing 2003). According to Hammah et al. (2008) the main capabilities of FEM technique are:

1. Possibility to use multiple materials in a single model (material heterogeneity).
2. Direct accommodation of non-linear material responses.
3. Possibility model complex boundary conditions.

Although the FEM is a continuum method, special elements (such as "Goodman joint elements") have been developed to represent discontinuous features such faults or joint sets and permitting the analysis discontinuum rock mass (Hammah et al; 2008 and 2009; Riahi et al., 2010). However, due to the fundamental basis of continuum approach related to compatibility of the displacement at each element node, FEM does not allow modelling the individual blocks detachment and generally all the situations in which block connectivity changes extensively (Hammah et al., 2008).

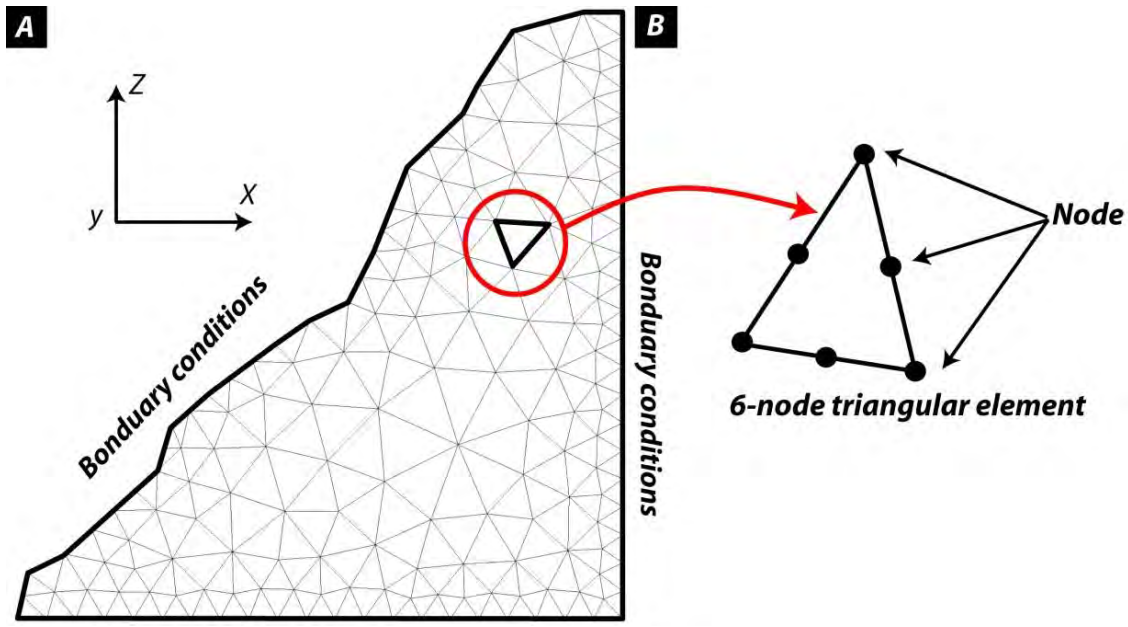

Figure 2.5-4: a) Example of finite element discretization of a 2D slope. b) Detail of single 6-node triangular element.

In rock slope stability FEM approaches was essentially applied to analysis large rock slope instabilities or deep open pit mines where failure can be considered controlled by the properties of the rock mass (Forlati et al., 2001; Ghirotti et al., 2011; Stacey et al, 2003). Styles and al. (2011) proposed a detailed back analysis of the Joss Bay chalk cliff (England) using FEM and hybrid numerical methods. The authors illustrated the potential of using an implicit FEM model to simulate progressive failure and to locate the zones within the slope where the failure take place (Figure 2.5-5). Sturzenegger and Stead (in press) adopted FEM analyses to characterize the in-situ stress and to simulate fracturing along rock bridges leading to the development of the Palliser rockslide (Canada). These authors suggested the importance of spatial relation between the joint-set and intact rock bridges on the development of shear or tension-like failures.

Recently, Hammah et al. (2008; 2009) proposed the application of shear strength reduction techniques (SSR; Dawson et al., 1999) in FEM analysis to analyse the stability of blocky rock slopes. By comparing the obtained results with distinct element method analyses (discontinuum approach), these authors highlighted the great potential of FEM-SSR techniques to analyse failure mechanisms in blocky rock masses (Hammah et al., 2008; 2009).

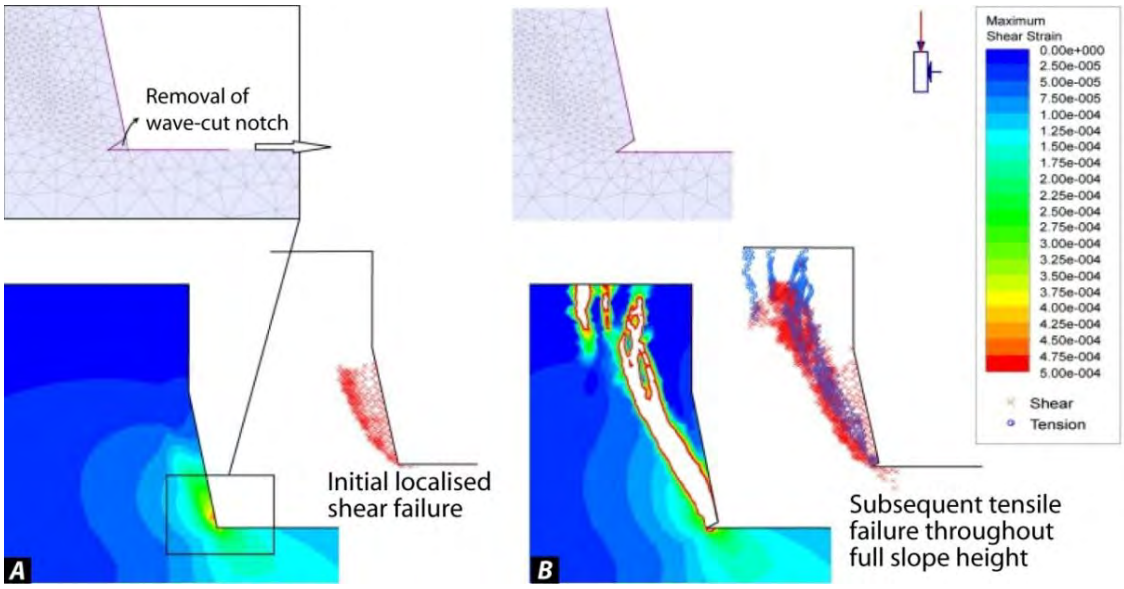

Figure 2.5-5: FEM modelling of the progressive destabilization of the Joss Bay chalk cliff (England). a) Stable model displaying just a localized shear failure at the bottom of the slope. b) Development of the tensile failure through the slope related to the removal of wave cut notch (from Styles et al., 2011).

2.5.2 DISCONTINUUM APPROACHES

In the previous section, the possibility to model the behaviour of jointed rock mass using continuum approaches has been highlighted. As demonstrated by Riahi et al. (2010), these techniques can accommodate rotations and strains of discrete objects as long as contacting node couples are not modified. However, continuum approaches cannot be adopted to complete block detachment and large deformations that represent current conditions within structurally-controlled rock slopes instabilities. Instead, discontinuum approaches, examines the problem assuming an assemblage of distinct (rigid or deformable) blocks exposed to gravity or external loads allowing a more accurate description of failure mechanisms in which block connectivity changes extensively. According to these characteristics, discontinuum represents the most common numerical technique to analyse structurally-controlled slope instabilities. There are three categories of discontinuum approaches that are commonly applied for slope stability problems:

- Distinct element method (DEM).
- Discontinuum deformation analysis (DDA).
- Bonded particle method (BPM).

2.5.2.1 Distinct element method (DEM)

Distinct element method (DEM) was proposed by Cundall (1971) to simulated movements in structurally controlled rock masses. Commercial computer code UDEC and 3DEC (Itasca 2004) have implemented this technique and represent nowadays the most used codes for rock slope stability modelling. In DEM approach, the slope is subdivided by different fully persistent joint sets delimiting a finite number of blocks (Figure 2.5-6). According to Eberhardt (2003), the principle of distinct element method is based on the repeated solving of the dynamic equations of equilibrium, for each block in the system until the boundary conditions, the contact and motion laws are satisfied. To perform this operation, DEM techniques needs to solve three key problems (Bobet 2010): (1) The representation of the contacts

between the blocks, (2) the representation of the intact block behaviour and (3) the continuous detection and revision of the contact type.

Displacements along the discontinuities (contacts) are controlled by force-displacement relations (linear or non-linear) in both normal and shear direction. The interaction between two contacting blocks is characterized by normal and shear stiffness (Figure 2.5-6). The calculations of the contact forces between two elements are obtained adopting algorithms for contact detection such as a penalty function or Lagrange multiplier (Jing 2003). Blocks can be considered rigid or deformable. Deformable blocks, with linear or nonlinear stress-strain behaviour, are discretised into a mesh of FDM elements, as for a standard continuum model (Figure 2.5-2). For rigid blocks, equations of motion are simply solved for the centroid. On the other hand, for deformable blocks, the equations of motion are solved and summed for each grid points within the blocks.

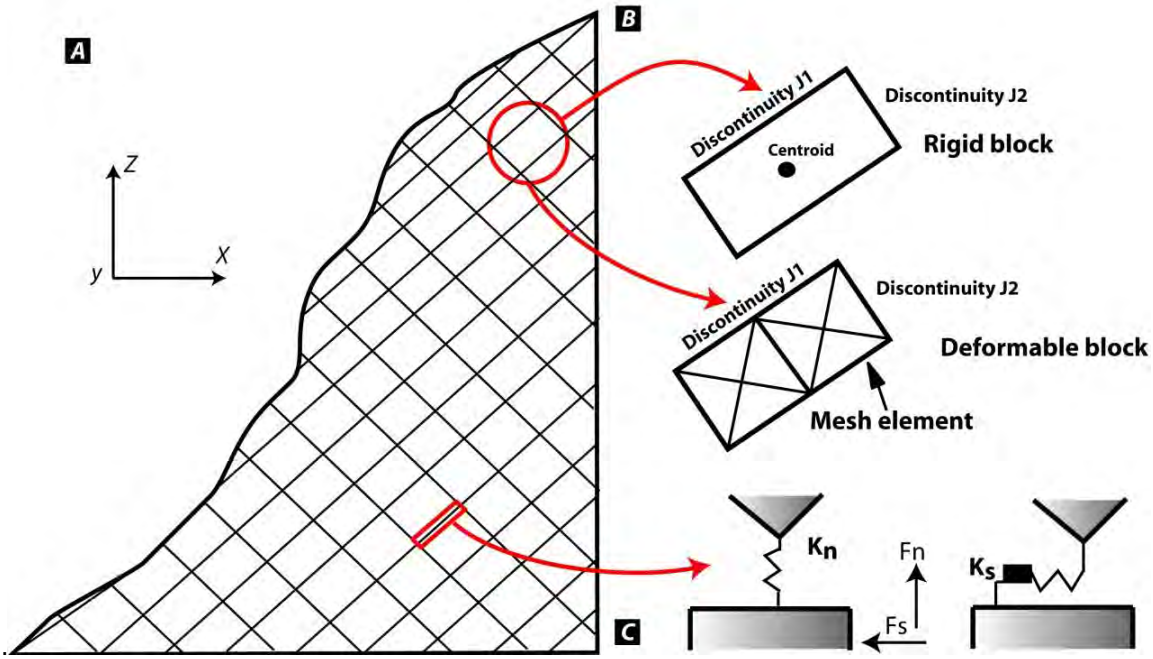

Figure 2.5-6: a) Example of distinct element method discretization of a 2D slope. b) Characteristics of rigid and deformable blocks adopted in DEM analysis. c) Representation of forces at the boundary of DEM elements.

Concerning natural or engineered rock slopes, several representative studies have been carried out adopting DEM techniques. Stead et al. (2006) provided a comprehensive overview of the innovative application and of the most representative case studies where DEM modelling was successfully applied. Recently, fast progresses in DEM techniques allow performing detailed study of complex rock slope situation requiring the application of hydro-mechanical, thermo-mechanical and dynamic approaches.

Eberhardt et al. (2007) showed the application of a coupled hydro-mechanical distinct-element model to analyse the efficacy of the deep drainage system installed to stabilize the Campo Vallemaggia landslide (Switzerland). The same authors (Eberhardt et al., 2005) based on a coupled hydro-mechanical DEM approach and field mapping, analysed the effect of progressive strength degradation and water pressure on the development of the 1999 Rufi slide (Switzerland). Fisher et al. (2011) adopted DEM approaches to assess the predisposing and the triggering factors influencing the slope stability for the 1988 Tschierva rock avalanche (Piz Morteratsch, Switzerland). In a first series of models, the authors proposed a

preliminary analysis of the progressive fracturing of the rock slope related to glacial unloading. In another series of models, they analysed the distribution of the hydraulic loading suggesting the potential influence of water pore pressure for the triggering of the instabilities (Fisher et al., 2011).

Gischig et al. (2011a) based on detailed remote sensing analysis and 3D geodetic patterns performed 2D numerical analysis to reproduce the hypothesized kinematic behaviour of the Randa rockslide (Switzerland). In the same way, Gigli et al. (2011) proposed a 2D distinct-element model to perform hazard scenarios of the Mt. Beni rockslide (Florence, Italy) calibrated on both conventional and GBinSAR monitoring data. Welkner et al. (2010) integrated field and numerical approach to investigate rockslide hazard of the Portillo Rock-avalanche site (Chile). The authors adopted hydro-mechanical and dynamic modelling to back–analyse the triggering and predisposing factors leading to the prehistoric Portillo rock-avalanche. Based on these results, they proposed a forward analysis to better assess the hazard associated to the potential rock slide events in the same area (Welkner et al., 2010).

Gischig et al. (2011 b and c) analysed the seasonal deformation trends of the Randa rockslide adopting a thermo-mechanical DEM approach. Based on instrumental observations and numerical modelling results, they suggested that seasonal thermal effects can drive deep rock-slope deformations and progressive failure in the upper portion of the Randa rockslide (Gischig et al., 2011 b and c).

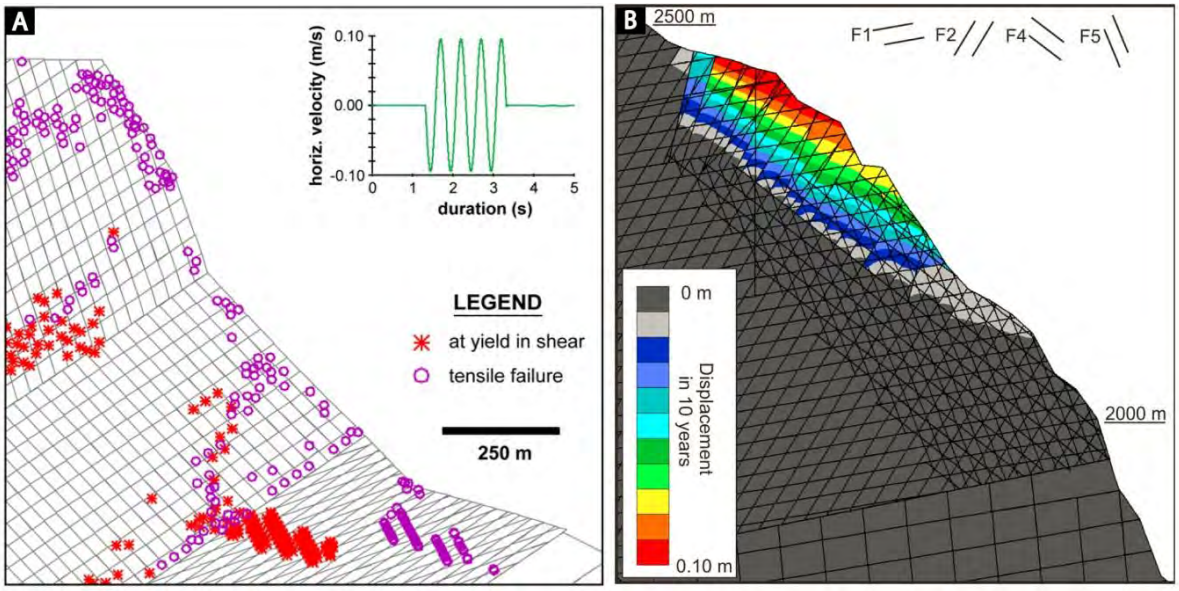

Figure 2.5-7: Example of advanced DEM modelling to analyse the failure mechanism of complex rock slope instabilities. a) UDEC modelling of Portillo rock slope response to an Mw=5.5 earthquake trigger (from Welkner et al., 2010). B) Displacements after 10 years of thermal cycling for the upper portion of the Randa rockslide obtained by thermo-mechanical distinct element model (from Gischig et al., 2011 b).

Application of three dimensional distinct element modelling of natural rock slope is still scarce. This is in particular due to the difficulty of 3D numerical code to model complex topography. Most of present-day publications discuss the 3D stability analyses for simple geometric configurations such as open pit mines and road cuts (Segalini et al., 2006; Sainsbury et al., 2007). Three dimensional DEM analysis for natural slope analyses have been recently proposed by Brideau et al. (2011; in press) to assess potential instabilities on Turtle Mountain and to analyse the potential failure mechanisms of the Chehalis lake

landslide. Kalenchuck et al. (2009) used 3D DEM to determine the influence of the failure surface geometry on the calculated displacements patterns at the Downie slide (Canada).

2.5.2.2 Discontinuous deformation analysis (DDA)

Discontinuous deformation analysis (DDA) has been originally developed by Shi (1988) and successively extended in 3D by the same author (Shi 2001). The discretization of the medium into different blocks divided by different discontinuity sets is similar to those presented for DEM approach in Figure 2.5-6. Even if DDA and DEM are similar in term of discretization of the medium, they show a different mechanical formulation. For instance, in DDA analyses, the unknown in the equilibrium equations are not represented by forces between the blocks but correspond to the relative displacements between blocks. Indeed, the system of equations in DDA approach is derived from minimizing the total potential energy of the whole system and it is then solved in the same way (implicit method) than the FEM formulation (Bobet 2010). Indeed, DDA can consider both statics and dynamics problems using a time-step marching scheme. The difference between static and dynamic analysis depends on the velocity assumed at the beginning of each time step. For static analysis, initial velocity is set to zero at each time step while for dynamic analysis the initial velocity is an accumulation of the velocities in the previous time steps (Lin et al., 1996). An important development of DDA approach, particularly useful to model rock mass fragmentation and fracture propagation has been proposed by Lin et al. (1996) by introducing the three–parameter Mohr-Coulomb criterion.

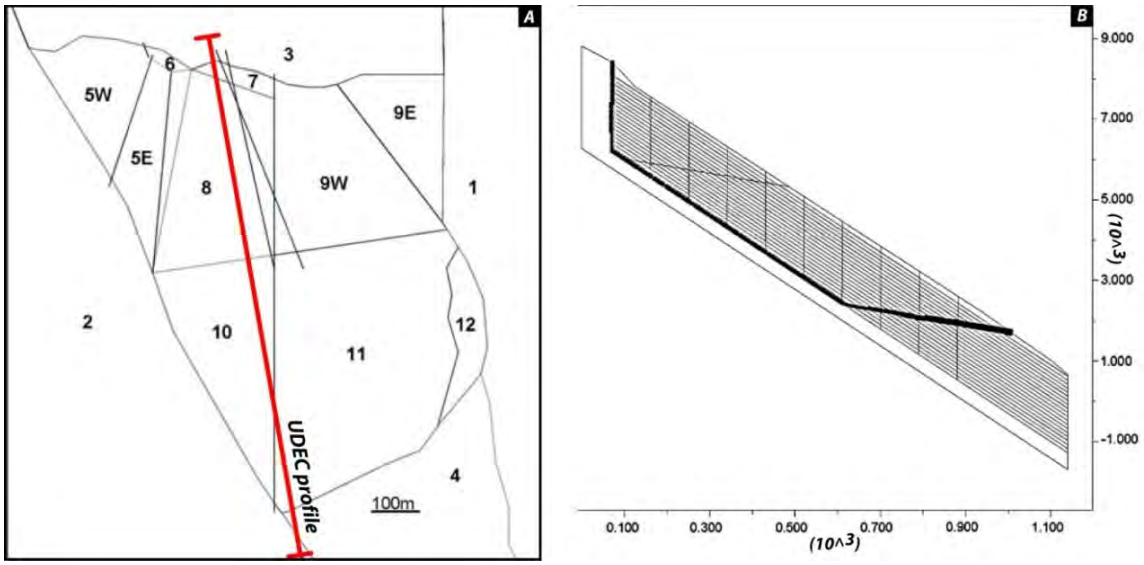

Figure 2.5-8: a) Subdivision of the Aakens rockslide in different blocks obtained based on displacement data and DDA modelling. b) Udec model (cross-section) displaying the maximum simulated shear displacements at depth of 200 m. The sliding depth depends on the location of the lower daylighting fracture (from Kveldsvik et al., 2009).

Practical applications of DDA technique for rock slope analysis are limited even if more than 100 validations of this approach have been reported by MacLaughlin and Doolin (2006). Hatzor et al. (2004) proposed a dynamic two-dimensional stability analysis of the King Herod's Palace (Israel) using time-dependent acceleration as input. These authors showed the capability of DDA approach to determine the failure mode of critical key blocks. On the other hand, the authors highlighted the necessity of an important calibration phase and the introduction of energy dissipation to obtain realistic models (Hatzor

et al., 2004). Kveldsvik et al. (2009) adopted DDA and DEM analysis to model the displacements observed on the Aaknes rock slides (Norway). These authors tested several potential subdivisions of the rock slope (2D slope surface) in different blocks and applied DDA modelling calibrated on different sets of displacements data and in-situ geomechanical characterization (Figure 2.5-8). Numerical model highlighted the possibility of three or four blocks located in the upper portion of the slope to fail catastrophically (Kveldsvik et al., 2009). Tommasi et al. (2009) adopted DEM and DDA modelling to investigate the development of shallow bucking deformations in the Lavini di Marco landslide (Italy). These authors emphasized the potential conditions promoting buckling deformations (water pressure, Young modulus of the intact rock, length of the slope, etc.) and suggested that this phenomenon may evolve into complete failure and influence the long term stability of the slope (Tommasi et al., 2009).

2.5.2.3 Bonded particle method (BPM)

The bonded particle method (BPM) represents a more recent improvement of the classical DEM techniques (Potyondy and Cundall 2004). Commercial numerical codes adopting this approach are PFC2D/3D (Itasca 2004). The basic idea of this method is that the rock mass material can be approximated by discs in two dimensions or by spheres in three dimensions. The interaction between the different particles is performed through their contacts such that deformation is produced at the particular contact or by the relative displacement between different particles (Bobet 2001). Clusters of particle, displaying the same mechanical characteristic, can be merged together to simulate the presence of jointed bounded blocks or local rock mass heterogeneities. Failure initiation occurs when tensile and/or shear strength of the contact are overcome. According to the classical DEM approach, the displacements and velocities of each particle is determined by solving the second Newton's law through a central finite difference algorithm (Bobet 2010). The forces-displacements calculation is then performed incrementally for each disc (sphere in 3D) adopting a small time step.

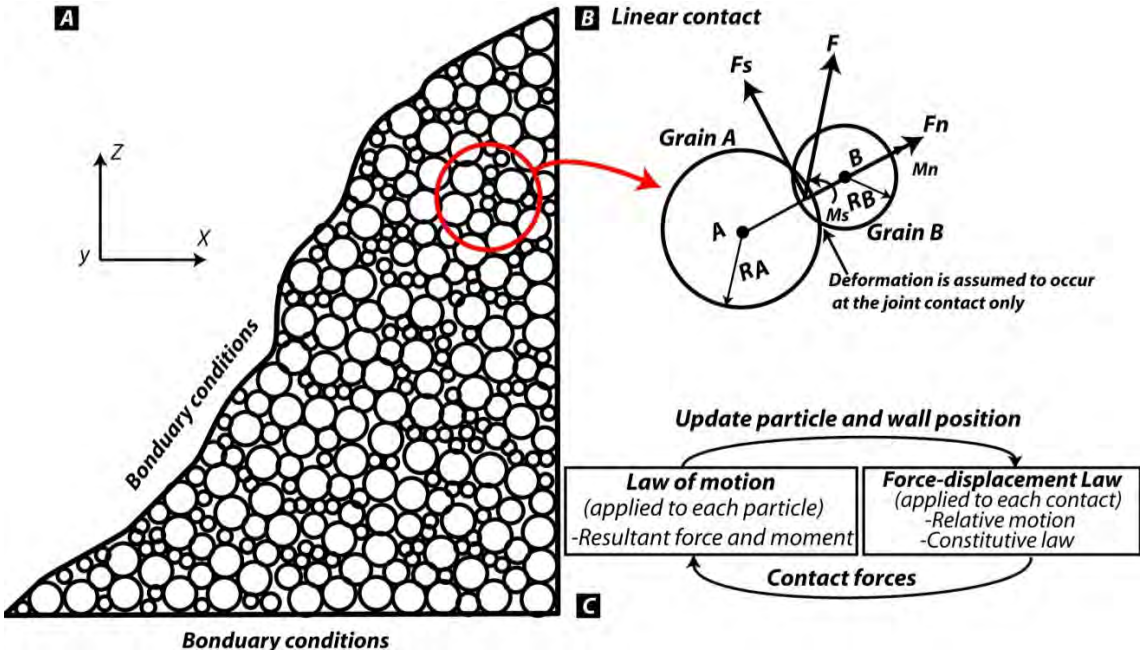

Figure 2.5-9: Example of bonded particle method discretization of a 2D slope. b) Contact logic of interacting particle used in BPM code PFC2D (adapted from Itasca 2004). c) Calculation steps in commercial code PFC2D (from Itasca 2004).

According to Eberhardt (2003) this approach allows an accurate modelling of the different phase of a rock slope destabilisation phases that include a granular-like behaviour since the pre-failure rupture to the transportation and the deposition phases. In particular, the capability of this approach to simulate fracture of intact rock through breaking of particle bonds, represent an important development to model progressive failure in heavily jointed rock slopes (Stead et al., 2006).

Early applications of rock slope analysis were proposed by Wang et al. (2003). These authors highlighted the capability of BPM technique to provide a full insight into the thorough process of rock slope destabilization (Wang et al., 2003). Utili and Nova (2008) developed a new contact bond model based on Mohr-Coulomb failure criterion. They validated the BPM approach by comparing it with classical limit equilibrium analysis and they proposed a complete model for a progressive slope destabilisation through weathering (Figure 2.5-10).

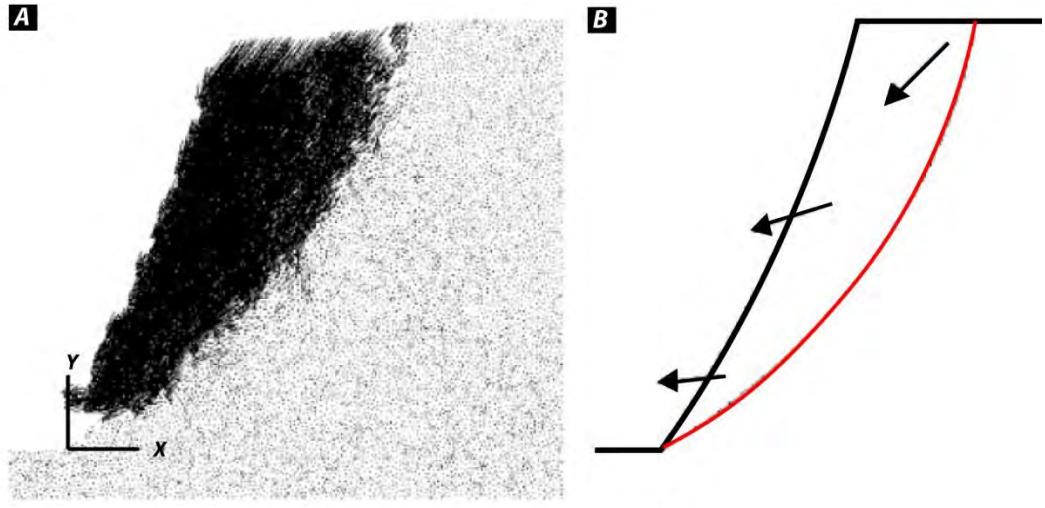

Figure 2.5-10: Comparison between particle velocity obtained using PFC modelling and failure surface (red line) obtained by limit equilibrium analysis for a hypothetical slope subject to uniform weathering (from Utili and Nova 2008).

Utili and Crosta (2011) compared BDM technique and classical limit analysis approach to analyze the evolution of natural cliff retreat subject to weathering. These authors highlighted the possibility of BPM technique to quantitatively associate the evolution of natural slopes to the degradation of strength properties of the intact rock with time (Utili and Crosta 2011). The BPM technique has been successfully applied also to model the propagation of large rock slope failure. Poisel et al. (2008) proposed a detailed back-analysis of the Punta Thurwieser rock avalanche and Frank slide by comparing results obtained using PFC3D and DAN3D (McDougall and Hungr 2004). The authors highlighted the great influence for both techniques of the early characterization of the run-out behavior and of the choice of appropriate mechanical parameters to obtain consistent simulations (Poisel et al., 2008).

2.5.3 HYBRID APPROACHES

In the recent years, new typologies of numerical technique called “hybrid techniques” are progressively being adopted to analyse rock slope stability. This technique combines the advantages of both continuum and discontinuum techniques allowing analysing complex rock slope failures involving displacements along pre-existing joint sets and progressive fracturing the intact rock. As suggested by Stead et al. (2006),

both continuum and discontinuum approaches only "imitate" the progressive fracturing of the intact rock but they do not respect strictly the basic principles related to brittle fracture mechanics. Conversely, hybrid techniques such as FEM/DEM codes can incorporate fracture mechanics principles and model explicitly the initiation and development of new fractures. At present-day, only few rock slopes have been analysed using hybrid FEM/DEM techniques. This is principally related to the difficulty to estimate the input parameters (damping factors; fracture energy release rate) for a real case study.

An early application of hybrid modelling was proposed by Eberhardt et al. (2004) to describe the failure mechanism of the Randa rockslide (Switzerland). These authors highlighted the difficulty in modelling the progressive sliding surface development with standard numerical approaches and proposed the implementation of FEM/DEM hybrid techniques to describe the link between initiation and degradation processes leading to the catastrophic failure of the Randa (Figure 2.5-11). Recently, Vyazmensky et al. (2010) adopted a hybrid finite/discrete element technique incorporating a coupled elasto-plastic constitutive criterion to analyse the subsidence development in open pit mines. Based on numerical experiment, the authors emphasized the importance of joint sets orientation and fault location on the subsidence mechanisms and the role of geological structure in defining the degree of surface subsidence asymmetry (Vyazmensky et al., 2010).

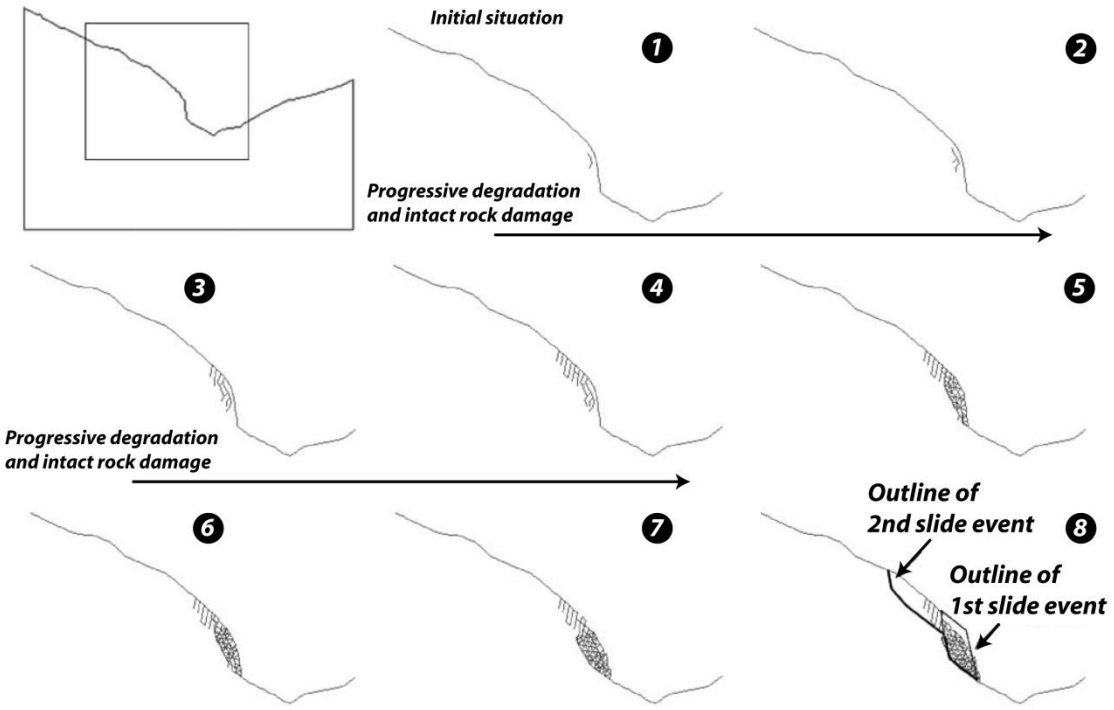

Figure 2.5-11: Example of hybrid FEM/DEM rock slope degradation model reproducing the progressive failure characterizing the 1991 Randa rockslide (modified from Eberhardt et al., 2004).

2.6 REFERENCES

Abellan, A., Vilaplana, J. M., Martinez, J. 2006. Application of a long-range terrestrial laser scanner to a detailed rockfall study at Vall de Nuria (Eastern Pyrenees, Spain), *Engineering Geology*, 88, 136-148.

Abellan, A., Jaboyedoff, M., Oppikofer, T., Vilaplana, JM. 2009. Detection of millimetric deformation using a terrestrial laser scanner: experiment and application to rockfall event, *Nat. Hazards Earth Syst Sci.*, 9, 365–372.

Abellan, A., Vilaplana, JM., Calvet, J., Blanchard, J. 2010. Detection and spatial prediction of rockfalls by means of terrestrial laser scanning modeling, *Geomorphology*, 119, 162–171.

Abele, G. 1974. Bergstürze in den Alpen, *Wiss. Alpenvereinshefte*, 25, 1–230.

Agliardi, F., Crosta, G., Zanchi, A. 2001. Structural constraints on deep-seated slope deformation kinematics, *Engineering Geology*, 59, 83-102.

Agliardi, F., Crosta, G. 2003. High resolution three-dimensional numerical modeling of rockfalls, *Int. J. Rock. Mech. Min*., 40, 455–471.

Agliardi, F., Zanchi A., Crosta, G. 2009a. Tectonic vs. gravitational morphostructures in the central Eastern Alps (Italy): Constraints on the recent evolution of the mountain range, *Tectonophysics*, 474, 250-270.

Agliardi, F., Crosta, G., Zanchi, A., Ravazzi, C. 2009b. Onset and timing of deep-seated gravitational slope deformations in the Eastern Alps, Italy, *Geomorphology,* 103, 113–129.

Ambrosi, C., Crosta, G.B. 2006. Large sackung along major tectonic features in the Central Italian Alps, *Engineering Geology*, 83, 183–200.

Ambrosi, C., Crosta, G.B. 2011. Valley shape influence on deformation mechanisms of rock slopes. In: Jaboyedoff, M. (ed.) *Slope Tectonics*, Geological Society, London, Special Publications, 351, 215–233.

Antinao, J.L., Gosse, J. 2009. Large rockslides in the Southern Central Andres of Chile (32-34.5°S): Tectonic control and significance for quaternary landscape evolution, *Geomorphology*, 104, 117-133.

Baltsavias, E.P., 1999. Airborne laser scanning: Basic relations and formulas, *ISPRS Journal of Photogrammetry and Remote Sensing*, 54, 199-214.

Baldi, P., Cenni, N., Fabris, M., Zanutta, A. 2008. Kinematics of a landslide derived from archival photogrammetry and GPS data*, Geomorphology*, 102, 435-444.

Barla, G., Atolini, F., Barla, M., Mensi, E., Piovano, G. 2010. Monitoring of the Beauregard landslide (Aosta Valley, Italy) using advanced and conventional techniques, *Engineering geology*, 116, 218-235.

Barletta, V.R., Ferrari, C., Diolaiuti, G., Carnielli, T., Sabadini, R., Smiraglia, C. 2006. Glacier shrinkage and modeled uplift of the Alps*, Geophysical Research Letters*, 33, L14307.

Bachmann, D., Bouissou, S., Chemenda, A. 2004. Influence of weathering and preexisting large scale fractures on gravitational slope failure: insights from 3-D physical modeling, *Natural Hazards and Earth System Sciences,* 4, 711–717.

Bachmann, D., Bouissou, S., Chemenda, A., 2006. Influence of large scale topography on gravitational rock mass movements: new insights from physical modeling, *Geophysical Research Letters*, 33, L21406.

Beck, A.C., 1968. Gravity faulting as a mechanism of topographic adjustment, *New Zealand Journal of Geology and Geophysics*, 11, 191–199.

Blair, T.C., Mc Pherson, E. 1994. Alluvial fan processes and forms. *In geomorphology of desert Environments*, Edited by A.D. Abrahams and A.J. Parsons. Chapman and Hall, London.

Bobet, A. 2010. Numerical method in geomechanics, *The Arabian Journal for Science and Engineering*, 35, 1B.

Bois, T., Bouissou, S., Guglielmi, Y., 2008. Influence of major inherited faults zones on gravitational slope deformation: A two-dimensional physical modelling of the La Clapière area (Southern French Alps), *Earth and Planetary Science Letters*, 272, 709–719.

Bouissou, S., Bois, T., Jaboyedoff, M. *In Press*. Influence of structural heterogeneities and of large scale topography on imbricate gravitational rock slope failures: New insights from 3-D physical modelling and geomorphological analysis, *Tectonophysics*, DOI: 10.1016/j.tecto.2011.08.001.

Bovis, M. J. 1982. Uphill-facing (antislope) scarps in the Coast Mountains, southwest British Columbia*. Geol. Soc. Am. Bull*., 93, 804-812.

Blikra, L. H. 2008. The Aknes rockslide; monitoring, threshold values and early warning, In: Chen, Z., Zhang, J.-M., Ho, K., Wu, F.-Q. & Li, Z.-K. (eds) *Landslides and Engineered Slopes*. From the Past to the Future: Proceedings of the 10th International Symposium on Landslides and Engineered Slopes, 30 June–4 July 2008, Xi'an, China. CRC Press, Baton Rouge, FL.

Bozzano, F., Cipriani, I., Mazzanti, P., Prestinizi, A. 2011. Displacement patterns of a landslide affected by human activities: insights from ground-based InSAR monitoring, *Natural Hazards*, DOI 10.007/s11069-011-9840-6

Braathen, A., Blikra, L. H., Berg, S. S., Karlsen, F. 2004. Rock-slope failures in Norway; Type, geometry, deformation mechanisms and stability, *Norw. J. Geol*., 84, 67–88.

Brideau, M.-A., Stead, D., Kinakin, D., Fecova, K. 2005. Influence of tectonic structures on the Hope Slide, British Columbia, Canada, *Engineering Geology*, 80, 342–359.

Brideau, M.-A., Stead, D., Couture, R. 2006. Structural and engineering geology of the East Gate Landslide, Purcell Mountains, British Columbia, Canada, *Engineering Geology*, 84, 183-206.

Brideau, M.-A., Stead, D., Roots, C., Orwin, J. 2007. Geomorphology and engineering geology of a landslide in ultramafic rocks, Dawson City, Yukon, *Engineering Geology*, 89, 171-194.

Brideau, M-A., Ming, Y., Stead, D. 2009. The role of tectonic damage and brittle rock fracture in the development of large rock slope failure, *Geomorphology*, 103, 30-49.

Brideau, M.A., Pedrazzini, A., Stead, D., Froese, C.R., Jaboyedoff, M., Van Zeyl, D. 2011, Three dimensional slope stability analysis of South-Peak, Crowsnest Pass, Alberta, Canada, *Landslides*, 8, 139-158.

Brideau, M.A., Sturzenegger, M., Stead, D., Jaboyedoff, M., Lawrence, M., Roberts, N.J., Ward, B.C., Millard, T.H., Clague, J.J. *In Press*. Stability analysis of the 2007 Chehalis Lake landslide based on long-range terrestrial photogrammetry and airborne-LiDAR data, *Landslides*, DOI 10.1007/s10346-011-0286-4.

Brückl, E., Brunner F.K., Kraus K. 2006. Kinematics of a deep-seated landslide derived from photogrammetric, GPS and geophysical data*, Engineering Geology*, 88, 149-159.

Burns, W.J., Coe, J.A., Kaya, B.S., Ma, L. 2010. Analysis of elevation changes detected from multi-temporal LiDAR surveys in forested landslide terrain in western Oregon, *Environmental Engineering Geoscience*, 16, 315–341.

Bye, A.R., Bell, F.G. 2001. Stability assessment and slope design at Sandsloot open pit, South Africa, *Int. J. Rock Mech. Min. Sci.,* 38, 449–466.

Canuti, P., Casagli, N., Ermini, L., Fanti, R., Farina, P. 2004. Landslide activity as a geoindicator in Italy: significance and new perspectives from remote sensing, *Environmental Geology*, 45, 907-919.

Cardenal, J., Mata, E., Perez-Garcia J.L., Delgado, J., Hernandez, M.A., A. Gonzalez, Diaz-de-Teran, J.R. 2008. Close range digital photogrammetry techniques to landslides monitoring, *International archives of Photogrammetry and Remote Sensing*, Vol. XXXVII, Part B8, 235-240.

Carranza-Torres, C., Fairhurst, C., Lorig, L. 1997. Insights on the Stability of Large Excavations from Analytical and Numerical Models, *Felsbau*, 15, 45-63.

Carrara, A., Guzzetti, F., Cardinali, M., Reichenbach, P. 1999. Use of GIS Technology in the Prediction and Monitoring of Landslide Hazard, *Natural Hazards*, 20, 117-135.

Casagli, N., Catani, F., Del Ventisette, C., Luzi, G. 2010. Monitoring, prediction, and early warning using ground-based radar interferometry, *Landslides*, 7, 291-301.

Catani, F., Casagli, N., Ermini, L., Righini, G., Menduni, G. 2005. Landslide hazard and risk mapping at catchment scale in the Arno River basin*, Landslides*, 2, 329–342.

Champagnac, J.D., Molnar, P., Anderson, R.S., Sue, C., Delacou, B. 2007. Quaternary erosion-induced isostatic rebound in the western Alps, *Geology,* 35, 195–198.

Chandler, J.H., Moore, R. 1989. Analytical photogrammetry: a method for monitoring slope instability, *Quarterly Journal Engineering Geology,* 22, 97-110.

Chemenda, A., Bois, T., Bouissou, S., Tric, E. 2009. Numerical modeling of the gravity-induced destabilization of a slope: example of the Clapière landslide, southern France, *Geomorphology*, 109, 86-93.

Chau, K.T., Sze, Y.L., Fung, M.K., Wong, W.Y., Fong, E.L., Chan, L.C.P. 2004. Landslide hazard analysis for Hong Kong using landslide inventory and GIS, *Computers and Geosciences*, 30, 429–443.

Chen, Y., Medioni, G. 1992. Object Modeling by Registration of Multiple Range Images, *Image and Vision Computing*, 10, 145–155.

Chen, R.F., Chan, Y.C., Angelier, J., Hu, J.C., Huang, C., Chang, K.J., Shih, T.Y. 2005. Large earthquake-triggered landslides and mountain belt erosion: the Tsaoling case, Taiwan, *Comptes Rendues de Geoscience*, 337, 1164–1172.

Chigira, M. 1992. Long-term gravitational deformation of rocks by mass rock creep, *Engineering Geology*, 32, 157–184.

Chigira, M., Wang, W-N., Furuyac, T., Kamaia, T. 2003. Geological causes and geomorphological precursors of the Tsaoling landslide triggered by the 1999 Chi-Chi earthquake, Taiwan, *Engineering Geology*, 68, 259–273.

Chigira, M., Duan, F., Yagi, H., Furuya, T. 2004. Using airborne laser scanner for the identification of shallow landslides and susceptibility assessment in an area of ignimbrite overlain by permeable pyroclastics*, Landslides*, 3, 203-209.

Choffat, P. 1929. L'écroulement d'Arvel (Villeneuve) de 1922, *Bulletin de la Société Vaudoise des Sciences Naturelles*, 57, 5–28.

Chorowicz, J., Dhont, D., Gundogdu, N. 1999. Neotectonics in the eastern North Anatolian fault region (Turkey) advocates crustal extension: mapping from SAR ERS imagery and Digital Elevation Model, *J. of Structural Geology*, 21, 511-532.

Corsini, A., Borgatti, L., Cervi, F., Dahne, A., Ronchetti, F., Sterzai, P. 2009. Estimating mass-wasting processes in active earth slides–earth flows with time-series of High- Resolution DEMs from photogrammetry and airborne LiDAR, *Natural Hazards Earth System Science*, 9, 433–439.

Clarke, B.A., Burbank, D.W. 2010. Bedrock fracturing, threshold hillslopes and limits to the magnitude of bedrock landslide, *Earth and Planetary Science Letters*. 297, 577-585.

Coe, J.A., Harp, E. L. 2007. Influence of tectonic folding on rockfall susceptibility, American Fork Canyon, Utah, USA, *Natural Hazards and Earth System Sciences*, 7, 1–14.

Coggan, J.S., Stead, D., Eyre, J.M. 1998. Evaluation of techniques for quarry slope stability assessment, *Transaction of the Institution of Mining and Metallurgy-Section B*, 107, B139-B147.

Colesanti, C., Wasowski, J. 2006. Investigating landslides with space-borne Synthetic Aperture Radar (SAR) interferometry, *Engineering geology*, 88, 173-199.

Cooper, M. 1992. The analysis of fracture systems in subsurface thrust structures from the Foothills of the Canadian Rockies. In McClay, K. R. (Ed), *Thrust Tectonics*, Chapman and Hall London, 391–405.

Crosta, G.B., Agliardi, F., Frattini, P., Zanchi, A. 2008. Alpine inventory of Deep-Seated Gravitational Slope Deformations, *Geophysical Research Abstracts*, Vol. 10, EGU2008-A-02709.

Crosta, G.B., Imposimato, S., Roddeman, D. 2009. Numerical modeling of entrainment/deposition in rock and debris-avalanches*, Engineering Geology*, 109, 135–145.

Cruden, D.M., Varnes, D.J. 1996. Landslide types and processes. In: Turner, A.K.; Shuster, R.L. (eds) *Landslides: Investigation and Mitigation*, Transp Res. Board, Spec Rep*.,* 247, 36–75.

Cundall, P.A. 1971. A computer model for simulating progressive large scale movements in blocky rock systems, *Proceedings of the symposium of the international society of rock mechanics (Nancy, France, 1971)*, Vol. 1, Paper No. II-8.

Cundall, P. 1976. Explicit Finite Difference Methods in Geomechanics in Numerical Methods in Engineering, *Proceedings of the EF Conference on Numerical Methods in Geomechanics*, Blacksburg, Virginia, Vol. 1, pp. 132-150.

Cullman, C. 1875 *Die Graphische Statik*, Meyer und Zeller, Zürich, 329 pp.

Dawson, E.M., Roth, W.H., Drescher, A., 1999. Slope stability analysis by strength reduction, *Geotechnique*, 49, 835-840.

Del Ventisette, C., Intrieri, E., Luzi, G., Casagli, N., Fanti, R., Leva, D. 2011. Using ground based radar interferometry during emergency: the case of A3 motorway (Calabria Region, Italy) threatened by a landslide, *Nat. Hazards Earth Syst. Sci.*, 11, 2483- 2495.

Densmore, A. L., Anderson, R. S, McAdoo, B. G., Ellis, M. A. 1997. Hillslope evolution by bedrock landslides, *Science*, 75, 369-372.

Derron, M.-H., Jaboyedoff, M., Blikra, L. H. 2005. Preliminary assessment of rockslide and rockfall hazards using a DEM (Oppstadhornet, Norway), *Nat. Hazards Earth Syst. Sci.*, 5, 285–292.

Derron, M.H., Jaboyedoff, M., Pedrazzini, A., Michoud, C., Villemin, T. 2011. Remote Sensing and Monitoring Techniques for the Characterization of Rock mass de formation and Change Detection. In: Lambert S., Nicot, F., *Rockfall engineering*, 39-65.

Dewez, T., Gebrayel, D., Lhomme, D., Robin, Y. 2009. Quantification de l'évolution des côtes sableuses et rocheuses par photogrammétrie et lasergrammétrie, *La Houille Blanche*, 1, 32-37.

Dorren, L., Seijmonsbergen, A. 2003. Comparison of three GIS-based models for predicting rockfall runout zones at a regional scale, *Geomorphology*, 56, 49–64.

Dramis, F., Sorriso-Valvo, M. 1994. Deep-seated gravitational slope deformations, related landslides and tectonics, *Engineering Geology*, 38, 231-243.

Dufresne, A. 2009. Influence of runout path material on rock and debris avalanches mobility: field evidences and analogue modeling, PhD thesis, University of Canterbury, 268 p.

Dufresne, A., Davies, T.R., 2009. Longitudinal ridges in mass movement deposits, *Geomorphology*, 105, 171–181.

Dufresne, A., Salinas, S., Siebe, C. 2010. Substrate deformation associated with the Jocotitlán edifice collapse and debris avalanche deposit. Central México, *Journal of Volcanology and Geothermal Research,* 197, 133-148.

Dussauge, C., Grasso, J.-R., Helmstetter, A. 2003. Statistical analysis of rockfall volume distributions: Implications for rockfall dynamics, *J. Geophys. Res.*, 108, 2286.

Eberhardt, E. 2003. Rock Slope Stability Analysis-Utilization of Advanced Numerical Techniques. Available online on http://www.eos.ubc.ca/personal/erik/e-papers/EE-SlopeStabilityAnalysis.pdf.

Eberhardt, E., Stead, D., Coggan, J. S. 2004 Numerical analysis of initiation and progressive failure in natural rock slopes–the 1991 Randa rockslide, *Int. J. of Rock Mech. Min.*, 41, 69–87.

Eberhardt, E., Thuro, K. Luginbuehl, M. 2005. Slope instability mechanisms in dipping interbedded conglomerates and weathered marls—the 1999 Rufi landslide, Switzerland, *Engineering Geology*, 77, 35-56.

Eberhardt, E., Bonzanigo, L., Loew, S. 2007. Long-term investigation of a deep-seated creeping landslide in crystalline rock – Part 2: Mitigation measures and numerical modelling of deep drainage at Campo Vallemaggia, *Canadian Geotechnical Journal*, 44, 1181-1199.

Fabbri, A.G., Chung, C.-J. F., Cendrero, C., Remondo, J. 2003. Is Prediction of Future Landslides Possible with a GIS? *Natural Hazards*, 30, 487-503.

Fasani, G.B., Esposito, C., Maffei, A., Mugnozza, G.S., Evans, S.G. 2004. Geological controls on initial failure mechanisms of rock avalanches in central Apennines (Italy), In: Larceda, E., Fontoura, Sayao (Eds.), *Landslides: Evaluation and Stabilization*, Balkema, Rotterdam, Rio de Janeiro, 501–507.

Fekete, S., Diederichs, M., Lato, M. 2010. Geotechnical and operational applications for 3-dimensioanl laser scanning in drill and blast tunnels, *Tunnelling and Underground Space Technology*, 25, 614-628.

Ferretti, A., Prati, C., Rocca, F. 2000. Nonlinear subsidence rate estimation using Permanent Scatters in Differential SAR Interferometry, *IEEE Trans. Geosci. Remote Sens.*, 38, 2202-2212.

Ferretti, A., Fumagalli, A., Novali, F, Prati, C., Rocca, F., Rucci, A. 2011. A new algorithm for processing interferometric data-stacks: SqueeSAR™, *IEEE Trans. Geosci. Remote Sens.,* 10.1109/TGRS.2011.2124465.

Fischer, L., Amann, F., Moore, J., Huggel, C. 2010. Assessment of periglacial slope stability for the 1988 Tschierva rock avalanche (Piz Morteratsch, Switzerland), *Engineering Geology*, 116, 32–43.

Forcella, F., Orombelli, G. 1984. Holocene slope deformations in Valfurva, Central Alps, Italy, *Geografia Fisica e Dinamica Quaternaria*, 7, 41–48.

Forlati, F., Gioda, G., Scavia, C. 2001. Finite element analysis of a deep-seated slope deformation, *Rock Mechanics and Rock Engineering*, 34, 135–159.

Fornaro, G., Pauciullo, A., Serafino, F. 2009. Deformation Monitoring over large areas with Multipass Differential SAR Interferometry: a new approach based on the use of Spatial Differences, *Int. Journal of Remote Sens.*, 30, 1455-1478.

Frayssines, M., Hantz, D. 2006. Failure mechanisms and triggering factors in calcareous cliffs of the Subalpine Ranges (French Alps), *Engineering Geology*, 86, 256-270.

Frattini, P., Crosta, G., Carrara, A., Agliardi, F. 2008. Assessment of rockfall susceptibility by integrating statistical and physically based approaches, *Geomorphology*, 94, 419–437.

Froese, C. Poncos, V. Skirrow, R. Mansour, R. Martin, D. 2008. Characterizing Complex Deep Seated Landslide Deformation using Corner Reflector InSAR: Little Smoky Landslide, Alberta, *Proceedings 4th Canadian Conference on Geohazards*, Quebec City, 287-293.

Galli, M., Ardizzone, F., Cardinali, M., Guzzetti, F., Reichenbach P. 2008. Comparing landslide inventory maps, *Geomorphology*, 94, 268-289.

Ghirotti, M., Martin, S., Genovois, R. 2011. The Celentino deep-seated gravitational slope deformation (DSGSD): structural and geomechanical analyses (Peio Valley, NE Italy). *In Slope Tectonics*, ed. M. Jaboyedoff, Geological Society, London, Special Publications, 351, 235–252.

Gigli, G., Casagli, N. 2011. Semi-automatic extraction of rock mass structural data from high resolution LIDAR point clouds, *International journal of rock mechanics and mining sciences*, 48, 187-198.

Gigli, G., Fanti, R., Canuti, P., Casagli, N. 2011. Integration of advanced monitoring and numerical modeling techniques for the complete risk scenario analysis of rockslides: the case of Mt. Beni (Florence, Italy), *Engineering geology*, 18, 48-59.

Gischig, V., Loew, S., Kos, A., Moore, J. R., Raetzo, H., Lemy, F. 2009. Identification of active release planes using ground-based differential InSAR at the Randa rock slope instability, Switzerland, *Nat. Hazards Earth Syst. Sci*., 9, 2027–2038.

Gischig, V., Amann, F., Moore, J. R., Loew, S., Eisenbeiss, H., Stempfhuber, W. 2011. Composite rock slope kinematics at the current Randa instability, Switzerland, based on remote sensing and numerical modeling, *Engineering Geology,* 118, 37–53.

Gischig, V. S., Moore, J. R., Evans, K. F., Amann, F., Loew S. 2011b. Thermomechanical forcing of deep rock slope deformation: 1. Conceptual study of a simplified slope, *J. Geophys. Res*., 116, F04010.

Gischig, V. S., Moore J. R., Evans, K. F., Amann, F., Loew, S. 2011c. Thermomechanical forcing of deep rock slope deformation: 2. The Randa rock slope instability, *J. Geophys. Res.*, 116, F04011.

Grelle, G., Revellino, P., Donnarumma, A., Guadagno, F. M. 2011. Bedding control on landslides: a methodological approach for computer-aided mapping analysis, *Nat. Hazards Earth Syst. Sci.*, 11, 1395–1409.

Guadagno, F.M., Martino, S., Scarascia Mugnozza, G., 2003. Influence of man-made cuts on the stability of pyroclastic covers (Campania, southern Italy): a numerical modeling approach, *Environmental Geology*, 43, 371– 384.

Günther, A. 2003. SLOPEMAP: programs for automated mapping of geometrical and kinematical properties of hard rock hill slopes, *Computer and Geosciences*, 29, 865–875.

Guthrie, R.H., Evans, S.G. 2004. Analysis of landslide frequencies and characteristics in a natural system, coastal British Columbia. *Earth Surface Processes and Landforms*, 29, 1321–1339.

Guzzetti, F., Cardinali, M., Reichenbach, P., Carrara, A. 2000. Comparing landslide maps: A case study in the upper Tiber River Basin, central Italy, *Environmental Management*, 25, 247-363.

Guzzetti, F., 2005. Landslide hazard and risk assessment. PhD thesis, Universität Bonn, 389 p.

Guzzetti, F., Ardizzone, F., Cardinali, M., Rossi, M., Valigi, D. 2009. Landslide volumes and landslide mobilization rates in Umbria, central Italy, *Earth and Planetary Science Letters*, 279, 222–229.

Habib, A. 2008. Accuracy, quality assurance and quality control of LIDAR data, Chap 9. In: Shan J, Toth CK (eds) *Topographic laser ranging and scanning: principles and processing*, CRC Press, Taylor and Francis, pp 269–294.

Haneberg, W.C. 2008. Using close range terrestrial digital photogrammetry for 3-D rock slope modeling and discontinuity mapping in the United States, *Bulletin of Engineering Geology and the Environment*, 67, 457-469.

Hammah, R.E., Yacoub, T.E., Corkum, B., Curran, J.H. 2008. The Practical Modelling of Discontinuous Rock Masses with Finite Element Analysis, *Proceedings of the 42nd U.S. Symposium on Rock Mechanics and the 2nd U.S.-Canada Rock Mechanics Symposium*, San Francisco, California, USA.

Hammah, R.E., Yacoub, T., Curran J.H. 2009. Variation of Failure Mechanisms of Slopes in Jointed Rock Masses with Changing Scale, *Proceedings of the CIM 2009 Conference,* Toronto, Ontario, Canada.

Hantz, D., Dussauge-Peisser, C., Jeannin, M., Vengeon, J.M. 2002. Danger d'éboulements rocheux : de l'opinion d'expert à une évaluation quantitative. *Symp. Geomorphology: from expert opinion to modelling, Strasbourg*, 115-122.

Hantz, D., Dussauge-Peisser, C., Jeannin, M., Vengeon, J.-M. 2003. Rock fall hazard assessment: from qualitative to quantitative failure probability, in: *Int. conf. on Fast Slope Movements*, Naples, 263–267.

Harp, E.L., Keefer, D.K., Sato, H.P., Yagi, H. 2011. Landslide inventories: the essential part of seismic landslide hazard analyses, *Engineering Geology*, 122, 9-21.

Hatzor, Y.H., Arzib, A.A., Zaslavskyc, Y., Shapirad, A. 2004. Dynamic stability analysis of jointed rock slopes using the DDA method: King Herod's Palace, Masada, Israel, *International Journal of Rock Mechanics and Mining Sciences,* 41, 813–832.

Haugerud, R.A., Harding, D.J., Johnson, S.Y., Harless, J.L., Weaver, C.S., Sherrod, B.L. 2003. High-resolution Lidar topography of the Puget Lowland, Washington—A Bonanza for earth science, *GSA Today,* 13, 4–10.

Heim, A. 1932. Bergsturz und Menschenleben, Fretz und Wasmuth, Zürich, 218 p.

Hewitt, K. 2002. Styles of rock avalanche depositional complex in very rugged terrain, Karakoram Himalaya, Pakistan. In Evans S.G. (ed.) *Catastrophic Landslides: effects, occurrence and mechanisms*, Reviews in Engineering Geology. Geological Society of America, Boulder, Colorado, 345-378.

Henderson, I.H., Lauknes, T.R., Osmundsen, P.T., Dehls, J., Larsen, Y., Redfield, T.F. 2011. A structural, geomorphological and InSAR study of an active rock slope failure development, *Slope Tectonics*, Geological Society, London, Special Publications, 351, 185–189.

Hermanns, R.L., Trauth, M. H., Niedermann, S., McWilliams, M., Strecker, M. R. 2000. Tephrochronologic constraints on temporal distribution of large landslides in Northwest Argentina, *Journal of Geology*, 108, 1, 35-52.

Hermanns, R., Niedermann, S., Villanueva, Garcia A., Gomez, JS., Strecker MR. 2001. Neotectonics and catastrophic failure of mountain fronts in the southern intra-Andean Puna Plateau, Argentina, *Geology,* 29, 619–623.

Hermanns, R.L., Niedermann, S., Villanueva Garcia, A., Schellenberger, A. 2006. Rock avalanching in the NW Argentine Andes as a result of complex interactions of lithologic, structural and topographic boundary conditions, climate change and active tectonics, in Evans, S.G., Scarascia Mugnozza, G., Strom, A., and Hermanns, R.L., eds., *Landslides from Massive Rock Slope Failure*, Netherlands, NATO Science Series, Springer, v. 49, p. 497–520.

Hippolyte, J.C., Brocard, G., Tardy, M., Nicoud, G., Bourlès, D., Braucher, R., Ménard, G., Souffaché, B. 2006. The recent fault scarps of the Western Alps (France): Tectonic surface ruptures or gravitational sackung scarps? A combined mapping, geomorphic, levelling, and 10Be dating approach, *Tectonophysics,* 418, 255–276.

Hoek, E., Grabinsky, M.W., Diderichs, M.S. 1993. Numerical modeling for underground excavations, *Transaction of the Institutions of Mining and Metallurgy*, Section A, 100, A22-A30.

Hoek, E., Brown, E.T., 1997. Practical estimates of rock mass strength*, International Journal of Rock Mechanics and Mining Sciences*, 34, 1165–1186.

Hovius, N., Stark, C.P., Allen, P.A. 1997. Sediment flux from a mountain belt derived by landslide mapping, *Geology*, 25, 231-234.

Huggel, C., Zgraggen-Oswald, S., Haeberli, W., KääB, A., Polkvoj, A., Galushkin, I., Evans, S.G. 2005. The 2002 rock/ice avalanche at Kolka/Karmadon, Russian Caucasus: assessment of extraordinary avalanche formation and mobility, and application of Quick-Bird satellite imagery*, Nat. Hazards Earth Sys. Sci.*, 5, 173–187.

Humair, F., Charrière, M., Pedrazzini, A., Güell I Pons, M., Volpi, M., Foresti, L., Jaboyedoff, M., Epard, J.-L.andFroese, C.R. 2010. The Frank Slide (Alberta, Canada). From the contributing factors to the processes of propagation. In *Proceedings of the 63rd International Canadian Geotechnical Conference & 6th Canadian Permafrost Conference*, Calgary, Alberta, Canada.

Hungr, O., Evans S.G., Hazzard, J. 1999. Magnitude and frequency of rock falls and rock slides along the main transportation corridors of southwestern British Columbia, *Canadian Geotechnical Journal,* 36, 224–238.

Hutchinson, J.N. 1995. Landslide hazard assessment. In: *Proceeding VI Int. Symp. on Landslides*, Christchurch, 1, 1805–1842.

Issler, D., De Blasio, F. V., Elverhoi, A., Bryn, P., Lien, R. 2005. Scaling behavior of clay-rich submarine debris flows, *Mar. Pet. Geol.*, 22, 187–194.

Itasca. 2004. Itasca Software Products—FLAC, FLAC3D, UDEC, 3DEC, PFC, PFC3D. Itasca Consulting Group Inc., Minneapolis.

Jaboyedoff, M., Baillifard, F., Derron, M.-H. 2003a. Preliminary note on uplift rates gradient, seismic activity and possible implications for brittle tectonics and rockslide prone areas: The example of western Switzerland, *Bull. Soc. Vaud. SC. Nat.,* 88, 393-412.

Jaboyedoff, M., Baillifard, F., Philippossian, F., Rouiller, J.-D. 2003b. Assessing the fracture occurrence using the "Weighted fracturing density": a step towards estimating rock instability hazard, *Nat. Haz. Earth Sys. Sci.*, 4, 83–93.

Jaboyedoff, M., Baillifard, F., Couture, R., Locat, J., Locat, P. 2004. New insight of geomorphology and landslide prone area detection using DEM. In: Lacerda WA, Ehrlich M, Fontoura A.B., Sayao, A. (eds) *Landslides evaluation and stabilization*, Balkema, 191–197.

Jaboyedoff, M., Derron, M.-H. 2005. Hazard assessment within an Integrated Risk Assessment Process for Landslides, (IRAPL). Proc., *International Conference on Landslide Risk Management*, Vancouver, Balkema, 187-197.

Jaboyedoff, M., Metzger, R., Oppikofer, T., Couture, R., Derron, M.H., Locat. J., Durmel, D. 2007. New insight techniques to analyze rock-slope relief using DEM and 3D-imaging clouds points: COLTOP-3D software. In: Eberhardt E, Stead, D., Morrison, T. (eds): *Rock mechanics: meeting society's challenges and demands*, Taylor and Francis, London, 61–68.

Jaboyedoff, M., Pedrazzini, A., Horton, P., Loye, A., Surace, I. 2008. Preliminary slope mass movements susceptibility mapping using LIDAR DEM, *Proceedings of 61st Canadian Geotechnical Conference*, Edmonton, Alberta, Canada, 419–426.

Jaboyedoff, M., Couture, R., Locat, P. 2009. Structural analysis of Turtle Mountain (Alberta) using Digital Elevation Model: Toward a progressive failure, *Geomorphology*, 103, 5-16.

Jaboyedoff, M., Oppikofer, T., Abellan, A., Derron, M-H., Loye, A., Metzger, R., Pedrazzini, A. 2010. Use of LIDAR in landslide investigations: a review. *Nat Hazards*, doi:10.1007/s11069-010-9634-2.

Jaboyedoff, M., Oppikofer, T., Derron, M.-H., Böheme, M., Blikra, L. H., Saintot, A. 2011. Complex landslide behavior and structural control: a three-dimensional conceptual model of Aknes rockslide, Norway. From: Jaboyedoff, M. (ed.) *Slope Tectonics*. Geological Society, London, Special Publications, 351, 1-10.

Jibson, R.W., Harp, E.L., Schulz, W., Keefer, D.K., 2006. Large rock avalanches triggered by the M 7.9 Denali Fault, Alaska, earthquake of 3 November 2002, *Engineering Geology,* 83, 144–160.

Jing, L. 2003. A review of techniques, advances and outstanding issues in numerical modelling for rock mechanics and rock engineering, *Int. J. Rock Mech. Min. Sci.*, 40, 253–283.

Jomard, H., 2006. Analyse multi-échelles des déformations gravitaires du Massif de l'Argentera Mercantour. Ph.D. Thesis, Sophia-Antipolis University, Nice, 217 p.

Jones, P. B. 1993. Structural geology of the modern Frank Slide and ancient Bluff Mountain Slide, Crownest, Alberta, *Bulletin of Canadian Petroleum Geology*, 41, 232–243.

Jackson, L.E., 2002. Landslides and landscape evolution in the Rocky Mountains and adjacent Foothills area, Southwestern Alberta, Canada. *Reviews in Engineering Geology,* XV, 325–344.

Kahle, H.G., Geiger, A., Buerki, B., Gubler, E., Marti, U., Wirth, B., Rothacher, M., Gurtner, W., Beutler, G., Bauersima, I., Pfiffner, O.A.1997. Recent crustal movements, geoid and density distribution; contribution from integrated satellite and terrestrial measurements. In: Pfiffner O.A., Lehner P, Heitzmann, P, Mueller, S, Steck, A (eds) *Deep structure of the Swiss Alps: results of NRP20,* Birkhäuser Verlag, Basel, 251–259.

Kalenchuk, K.S., Hutchinson, D.J., Diederichs, M.S. 2009. Influence of shear surface geometry on deformation processes in massive landslides, *Proceedings of the 3rd Canada-US Rock Mechanics Symposium, 20th Canadian Rock Mech. Symposium*, Toronto, May, 10 p.

Kastrup, U., Zoback, M. L., Deichmann, N., Evans, K., Giardini, D., Michael, A. J. 2004. Stress field variations in the Swiss Alps and the northern Alpine foreland derived from inversions of fault plane solutions. *J. Geophys. Res.*, 109, B01402.

Klar, A., E. Aharonov, Kalderon-Asael, B., Katz, O. 2011. Analytical and observational relations between landslide volume and surface area*, J. Geophys. Res.*, 116, F02001.

Kääb, A., Haeberli, W., Gudmundsson, G.H. 1997. Analyzing the creep of mountain permafrost using high precision aerial photogrammetry: 25 years of monitoring Gruben Rock glacier, Swiss Alps. *Permafrost and Periglacial Process*, 8, 409-426.

Kääb, A., Huggel, C., Fischer, L., Guex, S., Paul, F., Roer, I., Salzmann, N., Schlaefli, S., Schmutz, K., Schneider, D., Strozzi, T., and Weidmann, Y. 2005. Remote sensing of glacier- and permafrost-related hazards in high mountains: an overview*, Natural Hazards and Earth System Sciences*, 5, 527–554.

Kemeny, J., Turner, K. 2008. *Ground based LIDAR. Rock slope Mapping and assessment*, Technical report of the Central Federal Lands Highway Division US Department of Transportation, FHWA-CFL/TD-08-006.

Keefer, DK. 1984. Landslides caused by earthquakes, *Geological Society of America Bulletin*, 95, 406–421.

Keefer, DK. 1994. The importance of earthquake-induced landslides to long-term slope erosion and slope-failure hazards in seismically active regions, *Geomorphology*, 10, 265–284.

Kellogg, K.S. 2001. Tectonic controls on a large landslide complex: William Fork Mountains near Dillon, Colorado, *Geomorphology,* 41, 355–368.

Kinakin, D., Stead, D. 2005. Analysis of the distributions of stress in natural ridge forms: implications for the deformation mechanisms of rock slopes and the formation of Sackung, *Geomorphology,* 65, 85-100.

Koons, P.O. 2009. On the implications of low spatial correlation of tectonic and climate variables in the western European Alps, *Geology*, 37, 863–864.

Korup, O. 2006. Effects of deep-seated bedrock landslides on hillslope morphology, Southern Alps, New Zealand, *Journal of Geophysical Research,* 111, F01018.

Korup, O. 2005. Distribution of landslides in southwest New Zealand, *Landslides*, 2, 43-51.

Korup, O., Clague, J.J., Hermanns, R.L., Hewitt, K., Strom, A.L., Weidinger, J.T. 2007. Giant landslides, topography, and erosion, *Earth and Planetary Science Letters*, 261, 578–589.

Korup, O., Schlunegger, F. 2009. Rock-type control on erosion-induced uplift, eastern Swiss Alps*, Earth and Planetary Science Letters*, 278, 278-285.

Kveldsvik, V., Einstein, H.H., Nilsen, B., Blikra, L.H. 2009. Numerical analysis of the 650,000 m^2 Aknes rock slope based on measured displacements and geotechnical data, *Rock Mech. and Rock Eng., 42, 689-728.*

Lauknes, T.R., Piyush Shanker, A., Dehls, J.F., Zebker, H.A, Henderson, I.H.C., Larsen, Y. 2010. Detailed rockslide mapping in northern Norway with small baseline and persistent scatterer interferometric SAR time series methods, *Remote Sensing of Environment*, 114, 2097–2109.

Lorig, L., Varona, P. 2004. Numerical Analysis, in: *Rock Slopes—Civil and Mining Engineering* (Based on Rock Slope Engineering, 3rd Ed., 1977), Ch. 10. D. C. Wyllie and C. W. Mah, Compilers. London: Spon Press.

Loye, A., Jaboyedoff, M., Pedrazzini, A. 2009. Identification of potential rockfall source areas at a regional scale using a DEM based geomorphometric analysis, *Nat. Hazards Earth Syst. Sci.*, 9, 1643–1653.

Lugeon, M., Oulianoff, N. 1922. Sur le balancement superficiel des couches et sur les erreurs que ce phénomène peut faire commettre, *Bulletin de la Société Vaudoise des Sciences Naturelles*, 54, 381–388.

Lichti, D.D., Gordon, S.J., Stewart, M.P. 2002. Ground-Based Laser Scanners: Operations, Systems and Applications, *Geomatica*, 56, 21-33.

Lin, C.T., Amadei, B., Jung, J, Dwyer, J. 1996. Extensions of discontinuous deformation analysis for jointed rock masses, *Int. J. Rock. Mech. Min. Sci.,* 33, 671–94.

Lundgren, P., Usai, S., Sansosti, E., Lanari, R., Tesauro, M., Fornaro, G., Berardino, P. 2001. Modeling surface deformation observed with synthetic aperture radar interferometry at Campi Flegrei caldera, *Journal of Geophysical Research*, 106, 19355–19366, doi: 10.1029/2001JB000194.

Luzi, G. 2010. Ground based SAR interferometry.. A novel tool for Geoscience. In: *Geoscience and Remote Sensing, New Achievements*, edited by: P. Imperatore and D. Riccio, ISBN: 978-953-7619-97-8.

Mac Laughlin, M., Doolin, D.M. 2006. Review of validation of the discontinuous deformation analysis (DDA) method, *Int. J. Numer. Anal. Methods Geomech.*, 30, 271–305.

Mahr, T. Nemcok, A. 1977. Deep-seated creep deformations in the crystalline cores of the Tatry Mts., *Bulletin of the International Association of Engineering Geology*, 16, 104–106.

Malamud, B., Turcotte, D., Guzzetti, F., Reichenbach, P. 2004a. Landslide inventories and their statistical properties, *Earth Surface Processes and Landforms,* 29, 687–711.

Malamud, B., Turcotte, D., Guzzetti, F., Reichenbach, P., 2004b. Landslides, earthquakes, and erosion, *Earth and Planetary Science Letters* 229, 45–59.

Mantovani, F., Soeters, R., van Westen, C. 1996. Remote sensing techniques for landslide studies and hazard zonation in Europe, *Geomorphology*, 15, 213–225.

Marinos, V., Marinos, P., Hoek, E. 2005. The geological Strength index: applications and limitations, *Bull. Eng. Geol. Environ.*, 64, 55-65.

Martino, S., Moscatelli M., Scarascia Mugnozza, G. 2004. Quaternary mass movements controlled by a structurally complex setting in the Central Apennines, *Engineering Geology*, 72, 33-55.

Martinotti, G., Giordan, D., Giardino, M., Ratto, S. 2011. Controlling factors for deep-seated gravitational slope deformation (DSGSD) in the Aosta Valley (NW Alps, Italy). From: Jaboyedoff, M. (ed.) *Slope Tectonics*. Geological Society, London, Special Publications, 351, 113-131.

Metternicht, G., Hurni, L., Gogu, R. 2005. Remote sensing of landslides: An analysis of the potential contribution to geo-spatial systems for hazard assessment in mountainous environments. *Remote Sens. Environ.,* 98, 284-303.

Massironi, M., Genevois, R., Floris, M., Stefani, M. 2011. Influence of the antiformal setting on the kinematics of a large mass movement: the Passo Vallaccia, eastern Italian Alps., *Bull Eng. Geol. Environ*, DOI 10.1007/s10064-010-0340-9.

Meisina, C., Zucca, F., Notti, D., Colombo, A., Cucchi, A., Savio, G., Giannico, C., Bianchi, M. 2008. Geological interpretation of PSInSAR data at regional scale, *Sensors*, 8, 7469-7492.

Melchiorre, C., Matteucci, M., Azzoni, A., Zanchi A. 2008. Artificial neural networks and cluster analysis in landslide susceptibility zonation, *Geomorphology*, 94, 379–400.

McCalpin, J.P., Hart, E.W. 2003. Ridge-top spreading features and relationship to earthquakes, San Gabriel Mountains Region, Southern California: Part A. Distribution and description of ridge-top depressions (sackungen): Part B. Paleoseismic investigations of ridge-top depressions. In: Hart, E.W. (Ed.), *Ridge-Top Spreading in California*, California Geological Survey, Open-File Report, 1 CD-ROM.

McCalpin, J.P., 1999. Criteria for determining the seismic significance of sackungen and other scarp-like landforms in mountainous regions. Techniques for Identifying Faults and Determining their Origins. U.S. Nuclear Regulatory Commission, Washington, pp. 2.55–2.59.

McDougall, S., Hungr, O. 2004. A model for the analysis of rapid landslide motion across three-dimensional terrain, Canadian Geotechnical Journal, 41, 1084-1097.

McKean. J, Roering. J. 2004 Objective landslide detection and surface morphology mapping using high-resolution airborne laser altimetry, *Geomorphology*, 57, 331–351.

Molnar, P., Anderson, R.S., Anderson, S.P. 2007. Tectonics, fracturing of rock, and erosion, *Journal of Geophysical Research*, 112, F03014. doi:10.1029/2005JF000433.

Montgomery, D.R., Brandon, M.T. 2002. Topographic controls on erosion rates in tectonically active mountain ranges, *Earth and Planetary Science Letters*, 201, 481–489.

Monserrat, O., Crosetto, M. 2008. Deformation measurement using terrestrial laser scanning data and least squares 3D surface matching. *ISPRS Journal of Photogrammetry and Remote Sensing,* 63,142-154.

Nemcok, A. J., Pasek, J., Rybar, J. 1972. Classification of landslides and other mass movements, *Rock Mechanics*, 4, 71–78.

Nichol, J.E., Shaker, A., Wong, M-S. 2006. Application of high-resolution stereo satellite images to detailed landslide hazard assessment, *Geomorphology*, 76, 68–75.

Norini, G., Capra, L., Borselli, L., Zuniga, F. R., Solari, L., Sarocchi, D. 2010. Large scale landslides triggered by Quaternary tectonics in the Acambay graben, Mexico, *Earth Surf. Process. Landforms,* 35, 1445–1455.

Noverraz, F. 1990. Répartition géographique, origine et contexte géologique des glissements de terrains latents en Suisse, Hydrology in Mountainous Regions. Artificial Reservoirs; Water and Slopes (Proceedings of two Lausanne Svmposia, August 1990). IAHS Publ.,194.

Norton, K., Abbühl, L., Schlunegger, F., 2010. Glacial conditioning as an erosional driving force in the Central Alps, *Geology*, 38, 655-658.

Optech. 2011. ILRIS-LR, Summary Specification Sheet, Optech Inc. Available online on http://www.optech.ca.

Oppikofer, T., Jaboyedoff, M., Keusen, H.-R. 2008. Collapse at the eastern Eiger flank in the Swiss Alps, *Nature Geoscience*, 1, 531-535.

Oppikofer, T., Jaboyedoff, M., Pedrazzini, A., Derron, M.-H., Blikra, L. H. 2011. Detailed DEM analysis of a rockslide scar to characterize the basal sliding surface of active rockslides, *J. Geophys. Res.*, 116, F02016.

Oppikofer, T. Detection, analysis and monitoring of slope movements by high-resolution digital elevation models, PhD thesis, Univ. of Lausanne, Lausanne, Switzerland, 191p.

Owen, L. A., Kamp, U., Khattak, G. A., Harp, E. L., Keefer, D. K., Bauer, M. A. 2008. Landslides triggered by the 8 October 2005 Kashmir earthquake, *Geomorphology*, 94, 1–9.

Patikova, A., Digital Photogrammetry In The Practice Of Open Pit Mining. 2004. ISPRS Xx. Symposium, Commission Iv, Wg Iv/7, Istanbul.

Pedrazzini, A., Jaboyedoff, M., Loye, A. 2011. From Sackung to rock avalanche: the example of Sierre landslide (Switzerland), *Geophysical Research Abstracts*, 13, EGU2011-13069.

Penna, I., M., Hermanns, R., L., Niedermann, S., Folguera, A. 2011.Multiple slope failures associated with neotectonic activity in the Southern Central Andes (37° -37°30'S), Patagonia, Argentina, *Geological Society of America Bulletin, 123, 9-10, 1880-1895.*

Persaud, M., Pfiffner, O.A. 2004. Active deformation in the Eastern Swiss Alps: post-glacial faults, seismicity and surface uplift, *Tectonophysics,* 385, 59–84.

Petrie, G., Toth, CK. 2008. I. Introduction to laser ranging, profiling and scanning, II. Airbone and spaceborne laser profiles and scanners, III. Terrestrial laser scanners (chapters 1 to 3). In: Shan J, Toth CK (eds) *Topographic laser ranging and scanning: principles and processing*, CRC Press, Taylor & Francis.

Potyondy, D. O., Cundall, P. A. 2004. A Bonded-Particle Model for Rock, *Int. J. Rock Mech. & Min. Sci.*, 41, 1329-1364.

Poisel, R., Preh, A., Hungr, O. 2008. Run-Out of Landslides-Continuum Mechanics versus Discontinuum Mechanics Models, *Geomechanik und Tunnelbau*, 1, 358-366.

Pollet, N. 2004. Mouvements gravitaires rapides de grandes masses rocheuses: Apports des observations de terrain à la comprehension des processus de propagation et de dépôt. Application aux cas de la Madeleine (Savoie, France), Flims (Grisons, Suisse) et de Kofels (Tyrol, Autriche), PhD thesis, Ecole nationale des Ponts et Chaussées, 252 p.

Pollet, N., Schneider, J.-L.M. 2004. Dynamic disintegration processes accompanying transport of the Holocene Flims Sturzstrom (Swiss Alps), *Earth and Planetary Science Letters*, 221, 433-448.

Poon, C., Neufeld, A., El Madani, F., Castro, L. 2009. Enhancing the Collection of Rock Mass Fabric Data for Open Pit Mines ROCKENG09: Proceedings of the 3rd CANUS Rock Mechanics Symposium, Toronto, May 2009 (Ed: M.Diederichs and G. Grasselli).

Price, R.A., Carmichael, D.M. 1986. Geometric test for Late Cretaceous-Paleogene intracontinental transform faulting in the Canadian Cordillera, *Geology*, 14, 468-471.

Price, N.J., Cosgrove, J.W. 1990. *Analysis of Geological Structures*, Cambridge press, 516 p.

Prokešová, R., Kardoš, M., Medvedová, A. 2010. Landslide dynamics from high-resolution aerial photographs: A case study from the Western Carpathians, Slovakia, *Geomorphology*, 115, 90–101.

Radbruch-Hall, D. 1978. Gravitational creep of rock masses on slopes. In: Voight, B. (Ed.), Rockslides and Avalanches – Natural Phenomena. *Developments in Geotechnical Engineering*, vol. 14., Elsevier, Amsterdam, pp. 608–657.

Raucoules, D., Parcharidis, I., Feurer, D., Novalli, F., Ferretti, A., Carnec, C., Lagios, E., Sakkas, V., Le Mouelic, S., Cooksley, G., Hosford, S. 2008. Ground deformation detection of the greater area of Thessaloniki (Northern Greece) using radar interferometry techniques, *Nat. Hazards Earth Syst. Sci.*, 8, 779–788.

Ramsay, J. G., Huber, M. I. 1987. *The Techniques of Modern Structural Geology*, Vol. 2, Academic Press, London.

Read, J., Stacey, P. 2009. *Guidelines for Open Pit slope design*, Csiro Publising, Cayton, 512p.

Redfield, T.F., Osmundsen, P.T. 2009. The Tjellefonna fault system of Western Norway: Linking late-Caledonian extension, post-Caledonian normal faulting, and Tertiary rock uplift with the landslide-generated tsunami event of 1756, *Tectonophysics*, 474, 106–123.

Riahi, A., Hammah, R.E., Curran, J.H. 2010. *Proceedings of the 44th U.S. Symposium on Rock Mechanics and the 5th U.S.-Canada Rock Mechanics Symposium*, Salt Lake City, Utah, USA, June 2010.

Righini, G., Pancioli, V., Casagli, N. 2011. Updating landslide inventory maps using Persistent Scatterer Interferometry (PSI), *International Journal of Remote Sensing*, DOI:10.1080/01431161.2011.605087.

Roering, J.J., Kirchner, J.W., Dietrich, W.E. 2005. Characterizing structural and lithologic controls on deep-seated landsliding: Implications for topographic relief and landscape evolution in the Oregon Coast Range, USA, *Geological Society of America Bulletin,* 117, 654-668.

Rosser, N.J., Lim, M., Petley, D.N., Dunning, S.A. 2007. Patterns of precursory rockfall prior to slope failure, *Journal of Geophysical Research*, 112, F04014.

Sainsbury, D., Pothitos, F., Finn, D., Silva, R. 2007. Three-Dimensional Discontinuum Analysis of Structurally Controlled Failure Mechanisms at the Cadia Hill Open Pit, In *Slope stability 2007 (Proceedings, International Symposium, rock slope stability in open pit mines and civil engineering)* ed. Y. Potvin, pp. 307-320, Perth, Australia.

Saintot, A., Henderson, I. H. C., Derron, M.-H. 2011. Inheritance of ductile and brittle structures in the development of large rock slope instabilities: examples from western Norway. From: Jaboyedoff, M. (ed.) *Slope Tectonics*. Geological Society, London, Special Publications, 351, 27-78.

Sartori, M., Baillifard, F., Jaboyedoff, M., Rouiller, J.D. 2003. Kinematics of the 1991 Randa rockslides (Valais, Switzerland), *Natural Hazard and Earth System Sciences*, 3, 423–433.

Sauchyn, D. J., Cruden, D. M., Hu, H. Q. 1998. Structural control of the morphometry of open rock basins, Kananaskis region, southwestern Alberta, *Geomorphology*, 22, 313–324.

Savage, W. Z., Varnes, D. J. 1987. Mechanics of gravitational spreading of steep-sided ridges ('sackung'), *Bulletin of the International Association of Engineering Geology*, 35, 31–36.

Scarascia Mugnozza, G., Bianchi Fasani, G., Esposito, C., Martino, S., Saroli, M., Di Luzio, E., Evans, S.G. 2006. Rock avalanche and mountain slope deformation in a convex dip slope: the case of the Maiella Massif, Central Italy. In Landslides from massive rock slope failure. Edited by S.G. Evans, G. Scarascia-Mugnozza, A.L. Strom and R. L. Hermanns, NATO Science Series IV, v. 49, Springer, Dordrecht, 357-376.

Schlatter, A., Schneider, D., Geiger, A., Kahle, H., 2005. Recent vertical movements from precise levelling in the vicinity of the city of Basel, Switzerland, *Int. J. Earth Sci.*, 94, 507–514.

Schmidt, K.M., Montgomery, D.R. 1995. Limits to relief, *Science*, 270, 617–620.

Schowengerdt, R.A. 2007. *Remote sensing: models and methods for image processing, (3rd ed.).* Academic Press. 515p.

Schulz, W.H. 2007. Landslide susceptibility revealed by LIDAR imagery and historical records, Seattle, Washington, *Engineering geology*, 89, 67–87.

Segalini, A., D'Attoli, M., Ferrero, A.M., Migliazza, M. 2006. Stability analysis of fractured rock mass excavation in ornamental stone quarries by mean of 3D numerical modelling. In: *41st US Rock Mechanics Symposium-ARMA's Golden Rocks 2006—50 Years of Rock Mechanics*, Golden, Colorado, USA.

Selby, M.J., 1992. Hillslope Materials and Processes. University Press, Oxford.

Sharma, V.M., Saxena, K.R., Woods, R.D. 2001. *Distinct element modelling in geomechanics*, Rotterdam, Balkema.

Shea, T., van Wyk de Vries, B. 2008. Structural analysis and analogue modeling of the kinematics and dynamics of rockslide avalanches, *Geosphere*, 4, 657–686.

Shi, G.H. 1988. Discontinuous deformation analysis: a new numerical model for the statics and dynamics of block systems. Ph.D. Dissertation, Department of Civil Engineering, University of California, Berkeley.

Shi, G.H. 2001. Three dimensional discontinuous deformation analysis", 38th US Rock Mechanics Symposium, Washington, DC, 1421-1428.

Singhroy, V., Molch, K. 2004. Characterizing and monitoring rockslides from SAR techniques, *Advances in Space Research*, 30, 290-295.

Simonett, D.S. 1967. Landslide distribution and earthquakes in the Bewani and Torricelli Mountains. In: Jennings, J. N. & Mabbutt, M. A. (eds) New Guinea in Landform Studies from Australia and New Guinea. Cambridge University Press, Cambridge, 64–84.

Soeters, R., van Westen, C.J. 1996. Slope instability recognition, analysis and zonation. In: Turner, A.K. and Schuster, R.L. (eds.) *Landslide investigation and mitigation*, National Research Council, Transportation Research Board Special Report 247, 129-177.

Stacey, T.R., Xianbin, Y., Armstrong, R., Keyter, G.J. 2003. New slope stability considerations for deep open pit mines, *J. S. Afr. Inst. Min. Metall*., 103, 373–389.

Styles, T., Coggan, J., Pine, R. 2011. Back analysis of the Joss Bay Chalk Cliff Failure using numerical modeling, *Engineering Geology*, 120, 81–90.

Stark, C. P., Hovius, N. 2001. The characterization of landslide size distributions*, Geophys. Res. Lett*., 28, 1091–1094.

Stead, D., Eberhardt, E., Coggan, JS. 2006. Developments in the characterization of complex rock slope deformation and failure using numerical techniques, *Engineering geology*, 83, 217–235.

Stearns, D.W. 1968. Certain aspects of fractures in naturally deformed rocks, *Rock Mechanics Seminar*, R.E. Riecker, Bedford, Terrestrial Sciences Laboratory, 97–118.

Sturzenegger, M., Stead, D. 2009a. Close-range terrestrial digital photogrammetry and terrestrial laser scanning for discontinuity characterization on rock cuts, *Engineering Geology*, 106, 163-182.

Sturzenegger, M., Stead, D. 2009b. Quantifying discontinuity orientation and persistence on high mountain rock slopes and large landslides using terrestrial remote sensing techniques, *Natural Hazards and Earth Systems Science*, 9, 267-287.

Sturzenegger, M. 2010. Multi-scale characterization of rock mass discontinuities and rock slope geometry using terrestrial remote sensing techniques, PhD thesis, Simon Fraser University, 343 p.

Sturzenegger, M. Stead, D. *In press*. The Palliser Rockslide, Canadian Rocky Mountains: Characterization and modeling of a stepped failure surface, *Geomorphology*, doi:10.1016/j.geomorph.2011.09.001.

Slob, S., Hack, H., Turner, A.K. 2002 An approach to automate discontinuity measurements of rock faces using laser scanning techniques. In: Dinid da Gama, C., Riberia-Sousa, L. (eds): *Proceedings of ISRM EUROCK 2002, 25–28 November 2002*, Funchal, Portugal, Sociedade Portuguesa de Geotecnia, 87–94.

Storm, A.L. 2006. Morphology and internal structure of rockslides and rock avalanches: grounds and constraints for their modelling. Edited by S.G. Evans, G. Scarascia-Mugnozza, A.L. Strom and R. L. Hermanns, NATO Science Series IV, v. 49, Springer, Dordrecht.

Sue, C., Delacou, B., Champagnac, J.-D., Allanic, C., Tricart, P., Burkhard, M. 2007. Extensional neotectonics around the bend of the Western/Central Alps: an overview, *International Journal of Earth Sciences*, 96, 1101-1129.

Süzen, L.M., Doyuran, V. 2004. Data driven bivariate landslide susceptibility assessment using geographical information systems: a method and application to Asarsuyu catchment, Turkey, *Engineering geology*, 71, 303-321.

Tarchi, D., Casagli, N., Fanti, R., Leva, D., Luzi, G., Pasuto, A., Pieraccini, M., Silvano, S. 2003 Landslide monitoring using ground-based SAR interferometry: an example of application to the Tessina landslide in Italy, *Engineering Geology*, 69, 15–30.

Terzaghi, R.D. 1965. Sources of error in joint surveys, *Geotechnique*, 15, 287–304.

Teza, G., Galgaro, A., Zaltron, N., Genevois, R. 2007.Terrestrial laser scanner to detect landslide displacement fields: a new approach, *Int. J. Remote Sens.*, 28, 3425–3446.

Tommasi, P., Verrucci, L., Campedel, P., Veronese, L., Pettinelli, E., Ribacchi, R. 2009. Buckling of high natural slopes: The case of Lavini di Marco (Trento-Italy*), Engineering Geology*, 109, 93-108.

Travelletti, J., Malet, J.-P., Schmittbuhl, J., Toussaint, R., Bastard, M., Delacou, C., Allemand, P., van Dam, D.B. 2010. Multi-temporal terrestrial photogrammetry for landslide monitoring, In Malet, J.P., Glade, T., Casagli, N. (eds), *Proceedings of the Mountain Risks International Conference*, Firenze, Italy, 24-26 November 2010.

Ustaszewski, M.E., Hampel, A., Pfiffner, O.A. 2008. Composite faults in the Swiss Alps formed by the interplay of tectonics, gravitation and postglacial rebound: an integrated field and modelling study, *Swiss Journal of Geosciences,* 101, 223–235.

Utili, S., Nova, R. 2008. DEM analysis of bonded granular geomaterials, *Int. J. Numer. Anal. Methods Geomech*., 32, 1997–2031.

Utili, S., Crosta, G. B. 2011. Modeling the evolution of natural cliffs subject to weathering: 2. Discrete element approach, *J. Geophys. Res.*, 116, F01017, doi:10.1029/2009JF001559.

Varga, A.A. 2006. Gravitational creep of rock slopes as pre-collapse deformation and some problems in its modelling. In: Evans SG, Mugnozza GS, Strom A, Hermanns RL (eds) *Landslides from Massive Rock Slope Failure*, NATO Science Series. IV. Earth and Environmental Sciences, 49, Springer, Dordrecht, 103–110.

Van Den Eeckhaut, M., Poesen J., Verstraeten G., Vanacker, V., Nyssen, J., Moeyersons, J., van Beek, L.P.H., Vandekerckhove, L. 2006. Use of LIDAR-derived images for mapping old landslides under forest, *Earth Surface Processes and Landforms*, 32, 754-769.

Ventura, G., Vilardo, G., Terranova, C., Bellucci Sassa, E. *In press*. Tracking the evolution of complex active landslide by multi-temporal airborne LiDAR data, *Remote sensing of environment*, doi: 10.10167j.res.2011.07.007.

Vernon, A. J., van der Beek, P.A., Sinclair, H.D. 2009, Spatial correlation between long-term exhumation rates and present-day forcing parameters in the western European Alps, *Geology*, 37, 859–862.

Viero, A., Teza, G., Massironi, M., Jaboyedoff, M., Galgaro, A., 2010. Laser scanning-based recognition of rotational movements on a deep seated gravitational instability: The Cinque Torri case (North-Eastern Italian Alps), *Geomorphology,* 122, 191-204.

Voight, B. 1973. The mechanics of retrogressive block-sliding, with emphasis on the evolution of the Turnagain heights landslide, Anchorage, Alaska. In: De Jong, K. A. & Scholten, R. (eds), *Gravity and Tectonics*, Wiley, New York, 97–121.

Vyazmensky, A., Stead, D., Elmo, D., Moss, A. 2010. Numerical analysis of block caving-induced instability in large open pit slopes: a finite element/discrete element approach, *Rock Mech. Rock Eng.*, 43, 533–556.

Wang, C., Tannant, D.D., Lilly, P.A. 2003. Numerical analysis of the stability of heavily jointed rock slopes using PFC2D, *Int. J. Rock Mech. Min. Sci.*, 40, 415–424.

Wasowski, J., Casarano, D., Lamanna, C., Bovenga, F., Conte, D., Nutricato, R., Berardino, P., Manzo, M., Pepe, A., Zeni, G., Lanari, R., Refice, A. 2007. A comparative analysis of DInSAR results achieved by the SBAS and SPINUA techniques: the Maratea valley case study, Italy. Proc. 'Envisat Symposium 2007', Montreux, Switzerland, 23–27 April 2007.

Wehr, A., Lohr, U. 1999. Airborne laser scanning–an introduction and overview. *ISPRS J. Photogramm. Remote Sens.,* 54, 68–82.

Welkner, D., Eberhardt, E., Hermanns, R. L. 2010. Hazard investigation of the Portillo Rock Avalanche site, central Andes, Chile, using an integrated field mapping and numerical modelling approach*, Engineering Geology*, 114, 278-297.

Wieczorek, G.F., Jager, S. 1996. Triggering mechanisms and depositional rates of postglacial slope-movement processes in the Yosemite Valley, California, *Geomorphology*, 15, 17–31.

Wittmann, H., von Blanckenburg, F., Kruesmann, T., Norton, K.P., Kubik, P.W. 2007. The relation between rock uplift and denudation from cosmogenic nuclides in river sediment in the Central Alps of Switzerland*, Journal of Geophysical Research*, 112, F04010.

Wyllie, D.C., Mah, C.W. 2004. *Rock slope engineering,* Spoon Press, London, 431 pp.

Xu, Q., Fan, X.M., Huang, R.Q., Westen, C.V. 2009. Landslide dams triggered by the Wenchuan Earthquake, Sichuan Province, south west China, *Bulletin of Engineering Geology and the Environment,* 68, 373–386.

Yin, Y., Zhen, W., Li X, Sun, P., Li, B. 2011. Catastrophic landslides associated with the Mw 8.0 Wenchuan earthquake, *Bulletin of Engineering Geology and the Environment*, 70, 15–32.

Zaruba, Q., Mencl, V. 1982. Landslides and Their Control. Elsevier, Amsterdam; Academia, Prague.

Zischinsky, U. 1969. Uber Sackungen, *Rock Mechanics*, 1, 30–52.

3. REGIONAL SCALE ANALYSIS OF ROCK SLOPE INSTABILITIES

This chapter contains two sub-chapters written in a paper format:

1) "GRAVITATIONAL SLOPE DEFORMATIONS IN THE WESTERN ALPS: CHARACTERIZATION, SPATIAL DISTRIBUTION AND IMPLICATIONS FOR RECENT MOUNTAIN RANGE EVOLUTION".

This paper will be submitted to the journal "*Tectonophysics*" under the authorship: Pedrazzini, A., Jaboyedoff, M., Tonini, M., Derron M-H., Loye, A. The first author acquired, treated analysed and interpreted the data. M. Tonini assisted the first authors on statistical analyses. All the authors contributed to discussing the results and finalizing the manuscript.

2) "CHARACTERISTICS AND DISTRIBUTION OF ROCKSLIDE SCARS IN THE RHONE VALLEY (S-W SWITZERLAND)".

Part of this chapter will be reworked and submitted for publication to the "*Swiss Journal of Geosciences*" under the authorship: Pedrazzini, A., Jaboyedoff M., Derron, M-H., Loye, A.

3.1 GRAVITATIONAL SLOPE DEFORMATIONS IN THE WESTERN ALPS: CHARACTERIZATION, SPATIAL DISTRIBUTION AND IMPLICATIONS FOR RECENT MOUNTAIN RANGE EVOLUTION

3.1.1 ABSTRACT

In this chapter, an inventory of gravitational rock slope deformations, affecting the upper portion of the Rhone Valley (south-western Switzerland) were carried out to identify the different factors controlling their distribution. The study area represents a surface of about 5'000 km^2, along the Rhone valley and its tributary catchments. Lithological and tectonic characteristics as well as morphometric features display an important variability all along the study area leading to the development of different slope dynamics. Detection of potential unstable areas and main morphometric features was performed combining different remote sensing data as high resolution digital elevation model, aerial orthophotos and Google Earth™. Mapping and characterization of large slope instabilities was conducted according to their size, geometry and their morphological style. Based on these analyses, up to 300 rock slope deformations corresponding to 11% of the entire study area were identified. Statistical and morphometric analyses show that the coexistence of high local relief, large scale pre-existing tectonic weakness zones and active tectonic processes, including high uplift gradient and high seismic energy release predispose towards high rock slope deformations incidence in the Rhone valley. The strong influence of active tectonic processes on the rock slope instabilities distribution suggests that their significance need to be revaluated to better understand the uplift values of Western Switzerland and to quantify the spatial distribution of the Quaternary erosion rate.

3.1.2 RÉSUME

Les grandes déformations gravitaires représentent un phénomène fréquent qui influence la morphologie et le flux des sédiments de toute vallée Alpine. Ce chapitre présente le premier inventaire des grandes déformations de versant affectant la partie supérieure du bassin versant du Rhône (Valais, Suisse). La zone d'étude qui s'étend sur une surface de plus de 5000 km^2 présente des caractéristiques morphométriques très variables et traverse presque toutes les grandes unités tectoniques caractérisant la géologie des Alpes Occidentales. La cartographie des déformations gravitaires a été menée sur la base d'une analyse du modèle numérique de terrain à haute résolution et d'une visualisation tridimensionnelle à l'aide de Google Earth ™. La cartographie ainsi que les recherches bibliographiques ont permis d'identifier plus de 300 déformations gravitaires. Une analyse détaillée de paramètres tectoniques et morphologiques a permis de mettre en évidence que les grandes instabilités de versant se concentrent de préférence dans les régions caractérisées par un relief local important, par un fort gradient de soulèvement et par une activité sismique importante exprimée par une forte quantité d'énergie dissipée. Sur la basée de ces résultats, on a pu identifier que les processus néotectoniques, souvent indiqués comme secondaires dans les Alpes Occidentales, doivent être réévalués en particulier par rapport à leur influence sur la distribution spatiale du taux de soulèvement actuel et sur l'activité érosive postglaciaire.

3.1.3 INTRODUCTION

Large slope instabilities are common geomorphological features in mountain areas (Evans and Clague, 1994), which deeply shape the morphology of the mountain ranges (Crozier, 2010). Their impact on slope morphology and on past and on-going erosional processes is very significant, although they are difficult to quantify (Korup, 2005; Agliardi et al., 2009). The influence of bedrock landsliding on the erosion rate and hillslope gradient has been intensively studied using, in particular, available digital elevation models over large areas (Dramis and Sorriso-Valvo 1994; Schmidt and Montgomery, 1995; Burbank et al., 1996; Hovius et al., 1997; Densmore al., 1997; Korup, 2005). Potential correlations between tectonic processes and landslide distribution have been highlighted in active mountain belts, e.g. in the Southern Alps of New Zealand (Clarke and Burbank, 2010), in the Himalaya (Schmidt and Montgomery, 1995; Burbank et al,. 1996) and in the Andean belt (Antinao and Gosse, 2009; Hermanns et al., 2001). These regions are characterized by high tectonic activity mainly expressed by high uplift rate and intense earthquake activity. Bedrock fracturing and rock strength are often considered to be the main predisposing factors influencing erosional processes and landslide development (Molnar et al., 2007; Clarke and Burbank, 2010; Korup and Schlunegger 2009). The rock strength depends on lithological characteristics and weathering grade, whereas rock fracturing depends on the inherited geological and tectonic history of the study area (Selby, 1982). Molnar et al. (2007) indicate that the most important role played by tectonics in erosion processes is rock fracturing induced by tectonic strain accommodation. Based on this hypothesis, Clarke and Burbank (2010) explain the differences in landslide frequency and landslide volumes between more active belts like the Southern Alps of New Zealand and less tectonic active areas such as Fiordland (New Zealand).

The European Alps can also be considered as an active mountain belt even though neotectonic activity is lower than in the Southern Alps of New Zealand (Fitzsimons and Veit 2001) or the Himalaya (Burbank et al., 1996). In the European alpine context, neotectonic activity is often mentioned, as a possible predisposing factor influencing the development of large slope deformations (Forcella and Orombelli 1984; Dramis and Sorriso–Valvo 1994, Agliardi et al., 2009; Sanchez etal., 2010). However, few studies have investigated the potential link between high relief production, forced by tectonic stresses and the spatial distribution on large slope instabilities so far (Crosta et al., 2009, Agliardi et al., 2009). Active tectonic forcing here is poorly verified due to the lack of homogeneous and valid data over large areas (Agliardi et al., 2009).

In the Alps, research on large slope instabilities is rich in local case studies describing the potential predisposing and triggering factors for single slope failures (Agliardi et al., 2001; Reitner and Linner, 2009, Ghirotti et al., 2011, a. o.). However, regional scale studies on large slope instabilities, describing their characteristics and their regional distribution in term of surface processes, are less developed than in other ranges (e.g. Hovius et al, 1997; Jarman, 2006; Korup et al., 2007). After the pioneering works of Heim (1932), Abele (1974) and Eisbacher and Clague (1984), there are only few recent studies in Central Eastern Alps (Crosta et al., 2009; Agliardi et al., 2009).

This study presents a new detailed inventory of large slope instabilities and a lineament mapping of the entire upper Rhone valley (Western Switzerland) in order to quantitatively investigate the spatial relationship between slope instabilities and active tectonic processes, pre-existing structural features and

lithological characteristics. Aerial photo-interpretation, high resolution digital elevation model (HRDEM) analysis and Google Earth™ are used to map large landslides (named gravitational slope deformations, GSD, for this work) over more than 5'000 km^2 between Lake Geneva and sources of the Rhone. Descriptive statistical analyses are presented to identify the possible relationships among the litho-structural setting, the topography and the slope instabilities. Detailed lineament mapping and foliation attitude are spatially investigated to determine their influence on the localisation and on the magnitude of GSD. Spatial analyses are performed to define areas with high GSD density and to compare it to tectonic and climatic factors in order to spatially quantify their interrelationship. In contrast to recent mountain range scale analyses (Vernon et al., 2009) the results of the present study identify a correlation between large gravitational slope deformations and neotectonic activity leading to a better understanding of the link between erosion and tectonic processes.

3.1.4 STUDY AREA

The study area covers the entire upper Rhone catchment, including its tributary valleys from the Rhone delta on the Lake Geneva to the Rhone sources located in the central Swiss Alps (Figure 3.1-1).

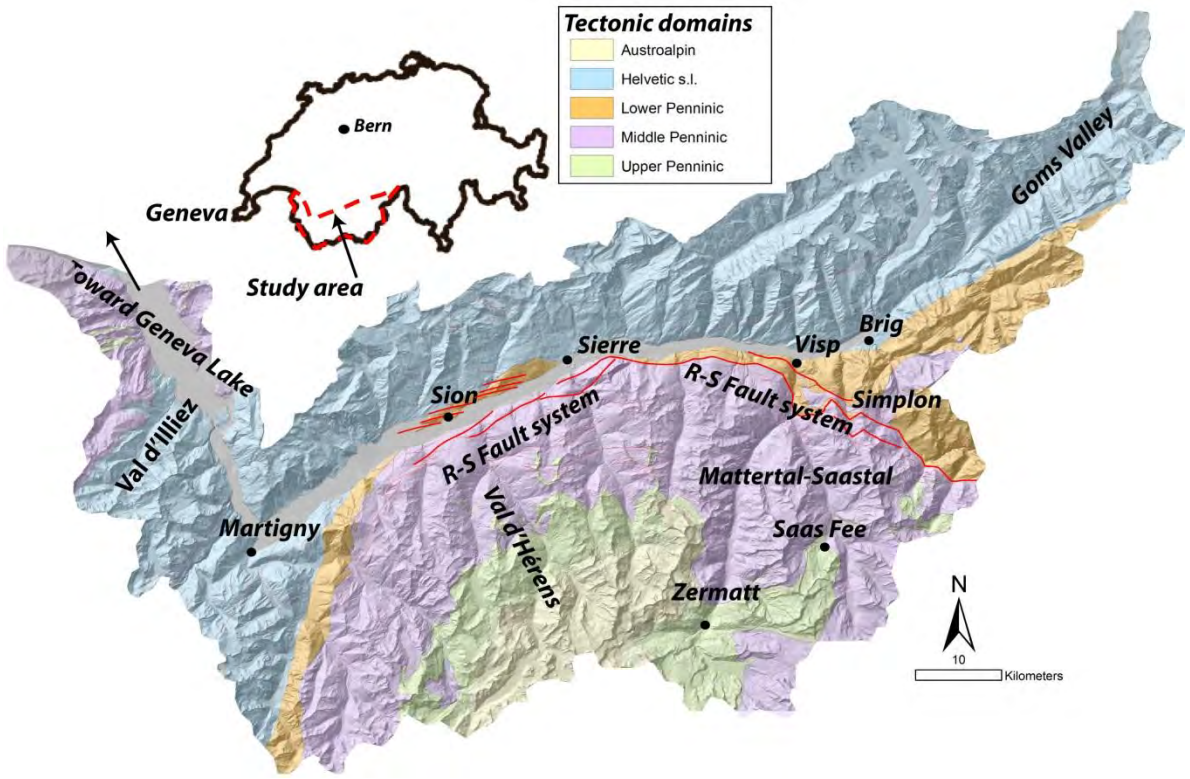

Figure 3.1-1: Geographical and geological setting of the Upper Rhone valley (South-Western Switzerland).

In the upper and central portions of the study area, the Rhone river flows toward SW parallel to the Alpine belt. Near Martigny its orientation changes toward NW to finally reach the Lake Geneva. In the catchment, elevation ranges from 372 m at Lake Geneva, up to 4634 m at the Dufour Peak that represent the highest summit of Switzerland. Climate conditions are heterogeneous. At high elevation and along tributary valleys the climate is typically Alpine whereas the intramontane Rhone valley has high insulation during all the year similar to Mediterranean conditions.

3.1.5 GEOLOGY

The geology throughout the study area is complex and encompasses almost all major tectonic units of the Western Alps (Figure 3.1-1). The western portion of the study area, close to the Lake Geneva, is characterized by the presence of the Prealpine Nappes. These are formed by several allochthonous sedimentary tectonic klippen (Mosar et al., 1996) of Sub-briançonnais and Briançonnais origin (Lemoine et al., 1986; Sartori 1987), comprising limestone, marly-limestone and marls with subordinate dolomite and sandstone. The Helvetic zone dominates the northern side of the Rhone valley. It is formed by the Infrahelvetic units, corresponding to the external polymetamorphic massifs and their cover (i.e. Aar, Aguilles Rouges and Mont Blanc Massif), as well as the Helvetic allochtonous sediment Nappes (Masson et al., 1980; Steck et al., 2001). The basement consists mainly of gneiss and granite with subordinate phyllites (von Raumer 1987; Steck et al., 2001). The Mesozoic-Oligocene sediments composing the Helvetic Nappes were detached and thrust toward the northeast (Escher and Beaumont, 1997; Brukhard et al., 1988). Since Miocene times, updoming of the external Massifs has led to substantial exhumation and controlled the formation of the Rawil axial depression where most of the sedimentary Nappes are preserved (Lugeon 1914; Heim 1921; Burkard et al., 1988). Helvetic Nappes comprise limestone and marly-limestone layers with subordinate shale and sandstone. The tertiary sediments are formed by Flysch sequences corresponding to syn-orogenic sedimentation characterized by intercalation of shale, sandstones and conglomerate. The Southern part of the Rhone catchment belongs to the Penninic and Austroalpine domains. This latter is almost completely eroded in the study area and the residual outcrops are constituted by the gneiss of the Dent Blanche Nappe (Steck and Hunziker, 1994). The Penninic Nappes consist of crystalline (gneiss and micaschist), meta-sedimentary (phyllites and marbles) and ophiolitic rocks. The Penninic units experienced strong deformations and a polyphasic Alpine metamorphic overprint corresponding to greenschist facies (Sartori et al., 2006). This was followed by important back folding and back-thrusting (Eocene and Miocene) and subsequently by an exhumation phase during Pliocene (Pfiffner et al., 2002).

Main regional brittle structures existing in the area are the Rhone –Simplon fault and the basal Penninic thrust. The Rhone-Simplon system corresponds to a dextral strike-slip post-nappe fault that was active from the late Paleocene to late Neogene (Steck 1984; Mancktelow 1992). It clearly drives the morphology of the Rhone valley and in particular the Rhone glacier incision by introducing a tectonic weakening (Preusser et al., 2010). The Penninic thrust corresponds to a gently south-dipping thrust dividing the Penninic units located above the thrust and the Helvetic units located below.

3.1.6 QUATERNARY EVOLUTION

The current geomorphic features of the Rhone valley are influenced by its glacial and paraglacial history. At the Last Glacial Maximum (LGM) around 21-19 Ka BP ice limits above sea level descended from Brig (2400 m) via Martigny (1800 m) to Lake Geneva (1400 m) (Florineth and Schlüchter, 1998; Kelly et al., 2003).

Erosion driven by the Rhone glacier created an important overdeepening of the Rhone valley (Preusser et al., 2010). Gravimetric (Rosselli and Olivier, 2003) and seismic reflection (Besson et al., 1992) studies showed that the quaternary valley infilling reaches a maximum of 900m close to Martigny and to the

Rhone delta. Eastward from Sion, the valley infilling progressively decreases to reach less than 300 m close to Brig (Rosselli and Olivier, 2003). Based on geophysical survey the total infilling material was estimated at 88 km^3 (Rosselli and Olivier, 2003). Jaboyedoff and Derron (2005) created a 3D model of the Rhone valley bedrock surface based on DEM modelling and estimated the total volume of the infilling material to 90-110 km^3. The retreat of the Rhone glacier after the LGM is marked by repeated advances /retreats until the Bølling interstade (Ivy Ochs et al., 2004; Schoeneich et al., 1998). After this period the main Rhone Valley is expected to be free of ice and characterized by an important torrential activity (Schoneich et al., 1998).

3.1.7 SEISMICITY AND ACTIVE TECTONICS

In the Central and Western Swiss Alps, several studies have recognized active tectonic processes. These were based on seismo-tectonic analyses (Sue et al., 1999, Kastrup et al, 2004 Delacou et al. 2004), geodetic analyses (Kahle et al., 1997; Schlatter et al., 2007), digital elevation model or orthophoto analyses (Sue et al., 2007; Ustaszewski and Pfiffner 2008) and in-situ analyses of fault populations (Champagnac al., 2003; Ustaszewski and Pfiffner 2008).

The Swiss Alps show a low to moderate seismicity compared to other tectonics belts (Sue et al., 2007). Nevertheless, the Rhone valley is among the most seismically active areas in the central Swiss Alps (Maurer et al., 1997). More than 2000 earthquakes with moment magnitude higher than 2 (Mw >2), and at least six historical events with an estimated magnitude higher than six (Mw> 6) were documented (Fäh et al., 2011). Almost all earthquake foci are located at depth smaller than 15 km. The accuracy of the epicentre location varies from less than 5 km for instrumentally recorded earthquakes up to 20 Km for historical events (Gisler et al., 2004). Figure 3.1-2 shows the distribution of earthquake epicentres with magnitude (Mw> 2) between 250 and 2010 AC in the study area.

The seismic activity is clearly heterogeneously distributed and two main clusters can be delimited. Two high earthquake density areas emerge (a) the Rawil axial depression in the north (b) Saastal-Mattertal valleys in the SE of the study area. The present-day tectonics of the Central and Western Alps are mostly driven by the counter-clockwise rotation of the Adriatic plate relative to the Europen plate (Sue et al, 2007).

In the Western Swiss Alps, fault planes solutions (Kastrup et al., 2004; Delacou et al., 2004) indicate a clear differentiation of the stress regimes between the Penninic domain and the Helvetic Nappes at the north. The Rhone-Simplon fault represents the separation line (Maurer et al., 1997) between the two stress regimes (Figure 3.1-2). To the north, the seismo-tectonic analyses indicate a strike-slip to normal faulting stress regime (Kastrup et al., 2004), whereas towards the south it is characterized by N-S extension (Figure 3.1-2).

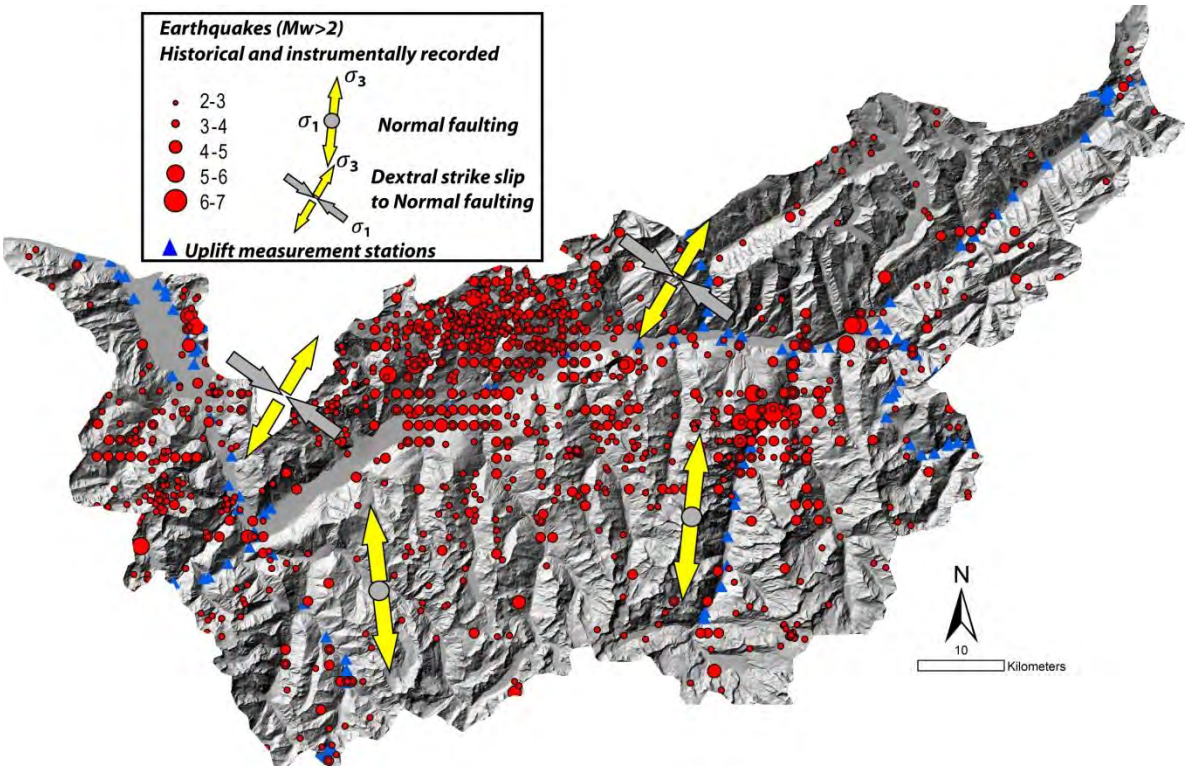

Figure 3.1-2: Distribution of historical and instrumentally-recorded earthquakes (ECOS-09 earthquake catalogue; Fäh et al., 2011). The global stress field within the study area is determined by seismo-tectonic analyses (Kastrup et al., 2004).

Geodetic data (Kahle et al. 1997; Schlatter et al., 2005; Schlatter, 2007) highlight strong uplift values for all the central portion of the study area with the presence of one of the maximal uplift values for Switzerland near Brig (1.2-1.3 mm/y). Different interpretations were postulated for this. Persaud and Pfiffner (2004) and Ustaszewski and Pfiffner (2008) proposed a tectonic origin related to post-collisional stress regime for the central Eastern Alps. Other researchers proposed that observed uplift could be related to isostatic reaction to crustal over-thickening and erosion (Schlunegger and Hinderer, 2001), rock-type control of erosion (Korup and Schlunegger 2009), rock material and climatic control (Koons, 2009) and/or glacial conditioning and surface processes (Norton et al., 2010).

3.1.8 MAPPING

3.1.9 GSD TYPOLOGIES

It is often difficult to assign specific RSFs within complicated classical classifications such as Hutchinson (1988) or Cruden and Varnes (1996). Complex sites that can fit several categories are common; hence Jarman (2006) identified just five broad categories for the Scottish Highlands. Here, sites have been classified by a three-way simplification of Hutchinson (1988):

1. Rockslide and rock-avalanches (RRA) characterized by monolithic rock masses with a failure surface defined by pre-existing discontinuity sets (Figure 3.1-3a). This class corresponds roughly to the translational slides defined by Hutchinson (1998).
2. Deep-seated creep and sagging (DSGSD) characterized by spreading ridges and counterscarps, possibly including minor landslides inside the deformed mass (Figure 3.1-3b). This class includes the deep sagging and creep deformation defined by Hutchinson (1998). This type broadly corresponds also to the definition of "Sackung" proposed by Zischinsky (1969).

3. Roto-translation slide (LRT) characterized by distinct headscarps, pronounced toe bulges and debris lobes (Figure 3.1-3c). This class includes the rotational slips and compound slides defined by Hutchinson (1998).

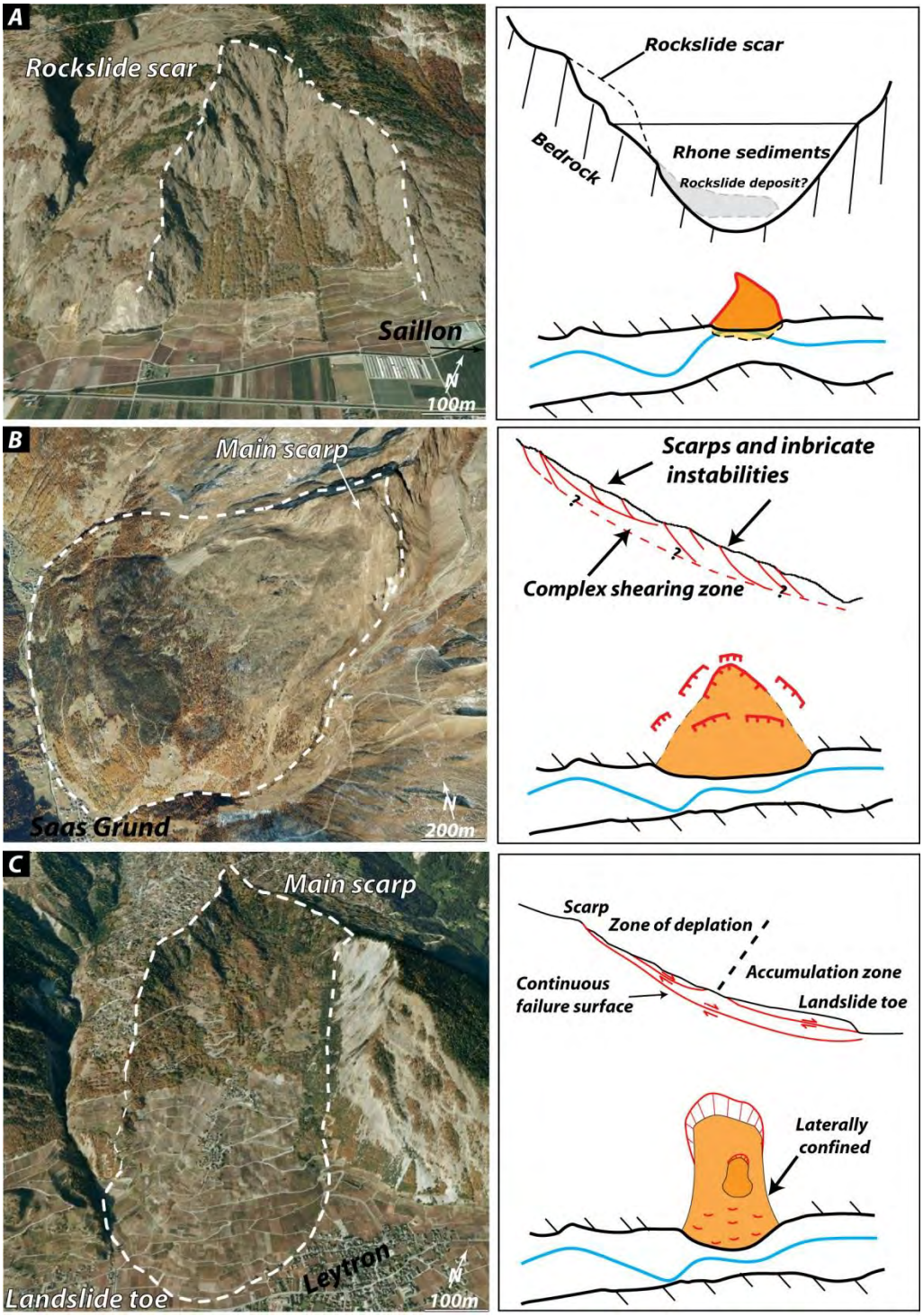

Figure 3.1-3: Google earth™ view and interpretive sketches of the three GSD typologies differentiated in this study. a) Rockslide scar of Saillon (Martigny area). b) Deep-seated gravitational slope deformation in upper Saastal valley. c) Roto-translational landslide of Montagnon (Sion-Martigny area).

3.1.10 GSD INVENTORY

Compared to the rest of the alpine chain, especially the Italian sides where extensive studies about DSGSD have been carried out (Martara and Sarzana 1987; Forcella and Orombelli, 1984; Agliardi et al., 2009), no recent or comprehensive inventory including all types of GSD categories has been compiled for the Western Swiss Alps. Detailed inventories carried out for the entire Alps by Heim (1932), Montandon (1933), Abele (1974) or Eisbacher and Clague (1994) focused mainly on "Bergsturz" (rock avalanche or rockslide) and large debris flows. At the opposite, Noverraz (1990) focused essentially on the characterization of large roto-translational slide. A new database was created sampling information about location and characteristics of GSD. Data have been extracted from four different sources of information:

-Review of scientific and of technical studies as well as analysing and digitising features described in the published 1:25'000 geological maps (Swisstopo).

- Aerial photograph (1:20'000 and 1:30'000) and orthophotos (15 and 25 cm pixel size).
- Digital elevation model (Swisstopo) at 2m / 25m cell size for areas below/above 2'000 m asl.
- Google Earth images (© Google 2010).

A lower size limit of 0.05 km^2 was adopted to obtain an inventory as complete as possible and to avoid scale discrepancy between GSD detected on remote sensing data, covering homogeneously the entire study area, and those extracted from 1:25'000 geological maps, that are very detailed but do not cover the entire study area. A similar size limit was also chosen by Korup (2005). The inventory is inevitably incomplete, especially for small size instabilities (<0.2 km^2). As proposed by Korup (2005), superimposed GSD were mapped separately according to their typology. For each detected GSD, an attribute table was compiled (based on descriptors proposed by Jarman 2006), containing (1) the typology of the slope deformation, (2) the degree of disintegration, (3) the geometrical descriptors, (4) the relative chronology, (5) the relative depth and (6) the degree of confidence. Figure 3.1-4a resumes the parameters adopted in the attribute table.

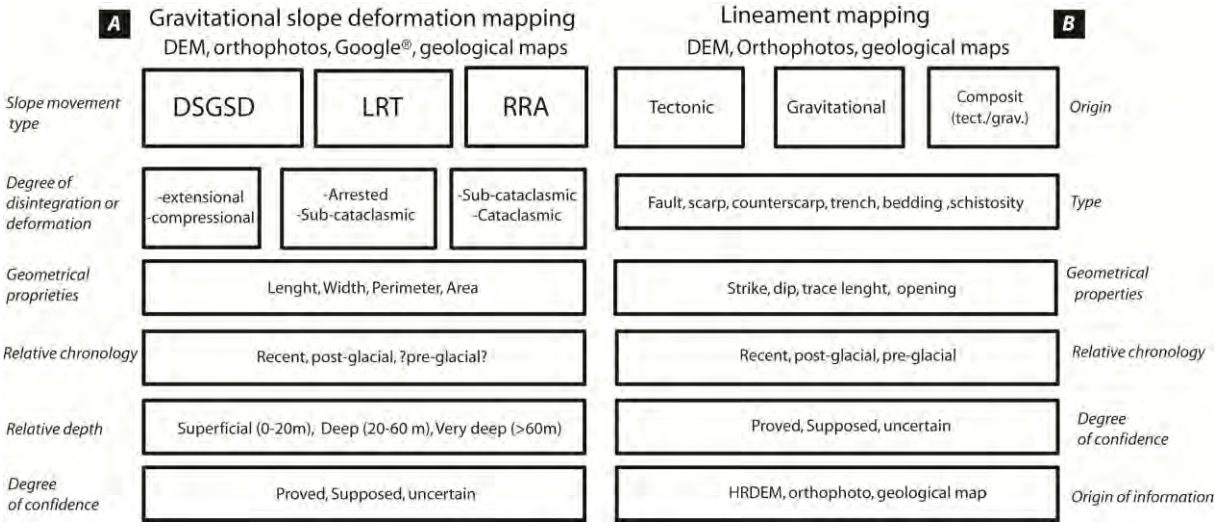

Figure 3.1-4: a) Main geometrical/geomorphological characteristics used to describe the slope movements forming the inventory database. b) Geometrical/geomorphological characteristics that describe the mapped lineaments.

3.1.11 LINEAMENT PATTERNS

A database including both tectonic and morpho-structural lineaments has been created based on analyses of DEMs and orthophotos as well as previously published studies (Steck et al., 1999; Champagnac et al. 2003, Ustaszewski and Pfiffner 2008, Gasser and Macktelow, 2008). The lineaments have been classified according to their potential tectonic, gravitational or composite origin based on morphological criteria as suggested by Mc Caplin (1999) and Agliardi et al. (2009). Tectonic lineaments include faults, persistent joints sets and undifferentiated structures where no precise information is available. Gravitational features represent the linear expression of slope instabilities, and are composed by scars, scarps, trenches, and counterscarps (Figure 3.1-4b).

3.1.12 DATA AND METHODS

3.1.12.1 Data

Uplift data, obtained by high precision levelling (Kahle et al., 1997), were extracted from the Swiss Federal Office of Topography geodetic database (Schlatter 2007). Uplift measurements (Kahle et al., 1997; Schlatter, 2007) are unfortunately not evenly distributed over the study area, but mainly taken in main valley floors. The spatial interpolation of this data was particular complex due to the distribution of the measurement points but also due to the non-stationary spatial structure of the uplift field in the Alps (Jaboyedoff et al., 2003). Different from Schlatter (2007), uplift data were interpolated using anisotropy natural neighbour to account for the uplift variation that occurs more rapidly transversal to the Alpine chain (Jaboyedoff et al., 2003).

Information about earthquake location and magnitude were extracted from the ECOS-09 earthquake catalogue (Fäh et al., 2011). This catalogue contains macroseismic earthquakes since 200 AD, yearly reports of the Swiss earthquake commission since 1879 and earthquake locations based on the instrumental networks since 1975 year. Potential control of precipitation on the GSD distribution was analysed based on Swiss Federal Office of Meteorology and Climatology (MeteoSwiss) database from 1961–1990. Mean annual precipitation data have been calculated and interpolated for the entire Swiss territory (Frei and Schaer, 1998).

3.1.12.2 Morphometric characterization

The main morphometric characteristics of the topography and the detected GSDs were analysed based on a 25 m cell size DEM, since there is no high resolution DEM above 2'000 m asl. Morphometric analyses of slope angle, slope aspect and local relief characterize the general topographic conditions leading to the development of slope instabilities.

3.1.12.3 Size distribution

Size-distribution is frequently used to analyse landslide inventories and to understand landslide dynamics (Malamud et al., 2004). The relationship between frequency and area is considered scale invariant and applies to both historical time series and single-event triggered landslides (Malamud et al., 2004; Van den Eeckhaut et al, 2007; Chaytor et al., 2009 a. o.). This relationship was tested by computing the probability density of GSD from Rhone valley. The GSD areas were extracted directly from the GIS database and were

analysed altogether and separately, according to their typology. In order to estimate the frequency density distribution, the methodology proposed by Malamud et al. (2004) and by Van den Eeckhaut et al. (2007) was adopted. The frequency density is then obtained by dividing each class by the bin width and plotting the result versus the lower boundary area of the given class.

3.1.12.4 Spatial distribution

The spatial distribution of GSDs in the Rhone valley has been analysed by means of quantitative geomatics tools and statistical methods. A Kernel density function (Silverman 1986) has been applied to calculate the density of the detected GSD. The distribution of GSD with respect to the lithology was investigated by overlapping the detected features with a modified version of the 1:500'000 Geological map of Switzerland (Swisstopo), completed and improved with available 1:25'000 geological maps. Geological formations were merged according to their geomechanical behaviour based on rock mass properties (geological strength index, Hoek and Brown, 1997). Limestone and marl lithologies were kept together because they are often intercalated, especially in the Helvetic Nappes. The distance between landslide centroids and large scale structures, such as the Rhone-Simplon fault system, has been measured.

3.1.12.5 Foliation and topography

The relationship between the orientation of the main foliation and the topography is a main parameter that can critically influence the stability of slopes at different spatial scales (Sauchyn et al., 1998; Cruden, 2003). Depending on the orientation of the main foliation with respect to the topography, different failure mechanisms are possible (Cruden 2003). The spatial relationship between the main foliation attitude in the study area and the distribution of the GSD was therefore investigated using the TOBIA index method proposed by Meentemeyer and Moody (2000). Following this index, the slopes are classified in three main classes: cataclinal (the foliation plunges in the same direction as the slope), anaclinal (foliation plunges in the direction opposite to the slope), and orthoclinal (foliation is perpendicular to the topography). Cataclinal and anaclinal slopes can then be subdivided in six different categories depending on the slope angle of the topography (Meentemeyer and Moody, 2000). To calculate the TOBIA index, main schistosity or bedding orientations were extracted from the 1:100'000 tectonic map of western Switzerland (Steck et al., 1999) and completed with structural information derived from the 1:25000 geological maps. In order to interpolate the foliation orientation values, they were first decomposed into direction cosines (de Kemp 1998) and then interpolated using ordinary kriging. Slope and aspect of the topography were extracted from 25m DEM. A pre-set focal filter of 3 x 3 meters was successively applied to erase local artefacts. The quality of the resulting map is strongly dependent on the availability of data and the local tectonic complexity.

3.1.12.6 Correlations and clustering

In order to identify if there is any relationship between seismicity, uplift, uplift gradient and GSD distribution several approaches have been applied. First, to identify possible correlations between GSD distribution and the above-mentioned parameters both the GSD area and the number of GSD within a given surface-based interval of the analysed parameter were analysed. The results were then cumulated

and normalized between 0 and 1. The obtained frequency density distribution was compared to a Beta cumulative function (Johnson et al., 1994):

$$f(x;\alpha,\beta) = \frac{1}{B(\alpha,\beta)} x^{\alpha-1}(1-x)^{\beta-1} \qquad \text{Eq. 3.1-1}$$

where B is the beta function with α and β the adjusting parameters.

This distribution is commonly used to evaluate the damage distributions related to earthquakes (Sengezer and Ansal, 2007). The advantage of using Beta cumulative function is that the curve presents different shapes leading to different probability density distributions depending on α and β values. An increasing cumulative beta distribution e.g. (α = 1 and β < 1), implies that the density is monotonically increasing with the x axis. At the opposite, a monotonically decreasing distribution is obtained when β = 1 and α <1. The uniform distribution corresponds to α = 1 and β =1. These characteristics are important in our study because, based on best fitting alpha and beta parameters; it is directly possible to determine what type of correlation can exist (uniform, increasing or decreasing) between the GSD distribution and the values of considered variables. The quality of the fitting was verified by using the Kolmogorov-Smirnov test with a significance level of 0.05.

In a second time, the spatial relationship (clustering) between GDS events and earthquakes has been performed using Ripley's K-function. This detects if a point process is randomly distributed or not (Ripley, 1977, 1995; Diggle, 1983). Analytically K(r) is the expected number of additional random points within a distance r of a randomly distributed event. K(r) can be plotted against r so that it is easy to compare the obtained curve with the theoretical one, computed for a completely random point process, for which $K(r)=\pi r^2$. Deviation between the two curves indicates spatial clustering or dispersion among punctual events. Moreover it is easy to find out at which range of distance data perform a non-random pattern. Here, a derivative of K-function was used, namely L-function which is defined as:

$$L(r) = \sqrt{\frac{K(r)}{\pi}} - r \qquad \text{Eq. 3.1-2}$$

Where K(r) is the Ripley K-function and r is the radius (in meters).

Its value is "zero" for randomness while positive and negatives values indicate respectively a clustered or dispersed data structure. To test for randomness, 999 simulations have been performed: the resulting envelopes allow accepting or rejecting the assumption of clustering. Since GDS and earthquakes represent non stationary point processes (i.e. intensity varies within the study area), a generalisation of K-function for inhomogeneous point pattern (Baddeley et al., 2000) has been adopted.

3.1.13 RESULTS

3.1.13.1 Inventory

The instability database comprises a population of 300 GSD (Figure 3.1-5a and b). Half of the dataset corresponds to deep seated creep/sagging (DSGSD= 142 events). The rest is represented by rockslides

and rock-avalanches (RRA=97 events) and by large roto-translational landslides (LRT=61 events). The areas of individual recorded GSDs ranges from the 0.05 km2 threshold up to 34 km², with the total cumulated area being about 575 km², corresponding to 11% of the entire study area. Figure 3.1-5b shows the kernel density map for all detected GSDs. It highlights that the GSDs are not uniformly distributed in the study area but are concentrated in six well-delineated zones: Val d'Illiez (considered surface = 130 km², percentage of instabilities = 8%), Martigny (350 km², 20%), Sion-Sierre (450 km², 20%), Visp-Brig (440 km², 23%) and Upper Mattertal zone (95 km², 6%), Val d'Hérens (113 km², 8%).

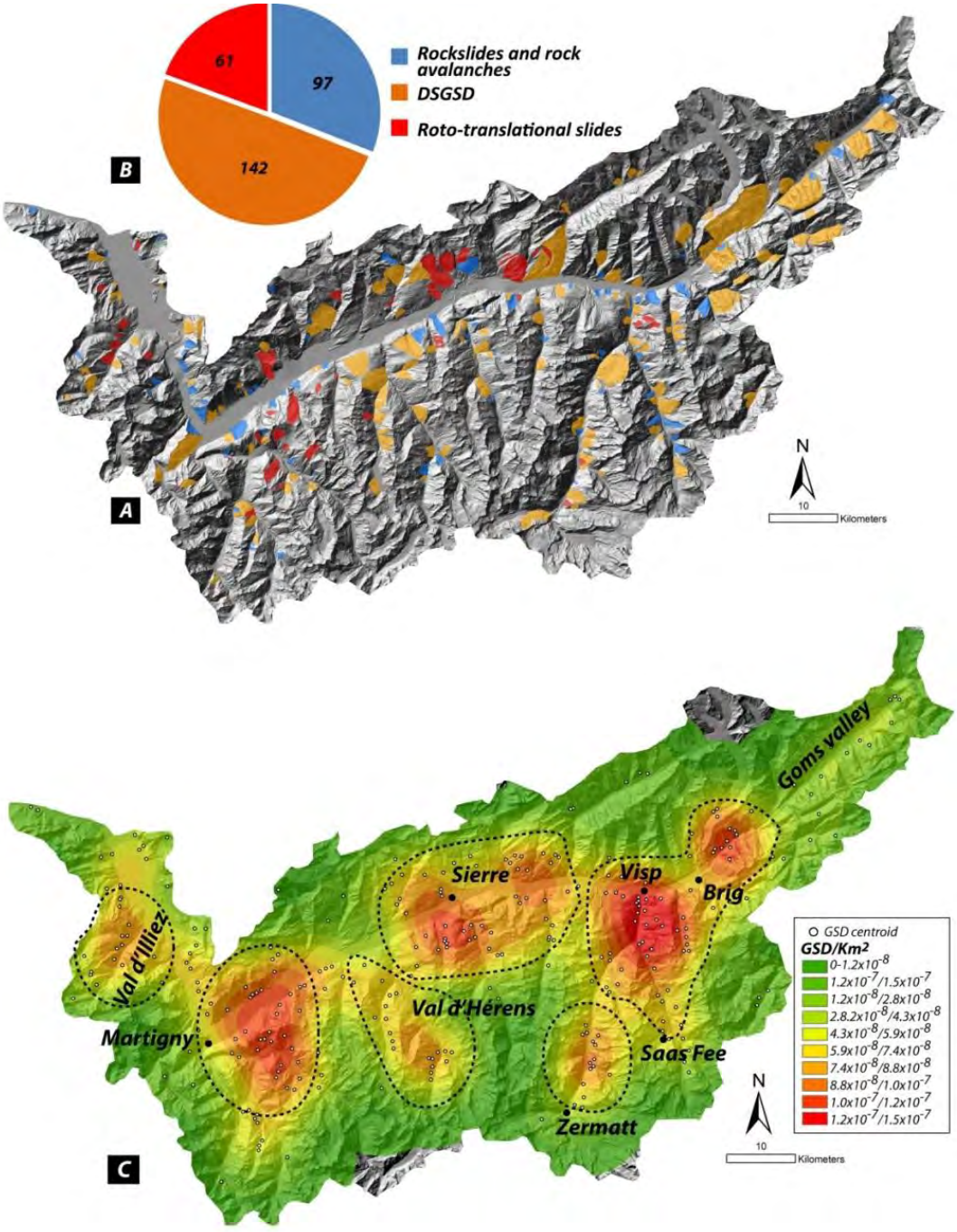

Figure 3.1-5: GSD inventory in the upper Rhone catchment. a) Distribution of the detected GSD within the study area. b) Pie chart showing the reparation of GSD typologies within the study area. c) Kernel density map based on the whole GSD dataset highlighting the presence of six distinct high density zones.

The six high density regions cover 33% of the total study area but enclose 85% of the instabilities detected in the entire dataset. When GSD typologies are considered separately (Figure 3.1-6), the six high density areas vary in significance. DSGSD almost follows the general spatial density, except in the Martigny area where few are observed (Figure 3.1-6a).

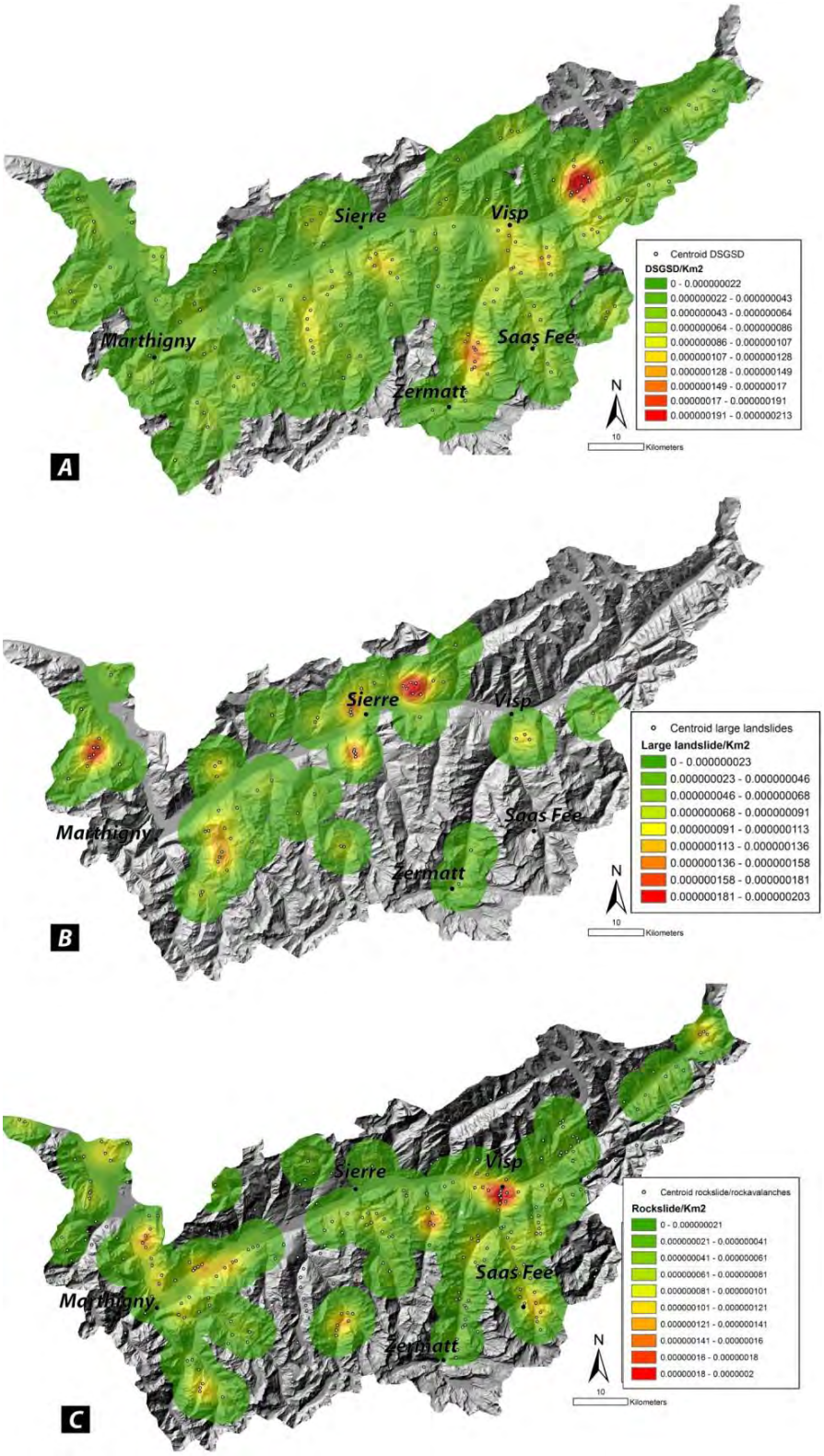

Figure 3.1-6: Kernel density maps obtained for each GSD typologies separately.

Conversely, LRT are well represented in the Val D'Illiez, Sion-Sierre and in Martigny areas, but are almost absent in the Visp-Brig area (Figure 3.1-6). RRA are scattered across all the study areas with a significant density in Mattertal-Saastal, also in the Visp and Martigny areas (Figure 3.1-6).

Ripley's K-function has been estimated to statistically explore the clustering of GSD events and envelopes have been generated to assess the goodness of the fitting (results not shown). Figure 3.1-7 displays the L-function (a derivative of K function) for the total population and for each one of the three classes of GSD. It shows that GSD events are not randomly distributed over the study area. Clustering can be observed for each GSD type for a distance between 0 and 10 km, with a maximum at about 2 km. This means that, considering the phenomena as inhomogeneous, the number of events inside a circle of radius equal to this distance from a chosen event, is higher than the expected number for a completely random point process. For a distance larger than 10 km, events (are more likely to) follow a random distribution.

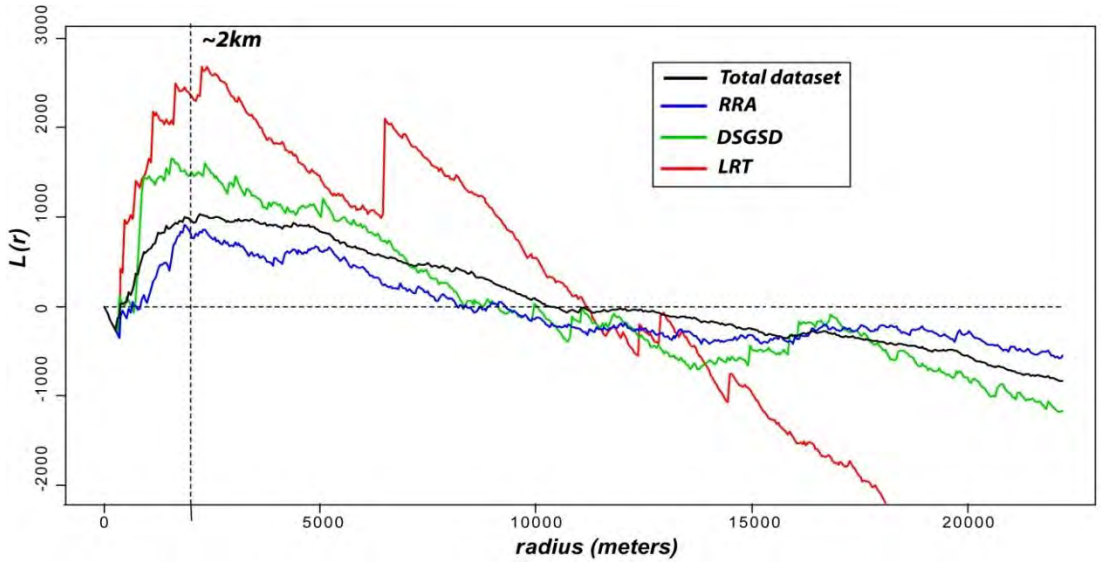

Figure 3.1-7: Ripley's L-function for all GSD events (black line) and for each landslide's category: GDT (red line), RSL (green line) and DGPV (green line). Horizontal dashed line represents the theoretical L-function while horizontal dash line corresponds to the L(r) maximum value. The distance r is in meters.

3.1.13.2 Lithology

Figure 3.1-8 reports the distribution of the outcropping lithologies in the entire study area compared to the GSD dataset (Figure 3.1-8a) and the different typologies separately (Figure 3.1-8b, c and d). When the total GSD dataset is considered, a clear predominance of a single lithology cannot be observed. However, Flysch, sandstone, and carbonate/marls interbedded layers are overrepresented while orthogneiss and metabasite are underrepresented. As found worldwide (Korup et al., 2007), this indicates a higher predisposition to failure of lithologies where persistent foliation/bedding are present. When the GSD typologies are considered separately, a clearer trend emerges. DSGSDs are concentrated in Flysch and in paragneiss, with more than 60% of cases. At the opposite, RRA are concentrated in stratified carbonates, marls and sandstones. Note that the largest rock avalanches of the study area occurred in marly-limestone rocks (e. g. Sierre 1.5-2 km^3 of volumes, Burri, 1997; Pedrazzini et al., 2011; Derborences 0.3-0.5 Km^3, Montandon 1933). LRT are clearly linked to Flysch and limestone-marls intercalation where more than 80% of the detected features are concentrated. The comparison between the spatial distribution of the

different outcropping lithologies and GSDs density does not show a clear spatial linkage, except for Val d'Illiez area, where bedrock geology is mainly Flysch leading to a local concentration of GSD. In this litho-tectonic context, LRT are preferentially developed (Figure 3.1-8d).

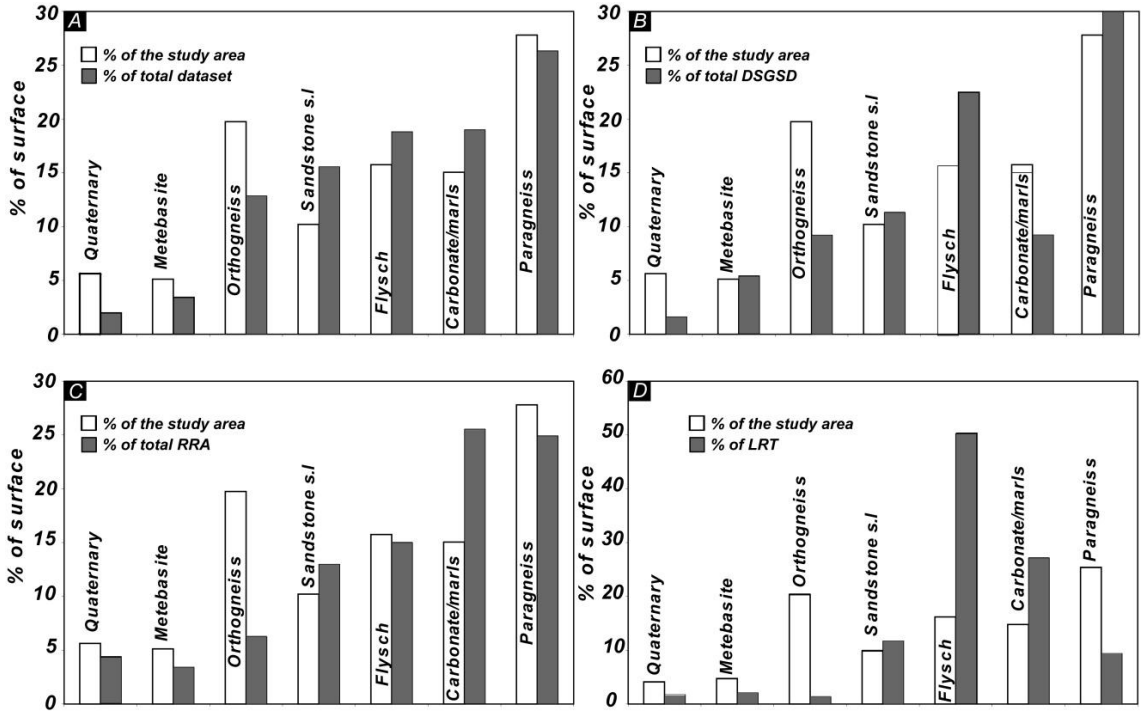

Figure 3.1-8: GSD distribution versus lithology. The areal frequency of each lithology and the percentage of outcrop area involved in GSD are shown. a) Comparison for the whole GSD dataset. b) Comparison for DSGSD. c) Comparison for RRA. D) Comparison for LRT.

3.1.13.3 Penetrative structures

A good correspondence between the TOBIA model and field observations was observed in the areas where bedding planes or foliation is persistent and almost homogeneous (e.g. Helvetic Nappes along central Rhone valley and gneiss of the Gotthard basement in upper Rhone valley). Inversely, in the Penninic domains the interpolation was found to be locally biased due to polyphased metamorphism leading to the presence of more than one main foliation orientation (Steck et al., 2001). The results of the TOBIA index computations are shown in Figure 3.1-9. Half of the study area, particularly lateral tributary valleys, is characterized by orthoclinal slopes (47%). Inversely, Cataclinal (28%) and Anaclinal slopes (24%) are mainly concentrated along the main Rhone valley (Figure 3.1-10a). GSDs are also widespread on the different slope categories with predominance in cataclinal and orthoclinal slopes (40% and 42% of the total landslide area respectively). Underdip configurations affect 33% of the total GSD area. Of the different GSD typologies, LRTs are clearly associated with underdip (60% of the LRT area). In contrast, RRA is linked to subdued escarpments (36% of the RRA area). DSGSDs are widespread in all structural settings. The structural configuration has also an important influence on the size of the GSD (Figure 3.1-10b). Larger failures (≥ $1x10^7$ m^2) are preferentially mobilized on cataclinal slopes (13% of the total dataset) rather than on orthoclinal or anaclinal slopes (6% for both) and this holds good for all GSD typologies. The observed GSD distributions within the different

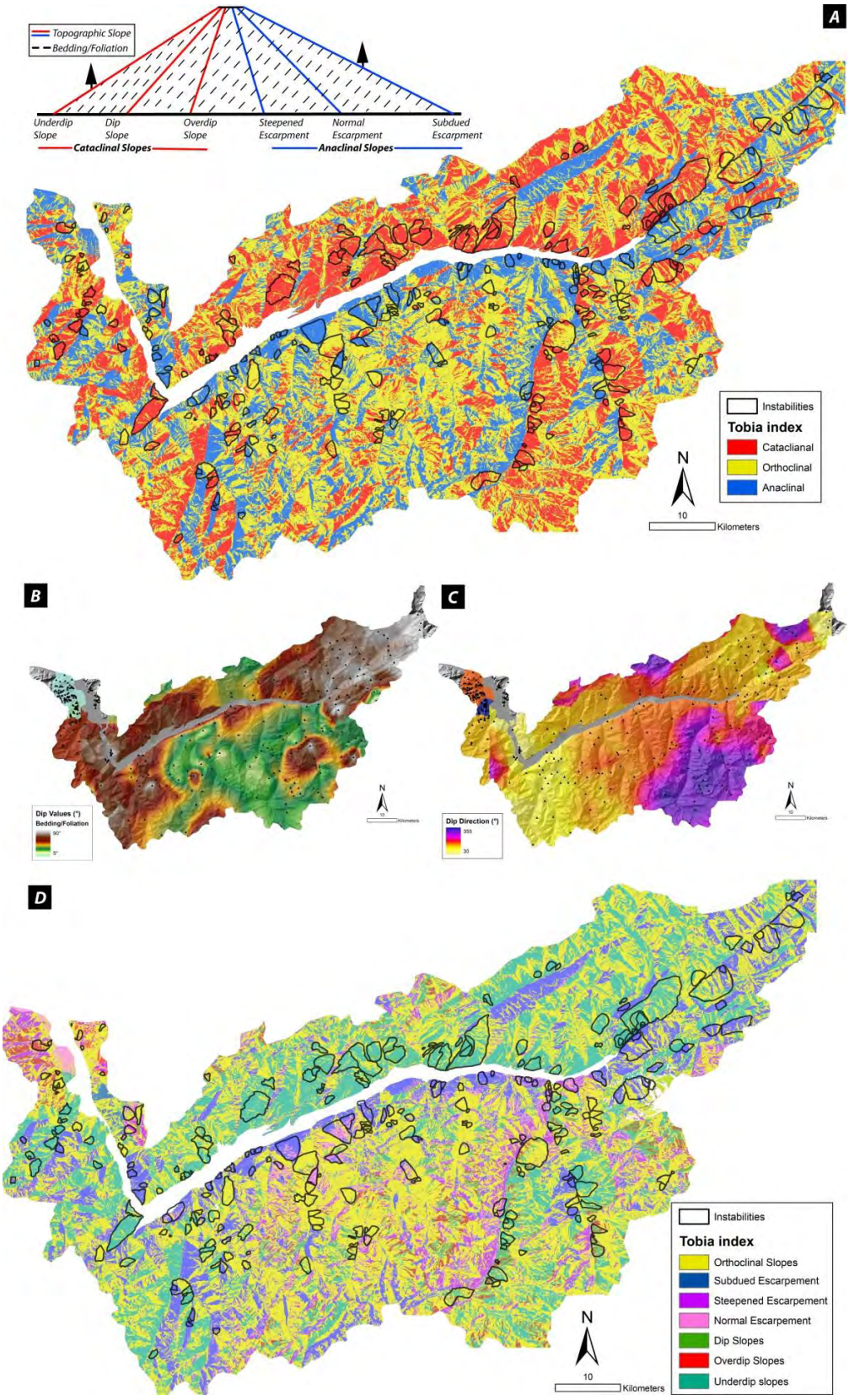

Figure 3.1-9:Spatial relationships between TOBIA index and GSD. The classification between topography and the main foliation, according to Meentemeyer and Moody (2000), is presented in the upper left corner. a) Three way categorical classification (simple TOBIA index). b) Interpolation of dip values of bedding planes or main foliation. Black points represent the location of the measurement. c) Interpolation of dip direction values of bedding planes or main schistosity. d) Detailed Tobia index classification dividing the slopes of the study area in seven different classes.

Tobia indexes are probably associated to the geometrical and the mechanical behaviour of the different geologicl units that can be found in the area. In particular, the small proportion of DSGSD in overdip or dip slope configurations can be explained by the fact that these geometrical setting represents directly an unstable situation that is prone to develop small scale instabilities and continuous erosion thought small scale destabilisation. At the opposite, underdip slopes represent, from a pure geometrical point of view a more stable configuration where GSD did not rapidly evolve in catastrophic failure after the glacial retreat. At the same time, it must emphasized that the overdip and dipslope configurations (respectively steepened and normal escarpment) represent particular geometrical setting that subject to a large uncertainties according to the spatial distribution on the study area of the foliation data. For this reason, the percentage of the GSD within the six subunits of the Tobia index needs to be critically analysed.

Large fault systems play an important role on the development of large slope instabilities by creating zones of weakness that passively control GSD (Agliardi et al., 2009). In the southern portion of the main Rhone Valley, it is possible to follow a clear alignment of GSD morphological features (both scarps and trenches) parallel to the Rhone-Simplon fault system. Euclidian distance calculation indicates that 10% (32) of the GSD are located within 1km from the Rhone-Simplon fault system. Field evidences (Sue et al., 2007) indicate an important ramification of the fault system which can locally exceeds 3 km width. Using this maximal extend, we found that at least 35% of the entire instabilities dataset are located close this main brittle tectonic accident.

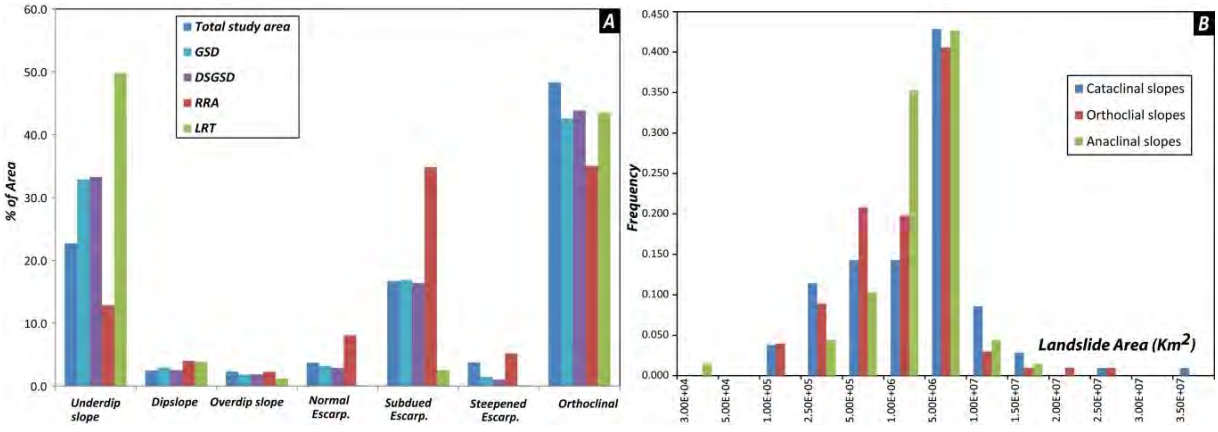

Figure 3.1-10: GSD and GSD typologies areal distribution versus slope and main foliation attitude (TOBIA index). b) Landslide area of the whole GSD dataset compared to three possible foliation configurations.

3.1.13.4 Slope and slope aspect

The slope angle distribution of the GSD populations was compared with that of the entire study area (Figure 3.1-11a). The modal angle value of the slope distribution within the GSD dataset (φ mod ~ 30°) is slightly smaller than the modal hillslope angle of the entire study area (φ mod ~ 31°). DSGSD shows little difference from non-failed slope angles, like the whole GSD dataset; LRT produces subdued topography as slopes relax into more stable configurations (φ mod ~ 25°); while RRA creates prominent scars and thus yields considerably steeper slopes (φ mod ~ 36°). These differences in the modal slope angle value can be linked to the rock mass strength of the lithology where they develop and also to the different degrees of disintegration (Jarman 2006) that characterize the different GSD typologies. The direct influence of the different GSD typologies on the hillslope slope angle is therefore different. For instance, RRA can lead to a

local increase of the hillslope angle by creating prominent scars, whereas LRT are more efficient to directly decrease the hillslope angle by creating a smoothed topography to reach a more stable configuration. Korup (2005) suggested that larger GSD have a greater impact on the topography by creating low–gradient slopes. Figure 3.1 11c tests the difference in slope distribution between GSDs </>1km2 and the entire study area, and confirms that larger GSDs create lower gradient slopes. The slope aspect distribution in the study area shows a NW-SE anisotropic distribution related to the orientation of the main Rhone valley. When normalized to this distribution, no preferential slope aspect is seen in the GSD population (Figure 3.1 11b). This also holds well for DSGSD, whereas RRA and LRT preferentially develop on NNW and SE slopes respectively. This reflects the geology of the Rhone valley since SE slopes are mainly meta-sediments of the Helvetic Nappes with an underdip configuration which is the typical environment where LRT develops, while NNW slopes are mainly hard rock masses of the Penninic front containing persistent faults and major joints that allow the creation of large catastrophic failures (RRA).

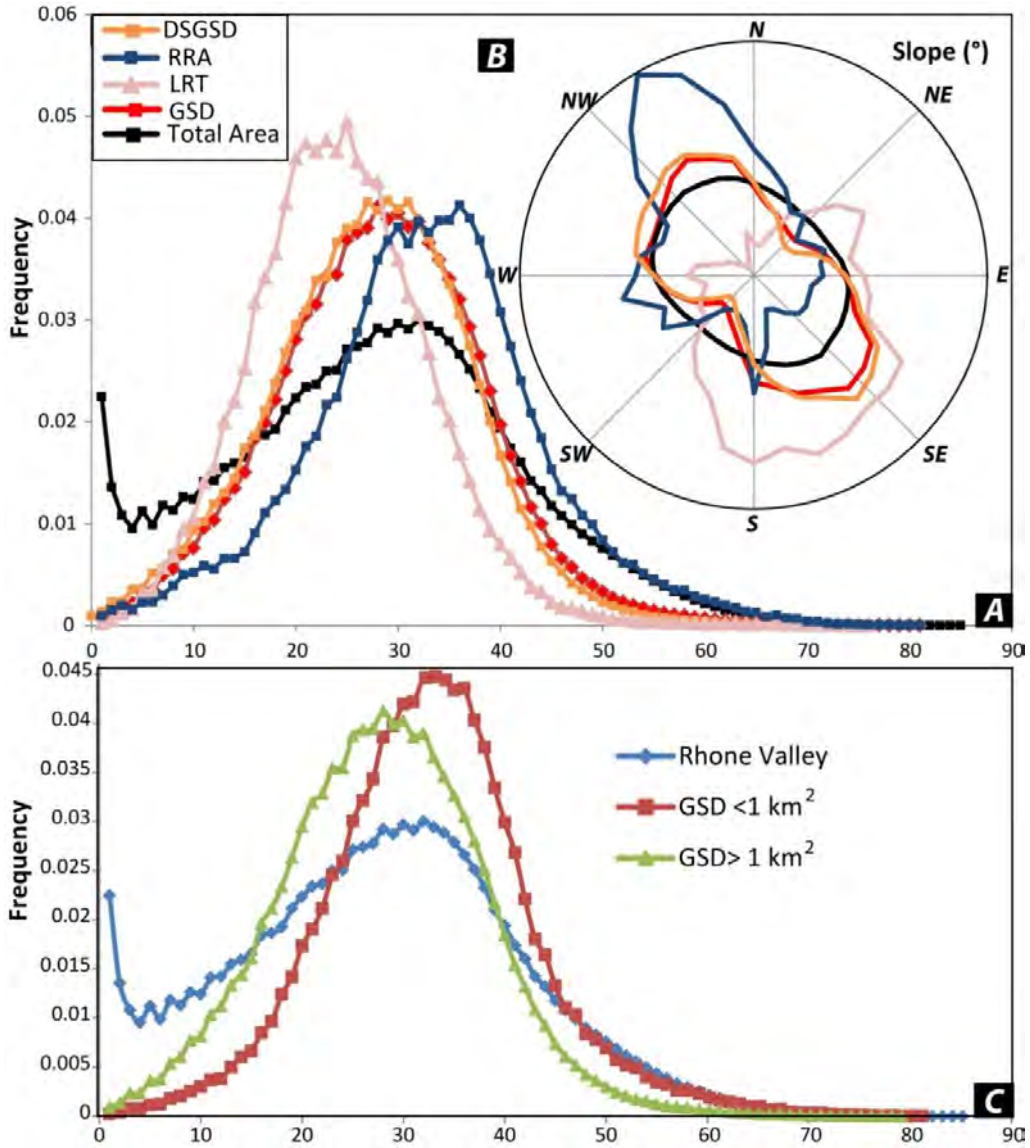

Figure 3.1-11: Morphometric analyses of rock slope instabilities based on 25 m DEM. a) Comparison between slope frequency distribution of the entire study area and slope frequency distribution for the different GSD typologies. b) Aspects of GSD-affected areas (scarps and deposits combined) and slope aspect, normalized by area, in the total Rhone catchment. c) Frequency distributions of surface-slope angles for GSD displaying a surface </> 1km².

3.1.13.5 Relief

Local relief can be calculated by subtracting the minimum elevation from the maximum elevation within a circular window of 5 km radius (Khueni and Pfiffner 2001; Montgomery and Brandon, 2002). The local relief is slightly higher than typical for the Alps (Agliardi et al., 2009), reflecting the presence of both deeply incised valleys and most of the highest peaks of the Alpine chain. 90% of the study area has a local relief greater than 1000 m, notably within the higher rock strength lithologies of the Penninic Nappes and gneissic basements (Figure 3.1-12a). GSD are associated with a local relief greater than 1500 m, with 90% of total GSD area having local relief greater than 1900 m. Modal values are 2200 m of local relief for the entire study area and 2400 m for GSDs with no major differences between the different GSD typologies (Figure 3.1-12b).

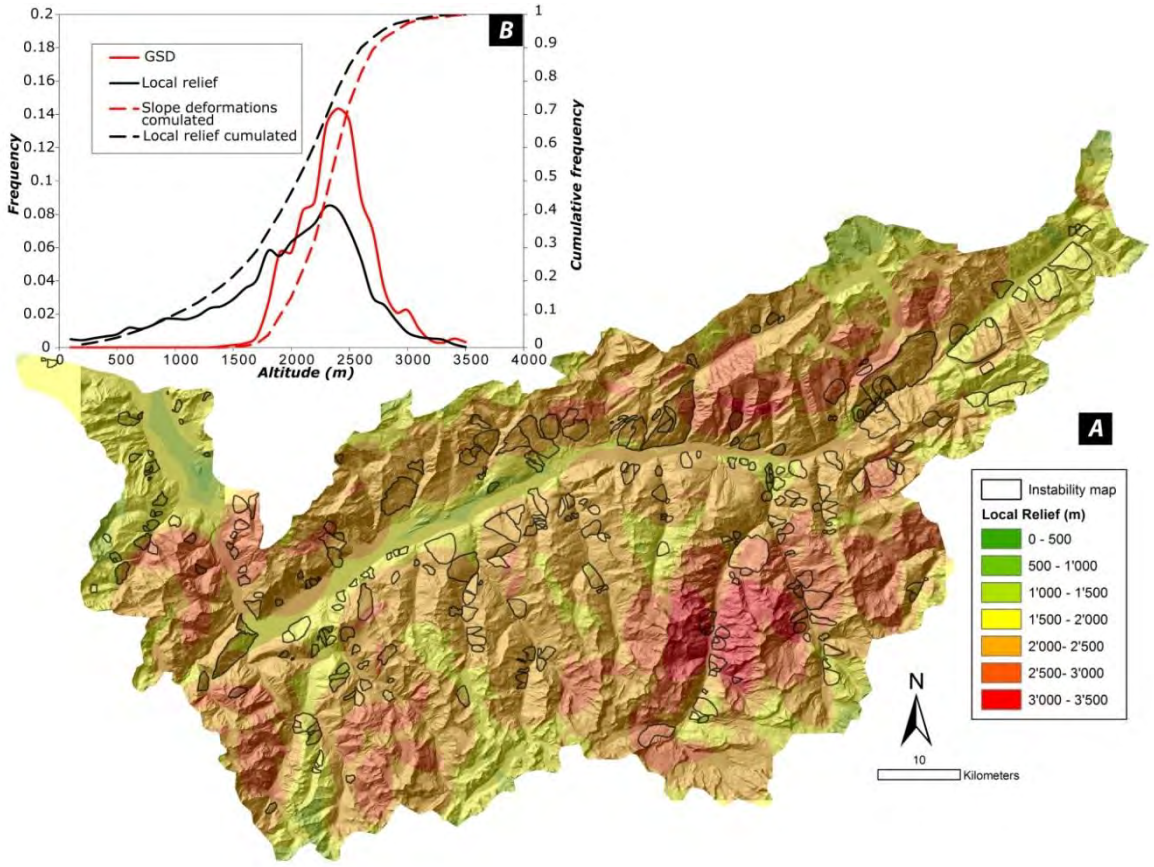

Figure 3.1-12: Local relief map for the upper Rhone catchment compared to the GSD distribution. b) Comparison between the mean local relief distribution in the entire study area and the distribution within GSD areas.

3.1.13.6 Precipitation and glacial forcing

In Figure 3.1-16a and b a clear inverse correlation is observed between GSD and precipitation (convex beta distribution according to alpha and beta values in Table 3.1-1). These results are not surprising because the study area, in particular the region showing a major GSD density, correspond to the driest regions of entire Switzerland. Although the quantity of present-day precipitations does not reflect early postglacial or Holocene conditions, the spatial distribution should have been almost similar, indicating that precipitations and paleoclimate do not control the spatial distribution of the detected GSD (Figure

3.1-13). Glaciation in term of paraglacial stress release and also in term of creation of new relief (i.e. glacial overdeepening or important glacifluvial/paraglacial stream incision) is considered a major predisposing factor for GSD development (Ballantyne 2002; Jarman 2006; Cossart et al., 2008). During the last glacial maximum (LGM), the study area was almost completely covered by ice. As a consequence, potential GSD areas are expected to be localized where the glacial shear stress and the glacial over deepening were the most important (Cossart al., 2009). In the Western Alps, this setting corresponds to the zones where the total ice thickness was highest and where the valley topography is characterized by a rapid change direction (Pedrazzini et al. in prep.).

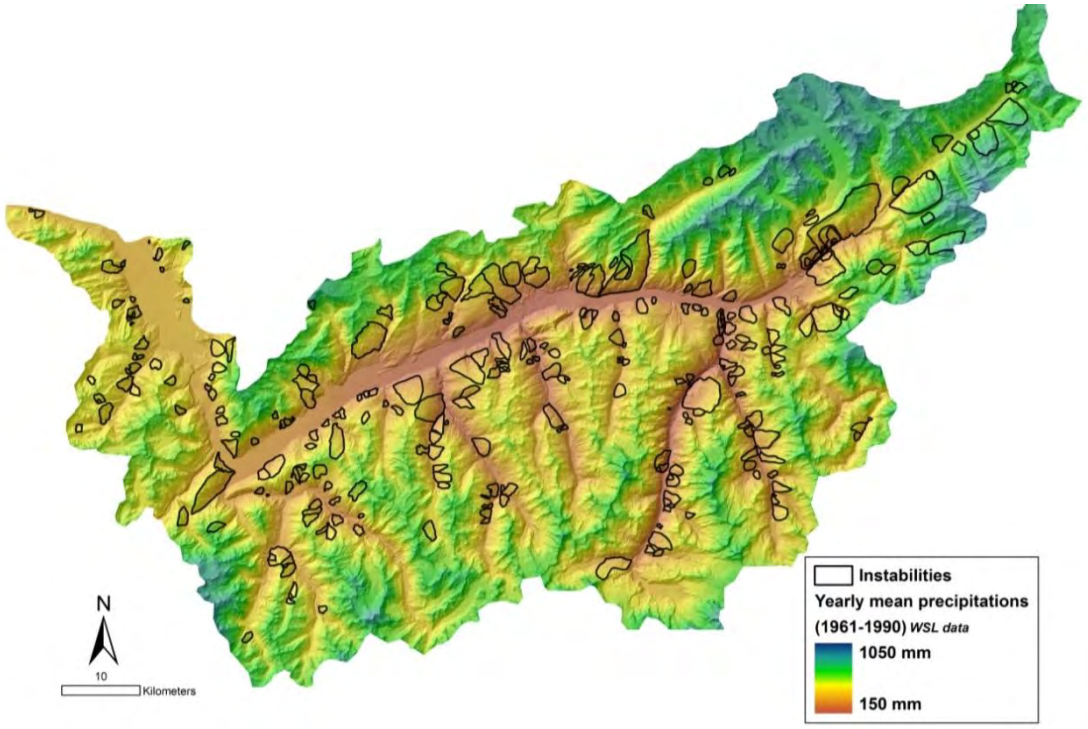

Figure 3.1-13: Comparison between the spatial distribution of yearly mean precipitations (mm/y) and the distribution of the mapped GSD.

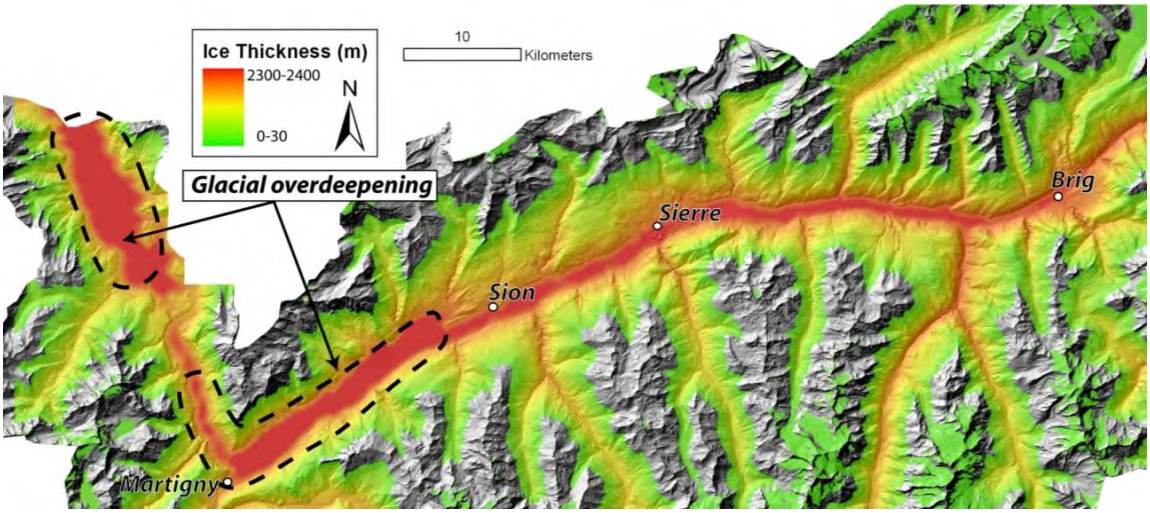

Figure 3.1-14: Maximal ice thickness within the main Rhone valley according to the published data about the maximal ice elevation during LGM (Kelly et al., 2004) and the bedrock model proposed by Jaboyedoff and Derron (2005).

Figure 3 14 shows a maximum glacial thickness of about 2.3 km close to Martigny and close to St. Maurice. This map was created by subtracting valley bedrock DEM proposed by Jaboyedoff and Derron (2005) to the LGM glacier surface (Kelly et al., 2004). The most important change on the main valley direction is located near Martigny. This area is associated with high RRA suggesting an important glacial and periglacial forcing. Concerning the others GSD typologies, a clear correlation to glaciation or paraglacial processes cannot be establish.

3.1.13.7 Uplift and uplift gradient

Figure 3.1-15 displays the interpolated uplift map for the upper Rhone catchment compared to the historical and instrumentally recorded seismic activity. No apparent correlation is observed between high uplift values and earthquakes distribution, high local relief or ice thickness. A quantitative comparison between landslide distribution and uplift was realized by calculating both landslide area and number of landslides within the surface of the study area corresponding to the different uplift values. Figure 3.1-16c and d show the results on a normalized cumulative chart. The normalized cumulative distribution shows a concave shape implying a non–uniform distribution of the landslides within the different uplift values. An increasing Beta distribution is statistically representative of this distribution (Table 3.1-1). This indicates that a correlation exist between high uplift values and both the number and the extent of the total landslide dataset. Graphically we can observe, on Figure 3.1-16, that less than 25% of the study area (corresponding to uplift values larger than 1.1 mm/y) contains more than 45% of the detected GSD and more than 55% of the total GSD areas.

Table 3.1-1: Parameters of Beta distribution adopted to fit the cumulative frequency distributions describing the relation between the number and the surface and a given surface–based interval of the analysed factors. Goodness of fitting is given by Kolmogorov-Smirnov test (α=0.05)

Parameter	Alpha	Beta	Goodness of fitting
Uplift number	1.1	0.45	0.302<0.318
Uplift surface	1.2	0.4	0.273<0.361
Uplift gradient number	1.15	0.85	0.164<0.287
Uplift gradient surface	1.15	0.64	0.216<0.224
Seismic energy release number	1.1	0.65	0.242<0.409
Seismic energy release surface	1.2	0.6	0.260<0.409
Precipitation -surface	0.7	1.20	0.31<0.39
Precipitation number	0.7	1.25	0.34<0.31

Jaboyedoff et al. (2003, 2005) suggested that the analysis of the uplift gradient can provide a good approximation of the location of highly strained zones, when the uplift is suspected to be related to tectonic activity. Highly strained zones can be considered to be seismically active and can potentially facilitate the development of GSDs. The gradient vector norm was calculated for the entire study area following the formulation proposed by Kreysig (1999):

$$\left|\vec{G}\right| = \left|\sqrt{\left(\frac{\partial z}{\partial x}\right)+\left(\frac{\partial z}{\partial y}\right)}\right| \qquad \text{Eq. 3.1-3}$$

where x, y and z are the spatial coordinates and the norm of the gradient vector is equal to the tangent of the slope angle of the terrain.

The quality of the uplift gradient map is strongly dependent on the location of the uplift measurements. Especially in the southern portion of the study area, where no measurements are available, the obtained interpolated results are uncertain and need to be critically analysed. Graphical representation of the gradient vector norm calculation is presented in Figure 3.1-15. Higher uplift gradient values are located near Sion, Marthingy, in Visp-Brig area and close to the Simplon Pass. The gradient vector norm shows a clear correlation with historical and instrumentally recorded larger earthquake clusters (Jaboyedoff et al., 2003; Ustaszewski and Pfiffner 2007). Almost the entire earthquake activity is associated with uplift gradients higher than 0.03 [mm/ (Km/y)] (Figure 3.1-15).

GSD distribution relates more strongly to uplift gradient than to simple uplift rate presenting a more marked concave shape (Figure 3.1-18 and Table 3.1-1). In this case, it also follows an increasing beta distribution indicating a correlation between GSD and higher uplift gradient values. An important variation of the slope in the chart is observed at 0.08 [mm/ (Km/y)] after which 15% of the total study area with higher uplift gradient encloses 30% of the total GSD dataset. When GSD areas are considered, the correspondence between higher uplift gradient and GSDs distribution is more obvious. In this case, 45% of the total GSD areas are enclosed in less than 15% of the total study area.

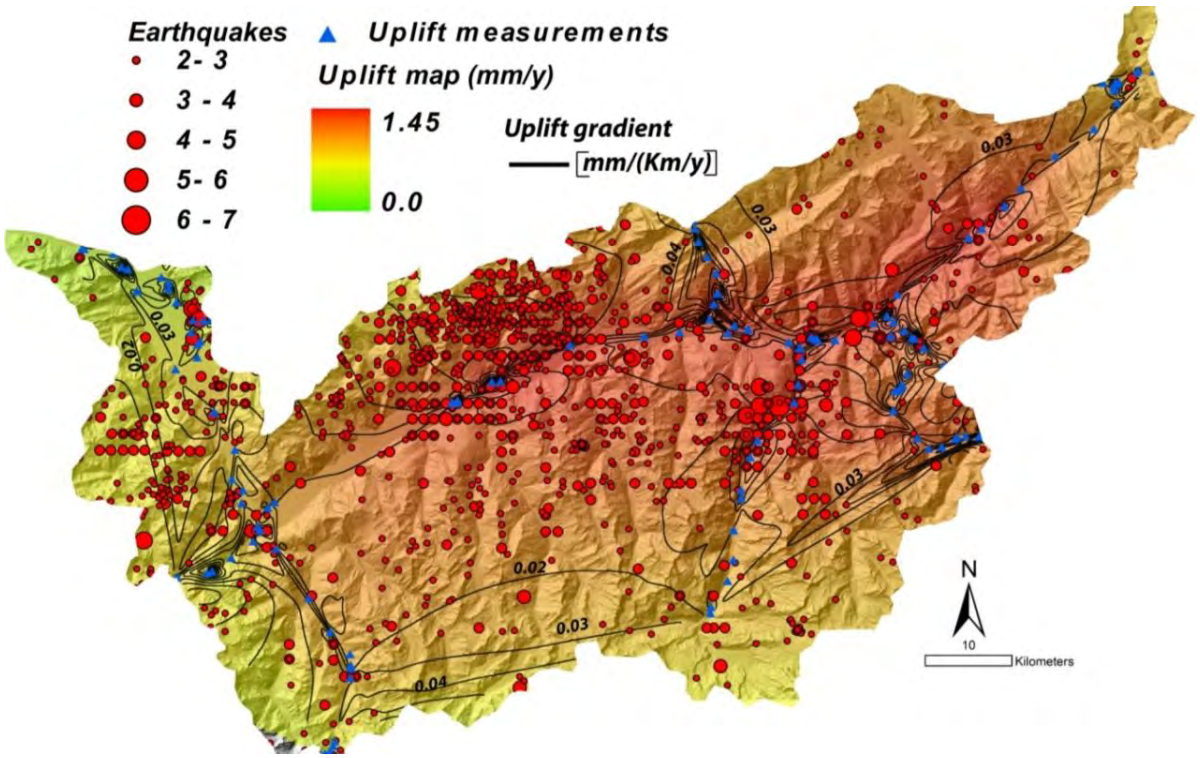

Figure 3.1-15: Interpolated uplift map and uplift gradient contours (black line) within the upper Rhone catchment compared to the historical and instrumentally recorded seismicity (red dots). Note the clear spatial relation between the seismic activity and the higher uplift gradient values.

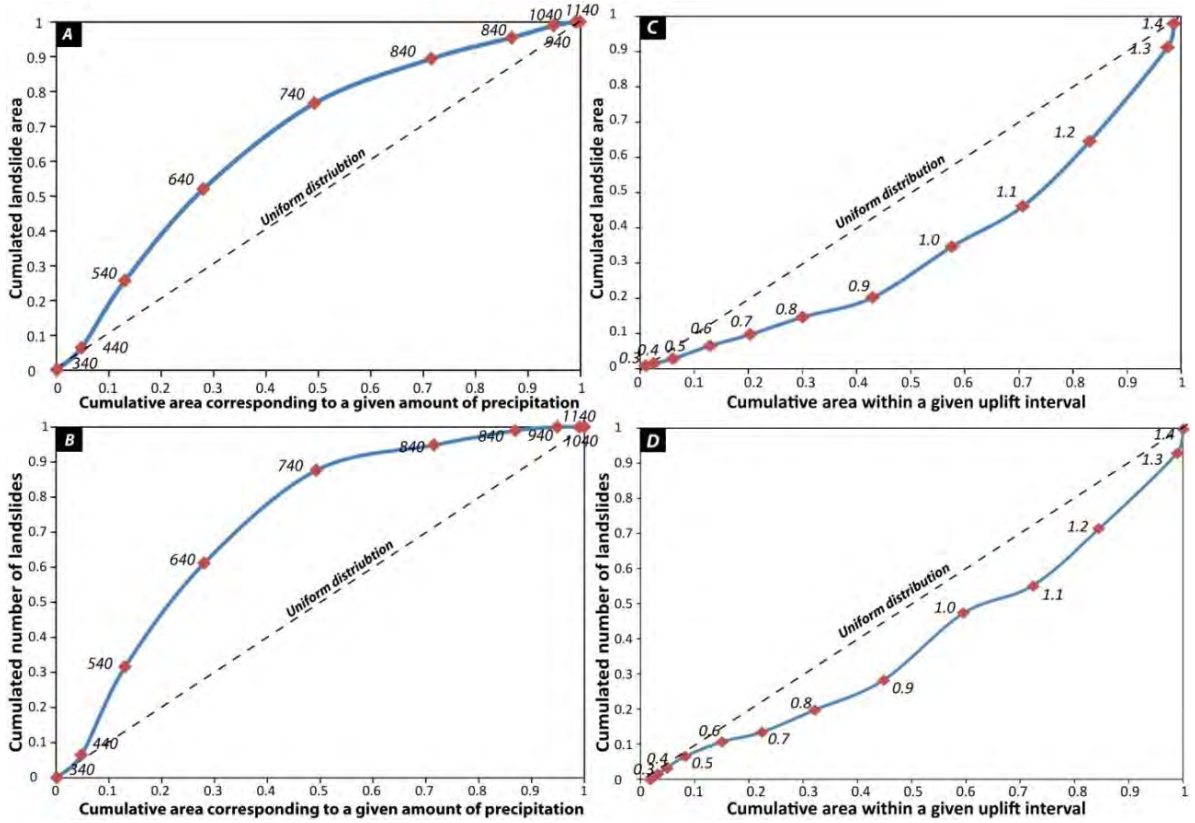

Figure 3.1-16: Cumulative distribution of the GSD (number and surface) within a given surface–based interval of mean annual precipitation (charts a and b) and within a surface–based interval of uplift (charts c and d). For each calculated point, the corresponding value of precipitation and uplift value is reported on the chart. Dotted lines correspond to a hypothetical uniform distribution of GSD (number or surface) within the different surface-based intervals.

3.1.13.8 Earthquakes and seismic energy release

The spatial relationship between seismic activity and rock instabilities in Rhone valley has been first pointed out by Jaboyedoff et al. (2003). Cases of rock instabilities triggered by historic earthquakes are also reported in the literature (Gisler et al., 2003; Fritsche and Fäh 2008).

In order to investigate this potential correlation, the total energy release of historical and instrumentally recorded earthquakes has been computed by summing the energy released within a circular window of 10 km radius. Conversion from magnitude to energy has been achieved based on the equation proposed by Richter and Gutenberg (1954):

$$LogE(s) = 4.8 + 1.5M \qquad \textit{Eq. 3.1-4}$$

Where *E(s)* is seismic energy (in Joule) and *M* is Earthquake Moment Magnitude.

A close spatial relationship exists between uplift gradient and the area of maximum seismic energy release (Figure 3.1-17). This implies that a potential correlation between seismic energy release and GSD might also exist. Indeed, GSD incidence is associated with increasing seismic energy levels following a concave beta distribution similar to previous analyses, notably above a seismic energy value of 1.3×10^{14} Joules (Figure 3.1-18 and Table 3.1-1). Only 30% of the entire study area has values above this energy level, but accounts for 55% of GSD cases and 65% of GSD area.

The association is strongest in the Sion –Sierre, Visp-Brig and Upper Mattertal areas, and is also observed in the Martigny and Val d'Hérens zones. Ripley's K-function can be used to define the spatial relation in the distribution of two or more events. L-function, a derivative of inhomogeneous K-function, has been calculated for GSD and earthquakes and the two curves have been plotted together to compare their trend (Figure 3.1-19).

The two curves display the same behaviour: both shows clustering of events at a distance between 0 and 10 km, with a maximum at around 2 km. This result also suggests that the pattern distribution of the GSD and earthquake events considered in the present study follow a similar spatial clustering.

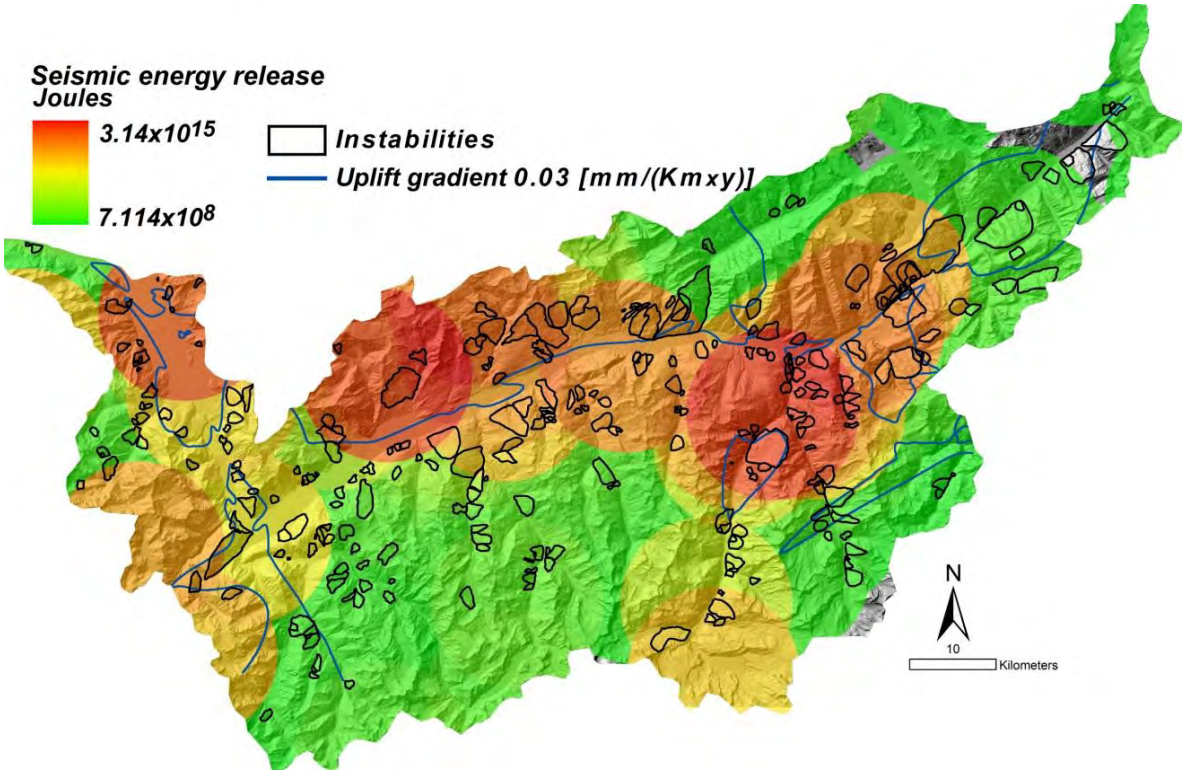

Figure 3.1-17: Map of earthquake energy release sum within a circular window of 10 km. Most of the seismic energy is released from areas displaying and uplift gradient > 0.03 [mm/ (Km/y)]. Note the good spatial relation between GSD distribution and seismic energy release areas.

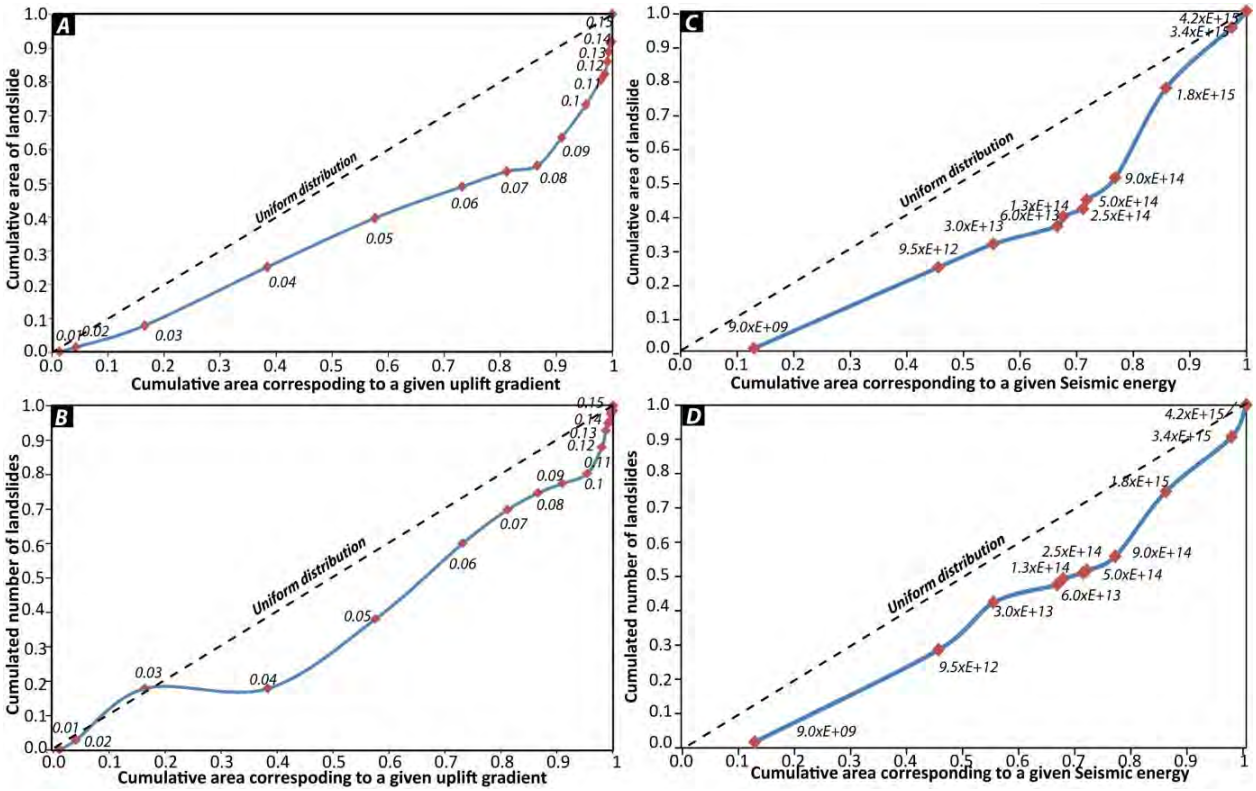

Figure 3.1-18: Cumulative distribution of the GSD (number and surface) within a given surface–based interval of uplift gradient (charts a and b) and within a surface–based interval of seismic energy (charts c and d). For each calculated point the corresponding values of uplift gradient and seismic energy is reported on the chart. Dotted lines correspond to a hypothetical uniform distribution of GSD (number or surface) within the different surface-based intervals.

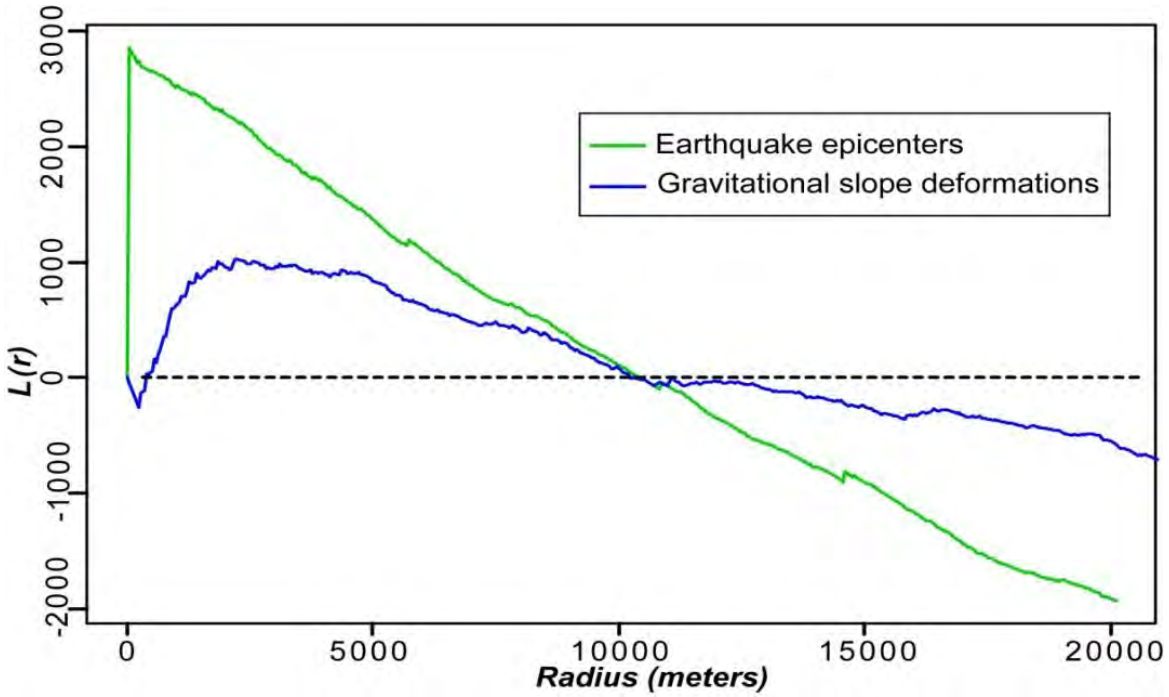

Figure 3.1-19: Ripley's L-function for GSD (blue line) and earthquakes (green line). Dashed line represents the theoretical L-function. The distance r is in meters. Ripley's L-function for earthquakes displays a bias for small values of radius (< 1000 m) related to the approximation in the coordinate values of the earthquake epicentres.

3.1.13.9 Magnitude-frequency distribution

Frequency density distribution indicates that GSD areas range between three orders of magnitude. As pointed out by Malamud et al., (2004) and Hovius et al., (1997) few larger GSD contribute massively for the total affecting area. In our dataset, the ten larger GSD (3% of the total dataset) correspond to 30% of the entire GSD surface. For the total GSD dataset the frequency density plot is shown in Figure 3.1-20a. Larger GSD (i.e. > 1km^2) are well described with a negative power-law with an exponent of 2.26 (R^2=0.99). The rollover that describes the area, after which data fall below the power-law line, is located at 1 km^2. This value is approximately 1.5 orders of magnitude larger than the minimum detected GSD. Similar correspondences between rollover and minimum landslide sample have been described by Guthrie and Evans (2004).

Below 1 km^2, the distribution flattens and suddenly decrease similar to what has been described by Malamud et al. (2004). Statistical distributions as double Pareto (Stark and Hovius 2001; Guthrie and Evans 2004), log normal (Chaytor et al., 2009) or inverse gamma (Malamud et al., 2004; Van den Eeckhaut et al., 2007) functions were tested to describe the entire landslide database. The best fit here was obtained using the three-parameter inverse-gamma probability density distribution (Malamud et al., 2004):

$$p(A_L;\rho,a,s)=\frac{1}{a\Gamma(\rho)}\left[\frac{a}{A_L-s}\right]^{\rho+1}\exp\left[-\frac{a}{A_L-s}\right] \qquad \textit{Eq. 3.1-5}$$

where (A_L) is the landslide area, (ρ) is the parameter controlling the power-law decay for medium to large landslides, (a) is the parameter controlling the location of the maximum probability distribution and (s) is the parameter controlling the rollover for small landslide areas.

For the total Rhone valley dataset, the best fit is obtained using the following parameters p=1.26, a=1.054x10^6 and s=-1.710x10^5 with a correlation coefficient of 0.93 (Figure 3.1-20b). The goodness of the fitted distribution was also confirmed based on Kolmogorov-Smirnov test (significance level of 0.05). The exponent of -2.26 for the power-law tail (corresponding to – (p+1) on the inverse gamma equation) is in good agreement with the average value of -2.3 calculated by Van den Eeckhaut et al. (2007). As already shown by Antinao and Gosse (2009), it suggests that the frequency density function of Malamud et al. (2004) is almost scale invariant and can also be applied for GSD inventories (1-100 km^2). Considering the three GSD typologies separately the exponent of the power-law tail typologies are quite similar (from -2, 14 to -2.17) but slightly smaller than the total dataset (Figure 3.1-21).

Following van den Eeckhaut et al. (2007) this indicates a more important contribution of larger GSD in the total inventory. In contrast, the distribution of the smaller slope deformations is quite different for the three typologies. The DSGSD with smaller surface are characterized by a positive power-law which is separated from large surface by a rollover. Smaller RRAs and LRTs are better described by a power-law with a negative exponent. This difference is probably related to the reduced geomorphological imprint of the small GSD on the topography leading to a recording bias especially with a historical inventory that covers a period since the LGM and where local morphological conditions have considerably evolved.

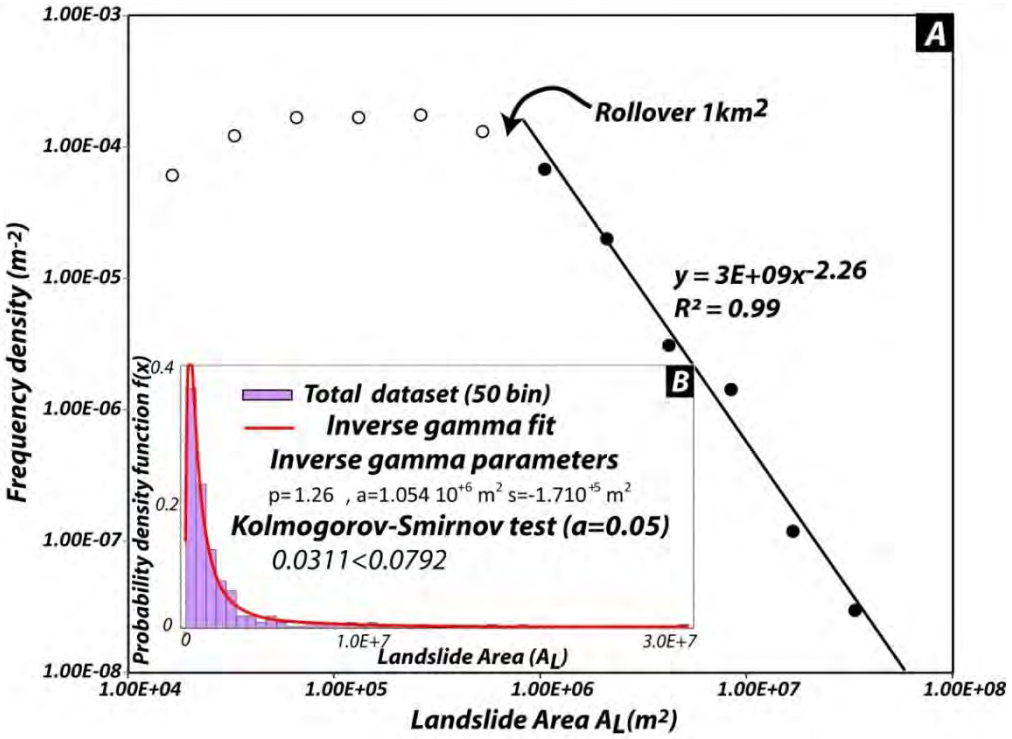

Figure 3.1-20: Non-cumulative probability density distribution of GSD dataset displayed in a logarithmic axis. Larger GSD are well described with a power-law. The total dataset can be described by an inverse gamma distribution. The rollover is approximately located at 1 km². b) Histogram of the same dataset displayed in a non-logarithmic axis where an inverse gamma function can be fitted. Best-fit values and results of Kolmogorov-Smirnov test are also reported.

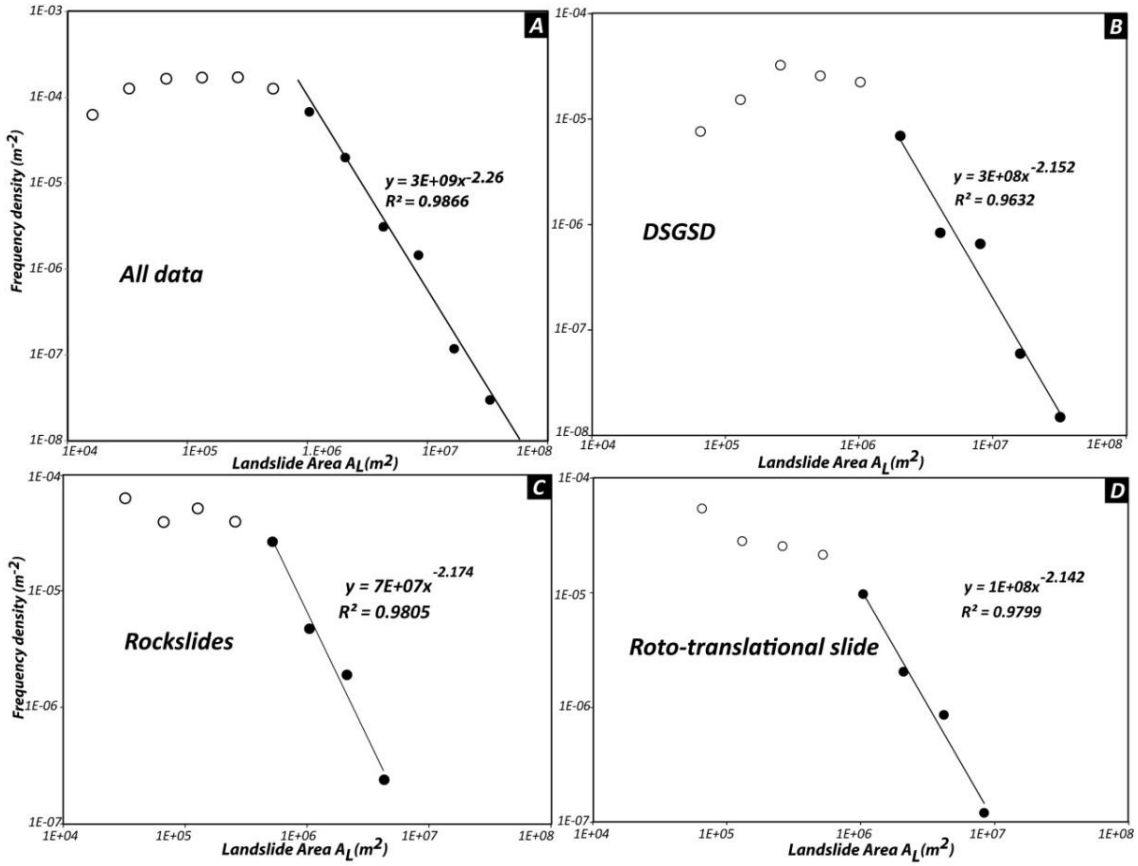

Figure 3.1-21: Non-cumulative probability density distribution of the different GSD typologies displayed in a logarithmic axis. Note that frequency distribution of larger GSD areas are very well described by a power-law. The rollover is approximately located for all GSD typologies at 1 km².

3.1.13.10 Tectonic control of large morpho-structures

Based on air images and DEM analyses, 6500 lineaments were detected. Figure 3.1-22 shows the distribution and orientation of the detected lineaments and the corresponding rosette plots. The lineaments are represented on different rosette plots according to the main tectonic units as suggested by Ustaszewski and Pfiffner (2008). The main lineament orientations clearly change from east to west of the Rhone valley. Above Brig, the upper Rhone valley is characterized by pervasive sub-vertical NE-SW foliation and lithological contacts. The mapped tectonic faults follow almost the same trend. Gravitational morpho-structures, in particular counter-scarps, are well developed in both side of the valley and follow predominantly the foliation orientation.

Lineaments detected in the Penninic Nappes have been divided in two zones and plotted separately according to the change in orientation of the Rhone-Simplon fault. In the western portion of the study area (Martigny-Sion) two main regional fracture orientations (NE-SW and NW-SE) can be observed. In the eastern part (close to Brig), ENE-WSW and NW-SE orientations are observed. In the western part NE-SW-lineaments are clearly visible at both regional and outcrop scale and, in particular along the main Rhone valley. These are probably related to the Rhone Simplon fault system and associated to normal and dextral strike-slip movements under the current stress field (Champagnac et al., 2004). In the eastern part of the study area, the orientation of the lineation related to the Rhone Simplon fault changes, becoming NW-SE according to the L-shape of the fault system.

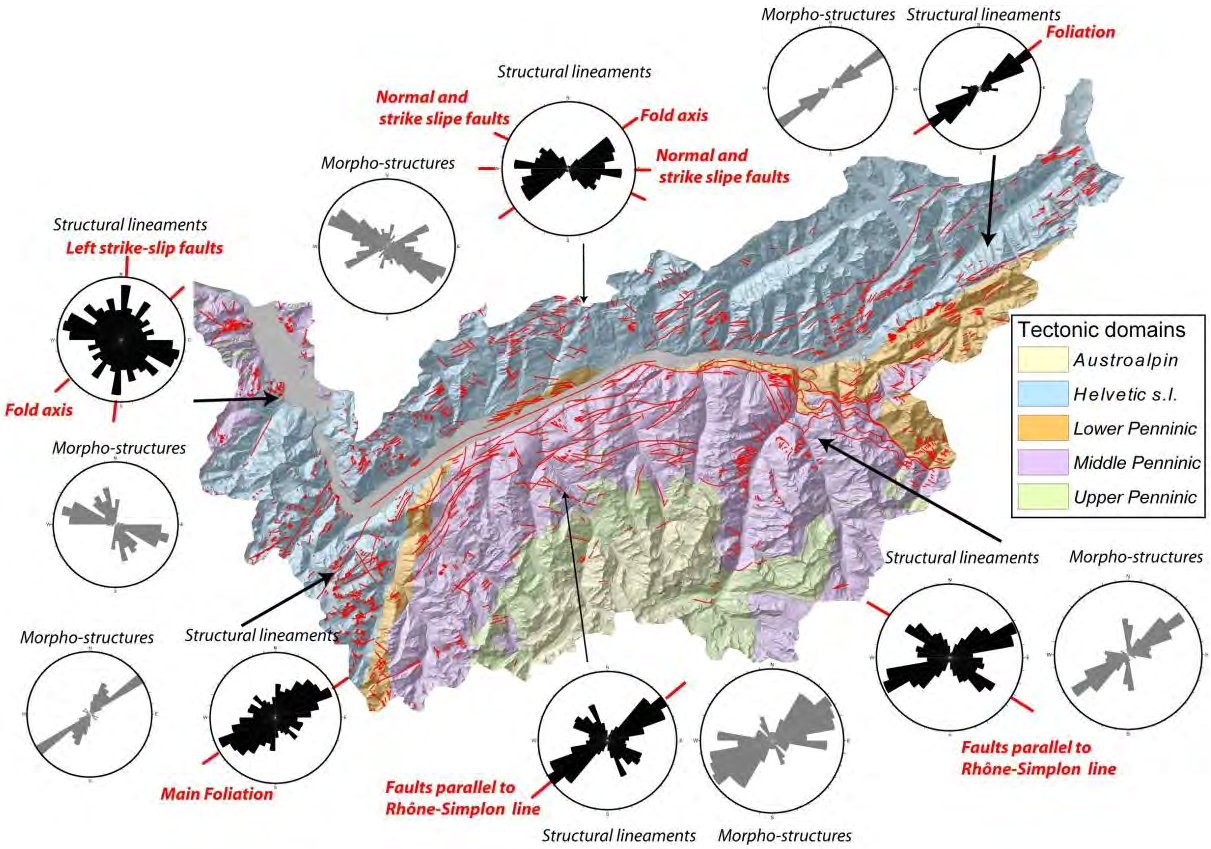

Figure 3.1-22: Main lineaments (tectonics and gravitational) identified in the Rhone catchment. Lineaments have been mapped and displayed in six sub-regions according to the regional tectonics setting. Grey rosette plot trend of morpho-structural features (gravitational and composite lineaments) and black rosettes correspond to the trend of tectonics lineaments.

In this area, NW-SE lineaments are more difficult to explain. Sue et al., (2007) suggest an older origin related to the Simplon fault during Neogene stress field. On the other hand, according to present-day stress regime, Jaboyedoff et al. (2003), indicate that NW-SE and ENE-WSW lineations can be related to large, new or pre-existing faults, permitting the uplift adjustment within the upper crust. Along the tributary valleys, morpho-structural features are mainly NE-SW trending, depending on the local topographic conditions.

Along the main Rhone valley, morpho-structures are predominately parallel the Rhone-Simplon fault system. In the Simplon Pass area, tectonic settings (Berisal syncline) induce morpho-structural features that are associated to the main foliation trend (NE-SW orientation). Recent gravitational reactivation of foliation or tectonic faults sub-parallel to the foliation creates evident deformations that are even visible on Holocene rock glaciers (Figure 3.1-23). In the Helvetic Nappes, two main and two subordinate lineament trends have been detected (NE-SW, NW-SE and WNW-ESE, WSW-ENE respectively). The observed orientations are in agreement with in-situ fault analyses performed in the area (Huggenberger and Aebli 1989; Ustaszewski and Pfiffner 2008; Gasser and Mancktelow 2010). NE-SW lineaments can be associated to normal faults parallel to the regional fold axis whereas the NW-SE trend correspond to normal faults or joint set perpendicular to the fold axis. ENE-WSW and WNW-ESE lineaments can be associated to normal and strike slip faults (Burkhard 1998). Morpho-structural features are generally extensional (scarp and trenches) and follow persistent NE-SW or NW-SE structures or a combination of both depending on local morphological setting. In the basement (Mont Blanc and Aiguilles Rouge crystalline massif) lineaments show a NE-SW trend sub-parallel to the main foliation.

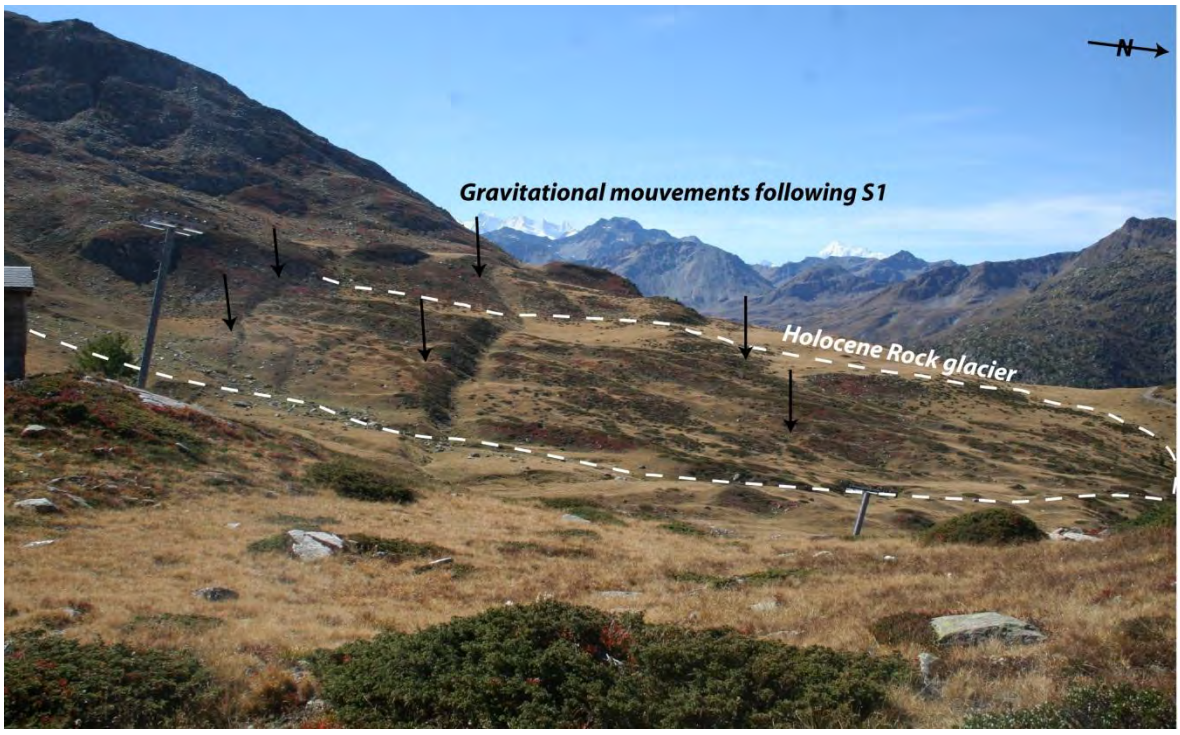

Figure 3.1-23: Example of recent reactivation of persistent foliation planes (S1) by a DSGSD in Simplon area (Berisal area). Note that active gravitational movements clearly cut a fossilized Holocene rock glacier.

In the Prealps, three main lineament trends have been detected N-S, NW-SE and subordinate NNE-SSW. The first two orientations are consistent with left lateral strike-slip movements in lower Rhone valley and might be related to the stress regime associated with the thrust development (Mosar and Borel 1992). The NNE-SSW lineament seems to correlate with faults developed parallel to the fold axis. The few detected morpho-structural features are developed along NW-SE on the main Rhone valley and along N-S faults on south-western tributary valley.

3.1.14 DISCUSSION

3.1.14.1 Controls on GSD occurrence

In our multidisciplinary approach, we have tested the relation between the distribution of GSD and their lithological, structural and tectonic factors that could influence the development and local occurrence. Based on these results, it is possible to highlight that the occurrence of large slope instabilities around the study area is not uniformly distributed and six main areas showing a higher GSDs density can be outlined. In contrast to other active mountain belts (Antinao and Gosse 2009; Keefer 1993; Hancox et al., 2003) where tectonic or climatic effects can be clearly identified, it is difficult to indicate a single causal relationship between the GSD clusters and a specific predisposing factor in the Alpine context.

The coexistence of high local relief, large scale pre-existing tectonic weakness zones and active tectonic processes, including varying uplift gradients and high seismic energy release predispose towards high GSD incidence in the Rhone valley. In particular, the five clusters (Marthigny, Sion-Sierre, Visp-Brig and Upper Mattertal, Val d'Hérens), including 80% of the GSD, can be quantitatively correlated with these factors. The spatial association between GSDs, high local relief, seismicity and uplift rate indicate possible tectonic forcing on GSD clustering in Western Swiss Alps. These general observations are in agreement with studies performed in the Eastern Alps (Agliardi et al., 2009) and at the Alpine range scale (Korup et al., 2007).

Even if the Rhone valley is one of the most seismically area of entire Switzerland and some evidences of earthquake-related instabilities have been observed, the primary influence of seismicity and differential uplift is via tectonic fracturing and rock mass strength reduction (Jaboyedoff et al., 2003; Molnar et al., 2007). This implies that seismicity and tectonic differential uplift need to be first considered as a long term predisposing factor and not only as potential triggering factors. Indirect confirmation of this assumption is the absence of clear postglacial neotectonic faults, indicating that the current tectonic strain is too low to produce large superficial deformation areas (Ustaszewski and Pfiffner 2008). Most of the tectonic strain is probably accommodated along minor pre-existing faults or neo-formed fractures (Molnar et al., 2007) within the upper crust (≤ 15km). When these rocks are exhumed to a depth sensible to surface processes, their lowered rock mass strength is a crucial predisposing factor to GSD development. This phenomenon can be emphasized in the Saastal–Mattertal region where massive outcropping lithologies (paragneiss and orthogneiss) are located in a region characterized by significant active tectonic processes (seismicity and uplift gradient). This leads to an unusual concentration of GSD compared to similar lithological and morphological settings like the Aar massive or the upper Penninic units (Dent Blanche Nappe) where the active tectonic strain is less.

Apart from tectonics, the role of glacial overdeepening of the Rhone valley requires critical examination. This is particularly the case for GSDs of the Martigny cluster where an important glacial overdeepening is associated to a main change of the Rhone valley orientation. Several rockslide scars along the main Rhone valley seems also to be related to similar geomorphological situations (Pedrazzini et al., 2009). GSDs related to breaches enlargement (Jarman 2006) seems to be limited in the Rhone catchment, because glaciers followed essentially pre-existing valleys (Kelly et al., 2004). However, during the LGM the Rhone glacier was characterized by an important ice cap (Kelly et al., 2004) that created an important regional transfluence in the upper Rhone valley (Goms valley). Here, some DSGSD characterized by compressional features (see chapter 4.9), can be associated with breach excavation and to important postglacial unloading.

As suggested by Agliardi et al. (2009) the occurrence of major structural features represents an important passive control, promoting the development of GSD. In the Rhone valley, the Rhone-Simplon fault system is a good example of this control. The orientation of morpho-structural features related to GSDs is clearly controlled by pre-existing and persistent weakness planes. However, in a complex tectonic context such as the western Alps, persistent tectonic features (foliation, faults) are, at least at local scale, ubiquitous and are readily exploited by GSD. Others factors control the GSD development include the influence of valley shapes (Backhmann et al., 2006; Ambrosi and Crosta, 2011) or structural and lithological weakness (Alberto et al., 2008). These factors have also an important influence on the GSD development but it was beyond the scope of this study to highlight those. However, these factors need to be considered as second order aspect related to the development of a single instability, but this cannot explain GSD clusters.

As shown in this paper, the lithological and structural conditions influence the hillslope processes by defining the typology and the extent of the GSD. The LRT are a good example of this control. Their distribution is frequently associated to overdip slope configuration of the Helvetic Nappes where weaker lithologies (as marly-limestone lithology and Flysch) crop out.

Morpho-structural and lithological properties can also explain the minor GSD cluster of Val d'Illiez. In this area, located outside the high relief of the Alpine chain, active tectonic processes and local relief are less significant (Cendrero and Dramis, 1996). Indeed, in this area, GSD are mainly expressed by large roto-translational landslides that developed in Flysch or in post-glacial sediments, driven by river incision and lateral erosion.

3.1.14.2 Implications for the understanding of the present-day uplift

In the eastern Swiss Alps, Korup and Schlunegger (2009) indicate that 25-40% of the Quaternary rock uplift can be theoretically accommodated by erosional unloading of weak rocks. This seems not to be the case in the Western Swiss Alps where maximal uplift rates correspond to lithologies with different rock strength. In the Rhone valley area high uplift is also difficult to correlate with glacial rebound or specific lithologies. Indeed the maximal uplift is not located near Martigny where the ice thickness was the highest or in Val d'Illiez where the weakest rocks crop out. Conversely, a good correlation between uplift gradient and seismic activity might indicate a possible correlation with the present-day tectonic stress regime (Jaboyedoff et al., 2003; Bistacchi and Massironi 2000; Sue et al., 2007; Ustaszewski and Pfiffner 2008).

In this study, we show the correlation between tectonic related fracturing (Molnar et al., 2007 Clarke and Burbank 2010) and GSDs. In addition, a strong correlation between the uplift gradient and GSD occurrence has been highlighted. These elements suggest that, according to present-day tectonic setting of Western Alps, the measured uplift rate is at least partially driven by tectonic forcing. In the extensional and strike-slip setting of the Rhone valley, tectonic origin of high uplift values are explained by partial detachment or warming of the lithosphere beneath the Western and Central Alps (Lyon-Caen and Molnar, 1989) and /or extrusion of ductile material (Escher and Beaumont, 1997) driven by the general context of convergence which leads to a bulge facilitating uplift and extension in the upper crust. Figure 3.1-24 shows a modified version of the tectonic model proposed by Bistacchi and Massironi (2000) and by Jaboyedoff et al., (2003) and allows explaining the relation between the extensional and strike-slip context, the measured uplift gradient and the distribution of GSD in the Western Swiss Alps. Based on this reconstruction, it is possible to highlight that, the presence of tectonic component, explain the coexistence of high uplift gradient values, important seismic activity and GSD clusters (Sion-Sierre, Brig-Visp and upper Saastal) in the same location.

The absence of lithologies characterized by low rock strength within GSD clusters also validates this hypothesis. This is not in contradiction with the models indicating that the present–day uplift in the Swiss Alps is mainly driven by erosion (Champagnac al., 2009) and glacial perturbations (Norton et al., 2010). In particular, areas characterized by high density of GSD might positively influence the erosion driven-uplift emphasizing this effect. As tectonic movements can be considered unchanged since 1-2 Ma (Sue et al., 2007), active tectonic processes have stable spatial contribution on the present-day rock uplift and, even if small (Champagnac et al., 2009; Glotzbach et al., 2010), this contribution needs to be considered as an important intrinsic factor facilitating and controlling the erosion-driven uplift in Rhone valley.

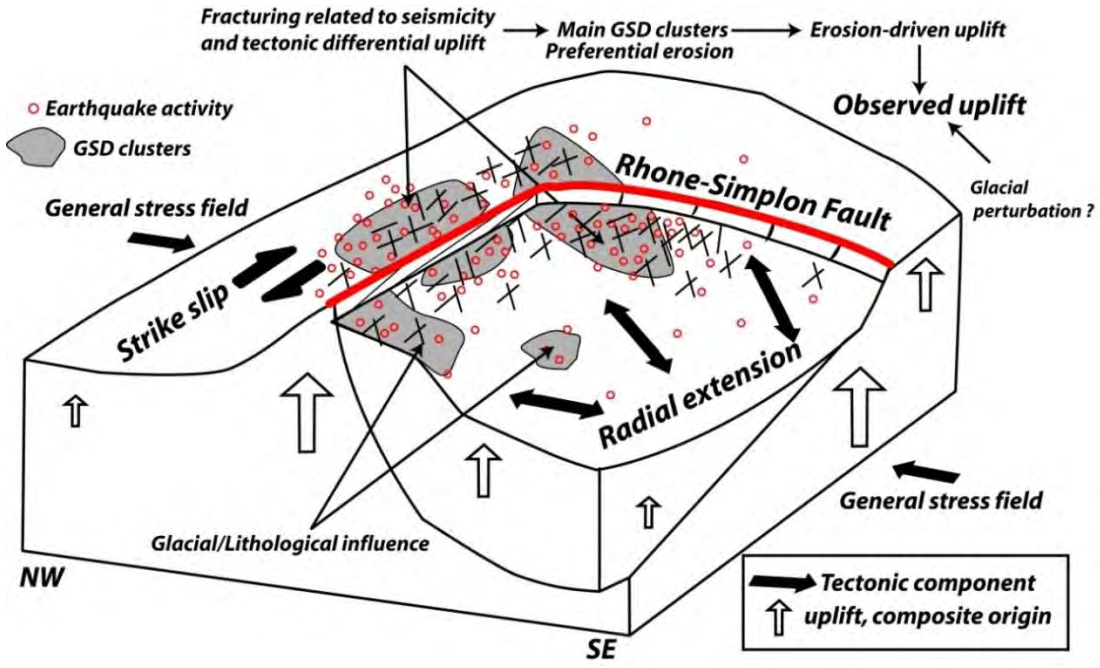

Figure 3.1-24: Schematic model illustrating the possible relation between tectonics, seismicity and observed uplift in Rhone valley catchment. The integration of on-going tectonic activity and tectonic fracturing is capital to understand the spatial distribution of the measured uplift values in the Rhone valley.

3.1.15 CONCLUSIONS

A detailed inventory of gravitational slope deformation was carried out in the Western Alps allowing the identification of more than 300 GSDs that cover 11% of the study area. They exert a profound influence on the rate and style of bedrock erosion and on the landscape evolution of this high mountain area. Frequency-area distribution indicates that GSD inventories follow an inverse gamma distribution with an exponent of the power-law tail comparable to previous studies. If the GSD typologies are considered separately, the power-law exponent decreases indicating the great influence of larger GSD on the inventory. These results highlight the difficulty of detecting medium and small landslides in an inventory that cover a period since the LGM and where local morphological conditions have considerably evolved.

The simplified three-way GSD typology adopted for this study is particularly helpful in bringing out the influence of the marked lithological and structural variations across the area. RSF development is strongly correlated with the large pre-existing tectonic features (faults, persistent joints) and to the orientation of the main foliation attitude. RSF distribution is far from uniform and six clusters have been identified. The five main clusters accounting for 80% of the recorded GSDs are associated with high uplift gradient, high seismic energy release, high local relief and large-pre-existing tectonic weakness. The strong influence of active tectonic processes on the GSD distribution suggested that their significance need to be revaluated and better integrated to understand the uplift values of Western Switzerland.

3.1.16 REFERENCES

Abele, G., 1974. Bergstürze in den Alpen-ihre Verbritung, Morphologie und Folge erschinungen, *Wissenschflitche Aplenvereinhefte,* 25.

Ambrosi, C., Crosta, G. B. 2011. Valley shape influence on deformation mechanisms of rock slopes. In: Jaboyedoff, M. (ed.) *Slope Tectonics*, Geological Society, London, Special Publications, 351, 215–233.

Agliardi, F., Crosta, G., Zanchi, A. 2001. Structural constraints on deep-seated slope deformation kinematics, *Engineering Geology*, 59, 83-102.

Agliardi, F., Zanchi, A., Crosta, G. 2009. Tectonic vs. gravitational morphostructures in the central Eastern Alps (Italy): Constraints on the recent evolution of the mountain range, *Tectonophysics*, 474, 250-270.

Alberto, W., Giardino, M., Martinotti, G., Tiranti, D. 2008. Engineering and environmental problems in karst, Natural and Anthropogenic Hazards in Karst Areas, *Engineering Geology*, 99, 147-159.

Antinao, J.L., Gosse, J. 2009. Large rockslides in the Southern Central Andres of Chile (32-34.5°S): Tectonic control and significance for quaternary landscape evolution, *Geomorphology*, 104, 117-133.

Baddeley, A., Moller, J., Waagepetersen, R. 2000. Non- and semiparametric estimation of interaction in inhomogeneous point patterns, *Statistica Neerlandica*, 54, 329–350.

Ballantyne, C.K. 2002. Paraglacial geomprohlogy, *Quaternary science Reviews,* 21, 1935-2017.

Besson, O., Rouiller, J.-D., Frei, W., Masson, H. 1992. Campagne de sismique-réflexion dans la Vallée du Rhone entre Sion et Martigny, *Bull. Murithienne*, 109, 45-63.

Bistacchi, A., Massironi, M. 2000. Post-nappe brittle tectonics and kinematic evolution of the northwestern Alps: an integrated approach,*Tectonophysics*, 15, 267-292.

Bonnard, C., Noverraz, F., Dupraz, H. 1996. Long-term movements of substabilized versants and dimatic changes in the Swiss Alps, *Proceedings International Symposium on Landslides*, Trondheim, Senneset (ed.), Balkema, 1525-1531.

Burkhard, M. 1988. L'Helvétique de la bordure occidentale du massif de l'Aar (évolution tectonique et métamorphique), *Eclogae Geologicae Helvetiae*, 81, 63–114.

Burbank, D.W., Leland, J., Fielding, E., Anderson, R. S., Brozovic, N., Mary, R., Duncan, C. 1996. Bedrock incision, rock uplift and threshold hillslopes in the northwestern Himalayas, *Nature*, 379, 505-510.

Burri, M., 1997. Géologie récente de Finges et des ses environs, *Bulletin de la Maurithienne*, 26 p.

Cendrero, A., Dramis, F. 1996. The contribution of landslides to landscape evolution in Europe, *Geomorphology,* 15, 191-211.

Champagnac, J.D., Sue, C., Delacou, B., Burkhard, M. 2003. Brittle orogen-parallel extension in the internal zones of the Swiss Alps (south Valais), *Eclogae Geol. Helv*. 96, 325-338.

Champagnac, J.D., Sue, C., Delacou, B. Burkhard, M. 2004. Brittle deformation in the inner northwestern Alp : from early orogen-parallel extrusion to late orogen-perpendicular collapse, *Terra Nova*, 16, 232-242.

Champagnac, J.D., Schlunegger, F., Norton, K., von Blanckenburg, F., Abbühl, L.M., Schwab, M. 2009. Erosion-driven uplift of the modern Central Alps, *Tectonophysics*, 474, 1, 236-249.

Chaytor, J.D., ten Brink, U.S., Solow, A.R., Andrews, B.D. 2009. Size distribution of submarine landslides along the U.S. Atlantic margin, *Marine Geology*, 264, 16–27.

Crosta, G.B., Agliardi, F., Frattini, P., Malusà, M. 2009. Deep-seated slope deformations, exhumation and relief in the Alps, *Geophysical Research Abstracts*, 11, EGU2009-13437.

Clarke, B.A., Burbank, D.W. 2010. Bedrock fracturing, threshold hillslopes and limits to the magnitude of bedrock landslide*, Earth and Planetary Science Letters*, 297, 577-585.

Cossart, E., Braucher, R., Fort, M., Bourlès, D.L., Carcaillet, J. 2008. Slope instability in relation to glacial debuttressing in alpine areas (Upper Durance catchment, southeastern France): Evidence from field data and 10Be cosmic ray exposure ages, *Geomorphology*, 95, 3-26.

Crozier, M.J. 2010 Landslide geomorphology: An argument for recognition, with examples from New Zealand, *Geomorphology,* 120, 3-15.

Cruden, D.M., Varnes, D.J. 1996. Landslide types and processes. In: Turner A.K.; Shuster R.L. (eds) *Landslides: Investigation and Mitigation,* Transp Res Board, Spec Rep 247, 36–75.

Cruden, D.M. 2003. The shapes of cold, high mountains in sedimentary rocks, *Geomorphology*, 55, 249-261.

Delacou, B, Sue, C., Champagnac, J.D., Burkhard, M. 2004. Present-day geodynamics in the bend of the Western and Central Alps as constrained by earthquake analysis, *Geophys Journal Int.*, 158, 753–774.

Deichmann, N. 1993. Structural and rheological implications of lower-crustal earthquakes below northern Switzerland, *Phys. Earth Plant. Interior*, 69, 270-280.

Densmore, A.L., Anderson, R.S., McAdoo, B.G, Ellis, M.A. 1997. Hillslope evolution by bedrock landslides, *Science*, 75, 369-372.

Dramis, F., Sorriso-Valvo, M. 1994. Deep-seated gravitational slope deformations, related landslides and tectonics, *Engineering Geology*, 38, 231-243.

Eisbacher, G.H., Clague, J.J. 1994. Destructive mass movements in high mountains. *Geological survey of Canada*, Paper 84-16.

Escher, A., Beaumont, C. 1997 Formation, burial and exhumation of basement nappes at crustal scale: a geometric model based on the Western Swiss-Italian Alps, *Journal of Structural Geology*, 19, 955-974.

Evans, S.G., Clague, J.J. 1994. Recent climatic change and catastrophic geomorphic processes in mountain environments, *Geomorphology*, 10, 107-128.

Fäh, D., Giardini, D., Bay, F., Bernardi, F., Braunmiller, J., Deichmann, N., Furrer, M., Gantner, L., Gisler, M., Isenegger, D., Jimenez, M.J., Kästly, P., Koglin, R., Masciadri, V., Rutz, M., Scheidegger, C., Schibler, R., Schorlemmer, D., Schwarz-Zanetti., S, Steimen., S, Sellami., S, Wiemer, S., Wössner, J. 2003. ECOS and the related macroseismic database, *Eclogae Geol. Helv.*, 96, 219–236.

Fäh, D., Giardini, D., Kästli, P., Deichmann, N., Gisler, M., Schwarz-Zanetti, G., Alvarez-Rubio, S., Sellami, S., Edwards, B., Allmann, B., Bethmann, F., Wössner, J., Gassner-Stamm, G., Fritsche, S., Eberhard, D., 2011. ECOS-09 Earthquake Catalogue of Switzerland Release 2011 Report and Database. Public catalogue, 17. 4. 2011. *Swiss Seismological Service ETH Zurich*, Report SED/RISK/R/001/20110417.

Fitzsimons, S. J., Veit, H. 2001. Geology and Geomorphology of the European Alps and the Southern Alps of New Zealand: A Comparison, *Mountain Research and Development*, 21, 4, 340-349.

Florineth, D., Schlüchter, C. 1998. Reconstructing the Last Glacial Maximum (LGM) ice surface geometry and flowlines in the Central Swiss Alps, *Eclogae Geol. Helv.*, 91, 391–407.

Forcella, F., Orombelli, G. 1984. Holocene slope deformations in Valfurva, Central Alps, Italy, *Geografia Fisica e Dinamica Quaternaria*, 7, 41–48.

Fritsche, S., Fäh, D., Gisler, M., Giardini, D. 2006. Reconstructing the damage field of the 1855 earthquake in Switzerland: historical investigations on a well-documented event, *Geophys. J. Int.*, 166, 719–731.

Frei, C., Schaer, J. 1998. A precipitation climatology of the Alps from high-resolution rain-gauge observations, *Journal of Climatolo*gy, 18, 873–900.

Gasser, D., Manktelow, N. 2010. Brittle faulting in the Rawil depression: field observations from the Rezli fault zones, Helvetic nappes, Western Switzerland, *Swiss Journal of geosciences*, 103, 15–32.

Gisler, M., Fäh, D. Kästli, P. 2004. Historical seismicity in Central Switzerland, *Eclogae geol. Helv.*, 97 221–236

Ghirotti, M., Martin, S., Genovois, R. 2011. The Celentino deep-seated gravitational slope deformation (DSGSD): structural and geomechanical analyses (Peio Valley, NE Italy), From: Jaboyedoff, M. (ed.) *Slope Tectonics*. Geological Society, London, Special Publications, 351, 235–252.

Glotzbach, C., Reinecker, J., Danišík, M., Rahn, M., Frisch, W., Spiegel, C. 2010. Thermal history of the central Gotthard and Aar massifs, European Alps: Evidence for steady state, long-term exhumation*, Journal of Geophys. Res*., 115, F03017.

Gutenberg, B., Richter, C.F. 1954. *Seismicity of the Earth and associated phenomena*, Princeton, New Jersey, Princeton University Press, 245 p.

Guthrie, R.H., Evans, S.G. 2004. Analysis of landslide frequencies and characteristics in a natural system, coastal British Columbia, *Earth Surface Processes and Landforms*, 29, 1321–1339.

Hancox, G.T., Cox, S.C., Turnbull, I.M., Crozier, M.J. 2003. Reconnaissance studies of landslides and other ground damage caused by the Mw 7.2 Fiordland earthquake of 22 August 2003, *Institute of Geological and Nuclear Sciences Science Report 2003/30,* Lower Hutt.

Hermanns, R.L., Niedermann, S., Villanueva Garcia, A., Sosa Gomez, J., Strecker, M.R., 2001. Neotectonics and catastrophic failure of mountain fronts in the southern intra-Andean Puna Plateau, Argentina, *Geology*, 29, 619–623.

Hovius, N., Stark, C.P., Allen, P.A. 1997. Sediment flux from a mountain belt derived by landslide mapping, *Geology*, 25, 231-234.

Heim, A. 1921. *Geologie der Schweiz*, Band II, Tauchnitz, Leipzig.

Heim, A. 1932*. Bergsturz und Menschenleben*, Fretz und Wasmuth, Zürich.

Hoek, E., Brown, E.T. 1997. Practical estimates of rock mass strength, *International Journal of Rock Mechanics and Mining Sciences*, 34, 1165–1186.

Hutchinson, J. N. 1988. General Report: Morphological and geotechnical parameters of landslides in relation to geology and hydrogeology, in: *Proceedings of the Fifth International Symposium on Landslides*, edited by: Bonnard, C., Balkema, Rotterdam, 3–35.

Ivy-Ochs, S., Schäfer, J., Kubik, P.W., Synal, H.-A., Schlüchter, C. 2004. Timing ofdeglaciation on the northern Alpine foreland (Switzerland), *Eclogae Geologicae Helvetiae*, 97, 47–55.

Johnson, N.L., Kotz, S., Balakrishnan, N. 1994. *Continuous Univariate Distributions* ,vol. 2, Wiley, New York.

Jarman, D. 2006. Large rock slope failures in the Highlands of Scotland: Characterisation, causes and spatial distribution, *Engineering Geology*, 83, 161–182.

Jaboyedoff, M., Derron, M. 2005. A new method to estimate the infilling of alluvial sediment of glacial valleys using a sloping local base level, *Geografica Fisica e Dinamica Quaternaria*, 28, 37-46.

Jaboyedoff, M., Baillifard, F., Derron, M.-H. 2003. Preliminary note on uplift rates gradient, seismic activity and possible implications for brittle tectonics and rockslide prone areas: The example of western Switzerland, *Bull. Soc. Vaud. Sc. nat.*, 88, 393-412.

Jaboyedoff, M., Derron, M.H., Manby, G.M. 2005. Note on seismic hazard assessment using gradient of uplift velocities in the Turan block (Central Asia), *Natural hazard and Earth System Science*, 5, 43-47.

Kahle, H.G., Geiger, A., Buerki, B., Gubler, E., Marti, U., Wirth, B., Rothacher, M., Gurtner, W., Beutler, G., Bauersima, I., Pfiffner, O.A. 1997. Recent crustal movements, geoid and density distribution; contribution from integrated satellite and terrestrial measurements. In: Pfiffner OA, Lehner P, Heitzmann P, Mueller S, Steck A (eds) *Deep structure of the Swiss Alps: results of NRP20*., Birkhäuser Verlag, Basel, 251–259.

Kastrup, U., Zoback, M. L., Deichmann, N., Evans, K., Giardini, D., Michael, A. J. 2004. Stress field variations in the Swiss Alps and the northern Alpine foreland derived from inversions of fault plane solutions, *J. Geophys. Res*., 109/B1, B01402.

Keefer, D.K. 1993. The susceptibility of rock slopes to earth-quake induced failure, *Association of Engineering Geologists Bulletin*, 30, 353-361.

Kelly, M.A., Buoncristiani, J.F., Schlüchter, C. 2004. A reconstruction of the last glacial maximum (LGM) ice-surface geometry in the western Swiss Alps and contiguous Alpine regions in Italy and France, *Eclogae Geologicae Helvetiae,* 97, 57–75.

Koons, P.O. 2009. On the implications of low spatial correlation of tectonic and climate variables in the western European Alps, *Geology*, 37, 863–864.

Korup, O. 2005. Distribution of landslides in southwest New Zealand, *Landslides*, 1, 43-51.

Korup, O., Clague, J.J., Hermanns, R.L., Hewitt, K., Strom, A.L., Weidinger, J.T. 2007. Giant landslides, topography, and erosion*, Earth and Planetary Science Letters*, 261, 578-589.

Korup, O., Schlunegger, F. 2007. Bedrock landslides, river incision, and transience of geomorphic hillslope-channel coupling: evidence from inner gorges in the eastern Swiss Alps, *Journal of Geophysical Research*, 112, F03027.

Korup, O., Schlunegger,F. 2009. Rock-type control on erosion-induced uplift, eastern Swiss Alps, *Earth and Planetary Science Letters*, 278, 278-285.

Korup, O., Clague, J.J. 2009. Natural hazards, extreme events, and mountain topography, *Quaternary Science Reviews*, 28, 977-990.

Korup, O., Schmidt, J., McSaveney, M.J. 2005. Regional relief characteristics and denudation pattern of the western Southern Alps, New Zealand, *Geomorphology*, 71, 402-423.

Kühni, A., Pfiffner, O.A. 2001. The relief of the Swiss Alps and adjacent areas and its relation to lithology and structure: topographic analysis from a 250 m DEM, *Geomorphology,* 41, 285-307.

Kreysig, E. 1999. Advanced engineering mathematics 8th ed. Wiley & Sons. 1056 p.

Lemoine, M., Bas, T., Arnaud-Vanneau, A., Arnaud, H., Dumont, T., Gidon, M., Bourbon, M., Graciansky, P.C., Rudkiewicz, J.L., Mégard-Galli, J. Tricart, P. 1986. The continental margin of the Mesozoic Tethys in the Western Alps, *Marine and Petroleum Geology*, 3, 179-199.

Lyon-Caen, H., Molnar, P., 1989. Constraints on the deep structure and dynamic processes beneath the Alps and adjacent regions from an analysis of gravity anomalies, *Geophysical Journal International*, 99, 19–32.

Lugeon, M. 1914. Les Hautes Alpes calcaires entre la Lizerne et la Kander (Wildhorn, Wildstrubel, Balmhorn et Torrenthorn). Fascicules 1, 2 & 3. En 2 vols. *Beiträge zur geologischen Karte der Schweiz*, N.F., Lfg. 30.

Masson, H., Herb, R., Steck, A. 1980. Helvetic Alps of Western Switzerland, excursion no. 1. In: Trümpy, R.: Geology of Switzerland, part II. - Wepf, Basel.Mancktelow N. S. 1990: The Simplon Fault Zone*, Beitr. Geol. Karte CH 163* (n.F.), 74 p.

Mancktelow, N. S. 1992. Neogene lateral extension during convergence in the Central Alps; evidence from interrelated faulting and backfolding around the Simplonpass; Switzerland, *Tectonophysics*, 215, 295–317.

McCalpin, J.P. 1999. Criteria for determining the seismic significance of sackungen and other scarp-like landforms in mountainous regions, *Techniques for Identifying Faults and Determining their Origins. U.S. Nuclear Regulatory Commission*, Washington, pp. 2.55–2.59

Meentemeyer, R. K., Moody, A. 2000. Automated mapping of alignment between topography and geologic bedding planes, *Computers and Geosciences*, 26, 815-829.

Montgomery, D.R., Brandon, M.T. 2002. Topographic controls on erosion rates in tectonically active mountain ranges, *Earth Planet.Sci. Lett.*, 201, 481–489.

Molnar, P., Anderson, R.S., Anderson, S.P. 2007. Tectonics, fracturing of rock, and erosion, *Journal of Geophysical Research,* 112, F03014.

Mortara, G., Sorzana, P.F. 1987. Fenomeni di deformazione gravitativa profonda nell'Arco Alpino Occidentale Italiano. Considerazioni lito-strutturali e morfologiche, *Bollettino della Società Geologica Italiana*, 106, 303–314 (in Italian).

Maurer, H., Burkhard. M., Deichmann. N., Green, A.G. 1997. Active tectonism in the Central Alps: contrasting stress regimes north and south of the Rhone Valley, *Terra Nova*, 9, 91–94.

Malamud, B.D., Turcotte, D.L., Guzzetti, F., Reichenbach, P., 2004. Landslide inventories and their statistical properties, *Earth Surface Processes Landform*, 29, 687–711.

Montandon, F. 1933. Chronologie des grands éboulements alpins, du début de l'ère chrétienne à nos jours. Socité géographique Génève, matériaux pour l'étude des calamites. 32, 271-340.

Mosar, J., Stampfli, G.M., Girod, F. 1996. Western Préalpes Médianes Romandes: timing and structure: A Review, *Eclogae geologicae Helvetiae*, 89, 389-425.

Mosar, J., Borel, G. 1992. Paleostress from the Préalpes médianes (Switzerland), *Annales Tectonicae*, 6, 115-133.

Norton, K., Abbühl, L., Schlunegger, F., 2010, Glacial conditioning as an erosional driving force in the Central Alps, *Geology*, 38, 655-658.

Noverraz, F. 1990. Répartition géographique, origine et contexte géologique des glissements de terrains latents en Suisse, Hydrology in Mountainous Regions. Artificial Reservoirs; Water and Slopes (Proceedings of two Lausanne Svmposia, August 1990). *IAHS Publ*. no. 194.

Pfiffner, O.A. Schlunegger, F., Buiter, F.S. 2002. The Swiss Alps and their peripheral foreland basin: stratigraphic response to deep crustal processes, *Tectonics*, 21, 1-16.

Pedrazzini, A., Jaboyedoff, M., Ornstein, P. 2009. Failure mechanisms analysis and reconstruction of pre-failure topography: examples of rockslide scars in Rhone valley, Switzerland, *Geophysical Research Abstracts, 11, EGU2009-11934-2*.

Persaud, M., Pfiffner, O.A. 2004. Active deformation in the Eastern Swiss Alps: post-glacial faults, seismicity and surface uplift, *Tectonophysics*, 385, 59–84.

Preusser, F., Reitner, J.M., Schlüchter, C. 2010. Distribution, geometry, age and origin of overdeepened valleys and basins in the Alps and their foreland, *Swiss Journal of Geosciences*, 3, 407-426.

Reitner, J.M., Linner, M., 2009. Formation and preservation of large scale toppling related to alpine tectonic structures-eastern Alps, *Austrian Journal of Earth Science*, 120, 69-80.

Ripley, B.D. 1977. Modelling spatial patterns (with discussion), *Journal of the Royal Statistical Society*, Series B, 39, 172–212.

Ripley, B.D. 1988. *Statistical inference for spatial processes*, Cambridge University Press, Cambridge, London.

Rosselli, A., Olivier, R. 2003. Modélisation gravimétrique 2.5D et cartes des isohypses au 1:100'000 du substratum rocheux de la Vallée du Rhone entre Villeneuve et Brig (Suisse), *Eclogae geol. Helv*., 96, 399-423.

Sanchez, G., Rolland, Y., Corsini, M., Braucher, R., Bourlès, D., Arnold, M. Aumaître, G. 2010. Relationships between tectonics, slope instability and climate change: cosmic ray exposure dating of active faults, landslides and glacial surfaces in the SW Alps, *Geomorphology*, 117, 1-13.

Sartori, M. 1987. Blocs basculés briançonnais en relation avec leur socle originel dans la nappe de Siviez-Mischabel (Valais, Suisse), *Comptes Rendus des Séances de l'Académie des Sciences de Paris*, 305, 999-1005.

Sartori, M., Guffon, Y., Marthaler, M., 2006. Harmonisation et définition des unités lithostratigraphiques briançonnaises dans les nappes penniques du Valais, *Eclogae Geologicae Helvetiae*, 99, 363-407.

Sauchyn, D.J., Cruden, D.M., Hu, X.Q. 1998. Structural control of the morphometry of open rock basins, Kananaskis region, Canadian Rocky Mountains, *Geomorphology*, 22, 313–324.

Selby, M.J., 1982. Hillslope materials and processes, Oxford University Press, 243p.

Schlatter, A., Schneider, D., Geiger, A., Kahle, H., 2005. Recent vertical movements from precise levelling in the vicinity of the city of Basel, Switzerland, *Int. J. Earth Sci.,* 94, 507–514.

Schlatter, A., 2007. Das neue Landeshöhennetz der Schweiz LHN95; Geodätisch-geophysikalischeArbeiten in der Schweiz: Schweizerische Geodätische Kommission, v. 72, 373 p.

Schmidt, K. M., Montgomery, D.R. 1995, Limits to relief, *Science*, 70, 617-620.

Schlunegger, F., Hinderer, M., 2001. Crustal uplift in the Alps: why the drainage pattern matters, *Terra Nova*, 13, 425–432.

Schoneich, P., Dorthe-Monachon, C., Jaillet, S., Ballandras, S. 1998. Le retrait glaciaire dans les Préalpes et les Alpes au Tardiglaciaire, *Bull. d'Ét. Préhist. et alpines de la vallée d'Aoste*, 9, 23-37.

Sengezer, B., Ansal, A. 2007. Probabilistic evaluation of observed earthquake damage data in Turkey, *Nat Hazards, 40, 305–326.*

Silverman, B.W. 1986. Density Estimation for Statistics and Data Analysis. New York: Chapman and Hall.

Spence, R., So, E., Jenkins, S., Coburn, A., Ruffle, S. 2011. A Global Earthquake Building Damage and Casualty Database, *Advances in Natural and Technological Hazards Research*, 29, 65-79.

Steck, A. 1984. Structures et deformations tertiaries dans les Alpes centrales, *Eclogae geol. Helv.*, 77, 55-100.

Steck, A., Hunziker, J., 1994. The Tertiary structural and thermal evolution of the Central Alps; compressional and extensional structures in an orogenic belt, *Tectonophysics*, 238, 229-254.

Steck, A., Bigioggero, B., Dal Piaz G.V., Escher, A., Martinotti G., Masson, H. 1999. *Carte tectonique des Alpes de Suisse occidentales et des régions avoisinantes,* 1:100000 [Tectonic map of the western Swiss Alps and neighbouring regions]. Special geological map no. 123, Service Géologique National, Bern.

Steck, A., Epard, J.L., Escher, A., Gouffon, Y., Masson, H. 2001. Carte tectonique des Alpes de Suisse occidentale et des regions avoisinantes 1:100000. *Notice explicative* [Tectonic map of the western Swiss Alps and neighbouring regions, explanatory note], Service Géologique National, Bern, 73 pp

Spence, R., So, E., Jenny, S., Castella, H., Ewald, M., Booth, E. 2008. The Global Earthquake Vulnerability Estimation System (GEVES): an approach for earthquake risk assessment for insurance applications, *Bulletin of Earthquake Engineering*, 6, 463-483.

Sue, C., Touvenout, F., Frechet, J., Tricart, P. 1999: Widespread extension in the core of the Western Alps revealed by earthquake analysis, *J.Geophys. Res. B,* 104/11, 25611–25622.

Sue, C., Delacou, B., Champagnac, J.-D., Allanic, C., Tricart, P., Burkhard, M. 2007. Extensional neotectonics around the bend of the Western/Central Alps: an overview, *International Journal of Earth Sciences*, 6, 1101-1129.

Strozzi, T., Delaloye, R., Kääb, A., Ambrosi, C., Perruchoud, E., Wegmüller, U. 2010 Combined observations of rock mass movements using satellite SAR interferometry, differential GPS, airborne digital photogrammetry, and airborne photography interpretation, *Journal of geophysical research*, 115, F01014.

Ustaszewski, M., Pfiffner, O. A. 2008. Neotectonic faulting, uplift and seismicity in the Central and Western Swiss Alps. In S. Sigmund et al. (Eds.), *Tectonic aspects of the Alpine-Carpathian-Dinaride System*, Geological Society of London Special Publication, 298, 231–249.

Vernon, A. J., van der Beek, P.A., Sinclair, H.D. 2009, Spatial correlation between long-term exhumation rates and present-day forcing parameters in the western European Alps, *Geology*, 37, 859–862.

Von Raumer, J-F. 1987. Les massifs du Mont Blanc et des Aiguilles Rouges: témoins de la formation de croûte varisque dans les Alpes occidentales, *Géologie Alpine*, 63, 7-24.

Van Den Eeckaut, M., Poesen, J., Govers, G., Verstraeten, G., Demoulin, A. 2007. Characteristics of the size distribution of recent and historical landslides in a populated hilly region, *Earth and Planetary Science Letters*, 256, 588–603.

Zischinsky, U., 1969. Uber Sackungen., *Rock Mechanics*, 1, 30–52.

3.2 CHARACTERISTICS AND DISTRIBUTION OF ROCKSLIDES SCARS IN THE RHONE VALLEY (S-W SWITZERLAND)

3.2.1 ABSTRACT

Along the main Rhone valley (south-western Switzerland), several rockslide scars are visible. For the majority of them, only their upper parts outcrop within the valley flanks, the bottom being buried below the sediment. Up to now, no regional mapping of these scars has been realized, and only few of them have been analysed in detail. In this study, a first catalogue of the rockslide scars along the Rhone valley will be presented. Geometrical and geological characteristics of the detected rockslide scars were analysed. In particular, their distribution, their volume and their failure mechanism characteristics were examined to identify the tectonic and the geological conditions promoting slope failure. Based on digital elevation model analyses and field mapping, 53 rockslide scars were identified along the main Rhone valley. The tectonic setting, in particular the orientation of the main foliation and the litho-structural characteristics of the outcropping lithologies was identified as the main predisposing factor influencing the morphology and the failure mechanism of the detected rockslides scars. Their spatial distribution along the main Rhone valley suggests the important influence of the preferential paraglacial stress release on the final location of the rockslide scar. Particularly, three specific morphological configurations including more than 80% of the entire dataset were identified to be the most prone to develop rock slope failures. Based on the volume-frequency distribution of the rockslide scars, a first quantitative estimation of the valley infilling and of the postglacial denudation rate associated to the rockslide activity was also proposed.

3.2.2 RÉSUMÉ

Le long de la vallée du Rhône plusieurs niches d'arrachement et de cavités témoignent la présence d'anciens glissements et d'avalanches rocheuses. Le matériel éboulé ainsi qu'une bonne partie de la surface de rupture originelle sont actuellement enfouis sous le remplissage quaternaire de la vallée du Rhône. Dans cette étude on présente le premier inventaire des niches situées le long de la vallée principale du Rhône. Pour chacune des niches, une étude des caractéristiques géométriques et structurales ainsi qu'une reconstruction du volume éboulé a été menée. L'analyse structurale a montré l'influence dominante du contexte tectonique général sur les mécanismes de rupture observés dans les différentes parties de la vallée. L'orientation de la foliation principale et les caractéristiques mécaniques des différentes lithologies affleurantes représentent les facteurs de prédisposition les plus importants. La distribution spatiale des niches souligne, par contre, un très fort conditionnement glaciaire. A l'échelle régionale, les zones montrant une forte densité d'anciennes niches d'arrachement sont principalement liées aux zones de surcreusement glaciaire qui permettent un accroissement du relief et de la pente des versants favorisant les phénomènes de déstabilisation gravitaire. A l'échelle locale, 80% des niches d'arrachement identifiées sont localisées dans trois situations topographiques spécifiques où les contraintes glaciaires étaient vraisemblablement les plus importantes. Sur la base de la distribution de la fréquence en fonction du volume des éboulements cartographiés, des premières estimations de l'influence des grands éboulements postglaciaires sur le remplissage de la vallée du Rhône et de leur influence sur le taux de dénudation post-glaciaire ont pu être calculées.

3.2.3 INTRODUCTION

Paraglacial rock slope failure (RSF) represents a widespread phenomenon affecting glaciated mountain ranges (Ballantyne 2002; Jarman 2009; Korup 2005). Recent works have indicated that this phenomenon may represent the main factor contributing to the erosion of the mountain belt (Hovius et al. 1997; Korup et al. 2007; Clark and Burbank 2010). A typical morphological feature associated with RSF is the formation of cavities. These features are created when the sliding material has been fully or partially displaced from the source area by the glacier/river, or is covered by the post-glacial filling of the glacial valley (Jarman 2009). Compared to roto-translational landslides or deep-seated gravitational slope deformations (DSGSD), cavities left by RSF generate the highest-impact single erosional events in the paraglacial land system (Jarman 2009). Their effect on the valley morphology is significant, in particular as scarp retreat processes but also by decreasing the slope gradient created by glacial deepening (Ballantayne 2002; Jarman 2009). Preferential destabilization of areas adjacent to old RSF cavities is also frequently observed (Blikra et al., 2006; Oppikofer 2009).

At a regional scale, few extensive studies have focused on the analysis of former scars, and their analysis were frequently associated with more general rockslides studies (Cruden 1976; Whellay et al., 1983; Blikra et al., 2005; Blikra et al., 2006; Antinao and Gosse 2009). Only recently some authors proposed a detailed geological and geomorphological investigation focused on rockslide scars only. Oppikofer (2009) proposed a detailed investigation of the failure mechanisms associated to RSF scars in western Norway. Jarman (2009) analysed the potential influence of rockslide scars for glacial trough widening in the Scottish Highlands. Size distribution of submarine rockslide scars was analysed in detail by ten Brink et al. (2006) and Chaytor et al. (2009) to obtain essential information for the assessment of the tsunami hazard generated by submarine landslides. Detailed analyses of the RSF cavities in term of size, failure mechanisms, and spatial distribution provide a valuable insight for the better understanding of the landslide dynamic and the paraglacial evolution of the study area (Chaytor et al., 2009). In particular, the possibilities of directly exploring the characteristics of the failure surface allow better identification of the main geometrical and mechanical factors controlling the failure (Brideau et al., 2010; Oppikofer et al., 2011). Such information, associated to detailed geometrical reconstruction (Oppikofer et al. 2009), size distribution analyses (Guzzetti et al. 2002; Malamud et al., 2004; Chaytor et al. 2009; Dussauges et al., 2002) and cosmogenic dating (Hermanns et al., 2001; Hermanns et al., 2004) could be extremely useful to provide a detailed rockslide hazard assessment. This is of primary importance in areas where potential rockslides and rock avalanches could induce tsunami waves (Blikra et al., 2005; Blikra et al., 2006) or directly hit the population or important transportation corridors (Froese et al. 2011; Pedrazzini et al., 2011).

Along the main Rhone valley (south-western Switzerland), several scars are visible, which apparently have not suffered glacial erosion. For the majority of them, only their upper parts outcrop within the valley's flanks, the bottom being buried below the sediment. Up to now, no regional mapping of these scars has been realized, and only few of them have been analysed in detail (Montandon 1932; Burri 1961; 1995; Pedrazzini et al., 2011). In this study, a first catalogue of the rockslide scars along the main Rhone valley will be presented. Geometrical, structural and geological characteristics of rockslide scars were analysed. In particular, their spatial distribution, their volume and their failure mechanism characteristics

will be investigated in order to identify the main predisposing factors promoting slope failure, and to quantify their impact on the post-glacial erosional history of the Rhone valley.

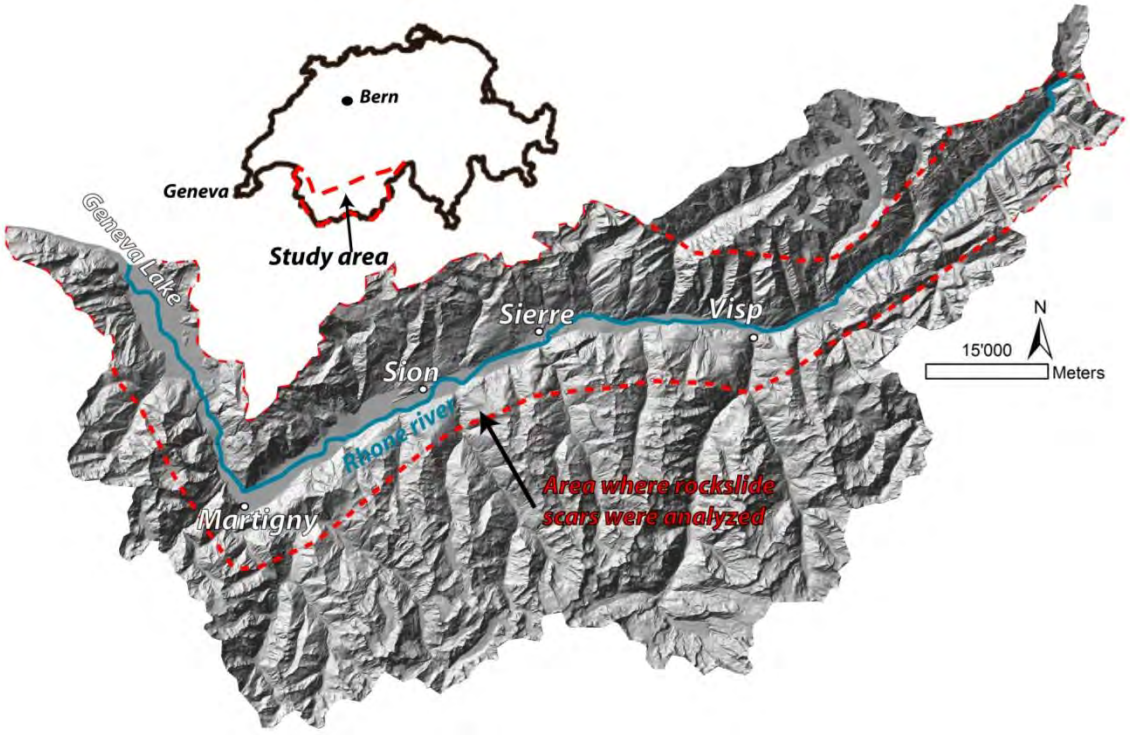

Figure 3.2-1: Overview of the Upper Rhone catchment (South-Western Switzerland). Detailed rockslides scar mapping have been performed for the area comprises within the red dotted line only.

3.2.4 REGIONAL SETTING

The study area is located in south-western Switzerland and covers the entire upper Rhone valley from Lake Geneva to the sources of the Rhone located in the central Swiss Alps (Figure 3.2-2). In the upper and central portions of the study area, the Rhone river flows towards the SE, parallel to the Alpine belt. Near Martigny, its orientation changes towards the NW to finally reach Lake Geneva. The Rhone valley presents an interesting case study owing to its particular geological situation. Indeed, the study area encompasses almost all the main tectonic units of the Western Alps (Steck 1984; Escher et al., 1997). The northern side of the Rhone valley is dominated by Helvetic sedimentary, Nappes (Lugeon 1914; Heim 1921). These are mainly formed by limestone, marly-limestone and shale (Figure 3.2-2). Bedding planes plunge into valley direction, creating complex convex dip-slope geometry. On the opposite side, the southern flank is made up of different Penninic Nappes, displaying a south-eastern orientation (Steck et al., 2001). Rocks types are quite different, with a predominance of terrigenous sediments such as sandstone, quartzite, and schist. Beddings and/or foliation plunges into the slope creating steepened to normal escarpments. From Martigny to Lake Geneva the valley crosses perpendicularly to the Aiguilles Rouges massif, characterised by gneiss and migmatites (von Raumer 1987), as well as to the pre-alpine Nappes. In the upper portion of the valley, the outcropping lithologies are characterised by gneiss, migmatites and meta-sediments associated with the Aar and the Gotthard massif. Post-orogenic tectonic is related to ductile and successive brittle dextral strike-slip movements along the Rhone-Simplon fault system (Steck 1984; Mancktelow 1992). The present–day morphology of the Rhone valley is clearly influenced by this complex glacial and

paraglacial history. The Last Glacial Maximum (LGM) was reached between 20,000 and 18,000 ^{14}C yr. BP and was followed by cyclic retreats and advances (Kelly et al., 2003). The main Rhone valley seems to have been free of ice since 11,000-10,000 ^{14}C yr. BP (Schoeneich et al., 1998). Erosion driven by the Rhone glacier created a significant overdeepening of the Rhone valley (Preusser et al., 2010). Gravimetric (Rosselli and Olivier 2003) and seismic reflection (Besson et al., 1992) surveys indicated the presence of two main glacial overdeepened zones: the first is located before Martigny where the valley changes its orientation, and the second just before Rhone river delta. Rosselli and Olivier (2003), based on gravimetric analysis, estimated the total infill material was estimated to 88 km^3. More recently, with a sloping base level modelling, Jaboyedoff and Derron (2005) created a 3D model of the Rhone valley bedrock and they estimated the total sediment infill to 90-110 km^3.

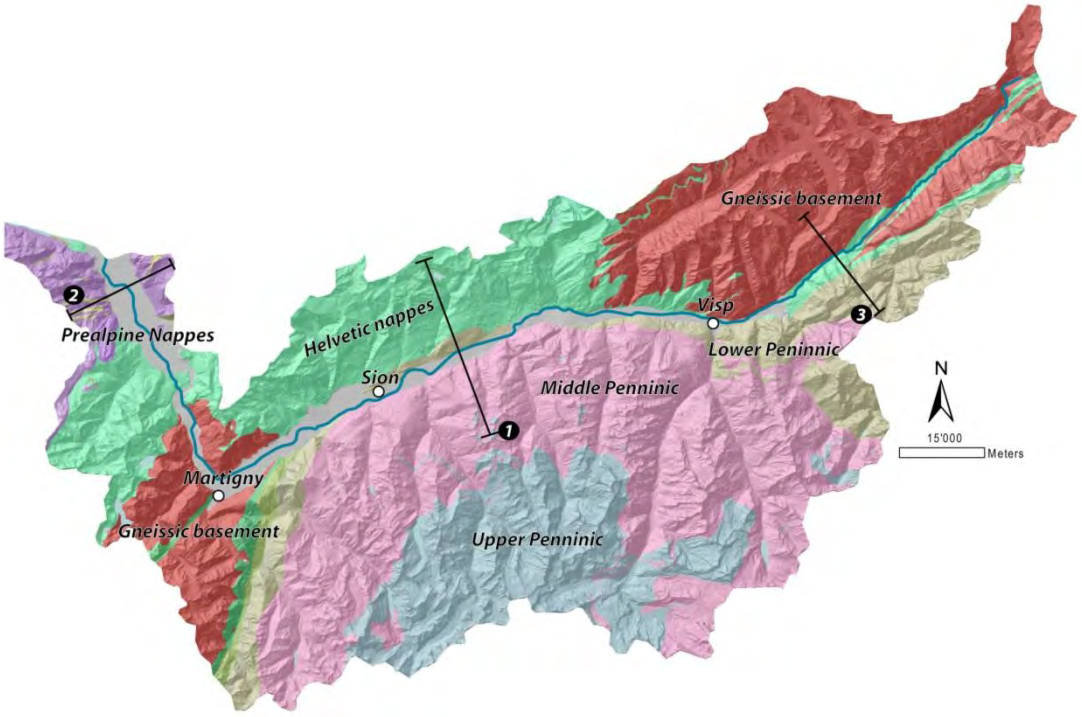

Figure 3.2-2: Simplified tectonic map of the upper Rhone catchment adapted from Steck et al. (2001). In this figure are also reported the traces of the cross section presented in Figure 3.2-23 8 (1), in Figure 3.2-24 (2) and in Figure 3.2-25 (3).

3.2.5 METHODOLOGY

3.2.5.1 Mapping and geomorphic characterisation

The inventory of RSF scars was performed using as primary geographic dataset a high resolution digital elevation model (2 metre cell size), obtained by the Aerial Laser Scanner survey (Swisstopo) up to 2000 m a.s.l. The investigated area covers the main Rhone valley from the source of the Rhone River until Lake Geneva. Rockslide scars were identified through different illuminations of the shaded relief map derived from the DEM. Additional visualisation and interpretation were also performed using Google Earth images (Google© 2010). In addition, for each detected rockslide scar, field analyses were carried out to validate the remote sensing analysis.

According to terminology proposed by Jarman (2006), two types of RSF scars were mapped:

- Cataclasmic scars (Figure 3.2-3a and b): corresponding to scars where the failed material was completely evacuated and the main portion of the failure surface outcrops.
- Sub-cataclasmic scars (Figure 3.2-3c and d): corresponding to scars in which part of the failure surface (< 50%) is still covered by the sliding mass, and that present a possibility of reactivation.

For each RSF scar, an attribute table containing the specific geometrical and geological characteristics were compiled. Owing to several RSF scars being located close to the valley bottom, an estimation of the percentage of the surface buried below the valley sediment was also added in the attribute table.

No lower size limits was adopted, and all detected scars were integrated into the database. However, the inventory has to be considered as incomplete, especially for small size instabilities (<0.1 km^2). This is related to the low quality of the DEM in dense forested areas and the subsequent difficulty of detecting the geomorphological indicators of rockslide scars. Another source of errors is related the absence of high resolution DEMs above 2000 m a.s.l, that drastically decreases the mapping quality in this areas.

The spatial distribution of the rockslide scar along the main Rhone valley has been analysed by means of GIS tools. A quadratic Kernel density function (Silverman 1986) has been applied to calculate the density of the detected rockslides. Analyses were performed both with and without adding a weight for the rockslide scar area.

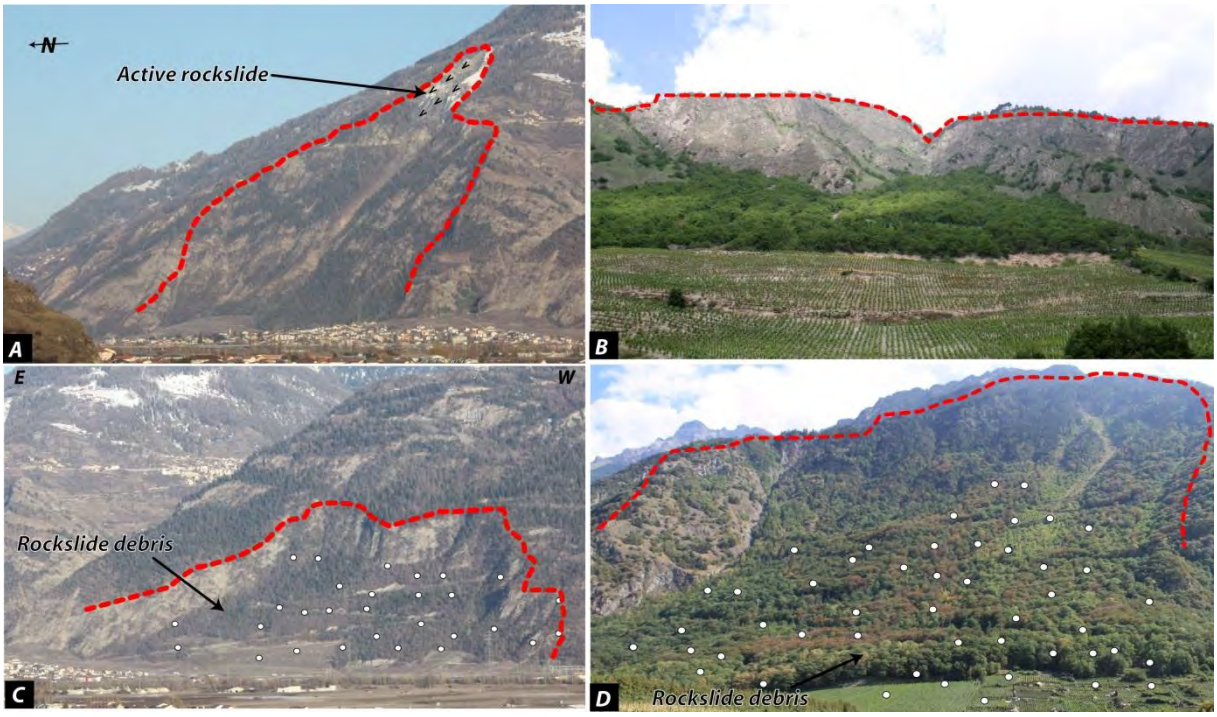

Figure 3.2-3: Examples of rockslide scars perturbing the morphology of the main Rhone valley. a) Cataclasmic rockslide of "Les Créteaux" on the southern side of main the valley. b) Cataclasmic rockslide scar located near Saillon on the northern side of the valley. c) Sub-cataclasmic rockslide located above the village of Riddes, southern side of the valley. d) Sub-cataclasmic rockslide near Martigny located in northern side of the valley.

3.2.5.2 Structural analysis and failure mechanism analysis

A detailed structural analysis of the rock slide scars was carried out based on DEM using COLTOP 3D software (Jaboyedoff et al. 2007; Jaboyedoff et al., 2009). This software allows the representation of a DEM by a 3D shaded relief that displays the orientation of the slopes by means of a Schmidt–Lambert

projection, with one colour for a given dip and dip direction. The main orientation of the discontinuity sets that shape the rocky outcrop can be successively extracted in a semi-automatic way. The discontinuity sets extracted using this software were employed to perform kinematic tests based on classical stereographic techniques (Richards et al. 1978), and to determine the most probable failure mechanism. The observed potential failure mechanisms were grouped into four main classes:

- Planar failure, when a pervasive discontinuity set daylights the pre-failure surface and/or the present-day shape of the scar morphology is mainly planar.
- Wedge failure, when the scar is controlled by two distinct joint sets forming clear gully–type morphology.
- Complex failure, where persistent joint set /foliation dipping with a high angle into the slope are visible. The failure surface is often complex and controlled by secondary joint sets creating complex and composite failure mechanism.
- Unknown, where no persistent joint sets are detected close to the scar or when the failure surface is completely covered by rockslide debris.

3.2.5.3 Pre-failure surface reconstruction and volume estimation

Performing an objective reconstruction of the pre-failure surface and volume calculation is often a difficult task, especially when it is necessary to evaluate it on a regional scale. Frequently, a rough estimation of the pre-failure surface is achieved from the landslide scar volumes by mapping the scar perimeter and assuming a mean thickness obtained by geomorphological observation or by geophysical analyses. Another approach consists in modifying the contour lines of the present-day topography within the rockslide scar, based on the morphology of the surrounding area (Rouiller et al., 1998; Bruckl 2001). Recently, the development of GIS-based analyses and the quality of DEM allow the improvement of valid tools for a more rapid and objective pre-failure topography reconstruction (Völker 2009) and volume estimation (Marchesini et al., 2009). In particular, Oppikofer (2009) developed and new approach combing the manual fitting of planes and ordering of simple forms directly on the 3D point clouds to constrain the SLBL computation (Jaboyedoff et al., 2009; Pedrazzini et al., in press) performed on the reversed topography.

A rapid method to reconstruct the pre-failure surface was presented by ten Brink et al. (2006). It consists of interpolating a smoothed surface (TIN) from the polygon that defines each of the failure scars. The volume is then calculated by subtracting the created TIN from the topographic DEM (Figure 3.2-4). This method is particularly suitable when the rockslide cavity is fully evacuated by the rockslide material. However, it could give erroneous and significant volume underestimations when applied to rockslide scar displaying a convex shape, or when part of the rockslide scar is partially buried below the valley sediments. In this study, the methodology proposed by ten Brink et al. (2006) was adopted. Manual corrections were performed to account for the volume buried below the alluvial planes and scree deposits located above the rockslide scar surface.

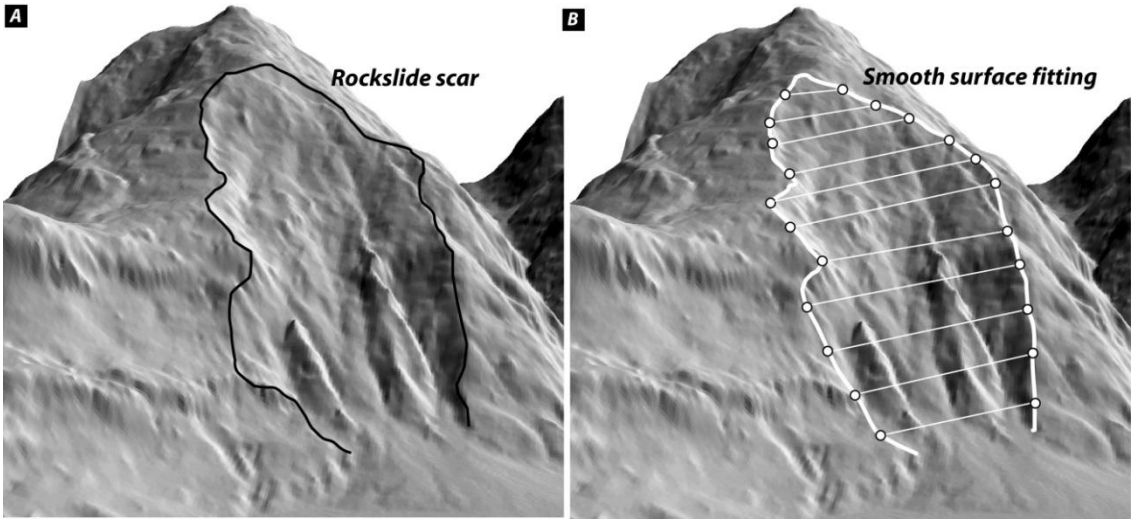

Figure 3.2-4: Example of rockslide volume reconstruction based on the method proposed by ten Brink (2006). The lateral limits of the rockslide are mapped precisely (a) and used to interpolate a smoothed surface (b) over the entire scar area.

In addition, for the most representative case studies a detailed volume reconstruction was performed by adapting the methodology proposed by Oppikofer (2009). In this approach, the volumes of scars are determined by the subtraction of the post-failure bedrock DEM from the early pre-failure DEM. However, to account for the rockslide scars partially buried below the valley sediments, this operation is preceded by a restoration of the post-glacial bedrock topography of the Rhone valley (Figure 3.2-5a). The post-glacial bedrock surface was deduced using the sloping local base level (SLBL) method developed by Jaboyedoff and Derron (2005). The SLBL method is based on an iterative deepening of the areas filled by sediments. The square meshed DEM (25 m cell size) representing the topography is deepened by an iterative routine. If a point (a pixel of the DEM) is located above the mean of its four neighbours its altitude is replaced by the mean value of the four extreme neighbours (minus a tolerance C). The routine is run until the calculated surface remains unchanged between two iterations. The area of the DEM processed with the SLBL is defined by the contour of the sediment filling the valley. SLBL calculation was constrained based on seismic and gravimetric information (Besson et al. 1992; Rosselli and Olivier 2003). This is performed by replacing the altitude of DEM cells where geophysical information are available, and considering these as fixed points during the SLBL calculation.

The post-failure bedrock DEM (Figure 3.2-5b) was then improved by computing an SLBL routine using the present rockslide scar limits separating sediments and bedrock at the border of the present valley as fixed points. Where the rockslide scars present a wedge-like form, the maximal vertical extension of the scar was estimated using the formulation proposed by Jaboyedoff et al., (1996) to calculate height of emergence of a wedge intersection:

$$h = \left\| \frac{d2}{\|\overrightarrow{n_1} \times \overrightarrow{n_2}\|} (\vec{\imath} \times \overrightarrow{n_1}) + \frac{d1}{\|\overrightarrow{n_1} \times \overrightarrow{n_2}\|} (\vec{\imath} \times \overrightarrow{n_2}) \right\| \qquad \textit{Eq. 3.2-1}$$

Where $\overrightarrow{n_1}$ is normal vector of the plane defined by discontinuity set J1, $\overrightarrow{n_2}$ is vector normal of the plane defined by discontinuity set J2, $\vec{\imath}$ is vector defining the wedge intersection line and d1, d2 the distance between the slope crest and the slip surfaces (mean spacing of the two discontinuities).

The rockslide debris, covering the failure surface, was removed by SLBL model based on available geomorphological and borehole data.

The pre-failure bedrock DEM was finally obtained by applying a SLBL calculation on the inversed DEM (Figure 3.2-5c and d). By inverting the DEM, crests become valleys and vice versa; this allows performing classical SLBL computation. After this operation, the DEM is re-inverted to obtain a model of the pre-failure topography. The SLBL computation was constrained by the present topography outside the landslide area, and the geometrical and failure mechanism model of the rockslide.

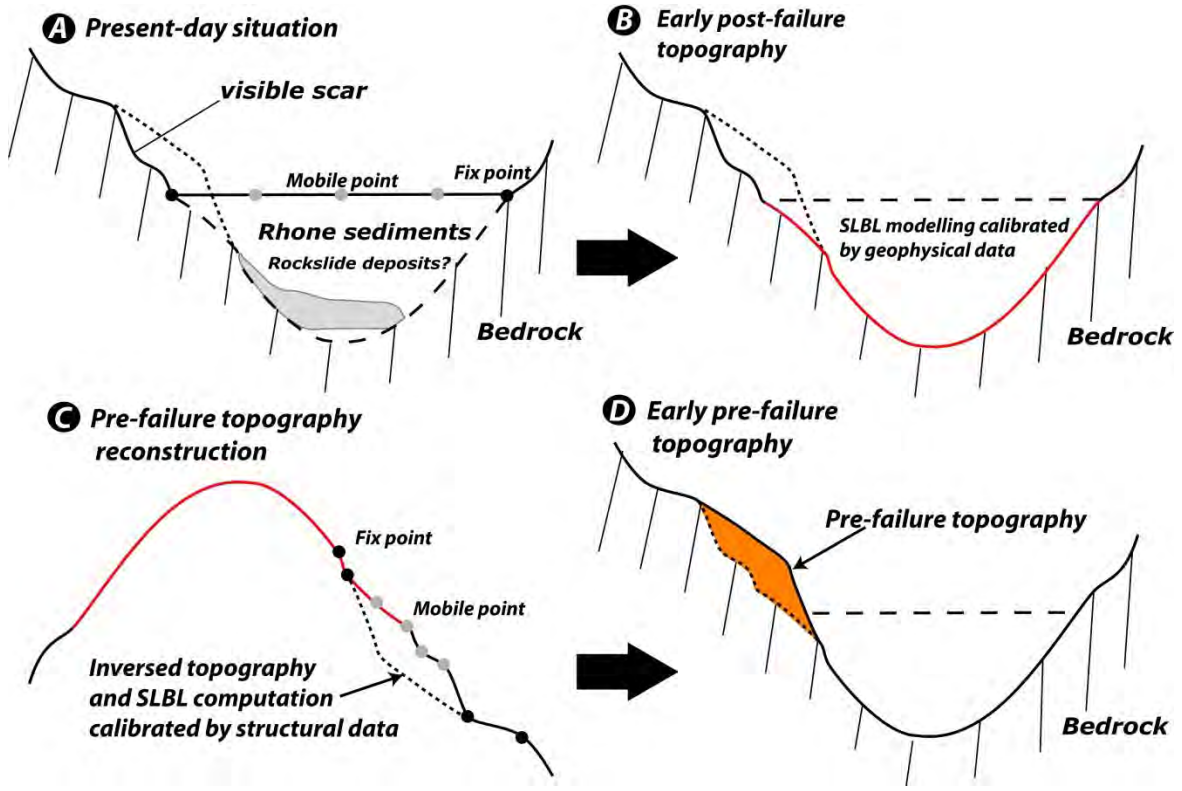

Figure 3.2-5: Methodology adopted for detailed a reconstruction of the pre-failure topography and rockslide volume calculation. a) and b) Estimation of the valley bedrock topography based on SLBL method and geophysical data. c) and d) Reconstruction of the pre-failure topography based on inverse SLBL calculation calibrated based on the height of emergence of potential wedge intersections.

3.2.6 RESULTS

3.2.6.1 General characteristics and spatial distribution

At total of 53 rockslide scars were identified along the main valley (Figure 3.2-6 and Appendix 1). The measured areas vary from 0.015 km^2 to a maximum of 7.4 km^2, corresponding to 2.5% of the total surface of the area investigated. The largest rockslide scar corresponds to the Sierre rock avalanche (Burri 1995; Pedrazzini et al., 2011). Geomorphic analyses indicate that for 77% of the detected scars the majority of the failure surface (90-100%) is located above the valley plain attitude. For the remainder of the dataset, part of failure surface is buried below the valley sediments. The number of the detected RSF scars is quite similar on both valley sides (25 for the northern side of the valley and 28 for the southern side). Figure 3.2-7 shows the kernel density maps for the detected rockslide scar. Kernel density map obtained without area weighting indicates the presence of a high density of scars close to the Martigny area. This region

representing only 17% of the total study area, contains 42% of the total detected landslides and 35% of the total rockslide surface. Three other areas with a high scar concentration are located in the upper portion of the Rhone catchment (Goms valley), near Visp and close to the Rhone delta. These three areas, corresponding to less than 35% of the total study area, contain almost the 70% of the entire rockslide dataset. The kernel density map, obtained by introducing a weighting factor taking into consideration the scar area, also highlighted the high rockslide density close to Martigny.

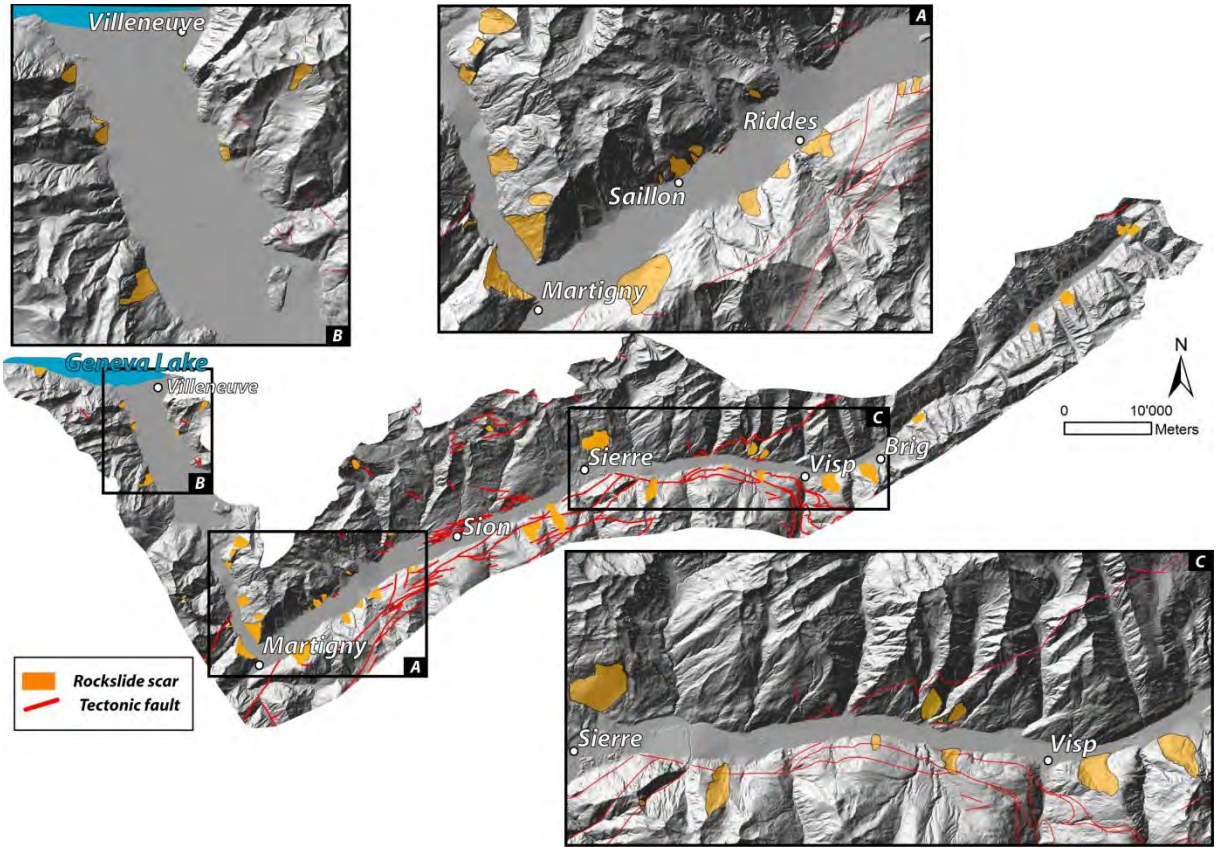

Figure 3.2-6: Map of the rockslides scar detected along the main Rhone valley. a), b) and c) Detail of the areas displaying the highest scar density.

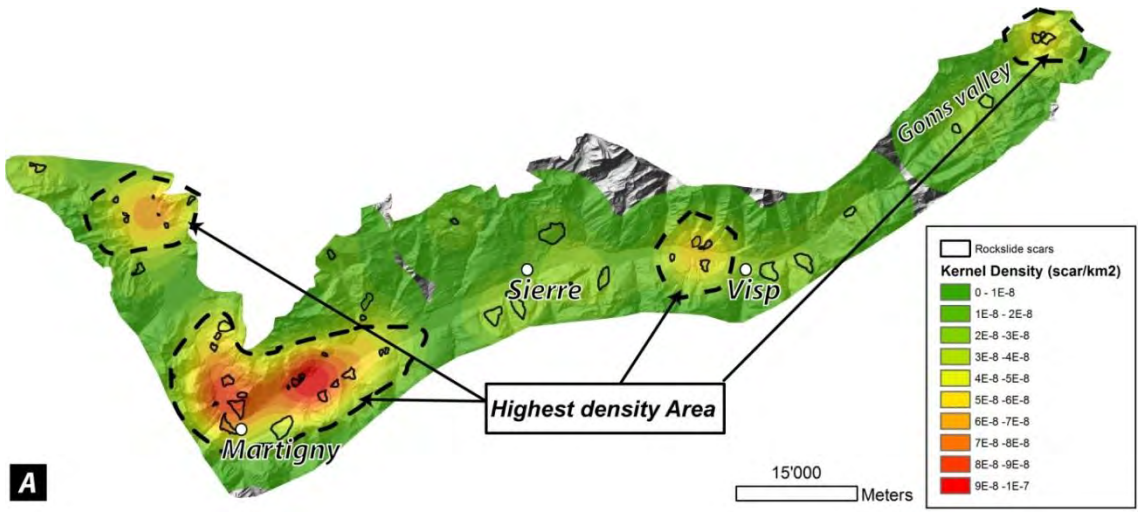

Figure 3.2-7: Kernel density map (obtained without area weighting) displaying the zones with the highest rockslide scar density.

The bedrock geology of each rockslide scar was extracted based on the 1: 25,000 Swiss geological maps (Swisstopo). The results indicate that more that 50% of the detected rockslide scars are found in limestone, malry-limenstone or gneiss. When compared to the surface occupied in the study area by the different lithology, the results indicate a higher concentration of RSF scars in marly-limestone and in Flysch (Figure 3.2-8). Competent brittle rock masses seem to be more susceptible to develop rockslide scars. On the other hand, schist seems to be underrepresented in the catalogue. An interesting propriety of the detected rockslide scar is the relation between the degree of disintegration and lithology type. It can clearly be highlighted that rockslides that develop in marly–limestone are more often completely evacuated compared to those that developed in gneiss or in schist (Figure 3.2-8b). This is in agreement with observations performed by Abele (1974) in the whole Alpine chain, indicating that rock-avalanches with a longer run-out are preferentially developed in sedimentary, well-stratified rocks.

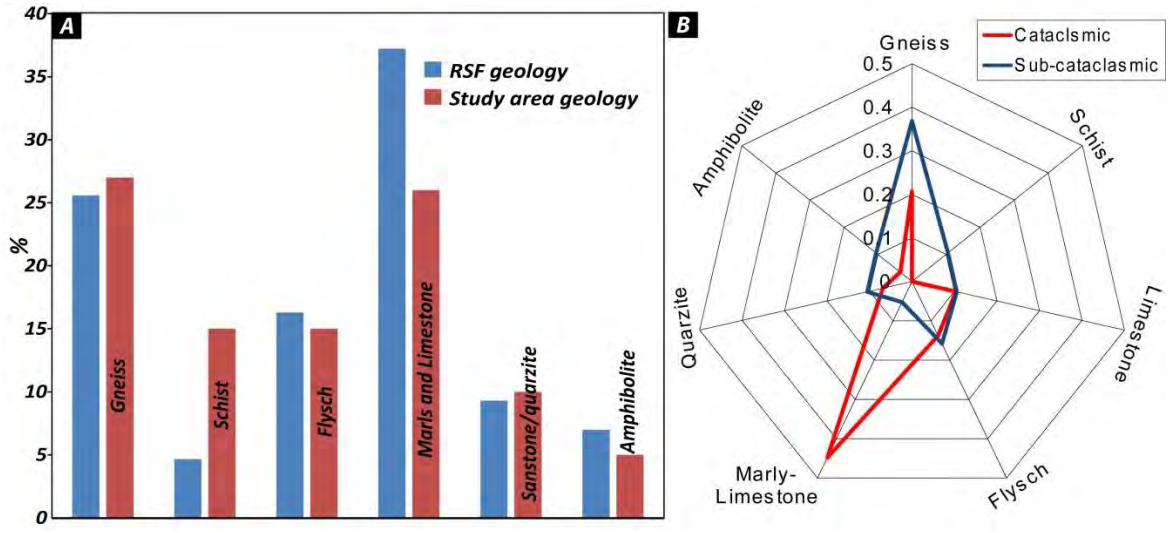

Figure 3.2-8: a) Rockslide scar areal distribution versus lithology. The areal frequency of each lithology and the percentage of outcrop area involved in rockslide scars are shown. b) Degree of disintegration (cataclasmic /sub-cataclasmic) versus lithology type highlighting the different behaviour between rockslides developed in gneiss and those developed in marly-limestone rocks.

3.2.6.2 Failure mechanism analysis

Based on the morphology of the rockslide scar and on the COLTOP 3D analyses, the potential failure mechanism leading to the formation of the rockslide scar was investigated. The analyses of the 53 rockslide scars reveal that the most recurrent failure mechanism corresponds to a wedge slide, controlled by persistent regional joint sets (61% of the total dataset). Spatially, it is possible to highlight a clear differentiation between the failure mechanism of the northern and southern sides of the Rhone valley (Figure 3.2 9a and b). On the southern flank, wedge sliding and topping/complex failures dominate. The main foliation/bedding plane does not seem to be actively involved in the wedge sliding and it occasionally appears as a passive rear release surface.

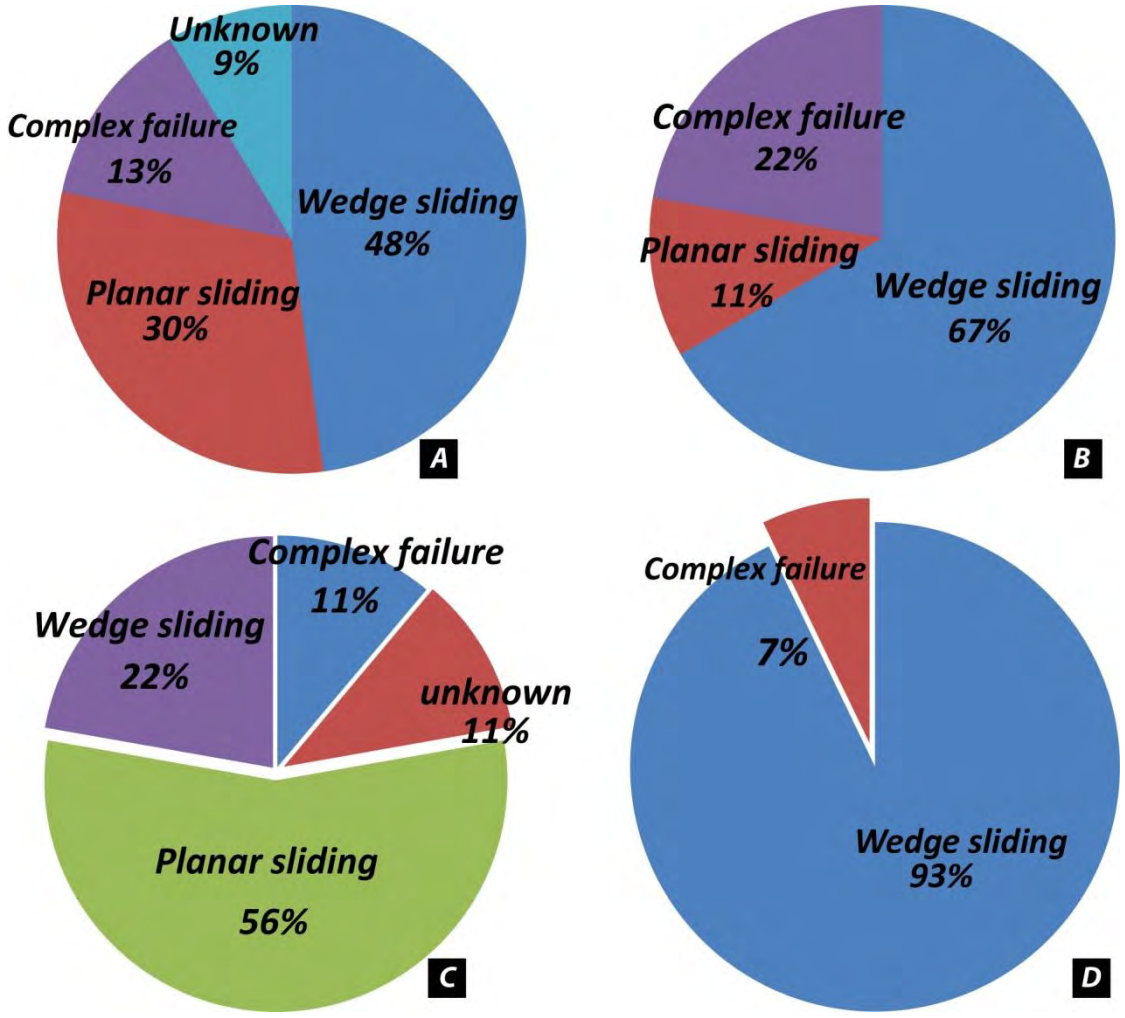

Figure 3.2-9: Failure mechanisms observed in the rockslide scars along the main Rhone valley. a) Failure mechanism observed in the northern side of the main Rhone valley. b) Failure mechanism observed in the southern side of the main Rhone valley) Failure mechanism observed in marly-limestone lithologies. d) Failure mechanisms observed in gneissic lithologies.

Only in the upper portion of the catchment, where the main foliation is almost vertical, these can play a significant role by promoting a diffuse flexural toppling destabilization. In the northern side of the valley, the planar slide mechanism is more developed and corresponds to 30% of the dataset analysed. Planar failures develop along bedding planes dipping in the valley direction. Wedge failures observed in this area also involve the bedding planes and auxiliary and steep joint sets. This clear differentiation of failure mechanism can also be highlighted by comparing the mechanisms affecting the different lithologies (Figure 3.2-9c and d). It is possible to observe that the scars formed in gneiss are mainly controlled by wedge sliding associated with regional joint sets (93% of the observed scars). Conversely, failure mechanisms in limestone and in marly-limestone rocks involve preferentially planar sliding along bedding planes (56% of the observed scars).

3.2.7 VALLEY BEDROCK RECONSTRUCTION AND SIZE DISTRIBUTION OF ROCKSLIDE SCAR

The SLBL calculation performed on the 25 m cell size DEM allowed the calculation of the total amount of the infill material in the Rhone valley. The total volume of sediment of the Rhone Valley is estimated to be 107 Km^3, which is in agreement to previous estimates (Hinderer 2001; Rosselli and Olivier 2003;

Jaboyedoff and Derron 2005). Figure 3.2-10 shows the spatial distribution of the thickness of the valley infill and clearly highlights the presence of the two main overdeepening areas where most of the infilling material is accumulated.

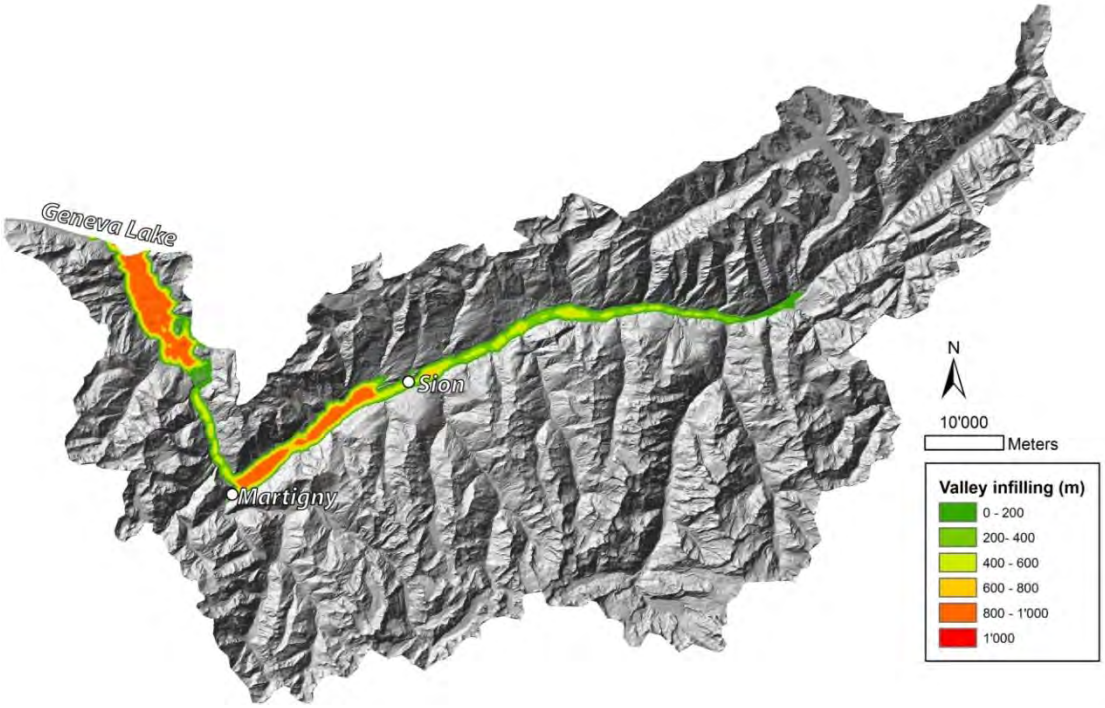

Figure 3.2-10: Results of the SLBL model displaying the distribution of the thickness depth of the valley infilling along the main Rhone valley. Note the presence of two main overdeepened areas close to Martigny and to the Rhone river delta.

The volume of the detected rockslides scar varies from 0.2 Mm^3 to 1600 Mm^3. The comparison between the volumes calculated adopting the two different methodologies varies form 5% to 40%, with a mean difference of 16% (Table 3.2-1).

Table 3.2-1: Comparison between the volume calculated by the method proposed by ten Brink et al. (2006) and by detailed geometrical reconstruction. Note that main differences in volume calculation concern RSFs where a significant portion of the rockslide scar is buried below the sediment (Nb. refers to the rockslide number reported in Appendix 1).

Rockslide Nb.	***Volume SLBL calculation (m^3)***	***Smoothed surface fitting (m^3)***	***Difference (+/-)***
2	4.32.E+08	3.8.E+08	20%
3	4.08.E+08	2.4.E+08	40%
7	1.00.E+08	7.5.E+07	20%
8	5.47.E+06	5.2.E+06	5%
10	2.10.E+08	2.0.E+08	4%
42	3.10.E+07	3.2.E+07	5%

The main differences are observed for the RSFs where a significant portion of the rockslide scar is buried below the sediment, or for RSFs displaying a complex shape. For these configurations, TIN-based surface reconstruction clearly underestimates the rockslides volumes compared to SLBL reconstruction.

The cumulative volume distribution of the detected rockslide scars can be approximated by two power-law distributions (Figure 3.2-11). For volumes smaller than 10 Mm^3 the exponent *b* is 0.13 (R^2 = 0.83). For volumes larger than 10 Mm^3 the exponent *b* increases to 0.73 with a higher correlation coefficient (R^2 = 0.96). The two exponents are similar to those obtained by Oppikofer (2009) from the analysis of rockslide scars in the Norwegian Fjords (b=0.68).

Concerning the smaller volumes, the exponent obtained is much lower than that found in the literature (Dussauge et al., 2002; Hungr et al., 1999). This difference is probably related to the reduced imprint on the topography of the smaller scar leading to a significant underestimation of their effective frequency. This sampling bias is particularly developed in inventories that cover large time spans (as in the preset one), and where the morphological conditions have considerably evolved over time (Van Den Eeckaut et al., 2007).

The relation between area and volume of the detected rockslide scars is reported in Figure 3.2-12. The area/volume relation can be approximated by a power-law distribution with a mean scaling exponent of 1.37 (R^2 = 0.89). As suggested by Chyator et al. (2009), this exponent value is characteristic of landslides where thick segments of unstable material are evacuated during single events, occasioning the formation of rockslides and debris avalanches. A histogram displaying the variability of the mean scaling exponent reported in the literature is presented in Figure 3.2-11b. The exponent obtained for the Rhone valley ranges in the highest frequency category and is very similar to those obtained in other landslide inventories (Simonett et al., 1985; Guthrie and Evans 2004; Guzzetti et al., 2009).

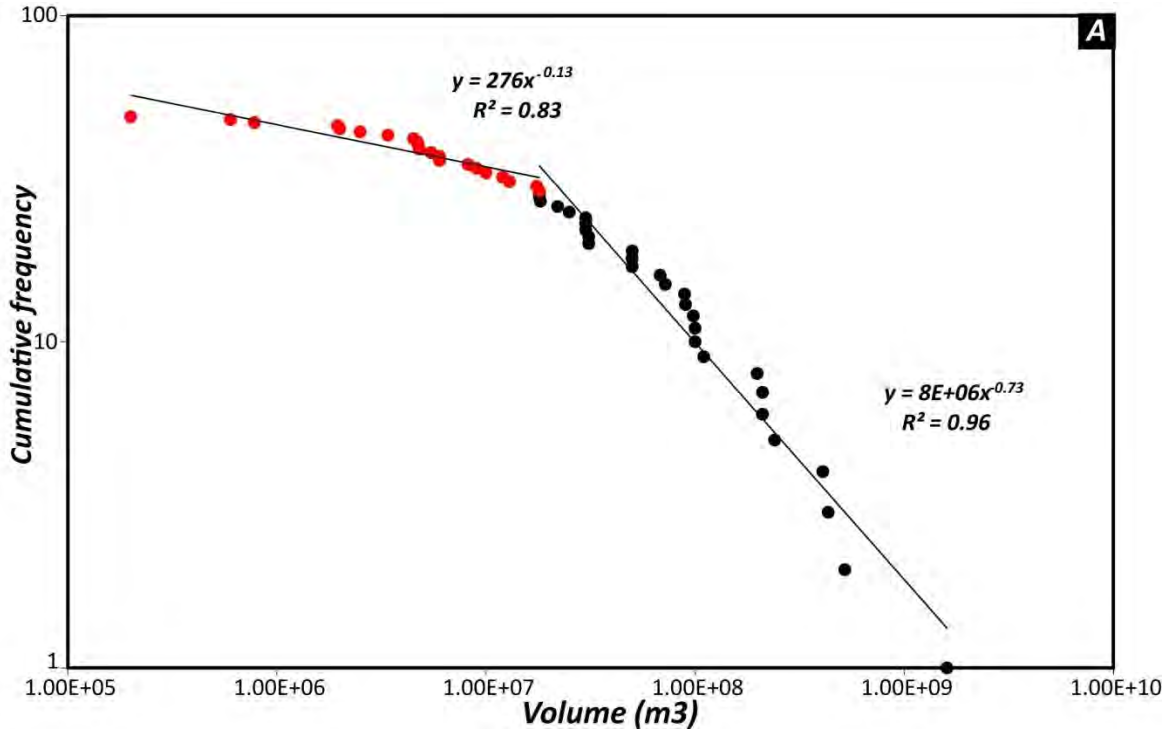

Figure 3.2-11: a) Cumulative frequency size distribution of the rockslides detected along the main Rhone valley. The distribution of the rockslide scar volume can be approximated by two distinct power-law distributions. The flexion point is located close to 10 M of m³.

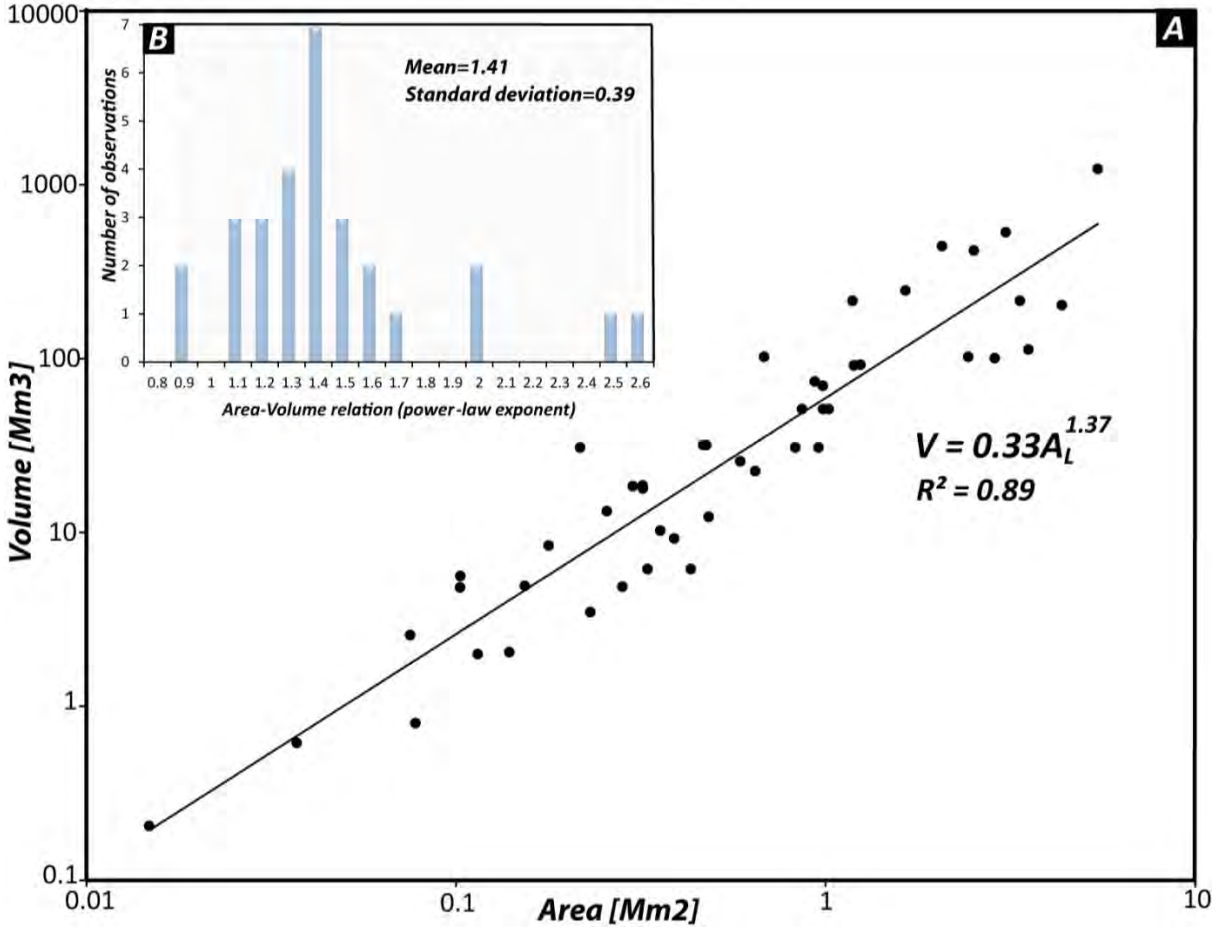

Figure 3.2-12: a) Relation between rockslide scars volume and rockslide scars area. The area-volume relation can be fitted by a power-law with an exponent of 1.37. b) Histogram of empirical power-law exponent obtained in different landslide inventories linking rockslide volume and area (data based on Guzzetti et al., 2009, Korup 2005 and ten Brink et al., 2006).

3.2.8 DETAILED CASE STUDIES

In this chapter, the specific geomorphological characteristics, the failure mechanisms and the volume reconstructions of five representative RSFs will be discussed in detail. Through these examples the influence of the tectonic setting and of the glacial preconditioning will be emphasised. For the localization of the different sites please refer to Figure 3.2-6a.

3.2.8.1 Martigny rockslides

The analysed zone is located close to changes in the direction of the Rhone valley from a NE-SW toward a NW-SE direction. From a geological point of view, the area is composed of massive gneissic and migmatitic rocks belonging to the Aiguilles Rouges massif. Two large concave rockslide scars are visible just after the change in the valley direction (Figure 3.2-13). These rockslide scars are well preserved and display an irregular morphology, shaped by persistent brittle structures. The lower portions of both scars are buried under post-glacial valley sediments. Gravimetric and electrical investigations suggest that part of the failed material is buried within the valley sediments below the RSF scars (Blanc 1976 and reference therein).

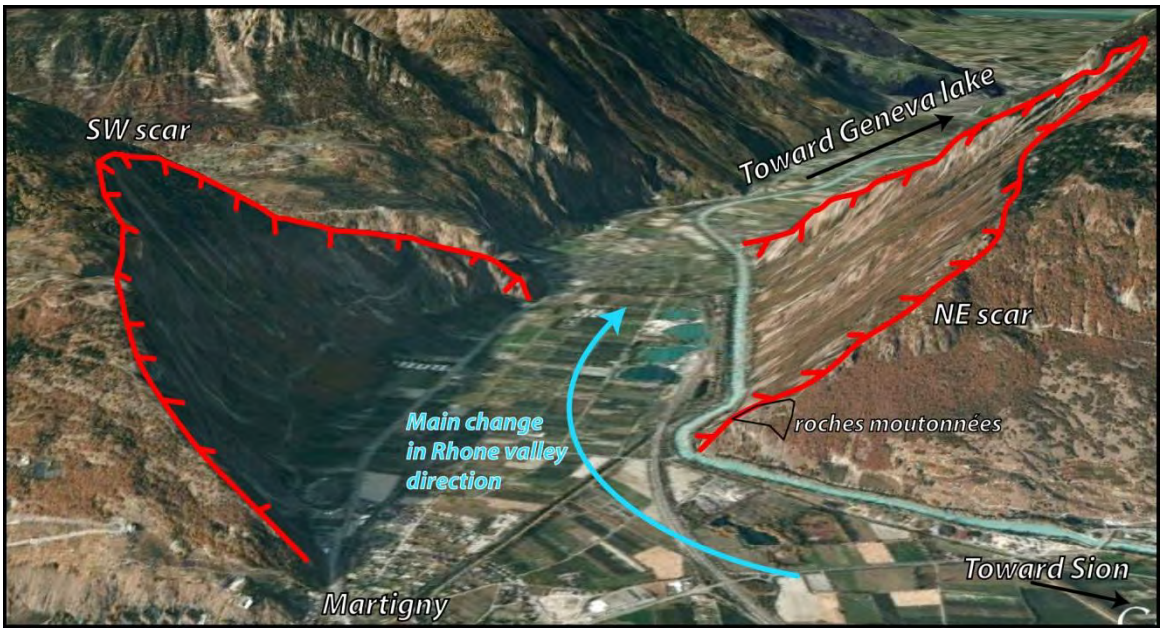

Figure 3.2-13: View toward north of the rockslide scar in Martigny area showing the important erosion associated to the main change in Rhone valley direction.

COLTOP 3D analysis indicates the presence of six persistent joint sets presenting a similar orientation in both rockslide scars (Figure 3.2-14). The detected joint sets are consistent with the results obtained in the same area by Loye et al. (accepted) indicating a homogeneous structural setting characterising all the terminal portions of the Aiguilles Rouges massif. The main foliation oriented NE-SW, does not form any clear morpho-structures and was only observed at the outcrop. The intersection of the main joint sets drives the formation, on both valley sides, of potential unstable wedges that drives the failure mechanisms of large instabilities. It is interesting that the structural configuration on both rockslide scars is characterised by a main wedge intersection line daylighting the topography, and by several potential wedges displaying a plunge angle close to the topography dip. This suggests that a steepening of the topography, as a result of glacial or river erosion have potentially amplified the failure susceptibility by permitting the development of wedge sliding.

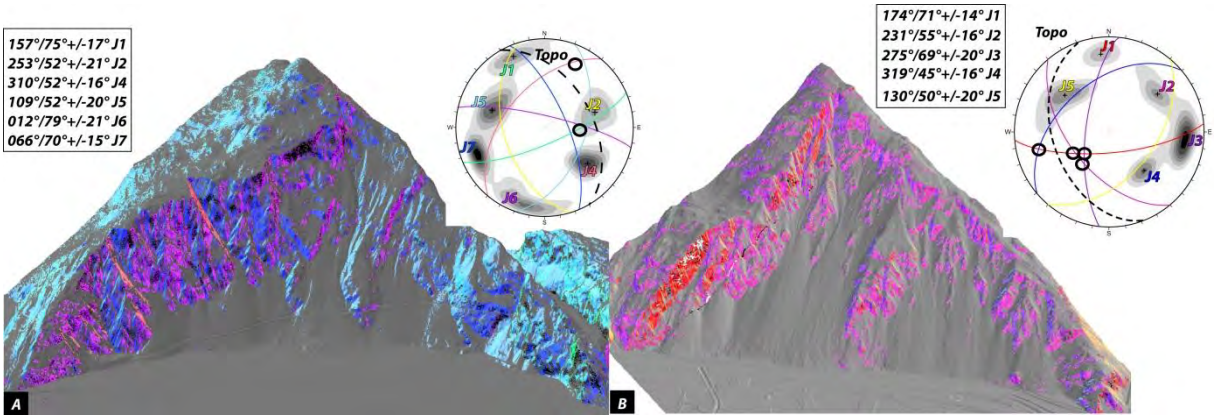

Figure 3.2-14: Structural analysis of the rockslide scars in Martigny area. a) Discontinuity sets detected in the SW scar. b) Discontinuity sets detected in the NE scar. Black circles indicate potential wedge intersection line plunging in the same direction than main topography Note that in the NE scar several potential wedges show a plunge angle greater than main topography. These wedges can be potentially activated if a steepening of the topography occurs.

No direct dating of the failure surface is available to determine the beginning of the rockslide activity. However, field observations indicate the presence of "Roches moutonnées" restricted to the outcrops located outside the rockslide scars suggesting a post-glacial origin. The pre-failure topography reconstruction reveals that at least 10 % of both original scars are now buried below the actual plain. The estimated volumes are 400 Mm^3 for the scar located on the eastern side of the valley and 430 Mm^3 for the one located on the western side (Figure 3.2-15).

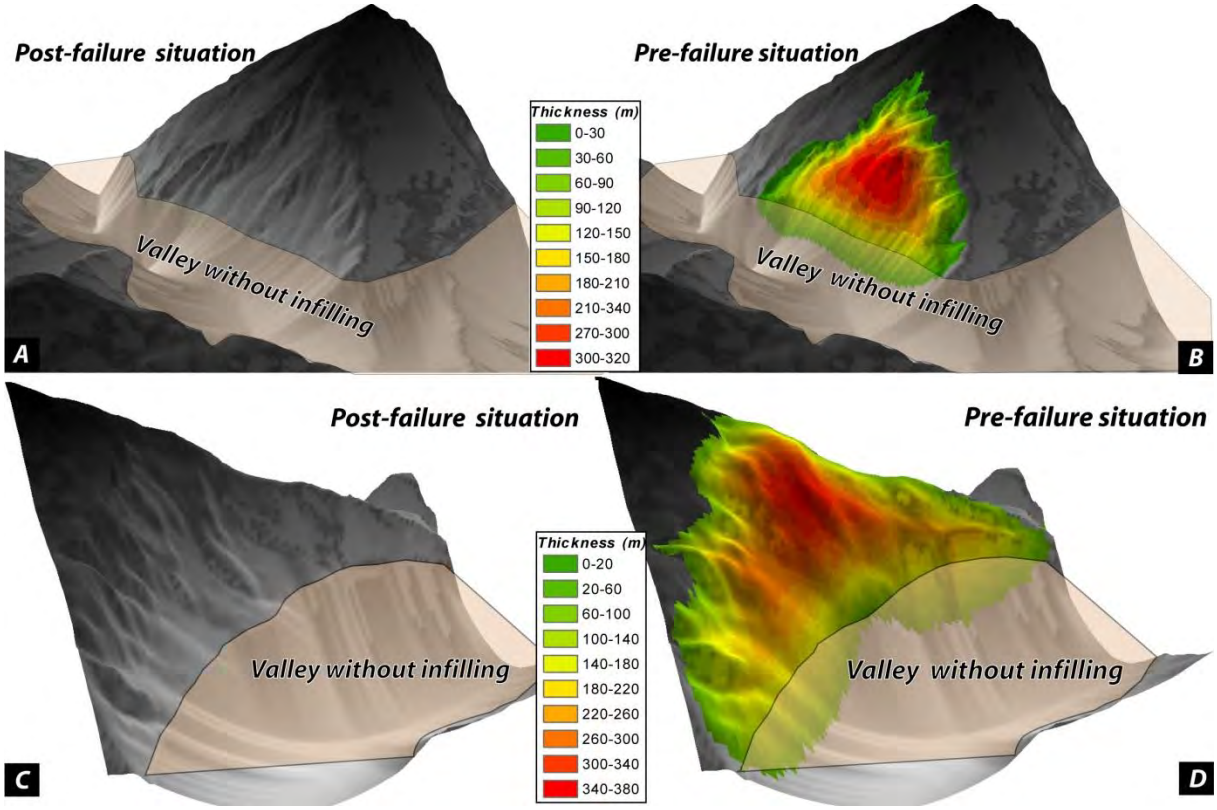

Figure 3.2-15: Detailed pre-failure topography reconstruction and volume calculation for the two rockslide scars located in Martigny area. a) and b) Reconstruction of the pre failure topography of the NE rockslide scar. The calculated volume is approximately 400 Mm^3. c) and d) Reconstruction of the pre failure topography of the SW rockslide scar. The calculated volume corresponds to approximately 430 Mm^3.

The location of these two rockslide scars suggests a significant influence of glacial stress and successive differential post-glacial unloading on the formation of these scars. Indeed, they are located at a point where the main Rhone valley experiences a dramatic change in its direction from NE-SW to NW-SE. This change in direction induces a local increase of glacial stress and slope steepening, in particular on the SW side of the valley. Indeed, this area displays a rugged topography and a more significant degree of disintegration compared to the NE side and almost all the failed material was evacuated from the RSF cavity. The RSF located in the eastern side displays a less evident concave shape. These suggest that its origin can be related to a fluvial-glacial undercut prompted by the valley obstruction created by the failed material coming from the western side.

3.2.8.2 Saillon area

The Saillon rockslide scar is located between Martigny and Sion (northern valley side). The outcropping lithology is the same as in the Martigny area, and is composed of massive migmatitic gneiss. In this area,

two rockslide scars and a sagging deformation were identified (Figure 3.2-16). The rockslide scars both display a clear concave shape. The failed mass is almost completely evacuated from the cavities. Recent colluvium material covers part of the lower portion of the slope, indicating significant post-failure activity. The morphology of the visible scars suggests that, also in this case, part of the rockslide scars are buried below the plain.

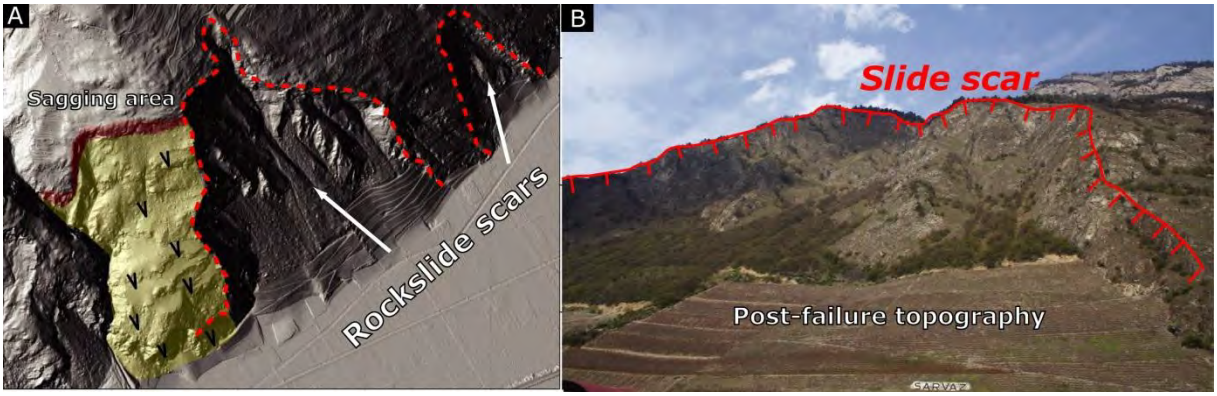

Figure 3.2-16: a) Hillshade view of the two rockslide scars and the sagging area identified in Saillon area. b) Frontal view of the main rockslide scar.

Structural analysis allows the detection of five main discontinuity sets influencing the slope morphology. The main foliation was not detected by the COLTOP 3D analysis, indicating a low morpho-structural imprint and its secondary role on erosional processes. In the field, it displays a significant dip and irregular NNE-SSW orientation (280°-320°/80°). Within both rockslides scars the detected discontinuity sets form four potential unstable wedges displaying a SE trend, and that create a clear preferential failure direction (Figure 3.2-17a and b). The rear release surface is shaped by joint set J1. The SE preferential failure direction is also in agreement with an analysis of the direction of the highest discontinuity frequency (Hudson and Priest 1983; Jaboyedoff et al. 1996) that also indicates a preferential structural weakness direction orientated towards the SE (25 toward 165 +/- 25°, Figure 3.2-17c). The presence of positive relief (rock spurs) within the scar and the irregular shape failure surface suggest that current morphology is the result of continuous rockslide activity driven by the wedge sliding mechanism.

Indirect dating of the rocky outcrops was obtained using Schmidt hammer rebound values (Godie et al. 2006). The results indicate that rebound values obtained within the rockslide slide scars are significantly higher compared to those measured in the surrounding area (Figure 3.2-18), suggesting clear post-LGM glacial development. The variability of the rebound values within the rockslide scar is probably related to local variability in the weathering grade, but it can also support morphological evidence suggesting that the present–day shape of the rockslide scars were not created by single events but are the result of continuous rockslide activity.

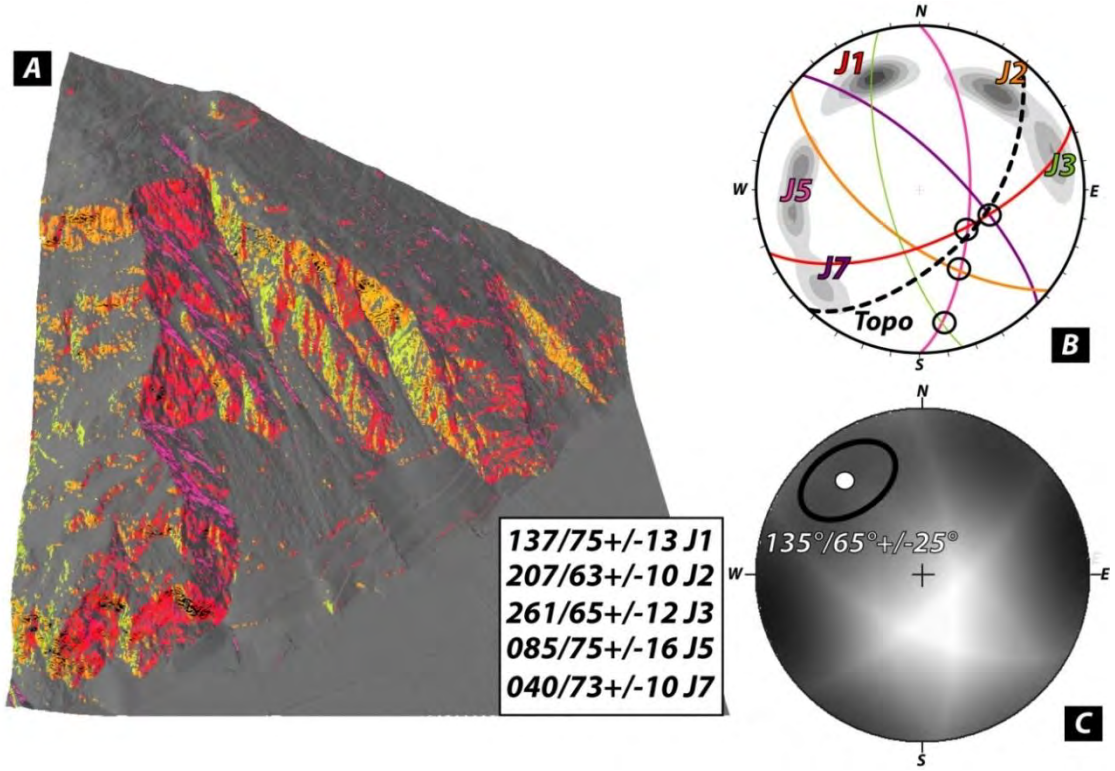

Figure 3.2-17: Structural analysis of the rockslide scars located in Saillon area. a) Selection on the DEM of all points whose spatial orientation match one of the major discontinuity sets. b) Stereonet displaying the joint sets detected based on COLTOP3D analysis. Black circles correspond to the wedge intersection line plunging in slope direction. c) Steronet displaying the direction of the highest discontinuity frequency.

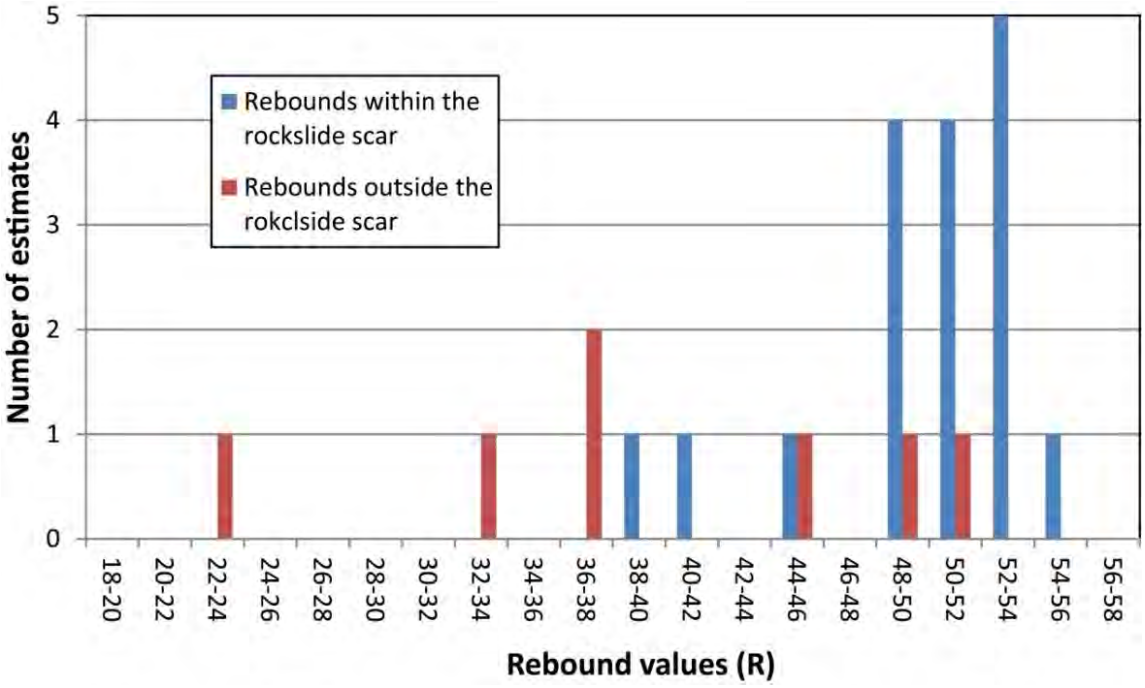

Figure 3.2-18: Indirect dating of the rocky outcrops located within and outside the rockslide scar based on Schmidt hammer rebounds. Each estimate corresponds to the mean values of 10 rebound values performed for the same outcrop.

The pre-failure topography reconstruction permits the estimation of the volume of the larger scar to approx. 100 Mm^3, and to 5.2 Mm^3 for the smaller scar (Figure 3.2-19). Geometrical constraints (estimation of the height of emergence of the wedge intersection line) and morphological characteristics (continuity

with the general slope of the area) suggest that the portion of the scars buried below the valley infill reaches 35% for the larger scar and 15% for the smaller one. The predisposing factors that have promoted the development of those rockslide scars are probably related to the favourable structural setting and to the topography configuration of the slope. Indeed, as shown in Figure 3.2-16 the area where the rockslides develop corresponds to a convex rock spur along the main Rhone valley. As pointed out by Eberhardt et al. (2004) and Oppikofer et al. (2008), this topographic situation leads to the preferential development of fracture damage parallel to the topography in relation to glacial unloading. This configuration represents an important predisposing factor for a post-glacial slope destabilization.

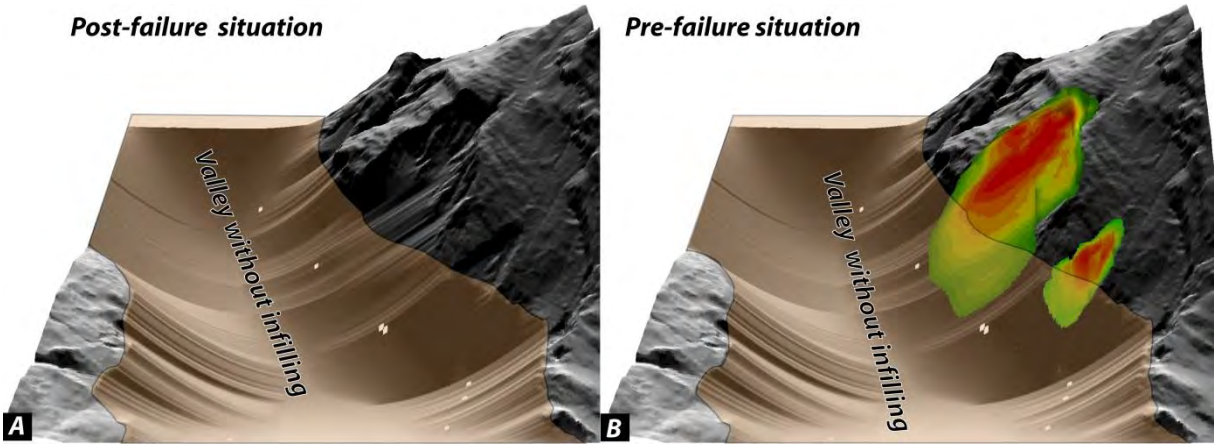

Figure 3.2-19: Detailed geometric reconstruction of the pre-failure topography for the Saillon rockslides. a) Early post-failure situation without the valley sediments. b) Pre-failure situation without the valley sediments. The pre-failure topography reconstruction indicates a rockslide volume of 100 Mm³ for the larger rockslide and of 5.2 Mm³ for the smaller one.

3.2.8.3 Creteaux area

The Creteaux RSF is located on the opposite side of the valley (southern side), in front of the rockslide scars of Saillon. Here the geology is complex, with the presence of three tectonic contacts within the scar area. The observed lithologies are composed of schist, calc-schist and quartzite belonging to the Penninic domain. The morphology is characterised by a clear concave shape and by debris deposits partially covering the lower portion of the slope (Figure 3.2-20). The upper portion of the scar displays a clear retrogressive erosional shape and is characterised by an active landslide (Rouiller 1990). Structural analysis identifies four main discontinuity sets and the main foliation (Figure 3.2-21). J3 is a common structure in the southern side of the Rhone valley and could be associated with faults sub-parallel to the Rhone-Simplon fault system (Champagnac et al., 2003; Sue et al., 2007). J2 and J4 are regional joint sets that were observed, at an outcrop scale, in the entire lower Penninic unit. Their origin can be related to the early Neogene stress field (Sue et al., 2007). As opposed to the Saillon and Martigny areas, the main foliation (152°/43°+/-12) is much more persistent and, even if it dips into the slope, it creates morpho-structures that are visible in the gorges of the la Fare River, SW from the rockslide scar.

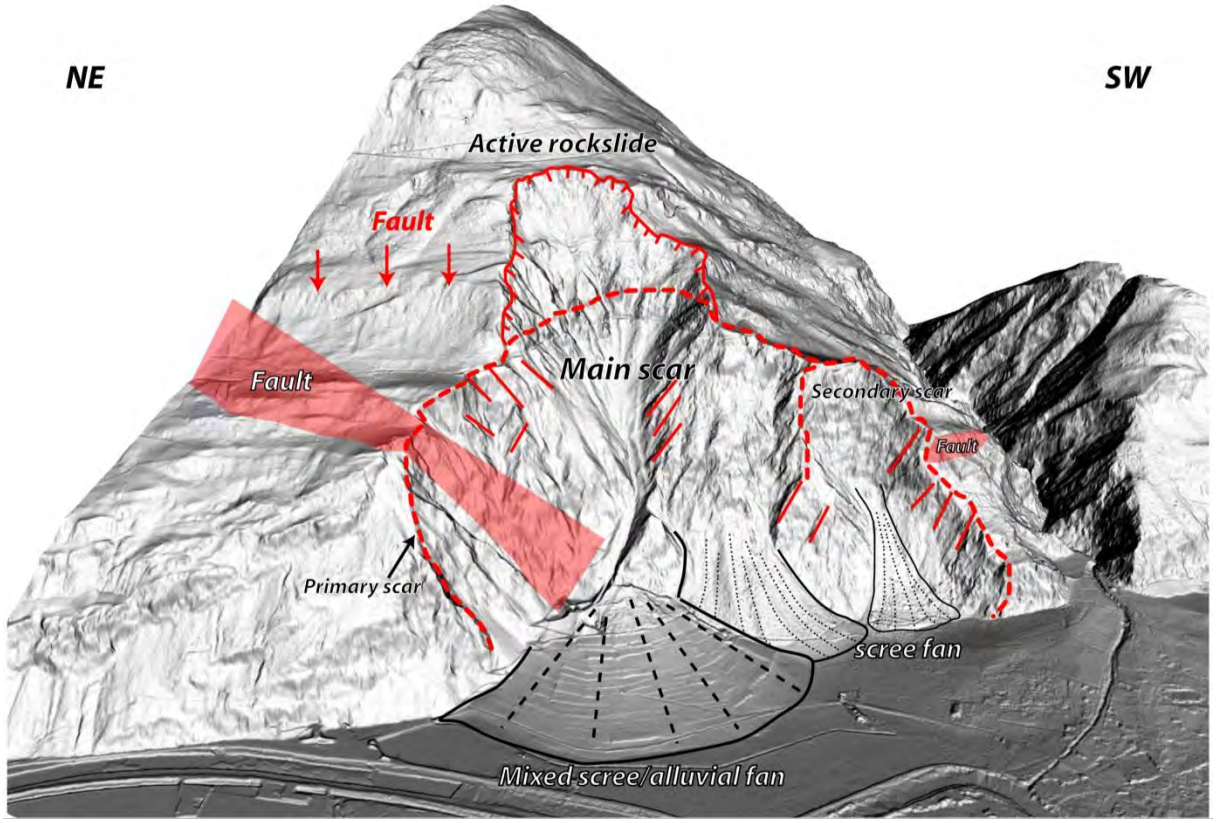

Figure 3.2-20: 3D hillshade view of the "Les Creataux rockslide scar" displaying the principal morphological and structural features observed in the area.

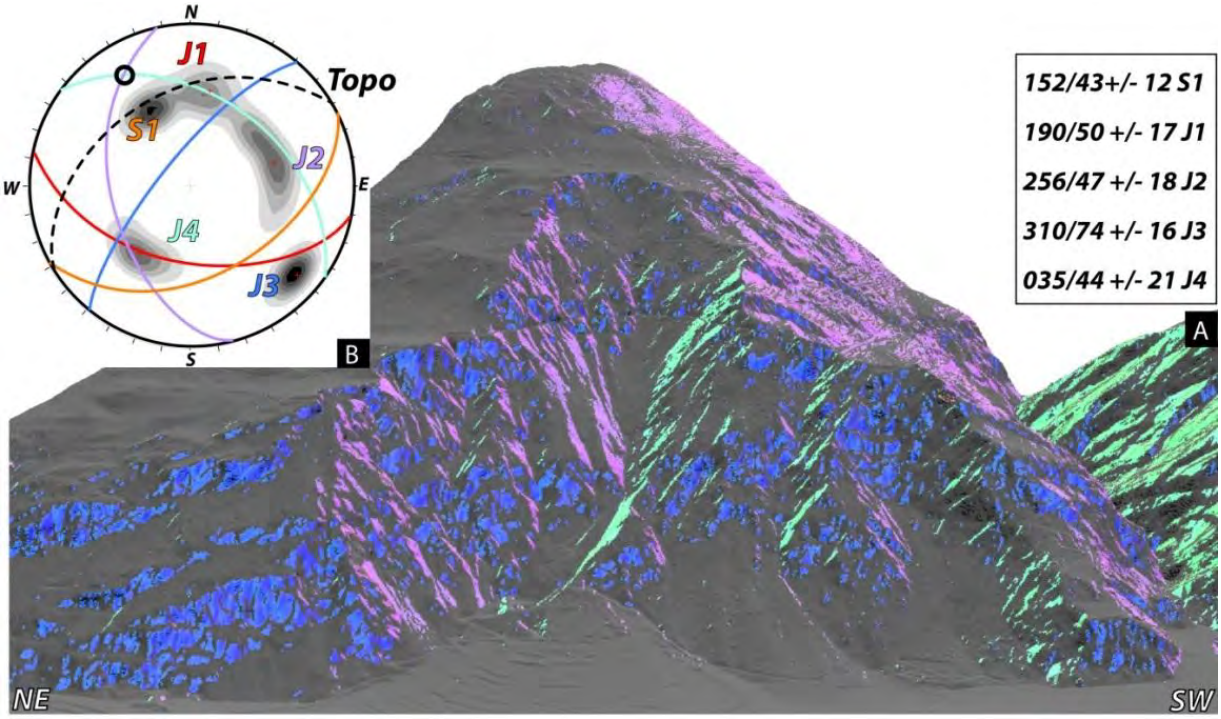

Figure 3.2-21: Structural analysis of Les Creataux scar. a) Shaded relief view of all points in DEM whose spatial orientation match one of the major discontinuity sets. b) Stereonet of the detected discontinuity sets. The black circle corresponds to the wedge intersection oriented toward the slope direction.

The rockslide scar itself is clearly controlled by the three regional discontinuity sets J2, J4 and J3 (Figure 3.2-21). Kinematic analysis indicates a potential wedge sliding created by the intersection of J2 and J4. Discontinuity set J3 acts as a rear release surface. Owing to its persistence, the main foliation can also influence the failure mechanism by the introduction of a toppling component.

The morphology of the main scar suggests that, at the slope scale, the wedge slide is the most effective mechanism to evacuate a large amount of material in a single event. On a local scale, as could be observed on the NW side of the scar, a complex mechanism involving a planar slide and/or toppling on J3 is also possible but generally involves a smaller amount of material. The pre-failure topography reconstruction indicates that, also in this case, the proportion of the failure surface buried below the surface is remarkably close to 30-35%. The estimated volume of the whole scar is about 210 Mm^3 (Figure 3.2-22). The predisposing factor location of this larger rockslide can be primarily related to the structural setting of the similar area. Indeed, the favourable structural conditions, in terms of discontinuity set orientations, are associated with a significant structural weakness and rock mass quality reduction accompanying the tectonic contacts visible within the rockslide scar. Glacial unloading seems to play here a secondary role in the development of the instability.

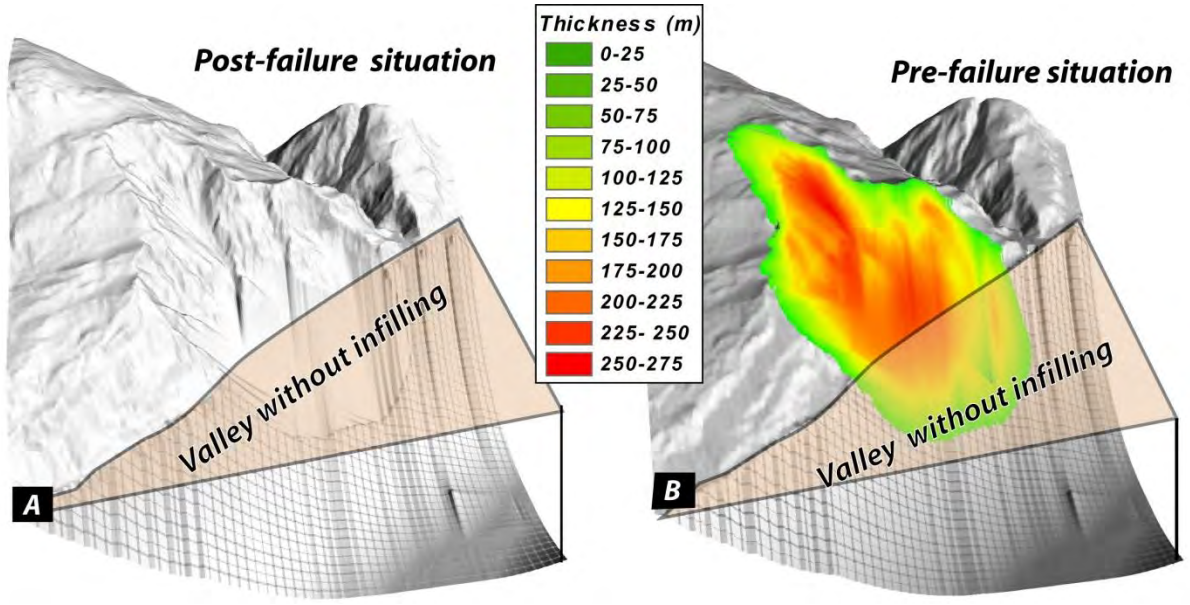

Figure 3.2-22: Detailed geometric reconstruction of the pre-failure topography for Les Creataux rockslides. a) Early post-failure situation without the valley sediments. b) Pre-failure situation without the valley sediments. The pre-failure topography reconstruction indicates a rockslide volume of 210 Mm^3.

3.2.9 DISCUSSION

3.2.9.1 Tectonic control on the failure mechanism and on the scar morphology

Analysis performed on the whole rockslide scar dataset, as well as detailed analysis of the selected case studies, show the main influence of brittle structures and rock mass characteristics on the failure mechanisms and on the morphology of the rockslide scars. This suggests a significant control of the general tectonic settings on the characteristics of the detected rockslide scars. Indeed, a preliminary subdivision of the Rhone valley into three main zones characterised by different rockslide failure mechanisms and scar morphology can be proposed:

a) Central area (Martigny-Visp)

In this area, the northern side of the valley is controlled by the convex dip-slope configuration related to Helvetic sedimentary Nappes. The observed failure mechanisms mainly involve planar slide along the bedding planes. Sub-vertical joint sets associated with the main folding phase or tardive extensional phases (Gasser and Mancktelow 2010; Burkard and Kerrich 1998) act as later rear release surfaces. The presence of marly-limestone interbeds also promote destabilization, creating local heterogeneity in water pore pressure and low shear strength layers that are more susceptible to sliding. This setting also leads to the preferential creation of cataclasmic RSF, where most of the failed masses are buried in the valley infill. The morphology of the rockslide scars detected is characterised by pronounced vertical scarps, but without a clear development of a concave shape (Figure 3.2-23) that is frequently difficult to identify. These characteristics can lead to a significant underestimation of their participation to erosion and create a bias on the rockslide inventory.

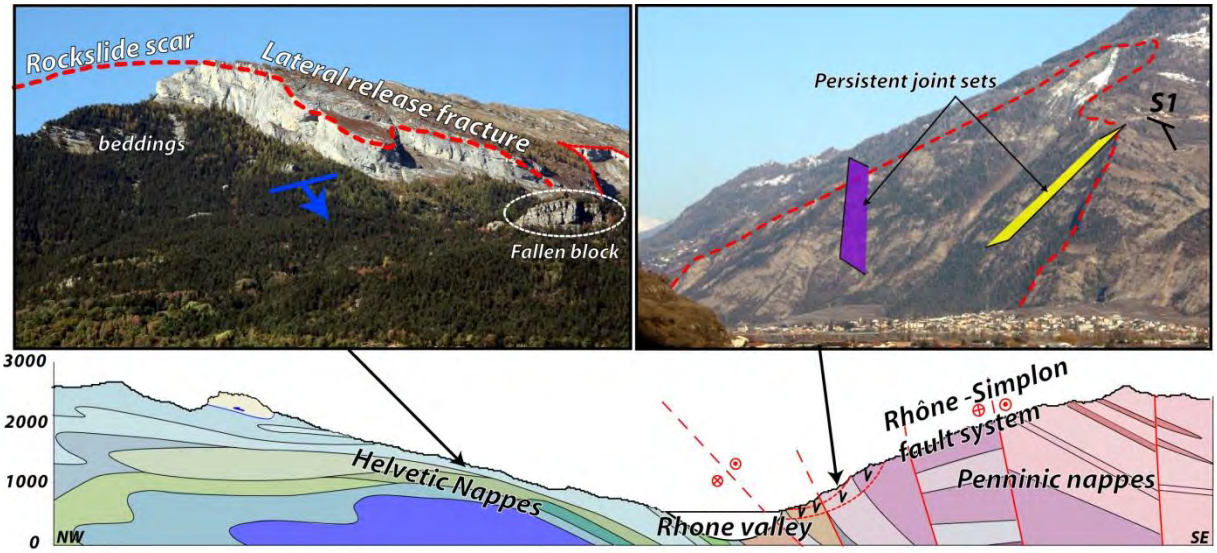

Figure 3.2-23: Geological cross-section through the central portion of the main Rhone valley (Sion area) and characteristics of the failure mechanism of the rockslide scar in this area. Note the clear differentiation on the slope morphology and on failure mechanisms between the two valley sides associated to the different tectonic setting.

The southern side of the valley is characterised by normal escarpments with bedding planes and/or main foliation dipping with a variable inclination into the slope. In this configuration, the main foliation only plays a passive role, and the failure mechanism is principally controlled by the regional joint sets (NW-SE) that create large wedges. The presence of sub-vertical faults related to the Rhone-Simplon fault system and the tectonic contacts between the Penninic units create a local rock mass weakening promoting the development of the instabilities. The heterogeneity of the bedrock characteristics (complex of lithology sequences with schist, gneiss and flysch deposits displaying a different mechanical behaviour) and the orientation of the main foliation do not promote the complete evacuation of the failed material. This leads to the formation of sub-cataclasmic RSF cavities, where part of the failed material is still present at the bottom of the scar. As opposed to the northern side of the valley, wedge-like failure mechanisms induce here the formation of a clear concave morphology that leads a significant overprint on the slope

topography. In this context, the RSF inventory can be expected to be more comprehensive than on the northern side.

A specific situation that cannot be categorised into the two precedent subdivisions is represented by the area near Martigny. The homogenous and high rock strength gneiss characterising the lithology of this area allows the perfect preservation of the RSF cavities, where the fundamental control of pre-exiting discontinuity sets on scar development can be clearly highlighted. The presence of persistent joint sets and of a homogenous structural domain for the entire Aiguilles Rouges basement allows the creation of several structural/topographic configurations that are susceptible to fail. In particular, several potential unstable wedges can be created with different slope orientations. This indicates that the structural predisposition is ubiquitous in the area and the final location of the RSF is defined by the presence of local tectonic accidents (faults or shear bands characterized by low rock mass quality) or by morpho-glacial constraints.

b) Lower Rhone valley (Martigny-Geneva lake)

In this area, the Rhone valley is characterised by a NW orientation sub- parallel to the Nappe vergence, perpendicularly incising the Prelapine Nappes. Also in this area, bedding planes do not participate actively to the failure mechanism. Besides, the presence of several persistent faults oriented WNW-ESE and NE-SW (Pedrazzini et al, in prep; Mosar and Borel 1992) promote the development of rockslides scars characterised by complex wedge failures (Figure 3.2-24). In this area, most of the RSF display only a small portion of the original scar, with the main part being buried below the valley bottom. This suggests a more significant infill rate within this area compared to the portion of the valley located upstream.

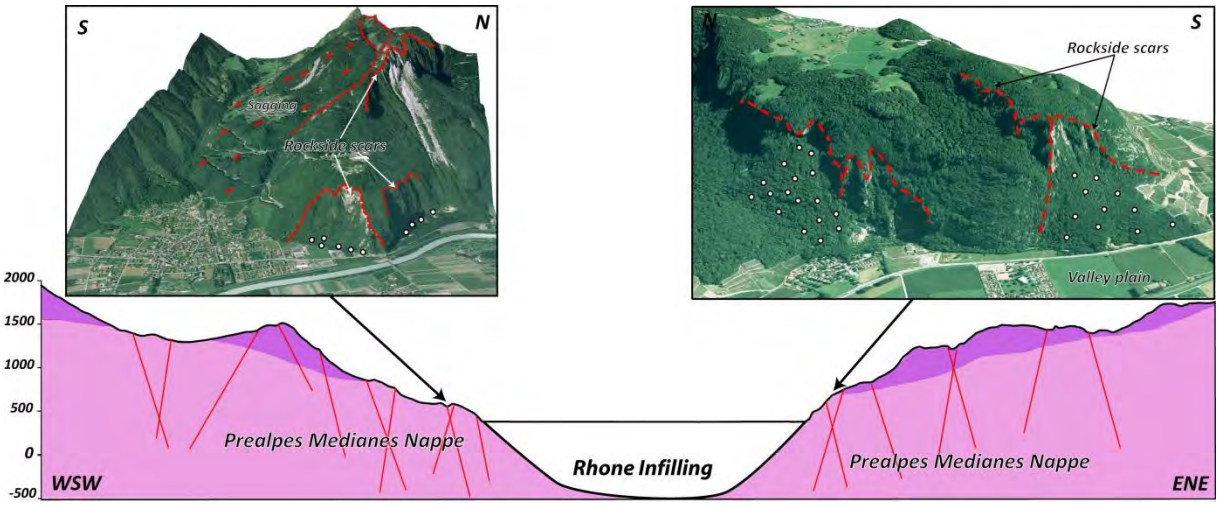

Figure 3.2-24: Geological cross-section through the lower portion of the main Rhone valley (Monthey area) and morphological characteristics of the rockslide scars detected in this area. Note widespread presence of early postglacial and more recent rockslides scars perturbing the slope morphology.

c) Upper Rhone valley (Visp –Goms)

In the upper portion of the Rhone valley, the two valley sides display almost the same structural configuration, characterised by a quasi-vertical foliation and the lack of persistent regional faults perpendicular to the main valley (Ustaszewski and Pfiffner, 2008). In this context, the development of large rockslide scars is limited compared to the central part of the valley. The postglacial morphology suggests that most of the erosion is achieved through fluvial erosion by lateral tributary torrents (Norton

et al., 2010) or by slow slope scale destabilization (DSGSD, and sagging features). Indeed, the mapped scars are frequently found inside large sagging areas (Pedrazzini et al., in prep). The failure mechanisms observed within RSF cavities are principally toppling on the main foliation and complex wedge sliding along regional joint sets (Figure 3.2-25).

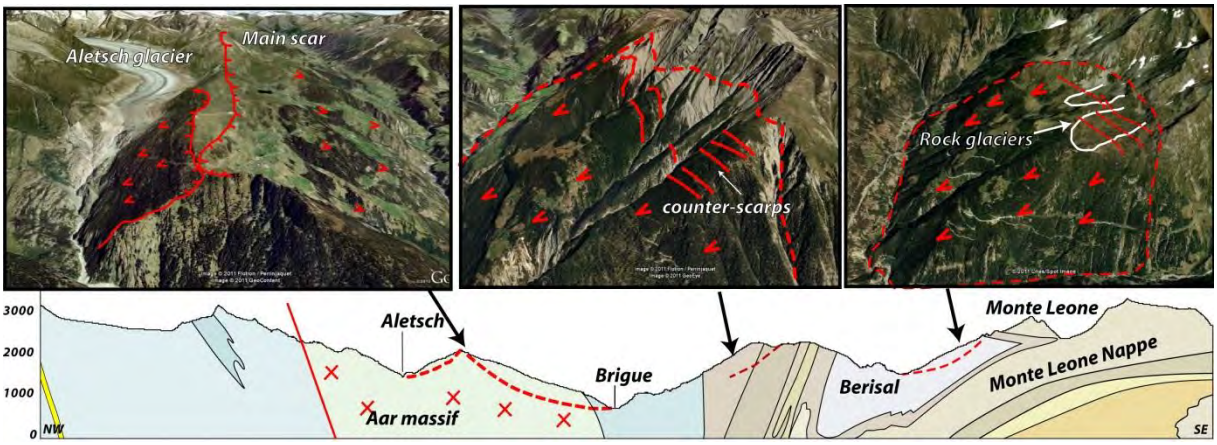

Figure 3.2-25: Geological cross-section through the upper portion of the main Rhone valley (Visp area) and morphological characteristics of the rock slope instabilities detected in this area. Rock slide scars are infrequent in this area and are principally located within large DSGSD areas.

3.2.10 INFLUENCE OF GLACIAL PRE-CONDITIONING ON ROCKSLIDE SCARS LOCATION

The results presented in the previous chapter clearly indicate the influence of the regional tectonic setting in defining the morphological characteristics and the failure mechanisms of the detected rockslide scars. However, as shown in Figure 3.2-6 the spatial distribution of high rockslide scars seems to be only marginally influenced by the lithology or by the structural factors. Besides, a potential correlation can be proposed between areas that experienced a significant glacial overdeepening (Martigny and Rhone delta areas) and areas displaying a high rockslide density. Indeed, more than 60% of the detected rockslide scars are found within these two areas, indicating significant glacial pre-conditioning developed by glacial erosion. As suggested by Ballantyne (2003) and Jarman (2009) the pre-conditioning is expressed by the creation of new reliefs and by valley flank steepening where the erosion can preferentially develop through large rockslides.

At the slope scale, these factors are associated with the subsequent para-glacial slope relaxation of the valley flank (Evans and Clague 1994; Jarman 2006; Cossart et al., 2008). During the last LGM, almost the whole investigated area was located below the trimline, suggesting that para-glacial relaxation affected almost all the slopes along the main Rhone valley. Therefore, more susceptible rockslide zones are expected to be located where the stress applied by a former glacier, and the related post-glacial relaxation, were the highest (Panizza 1973; Holm et al., 2004).

Detailed analysis of the spatial distribution of the detected rockslide scars allow identification of the presence of three main morpho-glacial configurations where the development of the rockslides can be clearly linked to the influxes of the paragalcial relaxation. These three configurations, encompassing almost 80% of the whole rockslide dataset, are presented below (Figure 3.2-26):

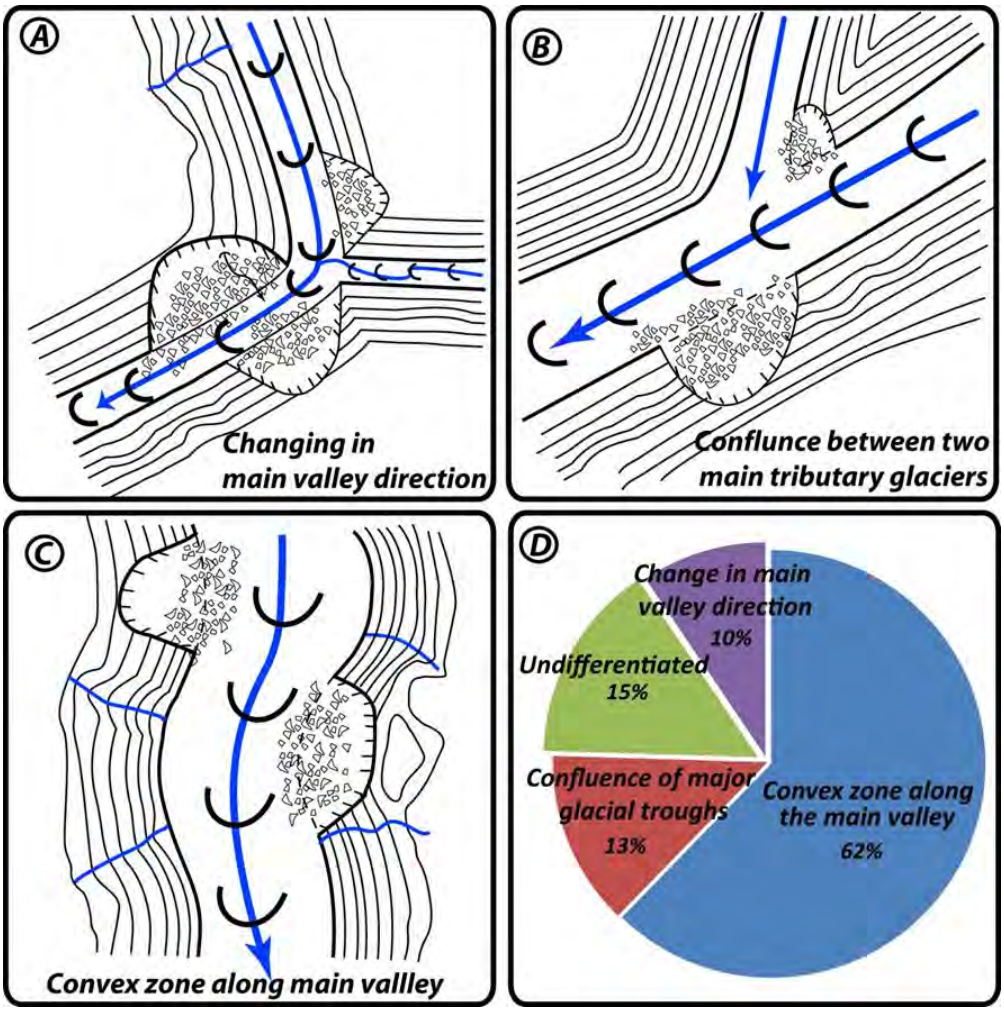

Figure 3.2-26: Typical morpho-glacial configurations susceptible to develop post-glacial RSFs along the main Rhone valley. a) Changing in the main Rhone valley. b) Confluence of an important tributary glacier within the main valley. c) Convex slopes along the main valley created by particular structural/morphological situations. d) Reparation of the detected rockslides scars in the three morpho-glacial configurations.

a) Main changes in the Rhone glacier direction.

Along the Rhone valley only two main changes in the valley direction are presents. The first one is located in the upper portion of the catchment (upper Goms valley) very close the Rhone glacier source area. The second one, which is more spectacular, is located near Martigny. Even if they only represent a limited surface of the study area, they encompass almost 15% of the rockslide scars detected. This is probably related to the significant shear stress applied by the glacier that was forced, by pre-existing structural constraints, to flow in a different direction.

b) Confluence of major glacial troughs.

This situation is quite common throughout the study area and it is related to a significant amount of tributary catchments converging on the central Rhone valley. Rockslides and other slope deformation types are frequently associated with this configuration (Panizza 1974). A good example is represented the rockslide scars observed near Brig. The formation of these scars can be associated with the confluence of the Aletsch Glacier into the Rhone valley. Another example is the Les Pics area (Pedrazzini et al., 2007) where a DSGSD and a large RSF scar are located in the zone of confluence of three different glaciers (Rhone, Dravenuese and Draversa glaciers).

c) Convex zone along the main Rhone valley.

As indicated by Holm et al. (2004), the presence of convex slope breaks, in particular ridge tops or crests of gullies are the most susceptible and the most widespread geomorphic environment where rockslides related debuttressing can develop. In the Rhone valley, 45% of the detected rockslide falls were found within this particular context. A typical example is related to the location of the rockslide scar in the lower portion of the Rhone valley, close to Lake Geneva (Figure 3.2-24). Here, almost all the main convex rocky spurs display the presence of rockslide scars.

3.2.11 SIGNIFICANCE OF ROCKSLIDES FOR MASS TRANSFER AND DENUDATION RATE

Slope movements, in particular, catastrophic rockslides have been highlighted as representing a major factor influencing the mechanical denudation rate of mountain belts (Hovius et al., 1997; Korup 2007; Antinao and Gosse 2009; Gutrie and Evans 2004). In the Rhone catchment, no studies have been carried out on the influence of landslides on denudation rates. Hinderer (2001), based on the estimation on the Rhone valley infilling, calculated a post-LGM denudation rate of 950 mm.kyr^{-1}. Considering the late glacial period only, the same author estimated a denudation rate reaching 2870 mm.kyr^{-1}. Recently, Norton et al. (2010), based on cosmogenic dating and geomorphic analysis, estimated, for the upper Rhone catchment, a post-LGM denudation rate of 1400 mm kyr^{-1}.

Using the volume frequency distribution obtained from the rockslide inventory it is possible to estimate the direct influence of post-LGM rockslides located along the main valley on the Rhone valley infilling. Hantz et al. (2002, 2003), based on detailed rockfall inventories, showed that the cumulated distribution of rock fall volumes follows a power-law distribution in a volume range covering at least 4 orders of magnitude. Assuming that the same relationship can be applied to the rockslide dataset in Rhone valley, the cumulative rockslide frequency can be described by:

$$n(V) = aV^{-b} \qquad \textit{Eq. 3.2-2}$$

Where n (V) is the mean number of rockslides with a volume greater than V, which occur after LGM and with *a* and *b* positive constants.

The total volume of the rockslides within the inventory (V_{tot}) can be then estimated by integrating the following relation (Hantz et al., 2003):

$$V_{tot} = \int_{Vmax}^{Vmin} Vdn = \frac{ab}{(1-b)}(V_{max}^{1-b} - V_{min}^{1-b}) \qquad \textit{Eq. 3.2-3}$$

Where: V_{max} is maximal expected volume of the inventory (m^3), V_{min} is minimal volume detected of the inventory (m^3)

Assuming that this law is valid for all rockslide volumes, the relation became:

$$V_{tot} = \int_{0}^{\infty} Vdn = \frac{ab}{(1-b)}(V_{max}^{1-b}) \qquad \textit{Eq. 3.2-4}$$

Within the analysed area, it is also possible to estimate, the quantity of the mechanical denudation rate related to the rockslide activity after the LGM. This is given by the following equation:

$$DR = \frac{Vtot}{S \times \Delta t} \qquad Eq.\ 3.2\text{-}5$$

Where S is the surface of studied area (m^2) and Δt is the considered time laps (years).

As show in chapter 3.2.7 the cumulative volume distribution of the rockslide scar volumes in the Rhone follow a two power-law distribution, where the slope changes occur close to 10 Mm^3 (Figure 3.2-11). However, according to the uncertainties associated with the rockslide inventory, it is reasonable to assume that only the power-law distribution describing the distribution of larger volumes is representative of the real distribution of the rockslide frequency. As adopted in similar studies, 20% of volume expansion and 1% of the compaction were considered to compare the rockslide volume derived from the inventory analysis to the volume of the valley sediment (Antinao and Gosse 2009 and reference therein).

Using equation (Eq. 3.2-3), the total post-LGM rockslides volume (rockslide > 10 Mm^3 only) is estimated to 5.9x 10^9 m^3 corresponding to 5-7% of the total valley infilling (Table 3.2-2). This variability related to the estimation proposed by previous authors concerning the total volume of the valley infilling. If the power-law distribution obtained for larger volumes (V > 10 Mm^3) is assumed to be representative of the entire rockslide dataset, Eq. 3.2-3 can be adopted. In this case, the calculated post-LGM rockslides volume increases to 7.9x10^9 m^3, corresponding to 5-9% of the valley infill (Table 3.2-2). According to the results obtained by Korup et al. (2007), our results indicate that the contribution of small rockslides (<10 Mm^3) to the total valley infill is relatively low compared to the contribution of larger, but infrequent rockslides.

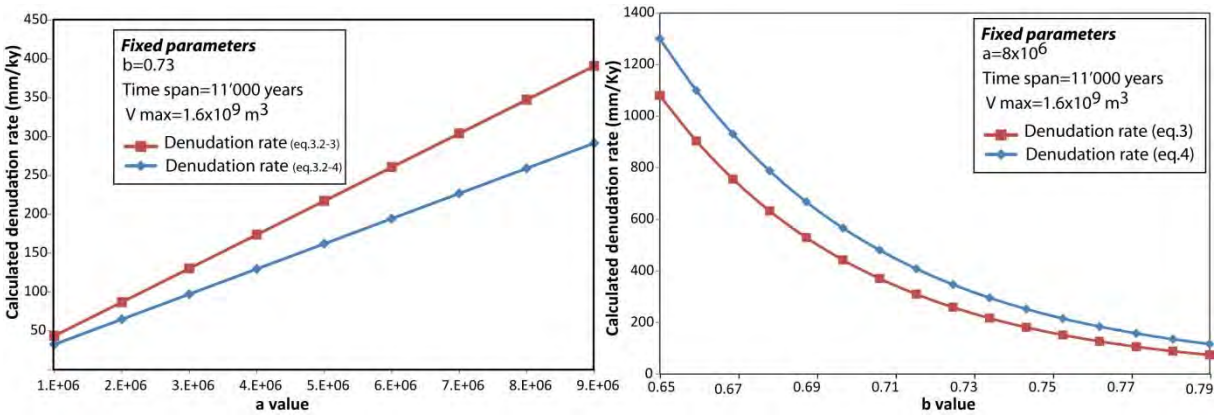

Figure 3.2-27: Sensibility analysis showing the influence of parameters (a) and (b) on the final denudation rate.

The estimation of the denudation rate related to the RSF activity was performed using equation (Eq. 3.2-5). The total active surface was calculated by subtracting the surface of the valley floor (12.7% of the study area) from the total study area. Two different time laps were adopted to perform this calculation. First, according to Hinderer (2001), a time lap of 16,700 years was used, corresponding roughly to the period since the formation of Lake Geneva. Then, another series of calculations were carried using a time lap of 11,000 years, corresponding to early ^{14}C dating obtained on the central and the upper part of the Rhone valley (Kelly et al., 2004; Schoneich et al., 1998; Ivy Ochs et al., 2006) indicating that the main valley was only completely free of ice (including the valley side) since the Holocene.

The calculated denudation rates are reported in Table 3.2-2. These values range from 143 to mm kyr^{-1} for a time laps of 16,700 years to 291 mm kyr^{-1} when a time laps of 11,000 years is considered. The

comparison with post-LGM denudation rate obtained by Hinderer (2001) for the entire Rhone catchment indicates that the contribution of rockslides located along the main Rhone valley to the total denudation rate ranges from 15 to 20%. If the rockslides are assumed to occur in lateglacial period only, their contribution to the late glacial denudation rate is estimated at 8-10%. These results suggest the important contribution of rockslides in particular largest ones on the postglacial erosion of the western Swiss Alps. Besides, this result is not surprising because most of the largest rockslides throughout the entire Rhone catchment are concentred along the main valley sides.

Table 3.2-2: Influence of rockslides on the infilling and on the denudation rate of Rhone valley calculated adopting the approach proposed by Hantz et al. (2002, 2003). According to the uncertainties associated to the infilling volume several different estimations are proposed. The % reported in bracket represents the contribution of the rockslides on the overall denudation rate estimated by Hinderer (2001) for the Rhone catchment.

Parameters	***Results***
Beta exponent	0.73
Alpha	8E+06
Maximal rockslide volume (V_{max}, m^3)	1.6E+09
Minimal rockslide volume (V_{min}, m^3)	1.0E+07
Total rockslide volume V_{tot} (>10 Mm^3) based on eq.*3.2-3*	5.9E+09
Total rockslide volume V_{tot} (all rockslides) based on eq. *3.2-4*	7.9E+09
Valley infilling volume based on results obtained in this study (m^3)	1.07E+11
Valley infilling volume based on results obtained by Jaboyedoff and Derron 2005 (m^3)	1.1E+11
Valley infilling volume based on results obtained by Rosseli and Olivier 2003 (m^3)	8.8E+10
% of rockslide volume in the total valley infilling (this study, eq. 3)	5%
% of rockslide volume in the total valley infilling (Jaboyedoff and Derron 2005, eq.*3.2-3*)	5%
% of rockslide volume in the total valley infilling (Rosselli and Olivier 2003, eq.*3.2-3*)	7%
% of rockslide volume in the total valley infilling (Jaboyedoff and Derron 2005, eq. *3.2-4*)	7%
% of rockslide volume in the total valley infilling (this study, eq. 4)	7%
% of rockslide volume in the total valley infilling (Rosselli and Olivier 2003 eq. *3.2-4*)	9%
Valley side surface without valley floor (Km^2)	205
Denudation rate associated to rockslide activity (eq.*3.2-3)*, 16,700 years ($mm.Kyr^{-1}$)	143 (15%)
Denudation rate associated to rockslide activity (eq. *3.2-4)*, 16,700 years ($mm.Kyr^{-1}$)	192 (20%)
Denudation rate associated to rockslide activity (eq.*3.2-3)*, 11,000 years ($mm.Kyr^{-1}$)	217 (8%)
Denudation rate associated to rockslide activity (eq. *3.2-4)*, 11,000 years ($mm.Kyr^{-1}$)	291 (10%)

Our results are similar to those obtained by Korup et al. (2007) in the Alpenrhein, where Late Pleistocene/Holocene rock avalanches contributed to 7% of the total post-glacial erosion. The uncertainties associated to the results presented in our study are difficult to estimate, in particular due to the several assumptions adopted for the characterisation of the total rockslide inventory. Figure 3.2-27 illustrates the important variability of the calculated denudation rate associated to small changes on parameter (*a*) and on the exponent *b* adopted in *eq. 3.2-3* and in *eq. 3.2-4*. In particular, it can be highlighted that variations of less 10% of exponent *b* can modify the final denudation rate by an order of magnitude. This indicates a large incertitude on the calculated denudation rate and the principal importance to dispose of a reliable volume frequency distribution allowing the extraction of reliable power-law parameters. For these reasons, these results presented here need to be critically interpreted as a preliminary attempt to quantify the role of rockslides on global the denudation rate of the Rhone valley.

3.2.12 CONCLUDING REMARKS

In this study we presented the first inventory of cataclasmic and sub-cataclasmic rockslides along the main Rhone valley. Based on digital elevation model analyses and field mapping, 53 RSF scars were identified. The analyses of their geometrical characteristics and their failure mechanisms reveal the fundamental control of the tectonic and structural setting on the development of the detected rockslide scars.

At a regional scale, Nappe geometry, in particular the orientation of the main foliation and the litho-structural characteristics of the outcropping lithologies, influence the main mechanism and predispose the morphology of the future RSF scars. According to general tectonic setting of the Rhone valley we proposed a first subdivision of the Rhone valley into three different sectors where rockslides are characterised by similar morphological and failure mechanism characteristics. At the slope scale, the relation between persisting joint sets, local tectonic weakness and the main topography orientation represent a primary predisposing factor facilitating the development of RSF and defining their failure mechanisms.

On the other hand, the spatial distribution of rockslides along the main Rhone valley suggests the important influence of the glacial pre-condition and preferential paraglacial stress release on the final location of the rockslide scar. At the valley scale, we identified a clear correlation between glacial overdeepened zones and high rockslide density. Besides, at a slope scale we identified three specific morphological configurations that includes more than 80% of the detect rockslides scar. These observations imply the fundamental role of rockslides on the adjustment of the reliefs and subsequent valley steepening, and the creation of reliefs that occurred during the last glaciation.

Statistical proprieties of the rockslide dataset revealed significant similarity with the landslide dataset that can be found in the literature. In particular, the exponent obtained for the power-law linking rockslide area and volume is very similar to those reported in the literature validating indirectly our volume estimation approach. Based on the observed cumulative frequency size distribution, we proposed a first estimation of the influence of the rockslides on the erosion rate of the Rhone valley. Our analysis indicated that at least 5-10% of the sediments forming the Rhone valley infill are composed of rockslide deposits that were directly discharged into the valley. Besides, we estimate the contribution of rockslides on the mechanical erosion rate of the Rhone catchment to be at least 8-10%. Even if the investigated area includes the main Rhone valley only, the calculated volumetric rockslide rate can be considered the minimal impact of the largest than ($>10^7$ m^3) rockslides within whole the Rhone catchment. This suggests that for less tectonically active mountain belts, such as the European Alps, the numerical erosion models need to explicitly account for large rockslides activity to dispose of a correct estimation of the quaternary erosion rate.

3.2.13 REFERENCES

Abele, G., 1974. Bergstürze in den Alpen-ihre Verbritung, Morphologie und Folge erschinungen, *Wissenschflitche Aplenvereinhefte*, 25.

Antinao, J.L., Gosse, J. 2009. Large rockslides in the Southern Central Andres of Chile (32-34.5°S): Tectonic control and significance for quaternary landscape evolution, *Geomorphology*, 104, 117-133.

Ballantyne, C.K. 2002. Paraglacial geomprohlogy, *Quaternary science Reviews*, 21, 1935-2017.

Besson, O., Rouiller, J.-D., Frei, W., Masson, H. 1992. Campagne de sismique-réflexion dans la Vallée du Rhône entre Sion et Martigny, *Bull. Murithienne,* 109, 45-63.

Blanc, P. 1976. Géologie du massif de l'Arpille, PhD thesis, University of Lausanne, Lausanne, 149p.

Blikra, L. H., Longva, O., Harbitz, C., Løvholt, F. 2005. Quantification of rock-avalanche and tsunami hazard in Storfjorden, western Norway, in: *Landslides and Avalanches*: ICFL 2005 Norway, edited by: Senneset, K., Flaate, K., and Larsen, J. O., Taylor & Francis, London, UK, 57–64.

Blikra, L. H., Longva, O., Braathen, A., Anda, E., Dehls, J. F., Stalsberg, K. 2006. Rock Slope Failures in Norwegian Fjord Areas: Examples, Spatial Distribution and Temporal Pattern, in: *Landslides from Massive Rock Slope Failur*e, NATO Science Series, 49, edited by: Evans, S. G., Scarascia Mugnozza, G., Strom, A., and Hermanns, R. L., IV. Earth and Environmental Sciences, Springer, Dodrecht, Netherlands, 475–496.

Brideau, M.A., Pedrazzini, A., Stead, D., Froese, C.R., Jaboyedoff, M., Van Zeyl, D. 2010. Three dimensional slope stability analysis of South-Peak, Crowsnest Pass, Alberta, Canada, *Landslides*, 8, 2, 139-158.

Bruckl, E.P. 2001. Cause-Effect Models of large landslides*, Natural Hazard*, 23, 291-314.

Burkhard, M., Kerrich, R. 1988. Fluid regimes in the deformation of the Helvetic Nappes, Switzerland, as inferred from stable isotope data, *Contributions to Mineralogy and Petrology*, 99, 416–429.

Burri, M. 1997.Géologie récente de Finges et de ces environs (VS), *Bulletin de la Murithienne*, 115, 5-27.

Burri, M. 1961. Les dépôts quaternaires de la vallée du Rhône entre St-Maurice et le Léman, *Bulletin de la Murithienne*, 78, 36-59.

Champagnac, J. D., Sue, C., Delacou, B. and Burkhard, M., 2003. Brittle orogen-parallel extension in the internal zones of the Swiss Alps (south Valais),. *Eclogae Geol. Helv*., 96, 325-338.

Chaytor, J.D., ten Brink, U.S., Solow, A.R., Andrews, B.D. 2009. Size distribution of submarine landslides along the U.S. Atlantic margin, *Marine Geology*, 264, 16–27.

Clarke B.A., and Burbank D.W., 2010. Bedrock fracturing, threshold hillslopes and limits to the magnitude of bedrock landslide, *Earth and Planetary Science Letters*, 297, 577-585.

Cruden, D.M. 1976. Major slides in the Rockies, *Canadian Geotechnical Journal*, 13, 8-20.

Dussauge-Peisser, C., Helmstetter, A., Grasso, J.-R., Hantz, D., Desvarreux, P., Jeannin, M., Giraud, A. 2002. Probabilistic approach to rock fall hazard assessment: potential of historical data analysis, *Nat. Hazards Earth Syst. Sci.*, 2, 15–26.

Eberhardt, E., Stead, D., Coggan, J.S. 2004. Numerical analysis of initiation and progressive failure in natural rock slopes--the 1991 Randa rockslide*, International Journal of Rock Mechanics and Mining Sciences*, 41, 69-87.

Froese, C.R., Moreno, F. 2011. Structure and components for the emergency response and warning system on Turtle Mountain, *Natural Hazards*, doi: 10.1007/s11069-011-9714-y.

Escher, A., Hunziker, J.C., Marthaler, M., Masson, H., Sartori, M. and Steck, A. 1997. Geologic framework and structural evolution of the Western Swiss-Italian Alps. In O. Pfiffner P. Lehner P. Heitzmann S. Mueller and A. Steck Eds. *Results of NRP 20 Deep structures of the Swiss Alps*, Birkäuser, 205-221.

Gasser, D., Mancktelow, N.S. 2010. Brittle faulting in the Rawil depression: field observations from the Rezli fault zone, Helvetic nappes, Western Switzerland, *Swiss Journal of Geosciences*, 103, 15- 32.

Goudie, A.S. 2006. The Schmidt Hammer in geomorphological research, *Progress in Physical Geography*, 30, 703–718.

Guzzetti, F., Malamud, B.D., Turcotte, D.L., Reichenbach, P., 2002. Power-law correlations of landslide areas in central Italy. *Earth Planet. Sci. Lett.,* 195, 169–183.

Guzzetti, F., Ardizzone, F., Cardinali, M., Galli, M., Rossi, M., Valigi, D. 2009. Landslide volumes and landslide mobilization rates in Umbria, central Italy, *Earth Planet. Sci. Lett*., 279, 222–229.

Hermanns, R.L., Niedermann, S., Villanueva Garcia, A., Gomez, J.S. and Strecker, M.R. 2001. Neotectonics and catastrophic failure of mountain fronts in the southern intra-Andean Puna Plateau, Argentina, *Geology*, 29, 619-623.

Hantz, D., Dussauge-Peisser, C., Jeannin, M., Vengeon, J.M. 2002. Danger d'éboulements rocheux : de l'opinion d'expert à une evaluation quantitative. Symp. *Geomorphology: from expert opinion to modelling*, Strasbourg: 115-122.

Hantz, D., Dussauge-Peisser, C., Jeannin, M., and Vengeon, J.-M. 2003. Rock fall hazard assessment: from qualitative to quantitative failure probability, in: *Int. conf. on Fast Slope Movements*, Naples, 263–267.

Hermanns, R. L., Niedermann, S., Ivy-Ochs, S.D. and Kubik, P.W. 2004.Rock avalanching into a landslide-dammed lake causing multiple dam failure in Las Conchas valley (NW Argentina) - evidence from surface exposure dating and stratigraphic analyses, *Landslides*, 1, 2, 113-122.

Hinderer, M. 2001. Late Quaternary denudation of the Alps, valley and lake fillings and modern river loads, *Geodin. Acta*, 14, 231– 263.

Hovius, N., Stark, C.P., Allen, P.A., 1997. Sediment flux from a mountain belt derived by landslide mapping, Geology 25, 231–234.

Heim, A. 1921. *Geologie der Schweiz*, Band II, Tauchnitz, Leipzig.

Holm, K., Bovis, M.J., Jakob, M. 2004. The landslide response of alpine basins to post-Little Ice Age glacial thinning and retreat in southwestern British Columbia, *Geomorphology*, 57, 201–216.

Hudson, J. A., Priest, S.D. 1983. Discontinuity frequency in rock masses, *Int. J. Rock Mech. Min. Sci. Geomech. Abstr.,* 20, 73-89.

Hungr, O., Evans, S.G., Hazzard, J. 1999. Magnitude and frequency of rock falls along the main transportation corridors of south-western British Columbia, *Canadian Geotechnical Journal*, 36, 224–238.

Ivy-Ochs, S, Kerschner, H., Reuther, A., Maisch, M., Sailer, R, Schaefer J, Kubik, PW., Synal, H.-A., Schlüchter C. 2006. The timing of glacier advances in the northern European Alps based on surface exposure dating with cosmogenic 10Be, 26Al, 36Cl and 21Ne, *GSA Special Papers,* 415, 43–60.

Jaboyedoff, M., Phillippossian, F., Mamin, M., Marro, C. and Rouiller, J. D. 1996. Distribution spatiale des discontinuités dans une falaise. Approche statistique et probabilistique. Vdf Hochschulverlag AG an der ETH, Zurich.

Jaboyedoff, M., Derron, M. 2005. A new method to estimate the infilling of alluvial sediment of glacial valleys using a sloping local base level, *Geografica Fisica e Dinamica Quaternaria*, 28, 37-46.

Jaboyedoff, M., Metzger, R., Oppikofer, T., Couture, R., Derron, M.-H., Locat, J., Turmel, D. 2007. New insight techniques to analyze rock-slope relief using DEM and 3D-imaging cloud points: COLTOP-3D software, *Proceedings of the 1st Canada – U.S. Rock Mechanics Symposium.*

Jaboyedoff, M., Couture, R., and Locat, P. 2009. Structural analysis of Turtle Mountain (Alberta) using Digital Elevation Model: Toward a progressive failure*, Geomorphology*, 103, 5-16.

Kelly, M.A., Buoncristiani, J.F., Schlüchter, C. 2004. A reconstruction of the last glacial maximum (LGM) ice-surface geometry in the western Swiss Alps and contiguous Alpine regions in Italy and France, *Eclogae Geologicae Helveticae,* 97, 57–75.

Jarman, D. 2006. Large rock slope failures in the Highlands of Scotland: Characterization, causes and spatial distribution, *Engineering geology*, 83, 161-182.

Jarman, D. 2009. Paraglacial rock slope failure as an agent of glacial trough widening, From: Knight, J. and Harrison, S. (eds) *Periglacial and Paraglacial Processes and Environments*.The Geological Society, London, Special Publications, 320, 103–131.

Korup, O. 2005. Distribution of landslides in southwest New Zealand, *Landslides*, 2, 43-51.

Korup, O., Clague, J.J., Hermanns, R.L., Hewitt, K., Strom, A.L., Weidinger, J.T. 2007. Giant landslides, topography, and erosion, *Earth and Planetary Science Letters*, 261, 578-589.

Lugeon, M. 1914. Les Hautes Alpes calcaires entre la Lizerne et la Kander (Wildhorn, Wildstrubel, Balmhorn et Torrenthorn). Fascicules 1, 2 & 3. En 2 vols. Beiträge zur geologischen Karte der Schweiz, N.F., Lfg. 30.

Malamud, B.D., Turcotte, D.L., Guzzetti, F., Reichenbach, P. 2004. Landslide inventories and their statistical properties, *Earth Surface Processes and Landform*, 29, 687–711.

Mancktelow, N.S. 1992. Neogene lateral extension during convergence in the Central Alps; evidence from interrelated faulting and backfolding around the Simplonpass; Switzerland, *Tectonophysics,* 215, 295–317.

Marchesini, I., Cencetti, Cencetti, C., De Rosa, P. 2009. A preliminary method for the evaluation of the landslides volume at a regional scale*, Geoinformatica*, 13, 277–289.

Mosar, J., Borel, G. 1992. Paleostress from the Préalpes médianes (Switzerland), *Annales Tectonicae*, 6, 115-133.

Montandon, F. 1933. Chronologie des grands éboulements alpins, du début de l'ère chrétienne à nos jours. Socité géographique Génève, *Matériaux pour l'étude des calamites*, 32, 271-340.

Norton, K.P., von Blanckenburg F., Kubik, P.W. 2010. Cosmogenic nuclide-derived rates of diffusive and episodic erosion in the glacially sculpted upper Rhone Valley, Swiss Alps*, Earth. Surf. Proc. Land*, 35, 651–662.

Oppikofer, T. 2009. Detection, analysis and monitoring of slope movements by high-resolution digital elevation models, Ph.D. thesis, Inst. of Geomatics and Anal. of Risk, Univ. of Lausanne, Lausanne, Switzerland.

Oppikofer, T., M. Jaboyedoff, Pedrazzini A., M.-H. Derron, Blikra, L. H. 2011. Detailed DEM analysis of a rockslide scar to characterize the basal sliding surface of active rockslides, *J. Geophys. Res.*, 116, F02016.

Oppikofer, T., Jaboyedoff, M., Keusen, H.-R. 2008. Collapse at the eastern Eiger flank in the Swiss Alps, *Nature Geoscience*, 1, 531-535.

Panizza, M., 1973. Glacio pressure implications in the production of landslides in the dolomitic area. Geologia Applicata e Idrogeologia, 1, 289–297.

Pedrazzini, A., Jaboyedoff, M., Loye A. 2001. From Sackung to rock avalanche: the example of Sierre landslide (Switzerland), *Geophysical Research Abstracts,* Vol. 13, EGU2011-13069, 2011 EGU General Assembly 2011

Pedrazzini, A., Froese, C.R., Jaboyedoff, M., Hungr, O., Humair, F. *In press*. Combining Digital Elevation Model analysis and run-out modeling to characterize hazard posed by a potentially unstable rock slope at Turtle Mountain, Alberta, Canada, *Engineering Geology*, doi:10.1016/j.enggeo.2011.03.015.

Pfiffner, O.A., Lehner, P., Heitzman, P.Z., Mueller, S., Steck, A. 1997. Deep structure of the Swiss Alps - *Results from NRP 20*.

Preusser, F., Reitner J.M., Schlüchter, C.2010. Distribution, geometry, age and origin of overdeepened valleys and basins in the Alps and their foreland, *Swiss Journal of Geosciences*, 103, 407-426.

Rosselli, A., Olivier, R. 2003. Modélisation gravimétrique 2.5D et cartes des isohypses au 1:100'000 du substratum rocheux de la Vallée du Rhône entre Villeneuve et Brig (Suisse), *Eclogae geol. Helv.*, 96, 399- 423.

Rouiller, J.D. 1990. L'éboulement des Crétaux – Isérables – Riddes (Valais), *Publication Société Suisse de Mécanique des Sols et des Roches*, 121, 15-17.

Richards, LR., Leg, G.M.M., Whittle, R.A. 1978. Appraisal of stability conditions in rock slopes. In: Bell FG (ed) Foundation engineering in difficult ground. Newnes-Butterworths, London, 449–512.

Simonett, D.S. 1967. Landslide distribution and earthquakes in the Bewani and Torricelli Mountains, New Guinea. In: Jennings, J.N., Mabbutt, J.A. (Eds.), Landform Studies from Australia and New Guinea. Cambridge University Press, Cambridge, pp. 64–84.

Schoneich, P., Dorthe-Monachon, C., Jaillet, S., Ballandras, S. 1998. Le retrait glaciaire dans les Préalpes et les Alpes au Tardiglaciaire, *Bull. d'Ét. Préhist. et alpines de la vallée d'Aoste*, 9, 23-37.

Silverman, B.W. Density Estimation for Statistics and Data Analysis. New York: Chapman and Hall, 1986.

Steck, A. 1984. Structures et deformations tertiaries dans les Alpes centrales*, Eclogae geol. Helv.*, 77, 55-100.

Steck, A, Epard, J.L., Escher, A, Gouffon, Y, Masson, H. 2001. Carte tectonique des Alpes de Suisse occidentale et des regions avoisinantes 1:100000. Notice explicative, Service Géologique National, Bern, 73 pp.

Sue, C., Delacou, B., Champagnac, J.-D., Allanic, C., Tricart, P., Burkhard, M. 2007. Extensional neotectonics around the bend of the Western/Central Alps: an overview, *Annu. Rev. Earth Planet. Sci.,* 96, 1001–1029.

ten Brink, U.S., Giest, E.L., Andrews, B.D. 2006. Size distribution of submarine landslides and its implication to tsunami hazard in Puerto Rico, *Geophys. Res. Lett*. 33, L11307.

Ustaszewski, M., Pfiffner, O. A. 2008. Neotectonic faulting, uplift and seismicity in the Central and Western Swiss Alps. In S. Sigmund et al. (Eds.), *Tectonic aspects of the Alpine-Carpathian-Dinaride System*. Geological Society of London Special Publication 298, pp. 231–249.

Völker, D.J. 2009. A simple and efficient GIS tool for volume calculations of submarine landslides, *GeoMarine Letters*, 30, 541-547.

Von Raumer, J-F. 1987. Les massifs du Mont Blanc et des Aiguilles Rouges: témoins de la formation de croûte varisque dans les Alpes occidentales, *Géologie Alpine*, 63, 7-24.

Van Den Eeckaut, M., Poesen, J., Govers, G., Verstraeten, G., Demoulin, A. 2007. Characteristics of the size distribution of recent and historical landslides in a populated hilly region, *Earth and Planetary Science Letters*, 256, 588–603.

Whalley, W.B., Douglas, G.R., Jonsson, A. 1983. The magnitude and frequency of large rockslides in Iceland in the Postglacial, *Geografiska Annaler*, 65A, 99–110.

Appendix 1: Characteristics of the rockslide scars mapped along the main Rhone valley.

Nb.	Coor X	Coor Y	Evidence	Degree of evolution	Area (m^2)	Area deposit (m^2)	Exposed failure surface	Volume (m^3)	Morph. type	volume estimation	Lithology	Tectonic Unit	Connected to main valley	Failure mechanism	Valley side
1	576566	106735	Uncertain	Sub-cataclasmic	4.4E+06	1.1E+06	0.9	2E+08	2	smoothed surface int.	Gneiss	Mont Blanc massif	Yes	WS	left
2	570133	106714	Uncertain	Cataclasmic	2.1E+06	0.0E+00	0.7	4E+08	1	volumes SLBL inverse	Gneiss	Aiguilles Rouges massif	Yes	WS	left
3	570862	109470	Uncertain	Cataclasmic	2.5E+06	0.0E+00	0.7	4E+08	1	volumes SLBL inverse	Gneiss	Aiguilles Rouges massif	Yes	WS	right
4	571621	110948	Uncertain	Sub-cataclasmic	5.9E+05	3.4E+05	1.0	3E+07	2	smoothed surface int.	Gneiss	Aiguilles Rouges massif	Yes	WS	right
5	581615	110766	Proved	Sub-cataclasmic	9.9E+05	6.9E+05	0.9	5E+07	2	smoothed surface int.	Schist	Sion-Courmayeur zone	Yes	WS	left
6	577380	111883	Proved	Sub-cataclasmic	7.5E+04	4.7E+04	1.0	3E+06	2	smoothed surface int.	Gneiss	Aiguilles Rouges massif	Yes	WS	right
7	578313	112468	Uncertain	Sub-cataclasmic	6.8E+05	3.8E+05	0.8	1E+08	2	volumes SLBL inverse	Gneiss	Aiguilles Rouges massif	Yes	WS	right
8	579007	112846	Proved	Cataclasmic	1.0E+05	5.2E+04	0.8	5E+06	2	volumes SLBL inverse	Gneiss	Aiguilles Rouges massif	Yes	WS	right
9	569859	112828	uncertain	Cataclasmic	1.2E+06	5.9E+05	0.8	9E+07	2	Large fault control	Gneiss	Aguilles Rouges massif	Yes	WS	right
10	584839	113542	Proved	Sub-cataclasmic	1.2E+06	0.0E+00	0.9	2E+08	2	volumes SLBL inverse	Flysch	Sion-Courmayeur zone	Yes	WS	left
11	568669	116001	Uncertain	Sub-cataclasmic	9.6E+05	9.0E+05	0.9	3E+07	3	smoothed surface int.	Gneiss	Aguilles Rouges massif	Yes	WS	right
12	568119	116796	Uncertain	Cataclasmic	4.8E+05	2.8E+05	0.9	3E+07	3	smoothed surface int.	Limestone	Aguilles Rouges massif	Yes	PL	right
13	568552	118226	Uncertain	Cataclasmic	3.9E+05	0.0E+00	1.0	9E+06	1	smoothed surface int.	Limestone	Infrahelvetics Nappe	Yes	PL	right
14	569563	119439	Proved	Cataclasmic	1.6E+06	0.0E+00	1.0	2E+08	1	smoothed surface int.	Flysch	North-Helvetics Flysch	Yes	WS	right
15	602800	120598	Uncertain	Sub-cataclasmic	2.9E+06	1.6E+06	1.0	1E+08	2	smoothed surface int.	Quartzite	Siviez-Michabel Nappe	Yes	WS	left
16	605586	122304	Uncertain	Sub-cataclasmic	3.5E+06	2.1E+06	1.0	1E+08	2	smoothed surface int.	Quartzite	Siviez-Michabel Nappe	Yes	WS	left
17	637051	126326	Uncertain	Cataclasmic	3.4E+06	1.9E+06	0.9	2E+08	3	smoothed surface int.	Flysch	Monte Leone	Yes	WS	left
18	629120	126995	Proved	Cataclasmic	9.4E+05	2.5E+05	1.0	7E+07	2	smoothed surface int.	Flysch	Sion-Courmayeur zone	Yes	WS	left

19	625049	127996	Uncertain	Sub-cataclasmic	3.6E+05	2.0E+05	1.0	1E+07	3	smoothed surface int.	Flysch	Sion-Courmayeur zone	Yes	WS/PL	left
20	641346	127585	Uncertain	Sub-cataclasmic	3.1E+06	1.5E+06	1.0	5E+08	3	smoothed surface int.	Flysch	Sion-Courmayeur zone	Yes	Top/complex	left
21	629441	129625	Uncertain	Cataclasmic	6.5E+05	0.0E+00	1.0	2E+07	2	smoothed surface int.	Marly-Limestone	Parauthoctone Aar massif	Yes	PL	right
22	610098	130954	Proved	Cataclasmic	5.5E+06	0.0E+00	1.0	2E+09	2	volumes SLBL inverse	Marly-Limestone	Doldenhorn Nappe	Yes	PL	right
23	557247	132667	Proved	Cataclasmic	3.0E+05	0.0E+00	0.8	2E+07	2	smoothed surface int.	Marly-Limestone	Prealpes Medianes	Yes	Ws	left
24	647107	133656	Uncertain	Cataclasmic	9.8E+05	3.2E+06	0.9	7E+07	2	smoothed surface int.	Marly-Limestone	Zone de Termen	Yes	Top/complex	left
25	660339	144037	Proved	Sub-cataclasmic	8.3E+05	5.4E+05	0.9	3E+07	2	smoothed surface int.	Gneiss	Gotthard Massif	Yey	WS	left
26	671811	155285	Proved	Sub-cataclasmic	1.2E+06	7.3E+05	1.0	9E+07	1	smoothed surface int.	Gneiss	Goms Massif	Yes	WS	left
27	671103	155676	Proved	Sub-cataclasmic	3.2E+05	1.9E+05	0.9	2E+07	1	smoothed surface int.	Amphibolite	Aar massif	No	WS	right
28	565296	135269	Proved	Cataclasmic	4.8E+05	0.0E+00	1.0	1E+07	2	smoothed surface int.	Amphibolite	Prealpes Medianes	Yes	WS	right
29	558725	126576	Uncertain	Cataclasmic	1.0E+06	4.9E+05	0.9	5E+07	2	smoothed surface int.	Marly-Limestone	Prealpes Medianes rigides	Yes	Top/complex	left
30	628546	129152	Proved	Sub-cataclasmic	7.8E+04	7.0E+03	1.0	8E+05	2	smoothed surface int.	Marly-Limestone	Parauthoctone Aar massif	Yes	PL	right
31	597984	132512	Proved	Cataclasmic	4.3E+05	1.0E+00	1.0	6E+06	2	smoothed surface int.	Marly-Limestone	Wildhorn Nappe	No	WS/PL	right
32	664013	147449	Proved	Sub-cataclasmic	2.1E+06	1.4E+06	1.0	2E+07	2	smoothed surface int.	Gneiss	Gotthard Massif	Yes	Top/complex	left
33	562216	131968	Uncertain	Sub-cataclasmic	2.2E+05	1.7E+05	0.7	3E+07	2	smoothed surface int.	Limestone	Prealpes Medianes	Yes	Unknown	right
34	670285	155137	Uncertain	Sub-cataclasmic	9.6E+05	6.4E+05	1.0	3E+07	1	smoothed surface int.	Amphibolite	Aar massif	No	Top/complex	right
35	560578	135490	Uncertain	Cataclasmic	3.7E+04	0.0E+00	0.3	6E+05	2	smoothed surface int.	Marly-Limestone	Prealpes Medianes	Yes	Unknown	right
36	561253	133312	Uncertain	Cataclasmic	2.4E+04	1.2E+04	0.4	5E+06	2	smoothed surface int.	Limestone	Prealpes Medianes	Yes	WS	right
37	545518	139554	Proved	Cataclasmic	1.5E+05	0.0E+00	0.9	5E+06	2	smoothed surface int.	Marly-Limestone	Prealpes Medianes	Yes	PL	left
38	546584	139060	Proved	Cataclasmic	8.6E+05	0.0E+00	1.0	5E+07	2	smoothed surface int.	Marly-Limestone	Prealpes Medianes	Yes	PL	left

39	588906	116181	uncertain	Sub-cataclasmic	2.3E+05	1.1E+05	1.0	3E+06	2	smoothed surface int.	Schists	Zone Houlliere	Yes	Ws	left
40	589596	116438	uncertain	Sub-cataclasmic	2.8E+05	1.8E+05	0.9	5E+06	2	smoothed surface int.	Sandstone	Zone Houllire	Yes	Top/complex	left
41	616522	125528	uncertain	Cataclasmic	2.4E+06	6.9E+05	1.0	1E+08	2	smoothed surface int.	Quartzite	Siviez-Michabel Nappe	Yes	WS	left
42	583116	112283	Proved	Cataclasmic	4.7E+05	2.9E+05	0.5	3E+07	2	volumes SLBL inverse	Flysch	Sion-Courmayeur zone	Yes	WS	left
43	581884	115991	Proved	Cataclasmic	1.8E+05	0.0E+00	1.0	8E+06	2	smoothed surface int.	Marly-Limestone	Morcle Nappe	Yes	WS/PL	right
44	555926	135100	Proved	Sub-cataclasmic	3.2E+05	0.0E+00	0.9	2E+07	2	smoothed surface int.	Limestone	Prealpes Medianes	Yes	WS	left
45	568250	109810	Proved	Cataclasmic	1.1E+05	0.0E+00	1.0	2E+06	0	smoothed surface int.	Gneiss	Aguilles Rouges massif	Yes	Ws	left
46	568248	110000	uncertain	Cataclasmic	1.5E+04	0.0E+00	1.0	2E+05	2	smoothed surface int.	Gneiss	Aguilles Rouges massif	Yes	WS	left
47	563046	113215	Proved	Cataclasmic	1.4E+05	0.0E+00	1.0	2E+06	0	smoothed surface int.	Marly-Limestone	Morcle Nappe	Yes	WS	left
48	612460	124734	Proved	Cataclasmic	1.0E+05	0.0E+00	1.0	4E+06	0	smoothed surface int.	Quartzite	Siviez-Michabel Nappe	Yes	PL	left
49	586679	120498	Proved	Cataclasmic	3.3E+05	9.7E+04	1.0	6E+06	0	smoothed surface int.	Marly-Limestone	Wildhorn Nappe	Yes	PL	right
50	582696	128409	Proved	Cataclasmic	6.84E+05	0.0E+00	1.0	2E+06	0	smoothed surface int.	Marly-Limestone	Wildhorn Nappe	No	PL	right
51	587619	123051	Proved	Cataclasmic	1.0E+06	0.0E+00	1.0E+00	1.0E+08	0	smoothed surface int.	Marly-Limestone	Wildhorn Nappe	Yes	PL	right
52	628179	122524	uncertain	Cataclasmic	1.2E+06	0.0E+00	1.0E+00	9.6E+07	0	smoothed surface int.	Marly-Limestone	Aar massif	Yes	PL	right
53	556980	133454	uncertain	Cataclasmic	1.2E+05	0.0E+00	8.0E-01	1.8E+06	0	smoothed surface int.	Marly-Limestone	Prealpes Medianes	Yes	WS	left

4. DETAILED FAILURE MECHANISM ANALYSES OF ROCK INSTABILITIES: THE ROLE OF INHERITED BRITTLE AND DUCTILE STRUCTURES

This chapter contains two sub-chapters written in a paper format:

1) ***"STRUCTURAL ANALYSIS OF TURTLE MOUNTAIN; ORIGIN AND INFLUENCE OF FRACTURES IN THE DEVELOPMENT OF ROCK SLOPE FAILURES"***.

This paper has been published in *Slope Tectonics*, Special Publication of the Geological Society of London under the authorship: *Pedrazzini A., Jaboyedoff M., Faroese C.R, Langenberg W., Moreno F.* The first author and M. Jaboyedoff acquired, treated and analysed the data. All the authors contributed to discussing the results and finalizing the manuscript.

1) ***"FROM DEEP SEATED SLOPE DEFORMATION TO ROCK AVALANCHE: DESTABILISATION AND TRANSPORTATION MODELS OF THE SIERRE ROCK AVALANCHE (S-W SWITZERLAND)".***

This paper will be submitted to the "*Landslide*" journal under the authorship: *Pedrazzini, A. Jaboyedoff M., Derron M-H., Loye A.* The first author acquired, treated and analysed the data. All the authors contributed to discussing the results and finalizing the manuscript.

4.1 STRUCTURAL ANALYSIS OF TURTLE MOUNTAIN; ORIGIN AND INFLUENCE OF FRACTURES IN THE DEVELOPMENT OF ROCK SLOPE FAILURES

4.1.1 ABSTRACT

Large slope failures in fractured rocks are often controlled by the combination of pre-existing tectonic fracturing and brittle failure propagation in the intact rock mass during the pre–failure phase. This study focuses on the influence of fold-related fractures and of post-folding fractures on slope instabilities with emphasis on Turtle Mountain, located in South-western Alberta (Canada). The structural features of Turtle Mountain, especially in the South of the 1903 Frank Slide, were investigated using high resolution digital elevation model combined with a detailed field survey. These investigations allowed the identification of six main discontinuity sets influencing the slope instability and surface morphology. According to the different deformation phases affecting the area, the potential origin of the detected fractures was assessed. Three discontinuity sets are correlated with the folding phase and the others with post-folding movements. In order to characterize the rock mass quality in the different portions of the Turtle Mountain anticline, the Geological Strength Index (GSI) has been estimated. GSI results show a decrease in rock mass quality approaching the fold hinge area owing to higher fracture persistence and higher weathering. These observations allow us to propose a model for the potential failure mechanisms related to anticline structures.

4.1.2 RÉSUMÉ

Le développement des grandes instabilités rocheuses est souvent contrôlé par la présence de discontinuités tectoniques préexistantes et par une rupture progressive de la roche intacte. Cette étude se focalise sur l'identification de structures cassantes associées aux phases de plissement et sur leur influence sur la stabilité des compartiments rocheux présents sur la Montagne de la Tortue en Alberta (Alberta Canada). L'étude de ces structures a été menée à l'aide du modèle numérique de terrain à haute résolution ainsi que par des analyses de terrain. Six familles principales de discontinuités ont pu être identifiées et caractérisées. Sur la base de critères géométriques, le développement des différentes discontinuités détectées a pu être associé aux différentes phases tectoniques qui ont affecté la zone d'étude au cours du temps. Une analyse détaillée de la qualité du massif rocheux à l'aide du GSI (Geological Strength Index) a permis de mettre en évidence que les grandes structures tectoniques et les structures cassantes associées ne contrôlent pas seulement la géométrie des instabilités mais elles influencent aussi la localisation des zones où la dégradation progressive du massif rocheux est la plus importante. Sur la base des observations réalisées sur la Montagne de la Tortue, un model géométrique préliminaire liant les caractéristiques structurales des plis et les mécanismes de ruptures potentielles a pu être formulé.

4.1.3 INTRODUCTION

The influence of structural features on the development of large rock slope instabilities has been investigated in several previous studies (Agliardi et al., 2001; Ambrosi and Crosta, 2006; Brideau et al., 2009; Jaboyedoff et al., 2009). These authors emphasized the role of pre-existing fractures for the initiation of the large rock slope instabilities. Brideau et al. (2009) discussed the origin and the influence of rock mass damage and their roles in the development of instabilities and highlight the importance of tectonic structures, not only on the 3D geometry, but also for the reduction of rock mass strength caused by induced damage. The damage is physically represented by weak zones in the rock mass, forming microcracks, mylonitic layers or void areas (Brideau et al., 2009).

Turtle Mountain is located close to the Crowsnest Pass in South-western Alberta, approximately 5 km South of Blairmore (Figure 4.1-1). This area became famous 1903 after the destruction of the village of Frank by Frank Slide rock avalanche destroyed. McConnell and Brock (1903) described the event as a rock slide and Cruden and Krahn (1973) re-examined the origin and the failure mechanisms and interpreted the Frank Slide as a rock avalanche. In the last few years, the southern part of Turtle Mountain (Third Peak and South Peak areas) has become an important field laboratory where different techniques related to the characterization and monitoring of large slope mass movements are tested (Moreno and Froese, 2007, Froese et al., 2009a). Moreover, a potential rockslide hazard has recently been re-emphasized in the South Peak area (Read et al., 2000).

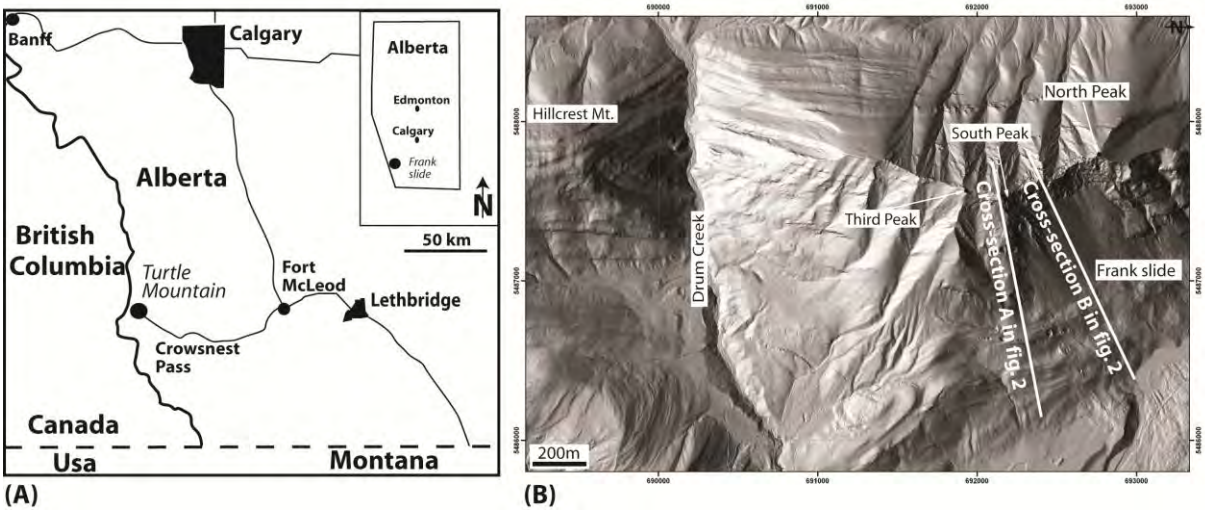

Figure 4.1-1: (A) Location of the Turtle mountain area. (B) Airborne LiDAR view of Turtle Mountain between North Peak and Hillcrest Mountain with the location of the geological cross section presented in Figure 4.1-2.

The structural and the geological settings in South Peak area were first studied in detail by Allan (1933). His work set the foundations for the present interpretation of the structure of the Frank Slide and South Peak area provided by Cruden and Krahn (1973). Langenberg et al. (2007) carried out a more detailed structural and geological investigation and Cruden and Martin (2007) analysed the situation and the predisposing factors before the 1903 event. Others researchers have undertaken more specific analyses of the joint sets based on field survey (Couture, 1998), as well as borehole logging analysis and ground penetrating radar (GPR) (Spratt and Lamb, 2005) in the South Peak area. Recent studies (Froese et al., 2009a; Jaboyedoff et al., 2009; Sturzenegger et al, 2007; Sturzenegger and Stead, 2009) provide a

structural analysis based on remote sensing datasets such as airborne laser scanning (ALS), terrestrial laser scanning (TLS) and the derived digital elevation model (DEM).

In this article, we first describe the structural characteristics of Turtle Mountain, and then we attempt to define the origin of the different detected discontinuity sets. Based on these data, we examine the influence of fold-induced joints on the three dimensional kinematic release of rock slope instability and their influences on the increase of rock mass damage near the fold hinge area.

4.1.4 GEOLOGY AND GEOMORPHOLOGY

Turtle Mountain lithologies range in age from Devonian to Cretaceous (Norris, 1993). The upper part of Turtle Mountain is composed of a fine to coarse-grained, sparitic limestone. This important lithological unit is called the Livingstone Formation (Visean) and was the main unit involved in the 1903 event. The Palliser Formation constitutes the central part of the mountain and consists of fractured dolomitic limestone. The Banff Formation is transitional between the Livingstone and Palliser formations and consists of shale, sandstone and cherty, argillaceous limestone. Outcrops belonging to the Mount Head Formation are present in particular in the western flank of the mountain and above the Turtle Mountain thrust (Langenberg et al., 2007). This formation is composed of an intercalation of coarse grained sparitic limestone and fine-grained silty-dolomitic layers. Below the Turtle Mountain thrust, three Mesozoic geological units could be identified: the Fernie Formation, the Kootenay group and the Blairmore group. Fernie Formation is mainly composed by shale and silty shale and the Kootenay group is composed by shale and siltstone and contains the coal bearing strata. The Blairmore group is composed of different detritic lithologies, especially sandstone and conglomerate.

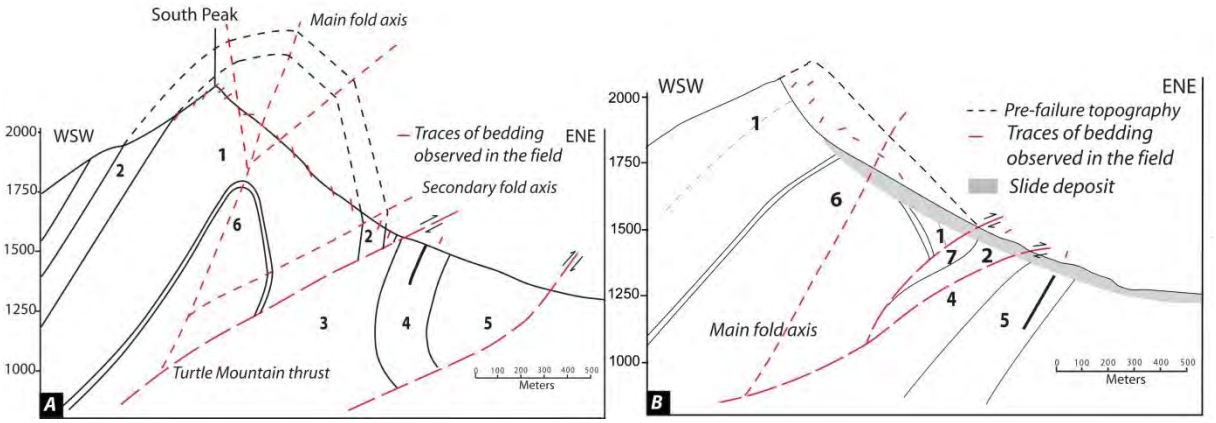

Figure 4.1-2: Cross-sections through Turtle Mountain area. (A) Cross-section under South Peak area. (B) Cross-section through the Frank slide scar. Lithological units: 1) Livingstone formation, 2) Mt. Head formation, 3) Fernie Formation, 4) Kootenay group, 5) Blairmore group, 6) Banff and Palliser formation.

The main structure in the area is the Turtle Mountain anticline (Figure 4.1-2). This fold can be described as a modified fault-propagation fold (Langenberg et al., 2007). In the North Peak area, the Turtle Mountain fold is cut by the thrust and only the western limb of the anticline remains. As the anticline has an asymmetrical shape plunging mainly to the West, the fold shape is not a perfectly cylindrical. In the field, its axis is difficult to follow due to the important fracturing of the hinge area and that is why, in two different zones, the fold axis has been deduced from the orientation of bedding planes (Figure 4.1-3). According to Ramsey and Huber (1987), the fold is assumed to be at least locally cylindrical in order to

reconstruct its axis orientation using the Π-diagram method. From Drum Creek to Third Peak area, the axis plunges gently toward the South (3° toward 181° in Drum Creek and 13° toward 193° in Third Peak area) but in the South Peak area, it changes and plunges gently toward North (2° toward 024°) (Langenberg et al., 2007). The fold axis trend also varies: in Drum Creek area the trend direction is mainly N-S, whereas in the North it is predominantly oriented NW-SE. This observation is also supported by the large scale view observed in the 1:50'000 geological map (Norris, 1993).

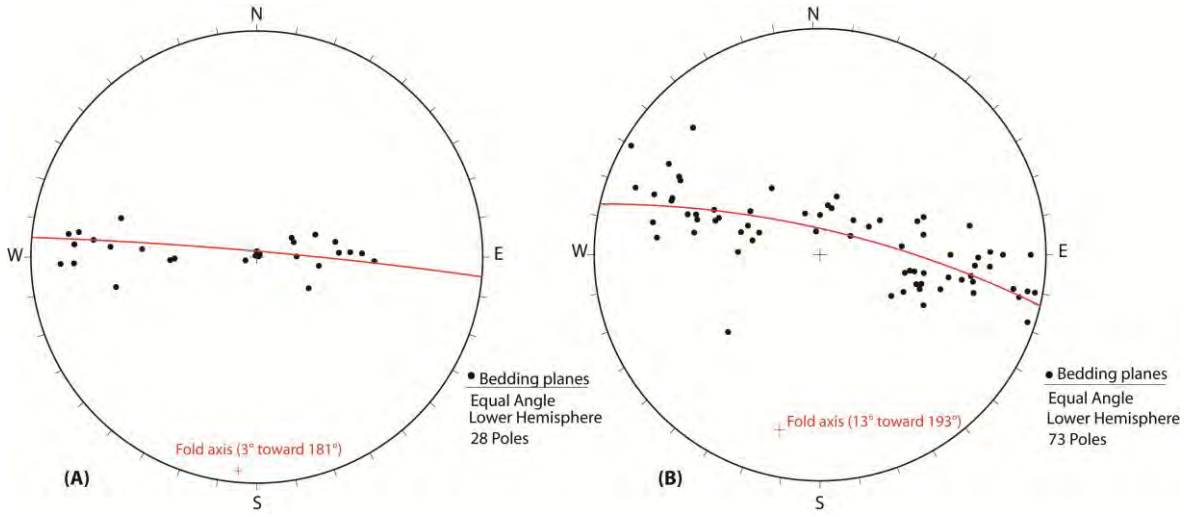

Figure 4.1-3: Determination of the fold axis orientation using the Π-diagrams method (from Ramsay and Huber, 1987). A) Results obtained for Drum Creek area, B) Results obtained for Third Peak area.

4.1.5 METHODS

In this study, classical method of geological field survey, (manual compass measurement of structures), is combined with semi-automated extraction of large scale structures by means of a High Resolution DEM (HRDEM). The main advantage of using the HRDEM is that the time spent in the field survey could be substantially reduced and investigations could be concentrated in the most representative areas. The structural analysis was performed in two separate areas corresponding to the two fold limbs (eastern and western fold limb). Using this approach, structural features related to the two fold limbs could be differentiated.

4.1.5.1 DEM analysis

Topographic analyses were performed using the software COLTOP 3D (Jaboyedoff et al., 2009; Derron et al., 2005; Jaboyedoff and Couture, 2003). This software allows the representation of a DEM by a 3D shaded relief that displays the orientation of the slopes by means of a Schmidt – Lambert projection with one colour for a given dip and dip direction. It results a coloured shaded relief map that combines slope and slope aspect in a unique representation where the slope orientation is coded by the Hue-Saturation-Intensity system (HSI).

4.1.5.2 Field survey

The results of previous scanlines in the South Peak area (Langenberg et al., 2007; Spratt and Lamb, 2005) were verified and completed. The field survey was performed in the Southern part of Turtle Mountain (between Third Peak and South Peak area) where 25 structural stations have been performed. In addition,

20 structural stations were established in Drum Creek-Hillcrest Mountain area. These were situated in an area where no rock instabilities or gravitational movements have been detected, in order to minimize the potential influence of the Frank Slide movements on the identification of the initial fracturing. For each station, we measured the characteristics of the joint sets and described the rock mass condition following the methodology suggested by the ISRM (1978).

4.1.5.3 Geological Strength Index

In order to provide an objective estimation of the rock mass quality, the geological strength index (GSI) (Hoek and Brown, 1997; Marinos et al., 2005) has been used. The GSI value is estimated taking into account the structural conditions (number of discontinuities, block geometry, persistent foliation) and the surface conditions (weathering, fracture infilling and roughness). As suggested by previous authors (Marinos et al., 2005), we used ranges of +/- 5 for the GSI estimation, in order to take into account the possible natural variations in the rock mass. The GSI estimation has been applied in 52 locations distributed in different parts of the anticline (Third Peak, South Peak Drum creek and Hillcrest Mountain). Even though the GSI is considered as a qualitative estimator of the rock mass quality based on geological observations, an attempt to quantify the GSI classification have been recently proposed (Cai et al., 2004; Cai et al., 2006). In this stud, we employed the GSI chart proposed by Cai et al. (2004) that taking in account the block volume and the discontinuity spacing to describe the decreasing the interlocking of rock pieces and the joint condition factor to characterize the surface quality. However, like suggested by Marinos et al. (2005), the GSI quantification has to be applied with caution and the visual observations and geological considerations still remains the best approaches. Each GSI value estimated in field have been considered as the mean values for outcrop having an extension of 50-100 m^2.

4.1.6 RESULTS

4.1.6.1 Characteristics of the fold hinge area

The Turtle Mountain anticline is characterized by a disturbed hinge area (Figure 4.1-4a). The general trend of the hinge could only be defined by distant observations and it is difficult to follow clearly the bedding planes and the progressive transition from normal to inverted limb, especially close to the hinge. In addition, some local limb thrusts (Figure 4.1-4a) along bedding planes close to the hinge area are suspected (Ramsey and Huber, 1987). The inverted limb shows steeper slope than the normal limb. Close to the hinge area, field survey indicates the presence of at least four discontinuity sets having frequently close spacing and a medium to high persistence (ISRM, 1978). Important local variations of spacing and persistence along the hinge zone are also recognizable. The fracturing is principally caused by compressive stress during the folding phase and by the presence of rock with different elastic characteristics (massive limestone vs silty-dolomite) in the stratigraphic sequence (Ramsey and Huber, 1987). These differences in the mechanical behaviour also affect the general morphology of the mountain. Silty-dolomite layers belonging to the Mount Head Formation are generally more eroded and form significant depressions in both fold limbs whereas positive relief is created by competent limestone beds. Dissolution phenomena are also abundant in the hinge area in coarse-grained limestone (Livingstone and Mount Head Formation) as the numerous cavities and heavy weathered zones show (Figure 4.1-4).

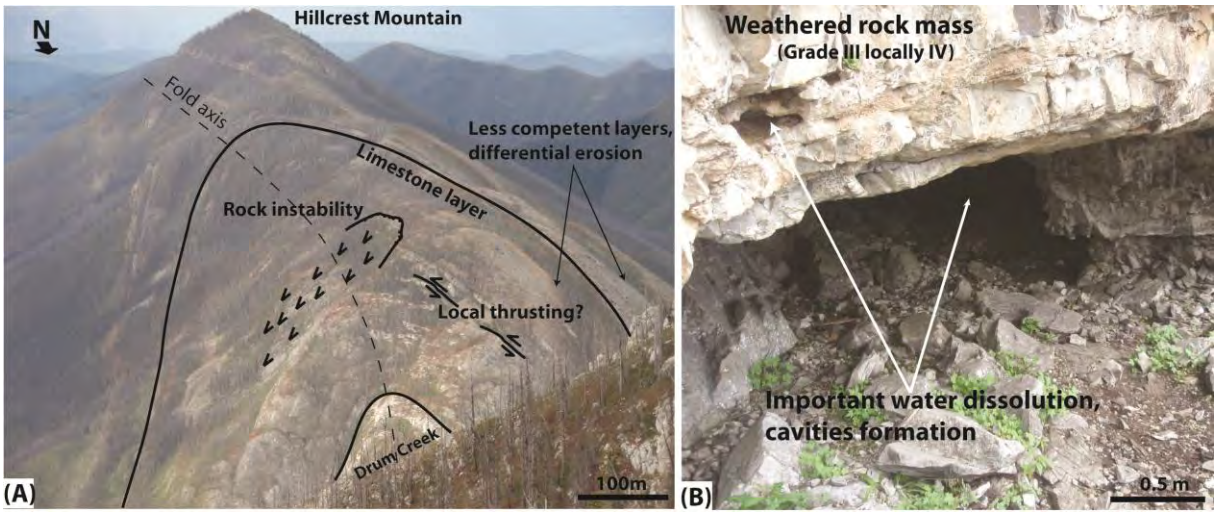

Figure 4.1-4: a) View of the Turtle Mountain anticline (Drum Creek area). The picture shows the asymmetric form of the Turtle Mountain anticline and the local uniformity in the anticline structure due to local thrusting. Differential erosion of less competent layers gives an important morphological signature. Evidences of rock instabilities located close to the hinge area are visible in eastern mountain flank. b) Example of rock weathering (Grade III-IV) and dissolution phenomena of limestone belonging to the Livingstone formation in Hillcrest area.

4.1.6.2 Main lineaments

The main lineaments extracted from the DEM and orthophotos (283 observations) were entered in a database and represented in rose diagrams (5° interval). Turtle Mountain was divided in five sectors with the same lineaments trend (Figure 4.1-5). These lineaments are expressions of dipping planes and represent apparent their strikes. These planes correspond on the field either to composite tension cracks, trenches, scarps or transfer faults (following two or more tectonic joint sets) or to gravitational fractures following a predominant tectonic joint set. In all of the five areas, a major lineament orientation NW-SE can be identified, whereas in the southern part, the trend is mainly NNW-SSE and changes progressively in the northern area to a WNW-ESE orientation. In the crest area, more particularly in the northern portion of Turtle Mountain, another predominant direction N-S is clearly defined.

4.1.6.3 Fractures in eastern fold limb

The slope morphology in the eastern limb of the anticline is mainly controlled by the orientation of the bedding planes, particularly those situated under Third Peak. Due to the thick vegetation cover and extensive deposits of rock fall debris, it is difficult to identify structures in portions of this area. In this case, the structural analysis using DEM became inefficient. Nevertheless, five main orientations were detected using COLTOP 3D between Drum creek and South Peak (Figure 4.1-6a).

In the lower Third Peak area, field measurements are difficult and often not representative of the discontinuity sets due to local fracture systems, toppled blocks, exfoliation and physical weathering (freeze and thaw cycles). Exfoliation and related weathering (that could reach locally grade IV) are much more developed in the dolimitic-siltstone of the Salter/Baril/Wileman member of the Mount Head Formation. In these rocks, exfoliation creates very to extremely close spaced discontinuities parallels to the general outcrop orientation. Freeze and thaw cycles cause the joint to enlarge, especially the close spaced exfoliation joints, and increase the rock mass fragmentation (Matsuoka, 2008). These effects are

evident at the outcrop scale and affect the first 2-3 meters of the rock mass. The typical block has columnar shape with a volume between 100 and 500 cm^3.

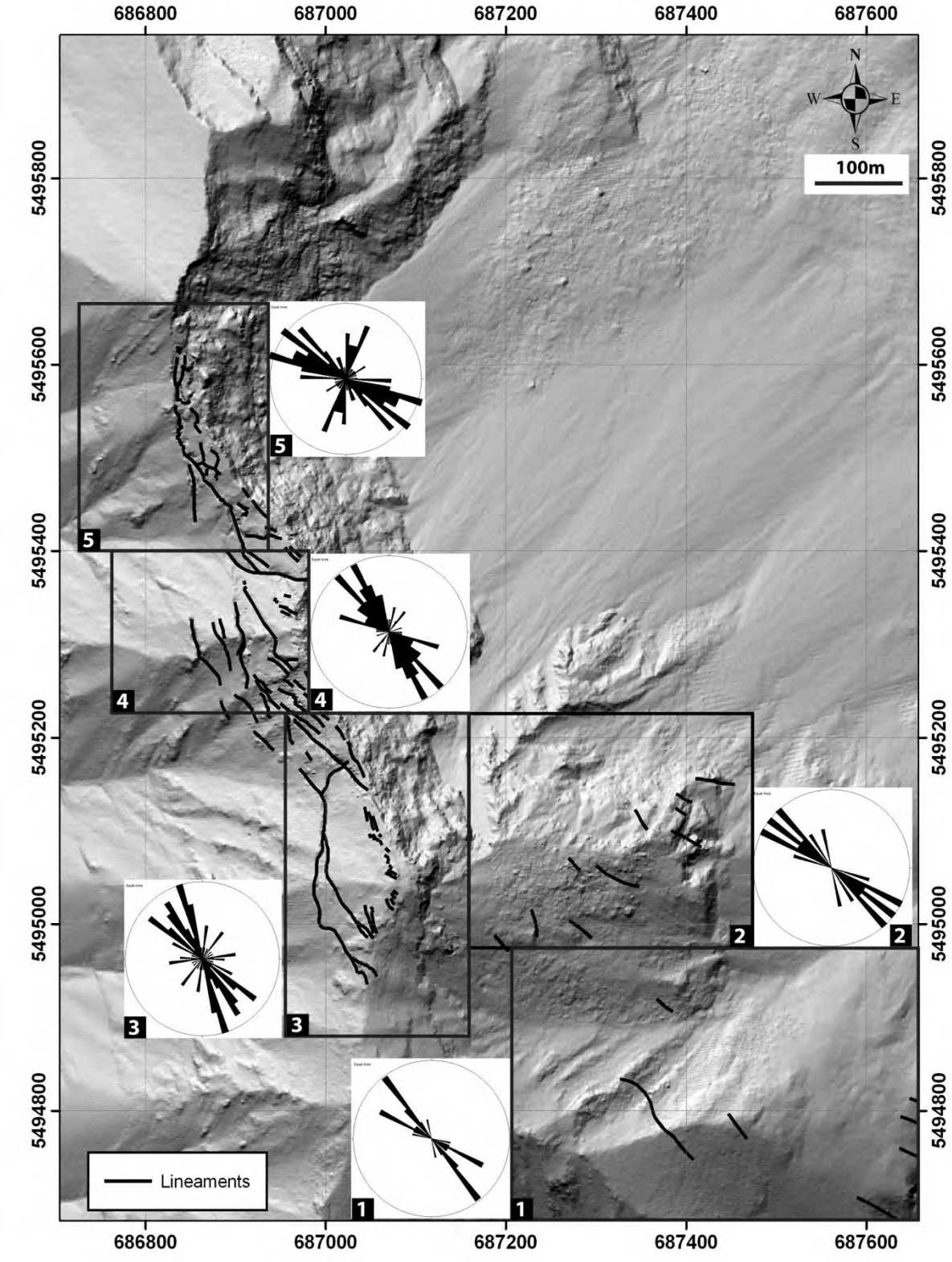

Figure 4.1-5: Main lineaments detected in different structural zones between North Peak and Third Peak.

Another factor is the occurrence of sedimentary anisotropy in the Livingstone formation, such as cross-bed structures, that influence the measurements at local scale. Field surveys show the same trend as the DEM analysis (Figure 4.1-6b), but with a greater dispersion. The majority of discontinuity sets are oriented toward East and J4 (215°/45°) and S0 (100°/55°) have been clearly identified in the two studies. Concerning discontinuity sets J1 (020°/45°) and J2 (060°/55°), field data show an important variation especially in dip angle. J3 is not visible on the outcrops but only locally on the DEM.

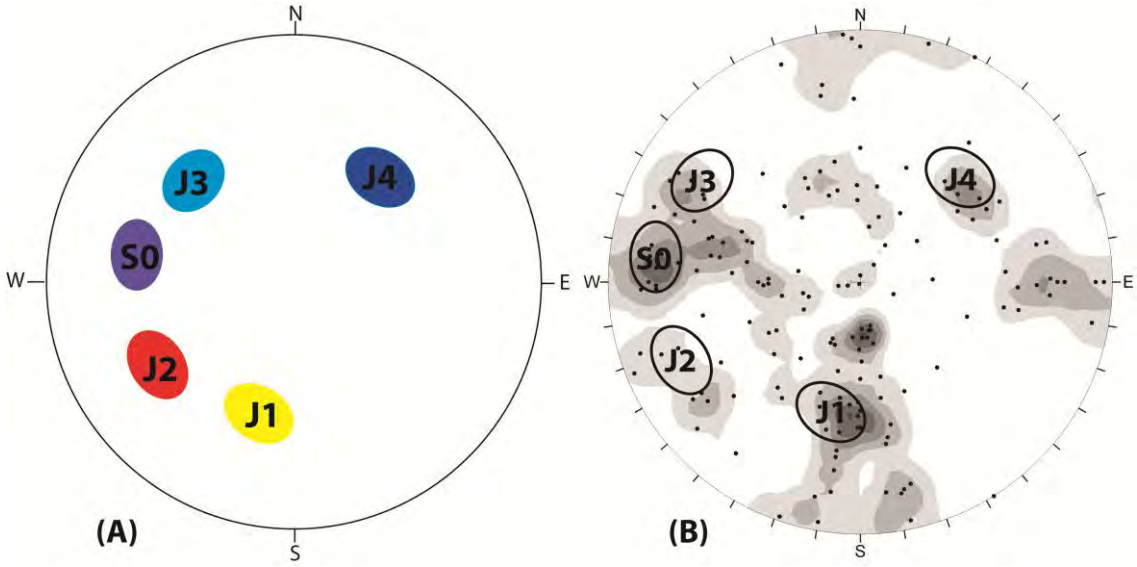

Figure 4.1-6: Comparison between the discontinuity sets detected using the Coltop3D software (A) and field survey (B) for the eastern fold limb, (Equal area, lower hemisphere projection).

Mean values of persistence, spacing and primary and secondary roughness were measured on different structural stations following the ISRM (1978) suggestions (Table 4.1-1). Important variations in discontinuity characteristics have been observed in the different structural stations. During the field survey, no important water flows were observed along discontinuity sets and the seepage rating for unfilled discontinuities could be described by classes II and III rarely IV (ISRM, 1978). However, due to the karstic hydrological system of the area, important water flow could be locally expected during important rainfall or during the snow melting period. The most important characteristics visible in almost all outcrops are the presence of at least four different discontinuity sets, the medium to high persistence of J1 set and the significant variation on the bedding thickness.

Table 4.1-1: Summary of general discontinuity sets characteristics of the eastern fold limb based on field and DEM analysis. Spacing and persistence values in brackets could show important local variations.

Name (color/variation)	***Dip direction***	***Dip***	***Persistence /spacing(m)***	***Primary roughness***	***Secondary roughness***
J1 (yellow, +/-10°)	*20*	*45*	*Medium to high persistence/1-2*	*Long wave undulation*	*Roug (dominant) Smooth (subordinate)*
J2 (red,+/-10°)	*60*	*55*	*Low to medium persistence/0.3-1*	*Planar*	*Rough*
S0 (violet, +/-10°)	*100*	*55*	*High persistance/0.1-3*	*Long wave undulation (folded)*	*Rough (dominant) Slickensided (local)*
J3 (light blue, +/-10°)	*135*	*50*	*Low persistence/(0.5-2)*	*Planar*	*Smooth*
J4 (dark blue, +/-10°)	*215*	*45*	*Low persistence/(0.5-1)*	*Sub-planar*	*Rough*

4.1.6.4 Fractures in western fold limb

The inclination and the position of the fold axis allow the outcropping of the western fold limb of the anticline, both in the upper eastern face (Frank Slide scar) and in the western face of the Turtle Mountain. As suggested by Cruden and Krahn (1973), on the western face of the Turtle Mountain the morphology is clearly influenced by the bedding orientation. Using the analysis performed by COLTOP 3D (Figure 4.1-7a), the bedding plane fractures are visible in the western face and their orientations correspond principally to 270°/45°. However in the South Peak area, the bedding orientation changes according to the evolution of the fold axis. In this zone, the orientation of J6 set (325°/45°) corresponds to a different discontinuity set parallel to the bedding, which that could not be related to the bedding orientation elsewhere (Langenberg et al., 2007). In fact, in the North Peak area the bedding is mainly parallel to J5-S0 (270°/45°) discontinuity set. Two others discontinuities are well-developed on the West side of the mountain: J4 (210°/50°) and J5-S0. These are likely encountered in the eastern face as well, but they do not influence the slope morphology and cannot be detected using an airborne LiDAR dataset. The upper eastern face is dominated by the Frank Slide scar, which is controlled by three main orientations: J1 (020°/45°), J2 (055°/65°) and J3 (115°/50°). Set J3 and J4 show a fair amount of variation in dip and in dip direction (Figure 4.1-7b). The mean characteristics of the different discontinuity sets derived from the compilation of all structural station are listed in Table 4.1-2.

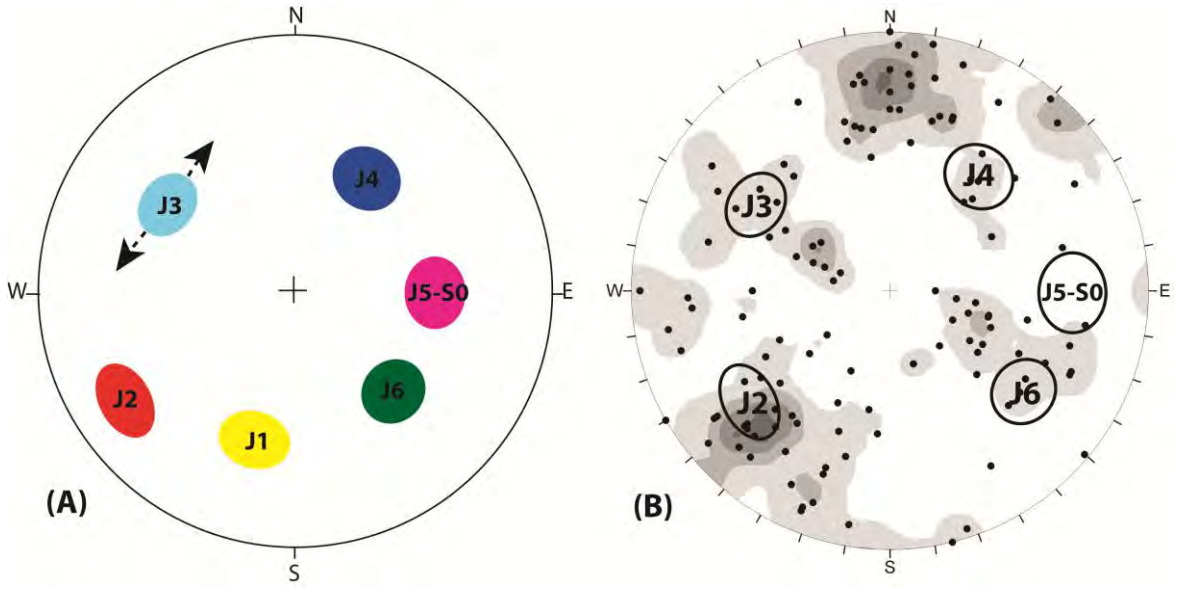

Figure 4.1-7: Comparison between the discontinuity sets detected using the Coltop3D software (A) and field survey (B) for the western fold limb, (Equal area, lower hemisphere projection).

Between the Frank Slide scar and South Peak, discontinuity sets J3, J6 and J2 show higher to very-high persistence values (Sturzenegger and Stead, 2009), which differ to the mean values reported in Table 2. This is probably related to the large gravitational movements that occurred before and during the 1903's event. In fact, J2 and J3 have been actively involved in the progressive failure of the upper part of the Turtle Mountain (Jaboyedoff et al., 2009). Discontinuity set J1 is the dominant set in lower South Peak area (both in eastern and western fold limb) and also in the scar are of the 1903's slide where it shows

medium-to-very high persistence. In South Peak crown area, field measurements indicate that J1 set is less frequent and show a lower persistence.

Table 4.1-2: Summary of general discontinuity sets characteristics of the western fold limb based on field and DEM analysis. Spacing and persistence values in brackets could show important local variations.

Name (color/variation)	***Dip direction***	***Dip***	***Persistence /spacing(m) (m)***	***Primary roughness***	***Secondary roughness***
J1 (yellow, +/-10°)	*20*	*45*	*Medium to high persistence/(1-2)*	*Long wave undulation*	*Rough (dominant) Smooth(subordinate)*
J2 (red, +/-10°)	*55*	*65*	*Low to medium persistence/(0.1-0.5)*	*Planar*	*Rough*
J3(light blue, +/-15°)	*115*	*55*	*Medium persistence/(0.5-2)*	*Stepped*	*Rough*
J4 (dark blue, +/-15°)	*210*	*50*	*Low persistence/(0.5-1)*	*Planar*	*Rough*
J5-S0 (violet, +/-10°)	*270*	*45*	*High persistence/(0.5-1)*	*Planar*	*Rough(dominant) Slickensided(local)*
J6 (green,+/-10°)	*325*	*45*	*Low persistence/(0.2-1)*	*Long wave undulation*	*Rough*

Primary and secondary roughness of discontinuity seem to be quite constant along the different structural stations and could be defined as undulating (subordinate planar) for intermediate scale and rough (only locally smoothed or slikensided) for small scale observations. It is important to note that only few structural stations (located in the Frank Slide scar area) record some slickenside on bedding planes (pitch 35° W), which differ to first observations on Turtle Mountain (Cruden and Krahn, 1973) but it is in agreement with more recent studies (Langenberg et al. 2007). Like suggested by Langenberg et al. (2007), slickensides are mainly localized along steep faults orientated N-S or NW-SE. Like in the eastern fold limb no important water flows were observed along discontinuity sets. Infilling material of joint sets are often absent especially for discontinuity sets J1 and J5. However, under South Peak area, J1 fractures are unfilled or partially filled by frictional material (rock debris, coarse sand) indicating previous movements. Concerning discontinuity sets J2, J3 and J4, infilling is mainly composed by calcite mineralization. Locally, approaching the hinge area, karstification process progressively increases, especially along joint walls. It is also possible to observe the formation of calcite concretions. Infilling material along karstified joints is often absent or composed by residual insoluble material (iron deposit, clay).

4.1.6.5 Rock mass conditions

In Turtle Mountain, the rock mass conditions are changing depending on local geological conditions (lithology, fracturation) and the location of the outcrops related to the anticline geometry. Figure 4.1-8 shows the location of the different GSI estimates along the Turtle Mountain anticline. Silty-dolomite outcrops of the Mount Head Formation generally show a more important grade of weathering (generally between II and IV) and a closer spacing (close to extremely close) of bedding planes than limestone belonging to the Livingstone Formation. The typical GSI values for the Silty-dolomite (estimated in the eastern fold limb only) range between 35 and 45.

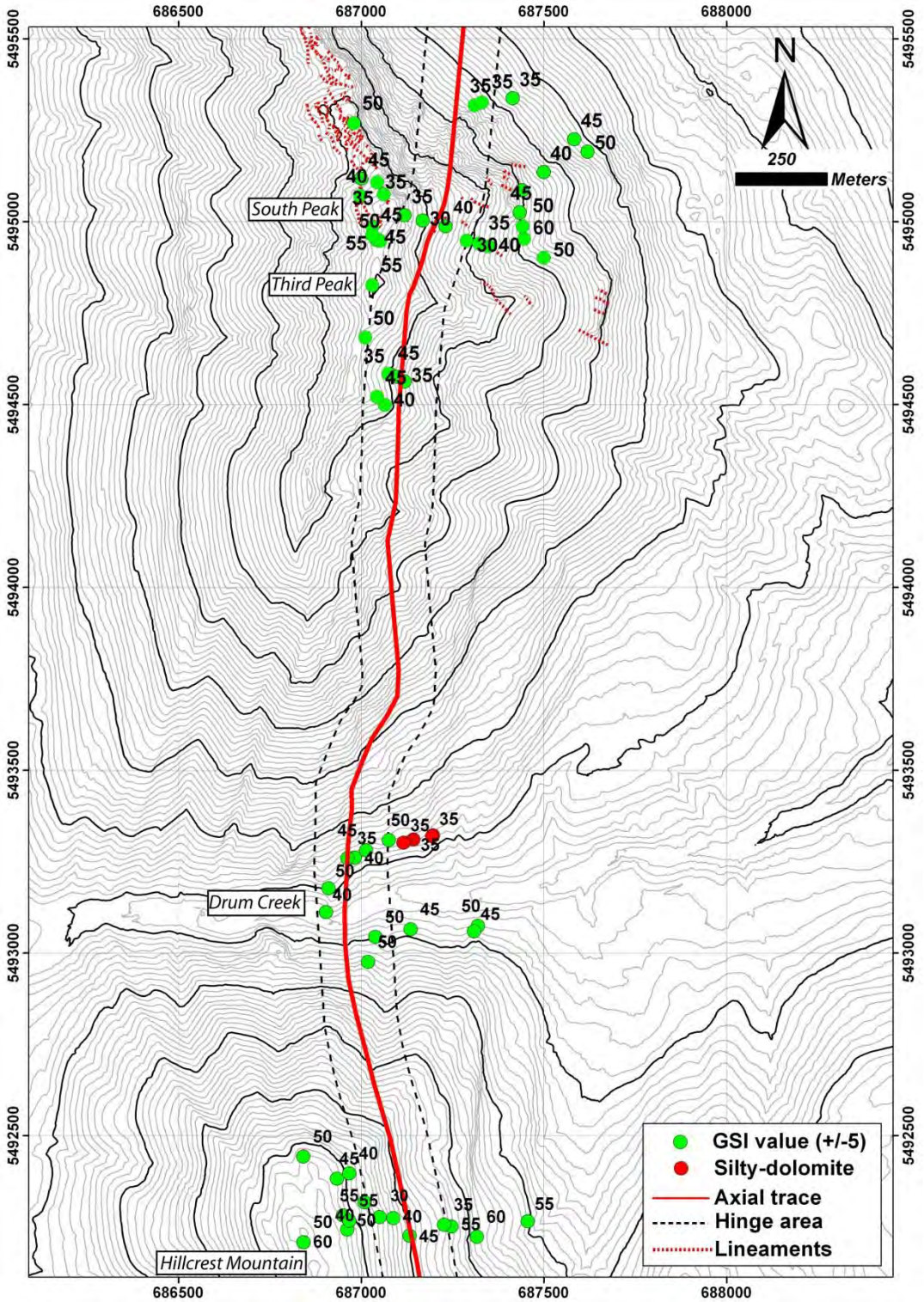

Figure 4.1-8: Rock mass characterization using GSI estimate: location of the structural stations where GSI values were estimate (red point correspond to silty-dolomite outcrops).

Figure 4.1-9 shows the histogram of GSI estimate obtained for the western and the eastern fold limbs and for the hinge area of the Turtle mountain anticline. Along the two fold limbs, limestone outcrops belonging to the Livingstone formation show local important variation on the rock mass quality. These variations are often related to the granulometry, to the presence of sedimentary anisotropy (mainly cross-bedding) and to precedent gravitational movements. Fine-grained limestone shows normally higher GSI values than

coarse-grained, well graded limestone. This difference concerns the surface conditions and the joint condition factor (J_c) and it is probably linked to the important porosity of coarse-grained limestone allowing a faster water infiltration and increasing the surface dissolution. Block shape and size were observed to be also locally influenced by large gravitational structures (tension cracks, reactivated joints), as a consequence the general rock mass conditions are also reduced. A clear example is represented by outcrops located between South Peak and North Peak. In this area especially close to the large crack the mean block volume is often smaller compared to outcrops where gravitational movements are less important. Approaching the hinge area both limestone lithologies shows a decreasing tendency in the GSI values. Common values for this zone range between 30-40 to 45-55.

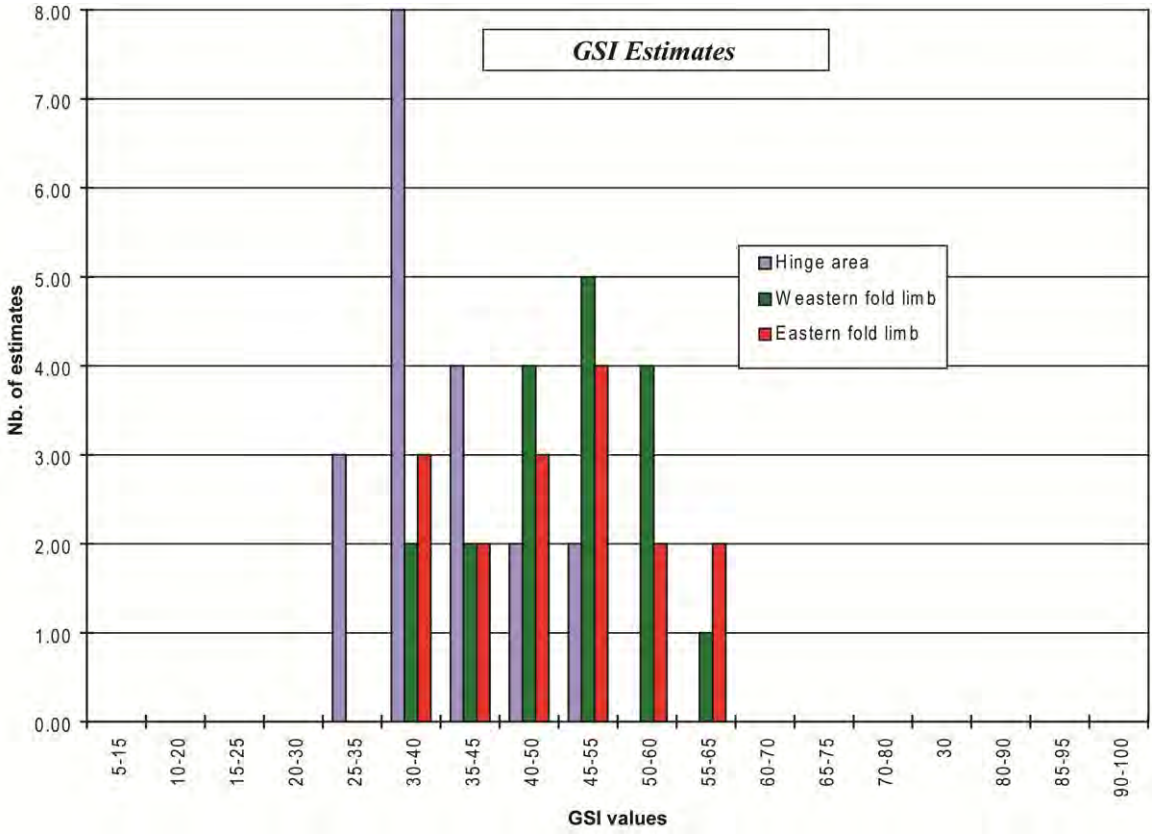

Figure 4.1-9: : Histogram of the GSI estimates obtained in the Hillcrest –South Peak area divided in three categories based on the structural location (only limestone lithology have been used).

In Figure 4.1-10, some examples of rock mass conditions for different outcrops in Turtle Mountain are reported. The potential extension of the hinge area was chosen according to previous works (Baillifard et al., 2003) indicating that large scale structures, like fault or thrust, induce local perturbations in the fracturing density and in the underground water flow, within 75-100 meters from each side of the structural feature. For these reasons, GSI stations within this distance have been used to create the histogram representing the characteristics values for the hinge area.

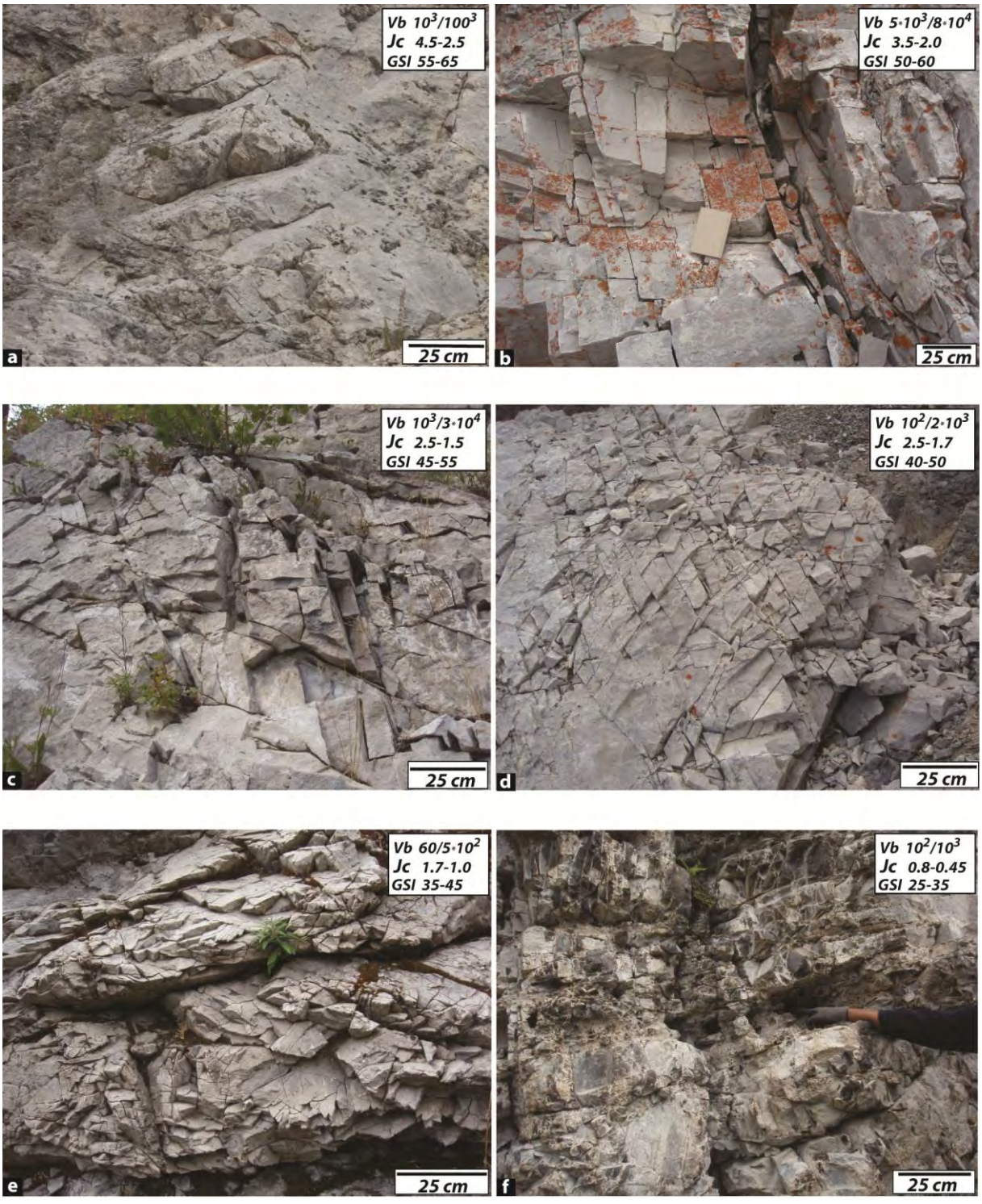

Figure 4.1-10: Examples of rock mass characteristics of different outcrops across Turtle Mountain. Each outcrop has been is described using the parameters proposed by Cai et al. (2004). For each outcrops coordinate are given in NAD 1983 UTM zone 32. a) 687440/5494953 b) 687027/5494964 c) 687441/5494984 d) 687029/5494987 e) 687137/5493067 f) 687046/5492282.

4.1.6.6 Rock instabilities

Several past and present-day instabilities involving limited volumes (generally <100,000 m^3) are observed along the hinge zone of Turtle Mountain anticline. Similar processes involving fold-related joint sets in the slope failure have been investigated in Rocky Mountain by different previous authors (Badger, 2002, Jackson, 2002, Jones, 1993). Field observations of the ancient scars show that an intense fracturing related

to the hinge area would limited instabilities to relatively small volumes. Depending on the structural position on the anticline, different instability mechanisms could be observed:

- Sliding/Toppling (on extensional fracture J3) and wedge failures (essentially J2^J4), affecting the western limb of the anticline but only in the eastern flank of the mountain. Toppling on bedding planes is kinematically possible but it was not observed during field survey.
- Step-like planar failure occurs along the bedding planes in the fold hinge zone. The prone areas for this mechanism are limited and concentrated where the bedding is parallel to the main topography (dip-slope).

In the upper part of Third Peak area, large gravitational movements, such as toppling or wedge failures, are not kinematically feasible due to rapid changes in the bedding orientation and the relative small fold interlimb angle. Potential shallow instabilities related to the hinge zone are evident below the Third Peak. Presently, the main unstable zone characterized with continued displacement, open gravitational cracks and rock fall activities is limited to the South Peak area (Moreno and Froese, 2007).

4.1.7 ORIGIN OF DETECTED DISCONTINUITIES

In order to understand the possible origin of detected discontinuity sets, the main tectonic phases affecting the studied area are reported below (Cooper, 1992; Price and Carmichel, 1986):

- Folding and thrusting phase, mainly E-W (Late Jurassic-Early Cretaceous).
- Right-lateral transpression phase, mainly NE-SW (Late Cretaceous-Paleocene).
- Left-lateral extension phase, mainly NW-SE (Early and Middle Miocene) and stress release during unloading between Early Miocene and present.

In addition to the chronological distinctions, it is possible to have the superposition of joints related to regional structural trends or to an individual geological structure. Currie and Reik (1977) showed that in the Rockies foothills it is possible to have the formation of fracture systems due to the local structural conditions (folds, faults) in addition to the regional trending fractures imposed by the large tectonic structure (anticlines, synclines, thrusts). The compilation of the data obtained by use of COLTOP3D and those measured in the field shows that four discontinuity sets (J1, J2, J3 and J4) appear in both limbs of Turtle Mountain anticline. J6 and J5-S0 are only visible in the western fold limb. No discontinuity sets are folded, meaning that no pre-folding discontinuity sets appear to be identifiable in this area. Several previous studies (Price and Carmichael, 1986; Cooper, 1992; Stearns, 1968) showed that the main fracturing can be related to the folding and thrusting. The development of fold-induced fractures depends on rheological conditions during the folding phase such as strain rate and temperature (Price and Cosgrove, 1990). In addition, local heterogeneities in the rock composition could induce fractures in different orientations than the main folding-induced fractures.

In order to understand their possible origins, we compare the orientation of discontinuity sets observed in the two fold limbs to the classical relationship between fold and fractures proposed by Cooper (1992) for the Alberta foothills. The results concerning the western fold limb, are presented in Figure 4.1-11 a. It is possible to identify some similarities between the conceptual model proposed by Cooper (1992) and the DEM or field measurements, where we can observe that three joint orientations (J2, J3, and J4) are often related to fracturing during the folding phase (Figure 4.1-11b). J3 could be interpreted as an extensional

joint sub-parallel to the fold axis and J2 and J4 could be interpreted as strike-slip conjugate faults with an acute bisectrix perpendicular to the fold axis (Muecke and Charlesworth, 1966).

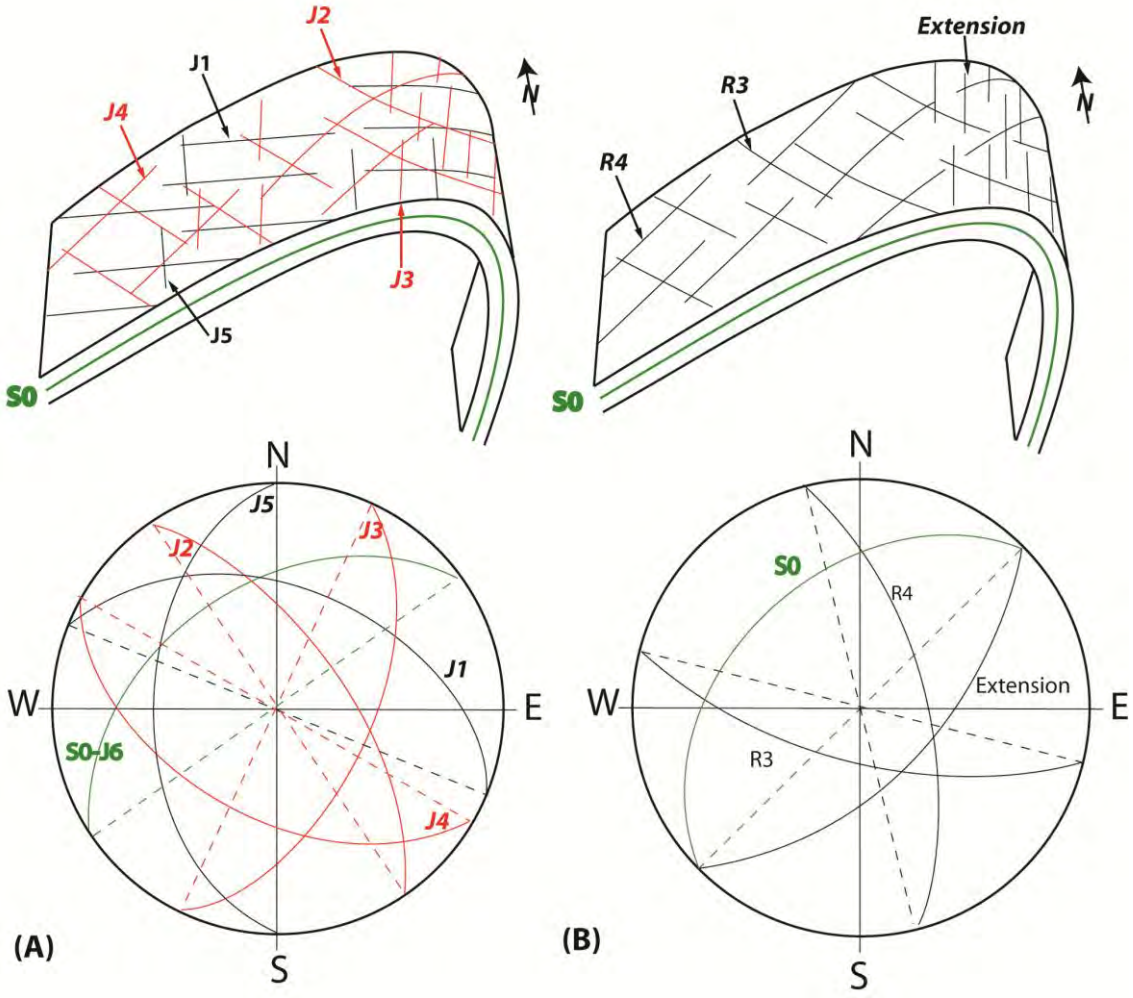

Figure 4.1-11: Comparison between the relationship of fold and fractures observed in the western Turtle Mountain anticline (A) and the general model (B) proposed by Cooper (1992).

In the western fold limb the strike-slip conjugate faults are only developed at a local scale; often only one of the two joint sets could be identified and this set tends to be sub-perpendicular to the fold axis. J5 and J1 are difficult to interpret using the fracturing models from Stearns (1963) or Cooper (1992). Concerning the eastern fold limb, a simple interpretation is more difficult to obtain due to the low rock mass quality and the strong influence of gravitational movements affecting the true fracture orientation. The same problems concerning the interpretation of the fractures of the forelimb zone have been pointed out by Cooley (2007) during his studies of the southern Livingstone range. We can speculate that conjugate strike-slip faults occur, but large scale extensional fractures are probably missing due to the compression stress encountered in the lower fold limb, which is overturned in the southern part of Turtle Mountain. The same origin could also be proposed for the discontinuity set J5. This joint is well developed in the western flank and controls the erosion as well as the channel incision. In general, J5 set is very close to bedding and its origin could also be linked to post-folding movements and could be associated to J1 set as

conjugate joint. This assumption is in agreement with the reconstruction of the mean stress direction influencing the area after the folding phase.

The NW-SE extension phase and the stress released during the thermal relaxation period have likely played an important role for the reactivation of syn-folding structures, like J2 and J3. This extension has probably enabled the development of the fractures in the two fold limbs. Other indications of post-folding movements can be seen in the lower part of Third Peak. In this area, we can suspect the presence of a post-folding fault oriented approximately N-S following the pre-existing bedding plane orientation with an estimated displacement of about 10 m. Normal fault and strike-slip fault with similar directions have been pointed out around South and North Peak (Langenberg et al., 2007). This suggests that the presence of different phases of movement in the same area induce often a reactivation and re-orientation of the pre-existing joints. Slickensides that could confirm or reject previous hypothesis are often absent due to the sub-superficial pressures / temperature regime during the last movement phases and due to dissolution phenomenon along the calcareous joint walls.

Another important reactivation of pre-existing discontinuity sets is probably related to recent gravitational movements. In fact, the orientation and the opening of cracks present in Turtle Mountain area are influenced by tectonic discontinuity sets such as suggested by Figure 4.1-12. The comparison of the dip directions of the discontinuity sets (Figure 4.1-12a) with the lineaments directions (Figure 4.1-12b) for the whole Turtle Mountain area, shows a close fit between the main discontinuity dip direction and the lineaments strike confirming the significant structural control of tectonic related joint on the slope deformation.

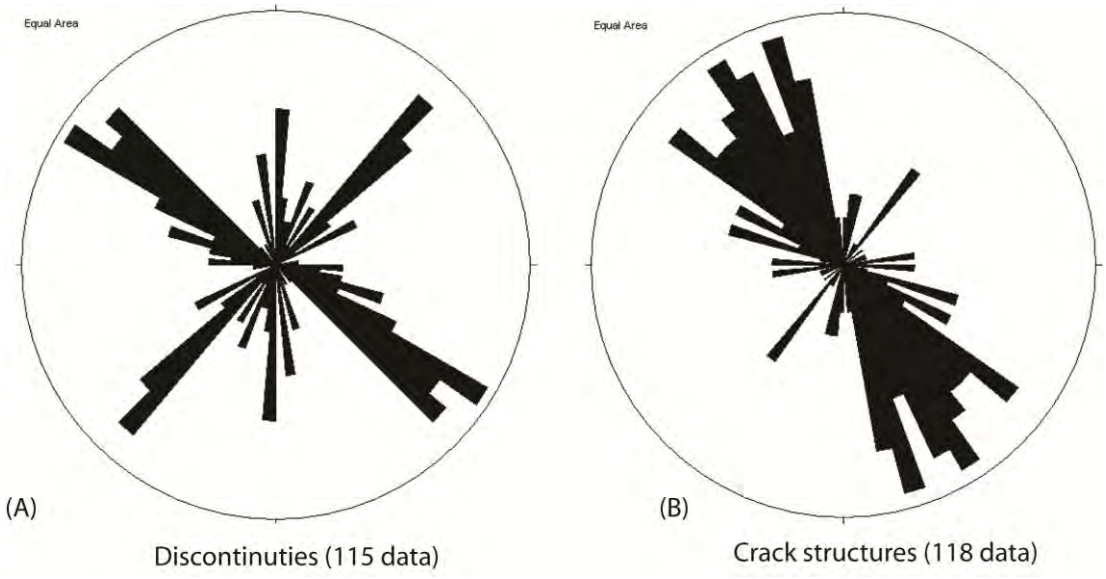

Figure 4.1-12: Rose diagrams (5° interval) comparing discontinuity set orientation (A) and crack orientation (B) between South Peak and the central part of the Frank slide crown area.

It is interesting to note that lineaments follow the NW-SE discontinuity (generally in the J1 or J2 dip direction) and also the NE-SW direction corresponding to the J3 discontinuity set. In upper South Peak the lineaments orientation highlights the irregular (saw-tooth) tension cracks disposition following two or more pre-exiting discontinuity sets. In the field, manual estimations of displacement directions have been

attempted along large cracks in lower South Peak area and also indicate a general movement plunging 10° toward NE.

4.1.8 INTERACTIONS BETWEEN FOLD STRUCTURE AND SLOPE INSTABILITIES

In this section, we analyse the structure and rock mass conditions in the hinge area of the Turtle Mountain anticline in relation to the past and potential failure instabilities. The primary influence of joints sets in rock slope instabilities is defined by the failure mechanism and the limits of the unstable volume (Hoek and Bray, 1981). As a result of tectonic features (shear zones, fault zones and fold hinge areas), the fracturing increases and the rock mass strength decreases (Brideau et al., 2009).

The fold hinge area represents an important structural feature where strain and related fracturing are often important (Badger, 2002; Price and Cosgrove, 1990; Ramsay and Huber, 1987). As a consequence, significant damage induced by extensional stress in the fold hinge could be expected. In these conditions, the deformed rock mass is more susceptible to weathering and the development of varied types of failure mechanisms.

4.1.8.1 Influence of fold-related fractures in the 3D kinematic release

The morphology of Turtle Mountain is dominated by the Frank Slide scar. The failure mechanisms of the 1903 event have been studied by different authors (Jaboyedoff et al., 2009; Benko and Stead; 1998; Cruden and Krahn, 1978). The influence of fold-related fractures on failure mechanisms has been indirectly suggested by Jaboyedoff et al. (2009). In their model, the fold-induced joint J2 is the rear limit of the toppled wedge formed by regional fault J1 and fold-induced fracture J3.

Kinematic analyses of sliding, toppling and wedge failure mechanisms were performed in order to verify the failure mechanisms observed in the field (Figure 4.1-13). A topographic attitude of 110°/50°corresponding to the mean value near the hinge area has been used as reference topography. A conservative friction angle of 30° has been chosen according to the worst discontinuity conditions observed in the field (roughness and weathering) and assuming that locally previous movements occurred along the discontinuity sets and the resulting shear strength will be close to the residual. The kinematic tests confirm these field observations concerning planar sliding on bedding, sliding/toppling on J3 and wedge sliding (J2^J4 but locally also J2^J3, J1^J3) mechanisms affecting the western fold limb, essentially in the eastern flank of the mountain. In addition, the presence of regional scale post-folding fractures (J1, J5) showing locally a very high persistence and crossing the entire anticline introduces another important instability factor not directly related to the presence of fold-related fractures. In the hinge zone, the presence of wedges formed by J1 and J5 sets allowing the back and the lateral release for the planar sliding along bedding planes. The influence of J1 set is also very important in the lower portion of South Peak, where it defines six large unstable areas, having volumes varying between 0.15 to 5 Million of m^3 (Froese et al., 2009b).

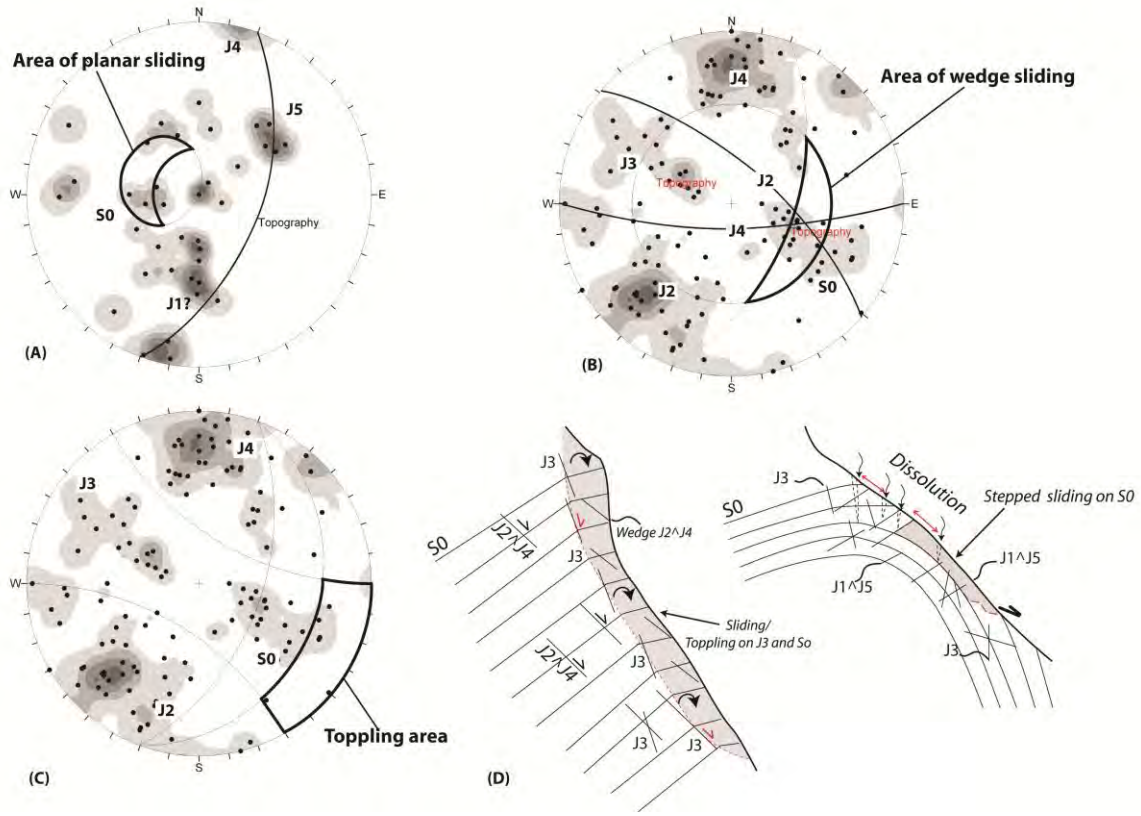

Figure 4.1-13: Instability mechanisms related to the fold hinge area. (A) Kinematic analysis of planar sliding for discontinuity sets detected close to the fold hinge (Equal area projection, lower hemisphere). B) Kinematic analysis of wedge sliding involving J2 and J4 discontinuity sets, affecting the western fold limb (Equal area projection, lower hemisphere). (C) Kinematics analysis of toppling mechanism involving S0 discontinuity set, affecting the western fold limb (Equal area projection, lower hemisphere). (D) Schematic representation of failure mechanisms and their location along the Turtle Mountain anticline.

4.1.8.2 Influence of fold-related fractures and karstification in the reduction of the rock mass strength

The evolution of rock mass quality along the Turtle Mountain anticline has been investigated by analysing the variations of GSI values obtained in the different structural stations. Figure 4.1-9 shows that GSI values in the two fold limbs are quite similar. However, values for the eastern fold limb have a tendency to be more dispersed compared to the values in the western fold limb. This is probably related to the post-folding movements (a fault sub-parallel to the bedding planes have been detected under Third Peak area) and recent gravitational movements. The GSI values in the hinge area show a large dispersion and a mean values clearly lower than the GSI values in the two fold limbs. In order to explain this trend, two main factors must be taken into account. Firstly, the fold-related joint sets, especially the extensional joint (J3), tend to be more persistent and open approaching the hinge. Referring to the GSI classification, we have a progressive evolution from a very blocky structure with multi faced angular blocks toward a blocky/disturbed rock mass. This evolution could be followed in Figure 4.1-8 in particular in picture a, b, c and d. Secondly, a decrease in structure quality involves also a decrease in surface conditions. In fact, along open joints in the hinge area it is possible to see a significant karstification involving the creation of cavities (Figure 4.1-4b and Figure 4.1-8). Moreover, along joints an important calcite recrystallisation can be observed, indicating previous fluid flows. In addition, a general decrease of surface condition (reaching

locally grade III-IV) could be observed approaching the hinge area (Figure 4.1-4b). Using the GSI chart (Figure 4.1-14), the influence of increasing of joint persistent and decreasing surface conditions in the hinge area could be illustrated. The vector A could be decomposed in two components: the vertical vector B corresponding to an augmentation of fracturing (in our specific case the increasing of persistence) and the horizontal vector C corresponding to a decrease in surface conditions such and an increasing of joint weathering related to karstification. Persistence is not directly taking in to account by the GSI chart proposed by Cai et al. (2004). However, assuming the presence of the same number of joint sets in the fold limb and in the hinge area, an increasing of the joint persistence could decrease the block size. The relation between joint sets persistence and block size is more complex, like suggested by Kim et al. (2007) and the correlation with Vector B (Figure 4.1-14) must be interpreted in a qualitative manner.

The influence in the strength reduction induced by karstification cavities is difficult to characterize using the GSI chart, because both GSI parameters are directly or indirectly affected. Concerning the Joint condition factor (J_c) fact, karstification influences manly the Joint alteration factor (J_a). In fact, when karstification occurs in calcareous rock, calcite is dissolved but often impurities remained (clay, quartz particles), and it results that shear strength is locally decreased. Joint walls are also influenced (macroscopic voids calcite) and show often higher alteration that the intact rock. Large scale (J_w) and small scale roughness (J_s) are just marginally influenced because, during karstification, no shear movements occurred along joint sets. At the same time, especially in porous coarse-grained limestone, water infiltration and related karstification decrease the rock strength promoting the rock mass disintegration and decrease the stability.

Cruden and Martin (2007) estimated the GSI value for each geological unit based on Norris's map (1993) and obtained for the Livingstone Formation a GSI value of 80, which appears much higher, compared to the ones in the present study. This discrepancy is principally due to the difference in the analysis scales. Our work focused on variations of GSI along the anticline and we describe the rock mass conditions at the outcrop scale (50-100 m^2). At this scale, the rock mass characteristics are influenced by local heterogeneities (lithological and structural) and by the climate effects (freeze and thaw cycles, exfoliation). This mean that outcrops used for the estimation of GSI show often lower values than estimation performed excavated slope and tunnel (Marinos et al., 2005). However, based on the outcrop conditions and suggestion proposed by Marinos et al. (2005) to project GSI values in to the ground a mean GSI value for the Livingstone Formation around 60-70 seems to be more realistic for describing the general condition of the Turtle Mountain anticline, especially the fold limb conditions (Figure 4.1-14). For the hinge, area the the projected GSI values in to the ground will probably lower (40-60) and more scattered depending on the relative position of the neutral surface and on the behaviour of the involved lithology. The suggested projection of GSI information from observations in outcrops to depth is reported in Figure 4.1-14.

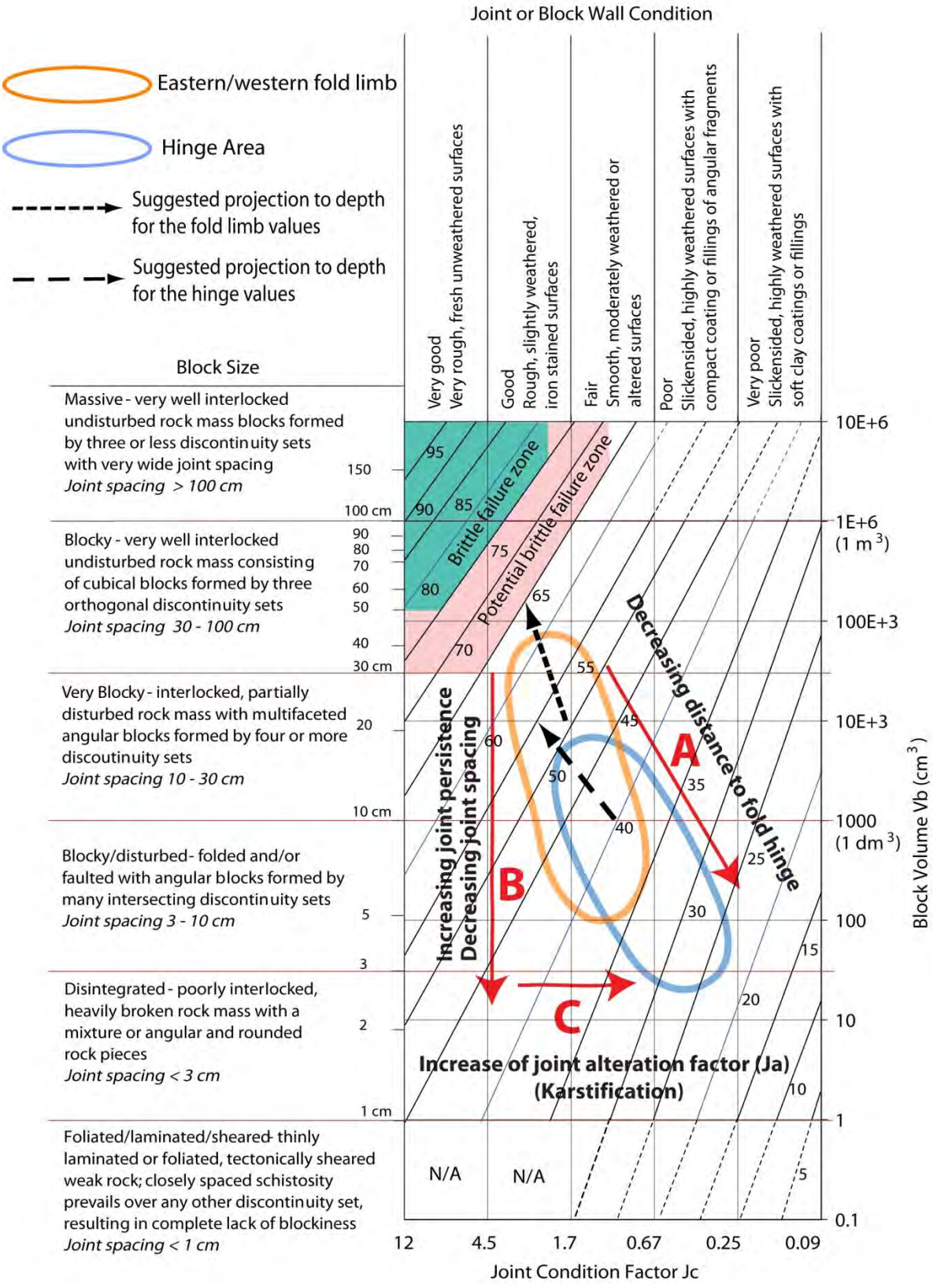

Figure 4.1-14: Factors influencing the decreasing of GSI values approaching the hinge area plotted in the GSI evaluation chart (from Marinos et al., 2005). Vector B corresponds to an increasing in fracturation and vector C corresponds to an increasing in rock weathering. The composition of these two vectors correspond to vector A.

4.1.9 GENERAL MODEL FOR FOLD-RELATED INSTABILITIES

Based on studies performed on the Turtle Mountain anticline, it is possible to propose a general relationship between the localisation and the specific characteristics of the fold and the potential failure mechanisms affecting the different portions of the mountain.

Two main parameters have been chosen for the failure mechanism description in the different portions of the mountain: the interlimb angle and the angle between the fold axis and the mountain axis.

The interlimb angle describes the minimum angle between two fold limbs measured in the profile section (Price and Cosgrove, 1990). In other words, the interlimb angle gives an indication of the tightness of the fold. The other important parameter is defined by the angle between the mean vertical axis of the mountain and the axial plane. This angle determines the relative position of the hinge zone in the mountain limb. According to the relative position of the hinge for different stability situations, we define three limit angles of 15°, 90° and 180°. The mountain slope angle plays a fundamental role in the effective kinematic feasibility of the different failure mechanisms (Cruden, 2003). In order to simplify the description of the theoretical potential failure mechanisms, we assume a mountain flank slope which is greater than the basal friction angle along the different discontinuity sets. Based on previous studies (Cruden and Hu, 1999), an angle of 30° was selected as an appropriate value for the basal friction angle of carbonate rocks. Figure 4.1-15 presents the nine different geometrical situations that could be obtained by combining the tightness of the fold (interlimb angle) and the different angles between the mountain's mean axis and the fold axis. For each situation, the potential failure mechanisms involving the bedding planes and the extensional fractures have been analyzed. Conjugate faults related to folding have not been taken into account in the general model because of their local extension and development. The presence of extensional joints is related to the fold mechanisms (flexural slip, flexural flow, and tangential longitudinal plane), the fold type and the strain and temperature conditions during folding (Price and Cosgrove, 1990; Ramsey and Huber, 1987). In this study, we focus on parallel folds where the bed thickness measured perpendicularly remains constant throughout the fold and assuming an analogous mechanical behavior for the different beds involved during the folding phase. Parallels folds correspond to the typical shape issued from a flexural-slip mechanism (Ramsey and Huber, 1987) and this appears to be the prominent process in Rocky Mountain Foothills and Front Ranges (Langenberg, 1992). Other fold shapes, such as similar folds, imply different folding mechanisms/conditions and the development of other type of discontinuities (cleavage schistosity, crenulations, etc.).

From a qualitative point of view, the failure mechanisms affecting the different portions of the mountain could easily be assessed using the chart proposed by Cruden (2003) for anaclinal and cataclinal slopes. This chart could be applied to the different configurations presented in Figure 4.1-15 assuming a correlation between kathetal (normal to bedding) joints and extensional joints related to the folding phase. Generally, a more stable configuration is reached when the angle between the axial plane and the mountain axis is close to 180°. In this configuration, the mountain is only affected by a potential toppling mechanism. According to previous observations in Canadian Rockies (Gadd, 1986), another favorable situation is represented by an angle close to 90° for tight folds. In this configuration, bedding is near horizontal. Gadd (1986) indicates that the higher peaks in the Canadian Rockies have this type of configuration.

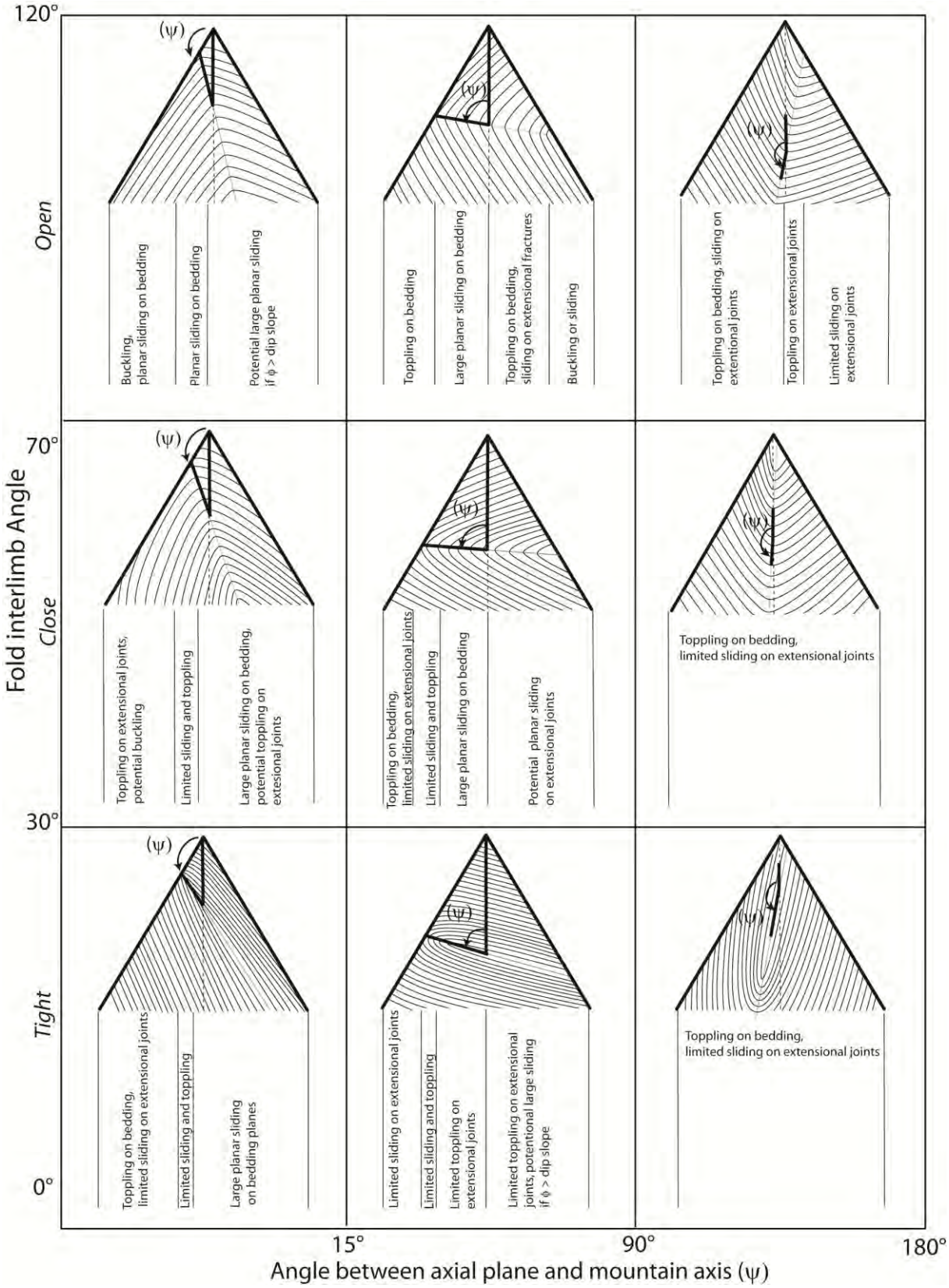

Figure 4.1-15: General model of potential fold-related instabilities. The potential failure mechanisms in the different mountain areas depend on the interlimb angle and the angle between the fold axis and the mountain axis. Φ symbolize the basal friction angle.

The folds with a tight interlimb angle present a very limited hinge area where instabilities seem to affect only limited volumes. In addition, failures mechanisms tend to be the same along a given mountain flank

because of sub-parallel bedding in the two fold limbs (constant anaclinal or cataclinal configuration). Folds with a more open interlimb angle show different failure mechanisms in the same flank. In fact, within the same flank, it is possible to have a change between a cataclinal and an anaclinal situation. Larger interlimb angles also signify a larger hinge area with its associated failure mechanisms.

4.1.10 CONCLUSIONS

The combination of a structural study performed using high-resolution DEM analysis with a detailed field survey has determined the main structural sets present at Turtle Mountain. At least three discontinuity sets (J2, J3 and J4) seem to be related to the folding phase. Regional post-folding movements must also be taken into account in order to understand the origin of the J1 and J5 sets. The fold-induced fracturing and the related rock mass damage in the hinge area seem to be the most significant elements to explain the presence of frequent small instabilities.

The influence of fold-related damage is an important factor not only for local-scale instabilities but also in the development of large rock slope failures. Particularly in a carbonate environment, the dissolution along fractures could play an important role in decreasing the rock mass strength and in increasing the water pressure along discontinuities. As suggested by Cruden and Martin (2007), water infiltration along karst-widened joints represented a major triggering factor for the Frank Slide. The GSI classification represents an interesting tool in characterizing the variation in rock mass quality variation along large structural features, such as a fold thrust or large fault. However, in order to have a reliable quantitative description of the rock mass strength variation more rigorous field investigations are necessary. In particular, a clear definition of the outcrop's extension considered for the GSI estimation and a homogeneous coverage of the study area (regular distribution of the GSI estimation along the slope) represent the main challenges when using this technique. Unfortunately, at Turtle Mountain, homogenous cover is difficult to perform owing to the difficulty in the field access.

A general model based on the location and the tightness of the fold in the mountain has been proposed to show the potential rock slope failures induced by the presence of fold and the fold-related fractures. This model represents a specific evolution of the model proposed by previous studies (Cruden and Hu 1999; Cruden 2003). The localization and opening of the anticline on the mountain influence the development of small or larger rock slope failures, and represents an important parameter in the assessment of hazards resulting from large rockslope failure.

4.1.11 REFERENCES

Agliardi, F., Crosta, G.B., Zanchi A. 2001. Structural constraints on deep-seated slope deformation kinematics, *Engineering Geology*, 59, 83-102.

Ambrosi, C., Crosta, G.B. 2006. Large sackung along major tectonic features in the Central Italian Alps, *Engineering Geology*, 83, 183-200.

Allan, J.A. 1933. Report on stability of Turtle Mountain, Alberta and survey fissures between North and South Peak. Department of Public Works, Edmonton, Alberta. Provincial Archives.

Badger, T. C. 2002. Fracturing within anticlines and its kinematic control on slope stability, *Environmental and Engineering Geoscience*, 8, 19-33.

Baillifard, F., Jaboyedoff, M., Sartori, M. 2003. Rockfall hazard mapping along a mountainous road in Switzerland using a GIS-based parameter rating approach, *Nat. Hazards Earth Syst. Sci.*, 3, 435-442,

Benko, B., Stead, D. 1998. The Frank Slide: A re-examination of the failure mechanism, *Canadian Geotechnical Journal*, 35, 299-311.

Brideau, M-A., Ming, Y., Stead, D. 2009.The role of tectonic damage and brittle rock fracture in the development of large rock slope failure, *Geomorphology*, 103, 30-49.

Cai, M., Kaiser, P.K., Uno, H., Tasaka, Y., Minami, M. 2004. Estimation of rock mass deformation modulus and strength of jointed hard rock masses using the GSI system. *International Journal of Rock Mechanics & Mining Sciences*, 41, 3–19.

Cai, M., Kaiser, P.K., Tasaka, H., Minami, M. 2007. Determination of residual strength parameters of jointed rock masses using the GSI system, *International Journal of Rock Mechanics & Mining Sciences*, 44, 247–265

Cooley, M. A. 2007. The structural, thermal, and fluids evolution of the Livingstone range anticlinorium, and its regional significance to the southern Alberta foreland thrust and fold belt. PhD thesis, Queen's University, 163 p.

Cooper, M. 1992. The analysis of fracture systems in subsurface thrust structures from the Foothills of the Canadian Rockies. In: McClay, K. R. (Ed), *Thrust Tectonics*. Chapman and Hall London, pp. 391–405.

Couture, R. 1998. Contributions aux aspects mécaniques et physiques des écroulements rocheux. PhD thesis, Laval University, 573 p.

Cruden, D.M. 2003. The shapes of cold, high mountains in sedimentary rocks, *Geomorphology*, 55, 249-261.

Cruden, D.M., Hu, X.-Q. 1999. The Shapes of some Mountain Peaks in the Canadian Rockies, *Earth Surface Processes and Landforms*, 24, 1 –13.

Cruden, D.M., Krahn, J. 1973. A re-examination of the geology of the Frank Slide, *Canadian Geotechnical Journal*, 10, 581-591.

Cruden, D.M, Martin, D.K. 2007. Before Frank slide, *Canadian Geotechnical Journal*, 44, 765-780.

Currie, J.B., Reik, G.A. 1977. A method of distinguishing regional directions of jointing and of identifying joint sets associated with individual geological structures, *Canadian Journal of Earth Sciences*, 14, 1211-1228.

Derron, M.-H., Jaboyedoff M., Blikra, L. H. 2005. Preliminary assessment of rockslide and rockfall hazards using a DEM (Oppstadhornet, Norway), *Natural Hazards and Earth System Science*, 5, 285-292.

Froese, C., Moreno, F., Jaboyedoff, M., Cruden, DM. 2009a. 25 Years of Movement Monitoring on the South Peak of Turtle Mountain: Understanding the Hazard, *Canadian Geotechnical Journal*, 46, 256-269.

Froese, C., Jaboyedoff M., Pedrazzini A., Hungr, O., Moreno, F. 2009b. Hazard Mapping for the eastern face of Turle Mountain, adiacent to the Frank Slide, Alberta, Canada. *Proceedings of the Landslide Processes Conference*, Strasbourg, 6-7 February 2009.

Gadd, B. 1986. *Handbook of the Canadian Rockies*, Corax Press

Hoek, E., Bray, J. 1981. *Rock Slope Engineering*, Spon Press.

Hoek, E., Brown, E.T. 1997. Practical estimates of rock mass strength, *International Journal of Rock Mechanics and Mining Sciences*, 34, 1165–1186.

International Society for Rock Mechanics (ISRM). 1978. Suggested methods for the quantitative description of discontinuities in rock masses, *International Journal of Rock Mechanics and Mining Sciences & Geomechanics Abstracts*, 15, 319–368.

Jaboyedoff, M., Couture, R. 2003. Report on the project COLTOP3D for March 2003: stay of Michel Jaboyedoff at GSC - Ottawa . Quanterra administrative document -Activity report-RA01.

Jaboyedoff, M., Couture, R., Locat, P. 2009. Structural analysis of Turtle Mountain (Alberta) using digital elevation model: toward a progressive failure, *Geomorphology*, 103, 5-16.

Jackson, E. L. 2002. Landslide and landscape evolution in the Rocky Mountains and adjacent Foothills area, southwestern Alberta, Canada. In Catastrophic landslides: effects, occurrence, and mechanisms edited by Stephen G. Evans, Jerome V. DeGraff, *reviews in Engineering geology XV*, Geological society of America.

Jones, P.B. 1993. Structural geology of the modern Frank Slide and ancient Bluff Mountain Slide, Crownest, Alberta, *Bulletin of Canadian Petroleum Geology*, 41, 232–243.

Langenberg, W. 1992. Styles of Deformation in the Rocky Mountain Foothills and Front Ranges, Alberta, Canada, *AAPG Bulletin*, 76.

Langenberg, C.W., Pana, D., Richards, B.C., Spratt, D.A., Lamb, M.A. 2007. Structural geology of the Turtle Mountain area near Frank, Alberta. EUB/AGS *Science Report 2007-01*, 30 p. World Wide Web Address: http://www.ags.gov.ab.ca/publications/ABSTRACTS/ESR_2007_03.html.

Kim, B. H., Cai M., Kaiser P. K., Yang, H. S. 2007. Estimation of Block Sizes for Rock Masses with Non-persistent Joints, *Rock Mech. Rock Engng*., 40, 169–192.

Marinos, V., Marinos, P., Hoek, E. 2005. The geological strength index: applications and limitations, *Bulletin of Engineering Geology and the Environment*, 64, 55-65.

Matsuoka, N. 2008. Frost weathering and rockwall erosion in the southeastern Swiss Alps: Long-term (1994-2006) observations, *Geomorphology*, 99, 353-368,

McConnell, R.G., Brock, R.W. 1903. Report on the great landslide at Frank, Alberta, Department of the Interior, Annual report for 1903. Ottawa, part 8. Edmonton Geological Society 2003, 52 p.

Moreno, F., Froese, C.R. 2007. Turtle Mountain Field Laboratory Monitoring and Research Summary report, 2005, *Earth Sciences Report 2006*.

Muecke, G.K., Charlesworth, H.A.H. 1966. Jointing in folded Cardium Sandstones along the Bow River, Alberta, *Canadian Journal of Earth Science*, 3, 579-596.

Norris, D.K. 1993. Geology and structure cross-sections, Blairmore (West Half), Alberta, *Geological survey of Canada*, Map 1829A, scale 1:50'000.

Price, R.A., Carmichael, D.M. 1986. Geometric test for Late Cretaceous-Paleogene intracontinental transform faulting in the Canadian Cordillera, *Geology*, 14, 468-471.

Price, N.J., Cosgrove, J.W. 1990. *Analysis of Geological Structures*, Cambridge press, 516 p.

Ramsay, J. G. and Huber, M. I. 1987. The Techniques of Modern Structural Geology, Vol. 2, Academic Press, London.

Read, R.S., Savigny, K.W., Oboni, F., Cruden, D.M., Langenberg, C.W. 2000. Geotechnical hazard assessment of the south flank of Frank Slide, Hillcrest, Alberta. GeoCanada 2000. Calgary, Alberta. May 29-June 2.

Spratt, D.A., Lamb, M.A. 2005. Borehole data interpretation and orientation, Turtle Mountain Project. Internal report of work Package WP15B, Alberta Municipal Affairs, 15 p.

Stearns, D.W., 1968. Certain aspects of fractures in naturally deformed rocks. Rock Mechanics Seminar. R.E. Riecker, Bedford, Terrestrial Sciences Laboratory, pp. 97–118.

Sturzenegger, M., Stead, D., Froese, C., Moreno, F., Jaboyedoff, M. 2007. Ground based and airborne LiDAR for structural mapping of the Frank slide. *Proceedings of the 1st Canada-US rock mechanics Symposium*, Vancouver, Canada, 27-31 May 2007.

Sturzenegger, M., Stead, D.2009.Quantifying discontinuity orientation and persistence on high mountain rock slopes and large landslides using terrestrial remote sensing techniques, *Nat. Hazards Earth Syst. Sci.*, 9, 267-287.

4.2 FROM DEEP SEATED SLOPE DEFORMATION TO ROCK AVALANCHE: DESTABILISATION AND TRANSPORTATION MODELS OF THE SIERRE ROCK AVALANCHE (S-W SWITZERLAND)

4.2.1 ABSTRACT

Sackung is a widespread post-glacial morphological feature affecting Alpine valley sides and creating typical geomorphological expressions that could be detected on the topography. Over long time evolution internal deformations can drastically increase leading to the formation rapid creeping phenomenon as a rock-slides or rock avalanches. In this study, a detailed description of the Sierre rock-avalanche (SW Switzerland) will be presented. This convex-shaped postglacial instability is one of the larger rock-avalanche in the Alps, involving more than 1.5 billion of m^3 with a run out distance of about 14 km an extremely low Fahrböschung angle. This study reports comprehensive analyses of structural and geological characteristics leading to the development of Sierre rock-avalanche. In particular, by combining field observations, digital elevation model analyses and numerical modelling, the strong influence of both ductile and brittle tectonics structures on the failure mechanism and on the failure surface geometry is highlighted. The detection of important pre-failure deformations indicates that the development of the rock avalanche corresponds to the last evolution stage of a pre-existing DSGSD. These analyses accompanied by the dating and the characterization of rock avalanche deposits, allow proposing a destabilisation model clarifying the different phases leading to the development of the Sierre rock avalanche.

4.2.2 RÉSUMÉ

Les tassements rocheux représentent un phénomène gravitaire très répandu dans les vallées Alpines. Dans certaines conditions, les déformations internes qui affectent de manière continue ces tassements, peuvent s'accélérer et donner lieu à une rupture rapide engendrant le développement d'avalanches rocheuses. Avec un volume estimé de 1.2-1.6 Km^3 et une distance de propagation de plus de 14 km, l'avalanche rocheuse de Sierre fait partie des cinq plus grandes instabilités de versants recensées dans les Alpes Européennes. Cette étude propose une évaluation des conditions structurales et morphologiques qui ont permis le développement de l'avalanche rocheuse de Sierre. Une modélisation géomecanique incluant une déglaciation progressive du versant a permis de confirmer l'importance de la géometrie de la surface de rupture, liée à la présence de plis à l'échelle kilométrique, sur la concentration des contraintes gravitaires et le développement de l'instabilité. Sur le terrain, l'identification au pied du versant d'importantes déformations ductiles et cassantes liées aux mouvements progressifs du versant, suggère que l'avalanche rocheuse de Sierre représente la dernière phase évolutive d'un grand tassement rocheux développé après la dernière glaciation. Les différentes analyses et les modélisations effectuées ainsi que des datations au carbone 14 des dépôts de l'avalanche ont permis de proposer des hypothèses concernant les différentes phases de déformations et de transports qui caractérisent l'avalanche rocheuse de Sierre.

4.2.3 INTRODUCTION

Deep seated gravitational slope deformations (DSGSD) are widespread morphological features affecting Alpine valley sides and creating typical geomorphological expressions (Agliardi et al., 2001; Pasquaré 2001; Ambrosi and Crosta 2001; Agliardi et al., 2009). Hazard generated by DSGSD is generally low especially if no velocity accelerations occur. However, over the long term, internal deformations affecting a DSGSD can drastically increase to rapid creep failure and create a more rapid and destructive phenomenon such as rock-slide or rock avalanche (Emery, 1978; Chigira and Kiho 1994; Jain and Nada 2010). This catastrophic evolution has been observed and documented in some historical cases such as in the Vayont (Semenza and Ghirotti 2000; Genevois and Ghirotti 2005), in the Val Pola landslides (Dramis et al., 1995; Crosta et al., 2003) or in the Todagin Creek landslide (Sakalas et al., 2007).

The geometric and the geomechanical characteristics of pre-exiting brittle structures, in particular, persistent bedding planes or foliations, are frequently identified as one of the main predisposing factors driving the failure mechanism of large slope instabilities (Sauchyn et al., 1998; Agliardi et al., 2001; Sartori et al., 2003 a. o.). Besides, few studies have focused on the influence of inherited tectonic ductile features (i.e. folds) in the development of rock slope instabilities (Badger 2002; Coe and Harp 2007; Pedrazzini et al., 2011; Saintot et al., 2011). Ductile tectonic features can create weakness zones (Brideau et al., 2009; Pedrazzini et al., 2011), can influence the shape and morphology of the failure surface (Oppikofer et al., 2011) or can drive the displacement patterns observed at the surface (Jaboyedoff et al., 2011). In particular, large scale antiforms, related to the presence of large scale anticline, have been identified to be susceptible areas for the development of DSGSD (Massironi et al., 2011) and rock avalanches (Scarascia Mungozza et al., 2003).

With an estimated volume of 1-2 km^3, the Sierre rock avalanche is one of the five largest mass movements of the entire European Alps (Abele, 1974). Even if this landslide has been mentioned and taken as example by different authors for his large volume and high mobility (Heim 1932; Scheidegger 1973; Abele 1974; Hsu 1978; Erisammn and Abele 2001; von Poschinger 2002), few studies have been carried out. In particular, no detailed description exists concerning the specific geometrical characteristics, the real extension of the scar and the potential failure mechanism.

This study reports comprehensive analyses of structural and geological characteristics leading to the development of Sierre rock-avalanche. In particular, by combining field observations, digital elevation model analyses and numerical modelling, the strong influence of both ductile and brittle tectonics structures on the failure mechanism and on the failure surface geometry is highlighted. The discovery of important pre-failure deformations indicates that the rock avalanche corresponds to the last evolution stage of a pre-existing DSGSD. These analyses associated to the characterization and to the dating of rock avalanche deposits, allow proposing a destabilisation and a transportation model for the Sierre rock avalanche.

4.2.4 GENERAL SETTING

The Sierre rock avalanche is located in the central part of the canton of Wallis in the South–Western Switzerland. The landslide scar is situated above the village of Varen, on the northern side of the Rhone

valley. The rock avalanche deposits are widespread on the Rhone valley from Varen to Grange village, located 12 Km downstream (Figure 4.2-1).

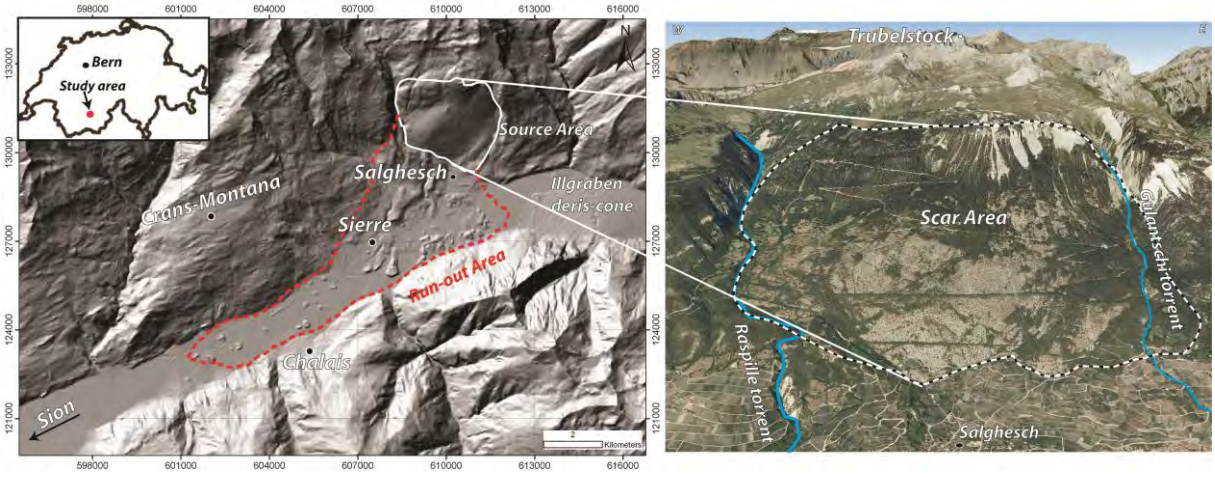

Figure 4.2-1: Shaded relief view of the DEM (10m cell size) of the source and the run-out area of the Sierre rock avalanche and detailed frontal view of the rockslide scar area (©Google 2010).

Tectonically, the study area is located at the eastern margin of the Rawil depression (Figure 4.2-2a). This zone represents a regional tectonic depression situated between the axial culmination of the Aiguilles Rouges massif to the West and the Aar massif to the East (Heim 1921; Burkhard 1988). The origin and geometry of the Rawil depression are still unclear (Gasser and Mancktelow 2010). According to Ramsay (1989), the Rawil depression could be associated to the change in thrusting orientation from top-to-N during the early stages of the Alpine collision to top-to-W during the late stage of the Alpine collision. In this context, Mesozoic and Tertiary rocks belonging to different Helvetic and Ultrahelvetic Nappes are preserved and characterize the outcrops at the northern side of the Rhone valley.

These tectonic units are characterized by limestone, marly-limestone and shale displayed in a dip-slope configuration. The main regional brittle structure existing in the area is the Rhône–Simplon system. This brittle tardive system corresponds to a dextral strike-slip fault that was active from the late Paleocene to late Neogene (Steck 1984; Mancktelow 1992). Several deformation indicators (faults, master joints and kink like folds) observed along the main Rhone valley have been related to the movements associated to this fault (Steck 1984). The Rhone-Simplon fault also drove the orientation of the main Rhone valley by introducing an important tectonic weakness that was preferentially followed by the glacial incision (Preusser et al., 2010). The morphology of the Rhone valley is clearly influenced by its complex glacial and paraglacial history. In the central Wallis, the maximum ice cap elevation reached between 21-19 Ka BP, was estimated to be 2000-2200 m (Jäckli 1962; Kelly et al., 2003). Glacial and paraglacial deposits cover partially the rocky outcrops on both valley sides. They consist mainly of till characterized by allochtonous elements (gneiss and granite clasts) deposited by the Rhone glacier or by tributary valley glaciers. In the lower portion of the slopes, fluvio-glacial and glacio-lacustrine deposit represents the most important outcrops. The present-day morphology of the northern side of the Rhone valley is characterized by the important overprint of gravitational movements. These latter are represented by translational landslides affecting the quaternary cover, and by deep-seated slope deformations affecting the entire slope (Figure 4.2-3).

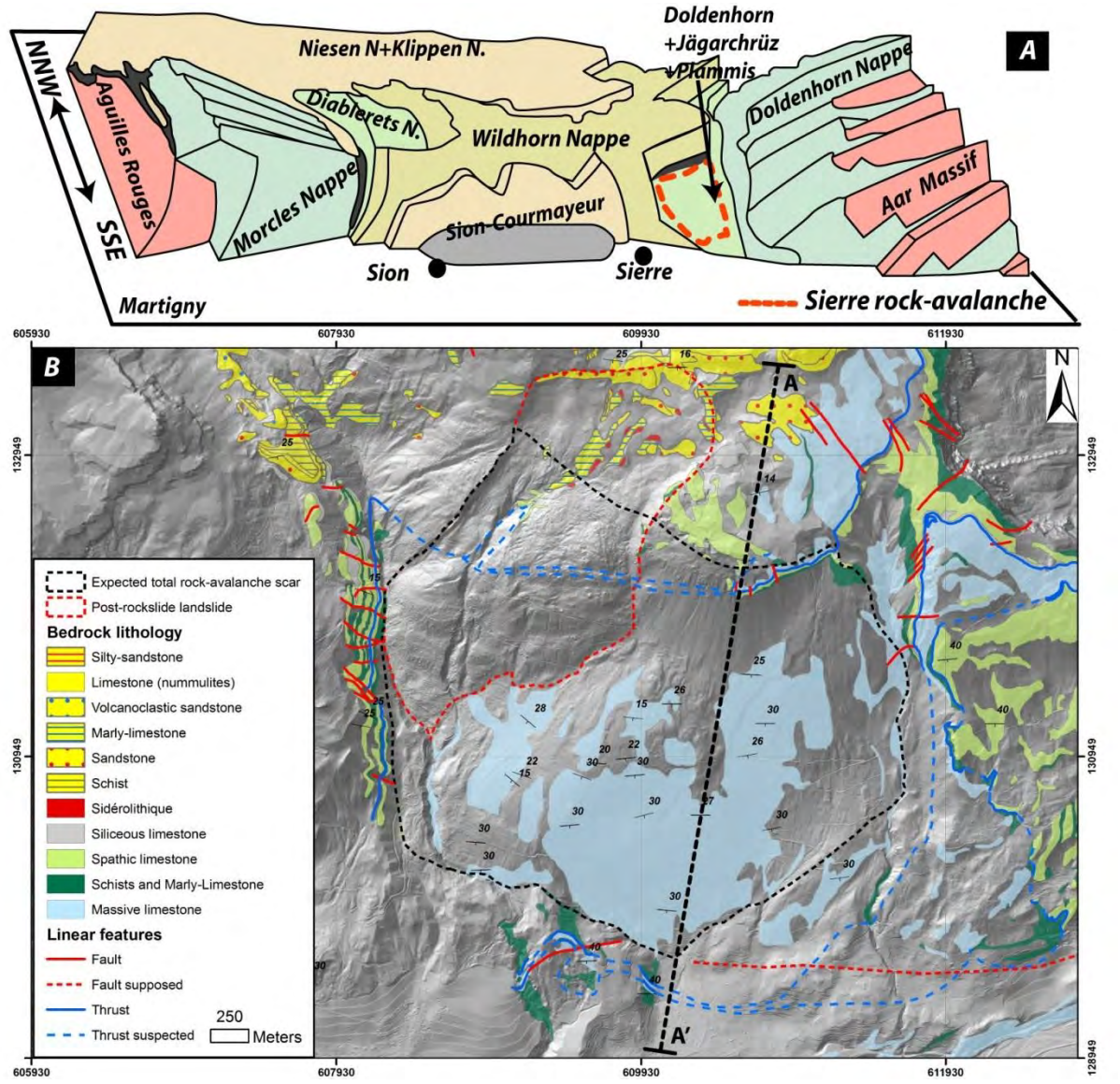

Figure 4.2-2: a) Tectonic sketch of the Rawil depression (northern side of the Rhone valley) showing the location of the Sierre rock-avalanche in the complex tectonic setting of the Helvetic Nappes. b) Geological map (bedrock lithology only) of the Sierre rock avalanche area (adapted from Bugnon, 1986 and completed by field investigations). The trace of cross section A-A' refers to Figure 4.2-4.

4.2.5 PREVIOUS STUDIES

The Sierre rock avalanche was first mentioned by Geralch (1883) and successively briefly described by Lugeon (1989), who was the first to describe the presence of till-like deposits above the rock avalanche. Abele (1974) suggested that the hummocky characteristic of the deposits is not directly related to the rock avalanche but is rather the results of the glacial remodelling. A first detailed description of the rock avalanche has been carried out by Burri (1955, 1995). In order to determine the conditions of the valley at the time of the slide, he described the granulometry and the lithology of the deposits and their relationship with adjacent quaternary sediments. In particular, he found some evidence of till-like and/or fluvio-glacial sediments deposited above the rock avalanche and the presence of fluvio-glacial terraces located 200 m above the actual valley level. In order to explain these observations, Burri (1995) proposed different scenarios implying: (a) the presence of the Rhone glacier at the time of the slide, (b) the re-advance of the Rhone glacier covering the slide deposits or (c) the formations of a lake by the re-advance

of lateral glaciers damming the main valley. Concerning the failure mechanisms and the real extent of the failure surface, no detailed studies have been carried out. Concerning the failure mechanism, the common accepted idea is that the rock avalanche was created by a simple planar slide along bedding planes dipping into the valley direction (Bugnon 1986; Burri 1995).

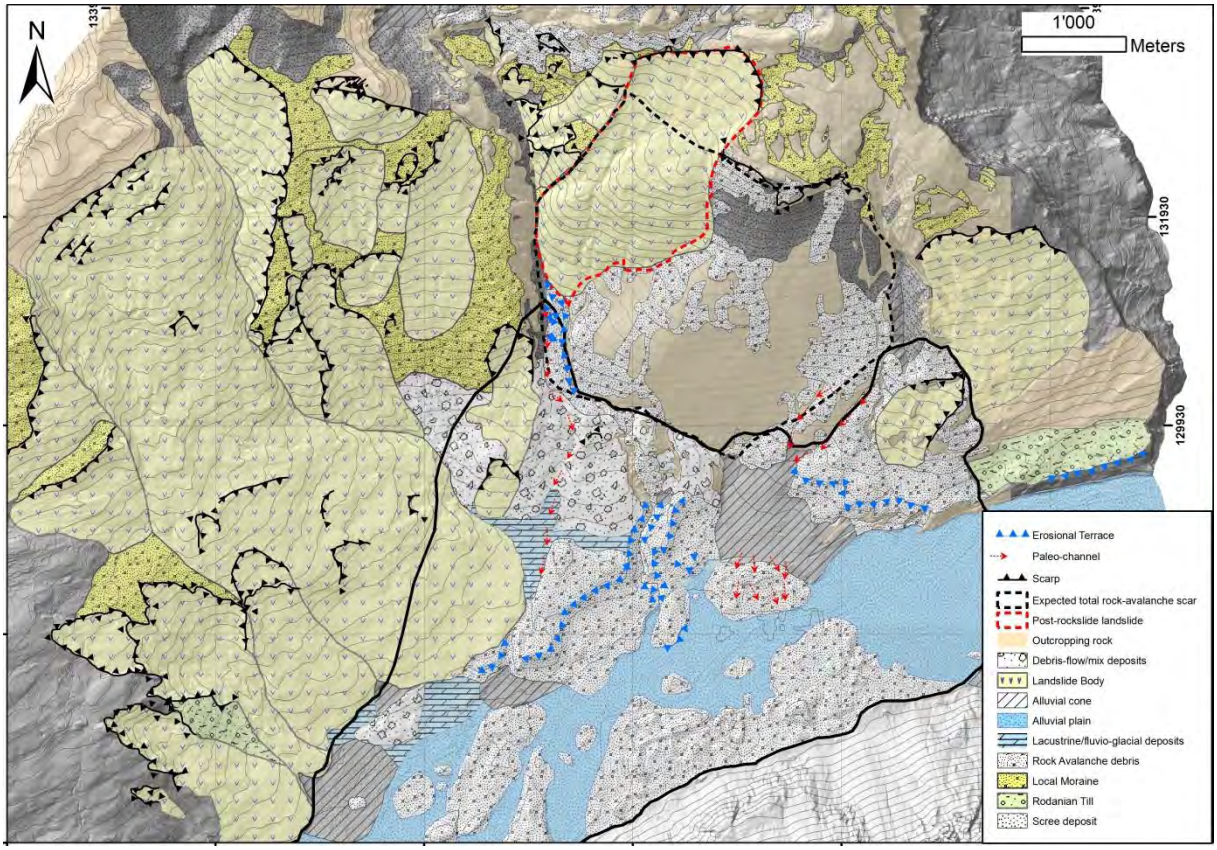

Figure 4.2-3: Geomorphological map displaying the gravitational features and the different quaternary sediments deposited before and after the rock avalanche development.

4.2.6 CHARACTERIZATION OF THE SOURCE AREA

4.2.6.1 Geology and geomorphology

The geology of the source area is characterized by the presence of three distinct tectonic units divided by two tectonics thrusts: The Doldenhorn Nappe, the Plammis unit and the Jägerchrüz unit. The last two units represent classical examples of a tectonic flake corresponding to incomplete sedimentary sequences that have been thrusted and slightly displaced from its reference Nappe (Bugnon 1986; Burkhard 1988). Bedding planes plunge into the valley direction with a dip of 35°- 40° in the lower portion of the slope and progressively flatten to 10°-20° in the upper part creating convex dip-slope geometry. The outcropping lithologies of the three tectonic units are similar and are composed by massive limestone (Malm), calcareous schist and marl (Valanginian inf.) and subordinated by micritic-limestone (Valaginien sup.) and siliceous limestone (Hauterivien). Detailed geological mapping performed by Bugnon (1986) and Burkhard (1988) indicates the presence of several tectonic faults oriented NE-SW and affecting the slopes at different height (Figure 4.2-2b). Most of them are sub- vertical and display normal to strike slip

movements (Burkhard 1988). Their origin has been associated to the shear zone of the regional Rhone-Simplon fault (Burkhard 1988).

East of the rock-avalanche area, a persistent gently dipping fault (15°-25°) has been detected at the bottom of the slope. Slickensides orientations suggest inverse movement direction (Bugnon 1986). Even though this has not been observed directly, its orientation suggests that the fault can potentially crosses the entire bottom the rock-avalanche scar. The visible failure surface is located at the contact between the massive limestone and the calcareous schist of the Doldenhorn Nappe. The massive limestone belonging to the Doldenhorn Nappe represents the most important rocky outcrops above the village of Salgesch. In the upper portion of the slope, a rock cliff of about 200 m is visible. In this area, representing part the rock avalanche scar, the contacts between the different tectonic units are visible. Above this cliff, several scarps and trenches can also be observed and indicate that the slope deformations extent behind the actual rock-avalanche scar. The lower portion of the slope is characterized by dip- slope lying directly above the recent alluvial fan. In the same area, evidences of paleo-channels developed parallel to the contact between the rock outcrops and the first unconsolidated deposit of the rock avalanche were observed. In the western side of the failure surface, the presence of a bench-like flatter section suggests break-out geometry. However, in this area, the delimitation of the rock-avalanche scar is more difficult. High resolution DEM (2 m cell size), allows identifying that the rock-avalanche scar and part of the failure surface are covered by a large rotational landslide (Figure 4.2-2b and Figure 4.2-3). Figure 4.2-4 shows a detailed cross-section through the rock-avalanche scar based on field observations and on previous geological mapping. On this cross-section, it is possible to distinguish the different lithologies forming the failed mass. The expected lithologies are: calcareous schist and marls (60%), massive limestone (35%) and micritic limestone (15%).

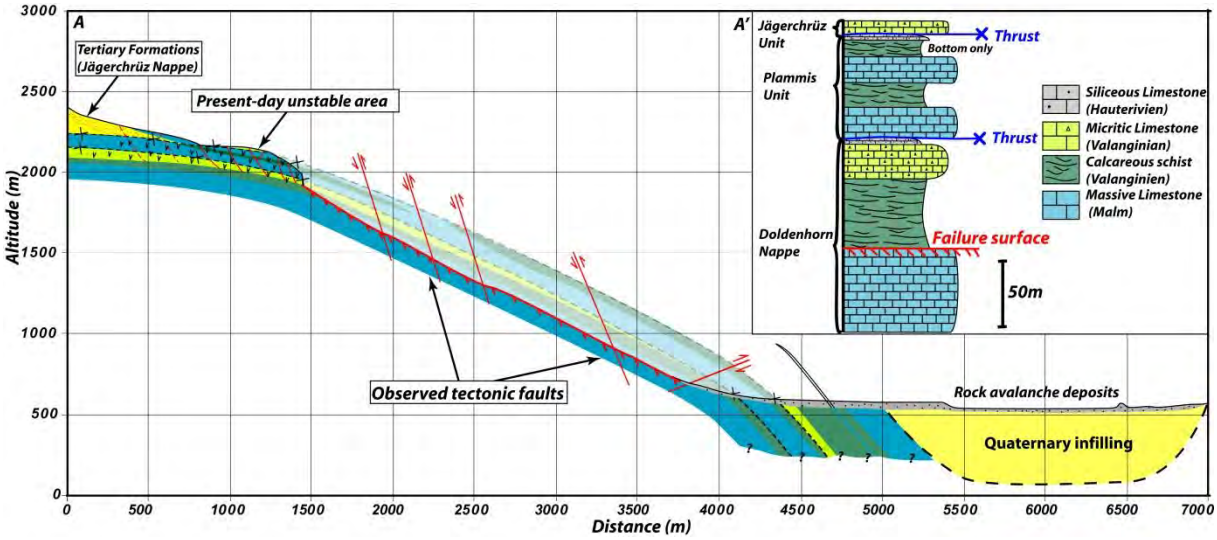

Figure 4.2-4: Geological cross-section through the scar area of the Sierre rock-avalanche. The location of the faults and the thickness of the different lithological formations were projected on the cross-section from the outcrops located in the adjacent areas.

4.2.6.2 Ductile structures

At least five different tectonic phases were identified in the Helvetic Nappes (Burkhard 1998). However, the identification of more than three phases within the same areas was never observed. In the study area,

based on outcrops investigations, two main ductile deformation phases were identified. The most evident deformation phase (Phase D1) is marked by folds displaying a gentle to open interlimb angle and can be observed both at metric and at hectometric scale. The fold axis plunges generally 20°-30° toward 245°. According to Burkhardt (1988) these folds can be related to the main phase of thrusting and deformation affecting the Doldenhorn Nappe.

The second deformation phase is less evident at the outcrop scale and it was observed in few outcrops only. It is marked by folds characterized by a close to thick interlimb angle that create small scale undulations on the bedding planes. The kink-style folds indicate a more brittle behaviour compared to the tectonic phase D1 (Figure 4.2-5b). Folds axes plunge 10°-20° toward 320°. At the slope scale, it forms an undulation oriented NNW-SSE more evident at the bottom of the slope and that progressively disappears in the upper part. The orientation fold axis (NW-SE, opposite of the main fold axis direction) and the folding style suggest that these structures are probably related to late Tertiary dextral strike-slip shear movements along Rhone-Simplon fault.

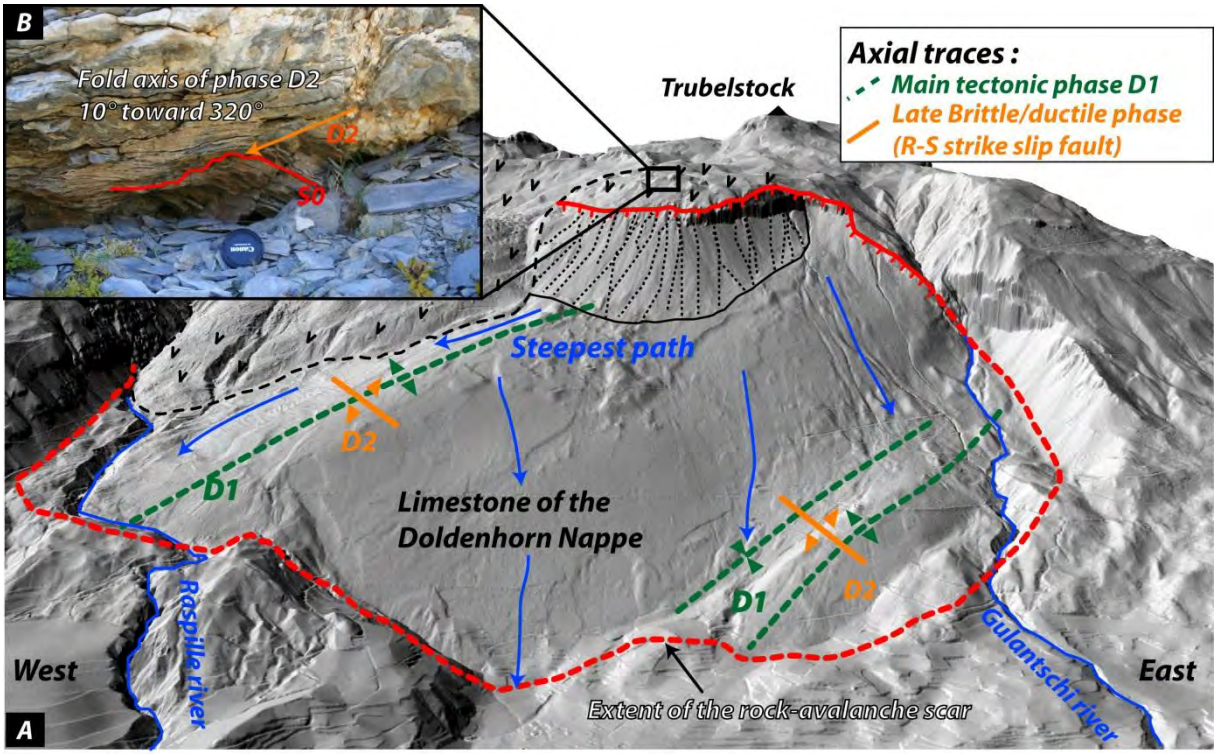

Figure 4.2-5: Ductile tectonic features identified in the Sierre rock-avalanche area. a) General 3D view of hectometric folds visible on the rockslide scar. Note in particular the considerable impact of folds belonging to Phase D1 on the morphology of the rockslide scar. b) Field example of folds associated to tectonic phase D2 creating small-scale undulations.

4.2.6.3 Brittle structures

Brittle structure analyses have been performed through field investigation in the different portions of the study area (Figure 4.2-6a). Attitude and geometrical characteristics (spacing, persistence, roughness and infilling) of the different discontinuity sets have been analysed within 13 structural stations following the methodology proposed by ISRM (1978). Four main discontinuity sets (J1, J2, J3 and J4) and the bedding planes were recognised (Figure 4.2-6b). Discontinuity sets J1 and J2 were recognized in all studied outcrops, whereas J3 and J4 were detected only in few outcrops located in the lower portion of the slope.

Except J4, all the detected discontinuity sets show a steep dip angle (Figure 4.2-7a). Specific geometrical characteristics of the detected discontinuity sets are reported in Table 4.2-1. The persistence and spacing estimations for discontinuity sets J1 and J2 indicate a medium to high persistence (3-20 m) and moderate spacing (20-600 mm) on the whole study area. Besides, J3 and J4 show a low persistence and a high variable spacing. Bedding planes display a variable spacing depending on the considered lithology. In Malm limestone, spacing ranges between 600-2000 mm and drastically decreased to 20-60 mm in Valanginian schist. Bedding planes were found to consist mainly of planar and smooth/slickensided surfaces. J1, J2 and J3 discontinuity sets show similar roughness characteristics with the discontinuity walls characterized by planar and rough faces. For all discontinuity sets, infilling is formed by calcite recrystallization. The block shape defined by the discontinuities can be described as tabular.

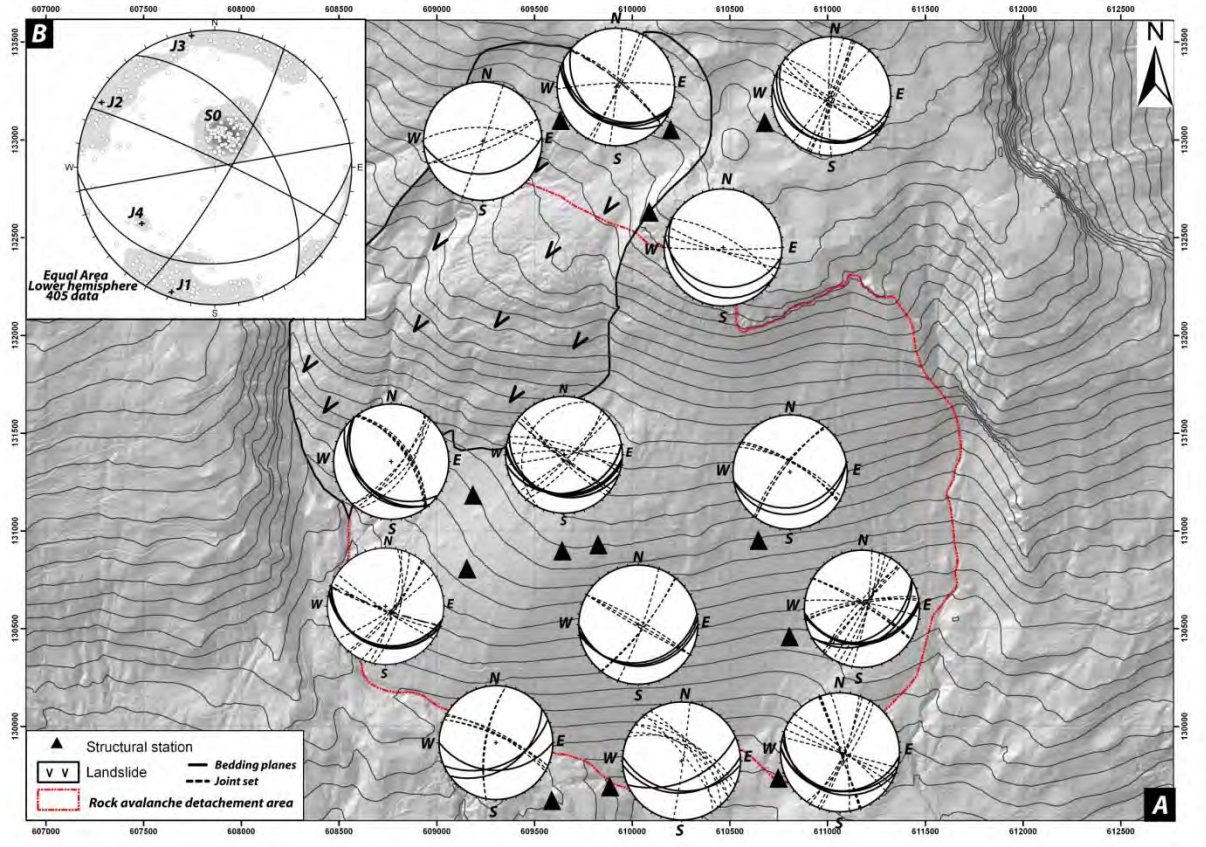

Figure 4.2-6: Analysis of the brittle structures identified on the Sierre rock-avalanche scar. a) Location of the different structural stations performed in the area. For each structural station a stereonet (lower hemisphere) displaying bedding planes (full line) and joint sets (dotted line) are presented. b) Stereonet summing up the structural measurements performed in the different structural stations. Note that the joint sets orientations remain quite uniform within the study area suggesting the presence of a single structural domain.

Discontinuity sets J1 and J2 show quite constant orientations through the study area. From a geometrical point of view, these joints display a fix relationship with the fold axis (NE-SW) of the main deformation phase D1: J1 is almost perpendicular to the fold axis and J2 is almost parallel. Kinematic indicators show that J1 set cut systematically the discontinuity set J2, suggesting a younger origin (Figure 4.2-7b). Discontinuity sets with similar orientations and kinematic evidences were observed in several locations within the Helvetic Nappes (Ustaszewski and Pfiffner 2008; Gasser and Mancktelow 2010) indicating that their origins is related to regional tectonic events. According to Gasser and Mancktelow (2010), it is

possible to correlate J1 discontinuity set to the development of tardive calcitic veins (type III described in Burkhard and Kerrich 1998) associated to a tardive extensional phase parallel to the fold axis.

Table 4.2-1: Main geometrical and geomechanical characteristics of the detected joint sets.

Name	***Dip direction***	***Variability***	***Spacing***	***Persistence***	***JRC***	***Infilling***
S0	193/23	14°	Variable	>20	4-6	-
J1	115/80	18	200-600	3-10/10-20	6-10	Calcite
J2	029/86	23	200-600	3-10/10-20	8-12	Calcite
J3	353/87	14	200-600	<1/1-3	12-14	Calcite

This tardive phase is related to the change in direction of overthrust shear (Dietrich, 1989). Besides, according to Burkhard (1988) and Gasser and Mancktelow (2010), J2 was formed during folding and thrusting phase of the Helvetic Nappes. Discontinuity set J3 is parallel to the main valley (ENE-WSW) and is probably related to strike-slip to normal faults movements along the Rhone-Simplon fault system.

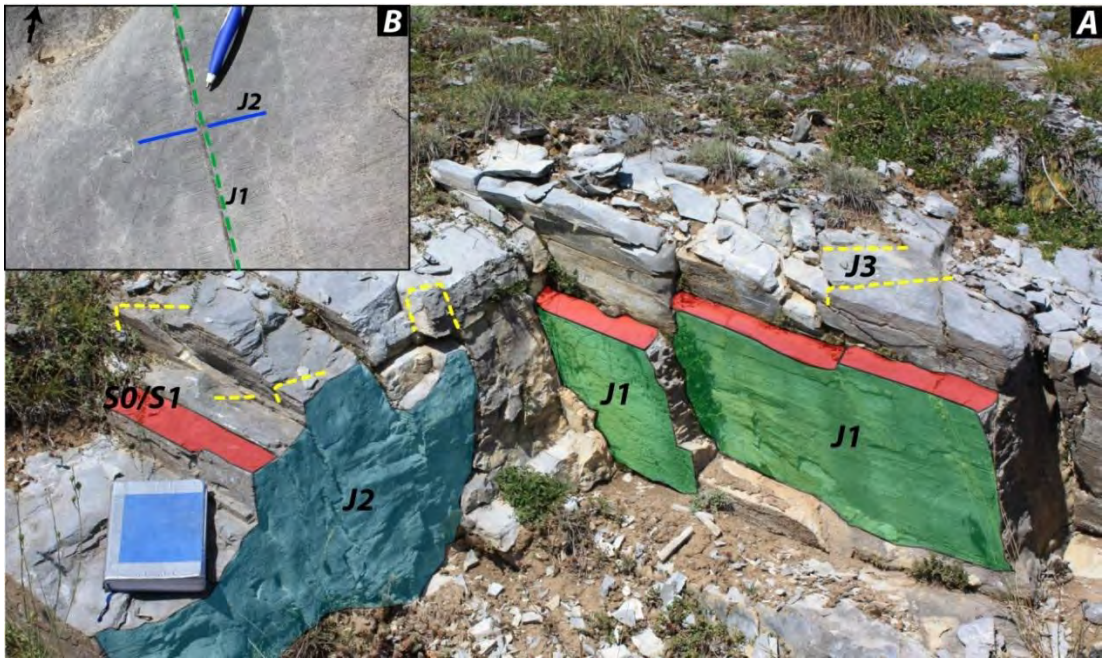

Figure 4.2-7: Field example of the joint sets detected on the Sierre rock avalanche scar. a) Outcrop displaying the presence of the three main joint sets. Note in particular the high persistence characterising joint set J1 and J2 compared to J3. b) Example of the kinematic relation between joint set J1 and J2. J1 systematically cuts J2 suggesting an older origin for J2.

4.2.6.4 Rock mass characteristics

The rock mass characteristics were analysed on the base of Geological Strength Index (GSI). The GSI classification (Hoek and Brown 1997) was developed to allow a field quantitative description of the rock mass quality based on structural and weathering condition of the rock mass. Figure 4.2-8 shows the distribution of the GSI values recorded on the different structural stations. The GSI estimates ranges from 15-25 for disintegrated and heavily broken rock mass to 55-65 corresponding to very block and partially disturbed rock mass. Higher GSI values (55-65) correspond to massive limestone outcrops. Uniaxial compressive strength obtained for this lithology by uniaxial test (Mathier pers. comm.) varies between 60-115 MPa. Lower GSI are mainly related to the Valanginian lithology where the closer spacing of the bedding planes (< 60 mm) and the fair to poor weathering grade generating bad to fair rock mass quality

(Figure 4.2-8a). For this lithology, field estimates of unconfined compressive strength indicate values between 40-65 MPa.

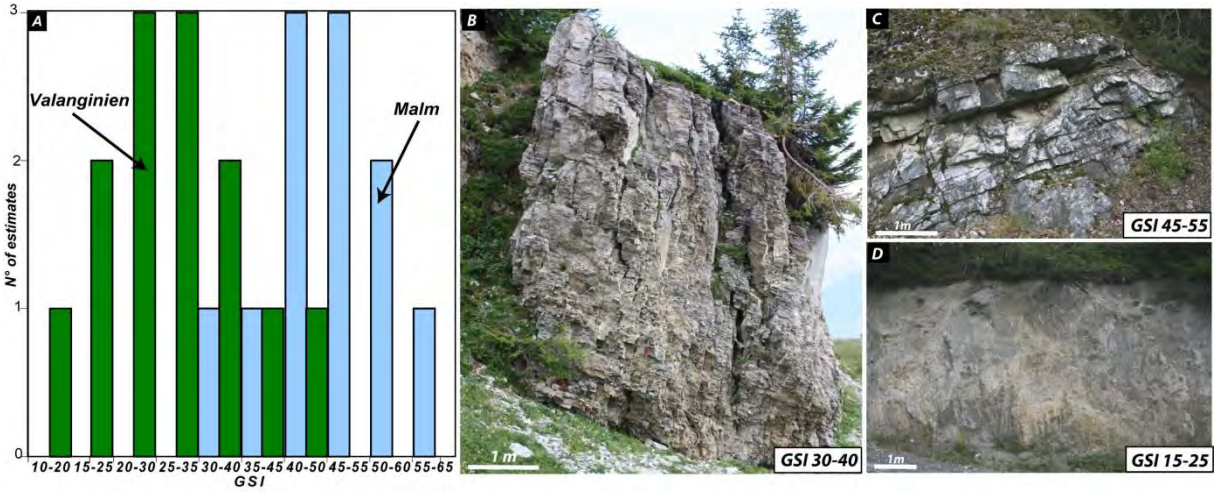

Figure 4.2-8: Rock mass conditions of the rocky outcrops in the Sierre rock avalanche area. a) Distribution of the GSI estimates as a function of the two main outcropping lithologies. b) Outcrop of calcareous schist (Valanginien) located in the upper portion of the scar. This outcrop corresponds to a GSI estimate of 30–40. c) Outcrop of massive limestone (Malm) located in the lower portion of the rockslide scar. The outcrop corresponds to a GSI estimate of 45–55. d) Outcrop of calcareous schist (Valanginien) located in the lower portion of the scar. Note the extremely small block-size and the important superficial weathering. The outcrop corresponds to a GSI estimate of 15–25.

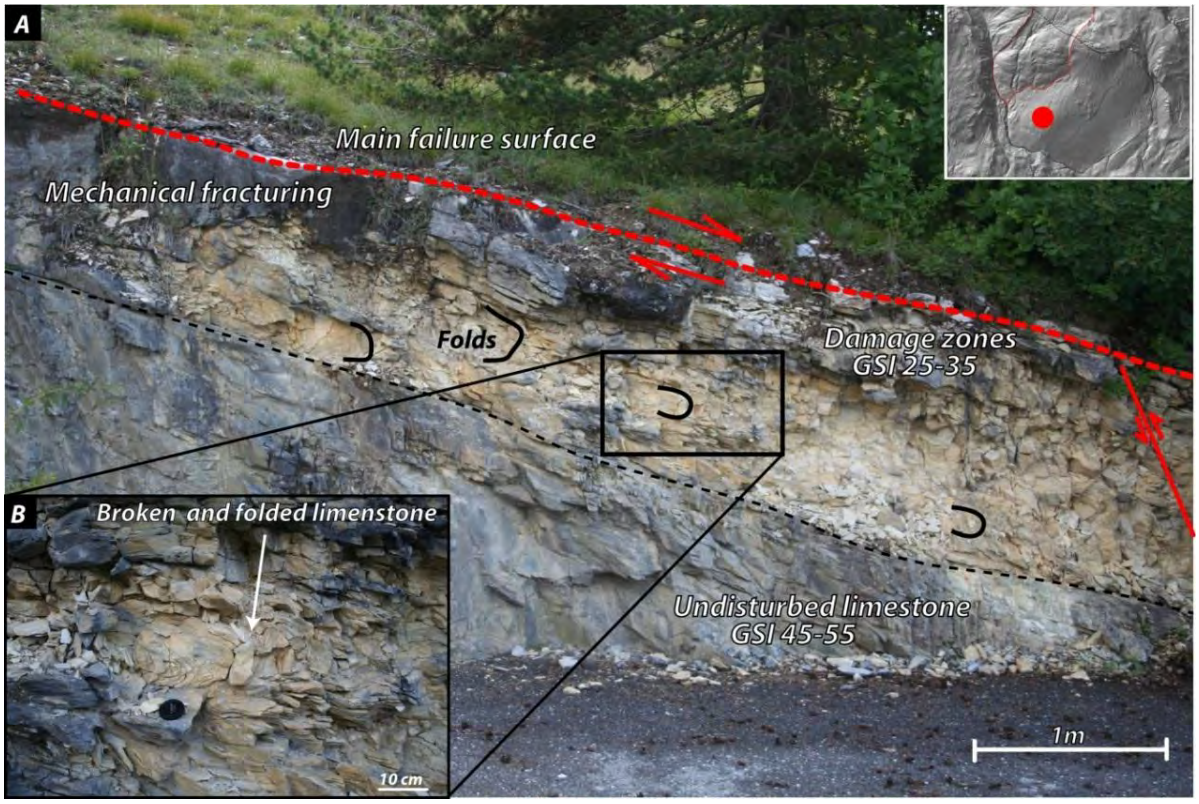

Figure 4.2-9: a) Detail of the failure surface of the Sierre rock avalanche. Note the presence of a damage zone within the first 1-2 m of the failure surface. b) Detail view of the damaged zone showing a poorly interlocked, heavy broken rock mass with the presence of small scale folds and partial rock recrystallization.

The lower GSI values were observed for the outcrops located at the bottom of the failure surface where the folded and weak rock mass is locally displaying centimetric scale kink-type folds (Figure 4.2-8). The

failure surface displays relative good rock mass quality (GSI 40-60). However, it is locally possible to observe an important rock mass quality degradation (GSI 25-35) of the Malm limestone within the first 0.5-1 m of the failure surface with the presence of small scale chevron-type folds (Figure 4.2-9). This local rock mass degradation might be related to friction and deformations that occurred during the rock avalanche displacement. Unlike the Kofels rock avalanche (Sorensen and Bauer, 2003) where thin bands of melted rock were observed, along the failure surface of the Sierre rock-avalanche there is no evidence that the mechanical heating was concentrated enough to produce rock melting.

4.2.7 INFLUENCE OF TECTONIC STRUCTURES ON THE INSTABILITY GEOMETRY

Based on geological cross section (Figure 4.2-4) and morphological observations it is now possible to highlight that the failure surface displays a complex concavo-convex shape. Figure 4.2-10 presents four cross-sections through the rock avalanche scar.

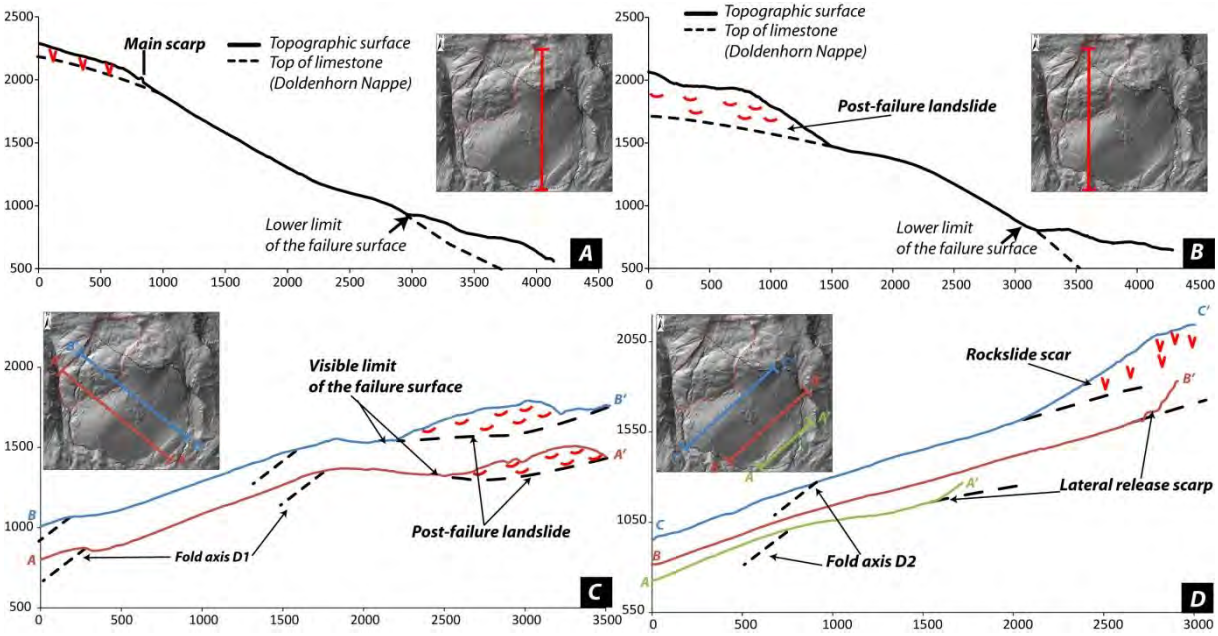

Figure 4.2-10: Cross-sections based on 2m DEM showing the influence of ductile tectonic structures on the shape of the rockslide failure surface. a), b) N-S cross sections showing the lateral variation of the shape of the failure surface from the eastern and the western portion of the scarp. In the eastern portion, the failure surface is almost planar but in the western portion it progressively changes to a convex shape according the orientation of the hinges related to deformation phases D1 and D2. c) Cross-section perpendicular to D1 fold axis displaying the relation between the failure surface morphology and the hectometric scale folds. d) Cross-section perpendicular to fold belonging to the folding phase D2. Note that at the slope scale, the influence of the folds associated to this tectonic phase is less evident.

It can clearly be underlined that the shape of the failure surface changes from the eastern side, where it shows a common concave form, toward west where it progressively changes into a convex configuration. On the central portion of the slope, the failure surface presents a planar dip slope configuration. This geometric change can be related to the presence of the hectometric-scale anticline oriented NE-SW and associated to the early folding phase (Phase D1). The existence of this tectonic feature leads to the clear separation between the lower eastern side and the upper western side of the failure surface. This separation is also shown by the cross-section parallel to the fold axis (Figure 4.2-10 and Figure 4.2-11c) and by different directions of drainage pattern characterizing the two sides of the failure surface. Additional complexity on the failure surface geometry are associated to tardive tectonic movements

(phase D2). Even if, the impact of this tectonic phase is less evident than for phase D1, it created large scale NW-SE undulation accentuating convex shape of the western portion of the scar by increasing the bedding plane inclination in the lower portion of the failure surface (Figure 4.2-10d).

The influence of brittle failure is particularly visible on the upper portion of the rock-avalanche scar. In this area, it is possible to observe several extensional gravitational morpho-structures (trenches scarp and counterscarps) related to the development of the rock-avalanche (Figure 4.2-11a). The comparison between the orientation of these structures and the main discontinuity sets is reported in Figure 4.2-11b and c. The close correspondence between discontinuity set J1 and the orientation of the morpho-structures indicates an important control of this joint set on the rear release surface of the different instabilities within the study area. The influence of the discontinuity set J2 is less evident on the morphology. However, as it can be observed in the eastern side of the instability (Figure 4.2-11a), J2 plays a fundamental role as a lateral release surface of the landslide occurred after the rock avalanche and also for the rock avalanche itself.

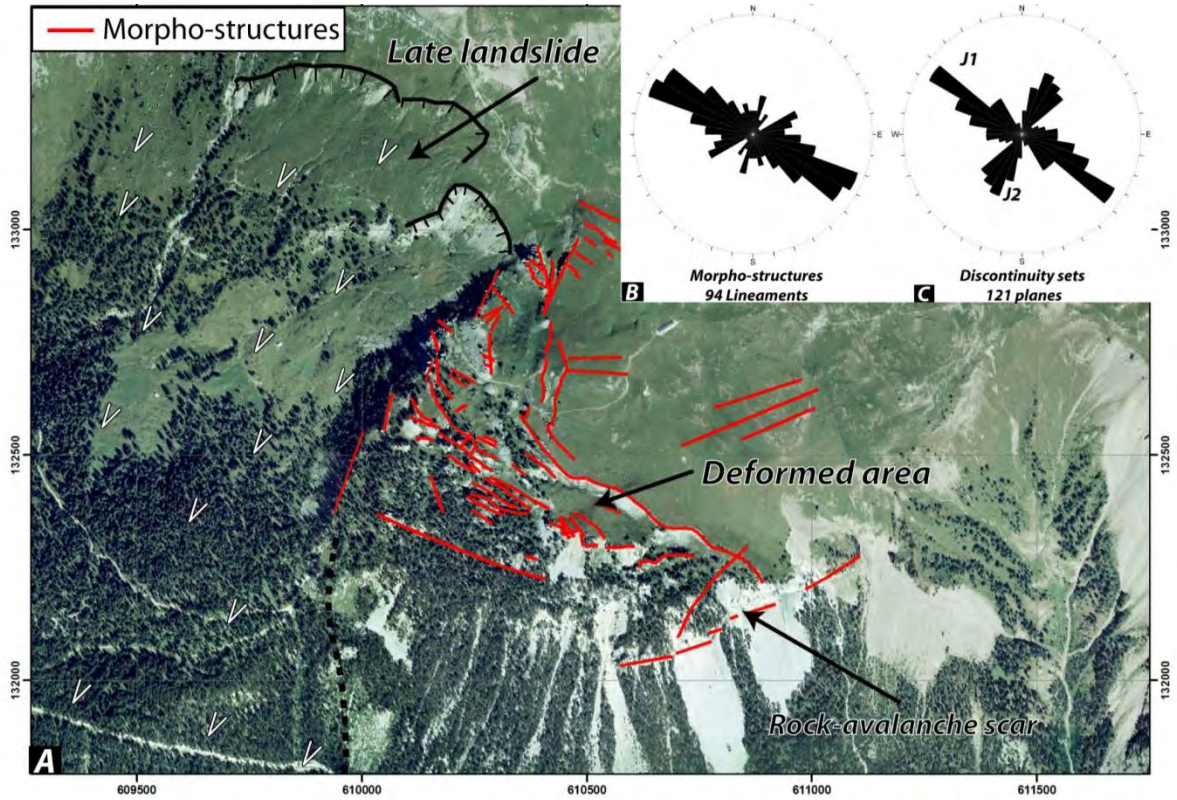

Figure 4.2-11: a) Orthophotos of the upper portion of the rockslide scar showing the presence of deformed area characterized by extensional gravitational morpho-structures. b), c) Rose diagram (10° interval) comparing morpho-structures (b) and joint sets orientations (c) in the upper portion of the rockslide scar.

4.2.8 EVIDENCES OF PRE-COLLAPSE DEFORMATIONS

In the lower portion of the slope, several outcrops show remarkable geological features indicating that important pre-failures deformation occurred before the development of the rock avalanches. A common feature, observed in almost all rocky outcrops located within the first 200-250 m from the failure surface, is the lower GSI values and the important tilting of the bedding planes. In this area, beddings show a dip angle varying between 75°-90° compared to the 30-40° characterizing the failure surface.

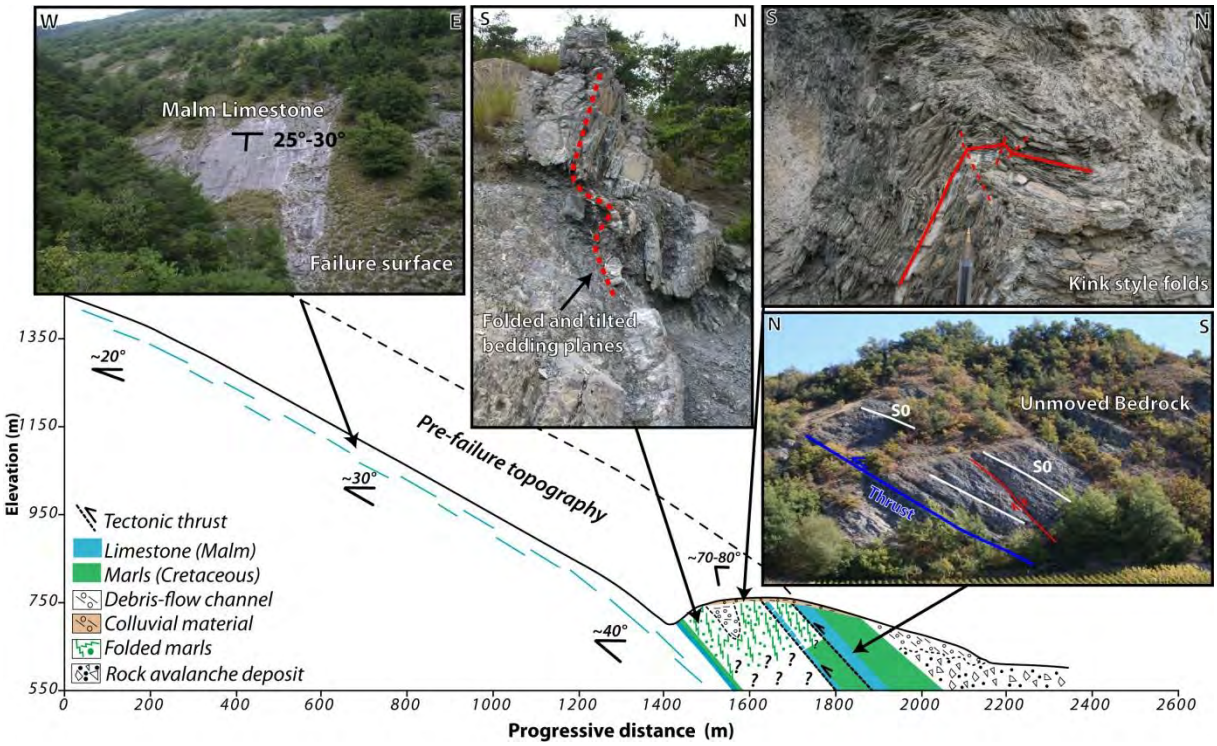

Figure 4.2-12: Cross-section through the lower portion of the rockslide scar displaying the different structures associated to the pre-failure movements preceding the Sierre rock-avalanche. It is interesting to note the formation of chevron folds and tilting of the bedding planes in the rocky outcrops located in the lower portion of the scar area.

This phenomenon is accompanied by chevron type folds affecting preferentially marl-rich layers and by a very low mean block size. Outcrops located at more than 250 m from the failure surface are not affected by these phenomena. They exhibit a bedding plan orientation (30-40°) in agreement with the regional trend and an undisturbed rock mass quality. Figure 4.2-12 displays a cross-section through the lower portion of the slope summarizing the different field observations. An example of complex deformed outcrops is reported in Figure 4.2-13. Here, the rock mass is completely disintegrated (GSI 20-30) and bedding planes are almost vertical (88°) displaying centimetric scale chevron folds. At the outcrop scale, these folds are disharmonic with small "décollement" faults parallel to the bedding. The fold hinges are completely broken with the presence of extensional fractures and several openings (Figure 4.2-13 and Figure 4.2-12b). Similar to what was observed by Chigira (1992) on DSGSD, detailed observations of the folds indicate that the axial surface is shaped like a card house (Figure 4.2-13b). The folding style and the orientation of the measured fold axes fold axes (0-10°toward 240-320°, sub parallel to the slope orientation) do not correspond to any tectonic phase observed in the area and suggest a gravitational origin for these deformations. In the west limit of the failure surface, another complex outcrop was observed (Figure 4.2-14c). In this area, the beddings show an important tilting (dip angle 75°-85°) compared to the dip of the bedding planes outcropping on the failure surface (Figure 4.2-14b). Associated to this phenomenon, the presence of titled (dip angle 55°-65°) glacio-lacustrine and fluvio-glacial sediments were also observed (Figure 4.2-14a). These deposits do not seem to be directly in contact with the tilted bedrock indicating a displacement from their initial position. Stratigraphically, these deposits are characterized by successions of silty/clay rhythmites that are irregularly intercalated with graded

sandy/gravel layers affected by several faults. For most of them, it was possible to define an inverse slip direction indicating that their development is related to a compressional regime.

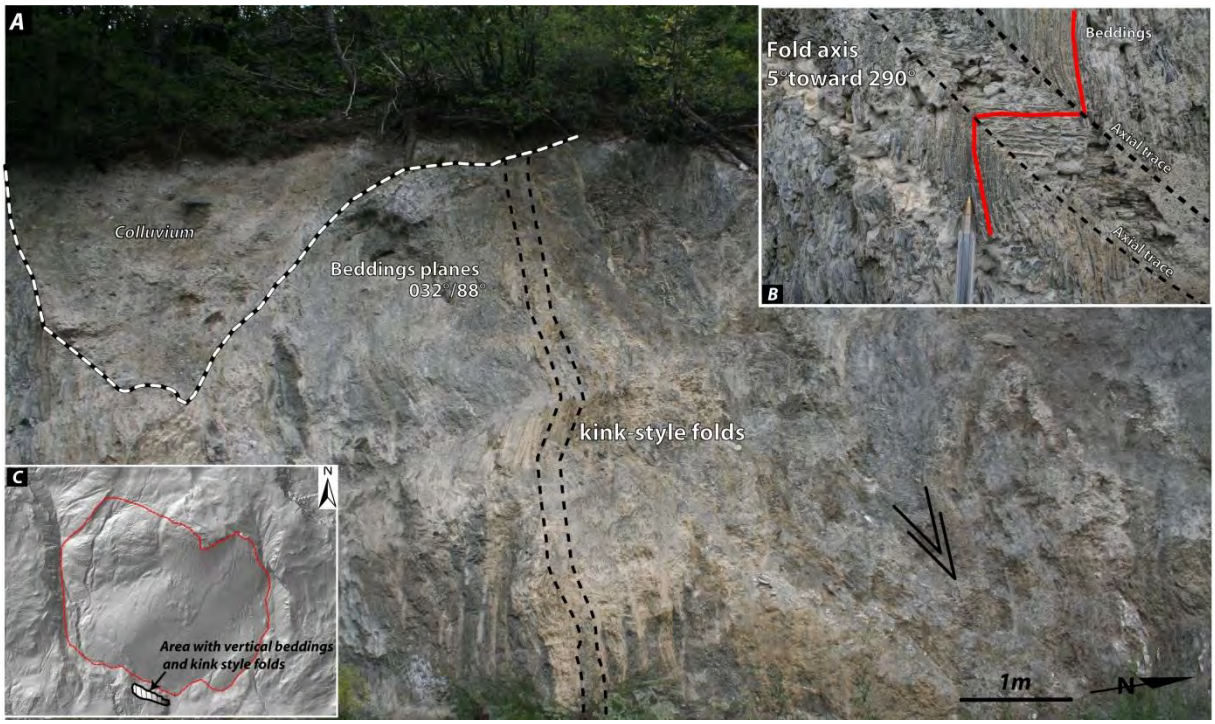

Figure 4.2-13: Deformed outcrops associated to gravitational movements preceding the development of the Sierre rock avalanche. a) General overview of the outcrop displaying very low rock mass quality and a tilted orientation of the bedding planes compared to general orientation of the bedding planes in the area. Decimetric–scale kink style folds are visible. b) Detail of the structures observed in the field showing the presence of centimetric–scale kink-style folds. c) Locations of the outcrop in relation to the extent rock-avalanche scar.

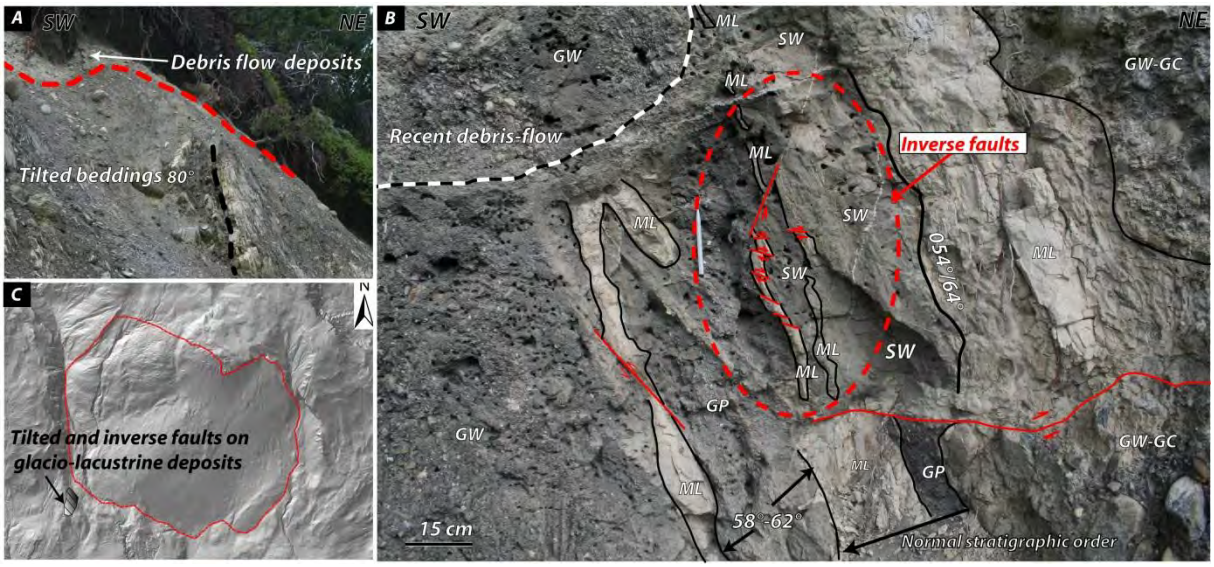

Figure 4.2-14: Deformed outcrops related to the development of the Sierre rock avalanche. a) View of tilted bedding planes (Valanginian lithology). b) Tilted fluvio-lacustrine deposits displaying the presence of inverse faults. Letters in the pictures correspond to USCS soil classification. c) Location of the outcrops.

Excluding an unlikely glacial re-advance reaching these altitudes, the creation of this inverse faults can be related to compressional regime at the bottom of the slope related to pre-failure movements of the rock-

avalanche. It indicates that this kind of structures and the increasing of the bedding plane dip angle are not related to tectonic deformations but associated to gravitational movements.

4.2.9 PRE-FAILURE TOPOGRAPHY RECONSTRUCTION AND VOLUME CALCULATION

The reconstruction of the pre-failure topography was performed by integrating structural and geomorphological observations in a modified version of the Sloping Local Base Level technique (Jaboyedoff et al., 2009). The SLBL method has been successfully applied to define the volume of the potential instabilities for both soil and rock slopes (Jaboyedoff et al., 2009; Travelletti et al., 2009; Pedrazzini et al., 2011). The modelling procedure is based on an iterative routine that progressively lowers the topography. This operation is performed by replacing the altitude of a DEM cell by the average altitude value of his direct neighbours (minus a given tolerance value if needed). A modified version of the SLBL technique also can be used to reconstruct the pre-failure surface. This is performed by inverting DEM. By this operation, the mountain peaks of the DEM became valley and vice versa. On this inverted DEM, the classical SLBL can be successively performed using all the points outside the landslide scar as fixed points and by varying the altitude of the points within the landslide surface. After the SLBL computation, the DEM is re-inversed to obtain the pre-failure topography (Figure 4.2-15).

For the Sierre rock-avalanche the application of this procedure is not straightforward and implies the following preparatory steps (Figure 4.2-15a and b):

1. Delimiting of rock-avalanche scar and define the anchor points (i.e. lithological limits, lateral cliff height) to constrain the SLBL calculation.
2. Restoring the early pre-failure surface (this implies the cleaning of the present-day failure surface from the rock-avalanche debris and late alluvial deposits).
3. Reconstructing the entire rock avalanche scar before the disturbance associated to the large landslide covering the western side of the rock avalanche scar. The reconstruction was performed by modifying the present-day topographic contours extracted from the DEM to fill the source area and to restore the lower slope (rock-avalanche scar) before the movements.
4. Checking the validity of the model based on lithological boundaries/morphology of the failure surface.

Several tests have been performed by changing the eastern limits of the rock-avalanche scar and by adding different tolerance in the SLBL calculation. Simple manual estimation obtained by the multiplication of the average thickness of the rock mass (200 m and 230 m) was also performed. The results obtained with different methods are reported in Table 4.2-2. The estimated volumes vary between 1.4-1.65 km^3 for the SLBL reconstruction and between 1.6-2.0 km^3 for the manual estimation. By assuming constant thickness, the manual estimation tends to be more conservative probably because the complex shape of the failure surface is not considered. The value is situated in between the previous estimates of Burri (1995) and Abele (1974) corresponding respectively to 1 km^3 and 2 km^3. Figure 4.2-15c and d show the simulation obtained by inverse SLBL calculation that presents the best correspondence with the geological and geomorphological constraints observed in the field.

Table 4.2-2: Estimation of the rock avalanche volume. Parameters and assumptions related to volume estimation based on «Manual" approach and on inverse SLBL calculation.

Method	***Calculated volume (Millions of m³)***	***Curvature tolerance***	***Assumption adopted***
Manual estimation	1.55	-	Maximal extent surface multiplied by constant thickness of 200 m.
Manual estimation	1.96	-	Maximal extent of the failure surface multiplied by constant thickness of 250 m.
Inverse SLBL calculation	1.15-1.25	-0.03/-0.05	Pre-failure surface limited by present-day lateral river and lower break-out zone.
Inverse SLBL calculation	1.55-1.65	-0.03/-0.05	Pre-failure surface limited by paleo-channels and preset day-lateral cliffs.

The estimated volume is about 1.6 km³. It is interesting to note that the maximal thickness of the unstable material (corresponding to 60-70% of the total volume) is concentrated in the western side of the failure surface, within the synform associated to deformation phase D1.

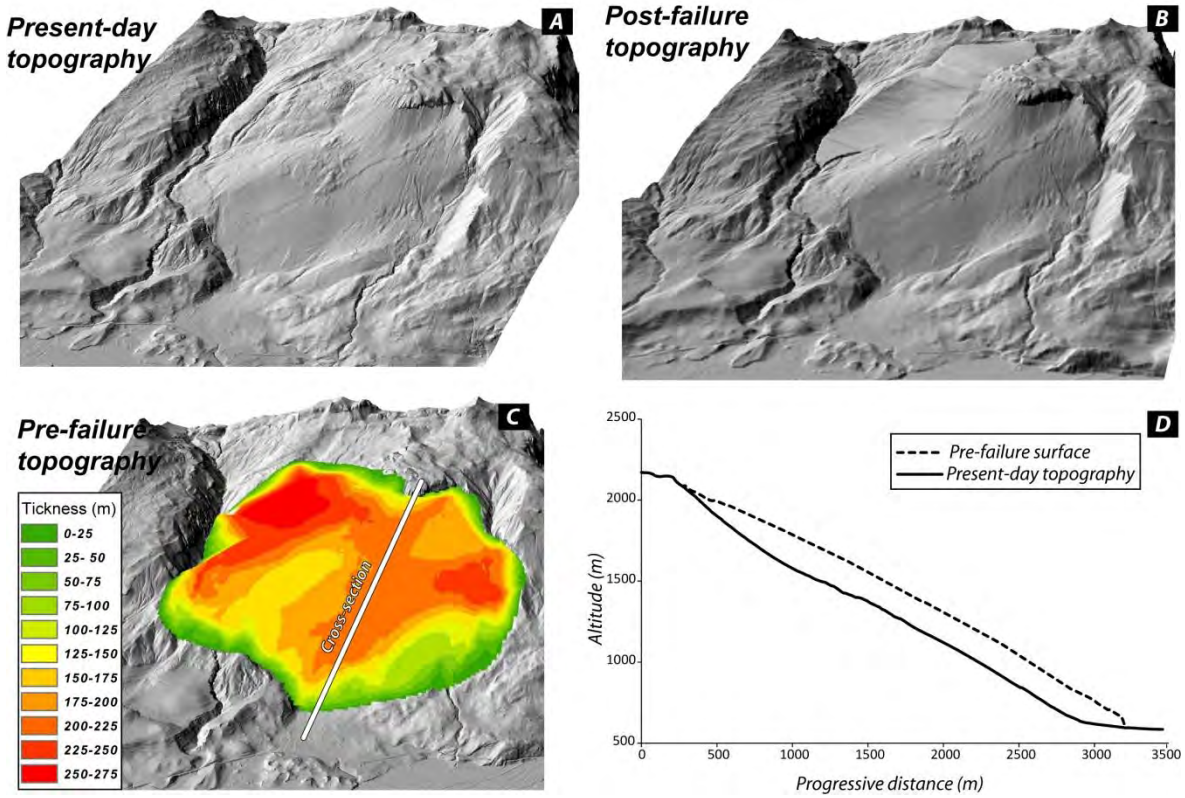

Figure 4.2-15: Pre-failure topography reconstruction of the Sierre rock-avalanche based on inverse SLBL calculation. a) 3D shaded relief view (2m DEM) of the present-day topography. b) Reconstruction of the early post-failure topography by before the disturbance associated to the large landslide covering the western side of the rock avalanche scar. c) Reconstruction of the pre-failure topography and estimation of the rock avalanche volume. d) Cross-section through the eastern portion of the rock-avalanche scar displaying the present-day and the pre-failure topography.

4.2.10 FAILURE MECHANISM ANALYSIS

The study of the potential failure mechanism was carried out by coupling field observations, limit equilibrium analyses and finite element numerical modelling. In order to propose a potential failure mechanism, the following key information derived from field analyses need to be integrated:

1. Pre-failure deformations are observed in the lower portion of the slope.
2. The average thickness of the failed mass is close to 200 m.

3. Paleo-channels, fluvio-glacial and glacio-lacustrine sediments are locally observed at the bottom of the slope.
4. A gently dipping tectonic fault is potentially present at the bottom of the slope.

Kinematic analyses based on detected discontinuity sets show potential planar sliding on bedding planes and toppling failures on J1 and J3. Some evidence of toppling mechanism was observed at the outcrop scale. However, spacing, persistence and hard calcite infilling of discontinuity sets J1 and J3 associated to the presence of a planar and smooth sliding surface indicate that this mechanism was not implicated in the development of the deformation at the scale of the slope. Concerning planar sliding all along the slope, the topography and the bedding planes exhibit an identical orientation indicating that the use of one mean value orientation for the topography for the kinematic analysis can lead to unrealistic failure mode. As observed on the Avalanche Lake slide (Evans et al., 1994), planar sliding became only possible at the slope scale by assuming intense fluvial erosion at the toe, which allows the bedding planes to daylight.
Field analyses at the bottom of the failure surface reveal the presence of paleo-channels and fluvial deposits suggesting the potential influence of fluvial erosion on the rock avalanche development. However, as observed in the eastern portion of the slope (Figure 4.2-3 and Figure 4.2-5), the major paleo-channels flow parallel to the slope direction. This indicates that the fluvial incision acting perpendicular to the slope is not a widespread phenomenon along the toe of the rock-avalanche and cannot explain the complete destabilization of the slope alone.

4.2.10.1 Limit equilibrium analysis

Based on the structural setting and the field evidence, the possibility to develop a buckling failure has also been tested. Buckling failure was observed and investigated in detail especially in surface coal mine (Cavers, 1981; Eberardth and Stead 1997). In this context, this failure mechanism involves frequently the failure of rock slab of few meters thick but can affect the slope face entirely.
Cavers (1981) proposes a series of limit equilibrium analyses for different slope configuration based on the Eulerian approach. More recently, different authors (Pant and Adhikary 1999; Stead and Eberhardt 1997; Tommasi et al., 2009) applied numerical techniques to investigate the sensibility of both geometrical and mechanical parameters on buckling failure modelling. The general geometric and geotechnical conditions that lead to the development of buckling failure are (Seijmonsbergen et al., 2005 and reference herein):

- Mostly tabular block shape.
- Same orientation and dip angle of both the main discontinuity and the topographic slope (dip-slope configuration).
- Inclination of the main discontinuity steeper than the basal friction angle.

In the case of the Sierre rock avalanche all the characteristics are observed. For this reason, a first series of simple sensitivity analyses of the possibility to produce flexural bucking failure was tested. In particular, the maximal thickness that can be mobilized by flexural buckling was investigated using simply limit equilibrium analyses as proposed by Cavers (1981).

The thickness of the zone affected by buckling is related to the elastic modulus of the rock, the length of the slope and the basal friction angle. Assuming a ratio of 0.5 (Cavers 1981) between the length of the slope subject to buckling and the total slope length, the maximal slab thickness (d) is given by:

$$d = \sqrt{\frac{l^3 2.25\left(\gamma sin\alpha - \gamma\, cos\,\alpha tan\Phi_j\right)}{\Pi^2 E}}$$

Where (l) is the length of the slope (m), (γ) is the unit weight (KN/m^3), α is the slope angle, (Φ_j) is the friction angle along discontinuity and (E) the young modulus. As shown by Stead and Eberhardt (1997), the limit equilibrium approach of Cavers (1981) is rather simplistic and flexural buckling failure of an unjointed slab is not a likely failure mechanism except for very thin rock mass. Nevertheless, it can be used to obtain a first estimate of the maximal thickness of the involved rock mass.

Figure 4.2-16 shows the results obtained through the sensitivity analyses. It can be clearly observed that, using the elastic modulus calculated for Valanginian schist (Vinard et al., 1993) or Malm limestone (Mathier pers comm.), the maximal thickness that can be destabilized by flexural toppling is less than 100 m. This indicates that Sierre rock avalanche was not developed by buckling failure only and the influence of other mechanism of destabilization is required to explain the thickness of the sliding slab. This does not exclude the important contribution of bulking mechanism especially on the early deformation phases. Indeed, in large slope instabilities particularly, flexural buckling phenomenon is commonly observed (Chigira, 1992) and associated to long term gravitational creep and can frequently precede catastrophic failures (Wang et al., 2003).

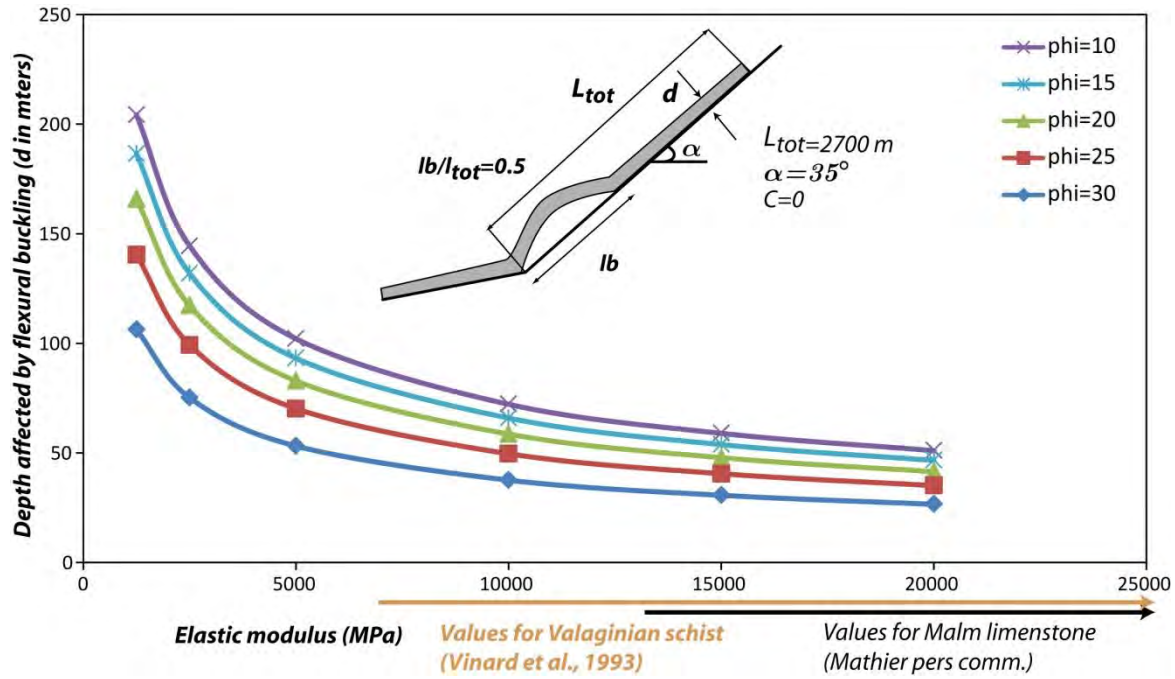

Figure 4.2-16: Relation between the Elastic modulus of the intact rock and the potential thickness of the slope affected by flexural buckling for different friction angles according to the limit equilibrium equation proposed by Cavers (1981). Note that adopting representative values the maximal thickness that can be destabilized by flexural toppling is always less than 100 m and cannot explain alone the development of the Sierre rock avalanche.

4.2.10.2 Numerical modelling

In order to investigate the potential failure mechanism and the observed deformations along the slope more in detail, sensibility analyses have been conducted using 2D finite element analyses (Phase^2 7.0 code, Rocscience 2010). A main advantage of this finite element technique is the possibility to model a wider range of continuous and discontinuous rock mass behaviours by introducing explicitly joints and joint networks in order to determine the initial failure mechanism. The main inconvenience is the difficulty to model large strains or complete separation of blocks (Hammah et al., 2008). A Mohr–Coulomb elasto-plastic yield criterion was used to simulate the response of the rock mass. Geomechanical properties of rock masses and joints (Table 4.2-3 and Table 4.2-4) were obtained through standard rock mass characterisation based on field analysis (Hoek and Brown, 1997) and by laboratory data obtained for similar lithologies (Vinard et al., 1993; Mathier per. Comm).

Table 4.2-3: Rock mass properties adopted in finite element model.

Parameters	***Doldenhorn limestone***	***Doldenhorn schist/marls***	***Jägerchrüz limestone/marls***	***Ice***
Young modulus (GPa)	25	20	25	10
Poisson ratio	0.33	0.3	0.3	0.3
Density (kg/m^3)	2700	2600	2700	900
Rock mass friction angle (°)	42	32	380	-
Rock mass cohesion (MPa)	2	0.5		-
Rock mass tensile strength (MPa)	0.1	0.1	0.1	-

The model was divided in three main sectors (Doldenhorn limestone, Doldenhorn/Plammis marls and schist and Jägerchrüz limestone and marls) according to the lithological and the tectonic setting (Figure 4.2-17a). Progressive deglaciation (6 stages) was simulated starting from the maximal ice elevation reached during the last glacial maximum (2100 m) based on Kelly et al. (2003).

The presence of lacustrine deposits at the bottom of the slope suggests saturated conditions of the lower portion of the slope after the complete valley deglaciation. Hence, water table level was explicitly integrated in the model. The in-situ stress ratio (horizontal to vertical stress ratio) was assumed to be 0.5 according to previous geomechanical analysis in the area (Eberhardt et al., 2004) and according to a fault plane solution of seismic events analysed by Kastrup et al. (2004), suggesting a strike-slip to normal faulting regime.

Table 4.2-4: Joint sets properties adopted in in finite element model.

Joint parameters	***Set S0***	***Set J1***	***Set J3***	***Basal fault***
Joint normal stiffness (GPa/m)	10	10	10	10
Joint shear stiffness (GPa/m)	1	1	1	1
Joint friction angle (°)	20	30	30	15
Joint cohesion (MPa)	0	0.1	0.1	0
Joint tensile strength (MPa)	0.05	0.05	0.05	0.01

In order to examine the influence of the different structural elements, five different models were analysed separately. In the first configuration, the geomechanical model was run without introducing any master joint (Figure 4.2-17b). Results show the development of tensile strength where the bedding steepens, indicating an important stress concentration related to the topographic/structural configuration. These two zones correspond to the scar and to the lower limits of the rock avalanche. In the upper portion of the slope, which corresponds to the rock avalanche scar, important shear strain deformations are observed

and extend further behind. The modelled displacements are small (< 1m) with vectors directions orientated parallel to the slope.

In a second series of models, the J1 discontinuity set was explicitly introduced on the Valanginen Layer. Owing to numerical constraints, the real average spacing of the discontinuity sets was multiple by a factor of 50 (Figure 4.2-17c). The introduction of this joint set increases both the tensile strength at the bottom and the movements along the unstable slab. In the lower portion of the slope, which corresponds to the topographic convexity, bulking-like deformations are visible. In the same area, inverse movements along J1 allow clockwise tilting of the bedding planes as observed in the field. However, the general displacements vectors still remains parallel to the slope.

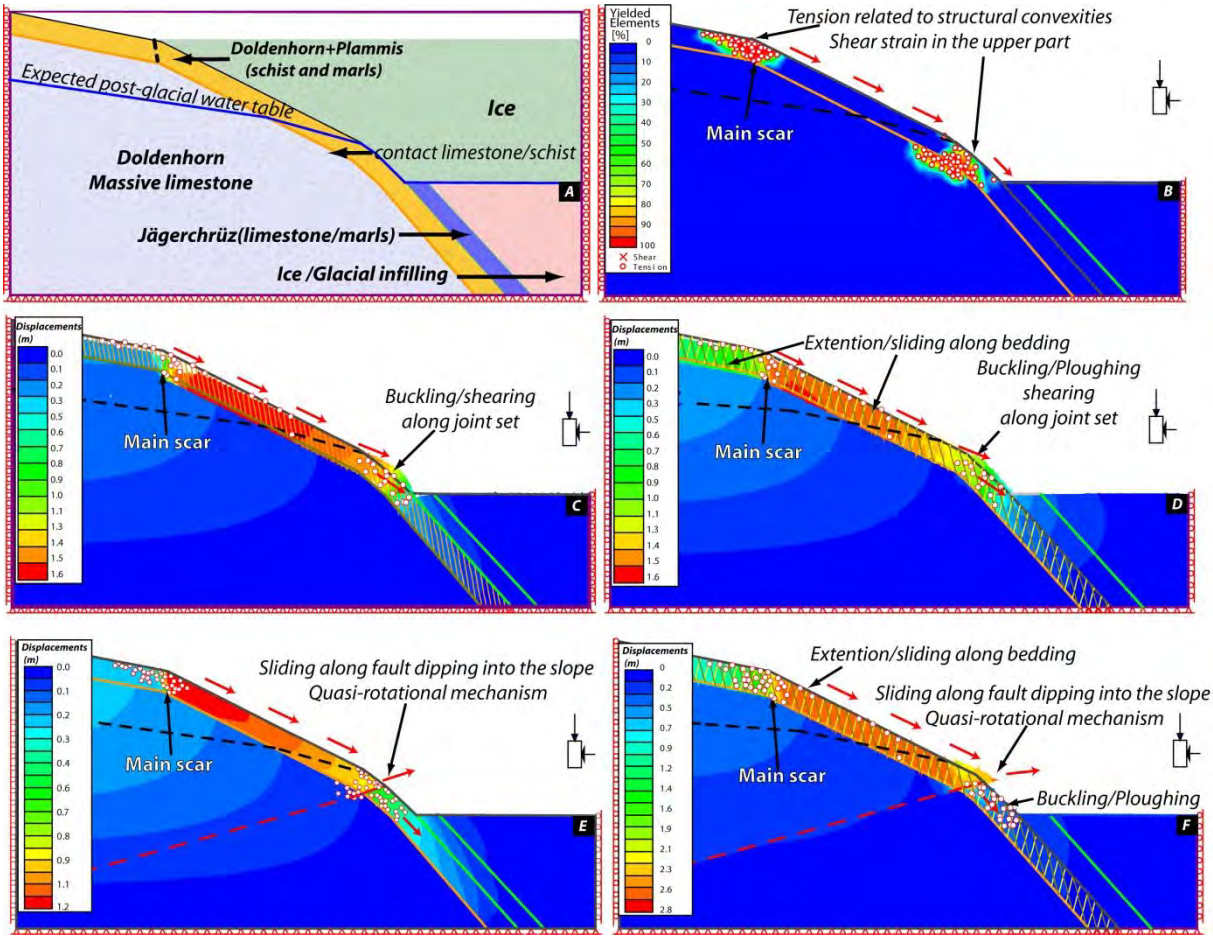

Figure 4.2-17: Finite-elements model of the post-glacial the destabilisation leading to the development of the Sierre rock avalanche. a) Simplified cross-section and subdivisions of the model according to the different tectonic units presents in the area. The ice elevation is based on the reconstruction performed by Kelly et al. (2003). b) Distribution of yielded elements in a simple model without the introduction joint sets. c) Displacements obtained by introducing joint sets plunging into the valley direction. d) Displacements magnitude and directions obtained by introducing a joint set plunging into the valley direction and a joint set plunging into the slope. e) Displacements magnitude and directions obtained by introducing a basal fault gently dipping into the slope at the bottom of the slope. f) Displacements magnitude and directions obtained by introducing a basal fault at the bottom of the slope and two joint sets.

A third series of model was run by introducing two sub-vertical joint sets (100 m spacing for both) to simulate discontinuity sets J1 and J3 (Figure 4.2-17d). In this case also, both buckling and ploughing-like deformations are observed in the lower portion of the slope. On the other hand, in this model deformations develop also behind the rock avalanche scar in agreement with the large scarps and

trenches observed in the field (Figure 4.2-11). Nevertheless, the main movement direction still remain parallel the main slope orientation.

Another series of model have been carried out by introducing tectonic faults identified by Bugnon (1986) on the outcrop close the rock avalanche scarp (Figure 4.2-17e). This fault shows a similar orientation that discontinuity sets J4 which was identified at the bottom of the slope even if it displays a shallower dip angle (15°-25°). Geomechanical modelling assuming residual friction angle values of 15° along the basal faults shows the development of a quasi-rotational failure mechanism (Stead and Eberhardt 1997). In this model, the movements are concentrated on the portion of the slab located between the two convex areas. The presence of the fault and the absence of persistent discontinuity set reduce the deformation at the bottom of the slope. In particular, the clockwise rotation of the bedding planes and buckling ploughing deformation cannot be reproduced by this model.

In the last series of models, both persistent discontinuity sets and a basal fault were explicitly integrated in the model (Figure 4.2-17f). Result shows a good agreement between the field observations and the numerical results. Compared to the previous models the introduction of persistent discontinuity sets J1/J3 allows the development of buckling and ploughing deformations below the fault plane and the extension of the deformations behind the rock-avalanche scar. Direction of modelled movements are constrained by planar sliding along bedding plane all along the failure surface and by quasi-rotational mechanism at the bottom of the slope promoting movement directed out of the slope. The calculated displacements are almost two times larger than the other models indicating the capability of this structural configuration to develop larger deformations.

4.2.11 CHARACTERISTICS OF THE ROCK AVALANCHE DEPOSITS

4.2.11.1 Geometry

The Sierre Rock avalanche deposit displays an L-type configuration (Nicoletti and Sorriso Valvo 1991). An important fraction the rock avalanche deposit is concentrated at the bottom of the slope where they cover entirely the Rhone valley width (Figure 4.2-18a). The rock avalanche then propagated toward SW occupying a planar surface of about 24-26 km^2. The proximal deposit is characterized by a hummocky morphology (cone-shaped or truncated cone-shaped hills formed by rock avalanche deposits). The calculated fahrböschung angle is around 6.5° (Δh = 1700 m, ΔL = 15000 m). The estimation of the volume of the deposit is difficult owing to the important reshaping performed by the Rhone River since the rock avalanche occurrence.

Several boreholes drilled for geotechnical purposes and described in Burri (1997) indicate the presence of several meters of paleo-channels filled by fluvio-glacial sediments incising locally the rock avalanche deposits by more than 20-30 m. In the proximal area, rock-avalanche deposits are less eroded, the small hills generating the hummocky morphology can reach an altitude of 80-90 meters above the actual river elevation. In the distal part, the maximal elevation above the alluvial plain of the sparse hills is always less than 45 m. According to these observations, a rough estimation of the volume can be assessed assuming an average thickness of 90 m for the proximal deposits (10 km^2 below the main scar) and 60 m for the central and distal part (16 km^2). The calculated volume is about 1.9 km^3 and is 20% greater than the

volume estimated by pre-failure topography reconstruction, which is in good correspondence with the SLBL calculation assuming the volume expansion between the deposits and the material in place.

4.2.11.2 Debris characteristics

According to Burri (1997), the texture of the rock-avalanche deposits is not homogenous as two main deposits facies can be differentiated: the structured (1) and the chaotic facies (2). The structured facies is characterized by the presence of large (decametric to hectometric scale) blocks separated by a sandy/silty matrix (Figure 4.2-19 a and c). The larger-blocks are mainly formed by calcareous marls (Valanginien) or by massive limestone (Malm). The main particularity of this facies is the preservation of the original structure of the rock mass, in particular the preservation of the bedding planes and of the sub-vertical discontinuity sets (J1 and J2 sets). This facies is particularly encountered in the proximal portion of the deposit where most of the observed hummocks are formed by a single large block. Toward the distal and the northern portion of the deposit, the large intact blocks disappear progressively.

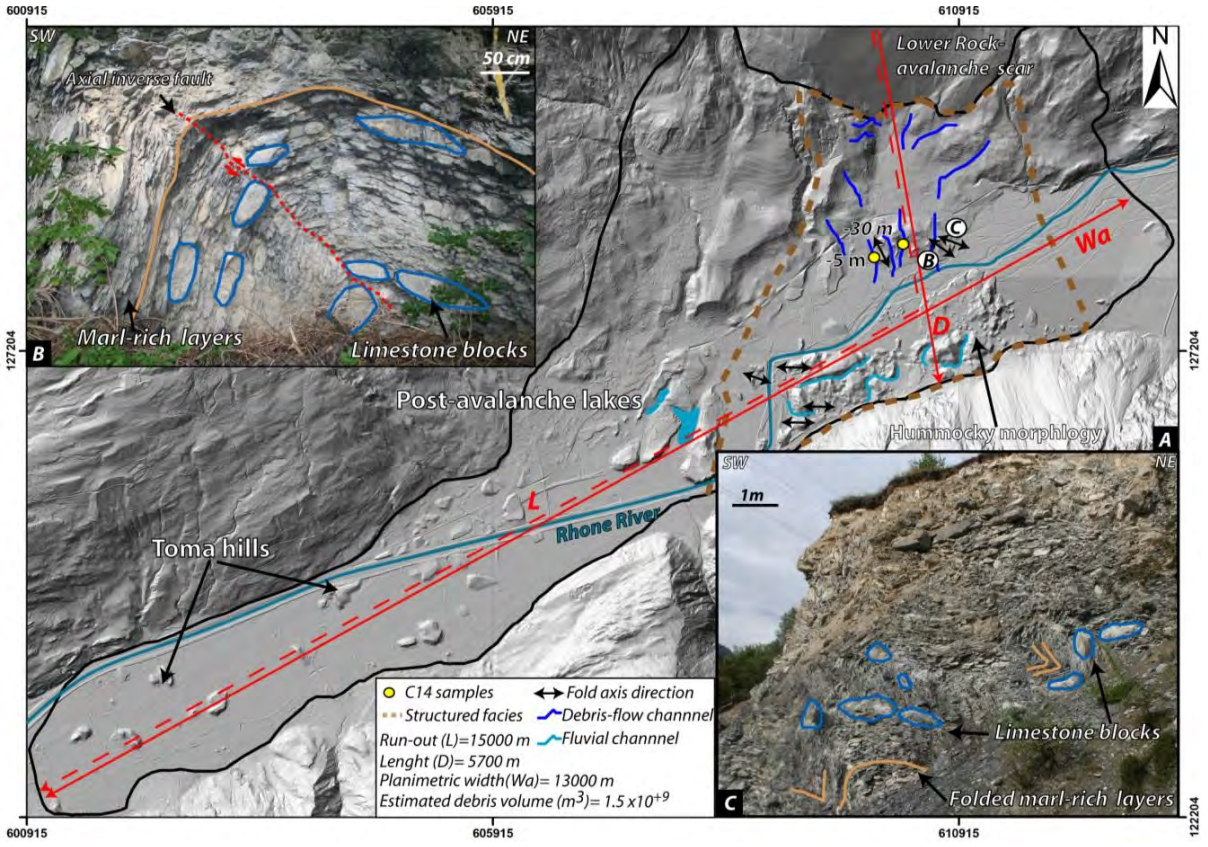

Figure 4.2-18: Overview of the geometrical and morpho-structural characteristics of the Sierre rock-avalanche deposits. a) Shaded relief view of the run-out area and orientation of the folds axis observed in the proximal portion of the deposit. Letters correspond to the location of picture (b) and (c). b) Metric scale gravitational folds observed in the proximal portion of the deposit. Note that more competent layers (massive limestone) are completely broken and form metric-scale blocks. c) Decimetric to metric-scale folds showing the different behaviour between marl-rich and limestone layers.

Analyses of the structures within the large preserved blocks reveal the existence of centimetric to metric folds affecting the bedding planes, principally when marl rich interbeds are present (Figure 4.2-18b and c). The fold hinges are characterized by the presence of several inverse faults and by fragmented limestone layers forming decametric to metric scale “boudins”. The folds axis orientation is quite variable (Figure 4.2-18a) but is globally sub-perpendicular to the run-out direction. These characteristics

associated to their locations within the deposits (mainly in the proximal portion of the deposit) suggest that these folds were created by the propagation of rock-avalanche.

The chaotic facies is characterized by limestone and marly-limestone blocks embedded in a silty to sandy matrix (Figure 4.2-19b). The block size varies from less than 1 m^3 to more than 100 m^3. Blocks of all scales are completely disintegrated but they often maintain their initial form suggesting the widespread development of the "jigsaw" phenomenon (Ui et al., 1986). The proportion of blocks varies between the observed outcrops and tends to decrease in the distal part of the deposits. In the proximal zone the chaotic facies displays a clast-supported texture. Inversely, in the distal part the matrix supported texture predominates.

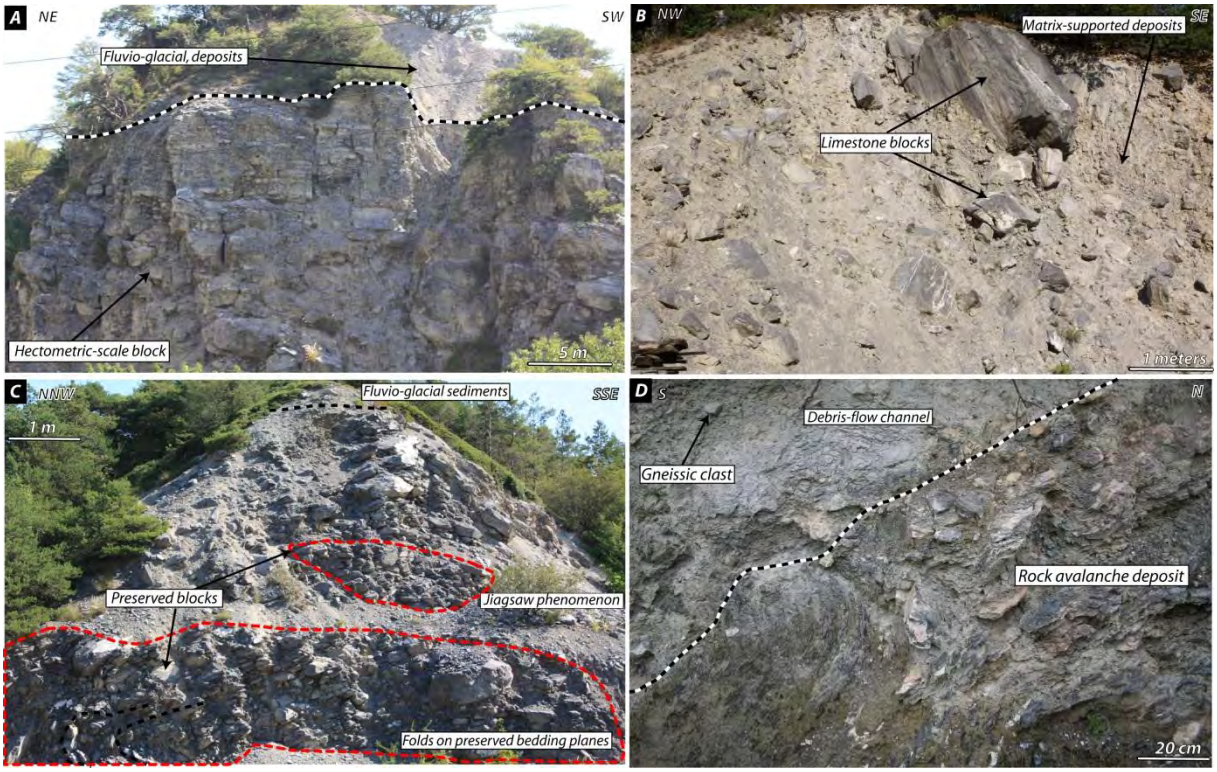

Figure 4.2-19: Characteristics of the rock avalanche deposits. a) Large intact hectometric block located in the proximal portion of the deposit (structured deposit facies). b) Decametric to metric scale limestone and marly-limestone blocks embedded in a silty to sandy matrix typical of the chaotic facies. C) Jigsaw phenomenon and gravitational folds within a decametric scale block in the distal portion of the deposit. d) Contact between the rock avalanche deposits and a channelized debris-flow deposit in the proximal portion of the rock avalanche deposit. Note that the debris flow deposits are characterized by the presence of clasts of different lithologies.

4.2.11.3 Post-collapse deposits

At the top of the rock-avalanche deposit, at least two different type of sediment can be differentiated. The first is represented by a roughly stratified sequence of silty sand and gravels. The clasts are formed by a great variety of rocks including gneiss, amphibolite and limestone. These sediments are particularly visible on the proximal portion of the deposits where they form a sort of cap that cover the cone-shaped hills (Figure 4.2-18a). Burri (1997) suggested that these deposits have a fluvio-glacial origin and are related to the Rhone river activity after the rock-avalanche.

The other types of post collapse deposits involves centimetric to metric blocks embedded in silty matrix, quite similar to the chaotic facies forming some parts of the rock-avalanche deposits. Clasts are formed by

different type of rocks and are often striated. The stratigraphic relationship with the rock-avalanche deposits is frequently difficult to establish because these sediments can be found above but also within the rock-avalanche debris. These deposits were interpreted by previous authors (Burri, 1955 and 1997; von Poschinger 2002) as glacial till that cover and/or that were incorporated during the rock-avalanche advance. These interpretations create several difficulties for the explanation of environment where the rock avalanche took place. In other to explain the presence of these sediments, these authors were forced to invoke an important glacier re-advance covering the bottom of the Rhone valley or a significant entrainment of a till-like substratum.

In this study, this type of deposit was found in association to paleo-channels incising the proximal portion of the rock-avalanche deposit (Figure 4.2-19d), suggesting that this type of deposits represents the material transported by debris-flow descending from the lateral tributary valley. This interpretation is confirmed by the observations done during the construction of the Hubil road tunnel, where several channels filled by this type of material were found to incise the rock-avalanche deposits at more than 30 m below the surface (Berthod pers. Comm.). In the central portion of the Rhone valley, Schoneich et al. (1998), based on several ^{14}C dating on alluvial fan deposit indicates that the post-glacial period was characterized by an important debris flow activity.

Within two debris-flows channels, crossed by the Hubil road tunnel, two large fragments of wood were found at respectively -5 m and -30 m below the ground surface. The dating of this wood was assessed by radiocarbon dating (^{14}C) performed using atomic mass spectrometry technique at the ETHZ facilities. The non-calibrated ages for the two samples are 8620± 40 BP for the deeper one and 8550 ± 40 BP for the shallower sample (Table 4.2-5). The deeper samples give an older age indicating a continuous debris flow activity incising/filling of the rock-avalanche deposits during the end of the Boreal chronozone. These data represent also the only available data defining a minimal age of the Sierre rock-avalanche.

Table 4.2-5: Characteristics and ^{14}C dating obtained by the two pieces of wood sampled in a debris-low channel crossing the proximal portion of the rock avalanche deposit.

Sample code	*Quantity (mg)*	*Depth (m)*	*^{14}C age BP*		*Delta C13 (‰)*		*Calibrated Age BC*	
ETH-39362	150	-5	8580	± 40	-28.8	± 1.1	7680	± 150
ETH-39363	600	-20	8620	± 40	-27.5	± 1.1	7730	± 160

4.2.12 DISCUSSION: DEVELOPMENT AND MECHANISM OF THE SIERRE ROCK-AVALANCHE

The studies performed on the failure surface area and on the deposits reveal complex destabilization history characterizing the early development and the run-out of the Sierre rock-avalanche. Based on these observations, the development of the rock-avalanche can be summarized in four distinct stages (Figure 4.2-20):

- ***Early pre-failure deformations***

This phase has been identified by field observations in the lower and upper portions of the failure surface, indicating that the slope experienced early deformation before the development of the rock avalanche (Figure 4.2-20). Compressional faults within glacio-lacustrine sediments and the presence of chevron-like folds are classical indicators of long term gravitational deformation induced by rock mass creep (Chigira

1992). Geomorphological analyses on the areas adjacent to the rock-avalanche scar (Figure 4.2-3) indicate that progressive rock creeping is widespread on the northern side of the Rhone valley. This phenomenon is promoted by the cataclinal configuration of the slopes and by intercalation of lithologies (i.e. massive limestone or marls) with a great contrast of competency, permeability and rock mass quality (Novara 1999; Pedrazzini et al., in prep.).

The influence of the regional tectonic configuration on the development of slope deformations is also visible at the scale of the slope. Simple numerical models show that the convex configuration, related to regional-scale folds geometry, induces important tensile stress concentrations at the points where beddings steepens and increases the development of gravitational deformations.

- ***Slab failure and early differentiation of the unstable mass***

The analyses performed to define the failure mechanism reveal that a simple failure mechanism cannot explain the early development of the destabilization. Even if residual shear strength could be assumed along bedding planes, the convex dip-slope configuration alone doesn't allow a simple translational planar sliding mechanism. Based on field observations and sensitivity analyses performed using numerical modelling, two distinct mechanisms can explain the failure: a classical planar sliding induced by (1) an important fluvial erosion and rock mass degradation at the toe of the slope and/or by (2) a quasi-rotational sliding on the gently dipping tectonic fault. These two mechanisms are not exclusive and a combination of the two can be imagined. Both mechanisms were probably facilitated by the high water pressure that characterized the lower portion of the slope. The lateral release surfaces were clearly controlled by orientation of pre-existing discontinuity sets (J1 and J3) and by fluvial erosion allowing the individualization of the potential unstable mass.

The triggering factors causing the ultimate collapse are unknown but two likely possibilities can be mentioned. The first can be related to a seismic trigger. In fact, the study area is located within one of the most seismic area of Switzerland (Gisele et al., 2004) and an earthquake-triggered rock-avalanche, the Sex des Eau Froude's (Marie tan 1946), was already observed in the region. The other reason could be a progressive degradation of the stressed rock mass after the glacial retreat, accentuated by the continuous seismic activity and ground water fluctuations.

The concavo-convex shape of the failure surface promotes, since the early stage of the collapse, the subdivision of the rock mass in two distinct sectors (Figure 4.2-20). The eastern portion located below the tectonic anticline was forced to follow the bedding plane and the steepest slope orientated perpendicular to the main valley direction. The unstable mass located in the western part was constrained by the anticline shape of the failure surface and had to move toward SW.

- ***Multi-slab shearing and rock-avalanche development***

The failure mechanism and characteristics of the rock-avalanche deposits, in particular the presence of two distinct facies reveals important information on the transportation model. Indeed, the presence of large intact blocks preserving the original structures, associated to high-fragmented granular deposits could be related to the slab-on-slab transportation model (Pullet and Schneider 2004; Pullet et al., 2005). This model implies a dynamic disintegration created by shearing and dilatancy along bedding planes.

Depending on degree of confinement, the dilatancy effect can be more or less important (Pullet and Schneider 2009).

Field observations of the disposition of the facies within the rock-avalanche deposits show the presence of different degree of fragmentation and indicate that the initial sliding mass evolved in different confinement environment. The eastern part of the deposit, characterized by the presence of hectometric blocks reveals a lower degree of disintegration that can be related to the impact of the moving mass on the opposite side of the valley which decreases considerably the kinetic energy. In this area, the formation of syn-displacements folds at the base of the rock column was observed. This phenomenon could be related to differential shearing along the beddings affecting the moving slab during the transport. In this context, less competent marl and schist interbeds captured most of the shear strain allowing the lower part of the rock column to deform in pseudo-ductile way. In the western side, the sliding mass does not encountered any major topographic obstacle. This enable the development of dynamic fragmentation and dilatancy (controlled by pre-existing sub-vertical discontinuity sets J1 and J2) transforming the sliding slab into a granular material promoting the long run out. This evolution is highlighted by matrix-supported texture of the rock-avalanche deposits situated in the distal portion and in the northern side of the valley which suggest a higher degree of fragmentation compared to those situated in the proximal portion.

The topographic control on the degree of disintegration of the sliding mass can be clearly highlighted in the Films rockslide where almost 70% of the rock mass stops on the opposite slope of the valley (Pollet et al., 2005). Conversely, for the Sierre rock-avalanche, by the early differentiation of the sliding mass in two distinct blocks, only the 30-40% of the rock-avalanche volume experienced a topographic confinement and drastic reduction of the kinetic energy.

Besides, the 60-70% of the rock mass do not experienced an important topographic confinement and consequently could move further and evolve in a granular flow. In addition to dynamic disintegration, the long run-out of the Sierre rock-avalanche was favoured by undrained loading and low friction coefficient of the substratum. Borehole analyses (Burri 1997; Fringer and Weidmann 1987) indicated that the pre-failure substratum was characterized by saturated peat, slits and glacio-lacustrine deposits. The rapid increase of pore pressure related to the arrival of the sliding mass in the water-saturated substrate caused a drastic reduction of effective stresses and decrease of the effective friction angle which permit a long run-out. The influence of water saturated valley sediments on the mobility of the rock-avalanche seems to be common feature in the Alps and was already observed in several other rockslides characterized by a long run-out such as Fernpass (Prager et al., 2006), Almtal (Abele 1974) or Wildalpen (Kellerer-Pirklabauer et al., 2009)

- ***Post-failure destabilization and erosion***

The detachment area of the Sierre rock-avalanche experienced an important stress release owing to the loss of frontal confinement creating the condition for a new destabilization stage.

This is marked by the progressive development of the large rotational landslide that covers the western portion of the rock-avalanche scar and by the development of the deep steed deformations behind the central and the eastern portions. This latest did not evolve in a rock-avalanche because of the progressive flatten of the bedding planes. The new destabilization of the valley flank also created an important stock of

unstable material that was mobilized by large debris flows incising the rock-avalanche deposits perpendicular to the main valley (Figure 4.2-20).

The deposition of the rock-avalanche debris on the main valley floor clearly influenced the fluvial regime of the Rhone valley. The presence of lacustrine sediments above the rock-avalanche deposits (Burri 1997 and reference herein) suggests that, in the proximal portion the rock-avalanche debris, a dam and a temporary lake were created. Successive dam destabilization by fluvial erosion promoted the creation of channels parallel to the main valley direction accentuating the hummocky morphology of the proximal portion of the deposit.

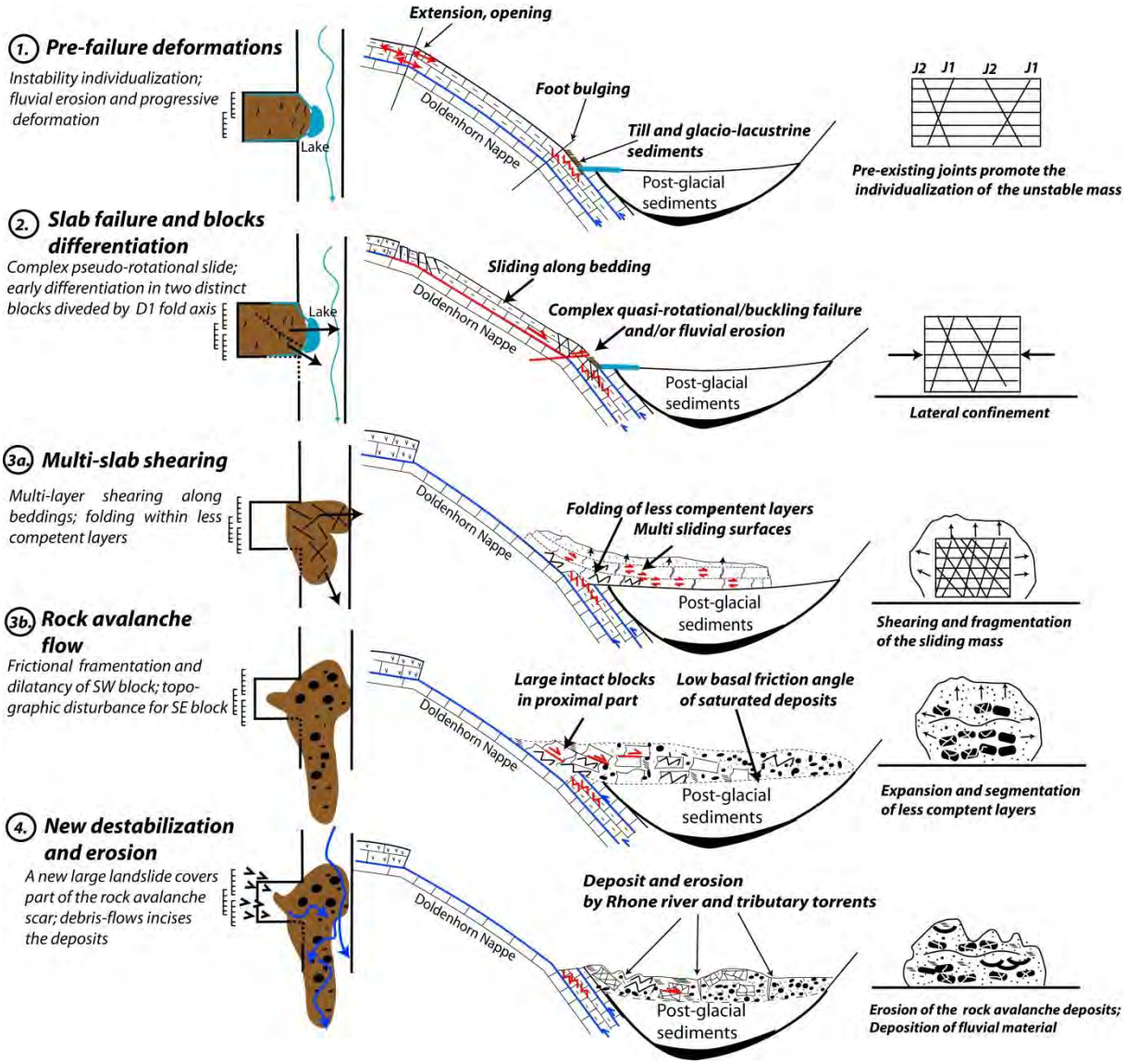

Figure 4.2-20: Reconstruction of the possible destabilization phases and the propagation of the Sierre rock avalanche. For each stage, a planimetric view and two cross-section view (parallel and perpendicular to the slope direction) have been drawn.

4.2.13 CONCLUSIONS

In this study, we presented a first detailed description of failure and transportation mechanisms of Sierre rock-avalanche. Field observations demonstrated that the detachment area was affected by at least three distinct generations of slope deformations that drastically changed the early post glacial morphology of

the slope. After an early rock mass creep deformation, which is a characteristic feature of the cataclinal slope of the northern side of the Rhone valley, the combination of the structural setting and the fluvial erosion created the local conditions for the instability to evolve into a rock-avalanche. The new topographic configuration and the loss of frontal confinement allow the development of a new generation of instabilities that partially reshaped the rock-avalanche scar.

Inherited brittle and ductile tectonic structures have a great influence on the development of the rock-avalanche. Even if not all the detected joint sets directly participate in the failure mechanism, they allow the delimitation of the unstable area by creating release surface and by driving the fluvial erosion that later defined the limits of the unstable area. Numerical modelling shows that pre-existing joint sets could promoted the tilting of bedding planes and the development of buckling deformations in the lower portion of the slope. Failure mechanism analysis underlines also the primary importance of a single and local tectonic feature (in our case the basal fault) on the evolution of the instability from a DSGSD to a rock-avalanche. The characteristics of the internal structures of the deposits associated to the sub-horizontally stratification of the initial rock mass, suggest that a slab-slab transportation model including frictional fragmentation and dilatancy (Pollet and Scheinder 2004; Pollet et al., 2005) can be adopted to explain the development and the mobility of the Sierre rock-avalanche.

Our study demonstrates the great importance of ductile inherited structures on the development and the displacement directions of a rock-avalanche. Field and digital elevation model analyses indicate that the complex concave-convex shape of the failure surface is controlled by the interference of at least two folds orientations related to two distinct tectonics deformations. Numerical modelling performed on the pre-failure surface shows that tectonic-related convexity corresponds to areas where higher tensile strength develop preferentially. In the field, these areas match to the upper and the lower boundary of the rock-avalanche.

The spatial distribution of the deposits facies on the rock-avalanche debris is related to the shape of the failure surface. Indeed, the antiform shape of the failure surface creates an early subdivision within the unstable rock mass that drives also the early movements of the rock-avalanche in two slightly different directions. Without this early subdivision, the sliding direction would have been completely perpendicular to the main valley and would have increased the dissipation of kinetic energy related by topographic confinement associated to the impact on the valley flank. In this case the mobility of the Sierre rock-avalanche would have been considerably reduced. This highlights the significance, in term of run out analysis and hazard assessment, to dispose of precise information concerning the shape of the failure surface and the differential movements affecting the active rockslides.

4.2.14 REFERENCES

Abele, G. 1974. Bergstürze in den Alpen, ihre Verbreitung, Morphologie und Folgeerscheinungen, *Wissenschaftliche Alpensvereinshefte*, 25, 230 pp.

Agliardi, F., Crosta, G. and Zanchi, A. 2001. Structural constraints on deep-seated slope deformation kinematics, *Engineering Geology*, 59, 83-102.

Badger, T.C. 2002. Fracturing within anticlines and its kinematic control on slope stability, *Environmental and Engineering Geoscience*, 8, 19-33.

Brideau, M-A., Ming Y., Stead, D. 2009. The role of tectonic damage and brittle rock fracture in the development of large rock slope failure, *Geomorphology*, 103, 30-49.

Bugnon, P-C., Géologie de l'Hélvetique à l'extremité sud-ouest du massif de l'Aar (Loeche, Valais). Unpublished PhD thesis, 106 pp.

Burri, M. 1955. La géologie du Quaternaire aux environs de Sierre, *Bull. Soc. Vaud. Sc. Nat.*, 289, 141-154.
Burri, M. 1997. Géologie récente de Finges et de ses environ (VS). *Bull. Murithienne*, 155, 5-27.
Burkhard, M. 1988. L'Helvétique de la bordure occidentale du massif de l'Aar (évolution tectonique et métamorphique), *Eclogae Geologicae Helvetiae*, 81, 63–114.
Burkhard, M., Kerrich, R. 1988. Fluid regimes in the deformation of the Helvetic Nappes, Switzerland, as inferred from stable isotope data*, Contributions to Mineralogy and Petrology*, 99, 416–429.
Cavers, D. 1981. Simple methods to analyze buckling of rock slopes, *Rock Mechanics*, 14, 87–104.
Chigira, M. 1992. Long-term gravitational deformation of rock by mass rock creep, Engineering Geology, 32, 157–184.
Chigira, M. Kihoa, K. 1994. Deep-seated rockslide-avalanches preceded by mass rock creep of sedimentary rocks in the Akaishi Mountains, central Japan, *Engineering Geology*, 38, 221-230.
Coe, J.A., Harp, E.L., 2007. Influence of tectonic folding on rockfall susceptibility, American Fork Canyon, Utah, USA, *Nat. Hazards Earth Syst. Sci.*, 7, 1-14.
Crosta, G.B., Chen, H., Lee, C.F. 2004. Replay of the 1987 Val Pola Landslide, Italian Alps, *Geomorphology*, 60, 127-146.
Dietrich, D. 1989. Axial depressions and culminations in the evolution of the Helvetic chain, *Schweizerische Mineralogische und Petrographische Mitteilungen*, 69, 183–189.
Dramis, F., Govi, M., Guglielmin, M., Mortara, G. 1995. Mountain permafrost and slope instability in the Italian Alps: the Val Pola landslide, *Permafrost and Periglacial Processes,* 6, 73–81.
Emery, J.Z. 1978. Simulation of rock creep. In Voight B. (editor). "Rockslides and avalanches natural Phenomena), *In Rockslides and avalanches Vol. 1. Natural phenomena*. Edited by B.Voight. Developments in Geotechnical Engineering 14A, Elsevier Science Publishers B.V., Amsterdam.
Eberhardt, E., Stead, D., Coggan, J.S. 2004. Numerical analysis of initiation and progressive failure in natural rock slopes--the 1991 Randa rockslide, *International Journal of Rock Mechanics and Mining Sciences*, 41, 69-87.
Erismann, H.T., Abele, G. 2001. Dynamics of Rockslides and Rockfalls. Springer, Berlin, Heidelberg, New York, 316 pp.
Evans, S.G., Hungr, O., Energreen, E.G. 1994. The Avalanche Lake rock avalanche, Mackenzie Mountains, Northwest Territories, Canada: description, dating and dynamics, *Canadian geotechnical journal*, 31, 749-768.
Finger, W. and Weidmann, M., 1987. Quelques données geologiques nouvelles sur la vallée du Rhone entre Sion et le Léman*, Bull. Murithienne*, 105, 27–40.
Gasser, D., Mancktelow, N.S. 2010. Brittle faulting in the Rawil depression: field observations from the Rezli fault zone, Helvetic nappes, Western Switzerland, *Swiss Journal of Geosciences*, 103, 15- 32.
Genevois, R., Ghirotti, M. 2005.The 1963 Vaiont Landslide, *Giornale di Geologia Applicata*, I, 41–53.
Gisler, M., Fäh, D., Kästli,P. 2004. Historical seismicity in Central Switzerland, *Eclogae geol. Helv.,* 97, 221–236.
Hammah, R.E., Yacoub, T., Corkum, B., Curran, J.H. 2008. The practical modelling of discontinuous rock masses with finite element analysis. *In Proceedings of the 42nd U.S. Rock Mechanics Symposium – 2nd U.S.-Canada Rock Mechanics Symposium*, San Francisco, US, 2008.
Heim, A. 1921. Geologie der Schweiz, Band II, Tauchnitz, Leipzig.
Heim, A. 1932. Der Bergsturz und Menschenleben. Zürich, Fretz und Wasmuth Verlag, 218 p.
Hoek, E, Brown, E.T. 1997. Practical estimates of rock mass strength, *International Journal of Rock Mechanics and Mining Sciences*, 34, 1165–1186.
Hsü, K.J., 1975. Catastrophic Debris Streams (Sturzstroms) Generated by Rockfalls, *GSA Bulletin*, 86, 129-140.
Hsü, K.J. 1978. Albert Heim: observations on landslides and relevance to modern interpretations. *In Rockslides and avalanches Vol. 1. Natural phenomena*. Edited by B.Voight. Developments in Geotechnical Engineering 14A, Elsevier Science Publishers B.V., Amsterdam, pp. 71–93.
International Society for Rock Mechanics (ISRM). 1978. Suggested methods for the quantitative description of discontinuities in rock masses, *International Journal of Rock Mechanics and Mining Sciences & Geomechanics Abstracts*, 15, 319–368.
Jaboyedoff, M., Couture, R., and Locat, P. 2009. Structural analysis of Turtle Mountain (Alberta) using Digital Elevation Model: Toward a progressive failure, *Geomorphology*, 103, 1, 5-16.
Jaboyedoff, M., Oppikofer, T., Derron, M.-H., Böheme, M., Blikra, L. H., Saintot, A. 2011. Complex landslide behaviour and structural control: a three-dimensional conceptual model of Aknes rockslide, Norway. From: Jaboyedoff, M. (ed.) *Slope Tectonics*. Geological Society, London, Special Publications, 351.
Jäckli, H. 1962. Die Vergletscherung der Schweiz im Würmmaximum, *Eclogae geol. Helv.,* 55, 285–294.
Kellerer-Pirklbauer, V-A., Nicolussi, K, Kain, H., Pilz, A., Thurner, A. 2009. Der Bergsturz von Wildalpen (Hochschwab, Steiermark):Neue dendrochronologische Ergebnisse eines Baumfragments aus der Bergsturzablagerung, *Mitteilungen des naturwissenschaftlichen Vereines für Steiermark*, 139, 57–65.
Kelly, M.A., Buoncristiani, J.F., Schlüchter, C., 2004. A reconstruction of the last glacial maximum (LGM) ice-surface geometry in the western Swiss Alps and contiguous Alpine regions in Italy and France, *Eclogae Geologicae Helvetiae*, 97, 57–75.
Kastrup, U., Zoback, M.L., Deichmann, N., Evans, K., Giardini, D., Michael, A. J. 2004: Stress field variations in the Swiss Alps and the northern Alpine foreland derived from inversions of fault plane solutions, *J. Geophys. Res.*, 109/B1, B01402.
Lugeon, M. 1898. L'éboulement de Sierre en Valais, *Le Globe*. T, XXVH. p. 82.
Mariétan, I. 1946. Le tremblement de terre du 25 janvier 1946. *Bull.Murithienne*, p. 63.
Massironi, M., Genevois, R., Floris, M., Stefani, M. 2011. Influence of the antiformal setting on the kinematics of a large mass movement: the Passo Vallaccia, eastern Italian Alps. *Bull Eng. Geol. Environ*, DOI 10.1007/s10064-010-0340-9.

Mancktelow, N. S. 1992. Neogene lateral extension during convergence in the Central Alps; evidence from interrelated faulting and backfolding around the Simplonpass; Switzerland, *Tectonophysics* ,215, 295–317.

Nicoletti, P.G., and Sorriso-Valvo, M. 1991. Geomorphic controls of the shape and mobility of rock avalanches. *Geological Society of America Bulletin*, 103, 1365–1373.

Noverraz, F. 1990. Répartition géographique, origine et contexte géologique des glissement de terrain latentes en Suisse. Hydrology in Mountainous Regions. H - Artificial Reservoirs; Water and Slopes(*Proceedings of two Lausanne Svmposia, August 1990*). IAHS Publ. no. 194.

Oppikofer, T., Jaboyedoff, M., Pedrazzini, A., Derron, M.-H.,Blikra, L. H. 2011. Detailed DEM analysis of a rockslide scar to characterize the basal sliding surface of active rockslides, J. Geophys. Res.,116,F02016.

Pasquaré, G. 2001. Tettonica recente e instabilità di versante nelle Alpi Centrali. Fondazione cariplo per la ricerca scientifica; CNR-Instituto per la dinamica dei Processi Ambientali, Milano, 218 pp. (in Italian).

Pedrazzini, A., Jaboyedoff, M., Froese, C.R., Langenberg, C. W., Moreno, F. 2011. Structural analysis of Turtle Mountain: origin and influence of fractures in the development of rock slope failures, From: Jaboyedoff, M. (ed.) *Slope Tectonics.* Geological Society of London, Special Publications, 2011, 351, 163-183.

Pedrazzini, A. Jaboyedoff, M., Tognini, M., Derron, M-H., Loye, A. (in prep for tectonophysics) Rock slope deformations in Western Swiss Alps: characterization, spatial distribution and implication on recent mountain range evolution.

Prager, C., Krainer, K., Seidl, V., Chwatal, W. 2006. Spatial features of Holocene sturzstrom-deposits inferred from subsurface investigations (Fernpass rockslide, Tyrol, Austria), *Geo Alps*, 3, 147-166.

Preusser F., Reitner, J.M., Schlüchter, C. 2010. Distribution, geometry, age and origin of overdeepened valleys and basins in the Alps and their foreland, *Swiss Journal of Geosciences*, 103, 407-426.

Pollet, N., Schneider, J.-L.M. 2004. Dynamic disintegration processes accompanying transport of the Holocene Flims Sturzstrom (Swiss Alps), *Earth and Planetary Science Letters*, 221, 433-448.

Pollet, N., Cojean, R., Couture, R., Schneider, J-L., Strom, A. L., Voirin, C., Wassmer, P. 2005. "A slab-on-slab model for the Flims rockslide (Swiss Alps)". Canadian Geotechnical Journal 42, 587-600.

Pant, S.R., Adhikary, D.P. 1999. Implicit and explicit modelling of flexural buckling of foliated rock slopes, *Rock Mech. Rock Eng*., 32, 157-164.

Ramsay, J.G. 1989. Fold and fault geometry in the western Helvetic Nappes of Switzerland and France and its implication for the evolution of the arc of the western Alps. In M. P. Coward et al. (Eds.), *Alpine tectonics*. Geological Society of London Special Publication 45, pp. 33–45.

Saintot, A., Henderson, I.H.C., Derron, M.-H. 2011. Inheritance of ductile and brittle structures in the development of large rock slope instabilities: examples from western Norway. From: Jaboyedoff, M. (ed.) *Slope Tectonics*. Geological Society, London, Special Publications, 351, 27-78.

Sakals, M E., Geersema, M., Schawab, J. W., Foord, V. N. 2011. The Todagin Creek landslide of October 3, 2006, Northwest British Columbia, Canada, *Landslides*, DOI 10.1007/s10346-011-0273-9.

Sartori, M., Baillifard, F., Jaboyedoff, M., Rouiller, J.-D. 2003. Kinematics of the 1991 Randa rockslides (Valais, Switzerland), *Nat. Hazards Earth Syst. Sci.*, 3, 423–433.

Sauchyn, D.J., Cruden, D.M., Hu, X.Q., 1998. Structural control of the morphometry of open rock basins, Kananaskis region, Canadian Rocky Mountains, *Geomorphology*, 22, 313–324.

Semenza, E., Ghirotti, M. 2000. History of 1963 Vaiont Slide: The importance of the geological factors to recognise the ancient landslide, *B. Eng. Geol. Env.*, 59, 87–97.

Seijmonsbergen, A.C., Woning, M.P., Verhoef, P.N.W., de Graaf, L.W.S. 2005. The failure mechanism of a Late Glacial Sturzstrom in the Subalpine Molasse (Leckner Valley, Voralberg, Austria), *Geomorphology*, 66, 277–286.

Sørensen, S., Bauer, B. 2003. On the dynamics of the Köfels sturzstrom, *Geomorphology*, 54, 11–19.

Scheidegger, A.E. 1973. On the prediction of the reach and velocity of catastrophic landslides, *Rock Mechanics*, 5, 231–236.

Schoneich, P., Dorthe-Monachon, C., Jaillet, S., Ballandras, S. 1998. Le retrait glaciaire dans les Préalpes et les Alpes au Tardiglaciaire, *Bull. d'Ét. Préhist. et alpines de la vallée d'Aoste*, IX, 23-37.

Scarascia Mugnozza, G., Bianchi Fasani, G., Esposito, C., Martino, S., Saroli, M., Di Luzio, E., Evans, S.G. 2006. Rock avalanche and mountain slope deformation in a convex dip slope: the case of the Maiella Massif, Central Italy. *In Landslides from massive rock slope failure*. Edited by S.G. Evans, G. Scarascia-Mugnozza, A.L. Strom and R. L. Hermanns, NATO Science Series IV, v. 49, Springer, Dordrecht, pp. 357-376.

Jain, S. K., Nanda, A. 2010. A Constitutive Model for Creep Rupture, *Mechanics of Advanced Materials and Structures*, 17, 459-466.

Steck, A. 1984. Structures et deformations tertiaries dans les Alpes centrales, *Eclogae geol. Helv.,* 77, 55-100.

Stead, D., Eberhardt, E. 1997. Developments in the analysis of footwall slopes in surface coal mining, *Engineering Geology*, 46, 41-61.

Travelletti, J., Demand, J., Jaboyedoff, M., Marillier, F. 2010. Mass movement characterization using a reflexion and refraction seismic survey with the sloping local base level concept, *Geomorphology*, 116, 1-10.

Tommasi, P., Verrucci, L., Campedel,P., Veronese, L., Pettinelli, E., Ribacchi, R. 2009. Buckling of high natural slopes: The case of Lavini di Marco (Trento-Italy), *Engineering Geology*, 109, 1-2, 93-108.

Ui, T., Yamamoto, H., Suzuki-Kamata, K. 1986. Characterization of debris avalanche deposits in Japan, *Journal of Volcanology and Geothermal Research*, 29, 231-243.

Ustaszewski, M., Pfiffner, O. A. 2008. Neotectonic faulting, uplift and seismicity in the Central and Western Swiss Alps, In S. Sigmund et al. (Eds.), *Tectonic aspects of the Alpine-Carpathian-Dinaride System*. Geological Society of London Special Publication 298, pp. 231–249.

Vinard, P., Blümling, P., McCord, J.P., Aristorenas, G. 1993. Evaluation of hydraulic under pressures at Wellenberg, Switzerland, *International Journal of Rock Mechanics and Mining Sciences & Geomechanics Abstracts*, 30, 1143-1150.

Wang, W-N, Chigira, M., Furuya, T. 2003. Geological and geomorphological precursors of the Chiu-fen-erh-shan landslide triggered by the Chi-chi earthquake in central Taiwan, *Engineering Geology*, 69, 1–13.

von Poschinger, A. 2002. Large rockslides in the Alps: a commentary on the contribution of G. Abele (1937–1994) and a review of some recent developments. In: S.G. Evans and J.V. De Graff, Editors, Catastrophic Landslides: Effects, Occurrence, and Mechanisms, *Geol. Soc. Amer. Rev. Eng. Geol.,* 15, 237–256.

5. KINEMATIC AND HAZARD ASSESSMENT OF CURRENT AND POTENTIAL INSTABILITIES

This chapter contains five sub-chapters written in a paper format (chapters 5.1 to 5.5):

1) ***"COMBINING DIGITAL ELEVATION MODEL ANALYSIS AND RUN-OUT MODELLING TO CHARACTERIZE HAZARD POSED BY A POTENTIALLY UNSTABLE ROCK SLOPE AT TURTLE MOUNTAIN, CANADA"***

This paper is at the present moment in press in "*Engineering geology*" under the authorship: *Pedrazzini A., Froese C.R, Jaboyedoff M., Hungr O., Humair F*. The first authors in collaboration with M. Jaboyedoff and F. Humair acquired, treated and analysed the data. O. Hungr performed the run-out modelling. A. Pedrazzini and C. Froese wrote the manuscript. All the authors contributed to discuss the results and finalize the manuscript.

2) ***"THE 2006 EIGER ROCKSLIDE, EUROPEAN ALPS"***

A modified version of this paper has been accepted for publication as book chapter in "Landslides; Types, Mechanisms, and Modelling" Edited by J. Clague and D. Stead, under the authorship*: Jaboyedoff M., Derron M.-H., Jakubowski J., Oppikofer T., Pedrazzini A*. The first author organised the research investigation on the Eiger rockslide and wrote part of the manuscript. T. Oppikofer acquired treated most of the TLS data and analysed displacements. J. Jakubowski developed the analytical model. A. Pedrazzini acquired part of TLS data, performed structural analyses and numerical modelling (continuum and discontinuum) and wrote part of the manuscript. All the authors contributed to discuss the results and to complete the manuscript.

3) ***"REINTERPRETATION OF DISPLACEMENT AND FAILURE MECHANISM OF THE UPPER PORTION OF THE RANDA ROCK SLIDE"***

This paper was presented at the Canadian geotechnical conference 2010 (Calgary, Candada) under the authorship: *Pedrazzini A., Jaboyedoff M., Derron M.-H., Abellan A., Vega Orozco C.* The first author and M. Jaboyedoff treated and analysed the data. All the authors contributed to discuss the results and finalize the manuscript.

4) ***"MONITORING AND FAILURE MECHANISM INTERPRETATION OF AN UNSTABLE SLOPE IN SOUTHERN SWITZERLAND BASED ON TERRESTRIAL LASER SCANNER"***

This paper was presented at Pan-Am CGS Geotechnical conference (Toronto, Canada) under the authorship: *Pedrazzini A., Abellan A., Jaboyedoff M., Oppikofer T*. The first author and T. Oppikofer acquired, treated and analysed the TLS data. All the authors contributed to discuss the results and complete the manuscript.

5) ***"RISK MANAGEMENT OF ROCKFALL/ROCKSLIDE HAZARD BASED ON REMOTE SENSING TECHNIQUES: THE EXAMPLE OF ARVEL QUARRY (SWITZERLAND)"***

This paper was presented at the Slope stability conference 2011 (Vancouver, Candada) under the authorship: *Pedrazzini A., Jaboyedoff M., Oppikofer T., Chantry R., Stampfli E*. The first author and M. Jaboyedoff analysed the data and proposed the risk mitigation measures. All the authors contributed to complete the manuscript.

5.1 COMBINING DIGITAL ELEVATION MODEL ANALYSIS AND RUN-OUT MODELLING TO CHARACTERIZE HAZARD POSED BY A POTENTIALLY UNSTABLE ROCK SLOPE AT TURTLE MOUNTAIN, ALBERTA, CANADA

5.1.1 ABSTRACT

Turtle Mountain in Alberta, Canada has become an important field laboratory for testing different techniques related to the characterization and monitoring of large slope mass movements as the stability of large portions of the eastern face of the mountain is still questionable. In order to better quantify the volumes potentially unstable and the most probable failure mechanisms and potential consequences, structural analysis and run out modelling were performed. The structural features of the eastern face were investigated using a high resolution digital elevation model (HRDEM). According to displacement datasets and structural observations, potential failure mechanisms affecting different portions of the mountain have been assessed. The volumes of the different potentially unstable blocks have been calculated using the Sloping Local Base Level (SLBL) method. Based on the volume estimation, two and three dimensional dynamic run out analyses have been performed. Calibration of this analysis is based on the experience from the adjacent Frank Slide and other similar rock avalanches. The results will be used to improve the contingency plans within the hazard area.

5.1.2 RÉSUMÉ

Le flanc Est de la montagne de la Tortue en Aberta (Canada) est marqué par la présence de nombreuses instabilités potentielles qui sont actuellement surveillées à l'aide de différentes techniques. Cependant, le volume et la cinématique des différentes instabilités sont encore peu connus. Pour obtenir une meilleure quantification de l'aléa et du risque lié au développement de grands éboulements rocheux, une analyse détaillée de structures et des mécanismes de ruptures potentiels a été menée. L'analyse des discontinuités à l'aide du modèle numérique de terrain à haute résolution ainsi que des campagnes de terrain ont permis de mieux comprendre l'agencement structural de la montagne. Sur la base des déplacements observés et des structures repérées, des modèles géométriques simples ont été développés pour contraindre la cinématique des différents compartiments instables. Les volumes des instabilités détectées ont été ensuite évalués par construction géométrique et par la méthode du Sloping Local Base Level modifiée pour prendre en compte l'orientation des discontinuités identifiées. Sur la base des volumes détectés, des analyses de propagation dynamique bi et tridimensionnelles, calibrées sur la base d'autres grandes avalanches rocheuses, ont été effectuées pour déterminer l'extension des zones potentiellement touchées par des éboulements. Les résultats de cette étude ont permis d'améliorer le zonage du danger et la planification du territoire situé au pied de la montagne de la Tortue.

5.1.3 INTRODUCTION

In western Canada, tectonic movements that resulted from the formation of the Rocky Mountains created complex folded and faulted structures (Price, 1994) that are locally prone to slope instability (Gadd, 1986). There have been numerous examples of large rock slides in these settings (Cruden, 1976). The most damaging of these was the 1903 Frank Slide, in southwestern Alberta, Canada (Figure 5.1-1), that killed over 70 people (McConnell and Brock, 1904). Due to the interest in the Frank Slide and to the potentiality for another large rock slide to originate from the eastern slopes of Turtle Mountain, significant investment in monitoring and hazard studies has been made since the eighties by the Alberta Provincial Government, in cooperation with communities of the region. The site is known as the Turtle Mountain Field Laboratory (Moreno and Froese, 2006) and is the ideal testing ground for new characterization techniques for unstable rock slopes. This chapter shows the application of airborne laser scanning (ALS) data to mapping of unstable areas, calculate potential unstable volumes and modelling of runout of the highlighted areas.

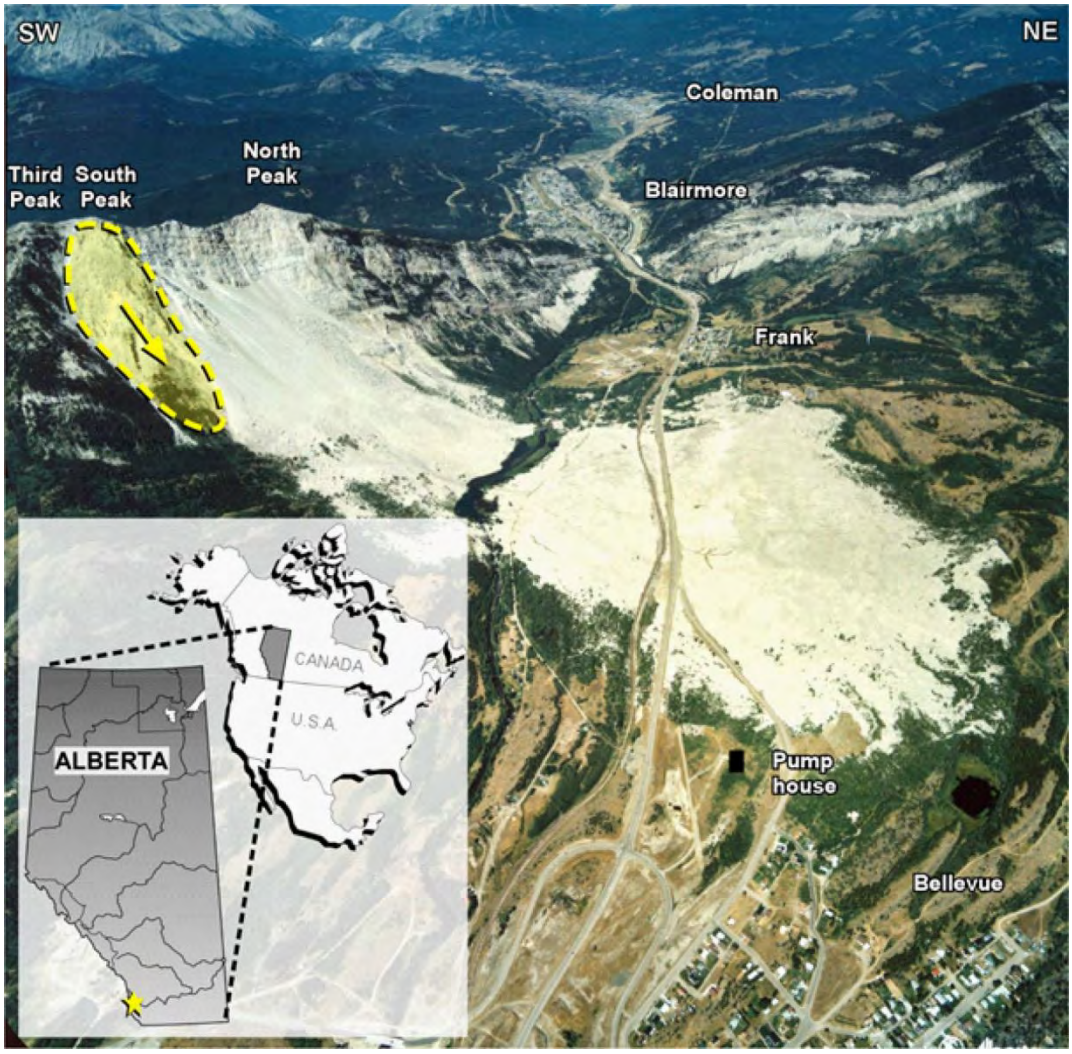

Figure 5.1-1: Aerial view of the Frank slide and the potential unstable areas located between South Peak and Third peak.

5.1.4 HAZARD CHARACTERIZATION

After the 1903 Frank Slide, focus of landslide specialists concerned with the locality shifted to potentially unstable areas on other portions of the eastern face of Turtle Mountain (Figure 5.1-1 and Figure 5.1-2). Initially, concerns regarding the stability of the North Peak (Daly et al., 1912) led to the relocation of the remaining portions of the Town of Frank. In the 1930's, studies by Allen (1931, 1932, 1933) mapped a series of deep fractures around the South Peak of Turtle Mountain and identified two different potentially unstable zones based on subjective estimates of run out for a 5 million m^3 volume of rock from the South Peak of the mountain.

Subsequent studies in the 1980's are worked under the assumption that a single large mass originating from the South Peak (Figure 5.1-2) could fail and travel into the valley below. In the late 1990's, as development around the mountain began to expand, the Government of Alberta (GOA) commissioned a review of the previous studies on the mountain and an updated risk assessment for a potential failure from the South Peak of Turtle Mountain. This study by BGC Engineering (2000) confirmed that the findings of Allan (1931, 1932, 1933) were valid and applied more modern empirical relations for rock fall and runout to estimate the potential impacted area for a rock avalanche with an approximate volume of 5 million m^3.

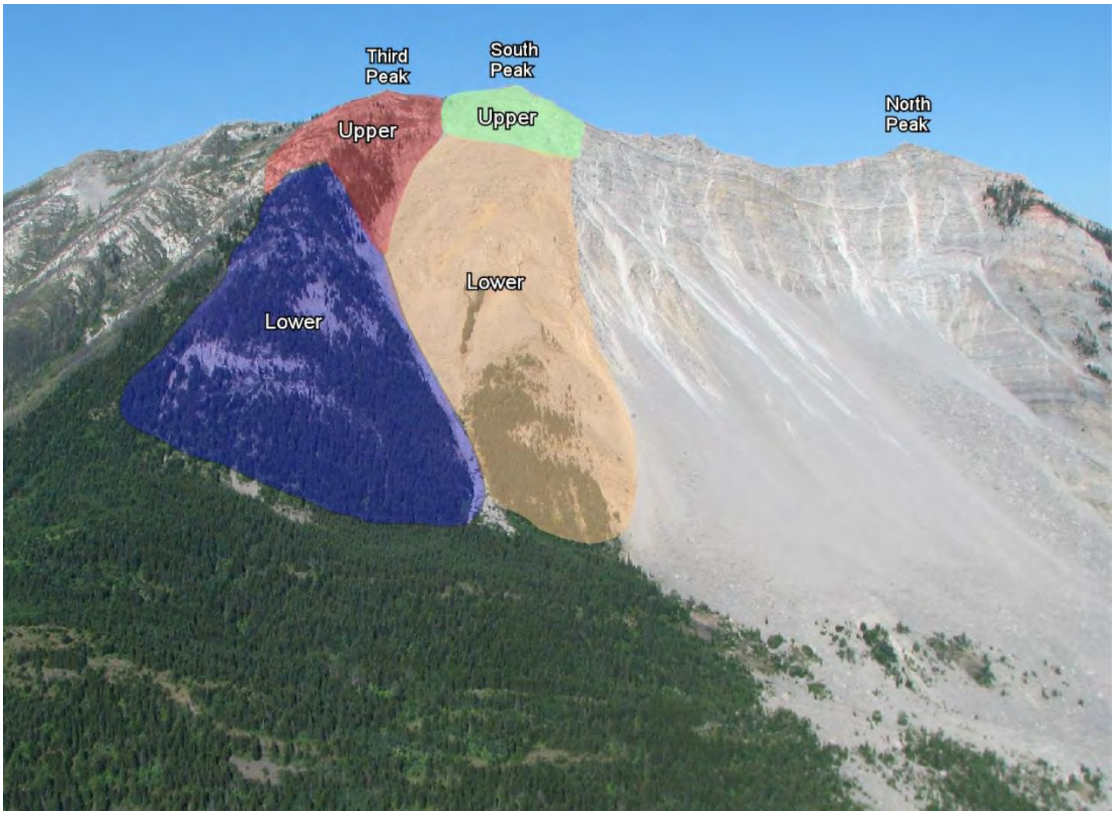

Figure 5.1-2: Photo of the eastern face of Turtle Mountain showing the main four zones discussed in this chapter.

One of the recommendations of the BGC (2000) study for managing the risk associated with a large rock avalanche was to install a monitoring and warning system on the South Peak of Turtle Mountain. Between 2003 and 2005, under a risk-management initiative of the GOA, a coupled state-of–the art monitoring system based on in-situ and remote devices (Froese et al., 2009) and warning system were designed and

installed on the South Peak of Turtle Mountain (Froese et al., 2005; Moreno and Froese, 2006; Froese et al., 2009), in order to characterize and provide warning related to deformations along a series of deep fissures. The design and the implementation of the monitoring system assumed that the rock slide volume and kinematics were as identified by Allan (1931) and sensors were installed to map movements consistent with these assumptions.

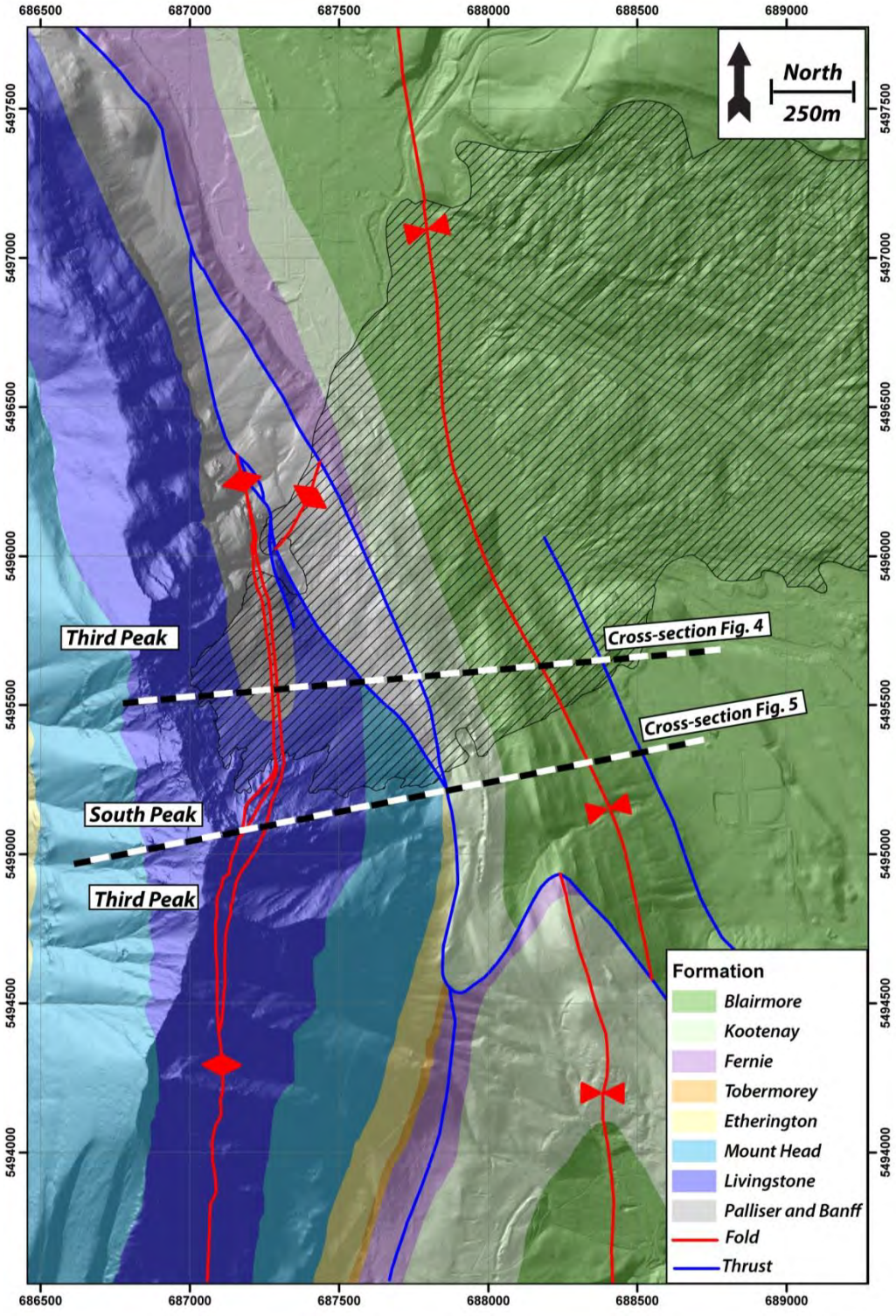

Figure 5.1-3: Geological and structural setting between South Peak and North Peak (adapted from Langenberg et al., 2007).

The initial focus was to develop the monitoring infrastructure and provide upgrades to increase reliability of the system. Subsequent to this, more detailed studies were undertaken to expand the understanding of the stability of the mountain as a whole using both conventional field mapping and newly available remote sensing techniques. The most valuable set of new data has been an airborne LiDAR survey completed in June 2005. The specifications of this data are described in more detail by Sturzenegger et al. (2007). By utilizing the 1 meter high resolution DEM (HRDEM) derived from interpolation of the ground returns, hillshade models were derived. It not only highlighted the visible morphology of the mountain, but also allowed to detail structural mapping of the features on the mountain.

5.1.5 GEOLOGICAL AND STRUCTURAL SETTING

The rocks that comprise Turtle Mountain range in age from Devonian to Cretaceous (Figure 5.1-3). The more important lithological unit is the Livingstone Formation (Visean), which forms the upper part of Turtle Mountain and forms the majority of the Frank Slide debris. It consists mainly of a massive limestone. The central portion of the mountain is formed by the Palliser and Banff formation and consists mainly of black mudstone, siltstone and sandstone (Figure 5.1-3). The most evident structure in the area is the Turtle Mountain Anticline. It has an asymmetrical form, with a westerly plunge (Figure 5.1-4 and Figure 5.1-5). This fold can be described as a modified fault-propagation fold involved in a break-thrust fold (Langenberg et al., 2007). Under South Peak, the fold interlimb angle is steeper than in other sectors and the anticline forms a kind of box fold. South of South Peak, both limbs are preserved over the Turtle thrust (Figure 5.1-5). The fold is cut by the thrust in the North Peak area allowing only the western limb of the anticline to be well outcropping. The fold axis orientation also changes near the South Peak, where it plunges 2° toward 024°.

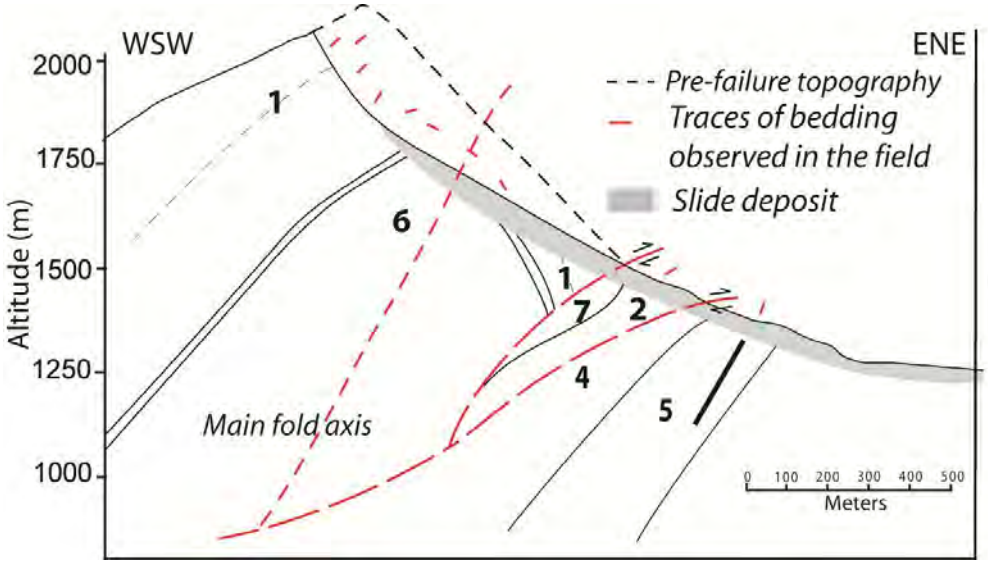

Figure 5.1-4: Cross-section of South Peak area (modified from Langenberg et al., 2007). The fold structures show a large interlimb angle. Cross-section legend (1: Livingstone formation. 2: Mt. Head formation. 3: Fernie Formation. 4: Kootenay group. 5: Blairmore group. 6 Banff and Palliser formation).

In the Third Peak area, the fold axis evolves and plunges to the opposite side, 4° toward Azimuth 194° (Figure 5.1-6). It is also interesting to note that the Turtle Mountain thrust is folded by the Hillcrest syncline, indicating that folding had taken place both prior to and during the thrust movements

(Langenberg et al., 2007).The structural and the geological settings in the South Peak area were first studied in detail by Allan (1933). An improved to modern interpretation of the peak's structure was provided in 1973 by Cruden and Krahn. Langenberg et al. (2007) carried out a more detailed revision of the structural and geological mapping.

Other researchers have undertaken more specifc analyses of the key joint sets based on field survey (Fossey, 1986; Couture, 1998), borehole analysis and ground penetrating radar (GPR) (Spratt and Lamb, 2005). These studies focused more strongly on the crown area, in particular near the South Peak. The result is a very large amount of structural data which is, however, heterogeneously distributed in space.

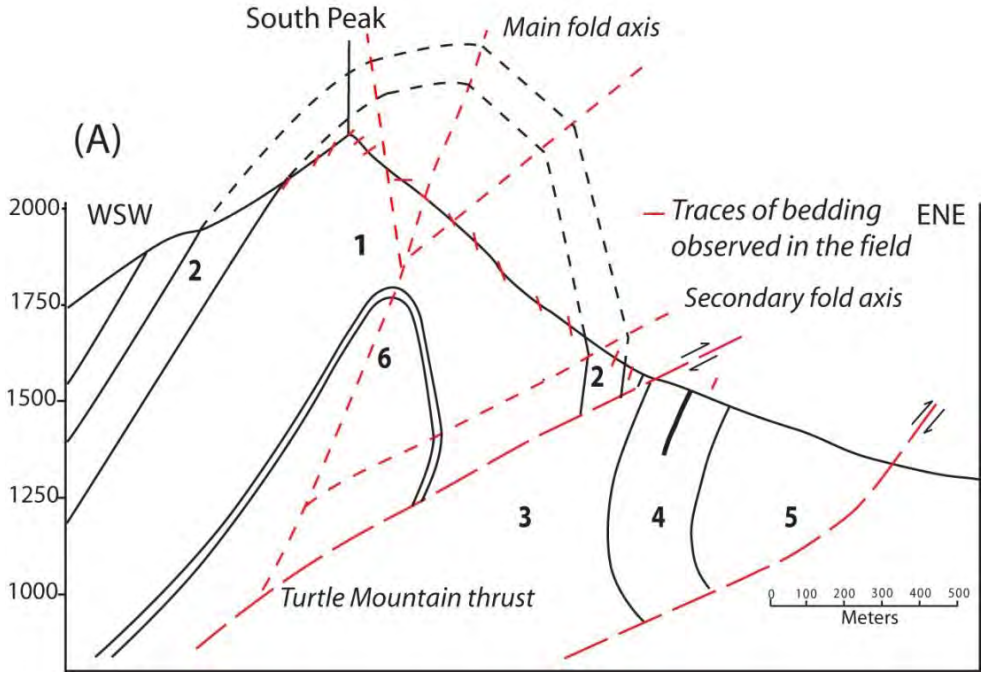

Figure 5.1-5: Cross-section through Frank slide (modified from Pedrazzini et al, accepted). Cross-section legend: (1: Livingstone formation. 2: Mt. Head formation. 3: Fernie Formation. 4: Kootenay group. 5: Blairmore group. 6 Banff and Palliser formation. 7: Etherigton formation).

The majority of structural measurements were taken in the western limb of the Turtle Mountain anticline without having a general overview of both fold limbs. Therefore, as the actual potential instabilities cover the two fold limbs; this gap represents the main limitation to dispose of a good comprehension of the potential kinematics.

5.1.6 DEM ANALYSIS

5.1.6.1 Methods

The analysis of the topography, particularly on unvegetated rocky outcrops, reveals the structural features (joints, faults) affecting the slope (Derron et al., 2005). Using the orientation of each of a series of quadrilateral surfaces (cells), a DEM can be represented by a 3D shaded relief that displays color representation of dip and dip direction. In the current version of the software COLTOP 3D (Jaboyedoff et al., 2007, 2009), this is performed by assigning colors according to the orientation of the normal vector of each DEM cell. The orientation-color relation is shown by means of a Schmidt - Lambert projection. The

slope orientation is coded by the Intensity Hue-Saturation system to perform statistics and fault drawing could be also performed. Grid data, as well as unstructured point cloud data, can be represented and analyzed in 3D using COLTOP 3D (Jaboyedoff et al., 2007). For the COLTOP3D analysis, the DEM of Turtle Mountain was divided in two portions following the fold axis orientation. Then a morpho-structural analysis was undertaken for the two fold limbs separately. If the fractures related to the folding tectonic phase forms morpho-structural features, these could be differentiated for the two fold limbs using this approach.

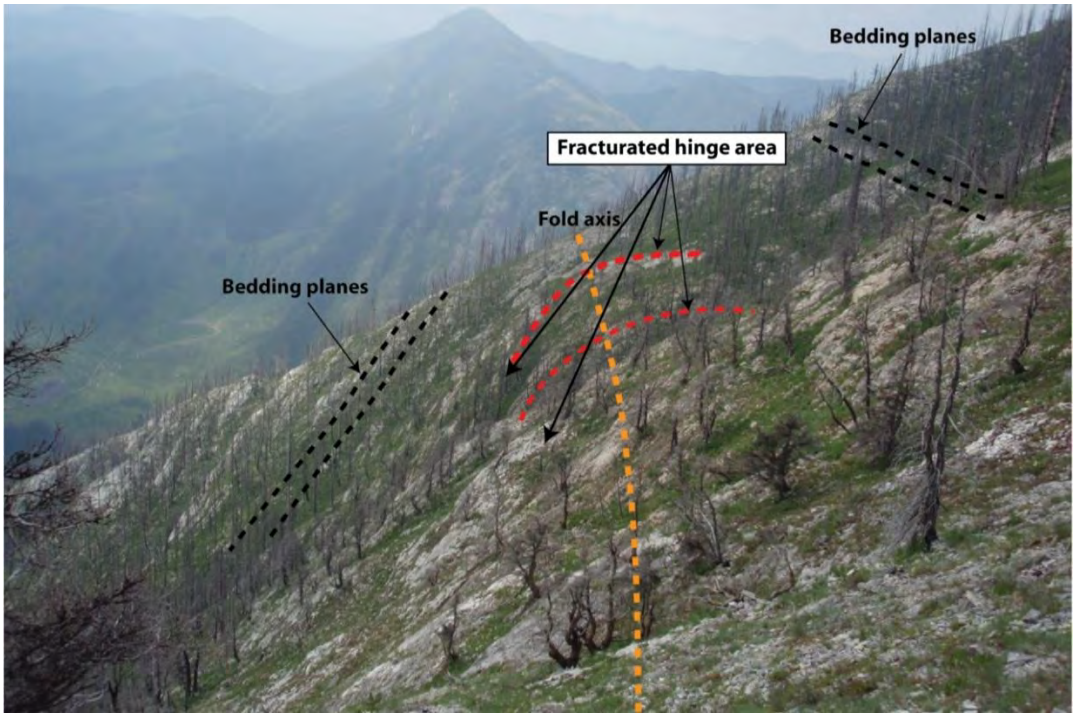

Figure 5.1-6: View (toward South) of Turtle mountain anticline under Third Peak. In this part of the fold the interlimb angle is relatively small, compared to South Peak situation.

5.1.6.2 Results for the Eastern fold limb

The slope morphology on the eastern limb of the anticline is significantly influenced by the orientation of the bedding planes, in particular under the Third Peak. As scree slope deposits and vegetation are abundant, especially in the lower part of the slope, the utility of the DEM to detect structural features in this zone is reduced. However, five main orientations have been detected (Table 5.1-1 and Figure 5.1-7) using COLTOP 3D:

- Medium violet, S0 (100°/55°) represents the predominant bedding orientation in the eastern flank of the anticline under Third Peak area.
- Yellow orientation J1 (020°/45°) also has an important influence on slope morphology, in particular in the lower part between the South Peak and the Third Peak.
- Red joint orientation J2 (060°/55°) forms the main rock outcrops and that are subparallel the slope surface.
- Light blue orientation J7 (135°/50°) and Dark blue orientation J4 (210°/45°), creating in association with J1 large gullies incising the eastern flank of the mountain.

Table 5.1-1: Characteristics of discontinuity sets detected in the eastern fold limb.

Name (color / variation)	***Dip direction***	***Dip***	***Main visibility***	***Large-scale roughness***
J1 (yellow,+/-10°)	20	45	Whole slope	Long wave undulations
J2 (red,+/-10°)	60	55	Whole slope	Planar
S0 (medium violet,+/-10°)	100	55	Entire eastern fold limb	Long wave undulation (folded)
J3 (light blue,+/-10°)	135	50	Upper part	Planar
J4 (dark blue,+/-10°)	215	45	Upper southern part	Sub-planar

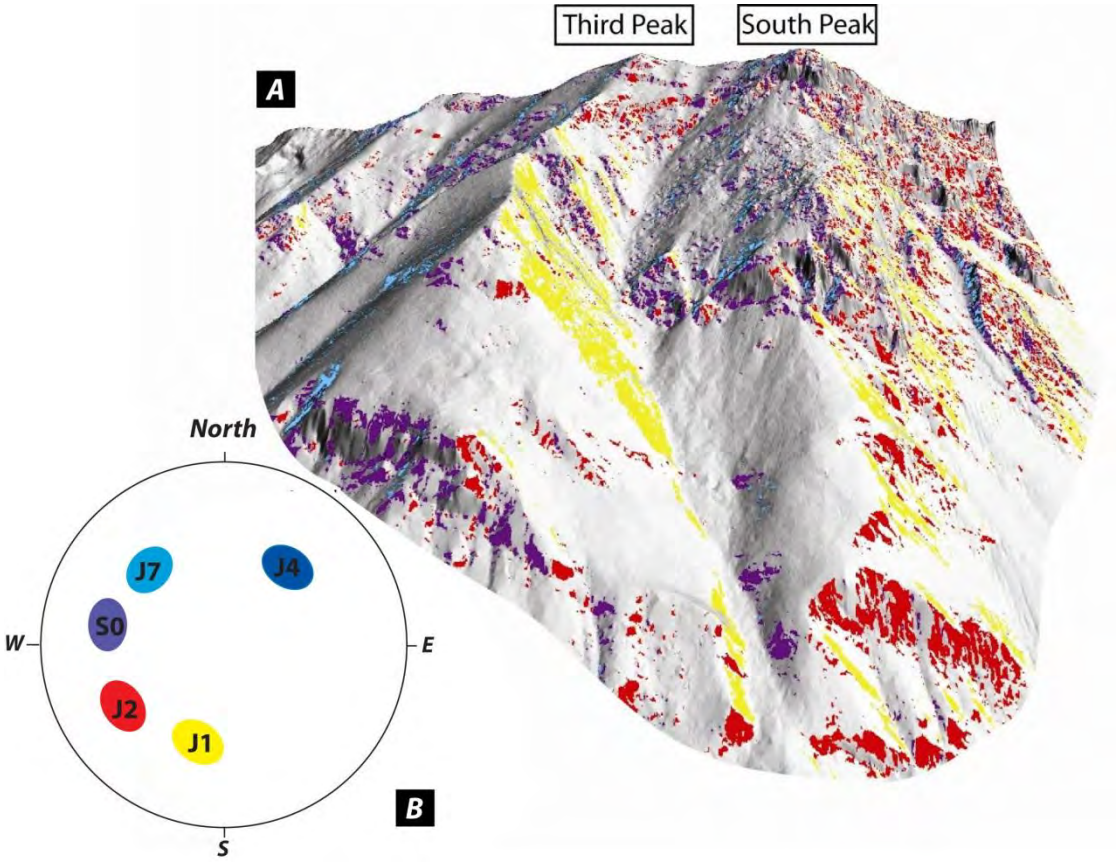

Figure 5.1-7: A 3D view of the eastern face of Turtle Mountain, showing discontinuity orientations detected using COLTOP 3D. B) Stereonet of discontinuity sets orientation detected by DEM analysis (Lower hemisphere projection). The size of the circle represents 1σ variability cone.

5.1.6.3 Results for Western fold limb

The western limb of the Turtle Mountain anticline represents the most visible outcrops in the upper east face and in the whole western face of Turtle Mountain (Figure 5.1-8 and Table 5.1-2). Using the analysis performed by COLTOP 3D, the bedding planes (S0) are clearly visible in the western face. Their orientation corresponds principally to green color (Figure 5.1-8). However, in the northern part of Turtle Mountain, the bedding orientation changes following the variation of the fold axis. In this zone, the morpho-structure named J6 corresponds to a true discontinuity set, which is different from the bedding planes (Jaboyedoff et al., 2009). In fact, in the North Peak area bedding is mainly parallel to J5 discontinuity set. For this reason, the orientation corresponding to the green color represents different discontinuity sets (S0-J6) depending on where they are situated along the anticline. Two others discontinuity sets are well-developed on the west side of the mountain (Blue –J4 - and magenta colors - J5). These are likely encountered in the eastern face as well, but they don't form important morpho-

structures and cannot be detected using an airborne LiDAR dataset (Figure 5.1-8). The upper eastern face is dominated by the Frank Slide scar, which is controlled by three main discontinuities, yellow J1 (020°/45°), red J2 (055°/65°) and light blue J3w (115°/50°).

5.1.6.4 Field characterisation

In order to better constrain the structural analysis computed on HRDEM extensive field survey in the different portions of Turtle Mountain have been carried out. More than 1300 data have been measured on both fold limbs (Figure 5.1-9). Six main discontinuity sets were identified between Third and South Peak. The nomenclature of discontinuity sets keeps consistent with Jaboyedoff et al. (2009) and Brideau et al. (2009). None of these sets are folded indicating a fundamental influence of folding and post-folding tectonic on the formation of the different discontinuity sets.

Table 5.1-2: Characteristics of discontinuity sets detected in the western fold limb.

Name (color / variation)	***Dip direction***	***Dip***	***Main visibility***	***Large scale roughness***
J1 (yellow, +/-10°)	20	45	Eastern flank	Long wave undulation
J2 (red, +/-10°)	55	65	Eastern flank	Planar
J3(light blue, +/-15°)	115	55	Eastern flank	Planar
J4 (dark blue, +/-10°)	210	50	Western flank	Sub-planar
J5 (violet, +/-10°)	270	45	Western flank	Planar
J6-S0(green,+/-10°)	325	45	Western flank	Long wave undulation

The study area is divided in six different structural domains characterized by distinct discontinuity sets orientations, distinct geometrical and geomechanical characteristics (persistence, spacing, JRC, JCS and GSI). Figure 5.1-9 represents the six structural domains recognized between South an Third Peak and their related rock mass characteristics. It is possible to note that the location of the structural domains is clearly related to the presence of the Turtle Mountain fold creating a quite clear subdivision between the structural domains located in the eastern and in the western limb. Excepted for the structural domains close to the hinge area, where important changing in the bedding planes orientation occurs, the other structural domains roughly show the same patterns in terms of discontinuity sets orientation. Indeed, five main discontinuity sets could be frequently observed:

- Axial joints, perpendicular to the bedding planes and parallels the fold axis (J3w western fold limb /J3e eastern fold limb).
- Steep transverse fracture cutting the entire anticline perpendicularly to the fold axis (J8).
- Conjugated strike-slip joints (J2 and J4).
- Persistent post-folding discontinuity set cutting the entire anticline (J1).
- A 325°/45° ± 20° discontinuity set (J6) presents in the western fold limb.

The rock mass quality for the different structural domains, was estimated using the Geological Strength Index (Hoek and Brown, 1997). Advantages and limitation of using GSI to describe natural unstable slope have been discussed by Brideau et al. (2009b). The mean rock mass quality corresponds to the limit between Very Blocky to Blocky/Disturbed/Seamy structure with good to fair discontinuity surface conditions. The zones showing the lower GSI values correspond to the structural domain close to the hinge area and to the structural domain corresponding to the lower South Peak area (Figure 5.1-9). For

those two areas, these lower GSI values are probably related to the vicinity of the fold axis and the disturbance effects of recent gravitational movements related to the 1903's event (Pedrazzini et al., in press).

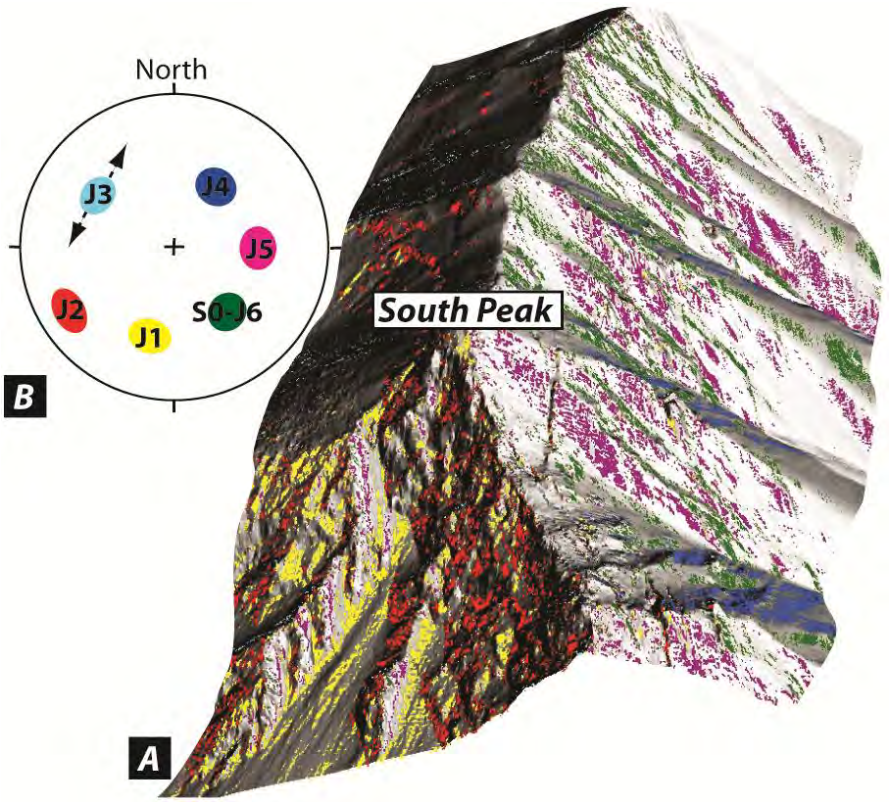

Figure 5.1-8: a) 3D view of the western limb of Turtle Mountain anticline, showing discontinuity orientations detected using COLTOP 3D. b) Stereonet of discontinuity sets orientation detected by DEM analysis (Lower hemisphere projection). The size of the circle represents 1σ variability cone. J3, as extensional fault related to the folding could change his orientation depending on mean pole of the bedding planes.

5.1.6.5 Comparison between DEM and field analysis

In general, field and COLTOP 3D analysis show good agreement especially concerning the results obtained for western limb of the Turtle Mountain anticline (Pedrazzini et al., 2008). Essentially, all the main orientations detected on DEM analysis are confirmed by field measurements. One important difference, however, is that field discontinuities are often steeper than the ones obtained from DEM analysis. This difference is evident for discontinuity set J2 (055°/60°). A possible explanation is that the slope angles deduced from DEM are smaller than the ones measured on the real relief due to the smoothing effect of the mesh size compared to the true discontinuity (Sturzenegger et al., 2007).

Field measurements allow the definition of two other discontinuities sets (J8 and J3e) that weren't pointed out by DEM analysis. Discontinuity set J8 is present almost in every structural station and cross the anticline but, due to it's orientation and steep dip it doesn't form any important morpho-structure and could not therefore be detected by DEM analysis. Discontinuity set J3a was observed in the eastern limb and shows fixed relationship with the fold axis. This joint is linked to J3, only pointed out in the western limb, as an extensional joint related to the folding phase. Unfortunately, in the eastern fold limb J3a

plunges into the slope and doesn't form any important morpho-structural feature that could be detected by DEM analysis.

In the western fold limb more specifically, the structural settings are relatively homogenous in space. However, J3w presents an important variation in dip and in dip direction. This is probably a consequence to his origin as extensional fracture related to the folding phase (Pedrazzini et al., in press). The fold is not cylindrical and small variations of its orientation influence J3w and J3e values (Figure 5.1-8b).

In the eastern fold limb the main structural settings have shown a more important variation. This is probably related to random local fracture systems and to exfoliation discontinuities. Exfoliation phenomenon is much more developed in the dolomitic-siltstone belonging to the Salter/Baril/Wileman member of the Mt. Head Formation. It is normally sub-parallel to the bedding planes or to the general outcrop orientation. Another complicating factor is the occurrence of syn-sedimentary cross-bedding structures in the Livingstone formation that may influences the measurements at outcrop scale.

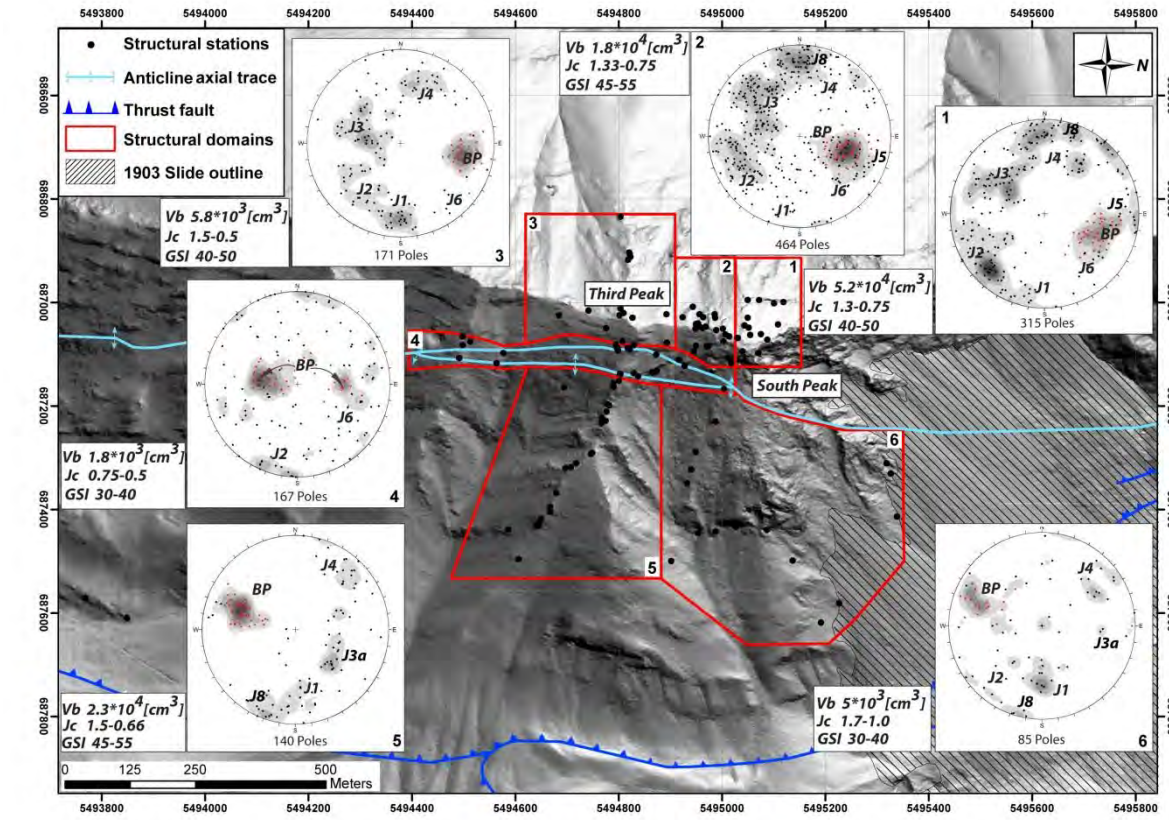

Figure 5.1-9: Structural domains identified between Third and South Peak and their related geomechanical characteristics (Vb = mean block volume, Jc = joint conditions from Cai et al. (2004), GSI = Geological Strength Index).

5.1.7 MOVEMENTS CHARACTERIZATION

At present day, the main effort to characterize the displacements has been carried out in the upper South Peak area. Based on photogrammetric and extensometers analysis, Froese et al. (2009) describe the main deformation patterns of this area. Concerning Third Peak and lower South Peak area, only limited quantitative information about the displacement are available. In order to dispose of preliminary information about the displacement direction, manual estimation has been performed on the main cracks fractures detected in the whole area between South and Third Peak. Practically, in the field, the opening

direction was measured based on the similarly between the two walls of the open cracks and the displacement vector was calculated using a classical geological compass. The measurement accuracy is estimated at ± 5° in plunge and ±10 ° in strike. The reliability of this approach has been tested comparing displacement direction obtained by field analysis with the available photogrammetric vector presented by Froese et al. (2009) for upper South Peak area (Figure 5.1-10a). Figure 5.1-10b and Figure 5.1-10c show the stereographic representations of the displacement vectors measured on the different cracks for upper South Peak and the for Third and Lower South Peak area.

Results concerning upper South Peak show a good agreement with the main movement directions calculated by Froese et al., (2009). In particular, field measurements allow confirming the subdivision of the upper instability in three distinct portions as suggested by Froese et al. (2009) and validated using numerical models by Brideau et al. (2009a). Superficial movements of the south–eastern face of South Peak were also pointed out. However, in the crown area, manual estimations are often biased by local displacement components that are not representative for the general movement directions. Displacement vector measured in Third and Lower South Peak areas are less numerous than in South Peak area, especially due to the debris covering and the access difficulties. However, it is possible to point out a quite constant trend indicating that the main movements affecting the lower portion of Turtle Mountain are oriented toward north-east.

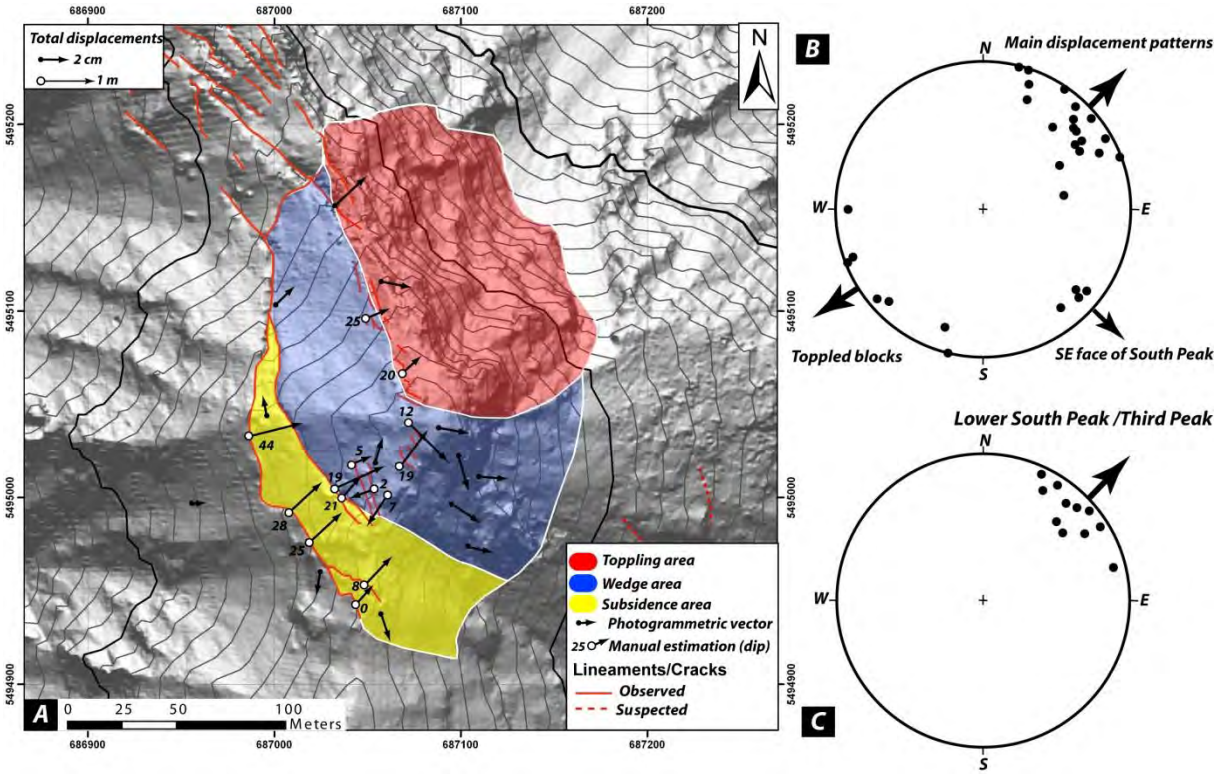

Figure 5.1-10: a) Comparison between the displacement vectors measured using photogrammetric techniques between 1984 and 2005 and total displacement measured by manual estimation on open cracks. b) Sterographic projection of displacement vector for the entire Upper South Peak area estimated by field measurement. c) Stereographic projection of manual estimated vector for the lower South Peak and Third Peak area.

5.1.8 FAILURE MECHANISM AND VOLUME ESTIMATION

Based on cracks and morphological evidence highlighted during field mapping, the COLTOP 3D analyses and available surface monitoring (Froese et al., 2009), various zones of potential instability were determined. Their volumes were estimated and preliminary kinematic analyses (Pedrazzini et al., 2008) were undertaken to determine whether or not they are susceptible to collapse.

5.1.8.1 Methods

Kinematic analyses (Pedrazzini et al., 2008; Brideau et al., 2009a; Pedrazzini et al., in press) have been performed based on method described by Hoek and Bray (1981). The orientation of the slope face was derived from the HRDEM data. Based on previous studies (Benko and Stead, 1998; Cruden and Martin, 2007) and roughness measurements in the field following techniques recommended by ISRM (1978), a friction angle of 35° was chosen to perform the kinematic analysis (Benko and Stead, 1998).

The volume estimation was performed using both (1) the Sloping Local Base Level (SLBL) method (Derron et al., 2005, Jaboyedoff et al., 2009; Travelletti et al., 2010) and (2) by fitting planes corresponding to mean discontinuity sets based on DEM point clouds analysis.

SLBL method allows to identify a surface, above which a rock mass is assumed to be kinematically capable of detachment. The SLBL method applied to a 3D surface (DEM) consists of replacing the altitude zij of a DEM node by the mean value of the highest and the lowest node altitude among the four direct neighbours, if the altitude zij is greater than the mean value (Jaboyedoff and Tacher, 2006, Jaboyedoff et al., 2009). When the difference between subsequent iterations of this process is near to zero, the computation is stopped. This procedure allows determining a straight line between two fixed nodes. The described analysis is linear. A quadratic-like surface is obtained when a tolerance is added to the mean value obtained by the highest and the lowest neighbour at each node. In order to account for the control of the discontinuity sets on the potential failure surface, another limiting parameter has been added in the SLBL calculation. This parameter called “slope limit factor” allows for constraint of the modeled surface based on the angle of the basal delimiting surface (for planar sliding) or intersection line (for wedge sliding). This means that the quadratic-like surface calculation stops when it reaches the dip of the limiting surface (Figure 5.1-11a). The use of this parameter is very effective to estimate potential unstable volumes of rock masses affected by composite deep-seated multi-block failure mechanism (Stead et al., 2006). In this instability configuration, discontinuity sets influence the mean failure extension and shape but also where progressive rock mass strength degradation occurs giving a more smooth failure surface morphology.

The rigorous geometrical reconstruction consists to fit plane corresponding to the mean orientation of the main fracture or discontinuity sets delimiting the rock instability. This operation has been carried out using 3D point cloud managing software Polyworks (InnovMetric, 2009). Based on the different planes defining the basal and the laterals releases surfaces, the volume of the potential instability is calculated in a GIS environment by subtracting from the HRDEM the TIN (Triangular Irregular Network) created from the constructed surface (Figure 5.1-11b).

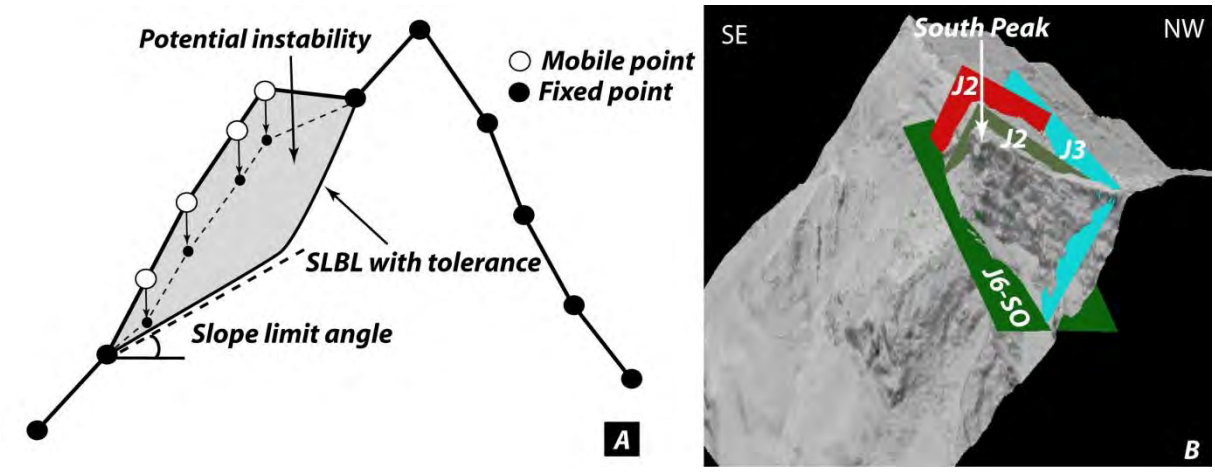

Figure 5.1-11: a) Illustration of SLBL calculation for a potential rock instability assuming a tolerance leading to rotational-like surface limited in the lower portion by the "slope limit angle". b) 3D geometrical delimitation of the potential instabilities in upper South Peak area by fitting plane corresponding to the mean orientation of the delimiting discontinuity sets.

5.1.8.2 Application to the Turtle Mountain area

The main unstable areas detected on Turtle Mountain have been analysed using the SLBL method. The limits of the mapped unstable areas have been chosen as invariant points. A tolerance has been added to the SLBL computation in order to better define the volume in accordance with the discontinuities orientation occurring in the area. The slope limit factor varies depending on the discontinuity sets influencing the geometry of the different areas. Table 5.1-3 defines the different slope limit factor adopted for the different potential unstable volumes. For all areas, a 5 m grid was created to perform the SLBL analysis. Several simulations have been performed in order to provide different volume scenarios (Table 5.1-3).

Table 5.1-3: Parameters and related volumes calculated using SLBL methods and geometrical construction.

Symbol	*Location*	*Curvature tolerance*	*Slope limit factor [°]*	*SLBL volume (M of m³) Min-Max*	*Geometrical calculation (M of m³)*	*Mean SLBL vs Geometrical*	*Max SLBL vs geometrical*
LSP-1	*Lower South Peak*	*-0.006/-0.008*	*35*	*1.5/1.65*	*1.85*	*-17%*	*-12 %*
LSP-2	*Lower South Peak*	*-0.009/ -0.011*	*35*	*5.5/ 5.9*	*6.4*	*-12%*	*-8 %*
LSP-3	*Lower South Peak*	*-0.0025/ -0.004*	*40*	*0.065/ 0.08*	*0.065*	*10%*	*19%*
LSP-4	*Lower South Peak*	*-0.0025/ -0.004*	*40*	*0.35/ 0.45*	*0.48*	*-20%*	*-7%*
LSP-5	*Lower South Peak*	*-0.004/ -0.005*	*40*	*0.5/ 0.65*	*0.74*	*-18%*	*-5%*
LSP-6	*Lower South Peak*	*-0.004/ -0.006*	*40*	*1.2/ 1.35*	*1.42*	*11%*	*-5%*
USP-1	*Upper South Peak*	*-0.008/ -0.01*	*65*	*0.20/ 0.25*	*0.2*	*11%*	*20%*
USP-2	*Upper South Peak*	*-0.03/ -0.05*	*30*	*0.57/ 0.85*	*0.8*	*-13%*	*6%*
USP-3	*Upper South Peak*	*-0.05/ -0.08*	*30*	*0.25/ 0.45*	*0.5*	*-43%*	*-11%*
3dP-1	*Third peak*	*-0.003/ -0.005*	*35*	*1.9/ 2.2*	*2.35*	*-15%*	*-7%*
3dP-2	*Third Peak*	*-0.03/ -0.05*	*35*	*0.57/ 0.85*	*1.0*	*-41%*	*-8%*

The calculated volumes correspond to the total volume of each detected instability and are not explicitly related to a potentially larger unstable volume for a single event.The calculation of the potential unstable volumes based on geometrical reconstruction has been carried out using the mean orientation of the discontinuity sets defining the different potential instabilities.

5.1.8.3 South Peak area

For the South Peak area, the COLTOP 3D and preliminary kinematic analyses were used to define two distinct zones: upper South Peak and lower South Peak (Figure 5.1-2).

For upper South Peak, studies by Froese et al. (2009) highlighted structural control of joints J2, J3 and J6/S0 on the deformations of the main unstable portion (wedge and subsidence zones) and the control of J1 on toppling from the eastern face of the upper South Peak. Kinematic analyses of these proposed mechanisms were undertaken by Froese et al. (2009) and Pedrazzini et al. (2008) along with numerical modelling conducted by Brideau et al. (2009a). Figure 5.1-12 provides a conceptual model of the main deformation zones on the South Peak. Based on the projections of the main joints and bedding controlling deformations on South Peak, volumes for the three zones were estimated and presented in Figure 5.1-13.

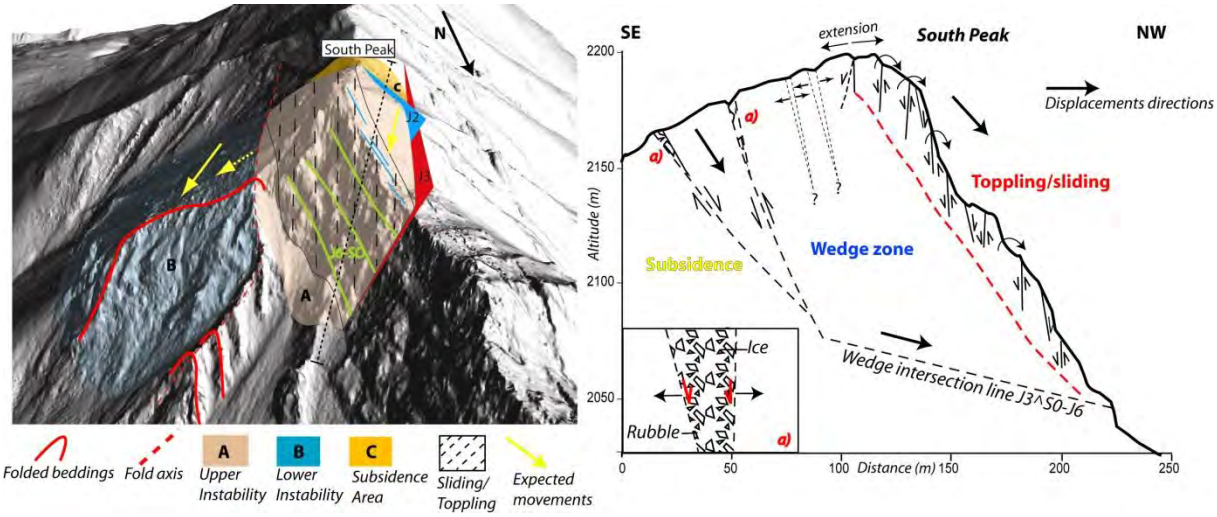

Figure 5.1-12: Conceptual model of South Peak unstable area based on structural and monitoring data. a) 3D view (toward south –west) of the different unstable zones. b) Cross section toward SE-NW showing the potential relationship between the structural data and the observed displacements directions.

For the lower South Peak, a variety of potentially unstable volumes were estimated based on the COLTOP 3D analysis and field mapping. The lower portion of the South Peak is heavily fractured and obscured by rock fall talus originating from the cliffs above. The fractured nature is likely due to the proximity of the anticline hinge (Pedrazzini et al., in press). Many open fractures in this zone appear to be related to movement and show visible indications of previous slope movement which are primarily oriented to the northeast, following in general the J1-J2 discontinuity sets (Figure 5.1-14a). The crack opening width is variable but it generally increases toward the NE. Based on the results of kinematic analyses, as well as field measurements of crack orientations, the lower South Peak area could be divided in at least 6 different potential unstable zones. The different areas appear to be moving towards the NE, following the J1 discontinuity set (Figure 5.1-14b).

Movements in the slope direction are possible following the wedge J2^J3w, but the cracks orientations observed during the field mapping did not provide evidence of such movements. Large scale planar sliding on the bedding seems unlikely due to the very steep dip angle of the bedding compared to the topography. However, in case of large slope movements involving the entire lower South Peak area, a flexural buckling slab failure on the bedding planes is not to exclude.

The SLBL method was applied to each potentially unstable block to estimate the potential failure volumes. The model gives volumes ranging from 0.12 to 1.89 million m^3. Considering a failure affecting the whole South Peak area, the potential unstable volume could reach 5.5 million of m^3 (Figure 5.1-15a). A cross-section representation of these unstable volumes is provided on (Figure 5.1-15b).

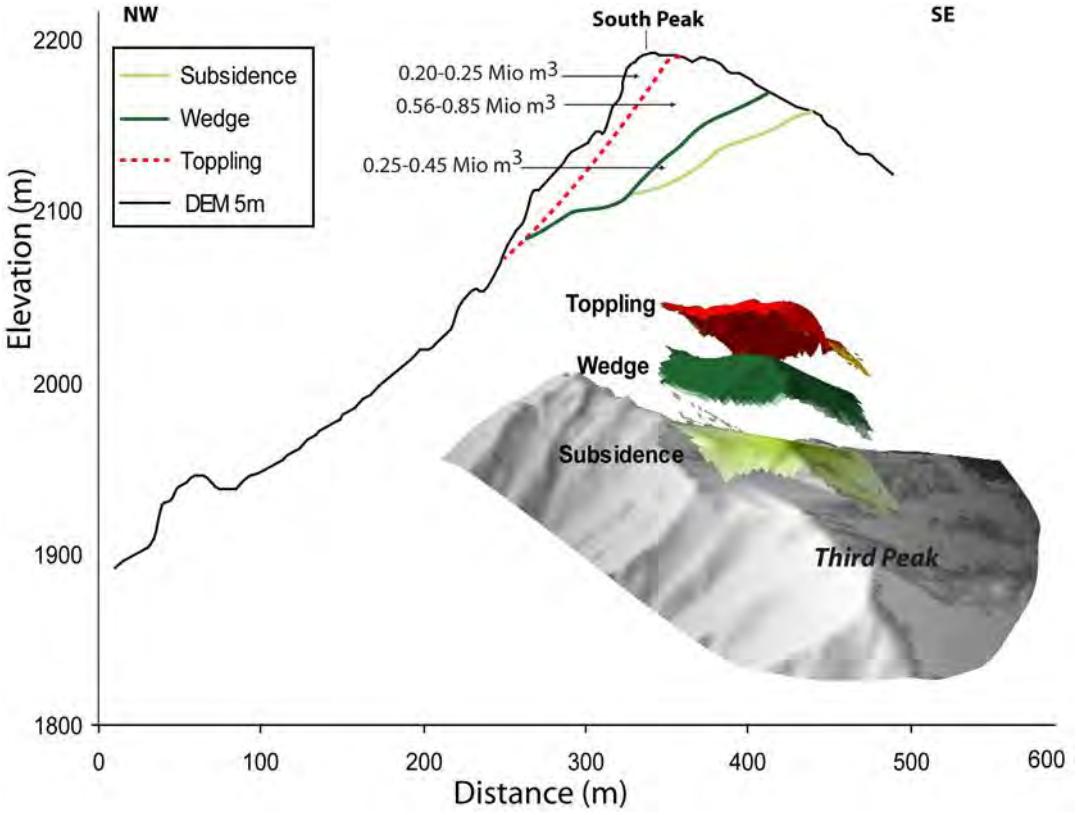

Figure 5.1-13: Representation of the SLBL calculation for the upper South Peak area, showing the potential relationship between the structural data and the observed displacement directions

5.1.8.4 Third Peak area

In the Upper Third Peak area, potentially unstable volumes are considered as very small. The absence of large instabilities is probably related to the location of the anticline hinge with respect to the mountain crest (Figure 5.1-16a). Large gravitational movements such as toppling or wedge failures are not kinematically feasible due to rapid changes in the bedding orientation and the relatively small fold interlimb angle. In addition, field observations of an ancient scar (Figure 5.1-16c) show that heavy fracturing is related and mainly limited to the hinge zone. Thus this intense fracturing would limit instability to relatively small volumes (<10'000m^3). Potential shallow instabilities related to the hinge zone are evident below the Third Peak, where two main types of failure mechanisms can be observed: toppling and planar sliding (Figure 5.1-16b). Toppling affects the western limb of the anticline. Planar failure occurs along the bedding plane and the discontinuity J3w (115°/55°) in the fold hinge zone. The

prone areas for planar sliding are limited to upper Third Peak and are concentrated where the bedding is parallel to the main topography (dip-slope). On the lower slope below Third Peak, two significant cracks have been detected, demonstrating that pre-failure movements occurred in this area. These cracks could be followed in both directions to the SE and to the NW from the apex of the ridge below Third Peak. The main orientation is generally 060°-070° (+/-10°), following the pre-existing discontinuity J2 direction (060°/55°). A cumulated displacement of about 20 cm toward 060/55 was observed. The rock mass at the surface often shows a low quality (GSI=40-50 for the Livingstone Formation). These characteristics, associated with the slope morphology and shallow instabilities, indicate the possible existence of a deep seated gravitational deformation (DSGSD) affecting the lower Third Peak area. Displacement vectors measured along cracks as well as kinematic analysis indicate that the most likely mechanism is stepped-like planar failure along discontinuity J1, with bedding planes as lateral release surface and J2 playing as back crack. The volume of a potential deep-seated slope deformation feature, (DGSD) outlined in the field by a large crack was estimated to define a volume between 1.9 and 2.2 million m^3. Potentially unstable zones were identified on the Lower Third Peak and are shown on Figure 5.1-18.

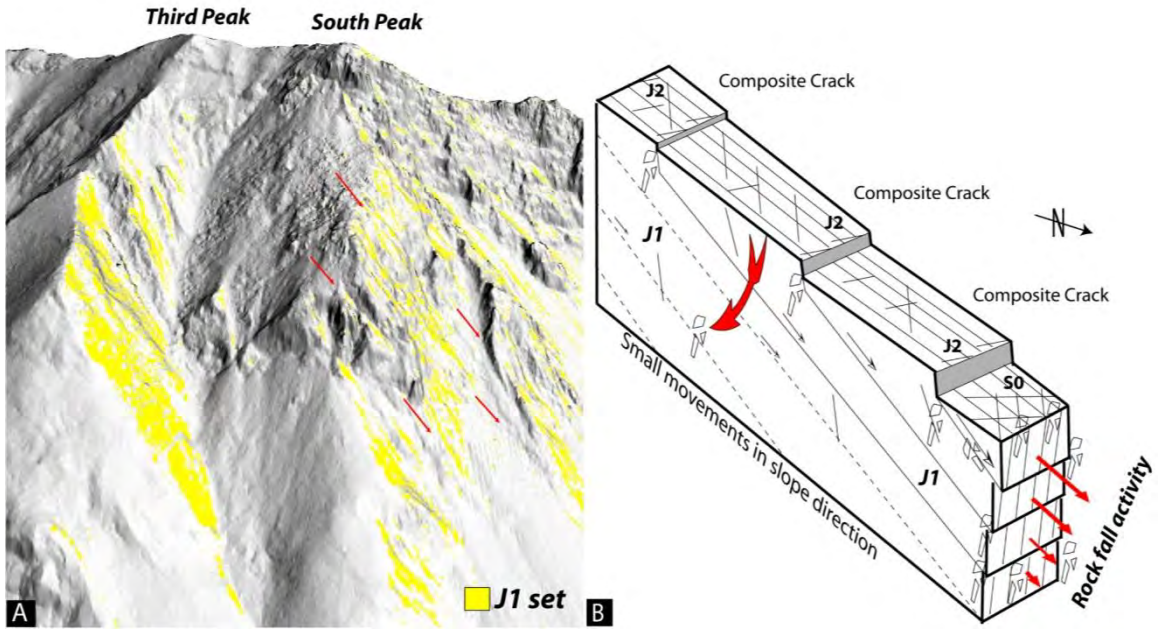

Figure 5.1-14: Influence on the eastern slope morphology of the discontinuity set J1 extracted directly from COLTOP3D and plotted on 3D HRDEM shaded view. The red arrows represent the expected movement direction B) Failure model for lower South Peak area: the different portions of the slope seem to move toward North-East following J1 discontinuity set.

5.1.9 LIMITATIONS AND UNCERTAINTIES OF VOLUME ESTIMATIONS

Using SLBL concept, the uncertainties of the calculated volumes essentially depend on the availability of 3D data delimiting the basal failure surface and the real extension of the unstable area. The SLBL volume estimation could be considerably refined by introducing 3D information derived from geophysical analysis or borehole data (Travelletti et al., 2010). 3D data are directly introduced in the SLBL calculation as invariant points, by subtracting the elevation to the depth of the potential failure surface for each DEM along the geophysical profile or close to the borehole location. Travelletti et al. (2010) coupled SLBL method and seismic survey to assess the failure surface of soil-like landslide and pointed out that results

of the SLBL calculations based only on geomorphological information (surface perimeter) are relatively close to the constraint volume based on the seismic reflection data. The differences between the constraint and the unconstraint calculations are less than 15-17%. Based on this example, it is pointed out that a reliable volume estimation could be obtained, using SLBL, based on geomorphological information. However, in these situations, the knowledge of the operator performing the SLBL computation, especially concerning the choice of the curvature tolerance, introduces some subjectivity on the calculation. When more 3D information about the location and the shape of the failure is available the influence of the operator decreases substantially and at the same time, the accuracy of the volume estimation increases quickly. The uncertainties also depend on the type of instabilities that are considered. If rock slope are considered, the main uncertainties are related to geometrical characteristics of the discontinuity sets influencing the failure mechanism, while uncertainties for soil slope are mainly related to the failure mechanisms (translational, circular or complex failure) and to the morphology of the sliding surface.

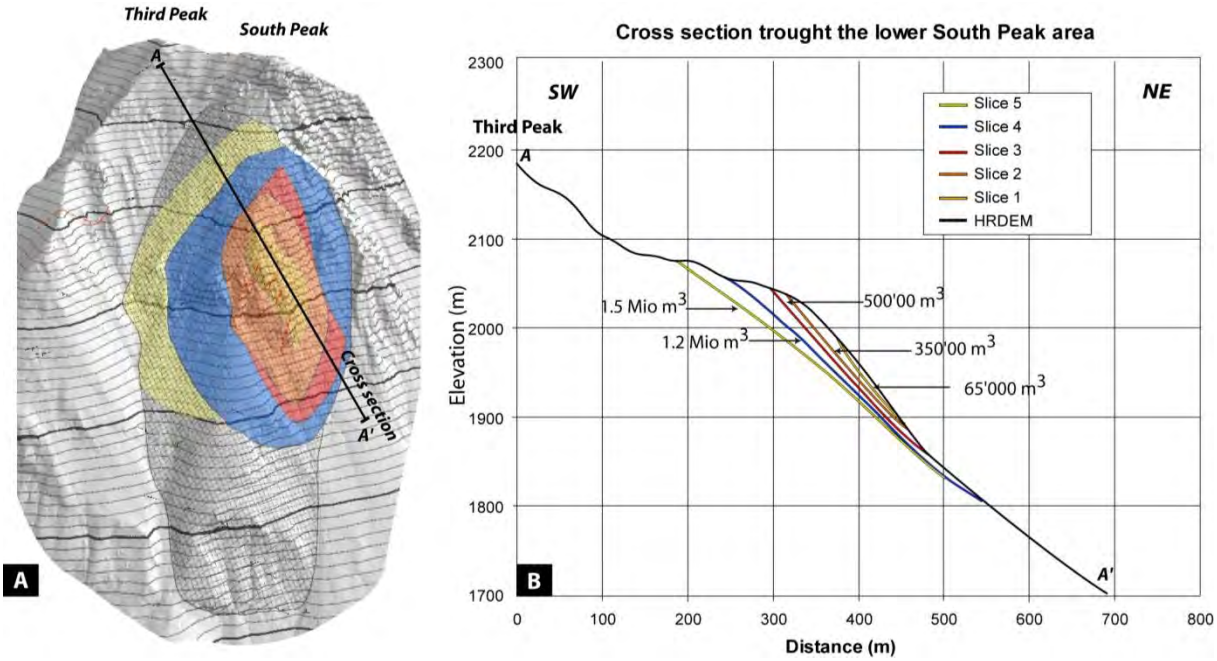

Figure 5.1-15: Representation of the instability areas detected in the lower South Peak area. The cross sections were performed in the direction of the expected movements. The gray potential instability corresponding to the entire lower South Peak area is not represented in the cross section because of his potential movement direction plunges toward east (flexural buckling).

For Turtle Mountain, no information about the real depth of the failure surface is available. However, the potential failure mechanisms and the dips of the potential failure surfaces are essentially known as well as the extension of the moving area. Based on that information, it is possible to define the maximal depth of the potential failure. The comparison between the volumes calculated using geometrical reconstruction indicates a good agreement (Table 5.1-3) with a mean difference of about 15% between the mean SLBL value and the geometrical reconstruction. This difference decreases to 10% when the maximal SLBL calculation and the geometrical reconstruction are compared. The main difference between the two methods concerns the volumes estimations. In fact, the geometrical method seems to overestimate the potential unstable volume, but the discrepancy decreases when smaller volumes are calculated. This tendency is probably related to the fact that SLBL methods assumes a pseudo-circular 3D shape allowing

better characterization of complex multi- failures instabilities (Stead et al., 2006). For smaller volumes, where failures along persistent discontinuity sets occur, geometrical reconstructions seem to give better results.

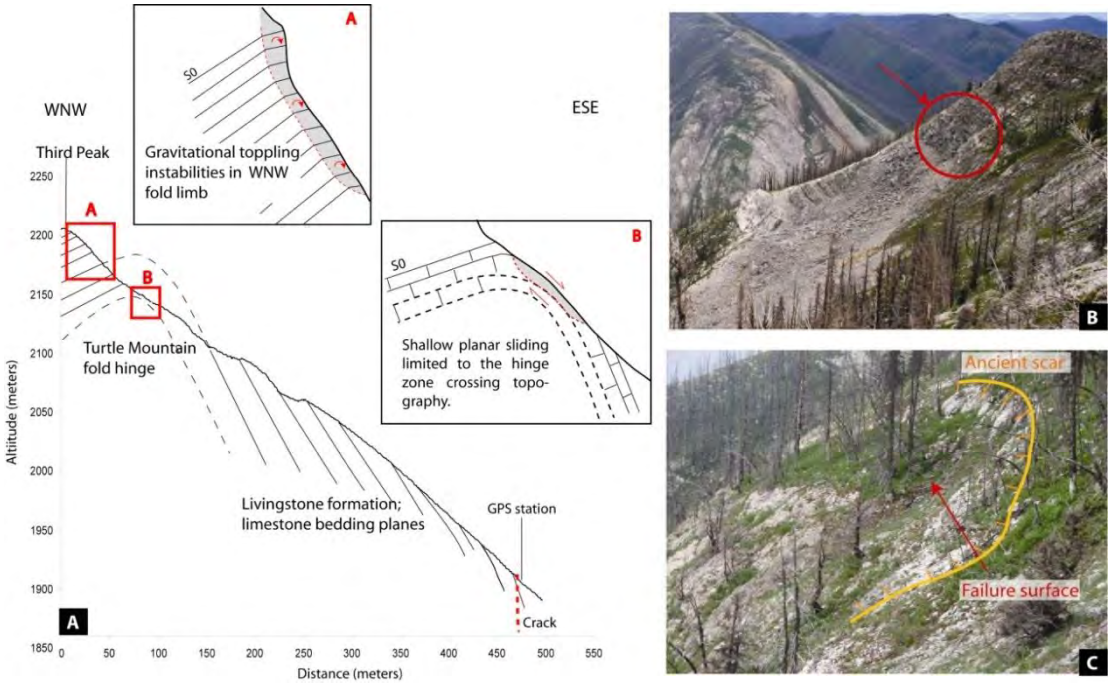

Figure 5.1-16: Shallow instability mechanisms detected in upper Third Peak area: a) Toppling mechanism affecting the western fold limb. b) Planar sliding localized in the fold hinge.

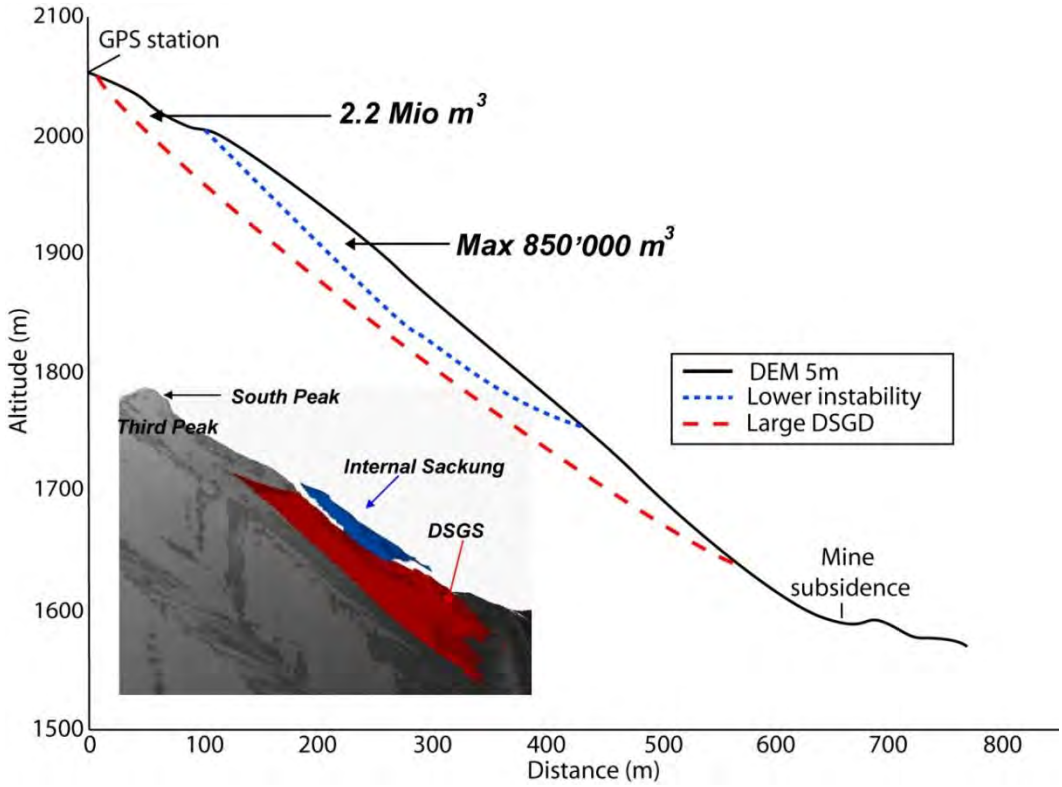

Figure 5.1-17: Cross-section of the Third Peak instability in the potential movement direction (based on crack orientation) showing potential unstable masses calculated using the SLBL method.

5.1.10 RUNOUT ANALYSIS

Several new areas of potential instability have been discovered on Turtle Mountain as described in the previous sections (Figure 5.1-18), in addition to the area initially recognized by Allan (1931). In order to determine the significance of these potential landslides on planning for emergency response and land-use below the eastern slopes of Turtle Mountain, the specific runout scenarios for the various zones needed to be determined. Within the period of time that had passed since previous hazard characterization studies (Allan, 1931, BGC, 2000), new numerical methods of landslide motion analysis have been developed and tested. As part of the recent studies, two such models have been used to estimate the possible consequences of the potential failures that have been identified. Analyses were completed using both a three-dimensional model DAN 3D and a two-dimensional model DAN. Descriptions of both models can be found in Hungr and McDougall (2009). Depending on the morphology of the slope, both models give comparable results when applied to the same travel paths with the same resistance parameters. However, in this case, the potential landslides would run over open slopes and ridges, without lateral confinement. The normal approach to dynamic modelling is to assume that the failing rock mass instantly disintegrates and changes into a frictional fluid. This may not correctly represent reality on unconfined paths, where the 3D models tend to predict excessive lateral spreading of the failing mass in the initial stages of movement (Hungr et al., 2007).

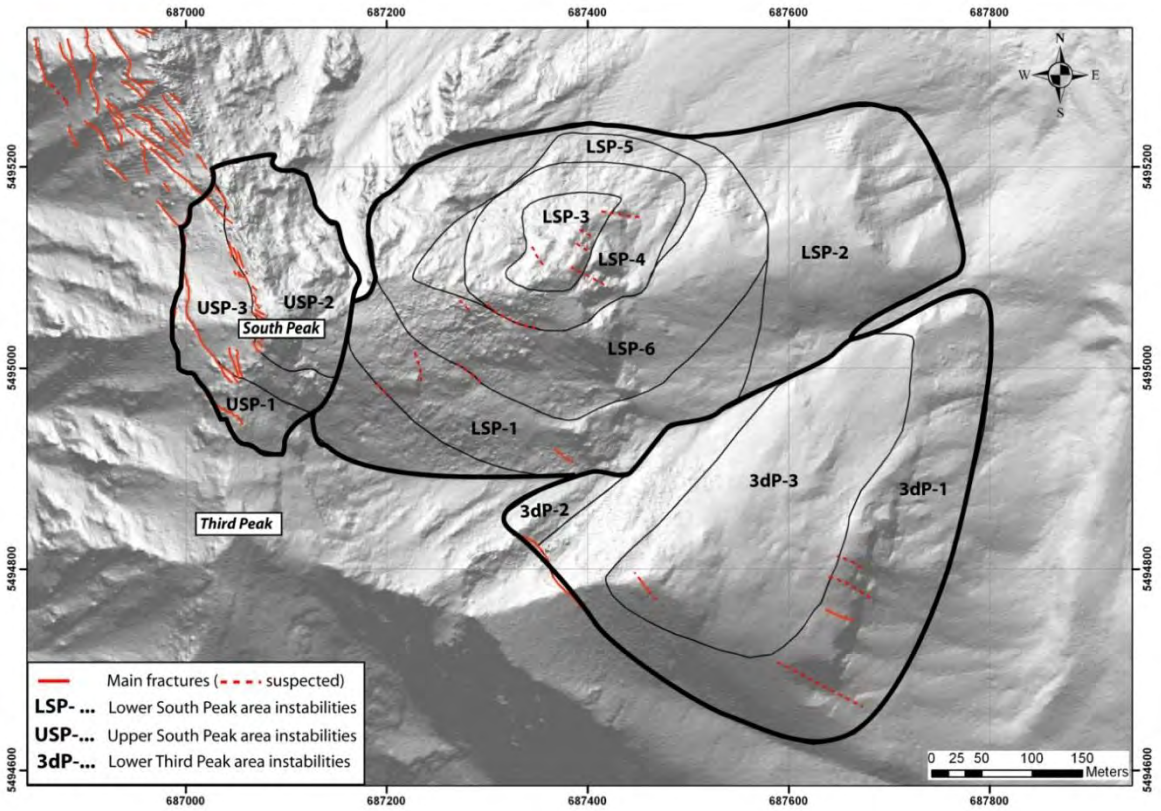

Figure 5.1-18: Outlines of the twelve unstable zones indentified from the combined COLTOP/SLBL analysis of the Third and South Peak areas.

The real rock mass may remain fully or partially coherent for a certain period after detachment and may thus follow a narrower path than would be predicted by the 3D model. With the 2D (or, rather, pseudo-

three-dimensional) model DAN, the width and direction of the travel path is prescribed subjectively by the user. This allows an alternative estimate of the runout distance to be made, assuming that the path may be narrower and/or straighter than that outlined by the 3D model. The final runout estimate is selected as the greater of the two alternative analyses. In most cases, the narrower path did, in fact, result in a somewhat longer runout, as shown later.

5.1.10.1 Model calibration

The two models were calibrated by back-analysis of the 36 million m^3 1903 Frank Slide and other smaller rock avalanches. A parametric study of the 1903 rock avalanche derived best fit parameters of the Voellmy type, including both a frictional and a velocity-dependent flow resistance term (Hungr, 2007). This is typical of large rock avalanches (Hungr, 2007, Sosio et al., 2009). Given the relatively small volume of most of the potential rock avalanches newly identified in this recent study for portions of South and Third Peaks and the dry, rocky character of the Turtle Mountain slopes, it is considered that motion of these landslides is most likely to remain frictional. In order to develop a predictive model for smaller detachments, calibration back-analyses were carried out of nine rock avalanche cases selected to represent rock avalanches that traversed relatively dry slopes, free of deep, saturated soil deposits (Table 5.1-4).

Table 5.1-4: Rock avalanche cases selected for calibration.

Location	***Volume (m^3)***	***Bulk FrictionAngle (°)***	***Reference***
Afternoon Ck	0.7 M	35	Strouth et al. (2006)
Thurwieser	1.9 M	26	Sosio et al. (2008)
Jonas North	2.4 M	25	Bruce (1978)
Jonas South	3.7 M	26	Bruce (1978)
Madison	33 M	15	Hungr and Evans (1996)
Frank, 1903	36 M	14	Cruden and Krahn (1978)
Val Pola	59 M	18	Hungr and Evans (1996)
Hope1965	64 M	22	Hungr and Evans (1996)
Diablerets	73 M	17	Hungr and Evans (1996)

Four of these are originated in limestone rock and five in strong igneous or metamorphic rocks. All the calibration cases ran out over steep mountain slopes, but only those larger than 10 million m^3 reached valley bottoms. In all cases, detachment volumes given by the references in the last column of Table 5.1-4 were used, but increased by a factor of 1.2 to account for fragmentation bulking. Table 5.1-5 gives the volumes of the rock avalanches and the effective (bulk) friction angle values (see Hungr et al., 2005) required to produce the observed runout in each case.

The frictional back-analyses clearly indicate an inverse relationship between volume and the friction angle, as shown in Figure 5.1-19. Such a trend has been observed in previous studies. The reasons for it are presently not clear, but may include:

- Increased likelihood for the larger slides to encounter unconsolidated saturated material on lower slopes,
- Greater intensity of possible undrained loading of material over-run by a larger slide,
- More intensive grain crushing and destruction of rock asperities in the larger events.

Table 5.1-5: Potential source volumes identified by HRDEM analysis and calculated using SLBL.

Symbol	***Location***	***Expanded Volume (m³)***	***Bulk friction angle (°)***
LSP-1	South Peak	1.89 M	25.0
LSP-2	Lower South Peak	6.59 M	20.0
LSP-3	South Peak	0.12 M	36.0
LSP-4	South Peak	0.46 M	30.4
LSP-5	South Peak	0.63 M	29.7
LSP-6	South Peak	1.44 M	26.2
USP-1	Upper South Peak	1.99 M	24.5
USP-2	Upper South Peak	0.30 M	31.0
USP-3	Upper South Peak	1.37 M	26.3
3dP-1	Third peak	2.59 M	23.2
3dP-2	Third Peak	54 000	37.0
3dP-3	Third Peak	1.37 M	26.3

A semi-logarithmic lower-limit envelope was drawn to the calibration data in Figure 5.1-19. This envelope was used to select bulk friction angles used in forward analysis, given the volume of each detachment. As a result, the larger rock avalanches are more mobile.

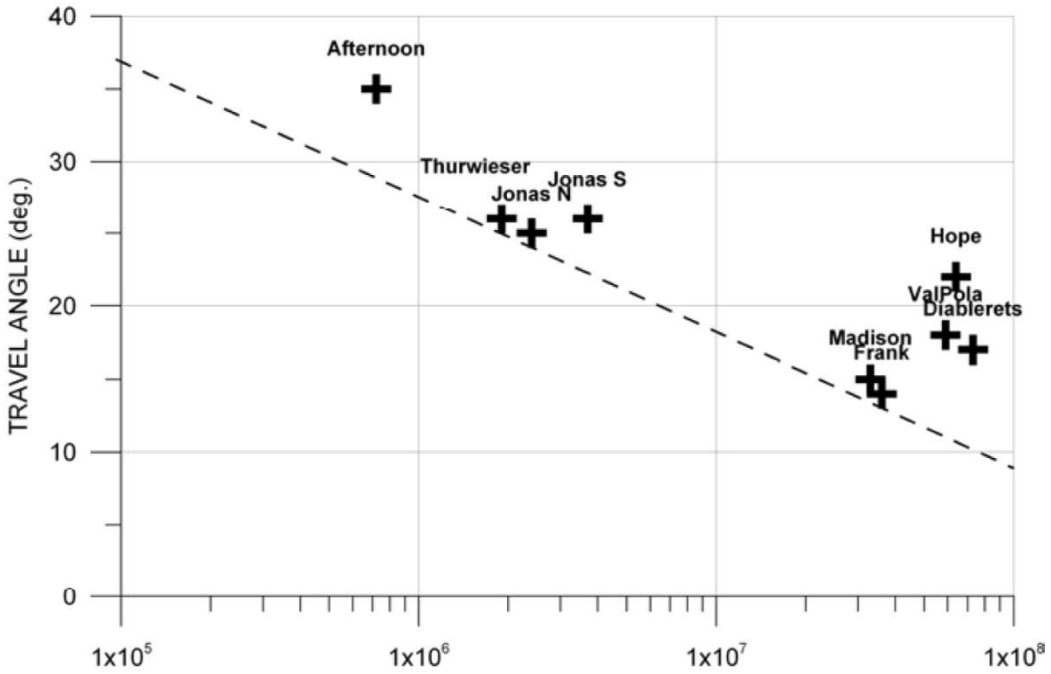

Figure 5.1-19: Calibration analysis, correlation between landslide volume and the back-calculated bulk friction angle (including pore pressure effects).

5.1.10.2 Results of Analyses

Two examples of frictional model analyses, using volume-related friction angles resulting from calibration are shown in Figure 5.1-20 and in Figure 5.1-21. These figures show the extent of the footprint of the landslide path (damage line) and the distribution of the debris deposits predicted by the 3D model. In addition, a line shows the location of the section selected for the 2D DAN analysis and the maximum runout predicted along this line. The 2D analyses were conducted using nearly constant path width and could be considered to represent landslides that remain narrowly channeled (smaller or closer to the

width or the source area) over most of their travel distance, possibly as a result of delayed fragmentation. As could be expected, the resulting runout distances are somewhat greater than those produced by the 3D model.

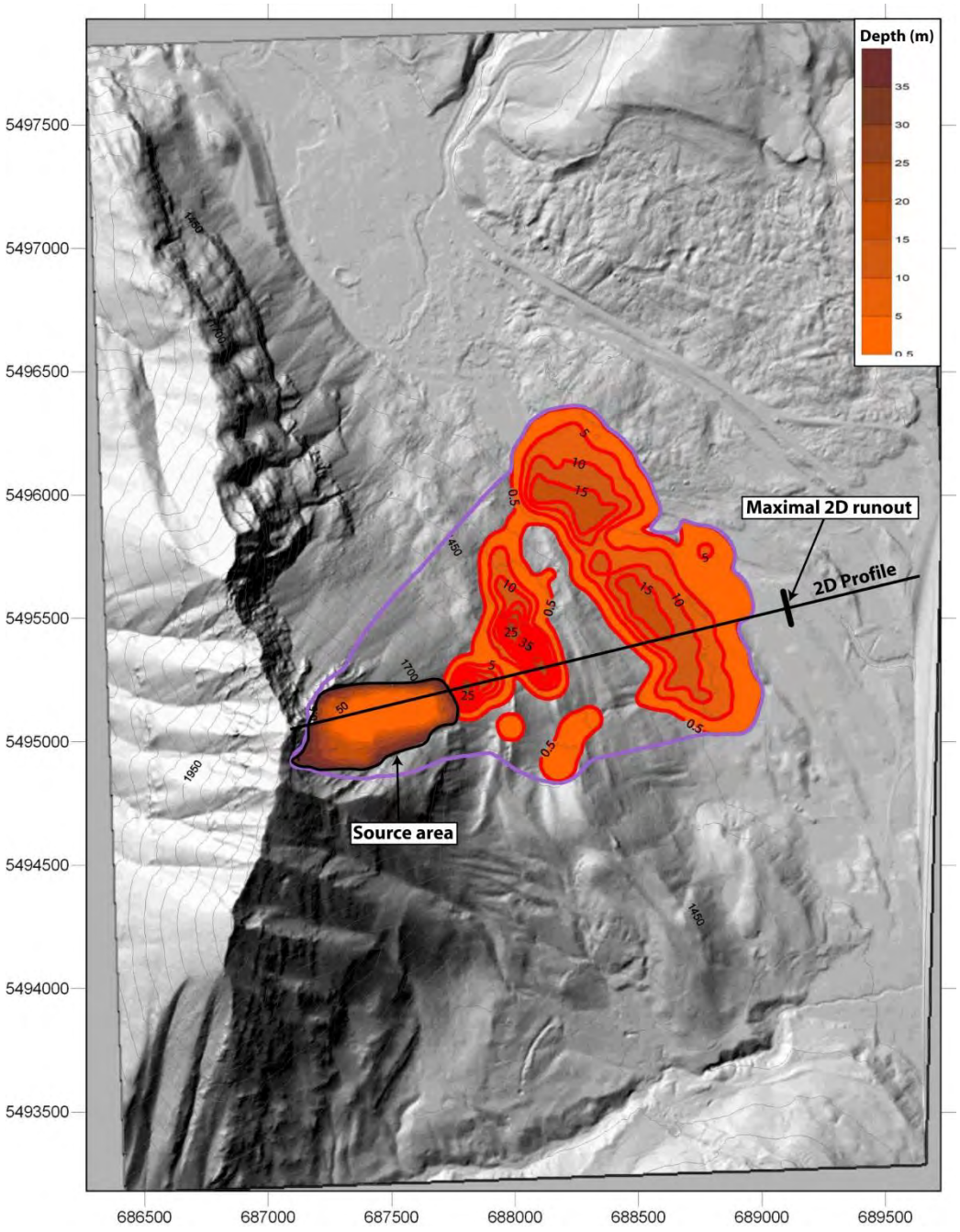

Figure 5.1-20: 3D prediction of the runout of the 6.59 M of cubic meters LSP-2 rock avalanche from the South Peak. The red areas indicate the final position of the 3D deposit, with 5 m contours. The black line on the map shows the location of the profile used in the 2D analysis. The thick, short black line shows the 2D runout.

All of the runout models stopped in less than 1.5 minutes, similar to the 1903 Frank Slide. The maximum estimated velocities were in excess of 50 m/s (180 km/h). The calculated deposit thicknesses, shown in Figure 5.1-20 and in Figure 5.1-21 (5 m contour intervals), were typically up to 10 m, but ranged up to 20 m. A summary of the maximum runout distances from the 2D and 3D analyses of the 12 new source zones identified by the present structural survey and listed in Table 5.1-5 is given by the maximum runout

envelopes in Figure 5.1-22. The 2D maximum runout distances are typically somewhat longer than the 3D results due to the concentration of energy on the narrow path. The direction of movement of the 3D slide and the assumed 2D profile often did not agree, showing the sensitivity of the 3D models to topographic details. Over most of the area, the largest runout is determined by LSP-2, the total failure of Lower South Peak, with a volume of 6.6 million of m^3. This is shown on Figure 5.1-20. For the Third Peak area the largest runout is determined by the 3dP-1 with an estimated volume of 2.6 million m^3 (Figure 5.1-21).

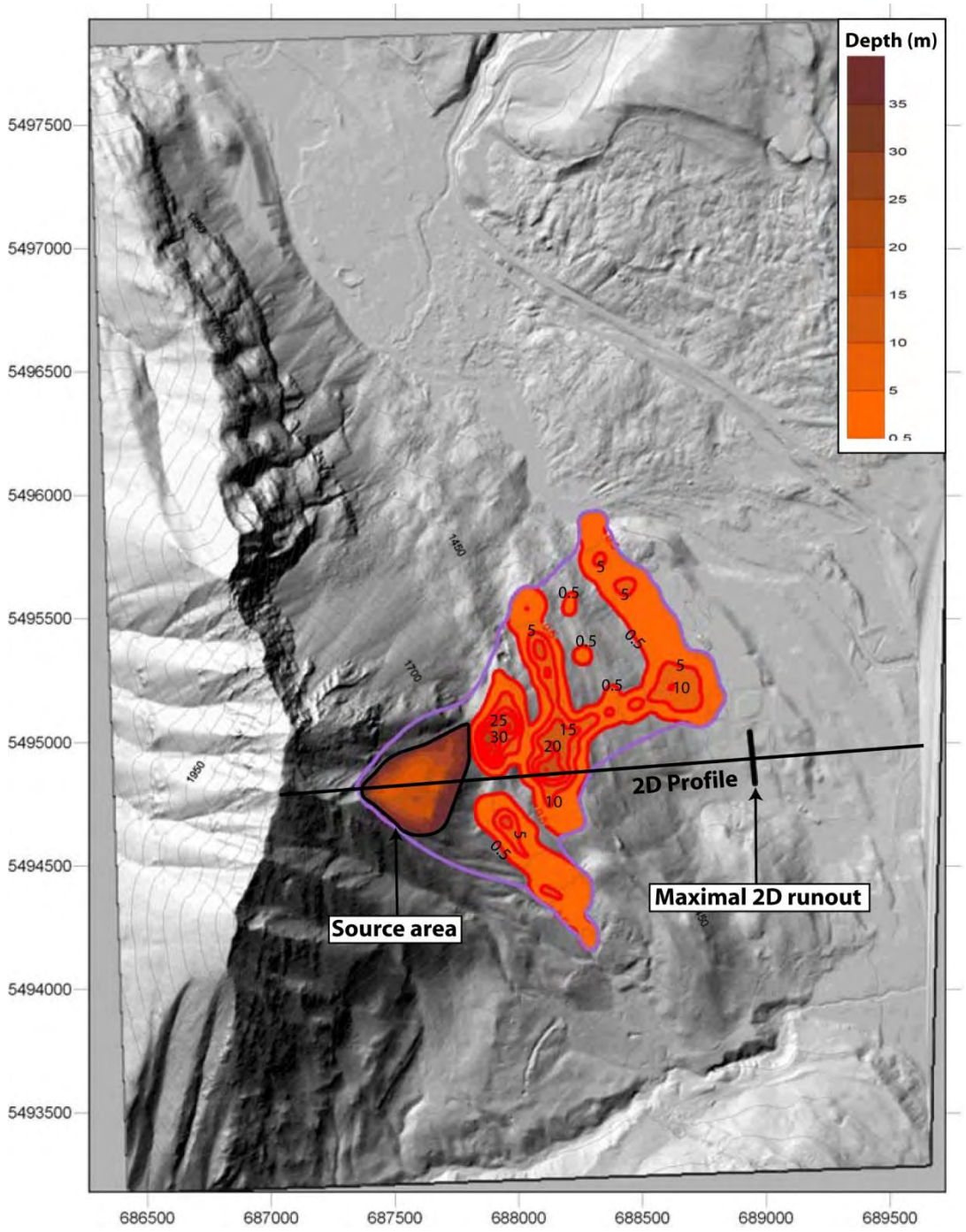

Figure 5.1-21: 3D prediction of the runout of the 6.59 Mio m3 LSP-2 rock avalanche from the Third Peak. The red areas indicate the final position of the 3D deposit, with 5 m contours. The black line on the map shows the location of the profile used in the 2D analysis. The thick, short black line shows the 2D runout.

5.1.11 NEW INSIGHTS FOR HAZARD MANAGEMENT

Understanding of the relative likelihood of various runout scenarios is important in managing the risk associated with the rock avalanche hazard at Turtle Mountain. Until recently, the single failure run out scenarios provided by Allan (1931) and BGC (2000) have been utilized for all discussions and planning for emergency response with the municipality and provincial emergency management officials (Froese et al., 2005; Moreno and Froese, 2009a, Froese and Moreno, submitted). These previous assumptions have been made without the advances in mapping technologies and runouts modeling that are available today. The present study contributed the knowledge that the most active movement areas are associated with smaller volumes and less substantial runout. These maximum extents of the smaller volumes runout modeling has been presented in relation to the previous large single event empirical scenarios on Figure 5.1-22 and communicated formally to the municipality and provincial emergency management officials. Although the visible signs of activity exhibits during field mapping indicate that a series of smaller volume failures is more likely, the potential for a single large volume failure cannot be ignored. Based on this the current planning for emergency response and evacuation still utilizes the larger volume runout estimate provided by BGC (2000).

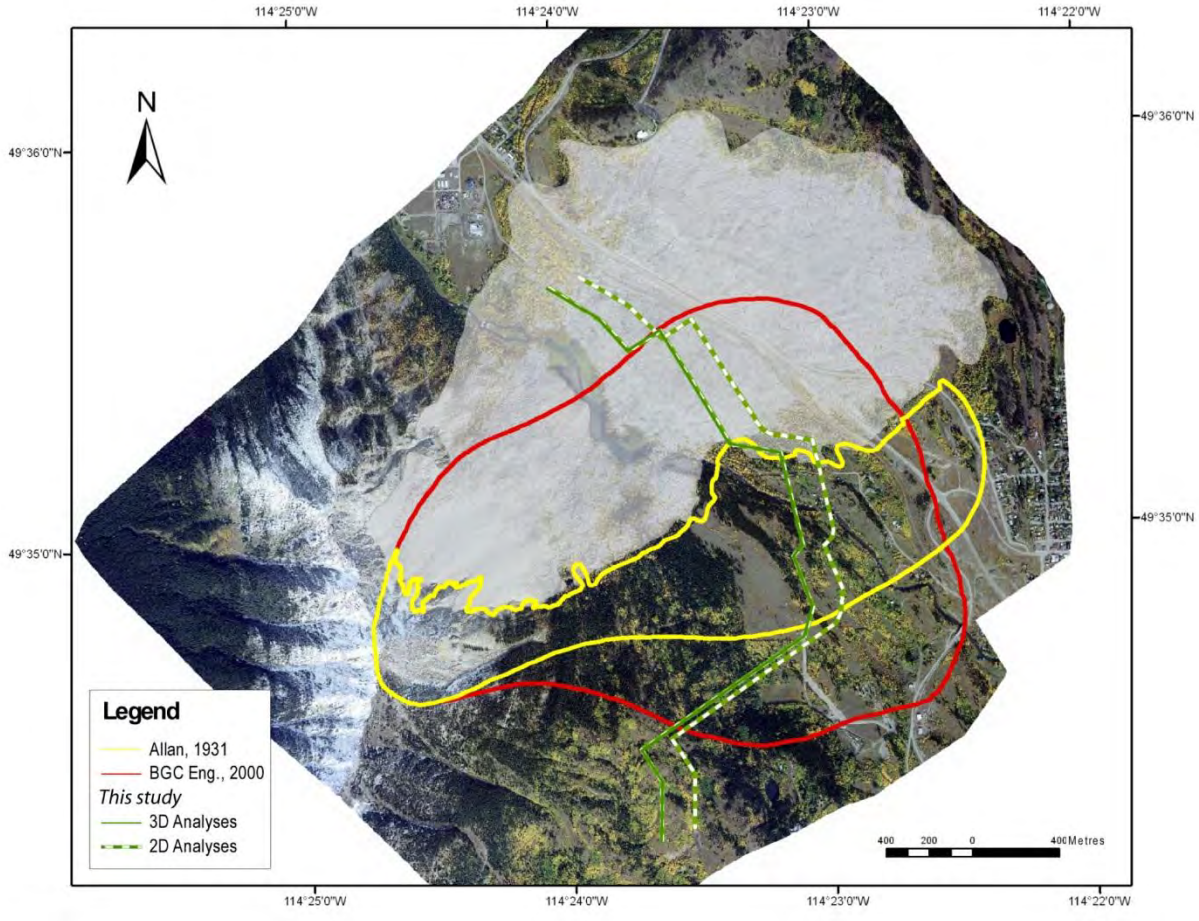

Figure 5.1-22: Updated piecewise run out scenario envelope as compared to the previous estimates for a single large event from the South Peak.

As the potentially unstable structures have only been identified and there is no information on the spatial and temporal characteristics of the deformations, a monitoring system has been installed on the lower

Third and lower South Peak areas, in order to characterize the movements. This system consists of an array of overlapping global positioning system (GPS) monitoring points (both continuously monitored and periodically monitored) and a series of 20 mirror prism which are monitored via robotic total station from across the valley. Details of the installations, performance and data trends are reported by Moreno and Froese (2008, 2009b) and are shown on Figure 5.1-23. In addition to the on-ground instrumentation a ground-based InSAR system was installed at Turtle Mountain in fall 2009 (Dehls et al., 2010) and monitoring campaigns were completed in the fall of 2009 and spring/summer of 2010 in order to test the application of the technology to the very slow movements at Turtle Mountain. As it is expected that deformation rates are likely in the millimeter to sub-millimeter level, many years of continuous monitoring will likely be required to gain confidence in the displacement trends. To this point the only detectable movements on the eastern face of the mountain are contained to the headscar of the 1903 Frank Slide, where large blocks with volumes of 100's to 1000's of m^3 detach from the crown area and fall onto the talus slopes below. While these movements are of low consequence they provide a test of differing monitoring technologies in detecting very slow (mm/year) rock slope movements. Based on the results of monitoring from the EDM system (Moreno and Froese, 2009b), photogrammetric targets (Froese et al., 2009), dGPS (Moreno and Froese., 2009b) and the ground-based InSAR (Dehls et al., 2010) movement rates of up to 5 mm/year have been observed on this active crown area.

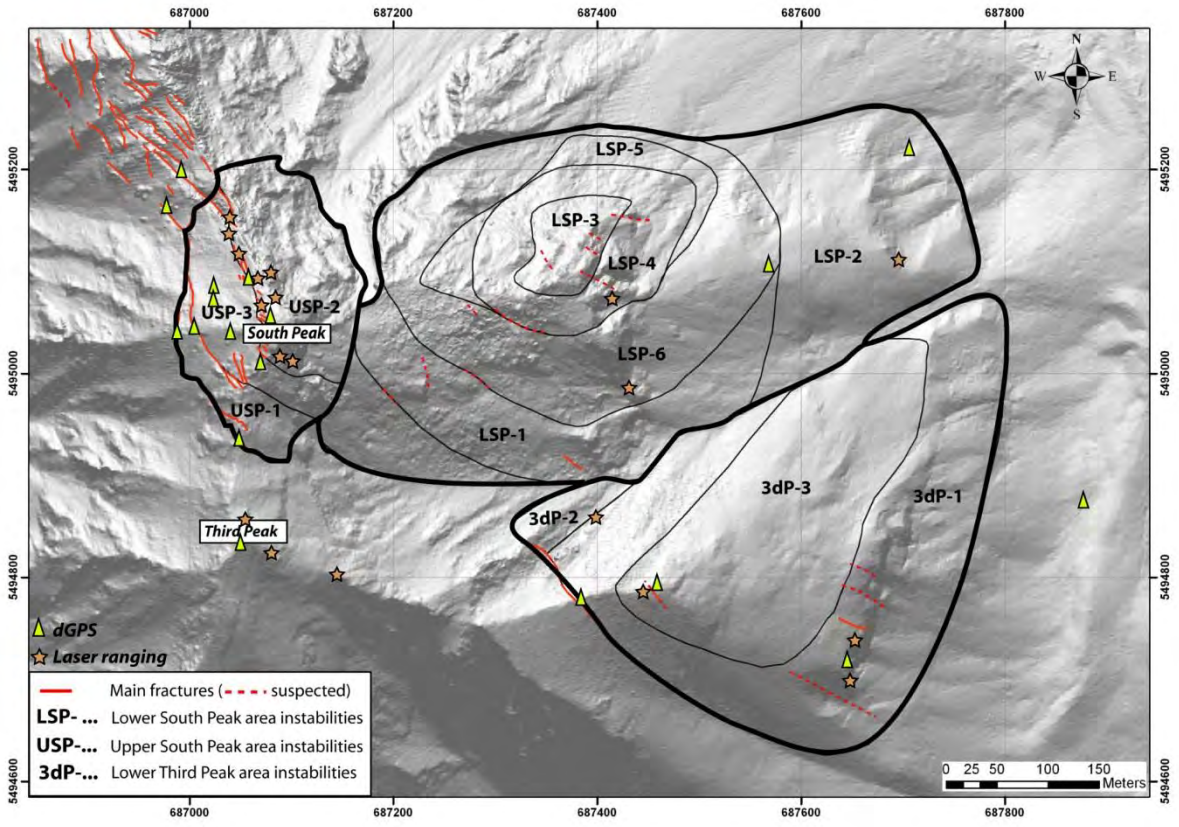

Figure 5.1-23: Plan view of the eastern side of Turtle Mountain showing the distribution of monitoring points below South and Third Peaks.

As there is quite good agreement between the various results it provides confidence in the fact that these technologies are able to quantify very slow movements and therefore confidence that any movements on other portions of the eastern face of the mountain are within these detectable limits.

The fact that no movements have been observed on these systems on other portions of the mountain provides confidence in the fact that any movements, if occurring, are lower than a few millimeters per year and therefore not currently of concern. Regular communication with the affected population regarding the risk associated with these hazards has been established. The most recent results of the ongoing studies are not only published (Moreno and Froese, 2008, 2009b, 2010) but also presented in public meetings to the municipal officials and residents in the affected zones. Frequent updates are also provided on the Alberta Geological Survey website at www.ags.gov.ab.ca.

5.1.12 REFERENCES

Allan, J.A. 1931. Report on the stability of Turtle Mountain, Crowsnest District, Alberta. Department of Public Works, Edmonton, Alberta. 14 p.

Allan, J.A. 1932. Second report on the stability of Turtle Mountain, Crowsnest District, Alberta. Department of Public Works, Edmonton, Alberta. Alberta Provincial Archives. 25 p.

Allan, J.A. 1933. Report on stability of Turtle Mountain, Alberta and survey of fissures between North Peak and South Peak; Alberta Department of Public Works, Alberta Provincial Archives, 28 p.

Benko, B., Stead, D. 1998. The Frank slide: A re-examination of the failure mechanism. Canadian Geotechnical Journal 35, 299-311.

BGC Engineering. 2000. Geotechnical hazard assessment of the south flank of Frank Slide, Hillcrest, Alberta. Report to Alberta Environment, No. 00-0153.

Brideau, M-A., Pedrazzini, A., Stead, D., Jaboyedoff, M., Froese, C.R. 2009a. Preliminary three-dimensional analyses of South Peak area, Turtle Mountain, Alberta. *In Proceedings of the 62nd Canadian Geotechnical Conference*. Bitech Publishers.

Brideau, M-A., Yan M., Stead, D. 2009b. The role of tectonic damage and brittle rock fracture in the development of large rock slope failures, *Geomorphology*, 103, 30-49.

Bruce, I. 1978. The field estimation of shear strength on rock discontinuities. Ph. D. Thesis, Departmentt Civil Engineering, University of Alberta. 318 pp

Couture, R. 1998. Contributions aux aspects mécaniques, et physiques des écroulements rocheux. PhD thesis, Laval University, 573 p.

Cruden, D.M., Krahn, J. 1973. A re-examination of the geology of the Frank slide, *Canadian Geotechnical Journal*, 10, 581-591.

Cruden, D.M., Krahn, J. 1978. Frank Rockslide, Alberta, Canada. in B. Voight (ed.), *Rockslides and Avalanches*,Vol. 1, 365-392. Amsterdam, Elsevier.

Cruden, D.M, Martin, D.K. 2007. Before Frank slide, *Canadian geotechnical journal*, 44, 765-780.

Daly, R.A., Miller, W.G., Rice, G.S. 1912. Report of the commission appointed to investigate Turtle Mountain, Frank, Alberta, *Geological Survey of Canada Memoir*, 27. 34 p.

Dehls, J., Guidici, D., Mariotti, F., Farina, P., Martin, D.C., Froese, C.R. 2010. Monitoring Turtle Mountain using ground-based synthetic aperture radar (GB-InSAR). *Proceedings of the 64th Canadian Geotechnical Conference*. Calgary, Alberta, 1635–1640.

Derron M.-H., Jaboyedoff M., Blikra, L. H. 2005. Preliminary assessment of rockslide and rockfall hazards using a DEM (Oppstadhornet, Norway), *Nat. Hazards Earth Syst. Sci.*, 5, 285-292.

Fossey, K.W. 1986. Structural geology and slope stability of the southeast slopes of Turtle Mountain, Alberta, M.Sc. Thesis, University of Alberta, 113 p.

Froese, C., Moreno, F. 2011. Structure and components for the emergency response and warning system on Turtle Mountain, Alberta, Canada, *Natural Hazards*, DOI 10.1007/s11069-011-9714-y.

Froese, C.R., Murray, C., Cavers, D.S., Anderson, W.S., Bidwell, A.K., Read R., Cruden, D.M., Langenberg, W. 2005. Development of a Warning System for the South Peak of Turtle Mountain. in Landslide Risk Management, O. Hungr, R. Fell, R.R. Couture and E. Eberhardt, A.A. Balkema, Leiden, Netherlands, p. 705–712.

Froese, C., Moreno, F., Jaboyedoff, M., Cruden, D. 2009. 25 Years of Movement Monitoring on the South Peak of Turtle Mountain (Alberta, Canada): An Understanding of the Hazard; Canadian Geotechnical Journal. 45: 256-269.

Gadd, B. 1986. *Handbook of the Canadian Rockies*. Corax Press.

Hoek, E., Bray, J. 1981. Rock slope engineering, 3rd edn, Inst Mining and Metallurgy, London, UK.

Hoek, E, Brown, E.T. 1997. Practical estimates of rock mass strength, *International Journal of Rock Mechanics and Mining Sciences*, 34, 1165-1186.

Hungr, O., Corominas, J., Eberhardt, E. 2005. State of the Art Paper #4, Estimating landslide motion mechanism, travel distance and velocity. In Hungr, O., Fell, R., Couture, R. and Eberhardt, E., Eds. *Landslide Risk Management. Proceedings, Vancouver Conference*. Taylor and Francis Group, London.

Hungr, O. 2007. South Peak of Turtle Mountain, Frank, Alberta: Runout analyses of potential landslides. Report prepared for Alberta Geological Survey. 13 p.

Hungr, O., McKinnon, M., McDougall, S. 2007. Two models for analysis of landslide motion: application to the 2007 Hong Kong benchmarking exercises. *Proceedings, 2007 International Forum on Landslide Disaster Management*, Ho, K. and Li, K., Editors, Geotechnical Engineering Office, Hong Kong.

Hungr, O., and McDougall, S. 2009 Two numerical models for landslide dynamic analysis, *Computers and Geosciences*, 35 : 978–992.

International Society for Rock Mechanics (ISRM). 1978. Suggested methods for the quantitative description of discontinuities in rock masses, *International Journal of Rock Mechanics and Mining Sciences & Geomechanics Abstracts*, 15, 319–368.

InnovMetric: PolyWorks: 3-D scanner and 3-D digitizer software from InnovMetric Software Inc., http://www.innovmetric.com/ Manufacturing/home.aspx, accessed: 10 October 2009.

Jaboyedoff, M., Couture, R., Locat, P. 2009. Structural analysis of Turtle Mountain (Alberta) using Digital Elevation Model: Toward a progressive failure, *Geomorphology*, 103, 5-16.

Jaboyedoff, M., Metzger, R., Oppikofer, T., Couture, R., Derron, M.-H., Locat, J., and Turmel, D. 2007. New insight techniques to analyze rock-slope relief using DEM and 3D-imaging cloud points:COLTOP-3D software, *Proceedings of the 1st Canada – U.S. Rock Mechanics Symposium*.

Jaboyedoff, M., Tacher, L. 2006. Computations of landslide slip surface using DEM, Geological Society of London, William Smith Meeting (2004).

Langenberg, C.W., Pana, D., Richards, B.C., Spratt, D.A., Lamb, M.A. 2007. Structural geology of the Turtle Mountain area near Frank, Alberta, *EUB/AGS Science Report 2006-01*, 30 p.

McConnell, R.G., Brock, R.W., 1904. Report on the great landslide at Frank, Alberta, Canada. Part 8, Annual Report, 1903. Canada department of the Interior, Ottawa, ont. pp. 3-17.

Moreno, F., Froese, C.R. 2006. Turtle Mountain field laboratory, monitoring and research summary report, January to December 2005. Alberta Energy and Utilities Board, *EUB/AGS Earth Sciences Report 2006-07*.

Moreno, F., Froese, C.R. 2008. Turtle Mountain Field Laboratory: 2007 Data and Activity Summary. Energy Resources Conservation Board, *ERCB/AGS Open File Report*, 2008-07.

Moreno, F., Froese, C.R. 2009a. ERCB/AGS Roles and Responsibilities Manual for the Turtle Mountain Monitoring Project, Alberta. Energy Resources Conservation Board, *AGS/ERCB Open File Report* 2009-06.

Moreno, F., Froese, C.R. 2009b. Turtle Mountain Field Laboratory, Alberta (NTS 82G): 2008 Data and Activity Summary. Energy Resources Conservation Board, *AGS/ERCB Open File Report 2009-15*.

Moreno, F., Froese, C.R. 2010. Turtle Mountain Field Laboratory, Alberta (NTS 82G): 2009, Data and Activity Summary, Energy Resources Conservation Board, *ERCB/AGS Open File Report 2009*.

Pedrazzini, A., Jaboyedoff, M., Froese, C.R, Langenberg, C.W., Moreno, F. 2011. Structural analysis of Turtle Mountain: origin and influence of fractures in the development of rock slope failures. From Jaboyedoff, M. (ed.) *Slope tectonics*, Geological Society, London, Special Publications 2011, 351, 163-183.

Pedrazzini, A., Jaboyedoff, M., Froese, C.R., Langenberg W., Moreno, F. 2008. Structure and Failure Mechanisms Analysis of Turtle Mountain. In : J. Locat, D. Perret, D. Turmel, D. Demers et S. Leroueil. *Proceedings of the 4th Canadian Conference on Geohazards : From Causes to Management*. Presses de l'Université Laval, Québec, 594 p

Price, R.A. 1994. Geological history of the Peace River Arch [accessed June 2004]; In Geological Atlas of the Western Canada Sedimentary Basin, Mossop G.D., Shetson I. (comp.), Canadian Society of Petroleum Geologists and Alberta Research Council, Calgary, Alberta.

Sosio, R., Crosta, G.B., Hungr, O. 2008. Complete dynamic modeling calibration for the Thurwieser rock avalanche (Italian Central Alps), *Engineering Geology*, 100,11-26.

Spratt, D.A., Lamb, M.A. 2005. Borehole data interpretation and orientation, Turtle Mountain Project: Internal report of work Package WP15B, Alberta Municipal Affairs, 15 p.

Stead, D., Eberhardt, E., Coggan, J.S. 2006. Developments in the characterization of complex rock slope deformation and failure using numerical modelling techniques, *Engineering geology*, 83, 217-235.

Strouth, A., Burk, R. L., Eberhardt, E. 2006. The Afternoon Creek rockslide near Newhalem, Washington, *Landslides*, 3, 175–179,

Sturzenegger, M., Stead, D., Froese, C., Moreno, F., Jaboyedoff M. 2007. Mapping the geological structure of Turtle Mountain, Alberta: A critical interpretation of field, DEM and LiDAR based techniques. In Eberhardt, E., Stead, D and Morrison T. (Eds.): *Rock mechanics: Meeting Society's Challenges and demands* (Vol. 2), Taylor & Francis. pp. 925-932.

Travelletti, J., Demand, J., Jaboyedoff, M., Marillier, F. 2010. Mass movement characterization using a reflexion and refraction seismic survey with the sloping local base level concept, *Geomorphology*, 116, 1-10.

5.2 THE 2006 EIGER ROCKSLIDE, EUROPEAN ALPS

5.2.1 ABSTRACT

In July 2006 approximately 2 million m^3 of massive limestone began to move on the east flank of the Eiger in central Switzerland. For more than two years after the initial failure, the rock mass moved at rates of up to 70 cm day^{-1}. A detailed analysis of the structures and velocities of the different moving blocks was conducted with the aid of terrestrial laser scanning. The moving rock mass included a rear block that slowly subsided, pushing a frontal block forward. Movement directions were controlled by discontinuity sets that form wedges bounded on one side by sub-vertical bedding planes. The instability was, until recently, buttressed by a glacier. Slope observations and results of continuum and discontinuum modelling indicate that the structure of the rock mass and topography were the main causes of the instability. Progressive weathering and mechanical fatigue of the rock mass appear to have led to the failure. A dynamic analytical model further indicates that the rockslide was primarily controlled by a reduction in the strength of discontinuities, the effects of ice deformation, and, to a limited extent, groundwater flow. This study shows that realistic and simple instability models can be constructed for rock slope failures if high-resolution data are available.

5.2.2 RÉSUMÉ

A partit de juillet 2006, un volume d'environ 2 million de m^3 de calcaire massif, situé dans le flanc est de l'Eiger (Suisse centrale), a commencé à montrer des signes d'instabilité importante. Plus de deux ans après les premiers signes d'instabilité, la masse rocheuse présentait des déplacements différentiels pouvant atteindre des vitesses de l'ordre de 70 cm par jour. Une analyse détaillée des mouvements ainsi que de l'agencement structural de la zone instable ont été effectuées à l'aide du Lidar terrestre. Ces analyses ont permis de mettre en évidence que l'instabilité était subdivisée en deux blocs principaux : un bloc arrière exhibait des mouvements de subsidence, et un bloc frontal qui se déplaçait passivement en suivent l'orientation décrit par deux discontinuités qui permettaient un glissement de type dièdre. Des modélisations numériques par éléments finis et par éléments distincts ont pu mettre en évidence que l'agencement structural et topographique de la zone représente le facteur de prédisposition principal qui a favorisé le développement de l'instabilité. La rupture et le développement rapide de l'instabilité sont vraisemblablement liés à une dégradation progressive du massif rocheux après la déglaciation rapide de la partie supérieure de l'instabilité. Un modèle mécanique dynamique a été développé pour étudier l'évolution rapide de cette instabilité. Les résultats de ce modèle suggèrent que les déplacements observés seraient liés à une réduction rapide de la résistance au niveau des discontinuités et à la déformation de la glace qui couvrait le pied de l'instabilité. Les pressions d'eau à l'intérieur de la masse rocheuse ont aussi pu contribuer au développement de l'instabilité. Cette étude montre l'importance d'intégrer des données structurales et topographiques à haute résolution ainsi que la cinématique tridimensionnelle des déplacements obtenus par acquisitions successives au Lidar terrestre pour développer des modèles numériques simples permettant d'étudier le comportement mécanique des instabilités rocheuses.

5.2.3 INTRODUCTION

In June 2006, a huge rock mass of approximately 2 Mm^3 started to move on the eastern flank of the Eiger peak in central Switzerland (Oppikofer et al., 2008). This event had considerable media impact because of the exceptionally fast displacement rates, frequent rockfalls/partial collapses and a preceding catastrophic rockfall event in May 2006 along the Gotthard highway, which killed two people and led to a five week closure of this important European transportation route (Liniger et al., 2006).

The particular location of the rockslide allowed 3-D imaging by terrestrial laser scanning (TLS) (Oppikofer et al., 2008). This was probably the first time that the movement of a natural rockslide was monitored periodically by TLS. This remote sensing technique enables the main structures controlling the orientations of the movements and the vectors of displacement of the different blocks to be mapped (Oppikofer et al., 2008). The combination of these data led to the creation of a conceptual model implying a bilinear wedge failure with sliding of a frontal block activated by a rear subsiding block (Norrish and Wyllie, 1996).

The development of the 2006 Eiger rockslide shows several features that are common to many rockslides. First, it affected a prominent spur in a glacial valley and, second, it occurred shortly (~150 years) after a major glacier retreat, which de-buttressed most of the slope. These conditions are likely similar to many Alpine valleys at the end of the last glacier advance (9'000 to 12'000 years B.P., Portman 1977; Florineth and Schlüchter, 1998). In postglacial alpine valleys, the influence of deglaciation processes and progressive rock mass degradation is considered an important preparatory factor in the development of both large and small rock slope instabilities (Agliardi et al., 2001, Ballantyne 2002, Eberhardt et al., 2004, Ambrosi and Crosta 2006, Fischer et al., 2010). In Swiss Alpine valleys, glacial retreat and glacial erosion processes represent the main preparatory factors that could lead to important changes in the slope equilibrium (Eberhardt et al, 2004) in two main ways: by unloading of the slope causing a stress relief in the rock mass (Ballantyne, 2002; Cossart et al., 2008; Ghirotti et al., 2011; Ambrosi and Crosta, 2011), and by oversteepening of the valley walls resulting in more adverse structures and stress concentration/rock mass damage at the slope toe (Eberhardt et al., 2004).

The 2006 Eiger rockslide provides a unique opportunity to analyse the destabilization of a slope in a paraglacial environment (Ballantyne, 2002). The specific evolution of the displacement rates of the 2006 Eiger rockslide is complex and difficult to model because of the large movements observed. Based on the conceptual bilinear wedge failure model, we have modelled the destabilisation and the movement of the Eiger rockslide by using Phase2 (Rocscience, 2010) and UDEC (Itasca, 2004), respectively, and providing an analytical solution to the implied stresses based on a two-dimensional bilinear wedge failure model (Sarma, 1979; Norrish and Wyllie, 1996) using optimisation (Bardet and Kapuskar, 1989). This agrees with our conceptual instability model implying failure initiation along the back crack and a weakening of the basal sliding zone to explain the displacement pattern over time. The simulated model results provide data useful to understand the destabilisation of spurs after debuttressing, and for hazard and risk assessment.

5.2.4 GEOLOGY AND MORPHOLOGY

Mt. Eiger is located in the central Swiss Alps near the village of Grindelwald and is part of the autochthonous Mesozoic sediment cover of the crystalline Aar massif, which dips steeply towards the northwest (Günzler-Seiffert and Wyss, 1938). At the rockslide location this Helvetic sedimentary cover is mainly consists of banded tabular upper Jurassic limestone with sub-vertical bedding (S0). More regionally, S0 is affected by a kilometric antiform syncline. The 2006 Eiger rockslide is located on a prominent spur (Figure 5.2-1). At this specific location, the morphology of the valley changes from a wide, U-shaped glacial valley to a narrow deep valley formed by the Lower Grindelwald glacier and its torrent (Figure 5.2-1c and d). This morphologic change is likely due to lithological differences and rock mass strength contrasts between the crystalline basement and Triassic to Middle Jurassic sediments in the southern part and the massive upper Jurassic limestone in the north (Günzler-Seiffert and Wyss, 1938).

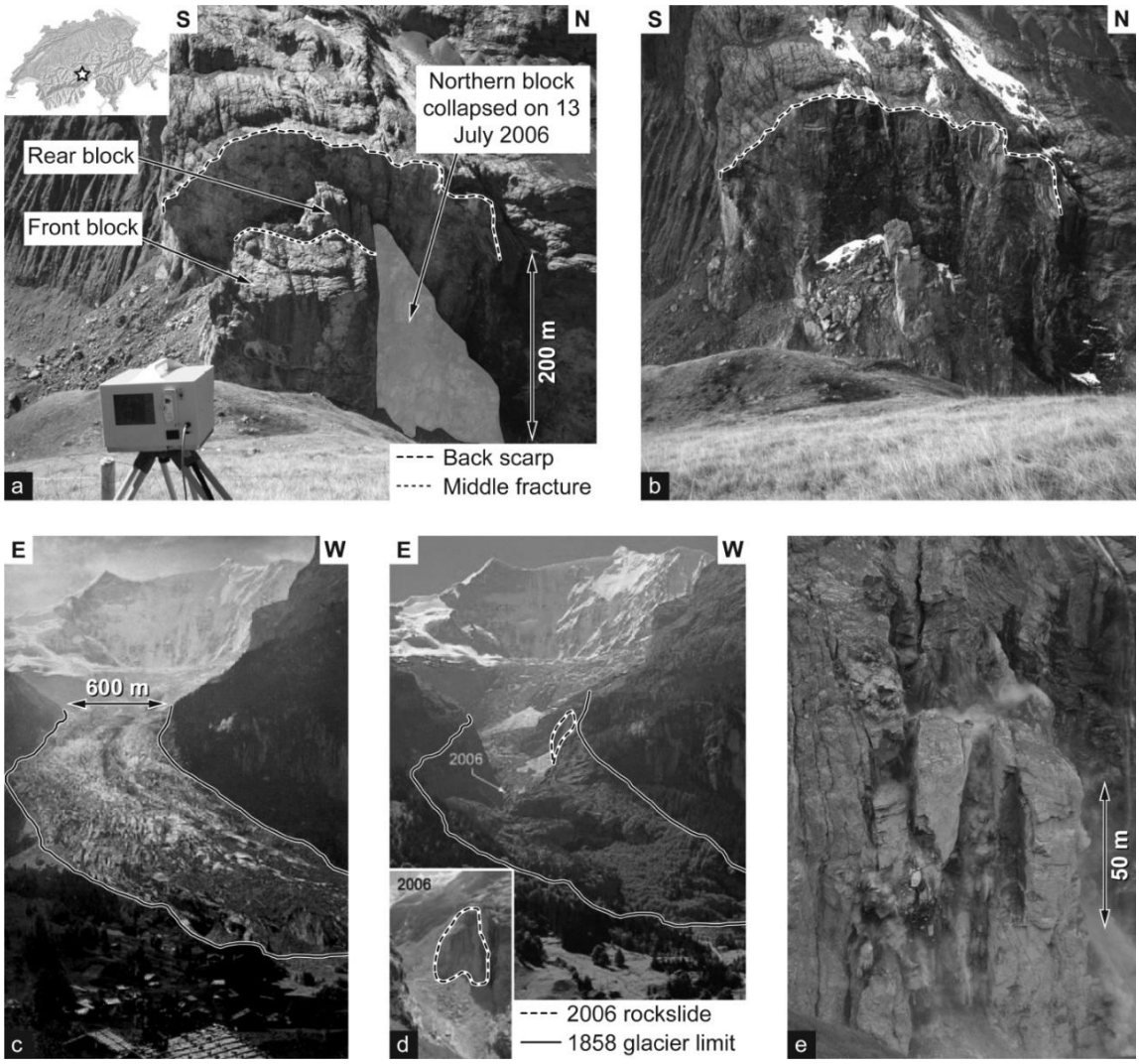

Figure 5.2-1: a) Photograph of the Eiger rockslide (22 September 2006) showing main rockslide features; b) Photograph of the remaining blocks on 21 October 2008; c) Historical photograph of the Lower Grindelwald Glacier in 1858 (© Frédéric Martens, Alpine Club Library London, modified from OcCC, 2007). c) Photograph of the Glacier in 1974 and in 2006 (inset), showing the important mass loss and the localization of the Eiger rockslide (© Heinz J. Zumbühl (1974) and Samuel U. Nussbaumer (2006), modified from OcCC, 2007); e) Photograph of the 13 July 2006 partial collapse of the northern block (photograph: B. Petroni).

The action of the ice of the glacier may have highly stressed this this rock spur as shown in Randa (Eberhardt et al., 2004). During the Little Ice age in 1860, the level of the Lower Grindelwald glacier was approximately 200 m higher than at present and reached the top of the slide back scarp (Messerli et al., 1978; OcCC, 2007) (Figure 5.2-1b).The glacier has retreated since the Little Ice Age, but at an accelerated rate since 1935 due to global warming (Messerli et al., 1978; Werder et al., 2010) (Figure 5.2-1c). The failure of the 2006 Eiger rockslide was probably caused by the removal of this glacier buttress and the subsequent stress relief within the rock mass (Oppikofer et al., 2008). During the last years irregular debris cover on the glacier tongue created differential melting and led to the formation of a surface depression located close to the Eiger rockslide. In this depression a glacier lake formed in 2005 and has been increasing in size until 2008. Sudden draining of this lake and outburst flooding has occurred on several occasions resulting in a major hazard to the communities living close to the river (Werder et al., 2010).

5.2.5 METHODS

5.2.5.1 Laser scanning technology

Laser scanning is a widely used remote sensing technique for the acquisition of point clouds of the Earth's surface (Baltsavias, 1999; Lichti et al., 2002). A laser pulse is emitted in a precisely known direction, back-scattered by the surface and the return pulse is recorded by the scanner. The distance between the instrument and the topography is calculated using the time-of-flight of the pulse. Mirrors inside the instrument deflect the laser beam in different directions and allow sweeping over the area of interest (Lichti et al., 2002); using a high acquisition rate (2500 points per second), a point cloud of the scanned area is obtained. The Optech ILRIS-3D used for this study has a wavelength of 1500 nm and a practical range of about 600 to 800 m on rock slopes. TLS uses a fixed position during the data acquisition and has a better point accuracy (1σ = ~1.5 cm at a distance of 300–400 m, Oppikofer et al., 2009) than aerial laser scanning (1σ = 5–20 cm, Baltsavias, 1999).

5.2.5.2 TLS data treatment and analysis

Typical data acquisition and analysis procedures include (based on Conforti et al., 2005):

1. TLS acquisitions from different viewpoints and/or different view directions.
2. Manual cleaning of scans and removal of vegetation.
3. Co-registration of the scans is a three-step procedure with 1) a rough manual matching, 2) the manual identification of common points in different scans, and 3) the minimization of co-registration errors using a point-to-surface Iterative Closest Point (ICP) algorithm (Besl and McKay, 1992; Teza et al., 2007). This procedure is also used for multi-temporal point clouds by limiting the iterative alignment procedure to the assumed stable part around the rockslide (Teza et al., 2007; Oppikofer et al., 2008; 2009).
4. Georeferencing of the TLS point cloud by co-registration on an ALS point cloud or using ground-control points.
5. The georeferenced TLS point cloud enables detailed structural analyses (Sturzenegger, and Stead, 2009), either by best-fitting planes on the selection of points forming a discontinuity

(Sturzenegger and Stead 2009) or by using specific software tools, such as Coltop3D (Jaboyedoff et al., 2007; 2009). Coltop3D computes the spatial orientation of each point relative to its neighbourhood. Using an orientation-specific colouring of the TLS point cloud allows identification of the principal discontinuity sets and computing their mean orientation (Jaboyedoff et al., 2007; Oppikofer et al., 2009).

6. Displacements between multi-temporal TLS datasets can be assessed by a shortest distance comparison using the ICP algorithm (Oppikofer et al., 2008; 2009). Positive differences mean that the data points are situated above or in front of the reference point cloud, for example due to an advance of the rockslide. Negative differences signify that the data points are behind or below the reference point cloud, for example due to vertical settlement or rockfall.
7. Displacement vectors are created by selecting identical points in multi-temporal point clouds. Errors on the measured displacements vectors are relatively high (length: 1σ = 10 cm; orientation: 1σ = 2–3°; Oppikofer et al., 2008).
8. The roto-translation matrix technique provides a detailed displacement analysis, including both translation and rotation of individual rockslide compartments (Monserrat and Crosetto, 2008; Oppikofer et al., 2009).
9. The rockfall volume is estimated by the volume between the pre-rockfall and post-rockfall surfaces (Rabatel et al., 2008; Abellán et al., 2010).
10. Combining the geometry of the main discontinuities, displacements and multi-temporal cross-sections parallel to the sliding direction allows creation of geometric models of the instability (Oppikofer et al., 2008; 2009).

Data treatment and analysis were performed using PolyWorks® software (InnovMetric, 2011)

5.2.6 STRUCTURAL INTERPRETATION

Four main discontinuity sets were detected on the TLS point cloud using Coltop3D and manual plane fitting (Figure 5.2-2). The presence of metric-scale folds with an open interlimb angle results in a significant variation in the mean orientation of the bedding planes. Fold-related dip variations, particularly in the area of the rockslide, have resulted in two distinct bedding orientations (S0 and S0* in Figure 5.2-2b). Bedding appears characterized as an undulating systematic discontinuity set (ISRM, 1978) showing a wide to very wide spacing. The eastern flank of the valley displays a stepped-like morphology linked to the presence of sub-vertical joint sets or faults (J2 and J3) and less steep discontinuities (J1) forming the flatter areas. This is also verified at outcrop scale based on TLS-DEM analysis. Joint sets J2 and J3 have a wide spacing with a medium to high persistence and are both predominantly planar and rough. However, J3 has a lower persistence (low to medium persistence following ISRM, 1978). The precise geometrical characterization of J1 is difficult because its orientation is especially sensitive to the "smoothing" effect created by the intense glacier erosion. Based on surface morphology, J1 could be described as moderate to widely spaced showing medium to high persistence. The shape of Eiger rockslide is clearly influenced by the discontinuity set orientations. Back-crack shows a saw-tooth shape controlled by the intersection of J2 and S0. The bedding planes also control the lateral extent of the instability, as well as the collapse of individual rock columns.

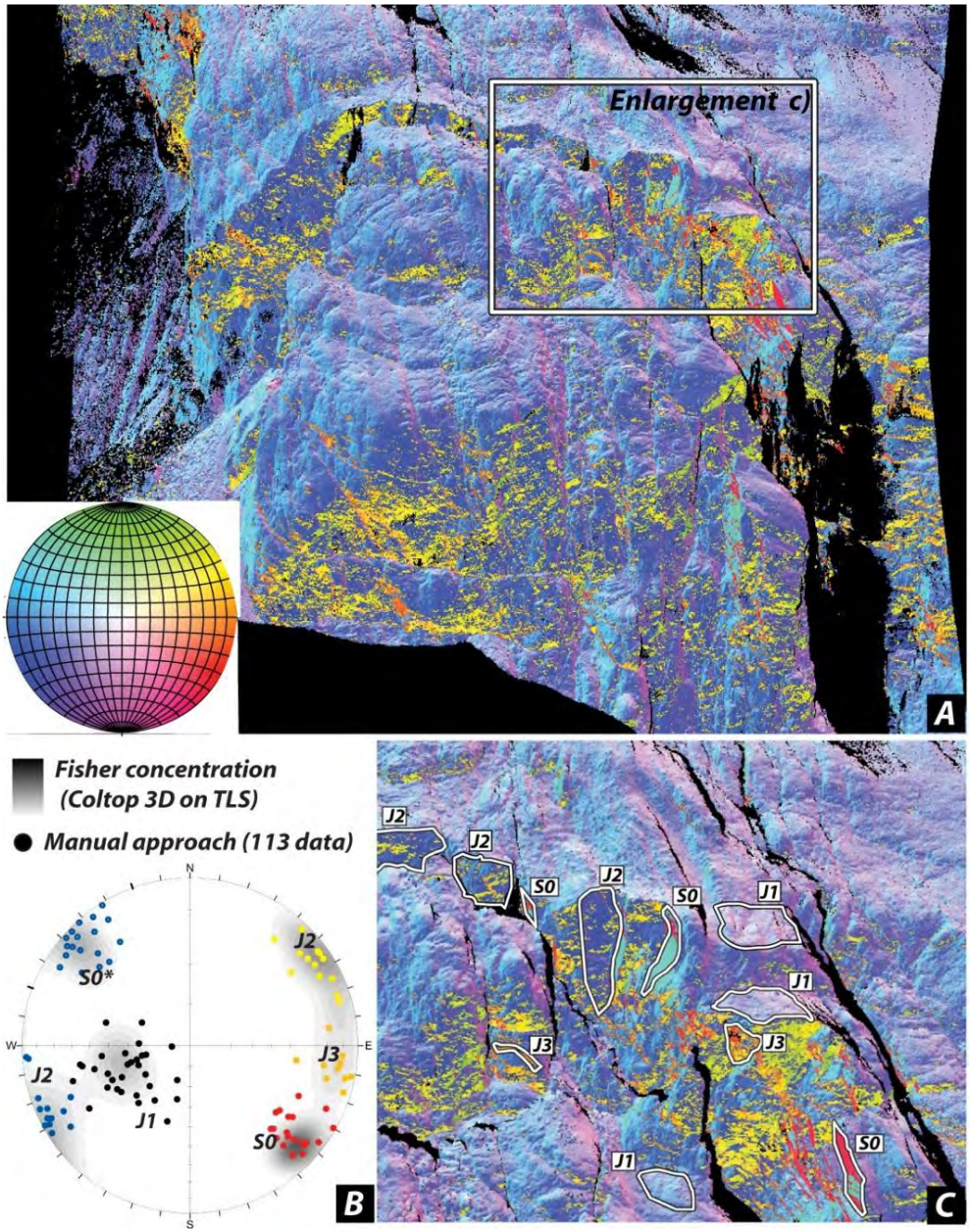

Figure 5.2-2: Structural analysis based on TLs data. a) TLS data of the upper portion of the Eager rockslide represented using Hue saturation system (COLTOP3D). Stereonet (lower hemisphere) showing the results of the structural analyses. Fisher concentration corresponds to poles of orientation orientations extracted by COLTOP3D analysis. Points correspond to poles of orientation obtained by manual fitting in PolyWorks (InnovMetric, 2011). C) Detail view of the upper portion of the rockslide scar showing the main joint sets characterized by their colour code.

5.2.7 EVOLUTION OF THE SLOPE INSTABILITY WITH TIME

After heavy rainfall in August 2005, eye witnesses reported the first rockfalls on the southern flank of the rock spur. Slope movements began on 10 June 2006 accompanied by large rockfalls of several hundred cubic meters. Two steep valley-parallel cracks were observed. One of these cracks forms the 250 m long back crack which detaches the spur from the stable rock mass. The other separates the spur into a front

and a rear block (Figure 5.2-1a). In addition, these blocks were separated by a bedding-parallel fracture into a southern and a northern part.

In the initial stage (June to August 2006) the slope movements were very fast (several dm per day) and caused frequent rockfalls and partial collapses. Initially, the back-crack opening was measured by perilous hand measurements, followed by total station surveys. As the installed targets were rapidly destroyed due to collapses and rockfalls, a contactless and reflectorless monitoring technique – terrestrial laser scanning – had to be deployed.

Sequential TLS point clouds allowed the progress of the slope movements in 3-D to be recorded using shortest distance comparisons with displacements of 80 cm/day for the rear block and 20 cm/day for the front block (see Oppikofer et al., 2008). A large partial collapse of the northern block that occurred on the evening of 13 July 2006 (measured volume: 169'000 m^3) was preceded by higher displacement rates (up to 125 cm/day) and large single rockfalls. Photographs of this collapse reveal that it started with failure of the fast-moving column (Figure 5.2-1e); this finding is important information for rockslide monitoring and especially for spatial and temporal failure prediction (Oppikofer et al., 2008; Abellán et al., 2009; 2010). These shortest distance comparisons provided a first assessment of the slope movements and highlighted the different displacement directions and velocities of the rear relative to the front block, with mainly negative differences in the rear (downward displacements) and positive differences at the front block (out of slope displacements on the basal sliding surface) (see Oppikofer et al., 2008). Periodic monitoring of slope movements continued for several months and showed a decrease in velocities for both the front and the rear block. During the first year of TLS monitoring, the total displacements reached 15 m for the front block and 50 m for the rear parts (Figure 5.2-3a). These high displacements were accompanied by the progressive lateral disintegration and break-up of the rear block. Between summer 2007 and autumn 2008, slope movements continued and rockfall activity once again increased in 2008, leading to a partial collapse of the front block (estimated volume: 60'000 m^3). The front block continued its break-up with several collapses until 21 October 2008 at which time only a blade-shaped, 90 m high needle remained (Figure 5.2-1b).

To allow a more precise analysis of the slope movements, displacement vectors were measured for the different blocks. Due to disintegration and break-up of the blocks, it became increasingly difficult to locate suitable point pairs as displacement vectors. Therefore, a roto-translation matrix technique was applied after June 2007 to obtain the blocks displacement vectors.

The measured sliding directions of the front block remained fairly constant throughout the measurement period (trend/plunge: 042°/34° ± 9°). The velocities decreased from 20 cm/day (summer 2006) to 2 cm/day (winter 2006/2007), before rising again to 4–6 cm/day in July 2007 (Figure 5.2-3b). The front of the northern block shows a similar velocity pattern (Figure 5.2-3b) and a constant displacement direction between July 2006 and July 2007 (038°/39° ± 11°) before starting to move more towards the north in summer 2008.

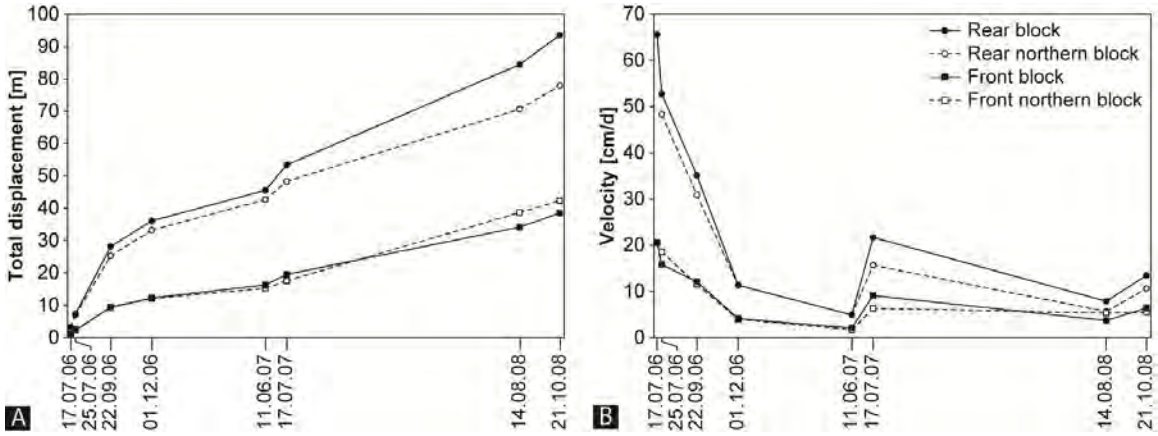

Figure 5.2-3: Graph of the total displacement since the beginning of the TLS monitoring (a) and the velocity (b) versus date of the TLS acquisition (modified from Oppikofer et al., 2008).

The sliding directions of the rear block also varied only slightly between July and September 2006 (mean orientation: 007°/68°) before moving more towards the east. This change is likely due to the blocks disintegration and toppling towards the east. In the final monitoring period (August to October 2008), the sliding direction was again similar to the summer 2006 direction (007°/77°). The rear of the northern block shows a more variable displacement direction pattern (on average 043°/75°). For both rear blocks the evolution of the velocity vs. time is similar to the front blocks (Figure 5.2-3b). The rear block velocity decreased between July 2006 and June 2007 (from 65 cm/day to 5 cm/day), increased in summer 2007 (up to 22 cm/day), before reaching a steady displacement rate of 8 to 13 cm/day between July 2007 and October 2008 (Figure 5.2-3b). Displacement vectors emphasize that the displacement directions are strongly controlled by the discontinuity sets intersections (i.e. a sliding wedge mechanism as opposed to a wedge collapse). The rear parts of the rockslide moved along the intersection line (wedge) of S0 and J2, while the front block moved forward parallel to the intersection line of S0 and J1 (see Oppikofer et al., 2008).On the basis of the measured 3-D displacements and the observed structures, a sliding mechanism involving a bilinear wedge failure has been proposed (Figure 5.2-4; Oppikofer et al., 2008). The front blocks are assumed to slide along a J1 and S0 discontinuity sets forming a wedge, while the rear blocks are suggested to move downward parallel to discontinuity set J2. Initially, the rear blocks which are the active one provide a driving force pushing the frontal blocks along their sliding surface (Sultan and Seed, 1987).

5.2.8 DESCRIPTION OF GEOMECHANICAL MODELS

Three different series of models were carried out based on continuum, discontinuum and analytical dynamic approaches. First, a series of continuum models was used in order to simulate the evolution and the stability conditions of the valley during deglaciation. Second, distinct element code is used to investigate, in more detail, the potential failure mechanism and the influence of pre-existing discontinuity sets. For both models, pore water pressure was neglected. Finally, based on previous initiation modelling and TLS analysis, we investigate a two-dimensional bilinear wedge failure model (Norrish and Wyllie, 1996) to perform a complete back analysis movement dynamic of the rockslide accounting for ground water conditions, shear strength degradation and progressive volume loss.

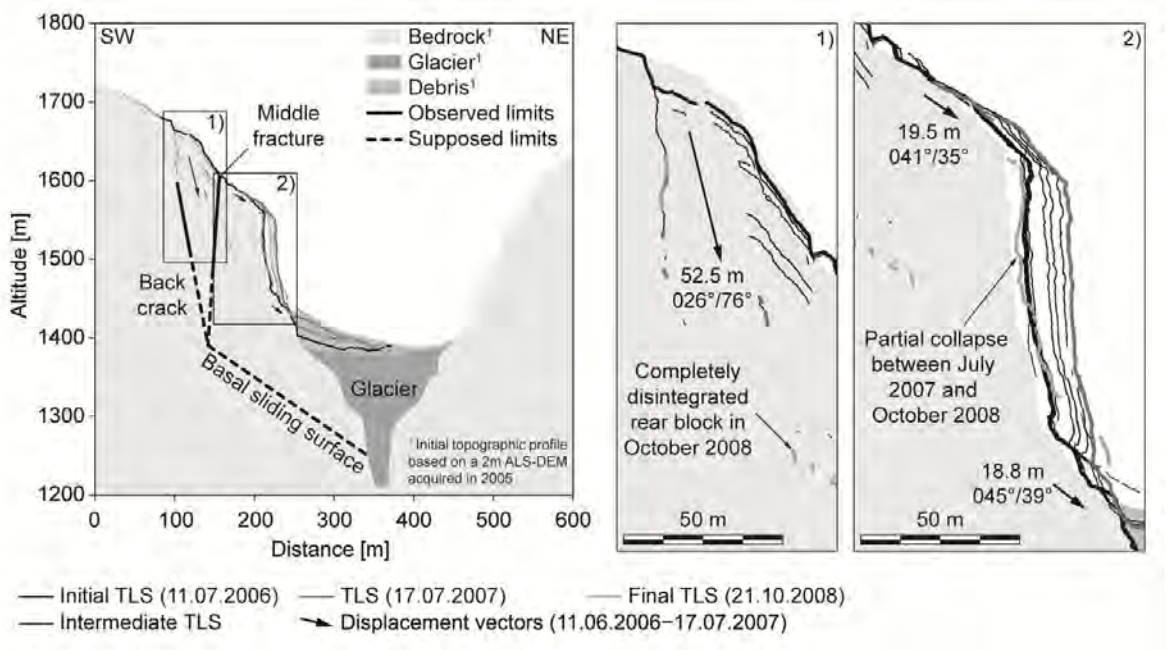

Figure 5.2-4: Profile across the Eiger rockslide parallel to the displacement direction of the front block. The cross-section series is based on TLS data (modified from Oppikofer et al., 2008). The 11 July 2006, 17 July 2007 and 21 October 2008 profiles are displayed with thicker lines than the other TLS acquisitions. Note the complete disintegration of the rear block in 2008 and the partial collapse on the front block between July 2007 and October 2008 (apparent retreat of the rock wall).

5.2.8.1 Continuum modelling

A multi-stage stress-strain analysis was carried out using the finite-element code Phase² 7.0 (Rocscience, 2010). Progressive deglaciation (in 6 stages) was simulated starting from the maximal ice elevation reached during the last recent glacial maximum in 1860 (Figure 5.2-1b). A Mohr–Coulomb elasto-plastic yield criterion was used to simulate the response of the rock mass. Successive unloading steps simulating glacial retreat were performed together with a progressive decrease in rock mass properties (Cai et al., 2007). Due to the difficulty of field mapping the rock mass was characterized using the Geological Strength Index (GSI) (Hoek et al., 2002) based on photographs, which was confirmed by TLS data and the analyses of the rocky outcrops located close to the TLS acquisition stations. This approach lead to potential uncertainties on the joint surface conditions, in particular concerning joint alteration characterization that need to be critically considered in the modelling interpretation.

Data concerning fifteen uniaxial compression tests performed in the same lithology at different depth (Mathier pers. comm.) have been also acquired to determine the uniaxial compressive strength and the Young modulus. These tests show an important variability of the intact uniaxial compressive strength varying between 65 MPa and 180 MPa with a mean and median value close to 100 MPa. The mean Young modulus is estimated to 25000 MPa. The rock mass strength was progressively decreased starting from a GSI of 70 (maximum values estimated in the area) down to GSI of 50 (corresponding to the lower observed present-day value). To account for glacial-induced stress relaxation, Disturbance factor D (Hoek et al., 2002), representing the degree of disturbance of the rock mass have been also decrease on the first 150 m of the model based results obtained by Bucher and Loew (2009) concerning the extension rock mass damage related to glacial unloading.

The failure criterion Mohr-Coulomb parameters and rock mass strength were estimated using Hoek and Brown criterion based on GSI (Table 1.1-1). It must be pointed out that Hoek and Brown criterion for lower tensile stress regime for hard rock masses overestimates tensile strength (Hajiabdolmajid et al., 2002; Diderichs, 2003). As a consequence, in the modelling the tensile failure will occurs in a later stage of degradation than using a more reliable criterion.

Table 5.2-1: Rock mass properties used in the continuum model.

	Stage 0 GSI =70 D=0.7 mi=12	***Stage 1 GSI =65 D=0.7 mi=12***	***Stage 2 GSI =60 D=0.7 mi=12***	***Stage 3 GSI =55 D=0.8 mi=12***	***Stage 4 GSI =50 D=0.8 mi=12***	***Stage 5 GSI =50 D=1.0 mi=12***
Equivalent friction angle (°)	*45*	*43*	*40*	*36*	*33*	*29*
Equivalent cohesion (MPa)	*2.9*	*2.3*	*1.9*	*1.5*	*1.3*	*1.0*
Tensile strength (MPa)	*1*	*0.9*	*0.85*	*0.8*	*0.75*	*0.75*
Poisson ratio	*0.3*	*0.3*	*0.3*	*0.3*	*0.3*	*0.3*
Young modulus (GPa)	*25*	*25*	*25*	*25*	*25*	*25*

Mechanical properties for ice were obtained from the published literature, (Schulson, 1999, Gagnon and Gammon 1995). In order to allow for ductile deformation, the remaining ice was modelled assuming a simple Mohr-Coulomb elasto-plastic constitutive law. The in-situ stress ratio (horizontal to vertical stress ratio) was assumed to be 0.5. This value is in agreement with previous geomechanical analysis in Swiss Alps (Eberhardt et al., 2004; Fisher et al., 2010) and with a fault plane solution of seismic events analysed by Kastrup et al. (2006), suggesting a strike-slip to normal faulting regime. The influence of the pre-existing joint set (J1) on the strength factor (ratio between the rock strength and the induced stress at every point in the mesh) and tensile stress distributions was investigated using a ubiquitous joint model.

5.2.8.2 Discontinuum model

Discontinuum modelling was performed using the two dimensional distinct element code UDEC (Itasca 2004) allowing a realistic analysis of discontinuous medium such as a jointed rock slopes (Eberhardt, 2004; Brideau et al., 2006). The goal of this analysis was to better define the potential failure mechanism and, in particular, to investigate the geometry of the failure surfaces/subsiding zones. The models assumed that the blocks (both rock mass and remaining ice) behaved as elasto-plastic Mohr–Coulomb materials (Table 5.2-2). Discontinuity sets behaviour was modelled using Mohr–Coulomb slip with residual strength. Strength properties of the rock mass were assumed based on average GSI values (stage 2 in Table 5.2-1). Intact rock bridges along large-scale discontinuities were modelled indirectly by assigning higher initial strength properties to discontinuities as described by Jennings (1970) and recently applied by Fisher et al. (2010) and Gischig et al. (2011). Using this approach, joint set properties are calculated based on a combination of discontinuity and intact rock properties. The location and the mean orientation of the rear and the middle fracture are known and were explicitly introduced in the model. The location of the basal sliding surface as well as her geometrical relationship with the middle and the rear surface are unknown. In a first series of models the basal failure surface was introduced explicitly at different depth. Then the consistency possibility to develop of step–like basal surface was also tested by

introducing discontinuity sets J1 and J2 in the lower portion of the model. The general consistency of the UDEC modelling models was tested comparing the orientation of the calculated displacement vector with the displacement vector direction obtained by TLS analysis in the early stage of the monitoring. In the same way, the velocity ratio between the rear and the frontal block obtained by TLS monitoring and UDEC models were also compared. This ratio gives important information about the interaction of the two blocks and the geometrical intersection of the middle and the basal surface. It is important to note that absolute velocity values of both methods are not directly comparable, since the modelling results show time machine velocity, while TLS represent real velocity.

Table 5.2-2: Rock mass properties used in the discontinuum models

Parameters	***Malm limestone***	***Ice***
Uniaxial compressive strength	*90-110*	
Young modulus (GPa)	*25*	*10*
Poisson ratio	*0.33*	*0.3*
Density (kg/m³)	*2700*	*900*
Intact rock friction angle (°)	*42*	*-*
Intact rock cohesion (MPa)	*2*	*-*
Joint normal stiffness (GPa/m)	*10*	*-*
Joint shear stiffness (GPa/m)	*1*	*-*
Joint friction angle (°)	*30-35*	*-*
Joint cohesion (MPa)	*0.2-0.8*	*-*
Joint dilatation angle (°)	*5*	*-*
Joint tensile strength (KPa)	*0.5*	*-*
Joint residual cohesion (MPa)	*0.1*	*-*
Joint residual friction angle (°)	*15*	*-*
Joint tensile strength (KPa)	*0*	*-*

5.2.8.3 Analytic model

An analytical model was employed to study the development of progressive failure and deformation in a dynamic way by testing different friction laws (see Figure 5.2-5 for the model geometry), including ice deformation. Rainfall infiltration and strength degradation were also considered. The moving wedges are assumed to slide against each other without losing contact (Coulthard, 1979; Sarma, 1979; Stamatopoulos and Petridis, 2006). Normal contact stresses are constant along the sliding surfaces and are assumed to be compressive only. Shear stresses (τ) depend on sliding velocities and normal contact stresses (σ_n) by the following equation:

$$\tau(u, \sigma_n) = \mu(u)\sigma_n \qquad \textit{Eq. 5.2-1}$$

where μ is a friction coefficient function that depends only on the sliding velocity (u). The function μ, however, strongly depends on materials on both sides of the sliding surface. We assume here that the friction coefficient decreases with sliding velocity, as argued by Spinnler (2001) in a mechanical design

context. A simple model is proposed (Figure 5.2-6a), whereby friction coefficient decreases with velocity at a rate that depends on a characteristic velocity u_0:

$$\mu(u) = \mu_1 + e^{-\frac{u}{u_0}}(\mu_0 - \mu_1) \qquad \textit{Eq. 5.2-2}$$

where μ0 is the static friction coefficient and μ1 is the asymptotical friction coefficient. Evolution over time of the static friction angle φ (related to μ_0 as $\mu_0 = \tan(\varphi)$), which simulates the progressive degradation of discontinuity strength (Alonso and Pinyol, 2010), is assumed to be the same for all sliding surfaces. Because strength degradation may cause the velocity to increase, the peak friction angle $\varphi(t)$ is decreased during the simulations to a given final value (Figure 5.2-6b):

$$\phi(t) = \phi_1 + \left(\frac{t}{t_d}\right)^a (\phi_0 - \phi_1) \qquad \textit{Eq. 5.2-3}$$

where φ_0 and φ_1 are initial and final friction angles, t_d the simulation duration, and $\boldsymbol{a}$ is an exponent that allows a faster decrease of friction angle at the beginning of the scenario ($\boldsymbol{a} < 1$) or at the end ($\boldsymbol{a} > 1$). This time-dependency was chosen because we made no a priori hypothesis that the friction angle is linearly dependent on deformation. Displacements have a significant influence on strength, but it is unclear when, and at what rate, strength degradation occurs in order to explain the late acceleration of the blocks without an assumption about the underlying mechanism. We also tested a constant friction angle (i.e. no strength degradation). Another possible explanation for the increase in sliding velocity in spring and summer 2007 is an increase in pore water pressure. We propose to use a simple groundwater model because there is little information about the permeability and porosity of the rock slope. The model stipulates, first, that the water table during a period of rain is zero at $t=t_0$, because at this time the water has not yet infiltrated the rock slope and is also zero at $t=\infty$, because water has completely drained from the slope. Second, the model stipulates that water table should be positive and continuous after the start of the rain at $t=t_0$ to $t=\infty$. In addition, full infiltration is assumed, that is all the rainfall infiltrates the slope. A groundwater model that meets these requirements is given by Eq. 5.2-4. Pore water pressure within the rock mass is defined by an impulse response function $\rho(t)$ that represents the degree of filling state of the reservoir (volume of water contained in the rock mass) resulting from a rainfall of intensity I_0, occurring at $t=t_0$. Such behaviour is expressed by the difference between a filling term of time constant T_{t1} (relaxation time) and a draining term of time constant $T_{t2} \geq T_{t1}$:

$$\rho(t) = I_0\left(e^{-\frac{t-t_0}{\tau_{t2}}} - e^{-\frac{t-t_0}{\tau_{t1}}}\right) \qquad \textit{Eq. 5.2-4}$$

If $\tau_{t2} = \tau_{t1}$ the water never fully fills up within the rock mass; if $\tau_{t2} >> \tau_{t1}$ water almost never drains. Figure 5.2-6c shows an example of the dynamic behavior of $\rho(t)$ in which groundwater remains in the rockslide mass after one specific rainfall (day 21). τ_{t1} is kept constant (1 day), whereas τ_{t2} varies from 1 day to 30

days. The water table and pore pressure also depend on the secondary porosity of the rock (η) created by fracturing. This parameter is used to create the relationship between quantity the water stored in the rock mass and the groundwater level. Input values of I_0 are proportional to the measured precipitation (data provided by Meteoswiss).

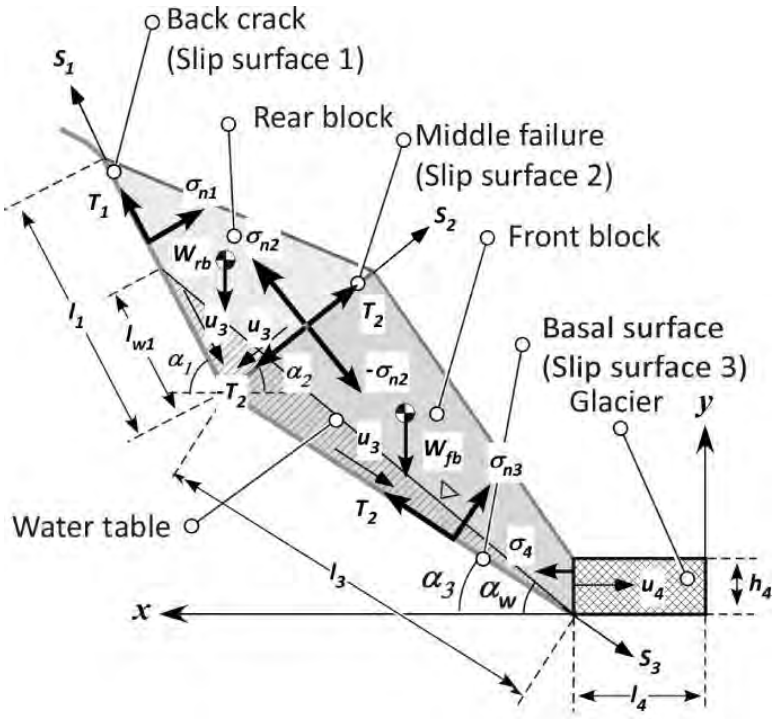

Figure 5.2-5: Simplified geometric representation of the double wedge model across the Eiger rockslide. The sliding part of the system is divided into the rear block (upper wedge), the front block (lower wedge) and the glacier. Groundwater level decreases linearly toward the glacier. The rear block and the front block are subjected to normal contact stress (σ_n), shear stress (τ), weight (W) and pore water pressure (not mentioned on the figure).

The resisting stress exerted by a glacier depends on the horizontal velocity of the ice through the Glen law (Glen, 1955):

$$\dot{\varepsilon} = \frac{u_x}{l_4} = Be^{-\frac{Q}{RT}}\sigma_4^n \qquad \textit{Eq. 5.2-5}$$

where $\dot{\varepsilon}$ is the glacier strain, l_4 is the length of the ice that is deforming, σ_4 is its normal stress, T is its temperature, and B, Q, R and n are constants, the values of which are considered unknowns in the back analysis. Parameters were determined using optimisation methods (Bardet and Kapuskar, 1989; Zhang *et al.*, 2010). The error between calculated and measured horizontal velocities of the moving part of the system was minimized by calibrating a given set of parameters using the Matlab-2009 *fmincon* function (Mathworks, 2009). Two sets of calibration parameters, which vary during the optimisation, were considered successively. The first calibration focused on time-dependent strength degradation without influence of pore pressure by using (1) two parameters from the strength degradation law in Eq. 5.2-3 (ϕ_1 and a), (2) two parameters from the friction law in Eq. 5.2-2 (the ratio of static-to-dynamic friction coefficients μ_1/μ_0, and the limit velocity u_0), and (3) the parameter n of the Glen law.

The last parameter is important because the front of the moving mass is constrained by the scree deposit, which changes the stress condition in the deforming ice.

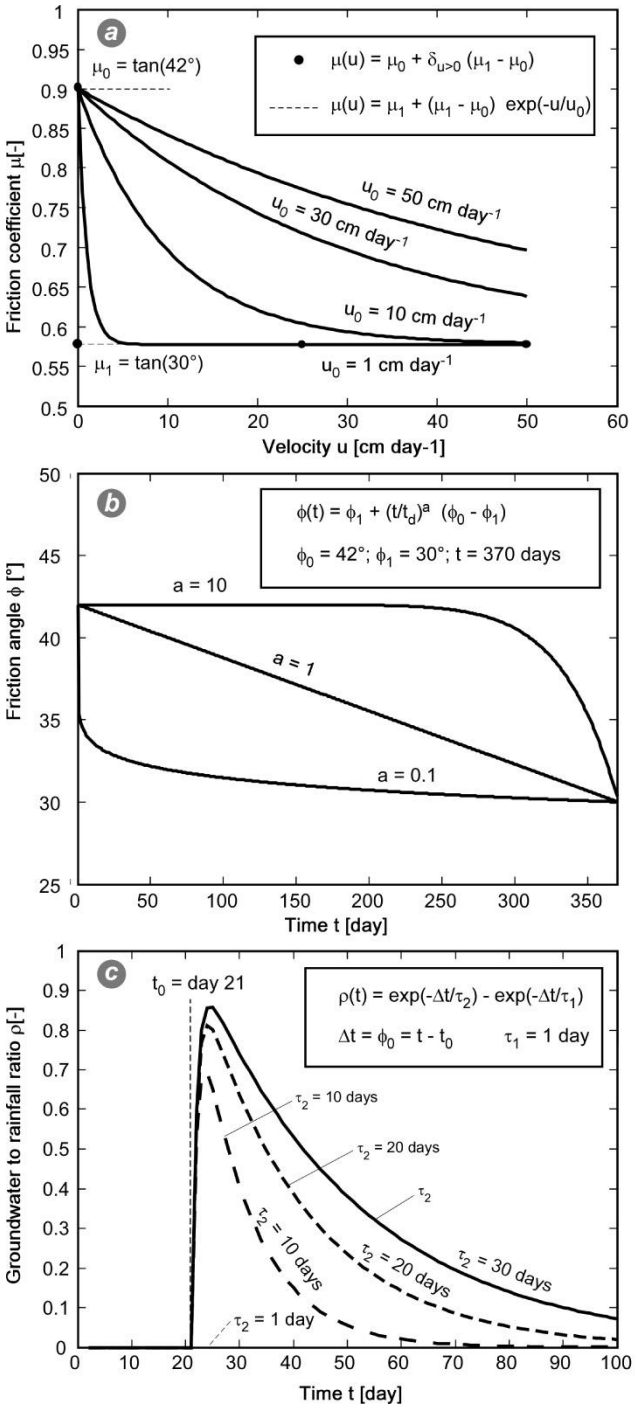

Figure 5.2-6: Models used in the back-analysis of the Eiger rockslide: a) Friction laws (given by Eq. 5.2-1), b) Infiltration law (Eq. 5.2-4), c) Strength degradation law (Eq. 5.2-2).

The infiltration law does not need to be parameterized in this first calibration because the pore pressure neglected. The second calibration investigated whether pore pressure triggered the increase of sliding velocity at the end of the modeling period (400 days; 17 July 2006 to 21 August 2007), with no consideration of strength degradation. The calibrated parameters comprise 1) rock porosity (η), 2) the ratio of the static-to-dynamic friction coefficients μ_1/μ_0, and (3) the parameter n of the Glen law. All

rainwater is assumed to enter the slope. Filling and draining time constants, τ_{t1} and τ_{t2}, are set to 1 day and 10 days, respectively. In both back analyses, collapses of the rear and front blocks are taken into account by linearly decreasing their mass to 40% and 70% of their initial mass, respectively.

We then set up equations describing the equilibrium of forces in the X and Y directions for both the rear and front blocks (see Figure 5.2-5). Velocity is influenced by the contribution of normal stresses over the sliding surfaces, but not by their distribution. Moment equilibrium does not have to be achieved, as solving for it only influences the distribution of the normal contact stress. The resulting wedge model at time t contains four unknowns: the normal contact stresses at sliding surfaces σ_{n1}, σ_{n2}, σ_{n3}, and the horizontal velocity of the moving part of the system, u_x

5.2.9 MODELLING RESULTS: INITIATION PROCESSES

5.2.9.1 Continuum models

Finite element analysis demonstrates the influence of progressive deglaciation on the stress and strain distribution in the Lower Grindelwald glacier valley. The coupled influence of glacial unloading and reduction of rock mass strength proprieties induces the formation of a yield zone due to shear damage near the base of the slope which transforms into a tensile failure zone sub-parallel to the valley in the central and upper portion of Figure 5.2-7a. The location of the maximum shear strain agrees closely with the expected instability geometry although in the rear portion of the slope it seems to extend further (20-25 m, 10%) than the observed rear release surface. It is interesting to note that using the lower present-day rock mass conditions (GSI 50), the tensile and shear yield indicators are not continuous within the central portion of the slope.

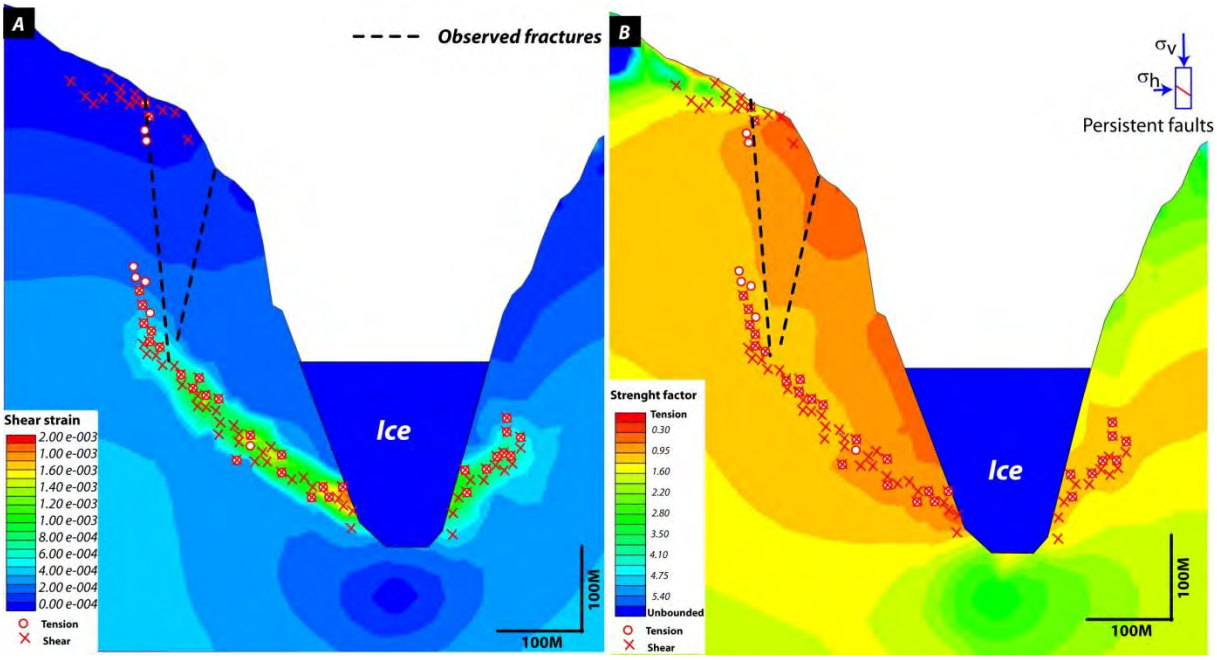

Figure 5.2-7: Finite element modelling of the initiation processes of the Eiger rockslide: a) Shear strain calculation for the last phase of deglaciation. The formation of a shearing zone at the bottom of the slope and a tension zone parallel to the valley can be recognized; b) Strength factor calculation (shear strength divided by the shear stress) obtained by introducing weakness planes corresponding to J1. The formation of an unstable area, matching the Eiger rock slide area could be observed.

This suggests that large slope failure cannot be developed without important external factors or the presence of persistent discontinuities. Numerical simulations are very sensitive to the rock mass strength anisotropy. Modelling results obtained by considering anisotropy associated with the orientation of joint set, J1 is presented in Figure 5.2-7b. It can be observed that the introduction of ubiquitous joints with the same orientation as J1 (assuming for instance, a residual friction angle of 30° and residual cohesion 0.1 MPa along the fractures) amplifies the results obtained using isotropic continuum modelling. The distribution of lower strength factors (<1) is in good agreement with the maximum extent of the expected rockslide geometry.

As suggested by Eberhardt et al. (2004), continuum modelling can be used to examine the evolution of stresses, strains and also to delimit the potential extent of the instability. However, results show a simplified representation of the failure mechanism involved in the rockslide. In particular, the development of the fracture located in the middle of the instability and the successively differentiation of the instability in two distinct blocks cannot be demonstrated using continuum modelling.

5.2.9.2 Discontinuum models

Using the UDEC code, different geometrical configurations were tested in order to reproduce the progressive deglaciation and related movements along discontinuity sets and to assess the orientation and magnitude of displacement vectors observed by TLS acquisition. According to this primary consideration, a series of sensitivity models was run in order to determine the equivalent cohesion and friction angle. During progressive deglaciation, the rock slope begins to be unstable when the peak friction angle has a value of 30°-35° and an apparent cohesion of 0.1 and 0.5 MPa. The early displacements along pre-existing fractures take place simultaneously in the upper and lower portion of the slope as previously indicated by finite element modelling (Figure 5.2-8). This implies that, during the initial phases of instability the discontinuity sets are not fully persistent and progressive fracturing of rock bridges occurs during deglaciation. A second series of UDEC models was run to better define the geometry and the potential failure mechanism. In particular, the orientation and the termination of the middle fracture and the shape and location of the basal failure surface were investigated. The first model was run with the middle fracture terminating directly on the basal failure surface (Figure 5.2-8). Results indicate that this configuration creates rotational-translational movements of the two blocks that begin to move simultaneously with similar velocities. The velocity ratio between rear and the frontal block is close to 0.8. These results are not in agreement with TLS analyses that indicate clear different displacement behaviour of the two blocks and in particular a velocity ratio of about 0.36.

The second model Figure 5.2-8b. is characterized by a middle fracture dipping 85° into the slope (following the joint set J2 orientation) and terminating on the rear fracture for which the frontal/rear velocity ratio and the orientation of the displacement vectors are in agreement with TLS results.

The real location of the basal failure surface is difficult to identify because velocity and displacement vectors are independent of its location as shown by the different models configurations. Nevertheless, the TLS measurements indicate a cumulative total settlement of the rear block of about 50 meters. Besides, models including a joint set that dips in the same direction as the failure surface indicate that most of the displacements occur between 40 and 60 m below the intersection of the rear and middle fractures (Figure

5.2-8c and d). The larger displacements are also obtained when the basal failure surface is closer to the surface. Based on these observations, it is suggested that the basal failure surface may be located between 50 and 60 meters below the intersection of the rear and the middle fractures.

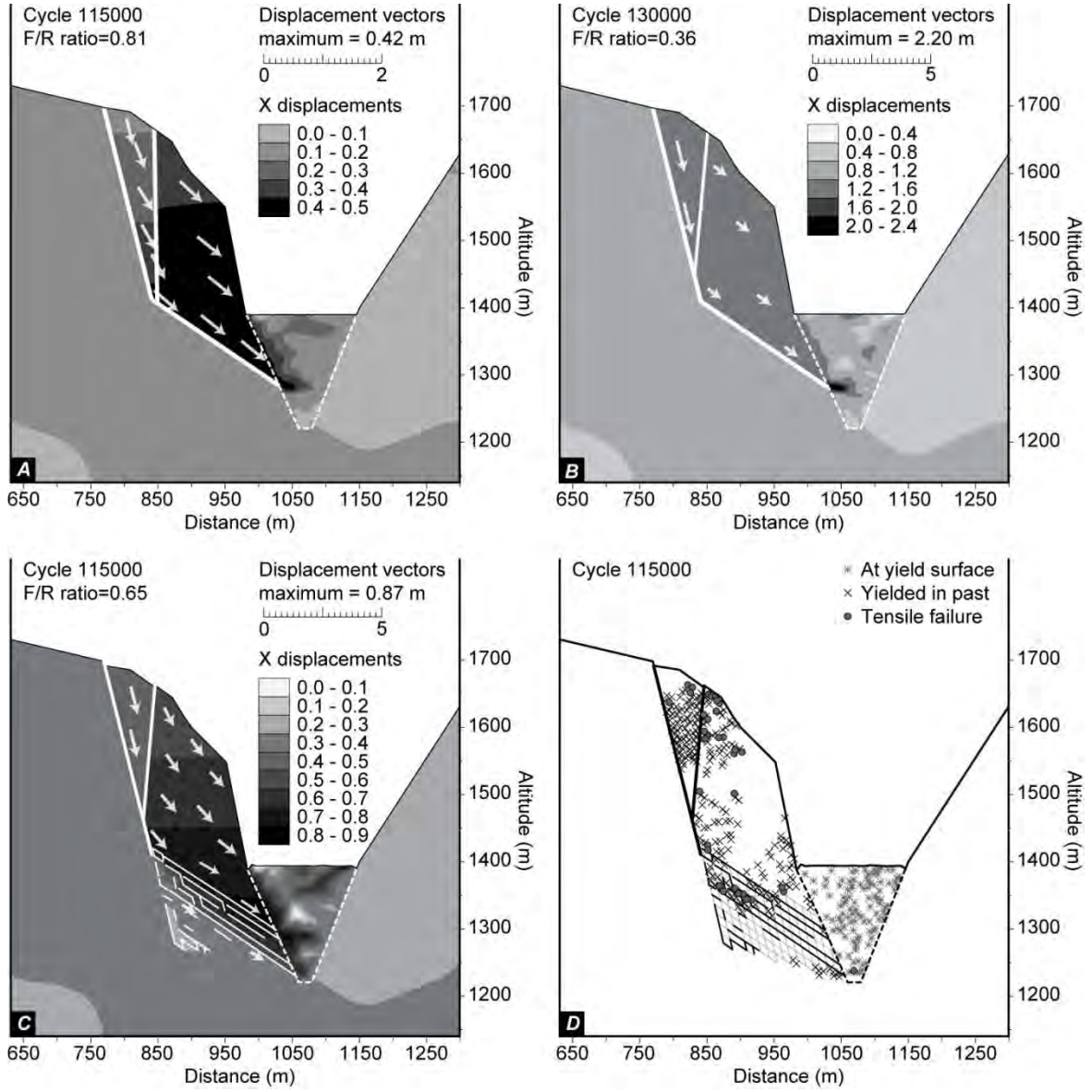

Figure 5.2-8: Discontinuum models of progressive failure associated with glacier confinement loss at the last stage of the model (pre-failure conditions). For all models withe arrow represent the calculated displacement vectors and white lines correspond to activated fully persistent discontinuity sets. F/R ratio corresponds to the calculated numerical velocity ratio between the frontal and the rear block. a) Model with middle fracture ending on the basal failure surface and planar basal failure. b) Model with middle fracture ending on rear fracture and planar basal failure. c) Model with middle fracture ending on rear fracture and multi-step-path basal failure surface. d) Distribution of plasticity indicators within UDEC model for the stepped-like basal surface model.

The failure surface geometry was also analysed using UDEC and assuming both planar and stepped failure surfaces. A stepped failure surface was modelled by introducing discontinuity sets J1 and J2 (mean spacing of 10 m for both) in the lower portion of the slope. Results indicate that movements take place along different planes, at different heights, creating a thick and dislocated stepped-like failure surface (Figure 5.2-8c and d). The directions of the displacement vectors for the rear block area are in good agreement with the TLS results. However, the directions of the frontal block displacement vectors,

particularly close to the middle fracture, show a steeper plunge than the TLS observations. The frontal/rear velocity ratio is also higher (0.65) than the TLS observations. These results indicate that the basal failure surface may follow a limited number of weakness planes parallel to joint set J1 without any (or subordinate) influence due to the steep discontinuity set J2.

5.2.9.3 Modelling results: dynamic evolution

Two types of back analyses were performed. In the first model, (Figure 5.2-9a and b; Table 5.2-3) based on time-dependent strength degradation, an "exponential" friction model and zero pore pressure were assumed. The calibration parameters are the two parameters from the strength degradation law (the final friction angle of the strength degradation model φ_1 and ***a***), the two parameters from the friction law (the static to dynamic friction coefficients ratio μ_1/μ_0 and the limit velocity u_0) and (*n*) from the Glen law. As no pore pressure was assumed the infiltration law does not need to be parameterized. In the second type of back analysis (Figure 5.2-9c, d; Table 5.2-4), we investigated whether increasing pore pressure triggered the increase in sliding velocity that was monitored at the end of the modelling period (400 days: 17.07.2006 to 21.08.2007), without no consideration of strength degradation.

The calibration parameters were the rock porosity η, the static to dynamic friction coefficients ratio μ_1/μ_0, the limit velocity u_0, and parameters of the glacier model (*n*). The total amount of rainwater is assumed to enter the rockslide. Filling and draining time constants τ_{t1} and τ_{t2} are set to 1 day and 10 days. In both back analyses the rear and front block masses decrease to 40% and 70% of their initial values, respectively. With no consideration of either strength degradation or pore water pressure the model can easily reproduce the early decrease in velocity.

This is mainly due to the loss in mass of the rear block. Indeed, if the rear block mass is kept constant the early deceleration fails to occur. However when neither strength degradation nor pore water is invoked the late stage acceleration cannot occur.

Table 5.2-3: Results of the analytical model based on strength degradation, using a strength degradation law, an exponential friction law, no hydrological law, and Glen glacier flow law.

Decision Variables	***Peak friction (42°)***	***Peak friction (38°)***	***Peak friction (35°)***	***Peak friction (30°)***
φ'_0	26.23	19.53	10.19	15.01
a	8.77	4.23	a = 5.56	a = 10 (upper bound)
μ_1/μ_0	0.71	0.58	0.50 (lower bound)	1 (upper bound)
u_0	1.87	4.04	5.5080	0.93
n (initial Glen law)	2.11	2.02	1.99	2.07
Function of error	0.176764 after 59 iterations and 492 functions evaluations.	0.176764 after 59 iterations and 492 functions evaluations.	0.188382 after 48 iterations and 369 functions evaluations.	0.425383 after 18 iterations and 138 functions evaluations.

Notes: Calibration parameters: final friction ratio - φ'0; strength degradation parameter – a; static to limit friction ratio - μ1/μ0; limit velocity for exponential friction law - u0; and Glen flow law exponent - n. Collapse ratio (rear/front) = 0.4/0.7. Glen flow law parameters: B = 22.2, Q = 28,000 cal/mol/K, T = 273°K.

For φ_0 values of 42°, 40° and 35° it appears that strength degradation results in the late increase in velocity (Table 5.2-4). However when pore water pressure alone is introduced, the calculated velocities seem to fit the early measured velocities very well, but not the late stage ones, and the late acceleration (that should occur at around day 320) is not simulated by the model for any value of φ_0. These results suggest that strength degradation could better explain the late acceleration of the blocks than the increase

of pore water pressure. Opening, loss of contact and shearing of 1st order roughness are the best arguments to explain the degradation along the failure surface.

Table 5.2-4: Results of the analytical model based on pore water pressure, no strength degradation, the exponential friction law, hydrological law (with porosity), and Glen flow law.

Decision variable	***Peak friction angle 42°***	***Peak friction angle 38°***	***Peak friction angle 35°***
Porosity	0.1	0.02	0.02
μ_1/μ_0	0.75	0.26	0.76
u_0	1.00	0.5949	0.1 (lower bound)
τ_{t1}	2.76	1.46	0.90
$\Delta\tau_t$	10.42	16.23	1.03

Notes: Calibration parameters: rock porosity; static-to-limit friction ratio (μ1/μ0); limit velocity for exponential friction law (u0); filling time constant (τt1); dewatering and filling time constants difference (Δτt); and Glen law exponent (n). Collapse ratio (rear/front) = 0.4/0.7 and the Glen flow law parameters: B = 22.2, Q = 28,000 cal/mol/K, T = 273°K.

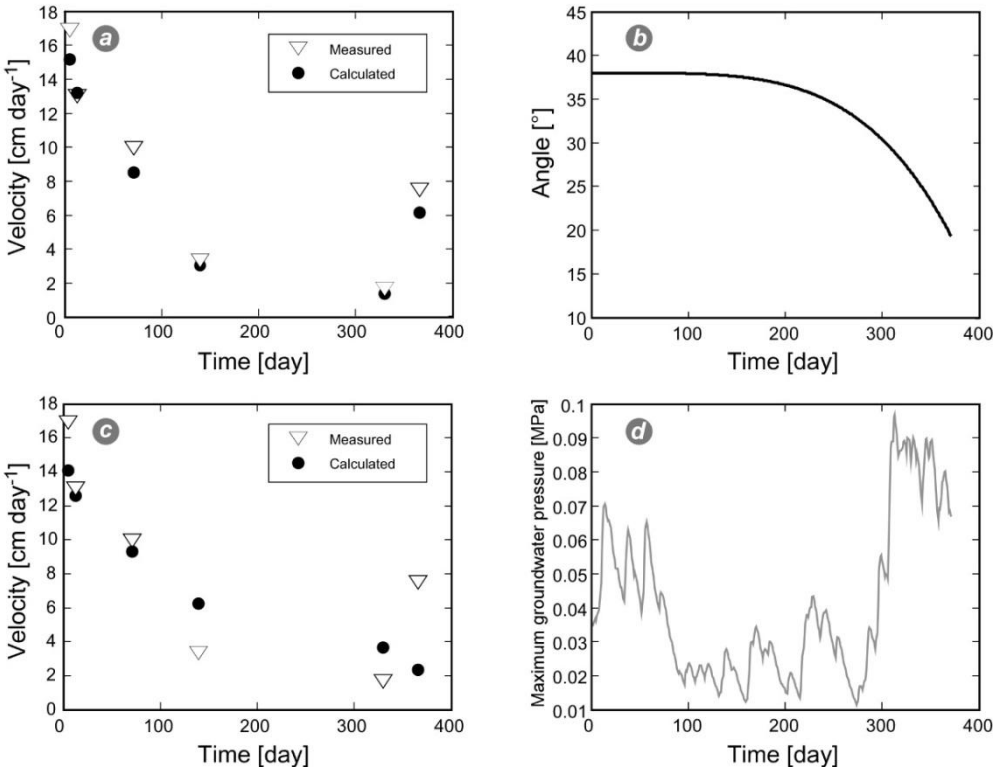

Figure 5.2-9: Numerical results obtained using an initial peak friction of 38°: a) Velocity histories with strength degradation and b) friction angle. c) Velocity histories with non-zero pore pressure and no strength degradation and d) pore pressure time dependence.

5.2.10 DISCUSSION

The geomorphic location of the 2006 Eiger rockslide is comparable to the 1991 Randa rockslide. Both rockslides occurred at spurs defined by high steep cliffs compared to their surroundings (Sartori et al., 2003; Pedrazzini et al., 2010). These spurs are the results of glacial erosion affecting rocks with different resistances to erosion, the most resistant rock forming more prominent topographical features. As suggested by Sartori et al. (2003), the spur locations are subjected to higher stresses due to the ice flow than alternative locations. The stress field created by these conditions appears to promote failure along pre-existing structures. The 2006 Eiger rockslide emphasizes the role of rock fatigue, because although this valley deglaciated ~6000 years ago (Portmann 1977), the spur did not fail before 2006.

This implies that mechanical fatigue and/or weathering are major factors in rock slope destabilisation (Jaboyedoff et al., 2004; Stead et al., 2006).However it remains unclear why the spur failed in 2006 and what triggered the initiation of the movement that led to the final collapse. It is clear that the last glacial retreat (Figure 5.2-1c and d) removed the final slope buttress and that the instability must have been very close to equilibrium as no exceptional precipitation or earthquake events are reported prior to the initiation of high velocity movements in 2006.

Stress and strain distribution within the rock slope were clearly favourable for instability development (Figure 5.2-7a), but the time scale for such a rock slope failure process would have been significantly longer without the pre-existing weaknesses in the rock mass. Medium to high persistent and moderate to widely spaced discontinuity sets define the size of the instability. The strain within the rock slope is mainly absorbed by pre-existing discontinuities. The strain has been localized along the pre-existing discontinuity set J2. The sliding surface discontinuity set J1 is ubiquitous in the area, forming large step-like surfaces. In addition, the very persistent S0 plays a primary role in the lateral release and break-up and participates in the formation of the wedge S0^J1 (Oppikofer et al., 2008) which controls the sliding direction of the front block. The displacement direction of the subsiding block is controlled by the wedge J2^S0 (Oppikofer et al., 2008) and is again close to the dip direction of J2. Since the sliding directions of both blocks are very close to the dip directions of J1 and J2, respectively, it is considered justified to model the basal sliding surface and the back-scarp as 2D planar surfaces.

The Mt Eiger rockslide did not move significantly before July 2006, which infers that the mechanical discontinuity properties changed slowly, allowing the breakage of the remaining rock bridges by localization of stress eventually creating through-going continuous structures (Figure 5.2-10a, b, and c). At this stage, the geometry was that of a subsiding wedge that pushed the frontal block. The base of the subsiding wedge may have been located well above the main basal sliding surface. The latter was controlled by the wedge J1^S0, without a stepped sliding surface as shown in Figure 5.2-4 and Figure 5.2-8. This quite simple geometry is demonstrated by observations and simulations.

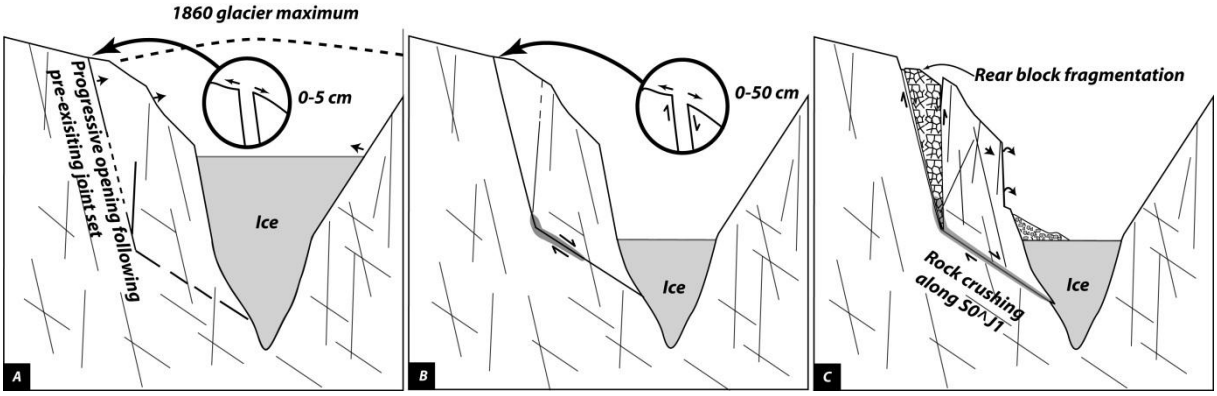

Figure 5.2-10: Progressive evolution of the Eiger rockslide. a) Early opening of the rear fracture (before July 2006), b) Progressive increase of displacement velocity relative to the creation of continuum basal failure surface, c) Fragmentation of the rear block and progressive velocity decrease.

The observed velocities were very rapid at the beginning, i.e. very uncommon for a rockslide without complete disintegration and collapse. These velocities then decreased primarily due to the loss of mass of the rock blocks. The analytical model shows that the other main parameters is the reduction of the friction

angle of the basal sliding surface occurred, A gouge filling must have been created along the slip surface making possible a strong decrease of φ as shown on Figure 5.2-9b or some local rock disintegration creating a short term stress change. This is supported by the fact that the rock mass was very fragmented as demonstrated by the progressive collapse by slow fragmentation of the instability (the instability disappeared almost completely in fall 2008). This behaviour is certainly caused by the ice, making a buttress that deformed slowly. A dumping effect of the debris can also be suspected (Figure 5.2-1e).

5.2.11 CONCLUSION

A subsiding wedge appears to provide an appropriate driving force for rock mass movement. Such situations are not uncommon (e.g. Turtle Mountain, Froese et al., 2009; Agliardi et al., 2001). In the present case of the 2006 Mt Eiger rockslide the well constrained geometry allowed testing of a dynamic model providing encouraging results. This indicates that it is possible to build a geologically realistic model using an optimisation procedure to fit the parameters of simple physical laws and may provide a future tool to forecast slope movements and improve our understanding of failure mechanisms (Zhang et al., 2010).

The validity of the analytical model presented leads to the following comments. The reduction in mass of the rear block seems to have sufficient impact to cause the initial decrease in slope displacement velocity. An additional physical phenomenon, such as a decrease in friction angle of the basal sliding surface, is however required to explain the reacceleration.

The Mt. Eiger rock slide is an important case study as it allowed the observation of a fast-moving rockslide without rapid collapse, because of the deceleration due to the deforming ice. The displacement data and structural measurements make it possible to obtain a reliable model geometry and to constrain the mechanism of sliding of wedges involving a basal surface (J1^S0) and rear surface (J2^S0). A subsiding wedge acting as driving mechanism seems to be a plausible and previously noted trigger for movements. The coherence of the model results, the structural analysis and the dynamics provide good arguments to highlight that when high resolution data are available, it is possible to use quite simple models. This provides new possibilities for extracting geomechanical parameters from back-analysis modelling and emphasizes the importance of acquiring relevant high resolution data in the field.

5.2.12 REFERENCES

Abellán, A., Jaboyedoff, M., Oppikofer, T. and Vilaplana, J.M. 2009. Detection of millimetric deformation using a terrestrial laser scanner: Experiment and application to rockfall event, *Natural Hazards and Earth System Sciences*, 9, 365-372.

Abellán, A., Vilaplana, J. M., Calvet, J., Blanchard, J. 2010. Detection and spatial prediction of rockfalls by means of terrestrial laser scanning modelling, *Geomorphology*, 119, 162-171.

Agliardi, F., Crosta, G., Zanchi, A. 2001. Structural constraints on deep-seated slope deformation kinematics, *Engineering Geology*, 59, 83-102.

Alonso, E.E., Pinyol, N.M. 2010. Criteria for rapid sliding. I. A review of Vaiont case, *Engineering Geology*, 114, 198-210.

Ambrosi, C., Crosta, G.B. 2006. Large sackung along major tectonic features in the central Alps, *Engineering Geology*, 83, 183-200.

Ambrosi, C., Crosta, G.B. 2011. Valley shape influence on deformation mechanisms of rock slopes. In *Slope Tectonics*, ed. M. Jaboyedoff. Geological Society, London, Special Publications, 351, 215-233.

Ballantyne, C.K. 2002. Paraglacial geomorphology, *Quaternary Science Reviews*, 21, 1935-2017.

Baltsavias, E.P. 1999. Airbone laser scanning: Basic relations and formulas, *ISPRS Journal of Photogrammetry & Remote Sensing*, 54, 199-214.

Bardet, J.-P., Kapuskar, M.M. 1989. A simplex analysis of slope stability, *Computers and Geotechnics*, 8, 329-348.

Besl, P., McKay, N. 1992. A method for registration of 3-D shapes, *IEEE Transactions on Pattern Analysis and Machine Intelligence*, 14, 239-256.

Brideau, M.-A., Stead, D., Couture, R. 2006. Structural and engineering geology of the East Gate Landslide, Purcell Mountains, British Columbia, Canada, *Engineering Geology*, 84, 183-206.

Bucher, S.P., Loew, S. 2009. Talklüfte im Zentralen Aaregranit der Schöllenen-Schlucht Kanton Uri, Schweiz), *Swiss Journal of Geosciences*, 102, 403-420.

Cai, M., Kaiser, P.K., Tasaka, H., Minami, M. 2007. Determination of residual strength parameters of jointed rock masses using the GSI system, *International Journal of Rock Mechanics and Mining Sciences*, 44, 247-265.

Carter, T.G., Diederichs, M.S., Carvalho, J.L. 2008. Application of modified Hoek–Brown transition relationships for assessing strength and post yield behaviour at both ends of the rock competence scale. In: *Proceedings 6th International Symposium on Ground Support in Mining and Civil Engineering Construction*. Ed. P. R. Stacey and D. F. Malan SAIMM, Johannesburg, 37–60.

Conforti, C., Deline, P., Mortara, G., Tamburini, A. 2005. Terrestrial scanning Lidar technology applied to study the evolution of the ice-contact Miage lake (Mont Blanc Massif, Italy). In *Proceedings of the 9th Alpine Glaciological Meeting*, Milano, Italy.

Cossart, E., Braucher, R., Fort, M., Bourlès, D.L., Carcaillet, J. 2008. Slope instability in relation to glacial debuttressing in alpine areas (Upper Durance catchment, southeastern France): Evidence from field data and 10Be cosmic ray exposure ages, *Geomorphology*, 95, 3-26.

Coulthard, M,A. 1979. Back Analysis of Observed Spoil Failures Using a Two-wedge Method. CSIRO Division of Applied Geomechanics, Melbourne, Australia, 83.

Diederichs M.S. 2003. Rock fracture and collapse under low confinement conditions, *Rock Mechanics and Rock Engineering*, 36, 339-381.

Eberhardt, E., Stead, D., Coggan, J.S. 2004. Numerical analysis of initiation and progressive failure in natural rock slopes – The 1991 Randa rockslide, *International Journal of Rock Mechanics and Mining Sciences*, 41, 69-87.

Fischer, L., Amann, F., Moore, J., Huggel, C. 2010. Assessment of periglacial slope stability for the 1988 Tschierva rock avalanche (Piz Morteratsch, Switzerland), *Engineering Geology*, 116, 32-43.

Florineth, D., Schlüchter, C. 1998. Reconstructing the last Glacial Maximum (LGM) ice surface geometry and flowlines in the Central Swiss Alps, *Eclogae Geologicae Helvetiae,* 91, 391-407.

Froese, C., Moreno, F., Jaboyedoff, M., Cruden, D. M. 2009. 25 years of movement monitoring on the South Peak of Turtle Mountain: Understanding the hazard, *Canadian Geotechnical Journal*, 46, 256-269.

Froese, C., Jaboyedoff, M., Charriere, M., Humair, F. and Pedrazzini, A. *In press*. Characterization and management of rockslide hazard at Turtle Mountain, Alberta, Canada, In *"Landslide; types, mechanisms and modelling*", Eds Clague, J. and Stead D. ; Cambridge University Press

Gagnon, R.E. Gammon, P.H. 1995. Triaxial experiments on iceberg and glacier ice, *Journal of Glaciology*, 41, 528-540.

Ghirotti, M., Martin, S., Genovois, R. 2011. The Celentino deep-seated gravitational slope deformation (DSGSD): Structural and geomechanical analyses (Peio Valley, NE Italy). In *Slope Tectonics*, ed. M. Jaboyedoff. Geological Society, London, Special Publications, 351, 235-252.

Gischig, V., Amann, F., Moore, J.R., Loew, S., Eisenbeiss, H., Stempfhuber, W. 2011. Composite rock slope kinematics at the current Randa instability, Switzerland, based on remote sensing and numerical modelling, *Engineering Geology*, 118, 37-53.

Glen, J.W. 1955. The creep of polycrystalline ice. Proceedings of the Royal Society of London. Series A, *Mathematical and Physical Sciences*, 228, 519-538.

Günzler-Seiffert, H., Wyss, R. 1938. *Swiss Geological Atlas*, Sheet 396 Grindelwald (Atlas Sheet 13). Swisstopo, scale 1:25,000.

Hajiabdolmajid, V., Kaiser, P.K., Martin, C.D. 2002. Modelling brittle failure of rock, *International Journal of Rock Mechanics and Mining Sciences*, 39, 731-741.

Hoek, E., Carranza-Torres, C.T., Corkum, B. 2002. Hoek-Brown failure criterion – 2002 edition. In Proceedings of the 5th North American Rock Mechanics Society, Toronto, ON, 267–273.

InnovMetric 2011. PolyWorks: 3d Scanner Software - 3d Scanning Software - 3d Digitizers. http://www.innovmetric.com/polyworks/3D-scanners/home.aspx?lang=en, accessed 6 July 2011.

International Society of Rock Mechanics (ISRM). 1978. Suggested methods for quantitative description of discontinuities in rock masses, *International Journal of Rock Mechanics and Mining Sciences & Geomechanics Abstracts*, 15, 319-358.

Itasca. 2004. UDEC—Universal Distinct Element Code (Version 4.0). Itasca Consulting Group, Minneapolis, MN.

Jaboyedoff, M., Baillifard, F., Bardou, E., Girod, F. 2004. Weathering, cycles of saturation-unsaturation, and strain effects as principal processes for rock mass destabilization, *Quarterly Journal of Engineering Geology and Hydrogeology*, 37, 95-103.

Jaboyedoff, M., Metzger, R., Oppikofer, T. 2007. New insight techniques to analyze rock-slope relief using DEM and 3D-imaging cloud points: COLTOP-3D software. In *Rock Mechanics: Meeting Society's Challenges and Demands*. ed. E. Eberhardt, D. Stead and T. Morrison. London, UK: Taylor & Francis, 1, 61–68.

Jaboyedoff, M., Couture, R., Locat, P. 2009. Structural analysis of Turtle Mountain (Alberta) using digital elevation model: Toward a progressive failure, *Geomorphology*, 103, 5-16.

Jennings, J.E. 1970. A mathematical theory for the calculation of the stability of open cast mines. *In Planning Open Pit Mines,* ed. P.W.J. van Rensburg. Johannesburg: South African Institute of Mining and Metallurgy, pp. 87–102.

Kastrup, U., Zoback, M.L., Deichmann, N., Evans, K.F., Giardini, D., Michael, A.J. 2004. Stress field variations in the Swiss Alps and the northern Alpine foreland derived from inversion of fault plane solutions. *Journal of Geophysical Research*, 109, B01402.

Lichti, D.D., Gordon, S.J., Stewart, M P. 2002. Ground-based laser scanners: operations, systems and applications, *Geomatica*, 56, 21-33.

Liniger, M. 2006. Die Herausforderung der Gefahrenprognose bei Massenbewegungen: Rutsch-und Sturzprozesse, *Bulletin for Applied Geology*, 11, 75–88.

Mathworks 2009. Matlab 9., Natick, Massachusetts: The MathWorks, Inc.

Messerli, B., Messerli, P., Pfister, C., Zumbühl, H.J. 1978. Fluctuations of climate and glaciers in the Bernese Oberland, Switzerland and their geological significance, 1600 to 1975, *Arctic and Alpine Research*, 10, 247-260.

Monserrat, O., Crosetto, M. 2008. Deformation measurement using terrestrial laser scanning data and least squares 3D surface matching, *ISPRS Journal of Photogrammetry and Remote Sensing*, 63, 142-154.

Norrish, N.I., Wyllie, D.C. 1996. Rock slope stability analysis. *In Landslides – Investigation and Mitigation*, ed. A.K. Turner and R.L. Schuster. Washington, DC: Transportation Research Board Special Report, 247, 391-425.

OcCC 2007. Climate Change and Switzerland in 2050. Expected Impacts on Environment, Society and Economy. Bern, Switzerland: OcCC/ProClim.

Oppikofer, T., Jaboyedoff, M., Keusen, H.R. 2008. Collapse at the eastern Eiger flank in the Swiss Alps, *Nature Geoscience*, 1, 531-535.

Oppikofer, T., Jaboyedoff, M., Blikra, L., Derron, M.-H., Metzger, R. 2009. Characterization and monitoring of the Åknes rockslide using terrestrial laser scanning, *Natural Hazards Earth Systems Science*, 9, 1003-1019.

Pedrazzini, A., Jaboyedoff, M., Derron, M.-H., Abellán, A., Vega Orozco, C. 2010. Reinterpretation of displacements and failure mechanisms of the upper portion of Randa rock slide. *In Proceedings of the 63rd Canadian Geotechnical Conference & 6th Canadian Permafrost Conference*, Calgary, AB, pp. 913–921.

Portmann, J.-P. 1977. Variations glaciaires, historiques et préhistoriques, dans les Alpes suisses. Les Alpes - *Revue du Club Alpin Suisse*, 4, 145-172.

Rabatel, A., Deline, P., Jaillet, S. and Ravanel, L. 2008. Rock falls in high-alpine rock walls quantified by terrestrial LIDAR measurements. A case study in the Mont Blanc area. *Geophysical Research Letters*, 35, L10502.

Rocscience 2010. Phase² Version 7.0. Toronto, ON: Rocscience Inc.

Sarma, S.K. 1979. Stability analysis of embankments and slopes. *Journal of the Geotechnical Engineering Division*, 105, 1511-1524.

Sartori, M., Baillifard, F., Jaboyedoff, M., Rouiller, J.-D. 2003. Kinematics of the 1991 Randa rockslides (Valais, Switzerland), *Natural Hazards and Earth Systems Science*, 3, 423-433.

Schulson, E.M. 1999. The structure and mechanical behaviour of ice. Journal of the Minerals, *Metals and Materials Society*, 51, 21-27.

Spinnler, G. 2001. Conception des Machines. Principes et Applications. Lausanne, Switzerland: Presses Polytechniques et Universitaires Romandes.

Stamatopoulos, C., Petridis, P. 2006. Back analysis of the Lower San Fernando Dam slide using a multi-block model. In Geohazards, ed. F. Nadim, R. Pöttler, H. Einstein, H. Klapperich and S. Kramer. Lillehammer, Norway: Engineering Conferences International Symposium Series, P0.

Stead, D., Eberhardt, E., Coggan, J.S. 2006. Developments in the characterization of complex rock slope deformation and failure using numerical modelling techniques, *Engineering Geology*, 83, 217-235.

Sturzenegger, M., Stead, D. 2009. Quantifying discontinuity orientation and persistence on high mountain rock slopes and large landslides using terrestrial remote sensing techniques, *Natural Hazards and Earth Systems Science*, 9, 267-287.

Sturzenegger, M., Yan, M., Stead, D., Elmo, D. 2007. Application and limitations of ground-based laser scanning in rock slope characterization. In *Rock Mechanics: Meeting Society's Challenges and Demands*, ed. E. Eberhardt, D. Stead and T. Morrison. London, UK: Taylor & Francis, 1, 29-36.

Sultan, H.A., Seed, H.B. 1967. Stability of sloping core earth dams. *Journal of the American Society of Civil Engineers*, 93, 45-47.

Teza, G., Galgaro, A., Zaltron, N., Genevois, R. 2007. Terrestrial laser scanner to detect landslide displacement fields: A new approach, *International Journal of Remote Sensing*, 28, 3425-3446.

Werder, M.A., Bauder, A., Funk, M., Keusen, H.-R. 2010. Hazard assessment investigations in connection with the formation of a lake on the tongue of Unterer Grindelwaldgletscher, Bernese Alps, Switzerland, *Natural Hazards and Earth Systems Science*, 10, 227-237.

Zhang, J., Tang, W.H., Zhang, L.M. 2010. Efficient probabilistic back-analysis of slope stability model parameters, *Journal of Geotechnical and Geoenvironmental Engineering*, 136, 99-109.

5.3 REINTERPRETATION OF DISPLACEMENTS AND FAILURE MECHANISM OF THE UPPER PORTION OF THE RANDA ROCK SLIDE

5.3.1 ABSTRACT

The Randa rockslide (South-western Switzerland) is one of the most studied rockslides in the world. In the last decade, different studies concerning the structural settings and the failure mechanism of the 1991 collapse were carried out. In the upper portion of the rockslide scar a potential unstable mass is still present is monitored since 1991 by different techniques. In this paper, after a review of previous studies, we focus on the integration of new monitoring data obtained by PSInSAR™ technique and new structural characterization based on Helicopter-based DEM for the reinterpretation of the kinematics of the unstable area. A methodology to obtain "quasi" three dimensional displacement patters for the entire upper unstable area was developed by coupling one dimensional displacements vectors obtained by PSInSAR and 1D geodetic instruments. These new displacements data have been reinterpreted and correlated to the structural setting to update previous conceptual models of the instability. Moreover, the potential unstable volume has been re-evaluated using a High Resolution DEM through the Sloping Local Base Level method, constrained by the main joint orientations.

5.3.2 RÉSUMÉ

Le glissement rocheux de Randa est l'un des glissements les plus étudié du monde. Au cours des vingt dernières années, plusieurs études ont été menées concernant les mécanismes de rupture des deux événements survenus en 1991. Au-dessus de niches d'arrachement de l'éboulement de 1991, une masse rocheuse potentiellement instable a été identifiée et présente des mouvements de quelques millimètres par ans. La zone est surveillée depuis 1991 avec plusieurs techniques. Dans ce chapitre, après une synthèse des études précédentes, une nouvelle approche pour estimer les déplacements en trois dimensions à l'aide de données géodésiques 1D et des vitesses issues des donnes PsinSAR est proposée. En particulier, l'interprétation de ces nouvelles données a permis de vérifier les hypothèses formulées par les auteurs précédentes concernant la présence d'une surface du rupture en escalier qui détermine la direction générale des mouvements dans la zone instable. Au même temps, les variabilités locales des mesures rendent difficile l'interprétation de la cinématique globale de l'instabilité ont pu être mis en évidence. En particulier, des mouvements à forte composante verticale dans la partie frontale de l'instabilité ont été identifiés. Ces mouvements sont vraisemblablement liés à une subsidence progressive contrôlée par des discontinuités sub-verticales très persistantes et par un basculement superficiel dans la partie frontale de l'instabilité. Une réévaluation du volume potentiellement instable a été proposée à l'aide de la méthode du « Sloping local base Level » et par construction géométrique basée sur le modèle numérique à haute résolution acquis par hélicoptère. Ces deux méthodes mettent en évidence un volume potentiellement instable d'environ 3.5-4 millions de m^3.

5.3.3 INTRODUCTION

The Randa rockslide, Wallis (western Switzerland), is one of the most studied rockslides in the world. In April 1991 a first large rockslides occurred involving 20 million of m^3. In May 1991, another rock mass of about 10 M of m^3 was released. From a geological point of view, the slope above Randa can be subdivided in two sub-regions. The lower portion of the slopes is composed of competent orthogneiss. In the upper portion the main outcropping lithologies comprise fractured paragneiss and micaschsits displaying a dominant foliation dipping toward west (Sartori et al., 2003).

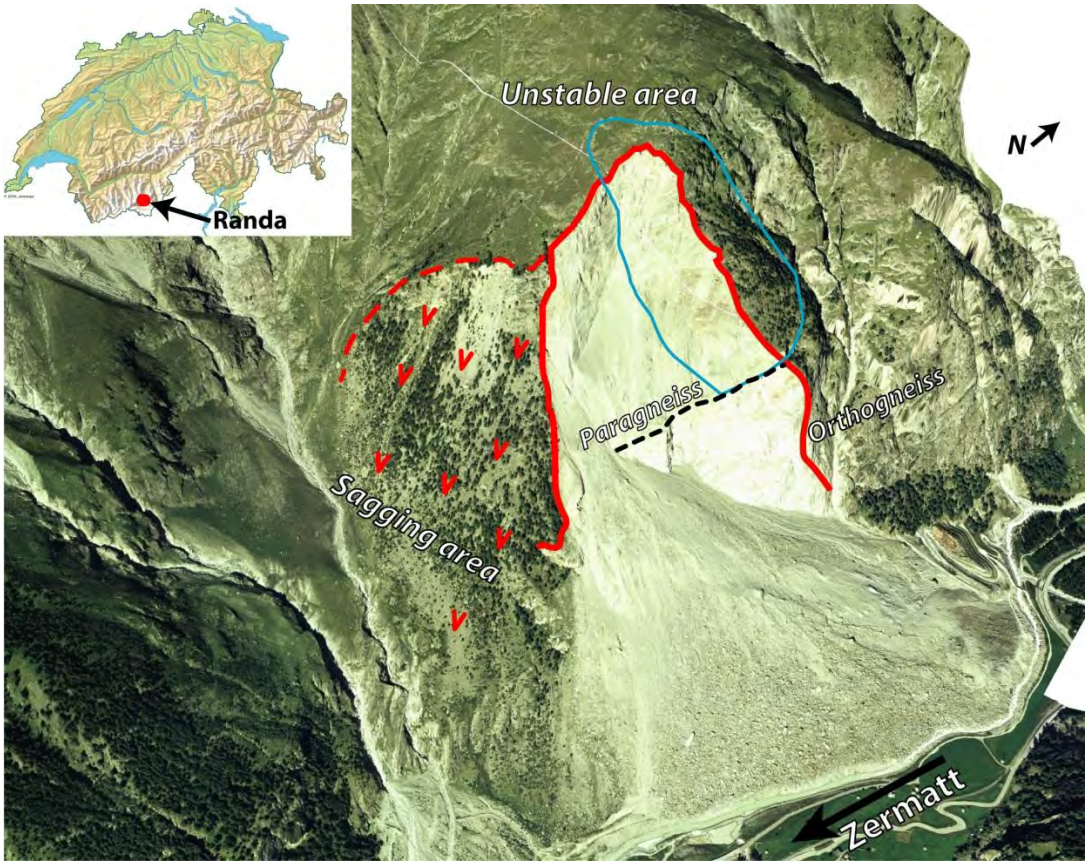

Figure 5.3-1: Geographical setting of the Randa rockslide displaying the extension of the upper unstable area defined by Jaboyedoff et al. (2004b) and by Gischig et al. (2009). In the Southern portion of the slope and active sagging area is visible.

A potential unstable mass is still present in the upper part of the scar and is monitored since 1991 by different techniques (Figure 5.3-1). During the last 20 years, new monitoring methods have been applied in order to better define the present-day kinematics and its possible evolution.

In this chapter, after a comprehensive review of the different monitoring techniques and the interpretations of the 1991 events and the upper potential unstable area, we focus on the impact and the improvement of the new monitoring techniques on previous failure mechanisms interpretation. More specifically, displacements data acquired by geodetic and remote sensing techniques have been reinterpreted and quantitatively constrained by detailed joint sets analyses based on LIDAR-DEM. A detailed re-evaluation of the potential unstable volume was performed adopting the Sloping Local Base Level techniques (Jaboyedoff et al., 2009) and based geometrical construction based on LiDAR points-cloud.

5.3.4 PREVIOUS STUDIES

The previous studies could be divided into four main categories, corresponding to the different stages in the understanding of the Randa instability.

5.3.4.1 Preliminary studies of the 1991 events

The investigations carried out during and just after the 1991 events mainly involved management of the crisis (Sartori et al., 2003). These analyses were focused on volume estimations, quick interpretations of the monitoring results and on the stability studies of the rockslide dam (Ischi et al., 1991; Pirocchi, 1992; Rouiller, 1992; Götz and Zimmermann, 1993). Indeed, detailed analysis of the structural and geomechanical conditions of the lower and upper parts of the slide were also performed and the early interpretations of the failure mechanism and the triggering factors were proposed by different authors (Wagner, 1991; Noverraz and Bonnard, 1992; Schindler et al., 1993).

5.3.4.2 Predisposing factors leading to the 1991 events

After the crisis management, researches have focused on the understanding of the kinematics of the 1991 events. The parameters controlling the 1991 collapse could be divided into two main categories: pre-existing factors and degrading factors (Sartori et al., 2003). For the first category, Sartori et al. (2003) indicated that the presence of a persistent fault at the base of the slope coupled with a steeply persistent joint is the major predisposing factors of the rockslide. Ground water circulation and the related mineralogical weathering (Girod et al., 1999, Jaboyedoff et al., 2004b) coupled with seismic activity were considered as the long term degrading factors (Schindler et al. 1993; Sartori et al., 2003). The ultimate triggering factor was identified as the important snow melting during April 1991 that increased the water pressure along discontinuity sets (Schindler et al. 1993, Sartori et al., 2003). Eberhardt et al. (2004), by mean of hybrid FEM/DEM geomechanical modelling highlighted the influence between the pre-existing joint set conditions and progressive shear strength degradation on the post-glacial destabilization of the slope. These authors also argued also that fully persistent geological features are not required to explain the rock slope collapse (Eberhardt et al., 2004).

5.3.4.3 Monitoring of the upper unstable area

The monitoring of the surrounding area of the Randa rockslide began just after the first rockslide event in April 1991. Until the second rockslide event (Mai 1991), 18 targets were installed and surveyed using Electronic Distance Meter (Ischi et al. 1991). After the second event, the destroyed targets were replaced and a total of 30 targets were monitored. Geodetic measurements were also carried out based on 14 reflectors between the two rockslide events and 19 reflectors after the second event (Ischi et al., 1991; Rey and Rouiller, 1995). After the second event, the northern part of the rockslide scar still showed some instability evidences. In order to study the displacements in the upper part of the slope and to monitor the potential fracture opening, twenty-four extensometers (tape-measure) and five automatic extensometers were installed. In 1995, seven 3-D retro-reflector prisms were installed in order to describe the movements on the three axes (Jaboyedoff et al., 2004a; Ornstein et al., 2005). Since 2001, an important research project was conducted to improve the understanding of the kinematics of the potential instability created after the two main rockslide events. New monitoring devices including borehole inclinometers,

extensometers and benchmark pairs were installed (Willenberg et al., 2008a; Willemberg et al., 2008b). Detailed geophysical investigations were performed to obtain a 3D overview of their fracture patterns and persistence (Spillmann et al., 2007). Recently, new monitoring devices including the use of modern monitoring techniques such as Ground-based InSAR (Gischig et al., 2009), and fiber-optic techniques (Moore et al., 2010) were installed and tested.

5.3.4.4 Kinematic of the upper unstable area

The movement of the potential unstable area located in the upper part of the rockslide were firstly interpreted by Jaboyedoff et al. (2004a) based on the 1D displacements data. According to the joint sets orientation defined by Sartori et al. (2003), these authors suggested that the kinematics of the upper unstable area is controlled by a shear band affecting the slope in the direction 135/40. Based on 3D displacement data, geophysical investigations and borehole analyses Willenberg et al. (2008b) confirmed the presence of a sub-planar shearing zone in the lower portion of the unstable area. Nevertheless, these authors suggested that the failure surface was not continuous (Willenberg et al. 2008b). The same authors, to explain displacement directions observed in the upper portion of the slope suggested the presence of block toppling. Recently, Gischig et al. (2009) comparing Ground–based InSAR data and geodetic distance measurements and confirmed the existence of a persistent basal rupture zone postulated by Jaboyedoff et al. (2004a).

5.3.5 DATA AND METHODS

5.3.5.1 New Available data

In 2008, a high resolution digital elevation model of the entire rockslide area was acquired through a helicopter survey (Helimap system®) with a 50 cm resolution. This allows a detailed topographical characterization and a precise delimitation of the morpho-structural features. Displacements dataset of the Randa rockslide area obtained by PSinSAR™ technique were recently processed by TRE® and acquired by the University of Lausanne. Satellites synthetic aperture radar (SAR) images were processed using the Local Permanent Scatter (PS) technique (TRE®, Ferretti et al., 2001) in order to detect permanent targets useful for the displacement monitoring. 51 SAR images from the satellites ERS taken in the ascending geometry and covering the period between May 1993 and July 2000 were used to determine the permanent scatters. The vector coordinates of the line of sight are N: -0.07993 E: -0.38993 H: 0.91737.
Even if, the geometrical and topographical characteristics of the study area are problematic, 1516 permanent targets were identified, distributed mainly in the upper part of the slope. The standard deviation on the velocity measurements is generally low, close to 0.2-0.5 mm/year, indicating the good reliability of the detected PS (Figure 5.3-2).

5.3.5.2 Methods

Available data concerning the discontinuity sets orientation were assembled and visualized using stereographic techniques. The helicopter base point clouds were treated using the software COLTOP3D (Jaboyedoff et al., 2007). This software combines slope angle and slope aspect determined on grid data as well as unstructured point cloud data in a unique representation by mean of Intensity-Hue-Saturation

system (IHS, see Figure 5.3-3). In the case of steep rocky outcrops the slope angle and the slope aspect of the topography can be associated to the orientation of the discontinuity sets present in the area (Jaboyedoff et al., 2007). This software also allows an easy semi-automatic delimitation and extraction of the different potential discontinuity sets.

The calculation of the potential unstable volume located in the upper portion of the scar was performed using the Sloping Local Base Level (SLBL) method (Jaboyedoff et al., 2009) and by performing a 3D geometrical reconstruction based on the point cloud acquired by helicopter. SLBL method applied to a 3D surface consists of replacing the altitude z_{ij} of a DEM node by the mean value of the highest and the lowest node altitude among the four direct neighbours, only when the altitude z_{ij} is greater than the mean value (Jaboyedoff et al. 2009). The geometrical analysis was performed using PolyWorks (InnovMetric©) and consists in fitting planes along the main discontinuity sets in order to calculate the maximal volumes that could be mobilized. A simple geomechanical model using finite-element model was performed using the software Phase² (Rocscience©).

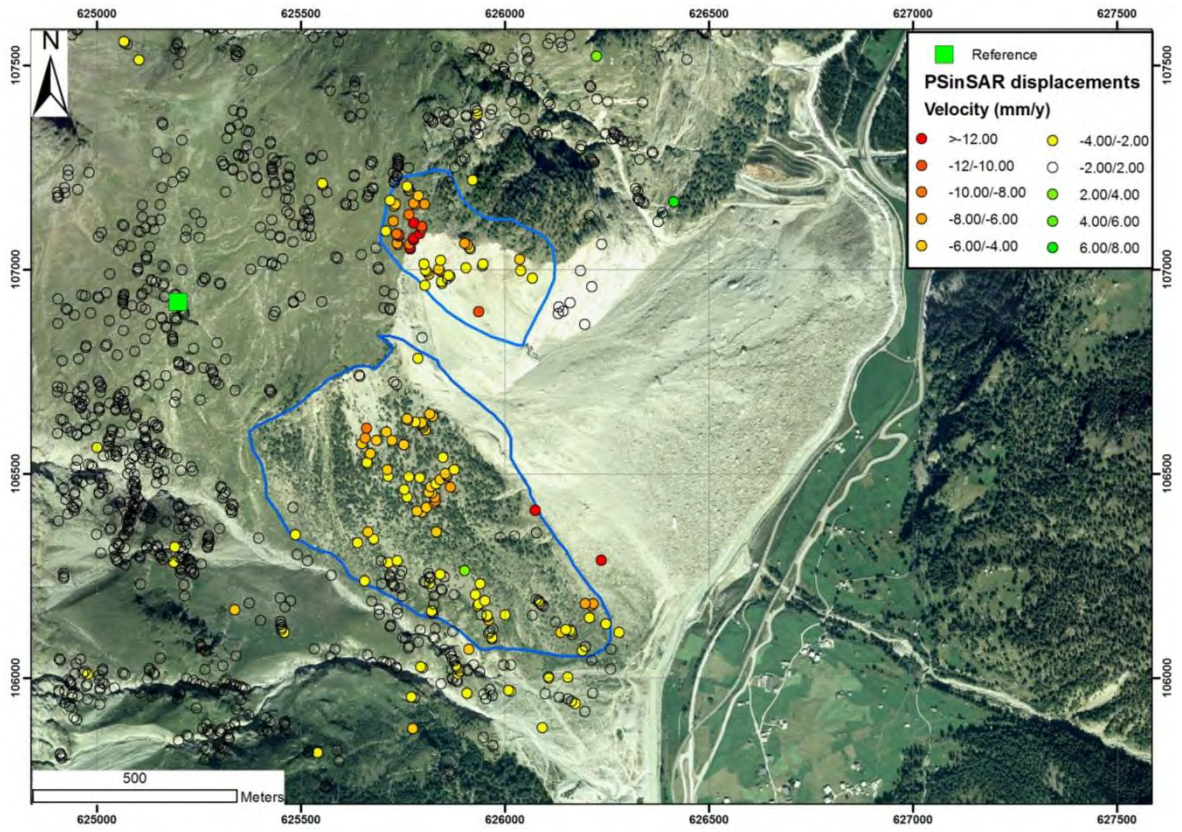

Figure 5.3-2: Distribution and displacements measured over the Randa rockslide obtained by SAR (Synthetic Aperture Radar) image processing (PSInSAR ™ technique, ascending satellite geometry). Note that in general the slope surrounding the Randa rockslide does not show any significant movements. Only two distinct areas (bleu lines) highlight clear movements.

5.3.6 RESULTS OF THE NEW STRUCTURAL ANALYSIS

Structural analysis performed using COLTOP3D software allowed the identification of height main discontinuity sets (Table 5.3-1). These results are consistent with previous fieldwork campaigns carried out by different authors (e.g. Wagner, 1991; Sartori et al. 2003; Willemberg, 2008a). In addition, another highly persistent joint (J8), with a dip direction sub-parallel to the main foliation were also identified. This

joint is primarily present in the upper portion of the slope and clearly influences the morphology of the western part of the slope (Light blue surfaces in Figure 5.3-3). On the other hand, COLTOP 3D analyses does not permit to identify joint sets dipping 60-70° into the slope (F2=355/60°) identified by Willemberg et al. (2008a) by borehole analyses. This is probably related to the fact that this joint set are developed close to the rockslide crown area only and they don't form clear morpho-structural features that can be detected by DEM analyses.

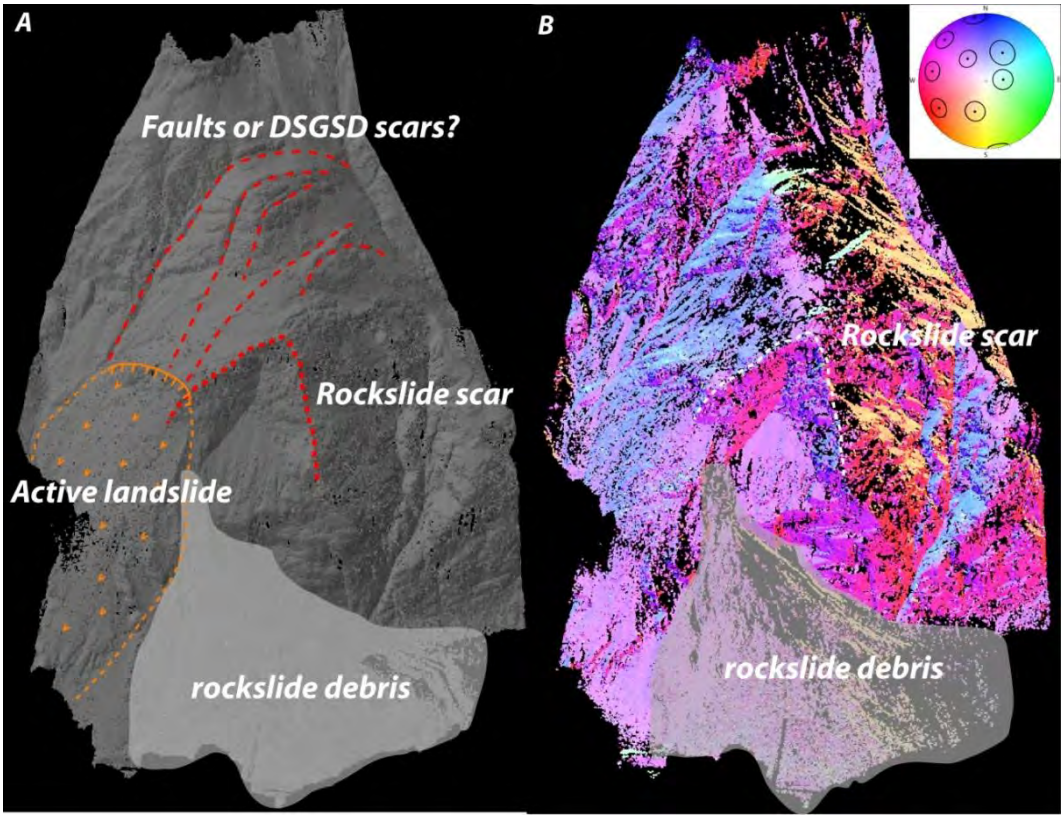

Figure 5.3-3: Hillshade 3D view of the Randa area showing the main morpho-structural features derived from helicopter-based point clouds. b) Visualisation of the same dataset by unique colour code (COLTOP 3D software) showing the significant structural control on the rockslide scar morphology.

In the slope located above the Randa rockslides, persistent lineation/faults parallel to J5 can be observed (Figure 5.3-3). These structures are mainly visible on the Randa rockslide area and became difficult to follow along the North-western side of the Mattertal valley because they don't form clear morphological features. The origin of these structures is unclear; they could be related either to a series of faults showing differential erosion or more probably to pre-glacial gravitational movements related to the presence of a deep seated slope deformation (DSGSD) affecting the entire slope above Randa. The hypothesis is supported by physical modelling performed by Bois et al. (in press) suggesting that the Randa rockslide represent only the most superficial expression of a deeper and larger slope deformation. Girod (1999) based on structural analysis performed in the by-pass tunnel highlighted that no joint sets can be clearly related to exfoliation phenomenon associated to the glacial unloading. However, according to field observation an increase of the persistence and a re-opening of pre-existing joints sub-parallel to the main valley (J2, J5 and J6), after the last glaciations can be expected.

Table 5.3-1: Characteristics of main discontinuity sets detected by COLTOP3D based on the helicopter point clouds.

Name (colour, variation)	***Dip direction***	***Dip***	***Relative distribution***
S1 (green, +/-12°)	*260*	*20*	*Whole area*
J2 (Red+/-10°)	*70*	*70*	*Central and lower area*
J3 (Light-orange, +/-12°)	*20*	*40*	*Whole area*
J5 (Red-violet, +/-10°)	*100*	*75*	*Whole area*
J4 (Light violet, +/-10°)	*140*	*35*	*Upper and central area*
J6 (Violet-blue, +/-10°)	*135*	*75*	*Central area*
J6'(Dark blue +/-10)	*170*	*85*	*Whole area*
J8 (Light blue +/-15°)	*210*	*40*	*Upper and central area*

The scar of the second rockslide event represents a clear example of complex structurally-controlled failure, especially in the south-eastern portion (Figure 5.3-3). The scar is delimited by three main orientation controlled by the pre-existing joint sets: (a) discontinuity set (J4) that controls the orientation of the main basal sliding surface; two sub-vertical joint sets (J2 and J5) delimits the southern lateral release surface; and (c) joint sets J4 and J6 define the orientation of the northern stepped-like auxiliary sliding surface. In this area, several evidences of brittle failure of the intact rock can be observed. These observations suggest that sliding planes (J4) were not fully developed. The failure were probably controlled by complex relation between the progressive fracturing and degradation of the intact rock mass and sliding along pre-existing joint sets.

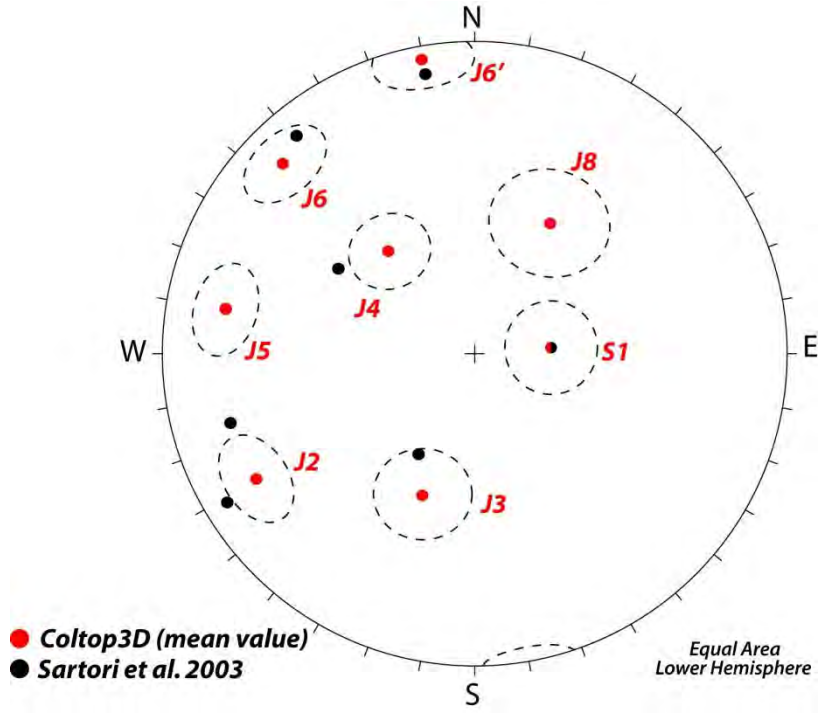

Figure 5.3-4: Stereoplot comparing the mean orientation of discontinuity sets detected on LiDAR point cloud using COLTOP 3D software (mean values red circles, 1 standard deviation dotted circles) and the mean values identified by Sartori et al., (2003) based on field observations.

5.3.7 DISPLACEMENTS ANALYSIS

The permanent scatters (PS) detected in the upper portion of the Randa rockslide were plotted on the high resolution orthophotos (see Figure 5.3-5). Negative PS InSAR velocity, indicating movements away from the sensor, can be interpreted as evidence of the progressive gravitational destabilization. According to accuracy to this monitoring technique only the points displaying a velocity over ± 2 (mm/y) were plotted. PS data of the Randa rockslide shows two areas with important negative velocities. These two areas closely corresponds to the previously monitored upper unstable area (Jaboyedoff et al., 2004a) and to a sagging area, identified by Sartori et al. (2003), in the eastern part of the rockslide.

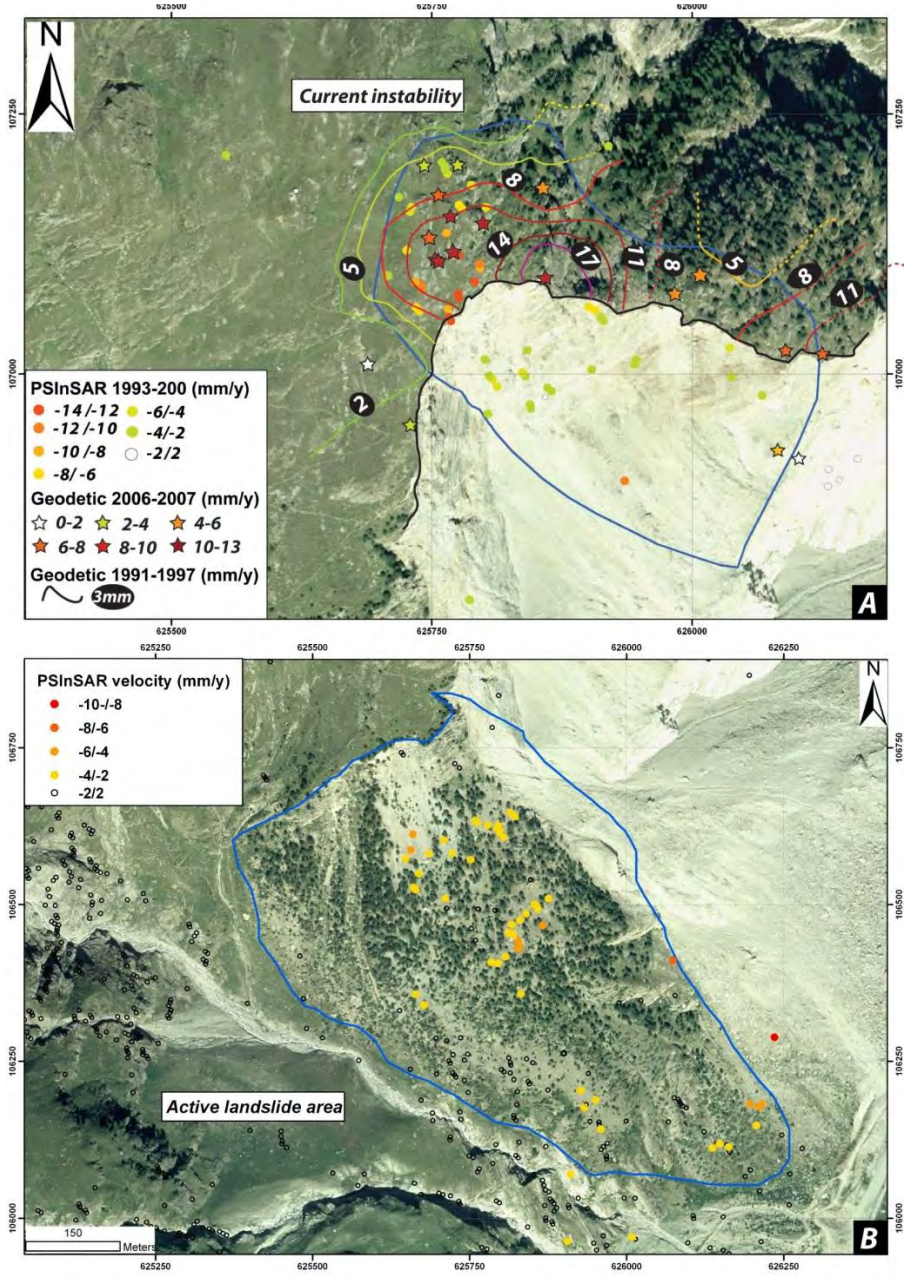

Figure 5.3-5: a) Comparison between geodetic monitoring displacement velocities (1991-1997 from Jaboyedoff et al., 2004a and 2006-2007 from Gischig et al., 2009) and PSInSAR velocities for the upper portion of the Randa rockslide. b) PSInSAR™ velocities in the landslide area located in the eastern part of the Randa rockslide scar. Displacements can reach -10 mm/y in the central portion of the instability.

The upper unstable area shows differential displacement velocities reaching -12/-14 (mm/y) close to the rockslide crown area decreasing progressively to -4/-6 (mm/y) toward NNE toward the rear portion of the unstable area (Figure 5.3-5a).The limit between the moving and stable areas is clearly visible, allowing for the clear delimitation of the potential unstable area. Concerning southern sagging area, the presence of PS is mainly concentrated in the central portion of the instability. In this area, uniformly displacements velocities of about -6/-4 (mm/y) were measured (Figure 5.3-5b). In the lower, velocities decrease progressively to -4/-2 (mm/y). In the main scar area only few permanent scatters were detected, showing slow displacements velocities (-2/-3 mm/y).

PSInSAR™ displacements observed in rockslide crown area have been compared to 1D geodetic measurement (Jaboyedoff et al., 2004) and ground based SAR analysis (Gischig et al., 2009). The three monitoring techniques show a good coherency in terms of mean velocities and extension of the moving area. Especially, all the monitoring techniques highlights that the rockslide crown area shows the higher displacement velocities (12-17 mm/y).

A progressive decreasing of velocities towards the rear part is also pointed out by the different data. It is important to remember that displacements derived from PSInSAR™ do not have the same orientation that displacements measured by geodetic method. The PSInSAR™ vector on which the velocities are projected plunges around 80° toward NE. Conversely, the geodetic vector plunges 25° toward SE.

5.3.7.1 Determination of quasi 3D displacements

Geodetic and PsinSAR™ techniques allow characterizing the displacements in one given direction only. Moreover, the 3D geodetic network installed in the upper portion of the slope is composed by seven prisms only and can be not considered fully representative of the movements affecting the entire instability. On the other hand, the 1D geodetic network and Permanent Scatterers (PS) are better distributed in the upper portion of the slope and can be used to obtain a more comprehensive view of the differential displacements in the whole area. A first approximation of the 3 dimensional displacements can be obtained by coupling the displacements measured along the two vectors coordinates defined by the 1D Geodetic devices and PSInSAR™. Let's define the PS vector as:

$$\overrightarrow{PS} = [PS_x, PS_y, PS_z]$$

and the geodetic velocity vector as:

$$\overrightarrow{GEO} = [GEO_X, GEO_y, GEO_z]$$

The "quasi" 3D vector can be defined as:

$$\vec{V} = \begin{bmatrix} V_x \\ V_y \\ V_z \end{bmatrix}$$

The velocities detected by geodetic and PSInSAR techniques can be considered as the projection of $\vec{V}$ on the unitary vectors $\vec{p}$ and $\vec{g}$ defined as:

$$\vec{p} = \frac{\overrightarrow{PS_{vel}}}{\left|\overrightarrow{PS_{vel}}\right|}; \vec{g} = \frac{\overrightarrow{GEO_{vel}}}{\left|\overrightarrow{GEO_{vel}}\right|}$$

Projecting $\vec{V}$ on the two directions and their perpendicular give a full 3D coordinate system:

$$\frac{\overrightarrow{v_n}}{|\overrightarrow{v_n}|} = \frac{\vec{p} \times \vec{g}}{|\vec{p} \times \vec{g}|} = \vec{V}_n$$

Setting the vector norm of $\vec{V}$ as the unknown we can write:

$$\begin{bmatrix} \vec{p} \\ \vec{g} \\ \overrightarrow{V_n} \end{bmatrix} \begin{bmatrix} V_x \\ V_y \\ V_z \end{bmatrix} = \begin{bmatrix} PS_{vel} \\ Geo_{vel} \\ 0 \end{bmatrix} \qquad \textit{Eq. 5.3-1}$$

And by inversing the matrix system we obtain:

$$\begin{bmatrix} V_x \\ V_y \\ V_z \end{bmatrix} = \begin{bmatrix} p_x & p_y & p_z \\ g_x & g_y & g_z \\ V_{n_x} & V_{n_y} & V_{n_z} \end{bmatrix}^{-1} \begin{bmatrix} PS_{vel} \\ Geo_{vel} \\ 0 \end{bmatrix} \qquad \textit{Eq. 5.3-2}$$

Where PS_{vel} and PS_{vel} correspond to the velocities (mm/y) measured along the vectors $\overrightarrow{PS}$ and $\overrightarrow{GEO}$.
It is important to note that this equation assumes that no displacements are considered outside of the normal plane of the two vectors ($\overrightarrow{PS}$ and $\overrightarrow{GEO}$). Hence, this formulation gives a minimal 3D displacement vector only and cannot be directly assumed as the real 3D vector. However, according to the magnitude and the direction of the expected 3D movements previously defined in the area (Jaboyedoff et al., 2004; Willenberg et al., 2008b) this formulation represents a good approximation of the real 3D displacement direction. This can be quantitatively tested by comparing the expected main sliding direction ($\overrightarrow{n}$), assumed to be parallel to the joint set J4, by maximizing the scalar product of the expected direction of sliding $\vec{n}$ with $\vec{V}$:

$$\vec{V} \cdot \vec{n} \qquad \textit{Eq. 5.3-3}$$

In order to analyse the possible orientation and norm variation of the real calculated vector, a sensitivity analysis was performed by setting non-zero displacement values along the cross-product direction ($\overrightarrow{v_n}$) in equation 5.3-2 (Figure 5.3-7). In a first test PSInSAR™ and geodetic displacements between 2006 and 2008, were used. The sensitivity analysis indicates that by adding positive or negative displacements, the plunge values of the calculated vector remain quite constant (between 55°-40°). On the other hand, vector trend values show more important variations (between 95°-180°). The final vector norm does show important differences varying from a minimum of 17 (mm/y) to a maximum of 20 (mm/y). Similar results were obtained using the geodetic displacements covering the period between 1991 and 1994.
According to equation 5.3-3 it is possible to show that the shortest 3D vector, calculated assuming $\vec{V}$ =0 is very close to the expected direction of sliding and it could be considerated representative of the real 3D vector (Figure 5.3-6). Indeed, the scalar product $\vec{V} \cdot \vec{n}$ is maximized assuming a value of $\overrightarrow{V}$ comprises between -1 and 0 (mm/y).

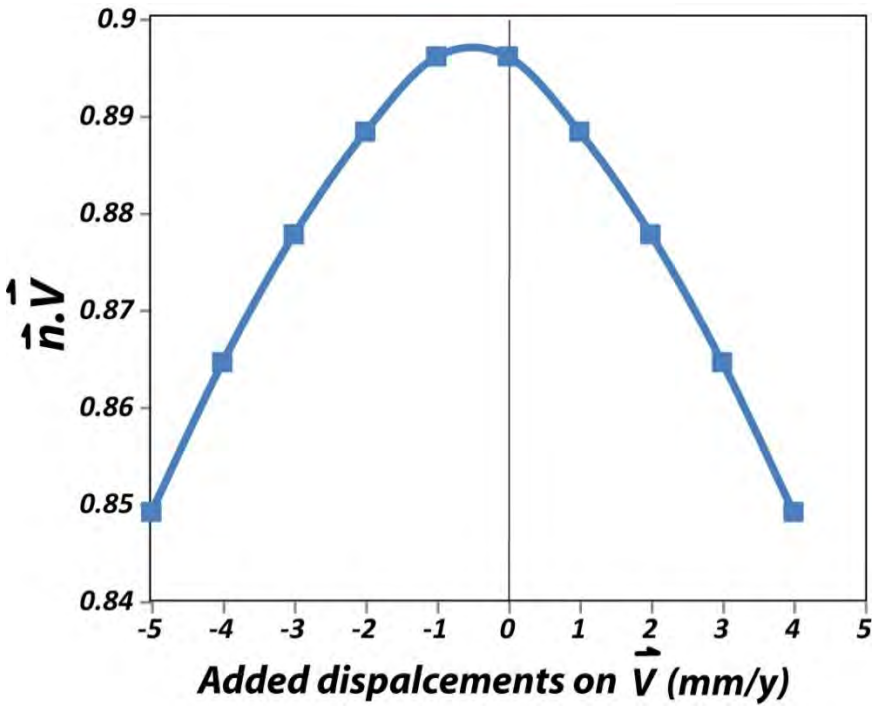

Figure 5.3-6: Results of the scalar product of equation 5.3-3 for different values of $\vec{V}$. Note that the scalar product is maximal between -1 and 0 (mm/y) suggesting that the shortest 3D vector calculated using the displacements values of PSInSAR™ and geodetic sensors is representative of the main kinematic of the area.

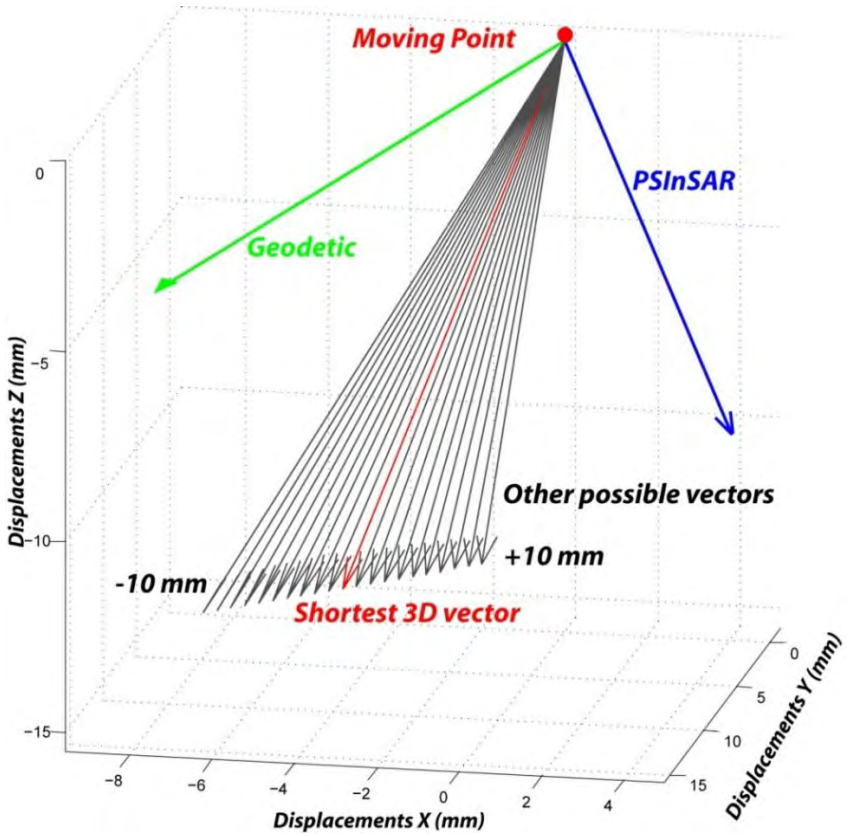

Figure 5.3-7: Example of a shortest 3D vector calculation using the displacements values of PSInSAR™ and geodetic sensors. These values correspond to the frontal portion of the unstable area (For example, coupling PSInSAR™ and geodetic displacements between 2006 and 2008, for the frontal part, a vector plunging around 55° toward 124° with a velocity of about 17 mm/y is obtained). The variation of the orientation of the composed displacement vector is calculated by replacing the result of the cross product in equation 5.3-2.

In order to examine the variations of the shortest vector along the entire unstable portion of the rockslide, geodetic and PSInSAR™ data were interpolated for the monitored area following the methodology detailed in Jaboyedoff et al. (2004). Figure 5.3-8 shows the evolution of the shortest vector calculated along a cross-section passing through the unstable area. The trend of the vector remains quite constant along the unstable area. On the other hand, the plunge of the vector decreases progressively from the frontal to the rear part (from 55° to 30°). The norm of vector shows the same trend, decreasing progressively in the rear part of the instability.

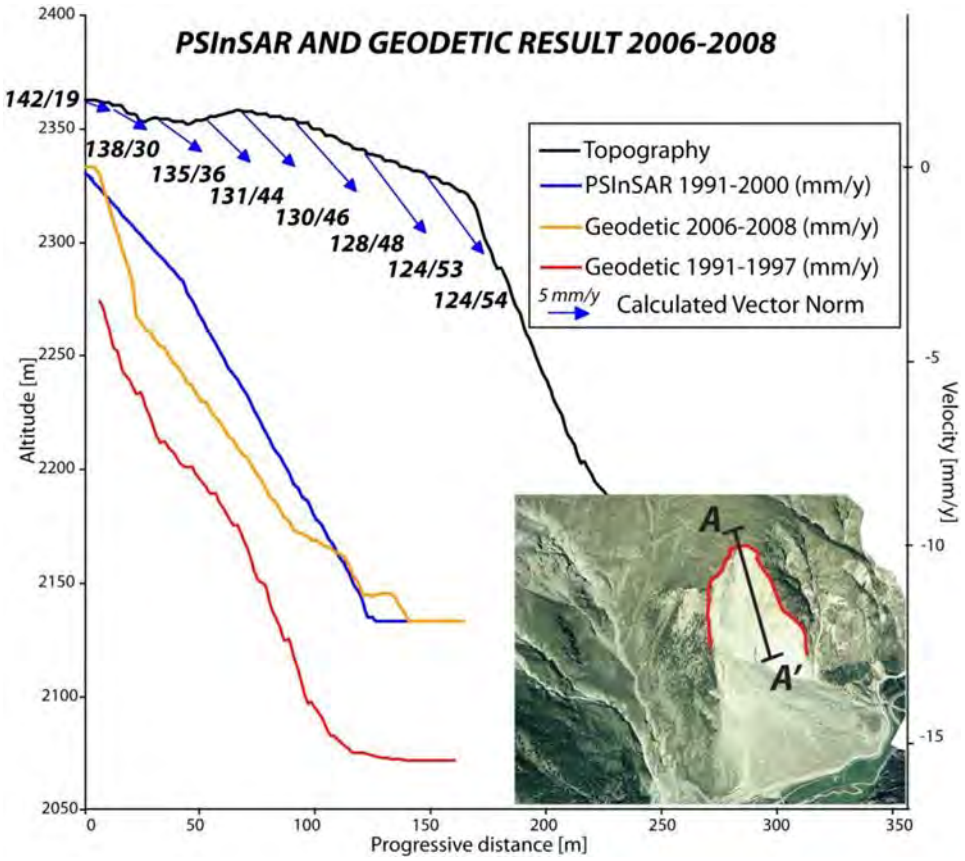

Figure 5.3-8: Variation of the shortest 3D vector calculated coupling the PSInSAR and geodetic velocities at different portion of the unstable mass.

5.3.8 FAILURE MECHANISM REINTERPRETATION

The structural setting characterizing the current unstable area (upper part of the slope) is very similar to the structural setting of the 1991 second rockslide area. Kinematics analyses performed using stereonet techniques indicate the possibility for planar sliding along J4 and for potential wedge sliding along the intersection line formed by J4^J2. J6 and J5 acting as rear release surfaces and J2 represents the main lateral release fracture.

The influence of these discontinuity sets on the kinematic of the upper unstable area was previously suggested by Jaboyedoff et al. (2004a) and by Gischig et al. (2009). In particular, these authors already suggested that general kinematics of the entire unstable area is probably controlled by a planar sliding along J4 or by a stepped-like planar slide formed by J4 and J6. However, the important movements detected by PSInSAR analysis along the line of sight, suggest that significant sub-vertical movements

occurs in the upper unstable area. Moreover, the presence of several open cracks with different orientations indicates that this area display a more complex behaviour.

The potential control of joint set J4 and J6 on the displacement directions was quantitatively tested by comparing the displacements direction calculated using equation 5.3-2 to the dip and the dip direction of the two joint set orientations. Figure 5.3-9 shows the possible variation of the quasi 3D vector calculated coupling geodetic and PSInSAR displacements by adding negative or positive displacements along the normal direction of the plane formed by the PSInSAR and geodetic vectors. In the same figure, the dip angle and dip direction of the main important discontinuity sets are also reported. It is possible to highlights that, by adding less than 2-3 mm of movements along the normal of the plane constructed by PSInSAR™ and geodetic vectors, the calculated 3D vector display almost the same trend than discontinuity sets J4 and J6.

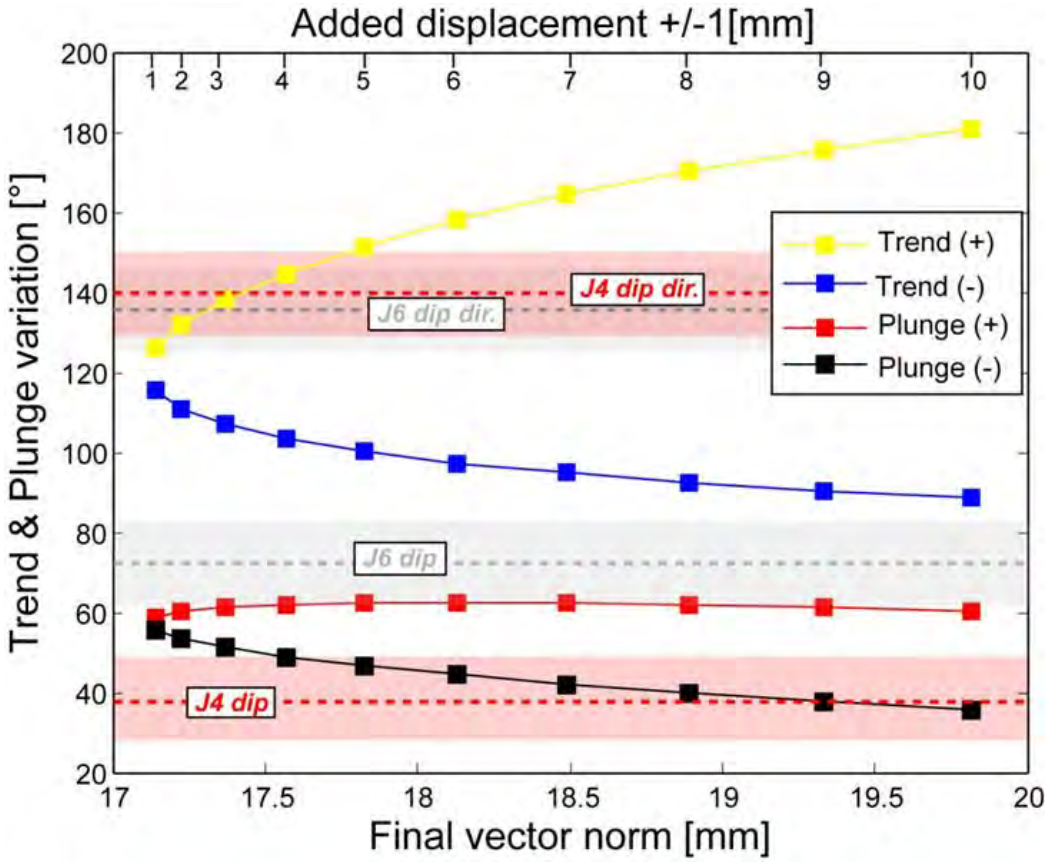

Figure 5.3-9: Comparison between the calculated trend/plunge of the "quasi" 3D vector and the dip and dip direction of the main important discontinuity sets limiting the basal failure surface. Note that the trend of the quasi 3D vector is very close to the dip direction of the two joint sets. At the opposite, the plunge of the vector not follows necessarily the joint set dip suggesting a complex behaviour of the unstable mass.

This suggests a clear control of these joint sets on the kinematic behaviour upper unstable partially confirming the schematic model proposed by previous authors (Jaboyedoff et al., 2004a; Gischig et al. 2009).

On the other hand, by adding the same amount of displacement, the plunge of the calculated vector is not comparable to the dip of the two main discontinuity sets involved in the planar failure. This indicates that more complex kinematics mechanism affects the entire unstable area. Indeed, if only planar sliding

kinematics was active, the plunge of the calculated vector will be closer to the flatter discontinuity set J4. To explain the calculated plunge values, an important vertical settlement affecting the entire upper unstable area need to be integrated in the kinematic model.

The variation of the shortest 3D vector calculated across the entire upper unstable area (Figure 5.3 7) highlight that the vertical movements are higher in the frontal portion of the instability and progressively decrease in the rear portion. According to joint set orientation detected by Willemberg et al. (2008b) in the boreholes located in the upper unstable area, the origin of this vertical movements can be associated to a close to moderate spaced joint set plunging into the slope (F-2 faults defined by Willemberg et al. 2008a) and to a discontinuity sets gently dipping out of the slope (J6). The intersection of these two joint sets define the formation of a horst and graben structure with some blocks displaying important subsidence and others blocks, especially close to the rockslide crown area that showing inverse faulting and toppling movements.

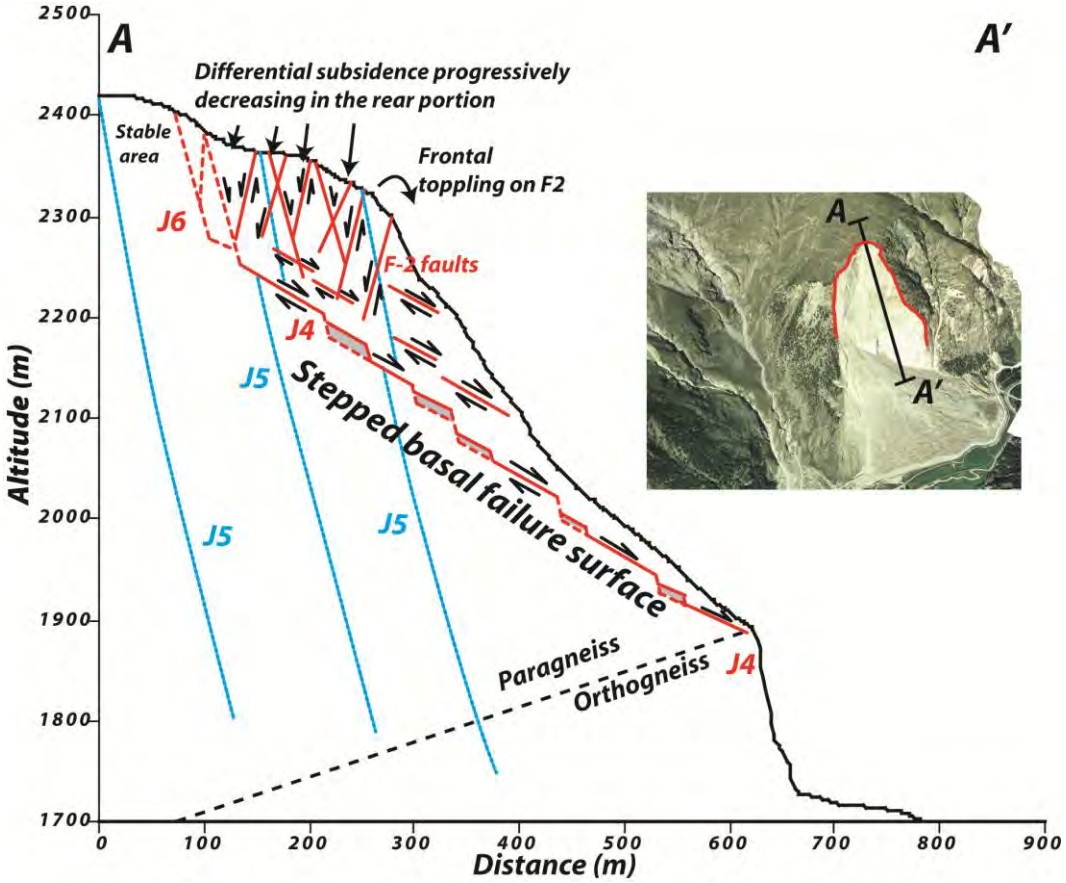

Figure 5.3-10: Schematic cross-section showing the potential kinematic of the upper unstable area. Differential subsidence movements in the upper portion are promoted by the presence of densely spaced discontinuity sets plunging into the slope together with cutting discontinuity sets gently dipping out of the slope (J4). Deeper movements are controlled by a stepped-like planar sliding.

According to these observations, the updated kinematic model for upper unstable portion of the Randa rockslide involve of shear movements along sub-vertical sets and progressive failure of rock bridges prompting the settlement of the entire upper area. This mechanism is coupled in depth with stepped-like planar sliding (J4 and J6 joint sets) that affects the slope probably until the lithological boundary separating paragneiss and orthogneiss lithologies. Toppling mechanism proposed by Willemberg et al.

(2008b) and Gischig et al. (2009) cannot not explain the important subsidence observed in the entire upper unstable area and need to be considered representative of the kinematic of the most superficial and frontal blocks only. Figure 5.3-10 presents a conceptual model of the upper unstable area the shallow fractured area and the deeper step-like failure surface.

To dispose of a mechanical corroboration of the displacements direction calculated adopting equation 5.3-2, a numerical model based on finite element approach was performed (Phase^2 code Rocscience©). Discontinuity sets and rock mass parameters and were derived from previous geomechanical model performed on the area (Eberhardt et al., 2004; Gischig et al., 2011) and adapted to be used in a finite element approach. The presence of intact rock bridges along discontinuities were modelled indirectly by assigning higher residual strength properties to discontinuities as suggested by Gischig et al. (2011).

The rock mass behaviour was modelled using elastic properties. In-situ stress was estimated to 0.6 according to sesismo-tectonic analyses performed by Kastrup et al. (2004). To avoid of potential meshing problems, only the three main joint sets (J4, J6 and F2) that are expected to influence directly the kinematic of the upper portion of the slopes were introduced in the model. The influence of the others joint was implicitly assessed by adapting the mechanical properties of the rock mass.

Table 5.3-2: Rock mass and joint set parameters adopted in finite element model.

Parameters	***Orthogneiss***	***Paragneiss***	***Set J4***	***Set J6***	***Set F2***
Young modulus (GPa)	26	14	-	-	-
Poisson ratio	0.21	0.2	-	-	-
Density (kg/m^3)	2700	2700	-	-	-
Rock mass friction angle (°)	55	41	-	-	-
Rock mass cohesion (MPa)	2	1	-	-	-
Rock mass tensile strength (MPa)	1	1	-	-	-
Joint normal stiffness (GPa/m)	-	-	10	10	10
Joint shear stiffness (GPa/m)	-	-	5	5	5
Joint apparent residual friction angle (°)	-	-	35	33	32
Joint apparent residual cohesion (MPa)	-	-	0.6	0.45	0.45
Joint apparent residual tensile strength (MPa)	-	-	0	0	0

The results of the geomechanical model shows a maximum displacement of 1.7 m. these results are in agreement with the range expected for rock slope relaxation following the rock slide occurred in 1991. The true cumulative displacements of about 1.5 m, derived by Gischig et al. (2011) summing the observed opening of cracks at the top of the instability, is also in agreement with the modelling results. The displacements direction obtained by finite element analysis show the same general trend highlighted by the displacement analyses and the geometrical model. The geomechanical model reproduces well the progressive decrease of the displacement dip toward the rear portion of the instability. Indeed, inside the unstable mass vertical settlement and superficial toppling close to the rockslides crown area have been correctly predicted. In the internal part of the instability geomechanical model highlights that movements are mainly controlled by joint set J4 that promote the development of a step-like planar sliding. In the lower portion of the slope, displacements modelled in the geomechanical model suggest that the step-like planar failure will not extent until the lithological boundary between paragneiss and orthogneiss but stops just above the scree deposits covering the upper portion of the rockslide scar.

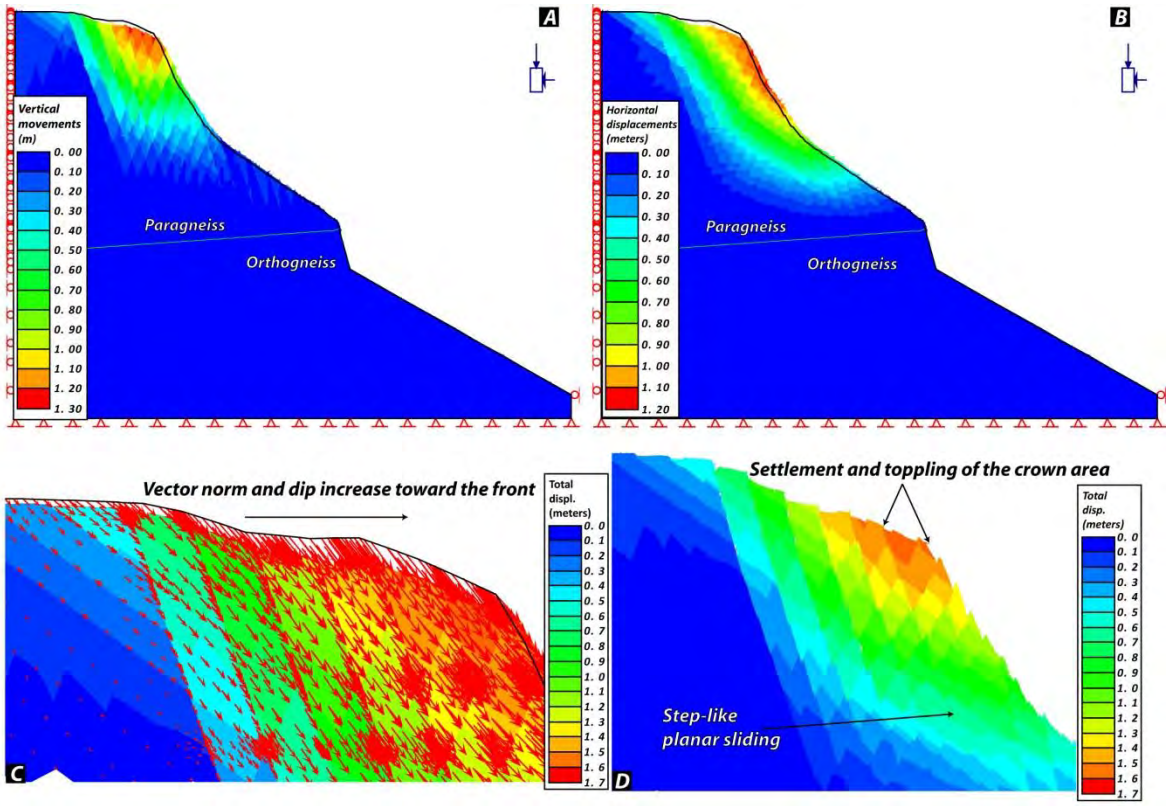

Figure 5.3-11: Preliminary finite–element model showing the magnitude and the orientation of the modelled displacement for the upper portion of the Randa rockslide. a) Magnitude and distribution of vertical movements showing the extension of the subsidence area on the upper portion of the slope. Note that vertical movements are higher close to the crown area and progressively decrease in the rear part. b) Magnitude and distribution of horizontal movements suggesting that in the internal zone of the instability movements are mainly controlled by planar sliding. c) Close-up of upper portion of the slope showing the total displacements and the displacement vectors observed in the upper portion of the instability. Note the progressive increase of the vector plunge toward to the frontal portion of the instability as suggested by PsinSAR and geodetic monitoring. d) Close-up of upper portion of the slope sowing the differential displacement along joint sets indicating the presence of differential subsidence and toppling movements.

Concerning the sagging area located in the southern portion of the Randa rockslide, only displacements data based on PSInSAR analysis are available therefore no information about the 3D displacements vector can be obtained. The detected Permanent Scatters are concentrated in the central and in the lower portion of the instability and no PS was detected in the upper portion. The displacement velocities measured by PSInSAR™ reach locally 10 mm/y and confirm the presence an active instability covering a surface of about 0.47 km^2. Clear evidences of gravitational movements are visible in the upper part of the slope (cracks scarp and counterscarps) and also at the southern margin of the Randa rockslide. In this area, after the development of the second rockslide event occurred in 1991, the shearing zone of the sagging area is clearly visible (Figure 5.3-12).

Preliminary structural analysis indicates that the displacements behaviour of this area is influenced by discontinuity sets J8 and J6'. These two joint sets allow developing a complex step-like planar surface where J8 acts as basal sliding plane and J6' creates steps and promoting vertical settlement. In the upper portion, it is possible to highlight that the back-cracks delimiting the unstable area follow essentially the pre-existing joint set J6'. As it can be highlighted in Figure 5.3-12a, it is not possible define a distinct failure surface. Nevertheless, a 15-20 m shear band, characterize by heavily fractured rock mass is visible. This disturbed area corresponds to the location of a multi-step shear failure zone (Figure 5.3-12b).

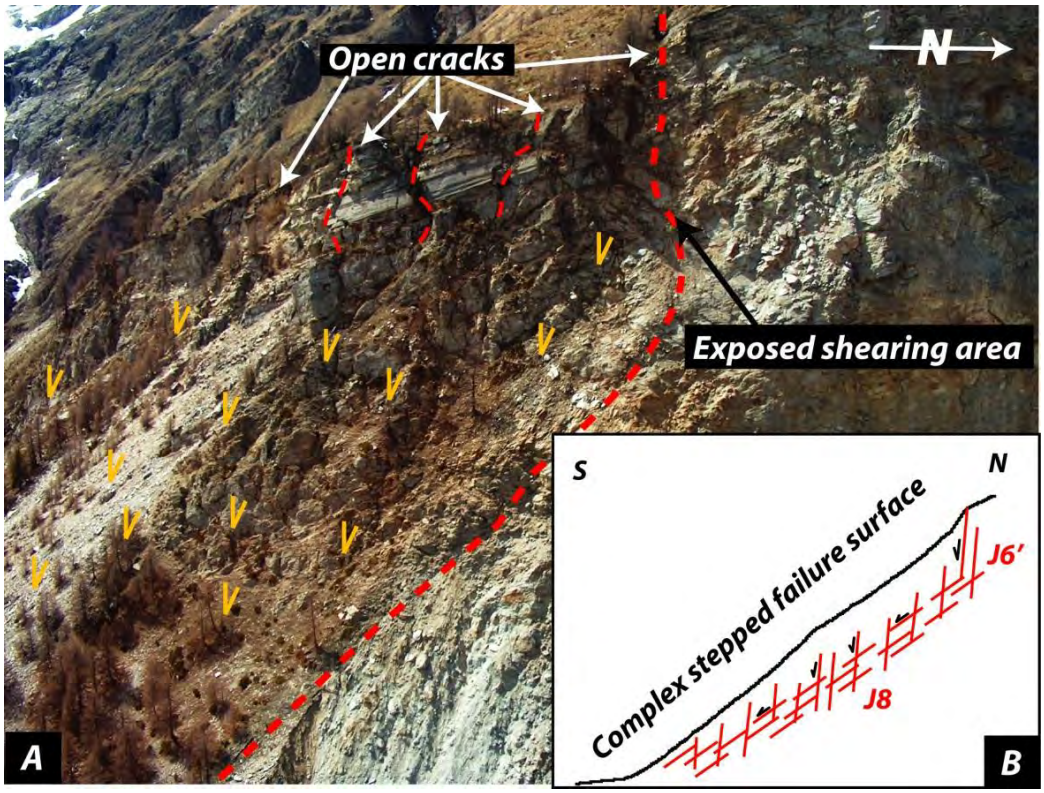

Figure 5.3-12: a) Oblique view of the upper portion of the sagging area located in the southern part of the Randa rockslide. A large portion of the multi-step shearing surface delimiting the basal sliding area is delimited with a discontinuous line. b) Schematic cross-section of the sliding area showing the potential dislocation mechanism related to the complex step-like shearing zone.

5.3.9 UNSTABLE VOLUME ESTIMATION

The geometrical reconstruction using the HRDEM allows delimiting a maximal potential unstable volume using two parameters: (a) discontinuity sets orientation and (b) extension of the moving area detected by PSInSAR. A maximal unstable volume of 4M m^3 was calculated (Figure 5.3-13). The SLBL method allows disposing to another estimation of the potential unstable volume. The SLBL calculation was constrained using the instability limits and the dip of the lower sliding surface as invariant points. An angle of 35° corresponding to the dip of joint set J4 was used to delimit the lower sliding surface. The SLBL result indicates a potential unstable volume of varying between 3.5-3.7 M of m^3 depending on the applied tolerance. A difference of about 15% between the two methods can be pointed out. This difference is probability related to the fact that using geometrical construction we do not account for large scale undulations of the main discontinuity sets and rectilinear later limits are assumed. On the other hand, SLBL model created a smoothed and curved surface approaching in a better way a complex and stepped failure surface. The estimated volumes are 20-25% lower than the volumes estimated by Gischig et al. (2009). This difference is probably related to a more detailed delimitation of the potential unstable area based on LiDAR point clouds and PSInSAR™ data.

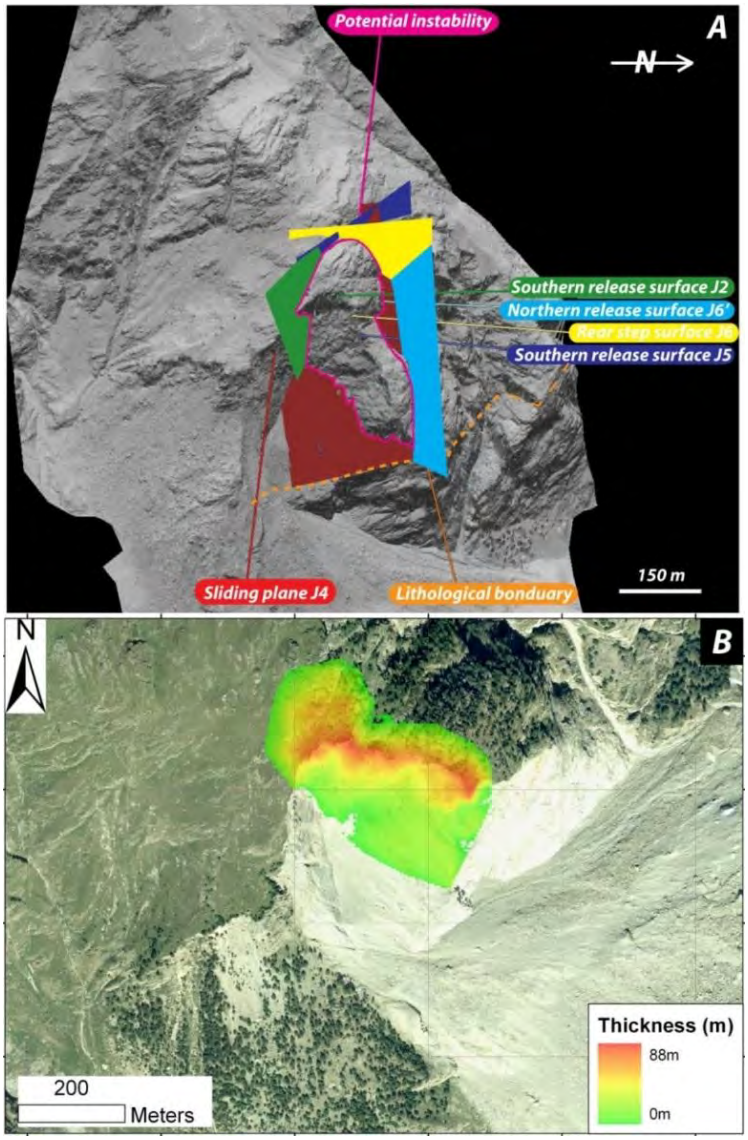

Figure 5.3-13: Estimation of the potential unstable volume located in the upper portion of the Randa rockslide scar. a) Volume estimation using geometrical reconstruction based on LIDAR point clouds and main joint set orientation. b) Thickness of the potential unstable area calculated using SLBL method.

5.3.10 CONTRIBUTION OF THE NEW AVAILABLE DATA

The integration of new joint set analysis and displacement data, allow updating the kinematic model of the upper portion of the Randa rockslide and improving the comprehension of the instability area in term of failure mechanism and present-day activity. The treatment of the helicopter-based point cloud permits to verify and update the joint sets orientations detected by previous authors by classical field mapping. New discontinuity sets influencing the stability and the morphology of the entire slope were also identified.

Based on persistent structures detected in the upper portion of the slope and the morphology of the entire slope above Randa, the presence of a potential pre-glacial DSGSD postulated by recent works of Bois et al. (in press) can be confirmed at least form a geomorphological point of view.

PSInSAR™ data show that important displacements occur in the upper unstable area but also in the sagging area located in the southern portion of the Randa rockslide. The detected velocities are comparable with the other monitoring techniques. Based on the integration of 1D geodetic and PSInSAR™ information, a quasi 3D displacement direction of the unstable are located below the Randa rockslide

crown area have been calculated and successively adopted to propose a new geometrical model of the instability. Previous postulations of a step-like planar sliding involving J4 seem to be verified especially concerning the deeper movements. However, the current kinematic remains very complex and involving progressive rock bridges failure and shearing movements along sub-vertical discontinuity sets that introduce important vertical component on the observed displacements. However, more reliable 3D displacement data are need to better constraint the kinematic behaviour of the upper instability.

5.3.11 REFERENCES

Bearth, P. 1964. Geologischer Atlas der Schweiz, Blatt N 1328 Randa mit Erklärungen, Schweizerische Geologische Kommission.

Bois, T., Bouissou S., Jaboyedoff M. In press. Influence of structural heterogeneities and of large scale topography on imbricate gravitational rock slope failures: New insights from 3-D physical modeling and geomorphological analysis, *Tectonophysics*, doi:10.1016/j.tecto.2011.08.001

Eberhardt, E., Stead, D., and Coggan, J. S. 2004. Numerical analysis of initiation and progressive failure in natural rock slopes–the 1991 Randa rockslide, *Int. J. of Rock Mech. Min.*, 41, 69–87.

Ferretti, A., Prati, C., Rocca, F. 2001. Permanent Scatterers in SAR Interferometry, *IEEE Trans. Geoscience And Remote Sensing,* 39, 8–20.

Girod, F. 1999. Altération météorique de roche granitique en milieu alpin: le cas de l'orthogneiss associé à l´´eboulement de Randa (Mattertal, Valais, Suisse). PhD Thesis, Université de Lausanne.

Gischig, V., Loew, S., Kos, A., Moore, J. R., Raetzo, H., Lemy, F. 2009. Identification of active release planes using ground-based differential InSAR at the Randa rock slope instability, Switzerland, *Nat. Hazards Earth Syst. Sci.*, 9, 2027–2038.

Götz, A., Zimmermann, M. 1993. The 1991 rock slides in Randa: causes and consequences, *Landslide News*, 7, 22–25.

Ischi, H., Keusen, H. R., and Scheller, E. 1991. Randa Kt. Wallis. Bergsturz Grossufer vom April/Mai 1991, Zusammenfassender Bericht ¨uber die Aktivit¨aten der Geotest AG., unpublished report 91126 Geotest AG, Martigny.

Kastrup, U., Zoback, M.L., Deichmann, N., Evans, K.F., Giardini, D., Micheal, A.J. 2004. Stress field variations in the Swiss Alps and the northern Alpine foreland derived from inversion of fault plane solutions, *Journal of Geophysical Research*, 109.

Jaboyedoff, M., Ornstein, P., and Rouiller, J.-D. 2004a Design of a geodetic database and associated tools for monitoring rock-slope movements: the example of the top of Randa rockfall scar, *Nat. Hazards Earth Syst. Sci.*, 4, 187–196.

Jaboyedoff, M., Baillifard, F., Bardou, E, Girod, F. 2004b. Weathering, cycles of saturation-unsaturation, and strain effects as principal processes for rock mass destabilization, *Quarterly Journal of Engineering Geology and Hydrogeology*, 37, 95-103.

Jaboyedoff, M., Metzger, R., Oppikofer, T., Couture, R., Derron, M.-D., Locat, J., and Turnel, D. 2007. New insight techniques to analyze rock slope relief using DEM and 3D-imaging cloud points: COLTOP-3D software, in: *Rock Mechanics: Meetings Society's Challenges and Demands*, edited by: Eberhardt, E., Stead, D. and Morrison, T., Taylor & Francis, 1: 61-68.

Jaboyedoff, M., Couture, R., Locat, P. 2009. Structural analysis of Turtle Mountain (Alberta) using Digital Elevation Model: Toward a progressive failure, *Geomorphology*, 103, 5-16.

Moore, J. R., Gischig, V., Button, E., Loew, S. 2010. Rockslide deformation monitoring with fiber optic strain sensors, *Nat. Hazards Earth Syst. Sci.*, 10, 191–201

Noverraz, F., Bonnard, C. 1992. L'écroulement rocheux de Randa, près de Zermatt, in: *Landslides, Proceedings of the 6th International Symposium*, Christchurch, edited by Bell, D. H., Balkema, Rotterdam, 1, 165–170.

Pirocchi, A. 1992. Laghi di sbarramento per frana nelle alpi: tipologia e evoluzione, PhD thesis, Università di Pavia, Pavia, 155 pp.

Sartori, M., Baillifard, F., Jaboyedoff, M., and Rouiller, J.-D. 2003. Kinematics of the 1991 Randa rockslides (Valais, Switzerland), *Nat. Hazards Earth Syst. Sci.*, 3, 423–433.

Spillmann, T., Maurer, H. R., Heincke, B., Willenberg, H., Green, A. G. 2007. Microseismic monitoring of an unstable rock mass, *J. Geophys. Res.*, 112, B07301.

Schindler, C., Cuenod, Y., Eisenlohr, T., Joris, C.-L. 1993. Die Ereignisse vom 18 April und 9 Mai 1991 bei Randa (VS) – ein atypischer Bergsturz in Raten, *Eclogae geol. Helv.*, 86, 643–665.

Wagner, A. 1991. Bergsturz Grossgufer Randa, étude structurale et gémecanique, Unpublished report number 91, CRSFA, Sion, 16p and annexes.

Willenberg, H., Loew, S., Eberhardt, E., Evans, K. F., Spillmann, T., Heincke, B., Maurer, H., and Green, A. G. 2008a. Internal structure and deformation of an unstable crystalline rock mass above Randa (Switzerland): Part I–Internal structure from integrated geological and geophysical investigations, *Engineering geology*, 101, 1–14.

Willenberg, H., Evans, K. F., Eberhardt, E., Spillmann, T., Loew, S. 2008b. Internal structure and deformation of an unstable crystalline rock mass above Randa (Switzerland): Part II–Three-dimensional deformation patterns, *Engineering geology*, 101, 15–32.

5.4 MONITORING AND FAILURE MECHANISM INTERPRETATION OF AN UNSTABLE SLOPE IN SOUTHERN SWITZERLAND BASED ON TERRESTRIAL LASER SCANNER

5.4.1 ABSTRACT

We present the application of terrestrial laser scanning (TLS) for the monitoring and characterization of an active landslide area in Val Canaria (Ticino, Southern Swiss Alps). At catchment scale, the study area is affected by a large Deep Seated Gravitational Slope Deformation (DSGSD) area presenting, in the lower boundary, several retrogressive landslides active since the 1990s. Due to its frequent landslide events this area was periodically monitored by TLS since 2006. Periodic TLS acquisitions provided new information on 3D displacements at the bottom of slope and the detection of centimetre to decimetre level scale changes (e.g. rockfall and pre-failure deformations). In October 2009, a major slope collapse occurred at the bottom of the most unstable area. Based on the comparison between TLS data before and after the collapse, we carried out a detailed failure mechanism analysis and volume calculation. TLS monitoring performed after the main collapse showed that the study area still present an important slope activity and new potential rock slope collapses can be expected especially in the eastern portion of the slope.

5.4.2 RÉSUMÉ

Dans cette étude, l'utilisation du scanner laser terrestre pour l'étude des mouvements d'un versant rocheux actif est présentée. Le site d'étude situé en Val Canaria (partie Sud des Alpes Suisses) est caractérisé par la présence de plusieurs zones de tassement de grandes ampleur qui présentent au pied, plusieurs zones de glissement particulièrement actives. L'analyse des caractéristiques géologiques et structurales ainsi qu'une cartographie détaillée des instabilités dans tout le bassin versant du Val Canaria a mis en évidence l'important contrôle de la dissolution du gypse au pied du versant et de l'orientation de la foliation principale sur le développement et la typologie des instabilités. Un suivi régulier par scanner laser terrestre, effectué depuis 2006, a permis une analyse très détaillée de l'activité de chutes de blocs et des déplacements. En octobre 2009, un important éboulement de 360'000 m^3 est survenu dans la partie inférieure du versant. Sur la base des acquisitions LiDAR effectuées un jour avant l'éboulement, des déplacements centimétriques de pré-rupture ont pu être détectés et validés par des mesures effectuées le même jour à l'aide du Radar terrestre.

Les données laser acquises avant et après l'éboulement ont permis ensuite une analyse détaillée du mécanisme de rupture et du volume mobilisé. Le suivi des mouvements effectué après l'éboulement d'octobre 2009 a mis en évidence que la zone montre encore des signes d'instabilité importante avec des mouvements de plus de 10 cm par an, ce qui suggère que des éboulements importants, en particulier dans la partie Est de la zone, sont encore possibles.

5.4.3 INTRODUCTION

Rockfalls and rockslides represent a major hazard in alpine valleys, especially along transportation corridors and populated areas (Remondo et al., 2008). Nowadays, almost all the alpine countries dispose of scientific studies to characterize rockfall hazard at least in areas where a potential conflict between human activities is present (Lateltin 1997; Raezo et al., 2002). Nevertheless, few studies investigated the indirect risk posed of landslide dam obstructing rivers and lakes in alpine catchment that could leads to downstream flooding (Bonnard, 2011; Eisbacher and Clague, 1984).

In this study, the characteristics of the Val Canaria in terms of type and distribution of slope instabilities will be presented. Firstly, the lithological and tectonic characteristics, influencing the location and type of movement will be analysed. Secondly, a more detailed study on a potential large collapse located directly above the Canaria River will be presented. This area represents a potential hazard to the village and the highway situated at the bottom of Val Canaria: Large rock collapse may create landslide dams in the narrow valley that could fail catastrophically and create an important downstream flooding. In this area, periodic Terrestrial Laser Scanning (TLS) acquisitions were carried out since 2006 aiming to characterize the instability in terms of structures and potential pre-failure displacements. In October 2009, an important rock collapse occurred on the monitored area. TLS datasets acquired the day before and the days after the event allowed the detection of pre-failure movements and the computation of the collapsed volume. Based on this information, an interpretation of main predisposing and triggering factors leading to the failure is proposed. The complex geological setting of Val Canaria represents also an interesting study area, where the type and the distribution of slope movements are clearly linked to tectonic and lithological characteristics. Detailed study of the relationship between lithology, tectonics and slope movements could also improve the understanding in term potential hazard posed by the different type of instabilities.

5.4.4 STUDY AREA

The study area is located in the Gotthard area, near the village of Airolo (southern Switzerland). Val Canaria is a lateral NE-SW valley (Figure 5.4-1). This 18 km^2-large catchment presents elevations ranging from 1100 m to 2700 m with mean annual rainfalls of about 1400 mm.

The area is historically well known for its susceptibility to slope instabilities since more than 150 years. According to Baruffini and Ambrosi (2010), an important rock collapse occurred in the southern part of the valley in 1846. Furthermore, a landslide located in the north-western flank of the valley was reactivated in spring 1992, after a rapid snow melting. This event created a temporarily landslide dam obstructing the Canaria River (Seno and Thüring, 2006). Val Canaria is dominated by the Mesozoic autochthonous cover of the Gotthard massif. The area is tectonically complex due to the presence of a large syncline (Piora syncline) that folds the meta-sediments covering the Gotthard massif. The outcropping lithologies are: (a) gypsum and dolomitic breccia in the lower part of the valley, (b) calc-schist in the eastern and in the central part of the valley; (c) orthogneiss and granite belonging to the Gotthard basement in the north-western flank of the valley (Figure 5.4-3).

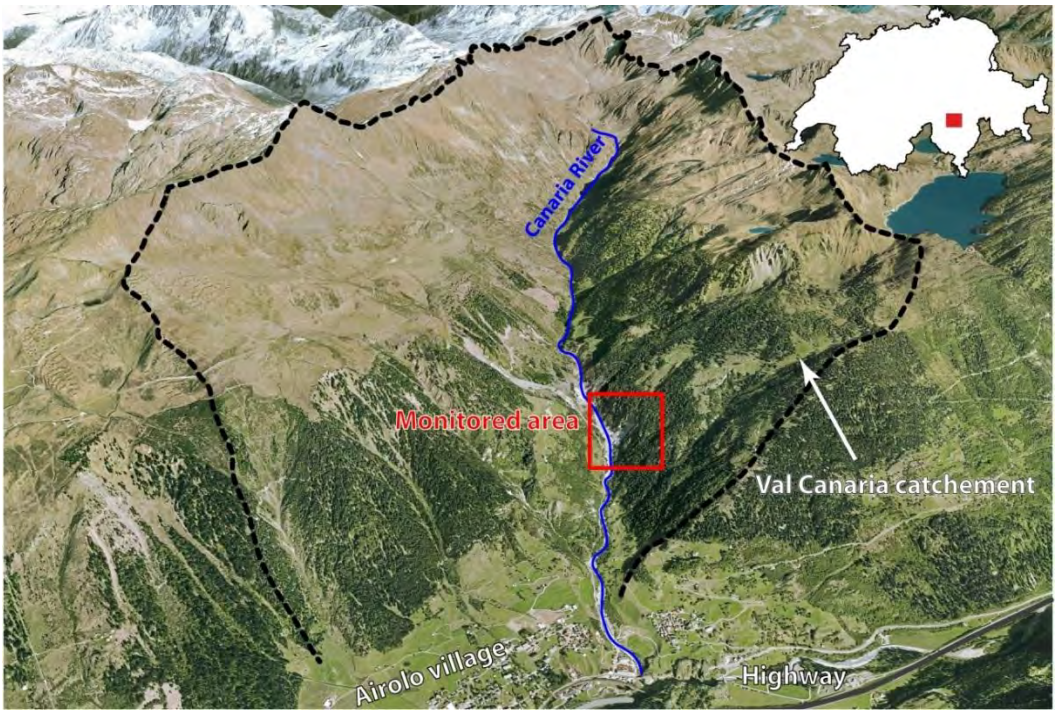

Figure 5.4-1: 3D view toward north of the Val Canaria catchment showing the TLS monitored area (red rectangle).

5.4.5 INSTABILITY MAPPING AT CATCHMENT SCALE

The first task of this study was to identify the main rock slope instabilities presented in the area. Digital support like orthophotos, a 10 m cell size digital elevation model (DEM), geological maps and Google Earth™ have been used for the first detection. Available literature on the previously known instabilities was also consulted and integrated in the mapping task (Seno and Thüring, 2006, Antognini al., 1996).

5.4.6 TERRESTRIAL LASER SCANNER METHODOLOGY

The lower part of most active landslide of Val Canaria has been surveyed using an Optech ILRIS3D. Distance measurement is based on the time-of-flight of the laser pulse, i.e. the time to travel and reflect from the rock surface. Maximum operational range of the ILRIS3D is around 700 m. TLS accuracy supplied by the manufacture is 7 mm at a distance of 100 m. More detailed information about TLS methodology and applications can be found in Rosser et al. (2007), Teza et al. (2007), Abellan et al. (2009) and in Oppikofer et al. (2009).

5.4.6.1 Data acquisition and Co-registration of the point clouds

Eight TLS surveys were acquired between June 2006 and October 2010. The rock slope was scanned from 4 different positions in order to completely cover the area. The mean point spacing on the rock face, depends on the site configuration and distances to the TLS, and ranges between 5 to 12 cm. After vegetation cleaning, each dataset contained between 4 and 7 million points. TLS datasets acquired during the same campaign were co-registered in a single point cloud using PolyWorks software (InnovMetrics). Merged scans were preliminary aligned using common points (N point pairs). A refinement of the alignment was carried out using Iterative Closest Point (ICP) algorithm (Chen and Medioni, 1992). Co-registration error could be estimated to 2.8 cm.

5.4.6.2 Displacements characterization and quantification

Two different methods have been applied in order to characterize and quantify the displacements:

- Point to surface comparison: Shortest Distances (SD) between the reference point cloud and the successive datasets (Oppikofer et al., 2008; 2009).
- Roto-translation matrix technique (Monserrat and Crosetto, 2008; Oppikofer et al., 2009).

As suggested by Oppikofer et al., (2009), SD analysis is a useful tool to detected 3D displacement allowing the identification of vertical, horizontal and oblique differences. The computation of SD was performed in PolyWorks software. For each point of a data point cloud the SD algorithm searches its nearest neighbour in the reference point could and computes the SD vector. Regarding sign criteria, positive SD indicate that the points in the data point cloud are situated above the reference point cloud (sliding mass advance from its initial position). Negative SD means that the data point cloud is behind or below the reference dataset. Negative SD could be interpreted as vertical settlement, subsidence or rockfalls (Oppikofer et al., 2008; 2009). The advantage of this method is the quick application that could be performed automatically to detect movements between the reference and the successive datasets. The main disadvantage is that SD analysis is performed for point pairs only. This implies that the quality of comparison results depends strongly on the point spacing and on the presence of shadow zones. In addition, the comparison must be ideally performed between datasets acquired almost from the same position. As suggested by Oppikofer et al. (2009), the error associated with the SD comparison can be estimated as the standard deviation obtained during the registration of sequential datasets, which is approximately 2.8 cm in this study.

To assess smaller displacements and to compare datasets acquired from slightly different positions the roto-translation matrix technique was applied. This method account for both translation and rotation of a selected area (e.g. rock slope compartment, block, portion of soil), considering all the data points. As suggested by Oppikofer et al. (2009) translation of the central point of the selected area can be expressed by trend, plunge and vector norm. The rotation is expressed by the toppling azimuth and angle of an initially vertical vector and the tilt rotation around the toppled vector. The methodology is described in detail in Oppikofer et al. (2009). Compared to the SD analysis, the roto-translation matrix technique presents a great advantage by using the high point density of TLS data to estimate mean displacements of a selected area. Using this method, displacements of approximately 1 cm can be detected. Main limitations of this technique are related to the detection of homogenous areas that could display constant deformation behaviour.

3.2.4 Volume estimation

In order to estimate rockfall and rockslide volume, we created DEMs from the TLS point clouds of the reference dataset and the successive acquisitions. Inverse distance weighted (IDW) interpolation was applied to create 0.2 m cell size DEMs. Failed volumes correspond to the sum of the differences between successive DEMs over the collapsed area.

5.4.7 STRUCTURAL ANALYSES

According to Brideau et al., (2009), structural analysis is one of the most important steps for the definition of the potential failure mechanism on hard-rock slopes. In this study, we obtained the orientation of the

main discontinuity sets on the base of TLS data using COLTOP3D software (Jaboyedoff et al., 2007). This software allows computing the spatial orientation (dip direction and dip angle) of each point with respect to its neighbourhood. An interactive selection of different orientations is possible, allowing a user-friendly exportation of the discontinuity orientation to common stereographic software (e.g. Dips). Main advantage of this technique is the possibility to obtain a quick and visual identification of the main orientation based on an orientation-specific colouring of the point cloud. This technique is relatively quick compared to manual techniques (Sturzenegger and Stead, 2009) and allows obtaining a large amount of structural data giving a more complete statistical description of the natural variability of different discontinuity sets.

5.4.8 RESULTS (1): INSTABILITY CHARACTERIZATION AT THE CATCHMENT SCALE

Photo-interpretation allowed for the identification and mapping of more than 30 slope instabilities affecting the Val Canaria catchment at different scales. 55% of the entire catchment is exposed to gravitational movements. We observed that the location and activity of the slope instabilities along the valley were not homogenously distributed (Figure 5.4-2). The most important slope destabilizations are concentrated in the lower part of the valley. In this area, both valley flanks are characterized by deep seated deformations and by several more superficial instabilities.

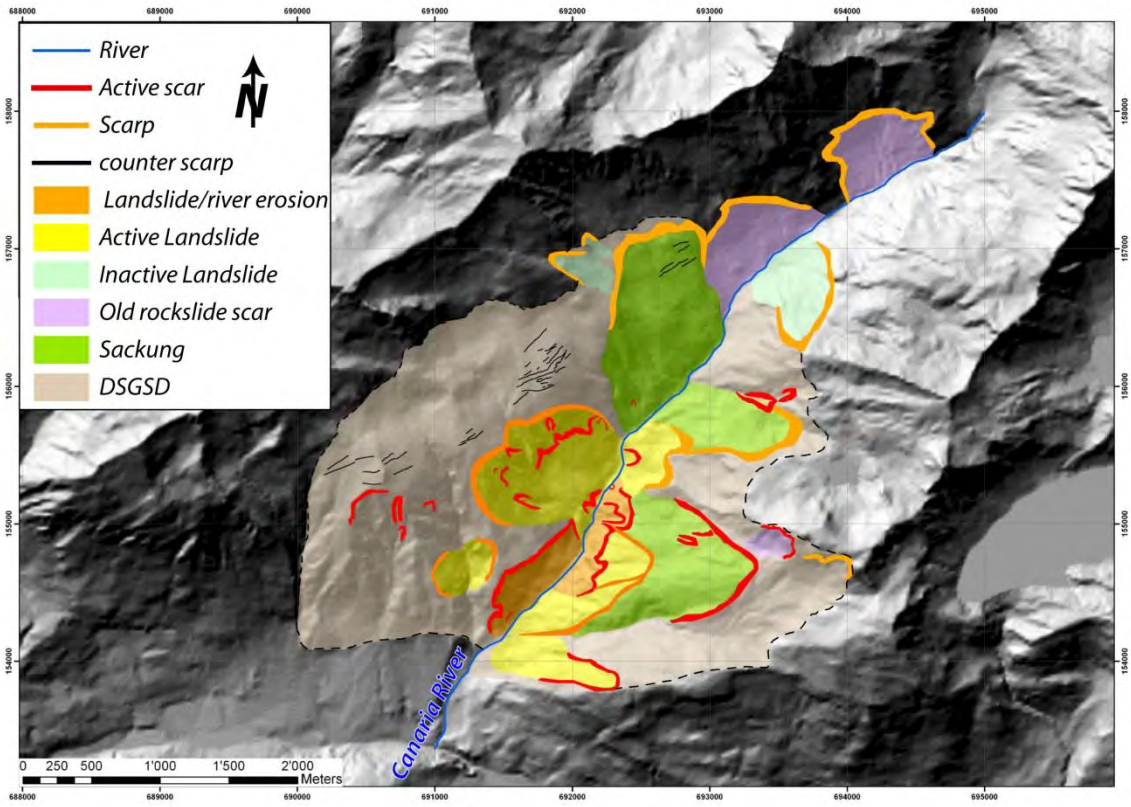

Figure 5.4-2: Map of the different slope instabilities detected through DEM analysis, aerial photos interpretation and field survey.

A clear distinction between the geomorphological features characterizing the two valley flanks is shown in Figure 5.4-3, as follows: (a) the upper part of the NW flank is characterized by a massif presence of large trenches and counter-scarp features. However, the present–day active scarps are located in the lower

part; (b) in the SE flank no counter scraps were observed. The topography is rough but the slope is quite uniform along the slope. In the lower portion of the slope close to the river, a series of active scars were observed. By analysing the distribution of slope instabilities in relation to tectonic features, it is possible to observe that the most active area corresponds to the lower part of the valley, where gypsum outcrops. In this area, the valley is sub-parallel to the Piora syncline axis. The presence of gypsum at the bottom of the slope represents a major destabilizing factor that was pointed out by several authors working in the Alpine area (Alberto et al., 2008; Dramis and Sorriso-Valvo, 1994). Dissolution of gypsum at the bottom of the slope favours the creation of large slope instabilities as deep seated creeping observed in both flanks of the valley. Typology and the style of activity are also influenced by tectonic heritage.

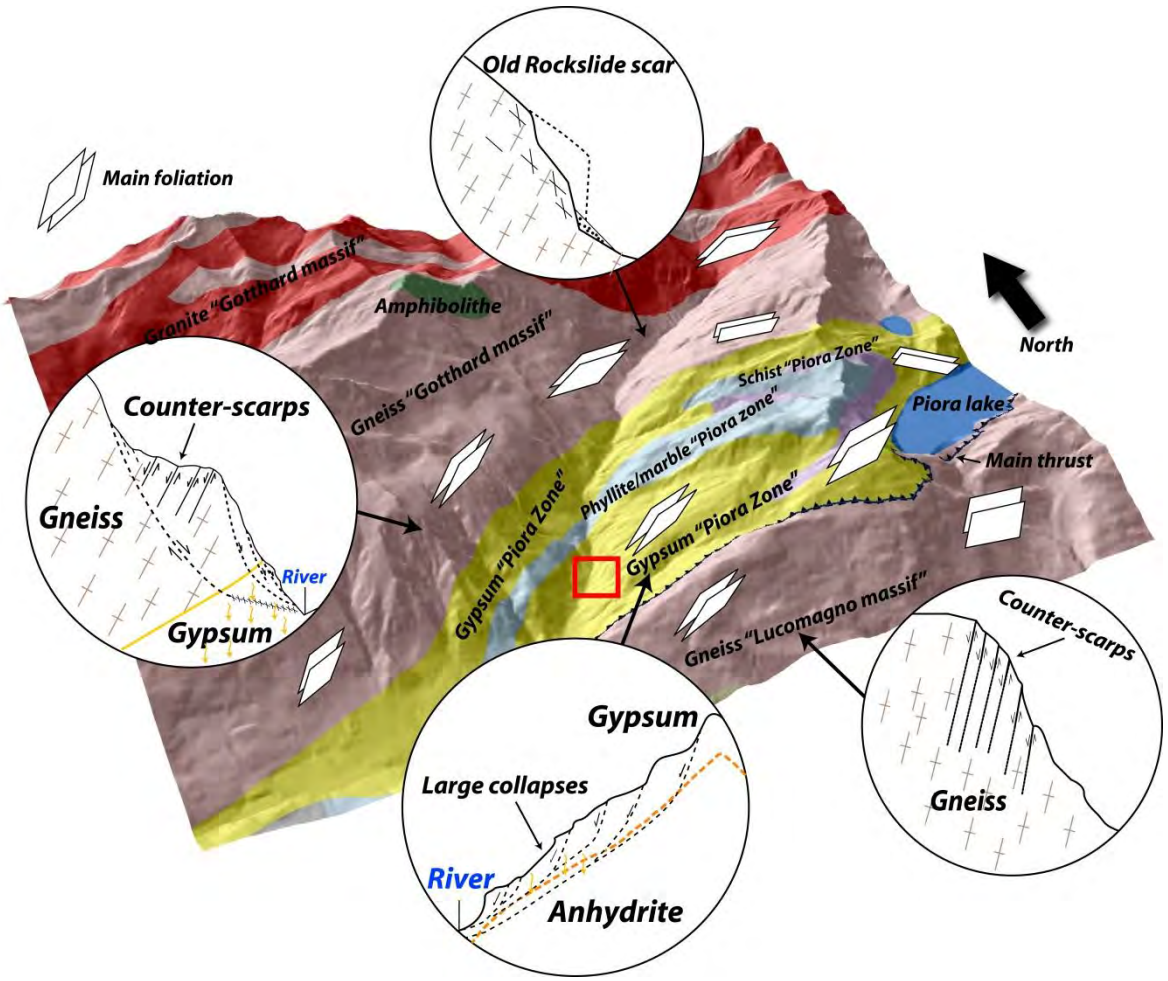

Figure 5.4-3: 3D sketch of the tectonic settings of the Canaria catchment, including the main instability types based on the foliation orientation and the lithological characteristics

In the south-eastern portion of valley, instabilities can be classified as large collapse and sliding. This is probably related to low rock mass strength of the lithology outcropping in the area and to the bedding attitude sub-parallel to slope direction. The NW flank of the valley shows the opposite situation with the main foliation of high strength orthogneiss dipping into the slope. This geological configuration induces the creation of compressional features, such as counter-scarps and trenches in the upper part of the slope (Figure 5.4-3). Gypsum dissolution at the bottom of the slope allows the development of large slope creeping. Slope activity decreases progressively in the more internal part of the catchment where the

Piora syncline and its related soluble rocks are not parallel to the valley. The outcrops are mainly massive orthogneiss with the main foliation orientated orthogonally to the slope orientation, which is less prone to slope instabilities (Figure 5.4-4).

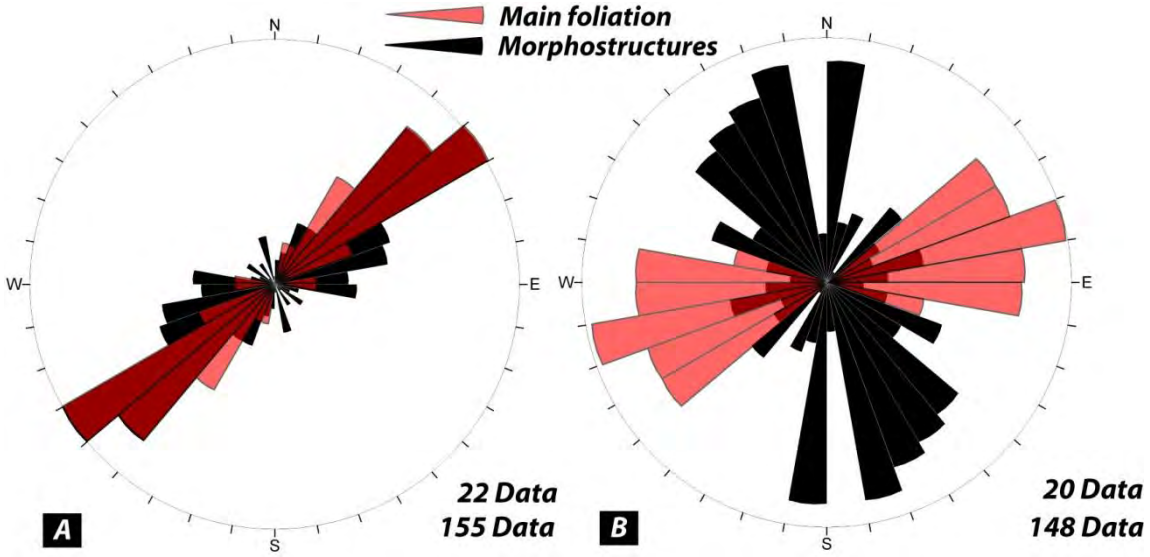

Figure 5.4-4: Comparison between bedding attitude and morpho-structures in the (a) NW valley flank and (b) in the SE flank, showing a clear distinction of structural and lithological control between the two valley flanks.

5.4.9 RESULTS (2): DISCONTINUITY SETS AND KINEMATIC ANALYSIS

At the bottom of the SE flank of valley an active scar formed on gypsum outcrop could be underlined (Figure 5.4-5). The area shows an increasing activity since the 1990s. Due to its proximity to the Canaria River and the possibility to create a landslide dam the area is monitored using total station techniques (Ambrosi, pers. comm.). Rockfall activity is frequently observed especially during melting periods and after rainfall events. In the past, the area experienced important rock collapse involving 10'000 m^3 of weathered gypsum.

A detailed structural analysis was carried out on TLS data acquired prior and after the 27 October 2009 landslide. Due to mechanical behaviour of gypsum, development of discontinuity sets is frequently scattered. Failure occurs commonly by rock mass collapse. However, field observations indicate that large structures are found also in gypsum and could influence the failure mechanism. By using the two TLS, it was possible to obtain a double control of the relevance of the detected structures.

Table 5.4-1: Main discontinuity sets detected on TLS point clouds acquired before and after the 27 October rockslide.

Joint set	*TLS 2007*	*Variability1σ/2σ*	*TLS 2010*	*Spacing (m)*	*Variability 1σ/2σ*
J1	178/72	11/18	172/69	2	12/19
J2	059/71	12/21	54/73	1.5	7/12
J3	153/64	12/20	153/64	2	12/20
J4	216/68	7/12	230/61	1	10/17
S0	341/55	14/23	324/69	0.2	9/16
J6	023/68	11/19	023/73	0.5	11/19
J7	260/60	10/17	266/54	0.5	11/18

Using COLTOP3D analysis, 6 discontinuity sets and the bedding planes were detected on both datasets with very similar values (Table 5.4-1 and Figure 5.4-6). A kinematic analysis was conducted for the

average topography of the cliff in order to detect the main potential failure mechanisms. Results indicated that planar sliding is locally possible along S0. Along intersections J4/J6, J7/S0, J7/J6 and S0/J4 wedge sliding is cinematically feasible and is marginally feasible along J7/J2 and J6/S0. Due to the high variability of discontinuity J3, toppling on this discontinuity is also locally possible. Rock instabilities in moderate to low rock mass qualities (e.g. gypsum, dolomitic breccia) are mainly controlled by rock mass strength (Brideau et al., 2009).

Nevertheless, rock mass anisotropy related to the presence of one direction of fracturing or to a preferential fracturing direction could reduce the strength in a preferential direction (Amadei and Savage, 1989). For this reason, the direction of the maximum discontinuity frequency (Hudson and Priest, 1983; Jaboyedoff et al., 1995) has been analysed in order to investigate the possible relationship between structural setting, potential strength anisotropy and the topography orientation (Figure 5.4-6d). Results indicate that the maximum discontinuity frequency direction (63° toward 340) defines a surface close to the mean orientation of the rockslide slope (300/55). This result pointed out that the surface of the scarp is not fully controlled by one distinct discontinuity set (i.e. beddings) or only by glacial or fluvial erosion but by the combination of discontinuity sets. Highest density direction calculated form of pre-existing discontinuities needs to be considered as important influence on slope orientation and failure direction.

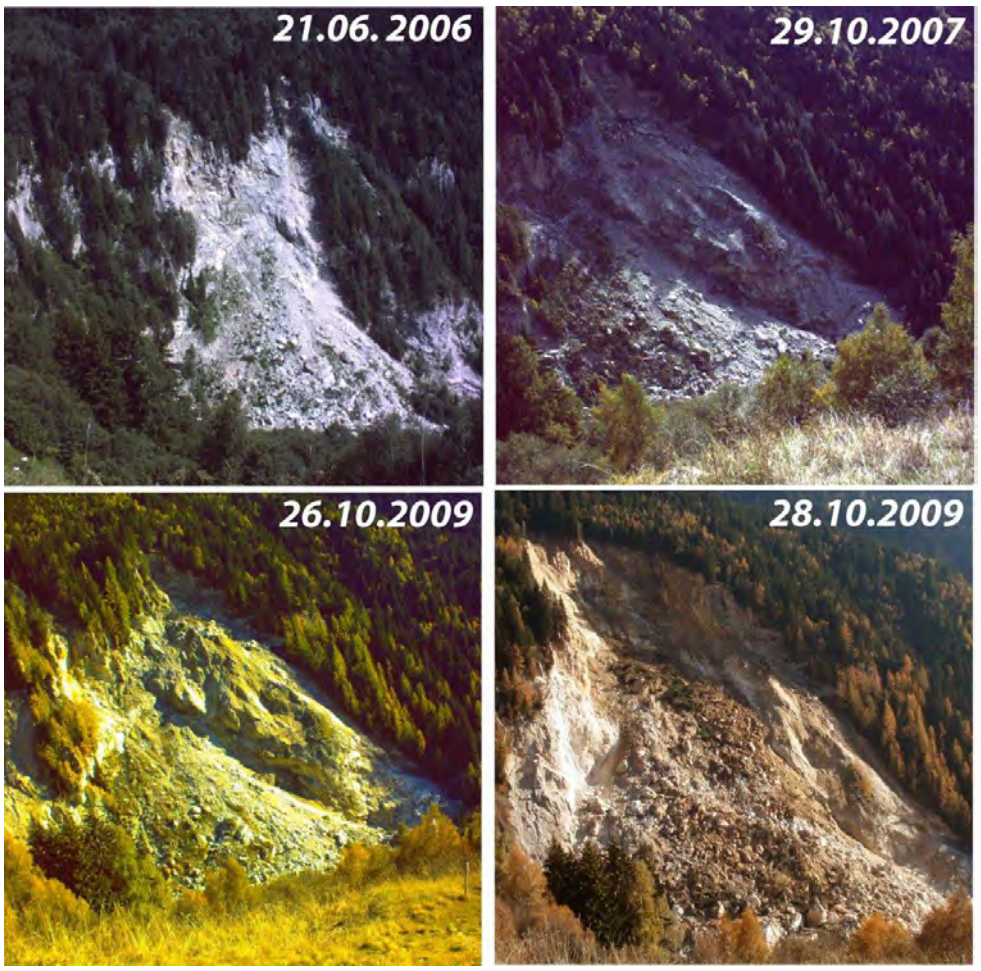

Figure 5.4-5: Picture showing the evolution of the monitored area between 2006 and 2009. Note the influence of the large collapse occurred on 27.10.2009 that completely modified the morphology of the monitored slope.

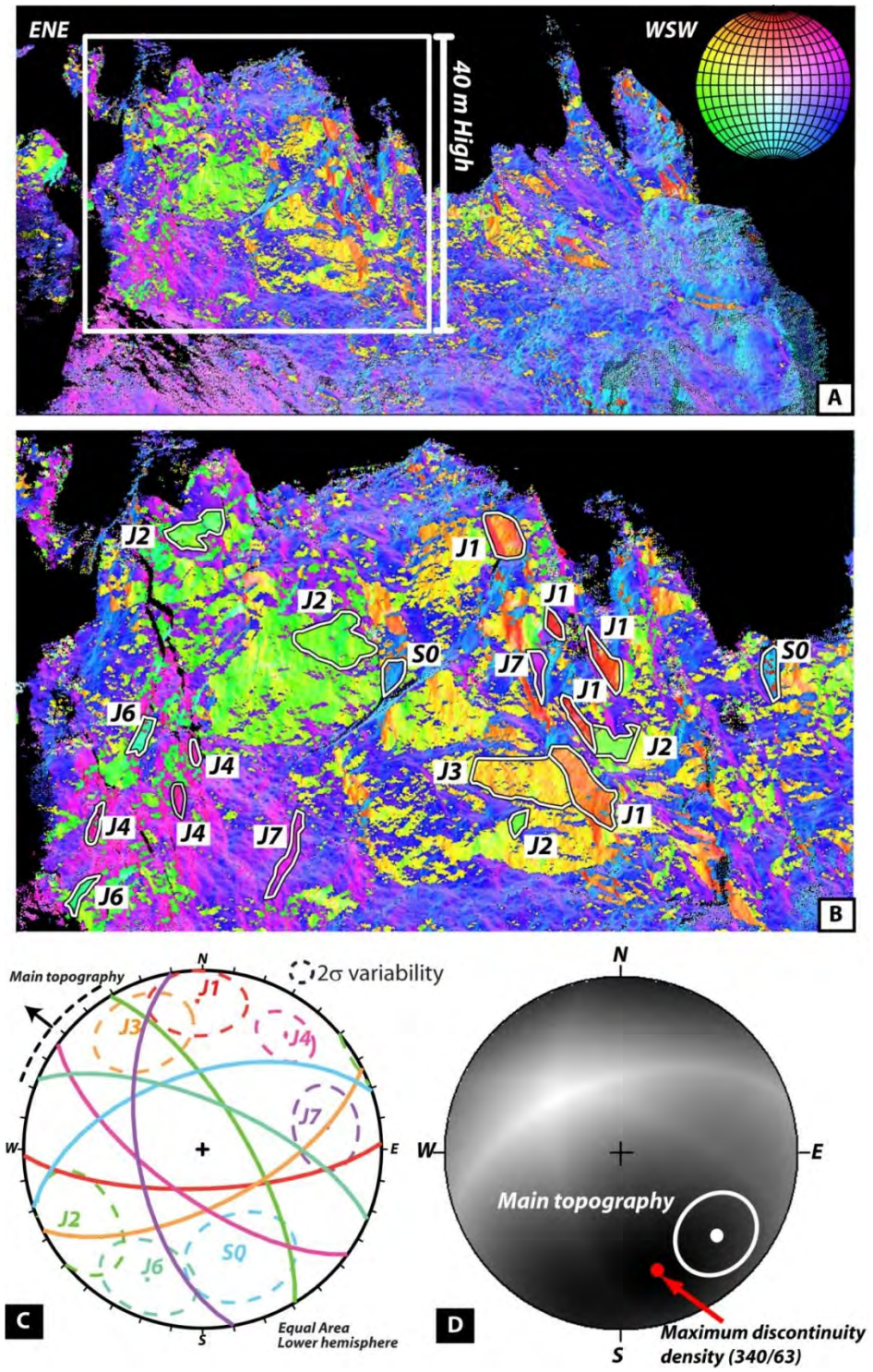

Figure 5.4-6: A) COLTOP3D representation of 2007 TLS dataset. B) Zoom showing the selected discontinuity set. C) Stereographic projection of discontinuity set detected on 2007 TLS dataset. D) Direction of the maximal discontinuity density obtained by introducing all the detected discontinuity sets compared to the local topography orientation (withe circle).

5.4.10 RESULTS (3): EVOLUTION OF THE MONITORED AREA DURING TIME

The activity of the area was evaluated by comparing the different TLS data acquired between 2006 and 2010. The comparison was carried out dividing the observation period in three different time spans, corresponding to pre, syn and post failure period. These three time spans will be analysed separately.

5.4.10.1 Time span 1: datasets acquired in 2006, 2007 and 2009.

We used the SD analysis to compare the TLS datasets acquired in 2006 (reference dataset) to scans acquired in 2007 and 2009 (26.10.2009). Displacement analysis between the first two datasets (2006 and 2007) reveals significant rock collapse in the WSW sector (Figure 5.4-7a) of the slope and pre-failure displacements, up to 15 cm in the central part of the rock mass (Figure 5.4-7b). Debris movements as well as material deposition are observed in the lower portion of the slope. Point cloud comparison between 2007 and 2009 shows an increasing displacement rate in the central part of the slope with movement that reach locally more than 1m in 2 years. The SW part of the slope shows smaller rock collapses.

The rock outcrops were divided into six blocks based on the morphology and differential displacements observed based on SD technique for a detailed 3D displacement analysis using the roto-translation matrix technique. This procedure ensures that the computed translational and rotational displacements of the blocks are representative for each analysed zones. In order to assess the errors with the given datasets, five areas that were assumed stable in the surroundings of the moving area were used as reference blocks. Analyses on reference blocks indicate an accuracy of the translation length varying between 0.02 and 2.41 cm with an average of 1.20 cm. The error on rotational components ranges from 0.008° to 0.227° with a mean value of 0.068° for the toppling angle and from 0.002° to 0.104° with an average of 0.041° for the tilt angle.

Translation vectors have a relatively constant trend and plunge (average of blocks between 2006 and 2009: 292°/34°) with only little variations between the different blocks (trend: [284°; 327°]; plunge: [24°; 51°] and the different epochs (1σ standard deviation between displacement vector orientations: mean: 11.4°; max: 22.4°). The translation velocity between 2007 and 2009 [22.9 cm/year; 50.8 cm/year] are 2.5 to 4 times higher than between 2006 and 2007 corresponding to 8.2 cm/year; 17.9 cm/year respectively. Most measured toppling angles are significant, although their accuracy is relatively low (mean error of reference blocks: 0.068°). Toppling angles vary between 0.011° and 0.382° and the toppling directions range from 210° to 037°, i.e. principally in down slope direction. Average toppling is 0.176°/year towards 301°N. For blocks that had significant toppling between 2006 and 2007, the annual toppling angle is slightly higher in the successive period between 2007 and 2009.

TLS analysis indicates an increase of the movement of the central part of the slope between 2007 and 2009.

The entire rock mass seems to be moving almost in the same direction, indicating that the frontal block is not completely disconnected from the entire rock mass. Displacement directions appear to be controlled by the structural settings: COLTOP3D analyses underline the presence of at least three potential wedges (S0/J4, S0/J7 and J6/J7) with similar trend and plunge as the observed movements. Blocks located in the WSW part of the slope show faster movements than blocks analysed in the ESE part. The WSW part of the rock slope experienced a large slope collapse between 2006 and 2007 that was estimated between 12'500 and 13'000 m^3 based on TLS comparison. A possible explanation of this collapse could be related to the concave topography allowing a water concentration inducing a drastic decrease of the effective rock mass strength. This explanation is also supported by measured tilt angles indicating a clockwise rotational movement for all monitored blocks.

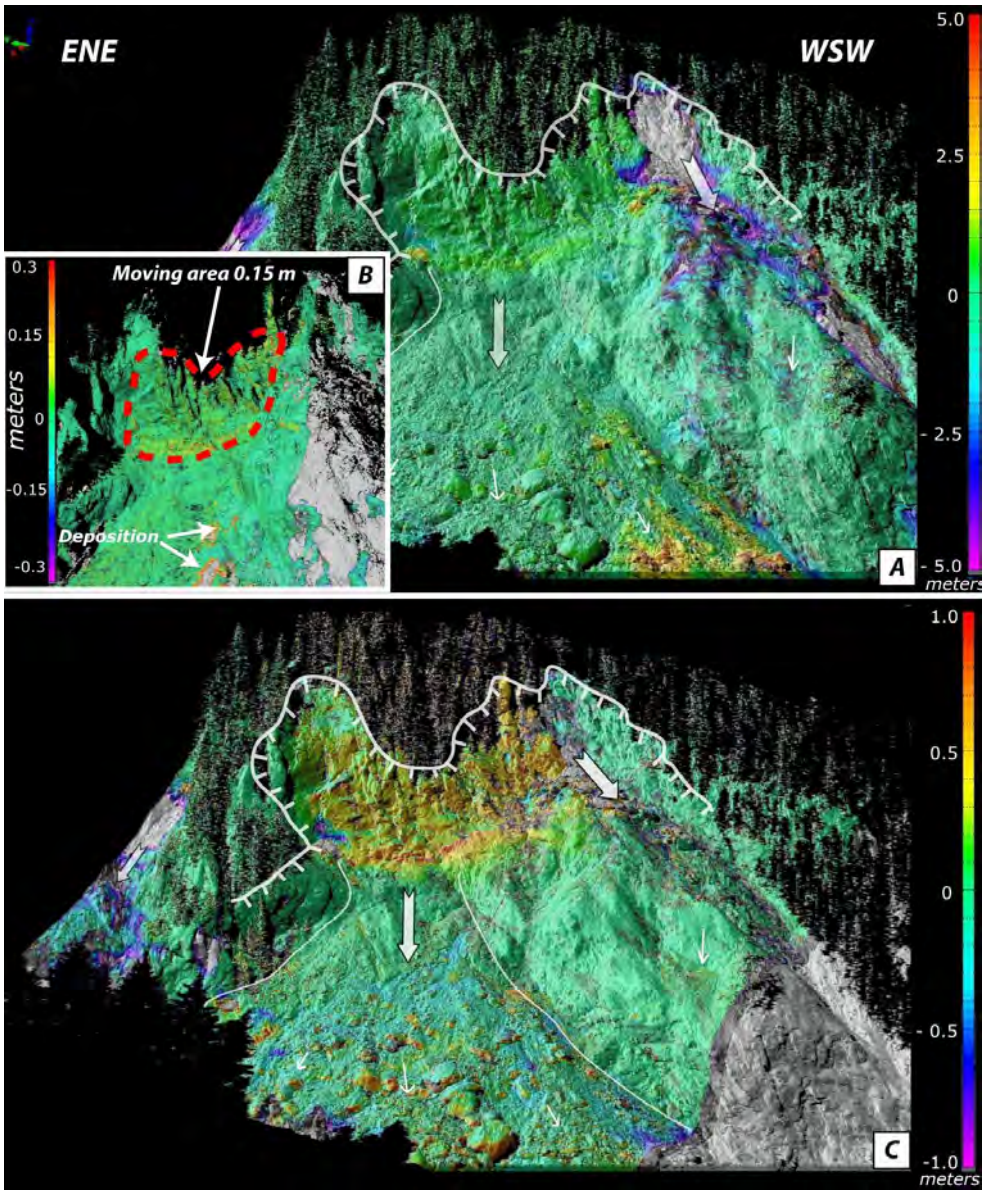

Figure 5.4-7: Shortest distance (SD) comparison between TLS data acquired in 2006, 2007 and 2009. A) SD comparison (+/- 5m) between 2006 and 2007 showing the rockfall that occurred in the WSW part of the rock cliff. B) SD comparison of the same period (+/- 0.3 m) highlighting uniform displacements of the entire central part of the slope. C) Displacements in the central part of the slope between 2007 and 2009.

5.4.10.2 Time span 2: Comparison of scans acquired the day before the main rockslide event (26.10.2009).

A complete TLS campaign of the unstable zone was conducted one day before the main rockslide event that completely changed the topography of the area. The area was scanned almost from the same position, in the morning (11.40 AM) and at the end of the afternoon (5.30 PM). SD analysis was applied to compare TLS datasets acquired in the morning (reference dataset) to scans acquired afternoon. This displacement analysis does not reveal significant differences, i.e. larger than the co-registration errors (1σ = 2.8 cm). The roto-translation matrix technique has been applied to the same compartments as in the 2006-2009 analysis. Two areas located in the lower part of the slope were assumed stable and were used as reference blocks (Figure 5.4-8). The calculated error for translation varies between 0.5 and 0.95 cm and average errors for the rotational components reach 0.05° for the toppling angle and 0.04° for the tilt angle.

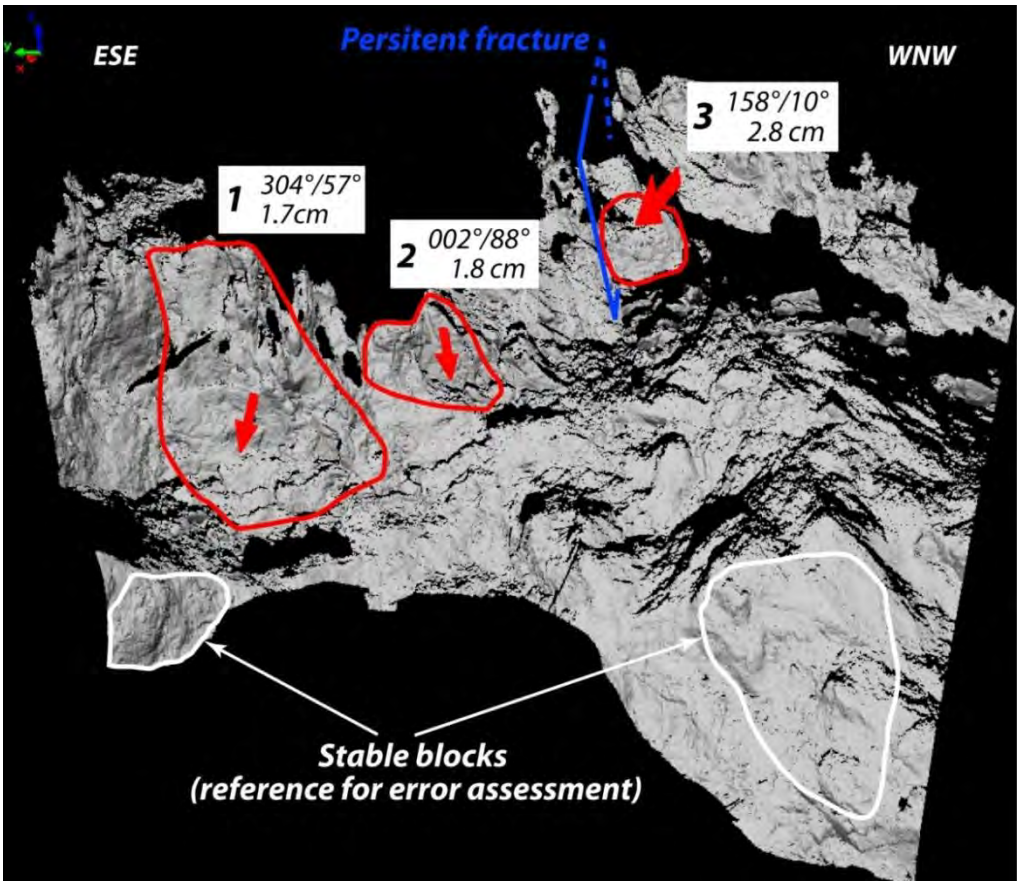

Figure 5.4-8: Results of roto-translation matrix technique applied to TLS dataset acquired the day before the main rock collapse. The time span between the successive scans is 5:15 hours.

The ENE portion of the slope, translation vectors have a similar length (1.7 and 1.8 cm for Block 1 and Block 2 respectively) and both blocks slide in the slope direction, but with different plunge angles. Block 3 located in the western part of the slope, shows a more important vector norm of about 2.9 cm with a direction plunging into the slope. Toppling and tilt angles are not significant with respect to the errors measured on the stable parts. The interpretation of the deformation is difficult because the measured movements are close to the limits of accuracy of the roto-translation matrix method. The measured translation displacements can be compared to ground-based radar measurements acquired the same day between 12.00 AM and 3.15 PM. The radar survey showed mean displacements of about 0.6-0.65 cm for the entire central part (Strozzi T., Pers. Comm., Figure 5.4-9). The agreement is good, considering that the displacement measured by the radar are related only to the line of sight and that the observation period (3:15 hours) is shorter than the time laps between the two TLS acquisition (5:15 hours). The differences in plunge angle of Blocks 1 and 2 could be related to the important fracturing and block individualization preceding the main collapse, which occurred 12 hours after the last TLS acquisition. During this phase, displacements of the rock mass could show different movement patterns. Block 3 shows a displacement direction pointing into the slope. These results are not surprising considering that block 3 is almost completely detached from the main rock cliff by a persistent fracture probably acting as strike-slip fault, allowing Block 3 to sag and to rotate. This corresponds, in the roto-translation matrix analysis, to a vector plunging in to the slope.

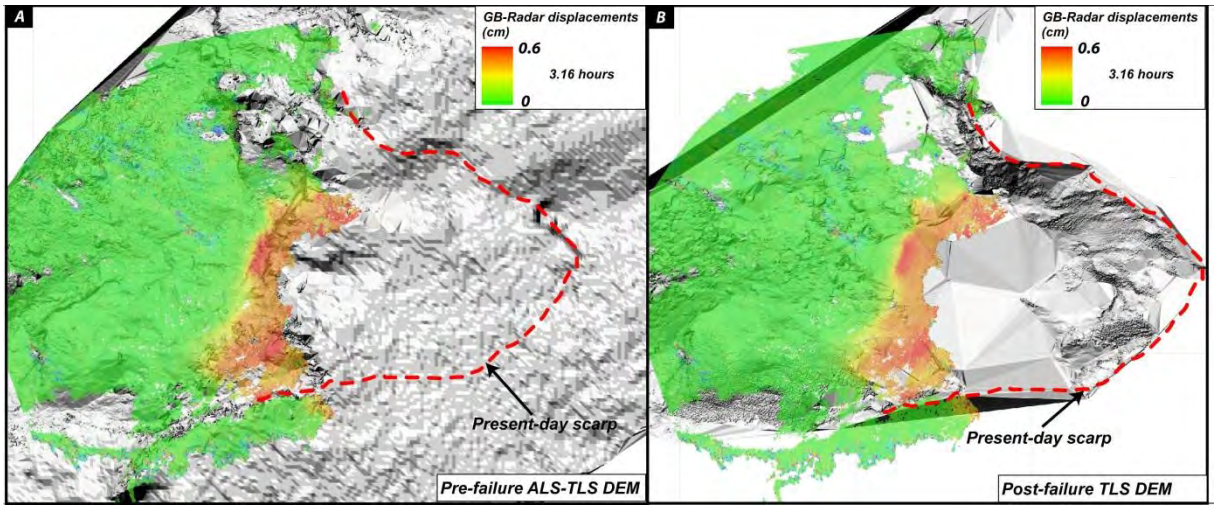

Figure 5.4-9: Displacements measured by ground–based real aperture radar one day before the main rockslide occurred the 26th October 2009 (data acquired by T. Strozzi). a) Ground-based radar displacements draped on shaded relief obtained by ALS and TLS data acquired before the rockslide event. b) Same displacements draped on shaded relief obtained by ALS data acquired after the rockslide event. Note the clear spatial correlation between the zones displaying the highest displacements and the location of the boundary of the collapsed area.

5.4.10.3 Time span 3: Comparison between scans taken after the main rockslide event (29.10.2009-28.10.2010).

After the main rockslide event, five TLS datasets were acquired in order to follow the slope evolution after the rockslide event. SD comparison of TLS data the entire period (29.10 2009 vs. 28.10.2010) indicates an important displacement of the upper portion of the debris cone (up to 5 m) toward the valley bottom (Figure 5.4-10).

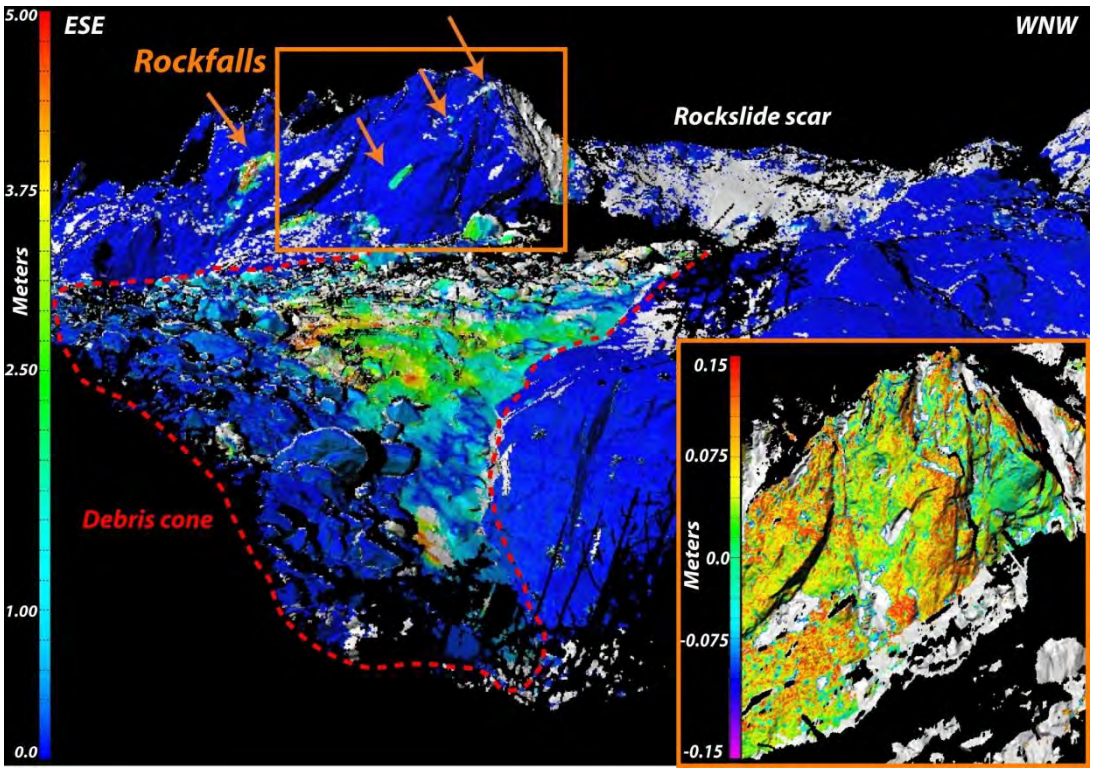

Figure 5.4-10: SD comparison between TLS data acquired in November 2009 and October 2010 showing the rockfall activity of the ENE sector of the slope. Zoom of the same area indicates post-failure displacements of about 10-15 cm of the most external block forming the rock mass.

The ENE part of the rockslide scar shows important differential movement of up to 15 cm (Figure 5.4-10). This indicates that new large instabilities could develop in the ENE part of the slope. In the same area, an important rockfall activity was observed all along the post failure period. The volume of the observed rockfalls progressively decreases from the early to the last TLS acquisition. In the first observation period (October - November 2009) detected rockfalls have a maximum volume of 5 m^3. In the following period the volumes decreases to maximum 1 m^3 for singular events.

5.4.11 CHARACTERIZATION OF THE OCTOBER 2009 ROCKSLIDE

The quantification of the failed volume was carried out by DEM differences derived from TLS point clouds. Results indicate a failed volume of 365'000 m^3 and the deposits are estimated to 430'000 m^3 (Figure 5.4-11). Differences between the two calculated volumes represent a swelling factor of 15-18%. The error on the volume calculation appear to be mainly related to the presence of shadow zones in the TLS datasets and to the interpolation of 3D point clouds and could be estimated as +/- 10% for both source and deposition volumes. The run-out length is about 316 m and the height difference is around 250 m correspond to a fahrböschung angle of 35-36°. Pre-failure movements observed in the frontal part of the instability were fairly uniform following a NW direction.

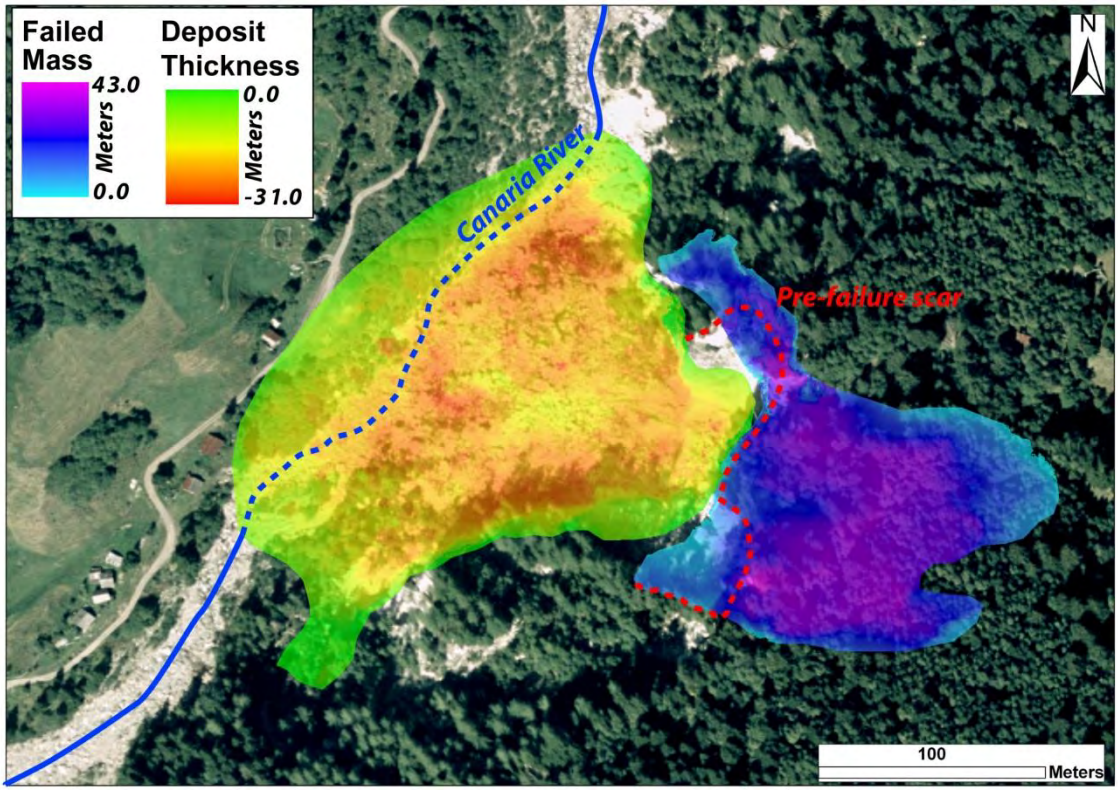

Figure 5.4-11: Map of deposit and failed mass thickness based on TLS DEM taken before and after the 27.10.2009 rockslide event. The DEM have a cell size of 20 cm.

Structural analysis indicates the possibility to have several wedges plunging in the same direction. Based on the structural setting, the movement may be explained by a retrogressive sliding/collapse driven by wedge intersection line S0/J4, S0/J7 or J6/J7 and by the progressive degradation of the gypsum, especially along the direction of the maximum discontinuity frequency. Based on the present-day scar morphology,

the rear release surface seems to be controlled by J1 and J3. The depth of the failure surface is controlled by the change of rock mass properties at the limit between weathered gypsum and fresh anhydrite. Based on borehole data located close to the rockslide area, the lithological change is located between 45 and 56 meters (Gassman et al., 1979). This depth corresponds quite well to the depth of the failure surface estimated by differences in DEM before and after the collapse (Figure 5.4-11). The topography of the surrounding area could also be pointed out as a potential predisposing factor for instabilities development. Above the main rock scarp, the topography is mainly concave allowing concentration of superficial and ground water behind the main rock face increasing pore pressure during rainfall. Identification of potential triggering factors is difficult to assess without disposing quantitative data about ground-water level. Based on evidences of other monitored instabilities in the area (Seno and Thüring, 2006) snow melting and rainfall associated to freeze and thaw cycles seem to be the main triggering factors. No seismic event has been registered before the event, so a potential triggering factor could be related to the precipitations occurring during the week before the landslide failure in combination with three days with minimal temperatures below zero before the rockslide.

5.4.12 CONCLUSIONS

The Val Canaria catchment shows an important slope activity that could be related to its complex geological settings and tectonic situation. Field evidences indicate different failure mechanisms in the two flanks of the valley. Local analyses based on periodic TLS monitoring allow creating a detailed geological model of the monitored area and an accurate description of pre-failure movements.

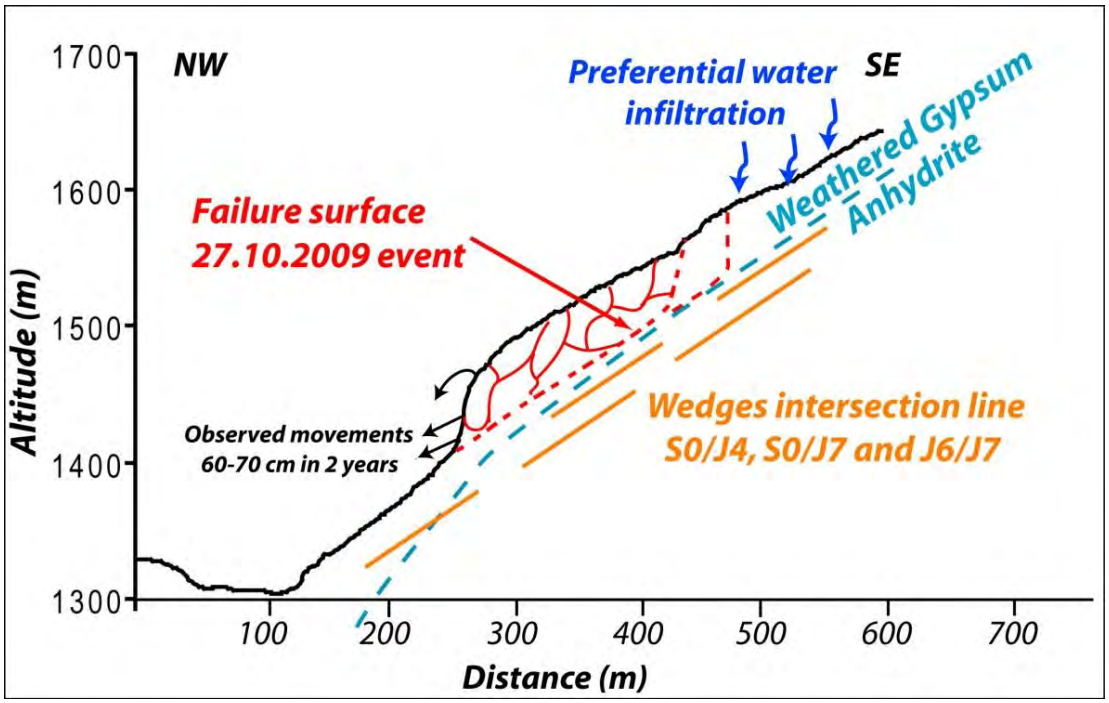

Figure 5.4-12: Schematic cross-section showing the structural and geological constraints on the 27.10.2009 rockslide. The failure surface depth is controlled by the changing of rock mass properties between gypsum and anhydrite.

The structural analysis based on TLS data indicated that discontinuity sets have an important influence on the main movement patterns, even in those lithologies that commonly do not exhibit a structurally

controlled failure mechanism. A detailed geometrical characterization of the 27.10.2009 rockslide was carried out based on TLS datasets acquired before and after the event. Coupling structural analysis and pre-failure movement, we proposed a possible failure mechanism corresponding to retrogressive sliding collapse driven by persistent wedge intersection lines and progressive decrease of the rock mass strength related to gypsum dissolution (Figure 5.4-11). Long-term displacements and continuous rockfall activity in the area is probably related with the Sackung affecting the entire area.

5.4.13 REFERENCES

Abellán, A., Jaboyedoff, M., Oppikofer, T., Vilaplana, J. M. 2009. Detection of millimetric deformation using a terrestrial laser scanner: experiment and application to a rockfall event, *Nat. Hazards Earth Syst. Sci.*, 9, 365-372.

Alberto, W., Giardino, M., Martinotti, G., Tiranti, D. 2008. Geomorphological hazards related to deep dissolution phenomena in the Western Italian Alps: Distribution, assessment and interaction with human activities, *Engineering Geology*, 99, 147-159.

Amadei, B., Savage, W.Z. 1989. Anisotropic Nature of Jointed Rock Mass Strength, *Journal of Engineering Mechanics*, 115, 525-542.

Antognini, M., Beffa, F., Valenti, G. 1996. Le glissement de Rutan dei Sassi, Val Canaria (Tessin, Suisse), *Bull. angew. Geologie*, 1, 1,55-64.

Baruffini, M, Ambrosi, C. 2010. A GIS-tool for risk assessment due to natural hazards in mountain regions. An exploratory study on an hypothetical event: the Val Canaria flood. Abstract Volume, *8th Swiss Geoscience Meeting*.

Bonnard, C. 2011. Technical and human aspects of historic rockslide dammed lakes and landslide dam breaches. In Natural and Artificial Rockslide Dams, Evans, S.G.; Hermanns, R.L.; Strom, A.; Scarascia-Mugnozza, G. (Eds.), *Lecture Notes in Earth Sciences*, 133, 101-122.

Brideau, M-A., Ming, Y., Stead, D. 2009.The role of tectonic damage and brittle rock fracture in the development of large rock slope failure, *Geomorphology*, 103, 30-49.

Chen, Y., Medioni, G., 1992. Object Modelling by Registration of Multiple Range Images, *Image and Vision Computing,* 10, 145–155.

Dramis, F., Sorriso-Valvo, M., 1994. Deep-seated gravitational slope deformations, related landslides and tectonics. Engineering Geology. 38, 231/243.

Eisbacher, G.H, Clauge, J.J. 1984. Destructive mass movements in high mountains: Hazard and management, Energy, Mines and Resources Canada (Ottawa).

Gassman, J., Gysel, M., Schnider, J.F. 1979. Anhydrit als wirtgestein für die endlangernung radioaktiver Abfälle in der Schweiz. *Technische Berich 12*, Nagra.

InnovMetric: PolyWorks: 3-D scanner and 3-D digitizer software from InnovMetric Software Inc., http://www.innovmetric.com/Manufacturing/home.aspx, access: February 10, 2011.

Jaboyedoff, M., Metzger, R., Oppikofer, T., Couture, R., Derron, M.H., Locat, J., Turmel, D. 2007. New insight techniques to analyze rock-slope relief using DEM and 3D-imaging clouds points : COLTOP-3D software. In: Eberhardt E, Stead D, Morrison T (ed*): Rock mechanics: Meeting Society's Challenges and Demands*, Taylor and Francis, 2:61-68

Lateltin, O. 1997. Prise en compte des dangers dus aux mouvements de terrain dans le cadre des activités de l'aménagement du territoire, Recommandations, OFEFP, 7.

Monserrat, O, Crosetto, M. 2008. Deformation measurement using terrestrial laser scanning data and least squares 3D surface matching, *ISPRS Journal of Photogrammetry and Remote Sensing*, 63, 142-154.

Oppikofer, T., Jaboyedoff M., Blikra L., Derron, M.-H, Metzger, R. 2009. Characterization and monitoring of the Åknes rockslide using terrestrial laser scanning, *Nat. Hazards Earth Syst. Sci.*, 9, 1003-1019.

Oppikofer, T., Jaboyedoff, M., Keusen, H.-R. 2008. Collapse at the eastern Eiger flank in the Swiss Alps, *Nature geosciences*, 1, 531-535.

Remondo, J., Bonachea, J., Cendrero, A. 2008. Quantitative landslide risk assessment and mapping on the basis of recent occurrences, *Geomorphology*, 94, 496–507.

Raetzo, H., Lateltin, O., Bollinger, D., Tripet, J. P. 2002. Hazard assessment in Switzerland – Code of practice for mass movements, *Bull. Eng. Geol. Env.*, 61, 263–268.

Rosser, N.J., Lim, N, Petley, D.N., Dunning, S., Allison, R.J., 2007. Patterns of precursory rockfall prior to slope failure, *Journal of Geophysical Research*, 112, F4.

Seno, S., Thüring, M., 2006: Large landslides in Ticino, Southern Switzerland: Geometry and kinematics, *Engineering Geology*, 83, 109-119.

Sturzenegger, M., Stead, D. 2009. Quantifying discontinuity orientation and persistence on high mountain rock slopes and large landslides using terrestrial remote sensing techniques. *Nat. Hazards Earth Syst. Sci.,* 9, 267-287.

Teza, G., Galgaro, A., Zaltron, N., Genevois, R. 2007. Terrestrial laser scanner to detect landslide displacement fields: a new approach, *Int. J. Remote Sens.*, 28, 3425–3446, 2007.

5.5 RISK MANAGEMENT OF ROCKFALL/ROCKSLIDE HAZARD BASED ON REMOTE SENSING TECHNIQUES: THE EXAMPLE OF ARVEL QUARRY (SWITZERLAND)

5.5.1 ABSTRACT

The Arvel quarry is located at the end of the Rhône valley (SW Switzerland) and is one of the most important producers of ballast and other construction materials in Switzerland. On the 12th December 2008, a rockslide of about 20'000 m^3 occurred in the upper part of the quarry inducing a partial interruption of mining operations. After this event, the stability of the entire quarry was analysed coupling classical field approaches, aerial and terrestrial laser scanner (ALS and TLS) analysis. Based on the updated structural configuration of the slope and detailed stability analyses, a new slope design concept was proposed to reduce the risk of new potential instabilities. A monitoring system was installed based on continuous Ground-Based Radar and periodic TLS measurements. After fourteen months of movement's observation, early warning systems as well as a new slope design concept were proposed to reach tolerable risk level allowing the partial reopening of the mining activities.

5.5.2 RÉSUMÉ

La carrière d'Arvel, située au bout du Lac Léman près de Villeneuve (Suisse), représente l'une des carrières de roche dures les plus importantes de Suisse. Dans le nuit du 12 décembre 2008, 20'000 m^3 de calcaire se sont éboulés dans la partie supérieure de la zone d'excavation principale. Suite à cet éboulement les travaux d'extraction et de minage ont été immédiatement arrêtés. Une analyse préliminaire de la zone supérieure de la carrière a montré la présence d'une autre instabilité potentielle avec des caractéristiques très similaires. Sur la base d'une analyse détaillée des caractéristiques structurales et des mécanismes de ruptures qui ont engendré l'éboulement de décembre 2009, la stabilité du dièdre potentiellement instable a été évaluée. L'analyse structurale a montré que la stabilité de cette zone est essentiellement contrôlée par des ruptures de dièdre par deux familles de failles tectoniques localement très persistantes. Sur la base de l'analyse structurale du massif et d'analyses de stabilité, une nouvelle conception des fronts d'excavation a pu être proposée. Un système de surveillance basé sur des acquisitions périodiques au Lidar terrestre ainsi que par un suivi en continu par radar terrestre a été mis en place pour suivre l'évolution des instabilités détectées. L'analyse des déplacements a pu mettre en évidence une forte activité de chute de blocs principalement associée aux cycles de gel et dégel. D'autre part, aucun mouvement généralisé n'a pu être observé pendant les 14 mois de suivi. Après une réévaluation des risques potentiels et la mise en place d'un système d'alarme, les activités ont pu être partiellement reprises dans la carrière.

5.5.3 INTRODUCTION

The Arvel quarry is located in SW part of Switzerland close to the eastern side of the Geneva Lake (Figure 5.5-1). The rock forming the slope above Villeneuve has been extensively exploited as construction material since the Middle Ages. The site of the actual quarry has been industrially exploited since 1905. The main rock exploited in the quarry is a siliceous limestone that represents a good material to produce ballast for railway construction. The annual production is about 500'000 tonnes. The site configuration, especially the steep and rough topography, represents a real challenge in quarry design. The Arvel quarry has experienced several rockslides and rockfall events during the last century. The most important one occurred on March 13th 1922, when a rockslide of about 600'000 m^3 destroyed all the installation located below the cliff. This rockslide also created an important deformation of the alluvial sediments on the Rhone plain (Choffat, 1929; Jaboyedoff 2003; Crosta et al., 2009). More recently, on December 12th 2008, a rockslide of about 20'000 m^3 occurred on the upper part of the quarry. The presence of a potential unstable rock spur in the same area, presenting the same characteristics, induces a temporary closure of the quarry activity.

In this paper, we illustrate the application of remote sensing techniques, in particular Terrestrial Laser Scanner (TLS) for slope monitoring but also as an important base to produce a reliable geotechnical model. In the first part, we analyse the main structural and lithological characteristics of the study area in order to define homogenous structural domains and the related failure mechanisms. Then, we present a detailed characterization of the rockslide of December 2008 and the potential unstable spur that is still present at the top of the quarry. In the last part, we describe the preliminary results of the monitoring system that has been installed and the design of the early warning system. Based on the new available information, a risk management procedure is proposed to permit the partial reopening of the quarry.

5.5.4 GEOLOGICAL SETTING

The Arvel quarry is located on the Préalpes Medianes Nappe. The rocks forming Les Monts d'Arvel belong to the normal limb of a kilometric-scale anticline (Tinière Anticline). The lower part of the slope is formed of an intercalation of weak marls and crinoid-rich limestone layers. The upper portion of the quarry representing from an economic point of view, the most interesting lithology, is composed by a regular intercalation of marls layers and thick (1-1.5 m) fine-grained siliceous limestone layers. Bedding planes plunge regularly 40°-50° into the slope. Two series of major tectonic faults (NNW-SSE and NE-SW) cross the entire area and display clear slickensided surfaces and a localized degradation of the rock mass quality. Tectonic movements associated to this fault are normal displaying frequently a dextral strike-slip component. The hydrogeological system is complex involving both karst and fracture permeability. Superficial drainage and seepage between rainfall periods are almost absent (Figure 5.5-1).

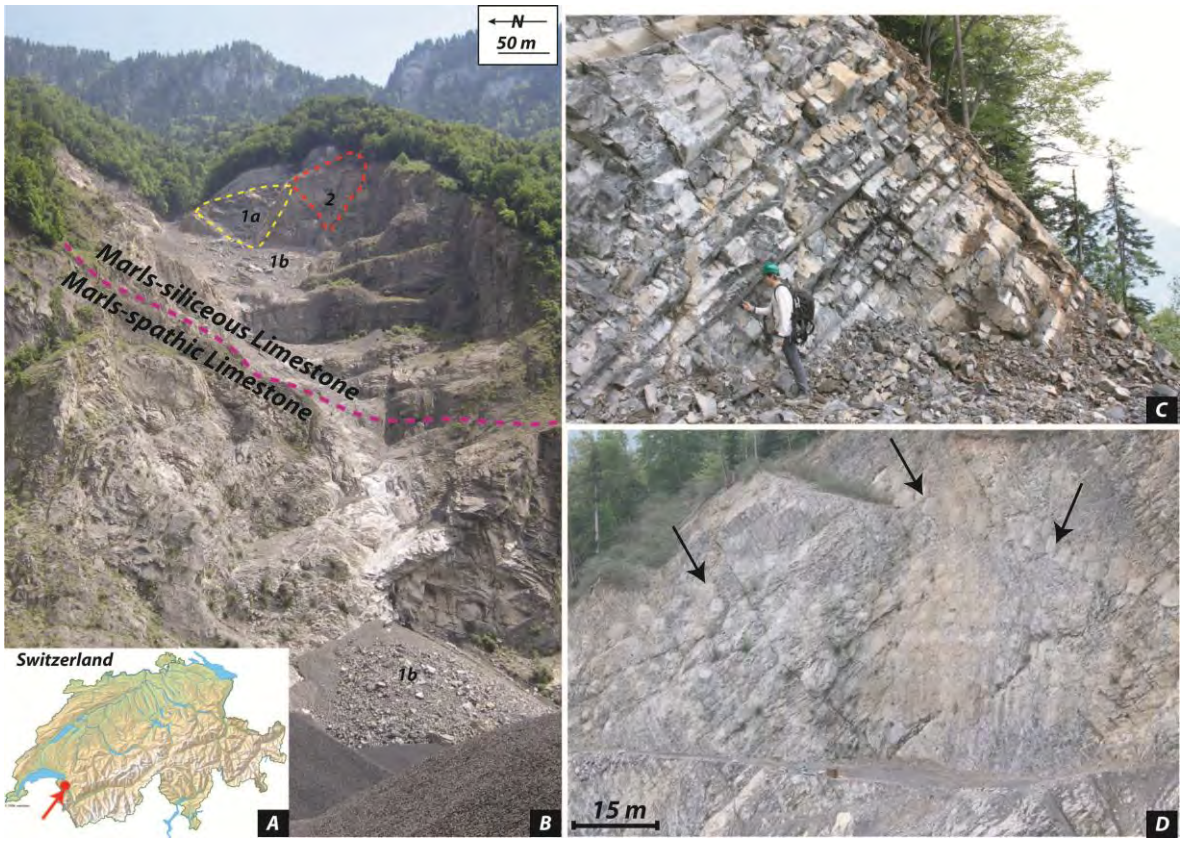

Figure 5.5-1: Overview and general setting of the Arvel quarry. a) Geographical location. a) View from the bottom of the main quarry excavation. Numbers on the picture correspond to the 2008 rockslide scar (1a) to the rockslide deposits (1b) and to the main potential unstable area (2). c) Rock mass characteristics in the upper portion of the quarry, showing regular intercalation of marls and siliceous limestone. D) View of upper bench face showing the important rock bolting necessary to stabilize the cliff (black arrows).

5.5.5 STRUCTURAL ANALYSIS AND ROCK MASS CHARACTERISTICS

5.5.5.1 Characterization of discontinuity sets

In this study, we combine a classical method of geological field survey, (manual compass measurement), with a semi-automated extraction of discontinuity sets by means of an aerial High Resolution DEM (HRDEM) and locally completed by TLS data. Structural analyses were performed using the COLTOP 3D software (Jaboyedoff et al., 2007; Pedrazzini et al., 2011). This software allows the representation of a DEM or 3D point clouds by a 3D shaded relief that displays the orientation of the slopes by means of a Schmidt – Lambert projection with one colour for a given dip and dip direction. It results in a coloured shaded relief map that combines slope and slope aspect in a unique representation coded by the Hue-Saturation-Intensity system (HSI). The main advantage of using the HRDEM and TLS based analyses is that the time spent in the field survey could be substantially reduced and investigations could be concentrated in the most representative/accessible areas. Recommendation and potential bias related to the remote sensing approaches can be found in Sturzenegger and Stead (2009).

COLTOP 3D analyses have been carried out on both 0.5 meters cell size DEM derived from helicopter-based LIDAR and TLS point clouds (Figure 5.5-2a). Thirteen discontinuity sets have been identified within five different structural domains (Figure 5.5-2b). The detected structural domains (SD) are mainly divided from the others by major faults crossing the entire area. A clear example is shown by the main gully

passing in the middle of the exploited area which follows a regional fault and creates an important distinction between the structural domains on the two side of the quarry. The slightly differences in term of discontinuity orientations between the upper and the lower portion of the quarry could be related to the lithological variations. Punctual field observations were performed to characterize the geometrical (spacing, trace length and roughness) and geomechanical characteristics (infilling materials and joint compressive strength) of the detected discontinuity sets (Pedrazzini et al., 2010 for details).

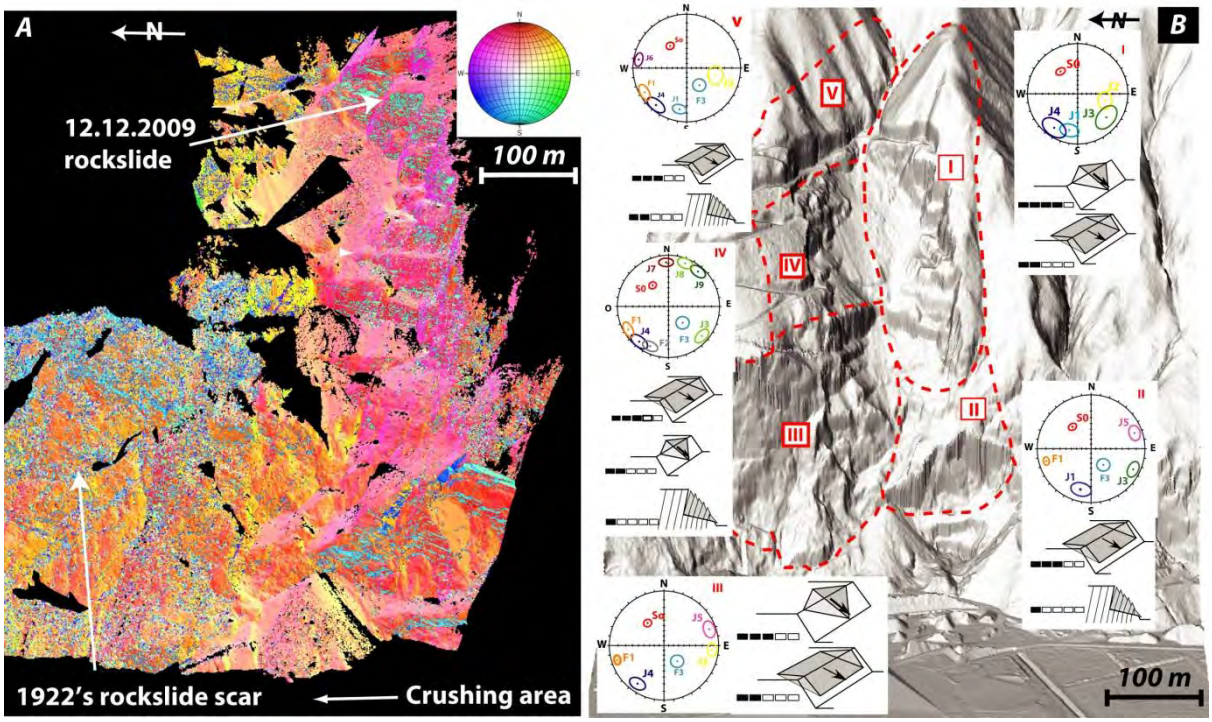

Figure 5.5-2: Structural analysis of the main quarry area based on COLTOP 3D software analyses on TLS point cloud. a) COLTOP 3D colour view of the entire quarry showing the orientations of the bench faces and the related discontinuity sets. b) Overview of the structural domains, potential failure mechanisms and the failure susceptibility based on COLTOP3D and Matterrocking analyses.

5.5.5.2 Rock mass quality

The Geological Strength Index (Hoek and Brown 1997; Marinos et al. 2005) was applied to describe and quantify the rock mass quality for the different parts of the quarry. Estimated GSI values in the study area vary from 45 to 60, corresponding to a good to fair rock mass quality. However, rock mass condition in quarry is quite variable and their spatial distribution is correlated to the detected structural domains (Pedrazzini et al., 2010). Local decrease of the rock mass quality is generally observed within 2-5 meters to the main regional faults particularly in term of weathering conditions (Weathering Grade III). This could be related to water circulation and previous tectonics movements. Intact uniaxial compressive strength has been estimated using manual index tests (ISRM, 1978) and Schmidt hammer test. It varies from 50 to 75 MPa for marls layers and from 100 to 150 MPa for siliceous and spathic limestone layers. As suggested by Brideau et al. (2009), the observed GSI values correspond to heavily jointed rock masses where slope failures are mainly structurally-controlled. This observation justifies the stability analyses proposed in the next sections where the discontinuity sets characteristics are explicitly integrate.

5.5.6 STABILITY ANALYSIS AT THE QUARRY SCALE

During feasibility and operational stages, stability analyses at the quarry scale are a very important step to point out the areas where potential instabilities could occur and to have a first estimation of the potential mobilized volume (Read and Stacey 2009). Here, we associated advantages from TLS and ALS data resolution to classical limit equilibrium stability analysis method to produce a fast and reliable analysis of the entire quarry, in term of rockslide and rockfall susceptibility. This allows prioritization of areas to where slope design reassessment is needed.

5.5.6.1 Spatial kinematic analysis and susceptibility index

Kinematic analyses are widely used as slope stability test for simple structurally controlled failure modes such as planar sliding, wedge and toppling. It takes into consideration the orientation of the discontinuities, the slope orientation and the assumed effective friction angle along the discontinuity surfaces. The main limitation of classical stereographic techniques is related to the choice of the main and "relevant" topographical slope orientation especially for complex situations (Brideau et al., 2010).

The Matterocking software (Jaboyedoff et al., 2004, available online at www.crealp.ch) compares planes or wedge intersection vector orientations with the topographic surfaces from a digital elevation model (DEM) to detect the areas where discontinuity sets daylight. This technique coupled with a GIS visualisation is very useful to analyse rugged slope topography. It allows a first screening of bench orientations susceptible to fail. The input parameters are orientation, spacing and trace length of discontinuity sets.

Main limitation of this approach is the impossibility to introduce the natural variability of the discontinuity sets in the analysis. DEM-based kinematic analyses were performed for all discontinuity combinations identified in the different structural domains. An example of the produced map is presented in Figure 5.5-3a. In order to provide a susceptibility level based on the two sliding mechanisms, the number of potential planar slides, as well as the number of potential sliding wedges were summed and normalized, for each structural domains separately, to a number between 0 and 1 by dividing the cell value by the maximal value (Figure 5.5-3b). The produced susceptibility map has been compared with the most active areas detected and to historical and recent zones of instabilities of the quarry. The comparison shows a very good agreement with field analysis validating the proposed approach. In particular, the slope orientations parallel to the slope of the 1922 rockslide and those benches located in the SE portion of the quarry show an important susceptibility of failure.

5.5.6.2 Limit equilibrium analysis

The susceptibility map reported in Figure 5.5-3 displays detailed qualitative information about the location of potential unstable areas. This kind of data is very useful especially at feasibility level. Stability problem concerning an active quarry like Arvel, also needs semi-quantitative information about the factor of safety and the expected unstable volumes for different bench orientations. For this reason, limit equilibrium code Swedge (Rocscience 2008) was used to investigate the volume and the stability of potential rock wedges formed on bench slopes. The combination analysis implemented in Swedge uses a user-defined list of discontinuities to calculate the factor of safety for valid wedge intersections for a given bench face.

Results obtained by the limit equilibrium analysis are reported in Table 5.5-1. It is interesting to note that SD 1 represents the most problematic zone as it is characterized by most important probability of failure and the largest potential unstable volumes. These results are in agreement with GIS-based susceptibility map and field observations, indicating a very useful complementarity of the two presented methods. SD 2 presents also an important probability of failure. However, in term of risk management, it does not represent a major issue, because the potential unstable volumes are relative small and easily manageable.

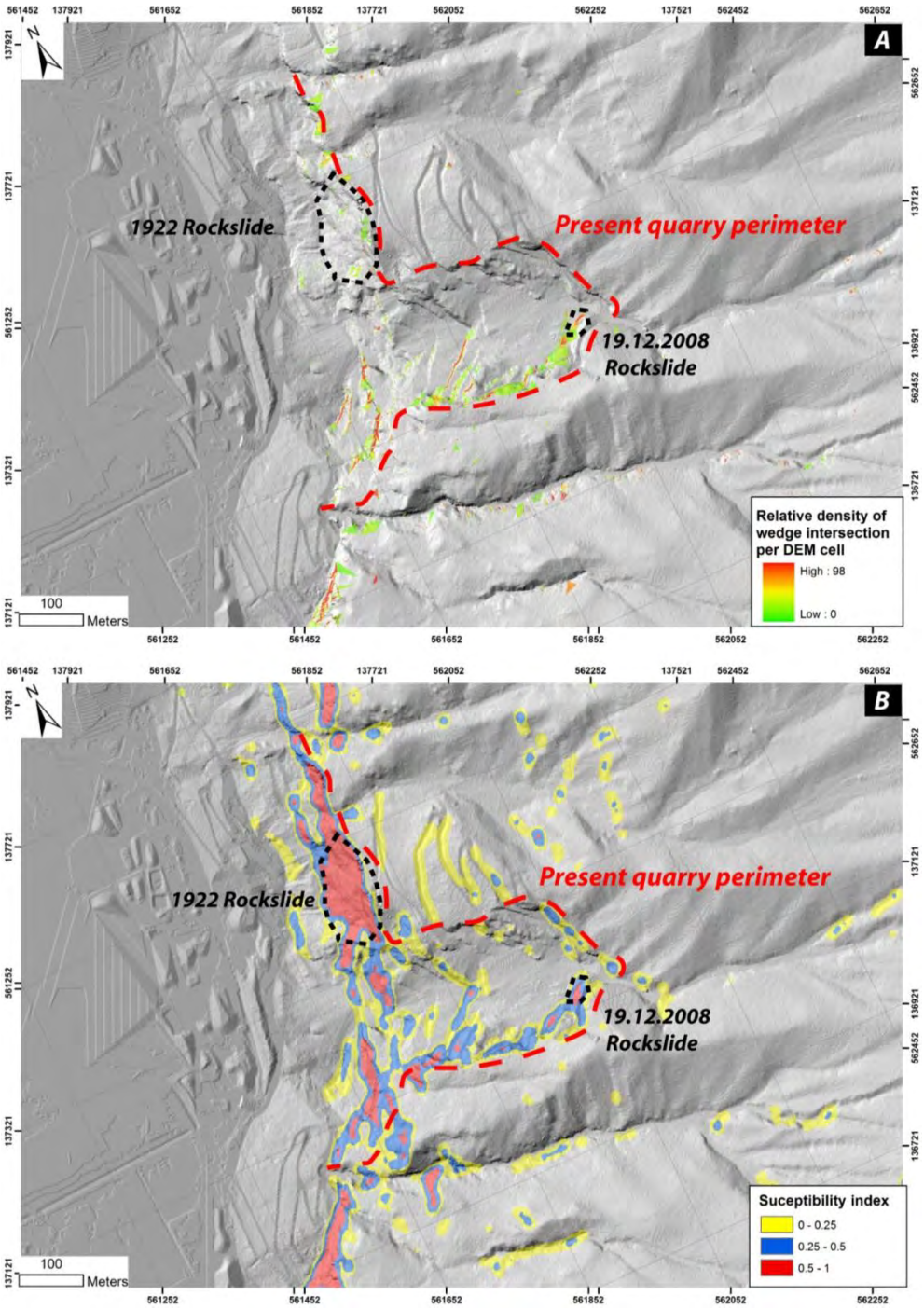

Figure 5.5-3 A) Example of kinematic analysis obtained for wedge sliding using Matterrocking software. B) Final failure susceptibility obtained by summing and normalizing the number of planar and wedge for each DEM cell, (0-0.15 = low susceptibility, 0.25-0.5 = moderate susceptibility, 0.5-1 = high susceptibility). The orientation and the discontinuity sets detected on the scar of the 1922 rockslide clearly pointed out as the highest susceptibility area indicating that potential instabilities could still occur in this area.

Table 5.5-1: Combination analysis computation obtained for different structural domain and main bench configurations.

Structural Domain	***Assumed slope surface (orientation and high)***	***Valid wedges (% of possible combinations)***	***Unstable wedges (% of valid wedges)***	***Max. wedge volume with FS<1 (m^3)***	***Probability of failure***
SD 1	*315/70 50 m*	*269440 (55)*	*138960 (51)*	*11'700*	*28%*
SD 2	*315/70 50 m*	*307730 (43)*	*110617 (35)*	*3'300*	*15%*
SD 3	*270/70 50m*	*230997 (32)*	*40499 (18)*	*4'500*	*6%*
SD 3	*230/70 35m*	*202913(28)*	*25777 (12)*	*5'500*	*3%*
SD 4	*230/70 35m*	*170049 (26)*	*42338 (25)*	*5'800*	*6%*
SD 4	*250/70 35m*	*346413 (53)*	*50395 (15)*	*8'500*	*5%*
SD 5	*230/70 35m*	*143048 (20)*	*9997 (7)*	*3'500*	*1.5%*
SD 5	*250/70 35m*	*147990 (20)*	*16177 (11)*	*1'700*	*2.5%*

5.5.7 ROCK FALL HAZARD

Small rockfalls (< $1m^3$) could have a great impact on the safety of the mine workers and it could induce important economic losses (Read and Stacey, 2009). Release zones are not often controlled by a simple failure mechanism but are mainly associated, in open pit environment, to poor blasting/scaling properties (Read and Stacey, 2009). However, relationship between structural setting and benches orientation could also have an important impact on small rockfall development. In particular, when the direction of maximum fracture density is perpendicular to the bench face, fragmentation destabilization and bench retreat increase. This situation can frequently increase the local rockfall susceptibility.

In order to identify the areas with high rockfall susceptibility, we computed the discontinuity frequency in all directions of space and in each structural domain, by using the equation proposed by Hudson and Priest's (1983) and implemented for stereographic visualization by Jaboyedoff et al. (1995). Zones where maximal frequency direction is perpendicular to the slope face orientation were extracted and visualized in GIS environment (Figure 5.5-4). This information, combined with other predisposing factors, (e.g. benches slope, proximity of large faults, rock mass and blasting quality) and structural-based susceptibility map allow a better identification of areas with important rockfall susceptibility.

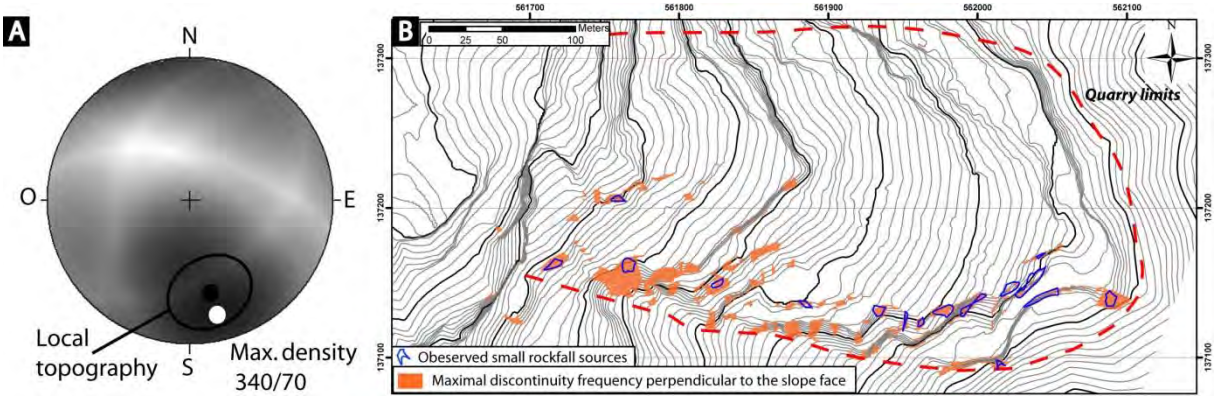

Figure 5.5-4: Frequency density calculation obtained for structural domain I. A) Comparison between maximal discontinuity frequency direction and local topography orientation. B) Spatial visualization of areas where maximal discontinuity density is perpendicular to the slope faces creating preferential rockfall activity. Blue zones correspond to the observed rockfall production areas.

5.5.8 DETAILED CHARACTERIZATION OF MAJOR INSTABILITIES

5.5.8.1 Back-analysis of the 12th December 2008 event

During the night between the 11th and the 12th of December 2008 in the upper portion of the quarry, a large rockslide of 20'000 m^3 occurred and destroyed two borehole machines (Figure 5.5-5a and b). This rockslide was investigated in detail to obtain precious information about the failure mechanism and the potential triggering factors. Kinematic analyses conducted on TLS point clouds by using COLTOP3D data, allowed the identification of a wedge failure involving wedges formed by the intersection between discontinuity sets J1^J2 and J2^J4. Field observations of the 2008's rockslide scar indicate that wedge formed by J2^J4 is less important in term of large slope stability due to the very low persistence of discontinuity set J4. The large wedge failure is mainly driven by the intersection of discontinuity sets J1^J2.

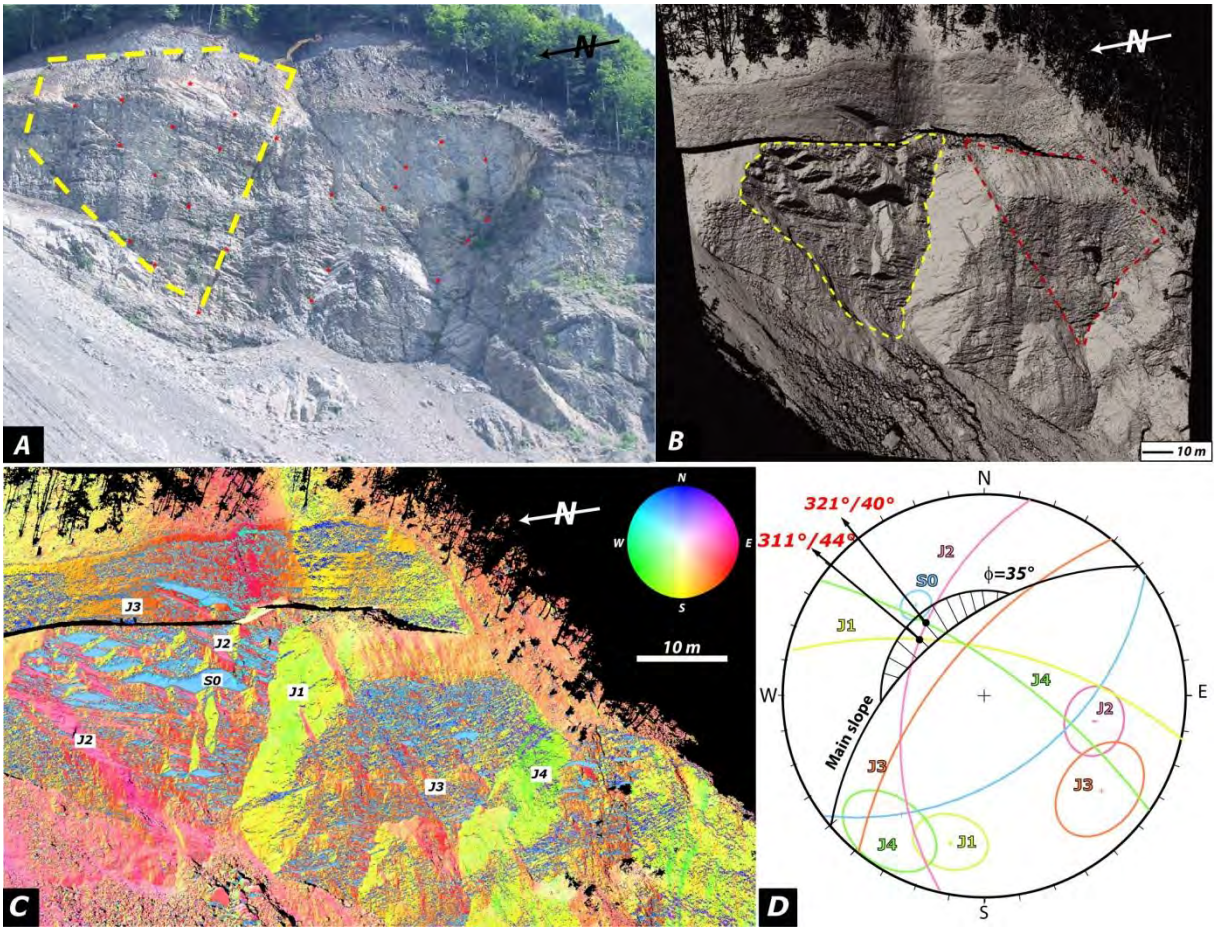

Figure 5.5-5: Characterization of the rockslide that occurred on 12th December 2008. A) View of the upper portion of the structural domain I before the rockslide event. Red dots correspond to old total station targets. B) TLS point cloud acquired after the rockslide event showing the rockslide scar and a potential unstable wedge with similar characteristics (dashed red line). C) COLTO3D view of TLS points clouds showing the main discontinuity sets delimiting rockslide scar. D) Kinematic analysis showing the possibility of wedge sliding by intersection of discontinuity sets J1^J2 and J2^J4.

A limit equilibrium back-analysis of the 2008 rockslide was also carried out in order to confirm (form a mechanical point of view) the most critical wedge and to estimate the apparent friction angle and the apparent cohesion along the failed wedge. Combination analyses performed using SWEDGE® confirm the structural observations indicating that the only small potential unstable wedges (1-1'000 m^3) could be

created by intersection of discontinuities J2^J4. In the other hand, the aforementioned confirm that larger wedges (> 1'000 m^3) are controlled by intersection of discontinuity sets J1^J2. Failure conditions (FS=1) are reached with an apparent friction angle of about 35°-38° and a residual cohesion of the infilling material of about 10-20 KPa. A preliminary 2D distinct element model (UDEC Itasca 2004) was also conducted to better characterize the failure mechanism (Pedrazzini et al., 2010). To simplify the model, only the bedding planes and the wedge intersection line have been introduced. The joint behaviour has been modelled using the strain softening model in order to account the effect of the silty-shale infilling of the discontinuities.

The general failure mode can be described as a wedge-topple mechanism (Jaboyedoff et al., 2009). Results show that the bedding planes act as an active toppling surface only in the upper part of the profile. In lower part of the profile, the failure is controlled by sliding along the wedge intersection line (Figure 5.5-6). Potential triggering factors of the 2008 rockslide are probably related to the important precipitations (snow and rainfalls) that had occurred the days before the rockslide event, coupled to the fast changes in temperature (freeze and thaw cycles) that had probably influenced the water pressure along fractures.

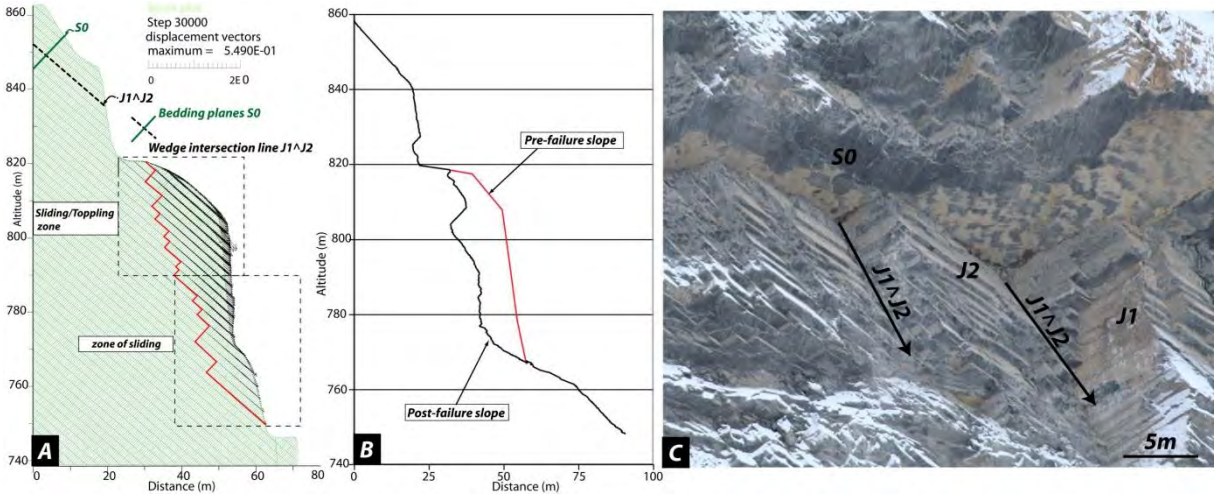

Figure 5.5-6: a) UDEC back-analysis of the failure mechanism indicating a topple-sliding failure mode in the upper part of the cliff and sliding on wedge intersection line in the lower portion of the cliff (modified from Pedrazzini et al., 2010). b) Cross-section on the failure scar extracted from TLS confirming the modelling results and displaying the formation of a step-like failure surface. c) Detail of the rockslide scar displaying the formation of several small wedges and outlining the influence of trace length and spacing of two discontinuities J1 and J2 on the final shape.

5.5.8.2 Comparison between remote sensing and in-situ analyses

In order to validate the structural analysis based on TLS point clouds and to define the continuity of structures in depth, three drill holes of about 60 m depth have been implemented close to the rockslide scar. Optical televiewer technique (Williams and Johnson, 2004) was applied to determine the orientation of the main structures. This technique provides a continuous and orientated 3D view of the drill hole allowing a precise detection and characterization of discontinuity planes. RQD (Deere, 1978) and visual rock mass quality investigation could also be carried out within the same borehole. Figure 5.5-7 shows the results of the televiewer analyses compared to COLTOP3D analysis. Results indicate the good agreement between surface and drill-hole measurement and show a homogenous and constant structural setting also

in depth. Low RQD values observed along the boreholes seem to be correlated to persistent faults defining the external limits of the 2008 rockslide.

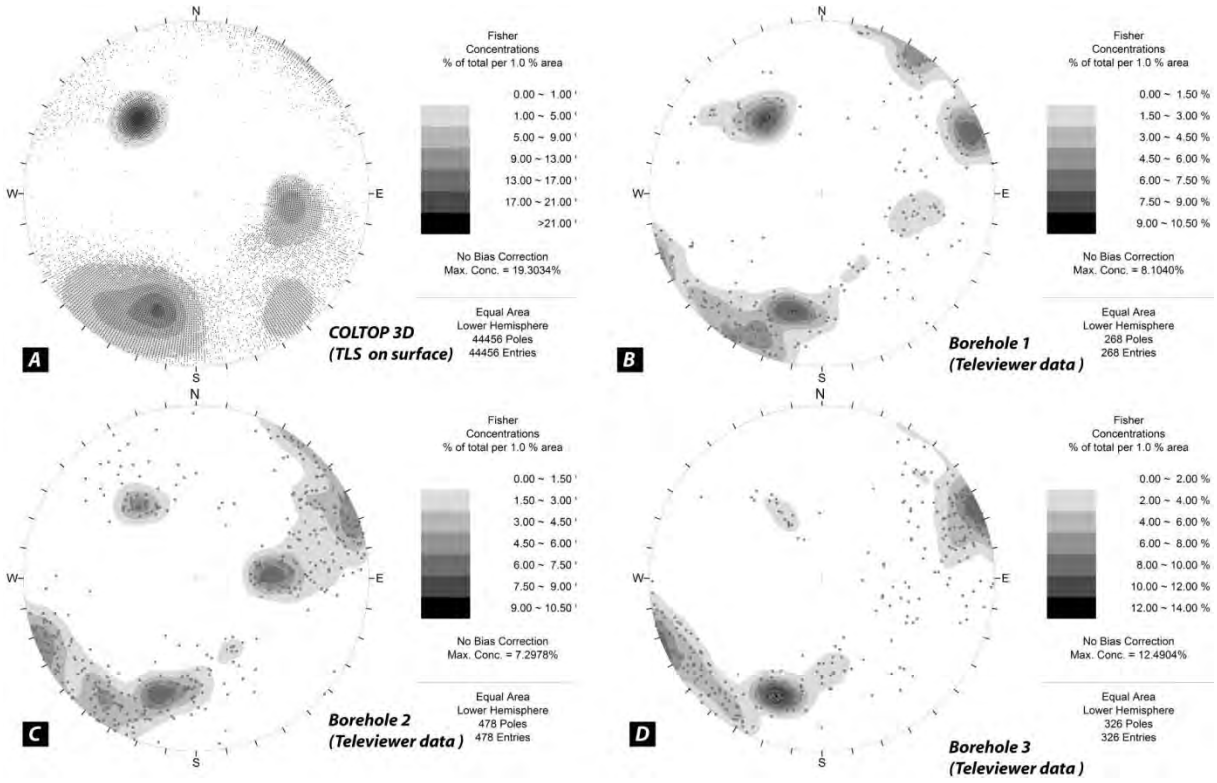

Figure 5.5-7: Stereonet of discontinuities detected in structural domain I. b) Discontinuities extracted by COLTOP3D analysis on TLS point clouds b), c) and d) Discontinuity sets identified by optical televiewer technique in three boreholes drilled close to the potential unstable wedge.

5.5.8.3 Potential instabilities

A detailed database of the different instabilities detected both by field and by spatial kinematics analysis has been created for the entire quarry in order to set up a monitoring program. More than fifteen potential unstable areas are detected in the different structural domains. Potential unstable volumes vary between few cubic meters to more than 10,000 m^3. In particular, an important potential unstable wedge was identified 50 metres south of the 2008 rockslide scar. Geomechanical parameters deduced from back-analyses were used to assess the present-day stability of potential wedge (Figure 5.5-5b). Limit equilibrium analysis were carried out using Swedge (Rocscience®, 2008) software. Deterministic approach indicates a factor of safety of 1.2-1.3 in dry conditions. Probabilistic analysis was realized assuming a normal distribution for the geomechanical and geometrical parameters and using the Fisher distribution for the discontinuity sets. Results show that in dry conditions the probability equals 10%. The influence of water pressure was also tested by a sensitive analysis. It shows that after 30% of joint filling the safety factor decreases exponentially. Volume calculation based on TLS point clouds analysis (details on methods in Longchamp et al., 2010 or in Pedrazzini et al., 2011) gives a potential unstable volume of about 21'000 m^3.

5.5.9 MONITORING SYSTEM

As field and modelling results indicating a high rockfall and rockslide susceptibility a monitoring system was built on. Most monitoring efforts are focused on the structural domain I where most important instabilities have been detected (see Figure 5.5-5). The monitoring system is based on continuous Ground-Based Radar coupled with repeated TLS acquisitions.

5.5.9.1 Terrestrial laser scanner

Between January 2009 and June 2009, six TLS acquisition have been carried out in the upper part of the quarry in order to detect the potential movements of the area. TLS datasets acquired during the same campaign were merged in a single file using a common coordinate system using PolyWorks® software (InnovMetric 2009). Details on TLS data treatment for movements' analysis could be found in Oppikofer et al. (2009) and in Abellan et al. (2009).

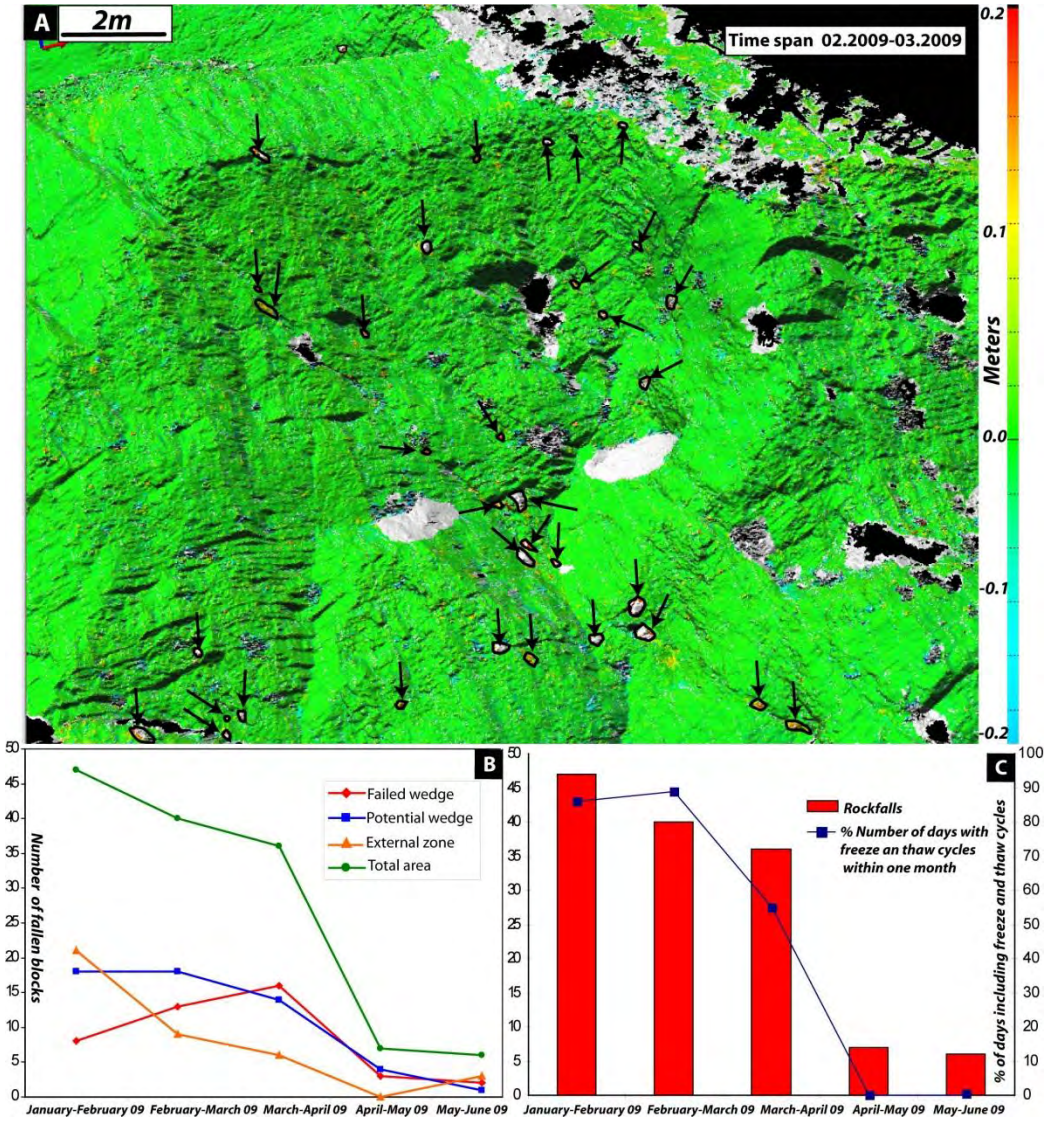

Figure 5.5-8: a) Spatial distribution of the rockfall activity between February and March 2009 on the potential unstable wedge located in structural domain I. Note the alignment of the rockfall along persistent fractures defining the limits of the unstable wedge. b) Number of rockfalls detected between the different TLS acquisitions. c) Correlation between the rockfall activity and the presence of daily freeze and thaw cycles.

The comparison of the different datasets indicates that the entire area is not affected by movements (at least larger than 1-2 cm). However, the comparison of TLS point cloud underlines an important rock fall activity. In the first months of 2009, more than 45 distinct rockfalls have been pointed out along the potential unstable area. The main active zone, where most of rockfall are concentred, corresponds to the northern external limits of the instability (persistent fracture parallel to J2 discontinuity sets). The general rockfall activity drastically decreases after April (Figure 5.5-8a). The attenuation of the rockfall activity is probably related to the changing in weather conditions after March. Indeed, a clear correlation between periods presenting freeze and thaw cycles and the number of rockfalls can be highlighted (Figure 5.5-8b).

5.5.9.2 Ground based radar

In order to provide a continuous monitoring of potential instabilities in structural domain I as well as in the entire the quarry, a Ground Based Synthetic Aperture Radar (GB-DInSAR) has been permanently installed at the bottom of the slope since 2009. Measurements were conducted by Ellegi Srl (Milano, Italy) using their GB-DInSAR system LiSA. Two subsequent SAR images can be combined to create an interferogram by extracting the phase difference between the two acquisitions (Tarchi et al., 2003). Displacements are then calculated between the two SAR images based on the phase differences and the wavelength of the signal. For LISA system the time span between two successive images is 3.5 minutes. The device accuracy, indicated by the manufacturer, is about 1 millimeter. Resolution is dependent on the acquisition distance and corresponds to 1.1 meters at a distance of 250 meters. More detail on this methodology can be found in Leva et al. (2003) and in Tarchi et al. (2003).

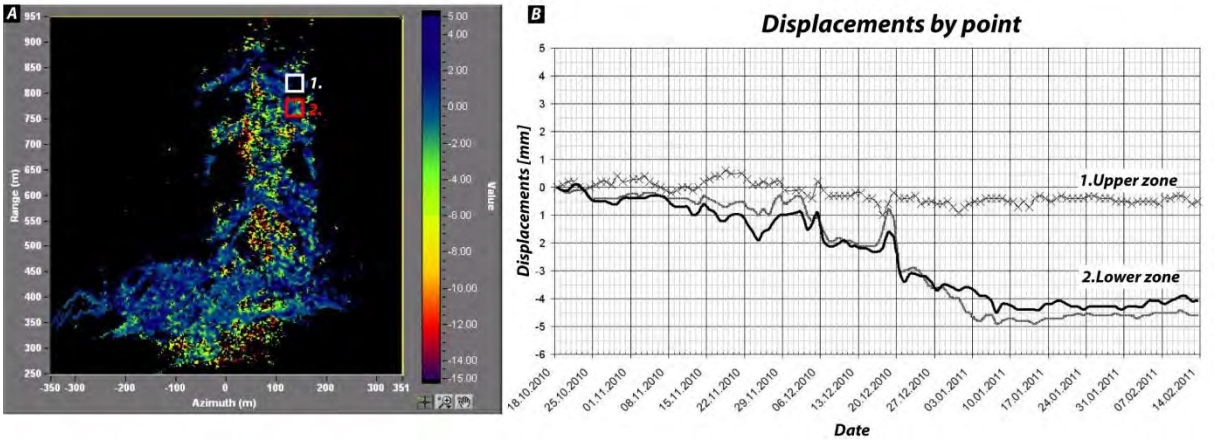

Figure 5.5-9: A) Cumulated displacements map produced using 24 hours averaged images between 18.10.2010 and 14.02.2011 (LISA system). B) History of movements for two selected points located in structural domain I. Small movements, concentred in the lower portion of the potential instability, could be highlighted, indicating small but continuous pre-failure movements.

GB-DInSAR has been positioned at the bottom of the slope to obtain a complete vision of the main quarry. First measurements confirm that most important slope activity in term of displacement and rockfall is concentred in structural domains I and III. In particular, several rockfalls with a volume varying between 3 and 30 m^3 have been identified based on millimetric pre-failure movements and a sudden pixel decorrelation. For larger rockfalls, pre-failure movements of about 3-4 mm were observed since one hour before the event. For the potential unstable wedge located in the structural domain I no movements was

detected since December 2010, then small movements of about 3-4 mm appear in the lower portion of the wedge (Figure 5.5-9). These movements were probably triggered by the important precipitation and temperature variations (freeze /thaw cycles) observed during this month. Similar climatic conditions were observed before the 2009 rockslide, suggesting an important correlation between the slope stability and the climatic factors, especially the coupled effect of rainfall and rapid temperature changes.

5.5.10 RISK MANAGEMENT AND EARLY WARNING SYSTEM IMPLEMENTATION

In order to permit the re-opening of the entire quarry with a tolerable risk level, passive and active mitigation measures have been proposed. Active measures consist of the construction of a rockfall barrier and of a new slope design for structural domain I. Passive measure involve the creation of an early warning system and of a connected emergency response procedure.

5.5.10.1 Active mitigation measures

Trajectography modelling shows an important lack of protection structures for installation located at the bottom of the slope. Trajectography modelling (obtained for blocks of 50 m^3, corresponding to the maximum block size of previous rockfalls) show that the actual barriers are not correctly designed to retain potential rockfall and rockslide falling from the upper part of the quarry (Figure 5.5-10a). In particular, installations located in the northern portion are not protected with the present–day barrier configuration. The calculated travel-time for a rockfall between the source and the maximal run-out distance indicate a very short response time (16-19s) that is not considered sufficient for workers safety (Figure 5.5-10). For this reasons, two additional geofabric barriers were designed to increase the safety of the crushing installation and of the material deposit. Pedestrian and vehicle accesses were also modified, in particular in the crushing installation area, to decrease the exposure to rockfall and to take advantage of the protection of the new and present-day barriers. Trajectography analysis indicates also that the debris cone created at the bottom of the slope after the 2008 rockslide event increased the potential rockfall propagation. In order to reduce the potential rockfalls run-out, re-profiling of the debris cone was proposed and replaced by a flat energy-absorbing area.

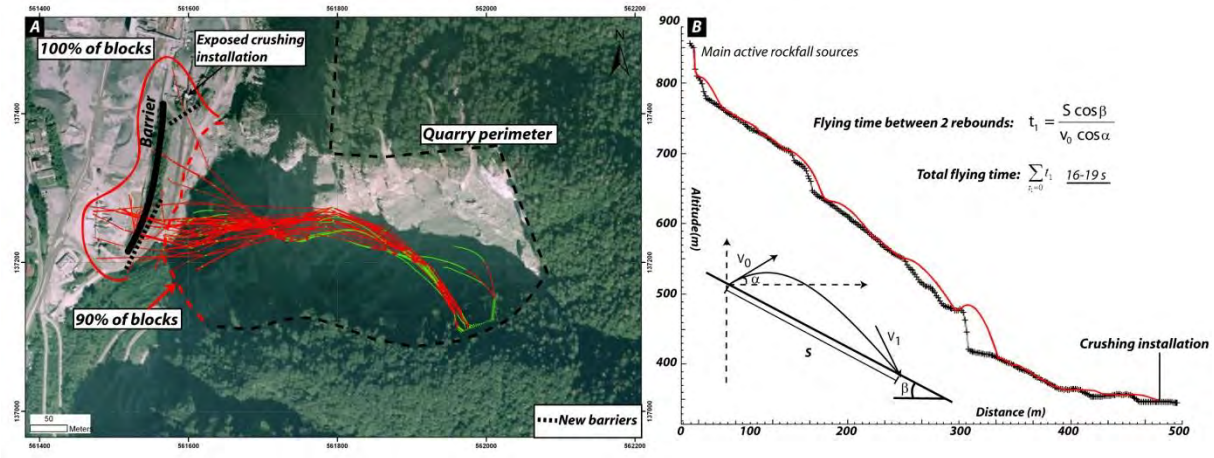

Figure 5.5-10: A) 3D trajectography modelling showing the potential exposure to rockfall of crushing installation and the ineffectiveness of existing measures, especially in the southern portion of the existing rock barrier. B) 2D rockfall modelling used to determine the time of propagation for a rockfall detaching from the source area and reaching the crushing installation.

5.5.10.2 Benches stabilization and new excavation concept

Geotechnical analyses conducted in structural domain I indicate clear dependence of the potential unstable mobilized volumes on the benches high and bench orientation (Figure 5.5-11b). Factor of safety calculation follow the same trend (Figure 5.5-11a). In order to decrease the rockfall/rockslide susceptibility of the structural domain I a complete re-profiling of the upper benches is proposed. In particular the slope height will be drastically reduced to 20 m and the bench orientation will be modified northward from 320° to 350°. The new slope configuration should allow reaching an acceptable safety factor (> 1.4) and manageable potential unstable volumes (< 2000 m^3).

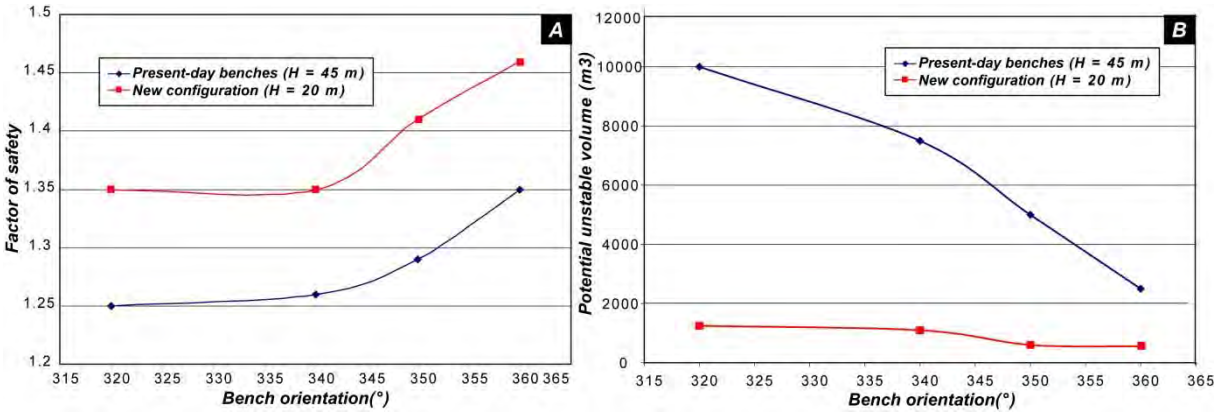

Figure 5.5-11: Variation of the safety factor (a) and the mean potential unstable volumes (b) as function of benches orientation for structural domain I. The factor of safety is calculated, for dry conditions, using limit equilibrium approach.

5.5.10.3 Early warning system and emergency response procedure

The continuous monitoring that has been set up for more than one year allows preliminary knowledge of the maximal variations on the normal trend recorded by Ground-based radar. Based on these observations, velocity thresholds have been proposed for the different potential instabilities. Back-analysis of the main rockslide event that occurred in the quarry indicates an important influence of climatic conditions on the development of large slope failures. For these reasons, a meteorological station was implemented in the upper portion of the quarry.

Table 5.5-2: Fixed critical threshold values of the selected criterion and corresponding number of point for the emergency response procedure.

Criteria	***Threshold values I (Nb. of points)***	***Threshold values II (Nb. of points)***
Rockfalls/slope activity	Sporadic rockfalls from potential unstable areas and/or small volumes (< 1 m^3) ***(1 Pt).***	Continuous rockfalls from potential unstable areas and /or large volumes (< 1 m^3) ***(2 Pt.)***
Precipitation/temperature variations	Rainfall (20 mm within 24h) or more than 1 day with freeze and thaw cycle ***(2 Pt).***	Intense rainfall (35 mm within 24h) or more than 3 days with freeze and thaw cycle (***3 Pt.)***
GB-Instar displacements	Cumulated displacements in 24 h > 2.5 mm and < 3.5 mm ***(2Pt.)***	Cumulated displacements in 24 h > 3.5 mm ***(4 Pt.)***

Critical threshold values for temperatures variations and rainfall quantity was also proposed based on historical data. Displacements and climatic parameters have been combined to create a quantitative emergency response flowchart (Figure 5.5-12). For each criterion (rainfall, temperature variation, and observed displacements), a threshold value and a relative score have been assigned. Table 5.5-2 presents the different threshold values and the corresponding score. The sum of each parameter corresponds to a

different alert level. For each alert level a risk reduction measure is associated. In particular, precise rules about the access and the activities that could be performed inside the exposed areas (potential rockfall/rockslide run-out areas, unstable benches) are clearly defined. For each alert level, roles and responsibilities of the different mine staff were also proposed.

Nb. of points	Alert level		Direct action	Response
⩾6	3	Very high	**Total closure of all risk areas** -Complete closure to machine and worker of risk areas -Operations allowed only outside the max. run-out zones -Monitoring and visual observations are increased	Site investigation by geotechnical engineer. Changing in alert level only after engineer's advice.
>3	2	High	**Total closure of high risk areas** -Closure of crushing installation for people's safety -No extraction works at the bottom of the slope	Movements/weather situation checked by geotechnical engineer. Changes in alert level only after engineer's advice.
>1	1	Moderate	**Partial closure of high risk areas** -Access to crushing installation behind the barriers -No extraction work at the bottom of the slope	Re-evaluation of the situation every 24h by the production manager. Geotechnical engineers are informed.
⩽1	0	Normal situation	**Acceptable risk level** -Normal quarry operations following classical safety rules	Real-time evaluation by quarry workers and Production Manager. Company and state safety rules are applied.

Figure 5.5-12: Emergency response procedure applied for Arvel quarry. The four alert levels are associated to different access restrictions and safety rules. For each level the responsibilities have been also clearly defined.

5.5.11 CONCLUSION

In this study, we propose an integrated approach covering the main steps of the slope design. The main challenge was to find a good compromise between a tolerable risk level and economic issues related to the quarry activity. Remote sensing techniques, in particular TLS and GB-DInSAR, have been adopted both in the hazard assessment analysis and for an early warning system. By applying the proposed approach, onerous analyses such as field investigations or borehole logging were focused on key locations only. Detailed back-analyses of previous instabilities occurred in the quarry reveal important information concerning the main predisposing and the triggering factors leading to the better hazard assessment of the new detected instabilities. Calibration of critical displacements and rainfall values defining the alert levels still remains an important issue that will be only partially solved with long-time monitoring analysis. Continuous actualisation and refining of threshold values are needed to improve both safety and economic productivity of quarry operations.

5.5.12 REFERENCES

Abellán, A., Jaboyedoff, M., Oppikofer, T., Vilaplana, J. M. 2009. Detection of millimetric deformation using a terrestrial laser scanner: experiment and application to a rockfall event, *Nat. Hazards Earth Syst. Sci.*, 9, 365-372.

Brideau, M.-A., Pedrazzini, A., Stead, D., Froese, C., Jaboyedoff, M., van Zeyl, D. 2010. Three-dimensional slope stability analysis of South Peak, Alberta, Canada, *Landslides*, 2, 139-158.

Brideau, M-A., Ming Y., Stead, D. 2009. The role of tectonic damage and brittle rock fracture in the development of large rock slope failure, *Geomorphology*, 103, 30-49.

Choffat, Ph. 1929. L'écroulement d'Arvel (Villeneuve) de 1922, *Bull. Soc., Vaud. Scin. Nat.*, 57, 5-28.

Chen, Y., Medioni, G. 1992. Object Modelling by Registration of Multiple Range Images, *Image Vision Comput.*, 10, 145–155,

Crosta, G.B., Imposimato, S., Roddeman D. 2009. Numerical modelling of entrainment/deposition in rock and debris-avalanches, *Engineering Geology*, 109, 135-145.

Hoek E., Brown, ET. 1997. Practical estimates of rock mass strength, *Int. J. Rock Mech. Min. Sci.,* 34, 1165–1186.

Hudson, J. A., Priest, S. D. 1983. Discontinuity frequency in rock masses, *Int. J. Rock Mech. Min. Sci. Geomech. Abstr.*, 20, 73-89.

International Society of Rock Mechanics (ISRM). 1978. Suggested methods for quantitative description of discontinuities in rock masses*, International Journal of Rock Mechanics & Mining Sciences & Geomechanics*, 15, 319-358.

InnovMetric. 2009. Polyworks: 3D scanner and 3D digitizer software from InnovMetric Software Inc. Canada

Itasca. 2008. UDEC 4.0, Itasca Consulting Group Inc., Minneapolis, Minnesota.

Jaboyedoff, M., Mamin, M., Philipposian, F., Rouiller, J.-D. 1996. Distribution spatiale des discontinuités dans une falaise, Rapport PNR31, VDF, 90 p.

Jaboyedoff, M, Baillifard, F, Couture, R, Locat, J, Locat, P 2004. Toward preliminary hazard assessment using DEM topographic analysis and simple mechanic modeling. In: Lacerda WA, Ehrlich M, Fontoura AB, Sayo A (eds) *Proceedings of the 9th International symposium on landslides*. Balkema, Rotterdam, 191–197.

Jaboyedoff, M., Metzger, R., Oppikofer, T., Couture, R., Derron, M.-H., Locat, J., and Turmel, D. 2007. New insight techniques to analyze rock-slope relief using DEM and 3D-imaging cloud points:COLTOP-3D software, Proceedings of the *1st Canada – U.S. Rock Mechanics Symposium*.

Jaboyedoff, M., Couture, R., Locat, P. 2009. Structural analysis of Turtle Mountain (Alberta) using digital elevation model: toward a progressive failure, *Geomorphology,* 103, 5-16.

Leva, D., Nico, G., Tarchi, D., Fortuny-Guasch, J., Sieber, A. J. 2003. Temporal Analysis of a Landslide by Means of a Ground-Based SAR Interferometer, *IEEE T. Geosc. Remote Sensing*, 41, 745–752

Longchamp, C., Pedrazzini A., Jaboyedoff, M., Dessauges A., Louis K., Buckingham T. Erni C. 2010. Structural and stability analyses of a rock cliff based on digital elevation model: the Obermatt quarry (Switzerland). *In Proceedings of the European Rock Mechanics Symposium (EUROCK 2010)*, Lausanne, Switzerland, 15–18 June (2010). CRC Press, Leiden, the Netherlands, 593–596.

Marinos, V., Marinos, P. Hoek, E. 2005. The geological strength index: applications and limitations,. *Bulletin of Engineering Geology and the Environment*, 64, 55-65.

Oppikofer, T., Jaboyedoff M., Blikra, L-H., Derron, M.-H, Metzger R. 2009. Characterization and monitoring of the Åknes rockslide using terrestrial laser scanning, *Nat. Hazards Earth Syst. Sci.*, 9, 1003-1019.

Pedrazzini, A., Oppikofer, T., Jaboyedoff, M., Guell i Pons, M., Chantry, R., Stampfli, E. 2010. Assessment of rockslide and rockfall problems in an active quarry: Case study of the Arvel quarry (western Switzerland). *In Proceedings of the European Rock Mechanics Symposium (EUROCK 2010)*, Lausanne, Switzerland, 15–18 June (2010). CRC Press, Leiden, the Netherlands, 593–596.

Pedrazzini, A., Froese, C.R., Jaboyedoff, M., Hungr O., Humair F., (In Press). Combining Digital Elevation Model analysis and run-out modelling to characterize hazard posed by a potentially unstable rock slope at Turtle Mountain, Alberta, Canada, *Engineering Geology*, DOI: 10.1016/j.enggeo.2011.03.015.

Read, J., Stacey, P. 2009. *Guidelines for Open Pit Slope Design*. CSIRO Publishing, Collingwood.

Rocscience. 2008. Swedge version 5.005, Rocscience Inc., Toronto, Canada.

Sturzenegger, M. Stead, D. 2009. Quantifying discontinuity orientation and persistence on high mountain rock slopes and large landslides using terrestrial remote sensing techniques, *Nat. Hazards Earth Syst. Sci.*, 9, 267–287.

Tarchi, D., Casagli, N., Fanti, R., Leva, D., Luzi, G., Pasuto, A., Pieraccini, M., Silvano, S. 2003. Landslide monitoring by using ground-based SAR interferometry: an example of application to the Tessina landslide in Italy, *Engineering Geology*, 68, 15–30.

Williams, J. H., Johnson, C. D. 2004. Acoustic and optical borehole-wall imaging for fractured-rock aquifer studies, *Journal of Applied Geophysics*, 55, 151-159.

6. CONCLUSIONS AND PERSPECTIVES

6.1 CONCLUDING REMARKS AND DISCUSSIONS

The specific conclusions for each study site were presented at the end of each sub-chapter. In the following section the main outcomes concerning the three main topics developed in this PhD are presented.

6.1.1 REGIONAL SCALE ASSESSMENT OF GRAVITATIONAL SLOPE DEFORMATIONS

The first two sub-chapters of this manuscript were focused on the regional scale assessment gravitational slope deformations within the upper Rhone catchment. A new mapping strategy based on the integration of high resolution digital elevation model and Google Earth™ analyses were adopted to dispose of a homogenous inventory of gravitational slope deformations for the entire study area. Spatial characteristics of the different gravitational slope deformations were analysed by different approaches including detailed field investigations, statistical analyses and GIS modelling. Detailed information obtained through the inventory was then compared to the geological, tectonic and the geomorphological characteristics of the study area to dispose of the key elements to propose comprehensive answers to two fundamental aspects of the regional slope evolution processes:

- *What are the main predisposing factors leading to the present-day distribution of large rock slope deformations?*
- *What is the contribution of rockslides and rock avalanches on the postglacial denudation rate and on the infill of main Alpine valley?*

In complex geological and morphological setting such as the Rhone valley, it was extremely difficult to define a single causal relationship between a specific predisposing factor and the gravitational slope deformation distributions. Lithological and structural conditions were identified to control the hillslope processes by defining the typology and the extent of the gravitational slope deformations. On the other hand, the occurrence of gravitational slope deformations within the Rhone valley is not uniformly distributed and six clusters encompassing more than 80% of the detected instabilities were identified.

These observations suggest that gravitational slope deformations are essentially related to coexistence of several factors leading to a preferential distribution of zones displaying a higher slope deformations density. In Rhone catchment, these zones are characterized by the coexistence of high local relief, large scale pre-existing tectonic weakness zones and active tectonic processes, including high uplift gradients and high seismic energy release was identified to be the most important predisposing factors constraining the present-day distribution of gravitational slope deformations.

In particular, the strong spatial and statistical relations between high seismic energy release, important uplift gradient and gravitational slope deformations represent an important discover that can potentially influence the current scientific debate concerning the existence and the magnitude of neotectonic processes in the Western Alps.

Climate forcing, which was identified by several authors as the most important factor controlling the denudation and the erosion rate in the Western Alps, seems also play an important role concerning the distribution of gravitational slope deformations. However, it requires a critical examination.

The creation of relief, in particular the formation of overdeepened areas operated by glaciers during LGM, was identified to be an important predisposing factor influencing the development rockslides and rock avalanches along the main Rhone valley. Moreover, at the slope scale, specific topographic settings that experienced a more rapid and important stress release was identified to be the most prone areas to develop rockslide and rock avalanches. On the other hand, especially along the lateral tributary valleys, no direct relation between glaciation and gravitational slope deformations development was clearly highlighted. Moreover, slope deformations associated to breaches enlargement seems to be limited in the Rhone catchment because last glaciation followed essentially pre-existing valleys.

At local scale, several others factors have been identified to predispose the development of gravitational slope deformations. For instance, the presence the structural and lithological weakness (e.g. local tectonic accidents or soluble rocks) and specific valley configurations can control the gravitational slope deformations development. However, all these factors need to be considered as second order aspects associated to the development of a single instability, but this cannot explain the regional distribution of the identified gravitational slope deformations. Figure 6.1-1 proposes an overview of the potential connexion between the inherited litho-tectonic context, active tectonic processes and climatic forcing in relation to gravitational slope deformations within the Rhone catchment.

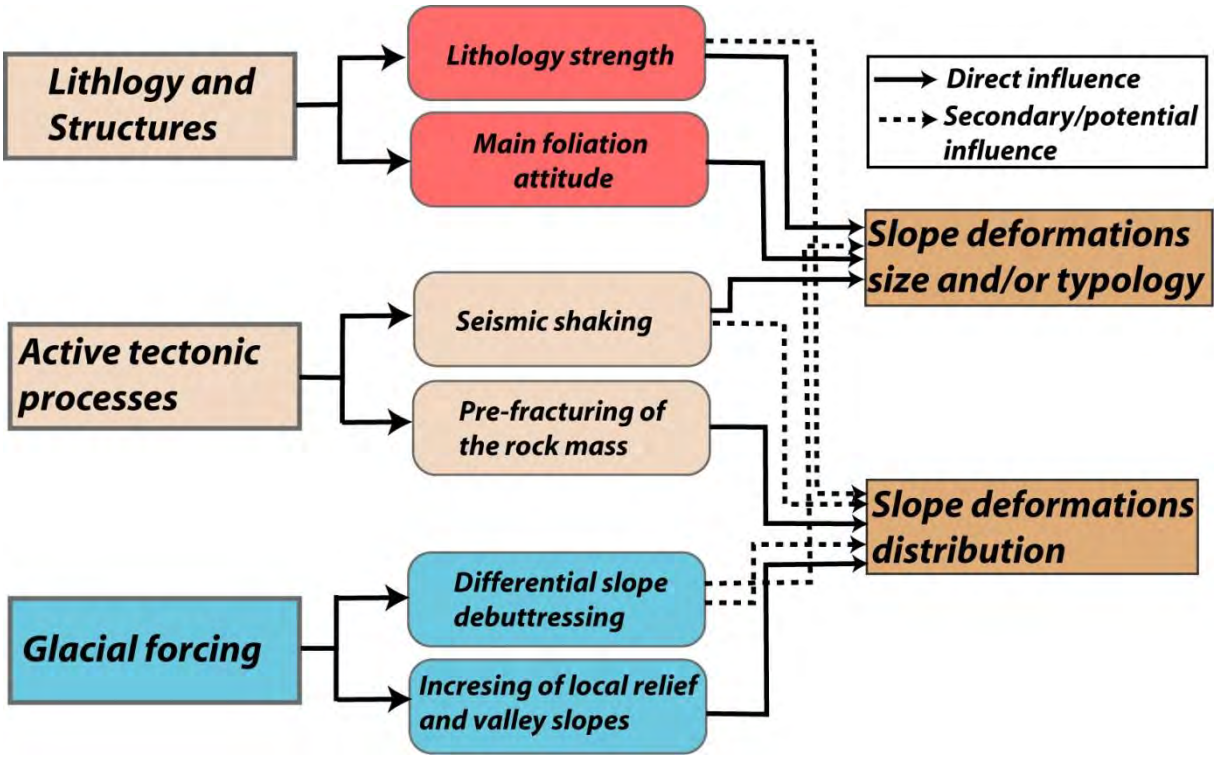

Figure 6.1-1: Potential connexion between inherited litho-tectonic conditions, active tectonic processes and climate forcing in relation to the distribution and the typology of slope deformations within the Rhone catchment.

As mentioned above, rockslides and rock-avalanches represent a particular typology of the gravitational slope deformations. Compared to other gravitational slope deformations, scars left by these phenomena

generate the highest-impact single erosional events in the paraglacial slope system. Detailed geometric reconstruction of pre-failure topography, based on high resolution digital elevation model, allowed the estimation of the volume associated to each rockslide scar. The obtained cumulative volume-frequency distribution was well described by fitting two power-law distributions; one describing volumes above 10 M of m^3 and other defining smaller volumes.

Based on the assumption that the power-law distribution for larger volumes is valid for the whole range of possible volumes, it was possible to estimate the total post glacial volume evacuated by rockslides and rock avalanches along the main Rhone valley. Depending on the assumption adopted, this volume represent between 5% and 9% of the whole quaternary sediments filling the Rhone valley. Compared to the total mechanical denudation rate estimated for the entire Rhone catchment, the contribution of rockslides and rock avalanches can be estimated in 8-10%. This highlights that important contribution of gravitational slope movements on the overall lateglacial erosion of the Rhone catchment but also for the overall evolution of the Alpine landscape. Moreover, these estimations need to be considered as minimum contributions to the overall denudation achieved by rock slope failures because they are based on the frequency-size distribution of large events only.

6.1.2 THE ROLE OF INHERITED BRITTLE AND DUCTILE STRUCTURES ON ROCK SLOPE INSTABILITIES DEVELOPMENT

In the second section of this manuscript, detailed structural and failure mechanism analyses of two of the large rock avalanches were presented. Classical field analyses of joint sets and rock mass conditions were improved by the extensive use of aerial high resolution digital elevation models. In the field, a special attention were spend to describe the rock mass conditions in order to characterize the potential variation or the rock mass damage within the slope and to dispose of preliminary information about the geomechanical parameters required by numerical modelling.

Investigation performed on Turtle Mountain highlighted the important control, at all spatial scales, of both ductile and brittle tectonic structures on the development of large rock slope instabilities. At the mountain scale, the overall stability conditions depend on the specific geometrical and tectonics characteristics of Turtle Mountain anticline and of the Turtle Mountain thrust. These kilometric-scale structures represent the primary conditions defining the location where large slope failures can develop preferentially. Outcrops-scale brittle structures, originated during the folding phase or associated to late tectonics movements were identified to control the three dimensional kinematic of rock slope failure. A general model based on the interlimb angle and on the location of the fold in the mountain was proposed to illustrate the potential failure mechanism induced by the presence of fold and fold-related fractures in anticline configuration.

The evaluation of rock mass quality along the Turtle Mountain anticline emphasized the important influence of both ductile and brittle structures, not only on the 3D geometrical control of rocks slope instability, but also for the local reduction of the rock mass strength. This phenomenon is particularly evident on the fold hinge area of Turtle Mountain anticline where significant damage induced by extensional stress increases the development of fracturing. Within this area, significant karstification along persistent fractures involve a preferential rock dissolution that drastically decrease the overall rock mass strength and create zones of preferential weakness prone to landslide. The influence of fold-related

damage was identified to be an important factor not only for local-scale instabilities but also in the development of large rock slope failures particularly in a carbonate environment.

The second case study investigated the influences of the tectonic context on the failure mechanism associated to the Sierre rock avalanche. Also for this study case, inherited brittle and ductile tectonic structures represent main predisposing factors facilitating the development of the rock-avalanche. At the slope scale, numerical modelling highlighted that the overall dip-slope geometry associated Nappe emplacement, drastically influences the tensile strength distribution within the slope outlining zones where tensile failure can preferentially develop. However, these conditions cannot explain alone the mobilization of the entire failed mass, suggesting the primary influence of a basal fault located at the bottom of the slope on the evolution of the instability from a DSGSD to a rock-avalanche. Slope-scale structures control also the overall morphology of the failure surface. Indeed, high resolution digital elevation model analyses indicated that the failure surface geometry is essentially controlled by the interference of two folds related to two distinct tectonics deformations. A surprising observation concerns the important control of failure surface geometry on the early phases of the rock avalanche propagation. Actually, the complex shape of the failure surface creates an early subdivision within the unstable rock permitting to the rock avalanche to move in two slightly different directions. Without this early subdivision, the mobility of the Sierre rock-avalanche would be considerably reduced. These observations highlight the significance, in term of run out analysis and hazard assessment, to dispose of precise information concerning the shape of the failure surface and the differential movements affecting active rockslides. Figure 6.1-2 proposes a first attempt to summarize the potential influence between outcrop and slope scale tectonic structures on the development of rock slope instabilities.

The trans-disciplinary approach adopted in this study permitted a more comprehensive overview of the complex interactions existing between inherited tectonic structures and rock slope deformations. Nevertheless several important questions remain concerning in particular the role of regional and local joint sets in defining the final location of the rock instability and the extent of rock mass damage associated to inactive tectonics accidents.

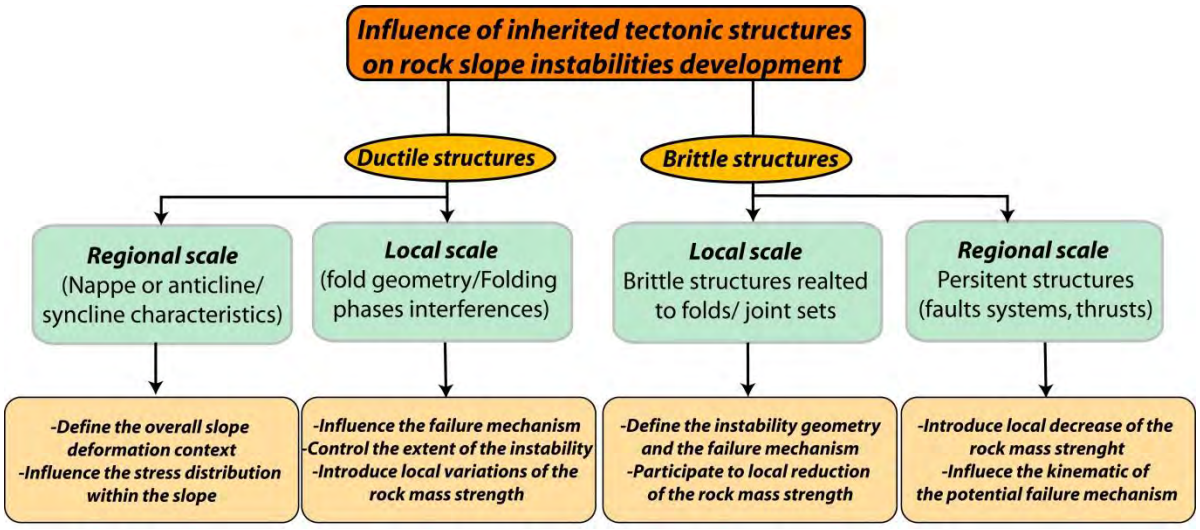

Figure 6.1-2: Potential influences of the brittle and tectonic structures on the development and on the failure mechanism of large rock slope instabilities.

6.1.3 HAZARD ASSESSMENT AND OF CURRENT AND POTENTIAL INSTABILITIES

The third section of this manuscript focused on the combination of different techniques to propose a comprehensive evaluation of the failure mechanism and the hazard posed by rock slope instabilities. A particular attention was spent to propose a 3D dimensional characterization of the instabilities in term of spatial delimitation and kinematic behaviour. Five study sites were analysed, displaying different characteristics in term of available data and stability conditions.

In the first case study, hazard posed by potential rock slope instabilities located in Turtle Mountain was analysed. In a first stage of the project, high resolution digital elevation model and field analyses were used to delimit the potential unstable areas and to propose a preliminary geometrical model of the instability. Available displacements data permitted a first validation of the early suppositions concerning the failure kinematic and the spatial extent of the different instabilities. In a second phase, geometrical and numerical analyses based on digital elevation models were applied to propose an objective estimation of the unstable volumes and to simulate the potential run-out of the detected instabilities. This two-steps approach represents a good example where information derived from different techniques was integrated to propose objective and quantitative hazard assessment. Indeed, the different methods presented above can also be applied to obtain a fast characterization of the hazard posed by other large potential rock slope instabilities in particular when high resolution digital elevation model and/or monitoring data are available.

In the second case study, the displacement patterns and the potential failure mechanism of the Eiger rockslide were investigated. The availability of sequential TLS point clouds provided detailed 3D displacement patterns over the entire instability and permitted a detailed structural characterization. The application of both continuum and discontinuum numerical models allowed identifying the main structural, topographic and geomechanical factors controlling the pre-failure stage and the early development of the instability. An analytical model developed specifically for this instability and constrained on TLS displacements data, was able to reproduce the displacement behaviours and to identify the main parameters controlling the uncommon evolution of this rockslide. The different approaches adopted in this study highlighted the importance to integrate detailed 3D displacement data and numerical modelling to understand the kinematic and the potential evolution of complex rock instabilities.

In the third case study, a new approach to identify and interpret the 3D displacements of the upper portion of the Randa rockslide was developed. One dimensional displacements data obtained by PsInSAR™ and geodetic techniques were combined to obtain “quasi” 3D displacement patterns within the unstable area. Detailed structural analyses based on new high relation digital elevation model allowed interpreting the calculated displacements in term of slope kinematic. The geometrical model was then validated based on simple numerical simulation. Even if preliminary, the proposed approach can open new perspectives for the determination of the 3D displacement patterns in complex rock slope instabilities where in-situ analyses are difficult and/or not representatives of the overall slope kinematic.

The fourth case study presented the results a four years monitoring based on sequential TLS acquisitions of a gypsum slope in located in Val Canaria. This case study represented a unique opportunity to study the slope behaviour before and after a large rock collapse. Analyses of successive TLS acquisition enable the

detection of significant pre-failure movements affecting part of the monitored slope since two years before the slope-scale collapse. The comparison between the displacements data acquired by real aperture ground-based radar and TLS techniques, one the day before the large collapse of October 2009 suggests that, in favourable conditions, displacements close to 1 centimetre can be potentially detected using TLS. These results open new interesting perspectives for temporal failure prediction of rock slope failures.

The last case study presented in this manuscript focused on the assessment and the mitigation of rockfall and rockslide hazards in the Arvel quarry. Similar to Turtle Mountain, a complete methodology was developed to characterize the stability of the quarry slopes. High resolution digital elevation models based on ALS and TLS techniques were implemented as basics information for the slope stability assessment and to design a more stable slope configuration. An early warning system and an emergency response procedure were developed based on sequential TLS acquisitions and continuous Ground-based radar monitoring. Early feedbacks about the reliability of this warning system are encouraging and highlighted the great potential of coupled approach, based on Ground-based radar and TLS techniques, to obtain more accurate spatial and temporal prediction of future rock failure.

6.1.3.1 Proposed approach to assess the kinematic and the hazard of current rock slope instabilities

A common feature connecting the approaches applied in the different study sites is the extensive use of high resolution digital elevation models derived from both ALS and TLS. Actually, information that can be derived from high resolution digital elevation models can be applied at the different stages of the rock slope analysis especially on the detection of the potential instability, the analyses of the mechanisms and monitoring of the slope activity in term of rockfalls and differential displacements. The Eiger and the Val Canaria and case studies are two good examples showing the different applications of digital elevation model analyses (chapters 5.4 and 5.4).

However, rock slope instabilities are complexes and require also a detailed description of the mechanical and hydrogeological characteristics of the rock mass and the joint sets. Therefore, field investigations implying a detailed geological characterization, in situ monitoring and subsurface characterization (geophysical survey, borehole logging) are extremely important to dispose of a more comprehensive description of the instability. This aspect has been clearly highlighted in the Val Canaria study site (chapter 5.4) where the maximal thickness of rock collapse is not structurally-controlled but is related to the geological contact between weathered gypsum and fresh anhydrite.

As showed in the Eiger case study (chapter 5.4), numerical models based on both continuous and discontinuum approaches represent also an important support to constrain and improve early geometrical interpretations. On the other hand, it is important remember that the reliability of the numerical models is strongly dependent on the quality of the input data; therefore the obtained results need to be critically interpreted.

A key point to assess the kinetic and the hazard related to rock slope instability is to integrate the different sources of information by creating a “conceptual” model of the instability. This latest corresponds essentially to a detailed geometrical 2D/3D representation of the instability where information about

displacements and in-situ characteristics of the rock mass are merged together to propose an interpretation of the involved volumes and of slope kinematic. Concrete examples of "conceptual" models are presented for the different instabilities identified in Turtle Mountain and for the upper portion of the Randa rockslide. The establishment of a conceptual model, even if it is preliminary, is extremely helpful because allow identifying the key areas where more detailed studies need to be focused on to dispose of a better overview of slope kinematic. Moreover, the monitoring system can be better developed/designed to detect displacements patterns that are more representative of the entire instability. The Arvel study site (chapter 5.5) highlighted the importance to dispose of an accurate characterization of the instability to define the most adapted monitoring techniques in order to dispose of a reliable early warning system.

The "conceptual" instability model is not intended to be a static description of the instability. A continuous update of the initial "conceptual" model, according to the new displacement data, detailed field analyses and more comprehensive numerical models is essential to constantly improve the understanding the unstable rock slope and to propose an objective hazard assessment. A good example of "conceptual" model updating is reported in chapter 5.3, where the early kinematic model for the Randa rockslide have been slightly modified according to new displacements information and modelling results.

The successive step to obtain a comprehensive hazard assessment of rock slope instabilities is the determination of the potential run-out zones. This can be performed adopting empirical or numerical propagation models. The integration in the run-out models of information concerning the potential instabilities (volume, shape, and general moving direction) is essential to dispose of reliable results. Analyses performed in Turtle Mountain (chapter 5.1) demonstrated the importance of these two aspects to obtain a reliable hazard zoning. An ideal workflow resuming the suggested key-points for an integrated rock slope hazard assessment is reported in Figure 6.1-3.

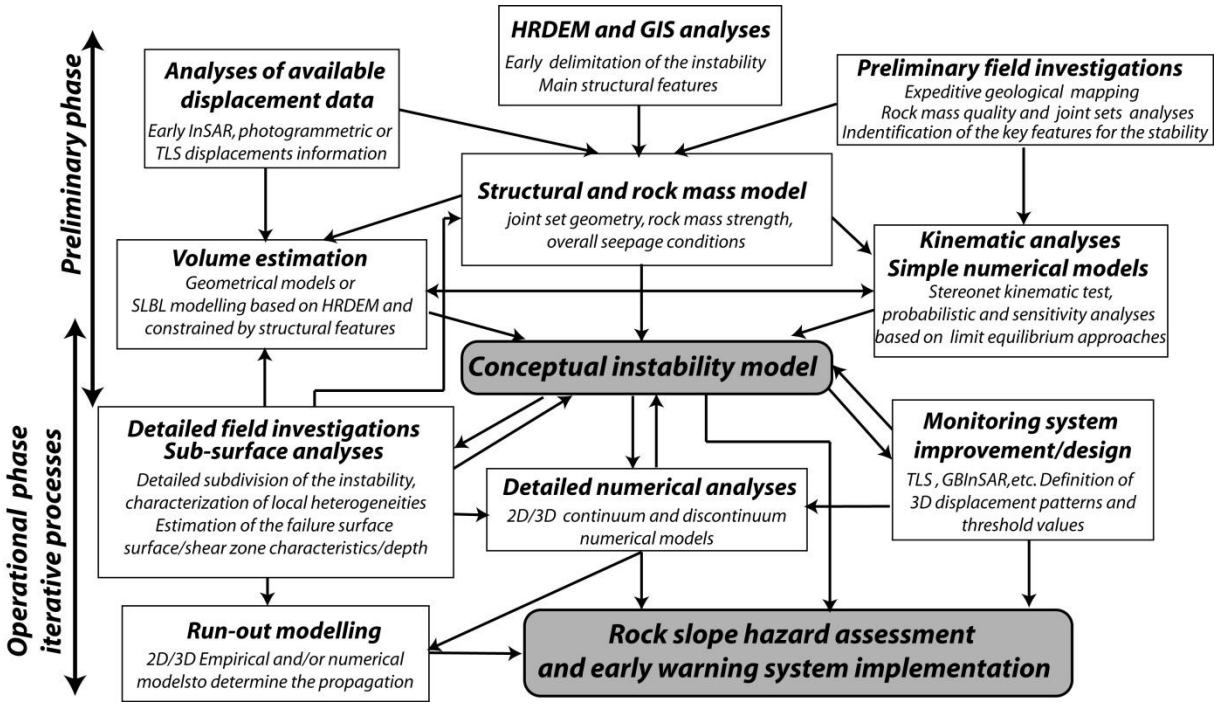

Figure 6.1-3: Workflow resuming the key points of the integrated approaches for a comprehensive hazard assessment of rock slopes instabilities.

6.2 GENERAL CONCLUSION

In this PhD manuscript three main aspects of the rock slope system have been analysed:

- The regional analysis of gravitational slope deformations.
- The influence of the inherited tectonic structures on the rock instabilities development.
- The combinations of different techniques to assess the stability of potential rock slope instabilities.

The first two aspects deal about two fundamental aspects of the slope instabilities characterization where rock slope instability is primary regarded as an agent influencing the landscape evolution. At the opposite, the third aspect developed in this thesis focused on more practical rock slope engineering problems where rock slope instabilities represent an important natural hazard. Even if the primary objectives and the study scales are different, significant connections exist between these three aspects. Through the different case studies presented in *chapter 5,* the strong influence of the tectonic and the lithological setting on the kinematic of current and potential rock slope instabilities was highlighted. This emphasizes the importance to develop a better comprehension, all spatial scales, of the relationship between tectonic structures and rock slope instabilities for constructing reliable geological models, which are necessary for the implementation of a monitoring system or mitigation measures.

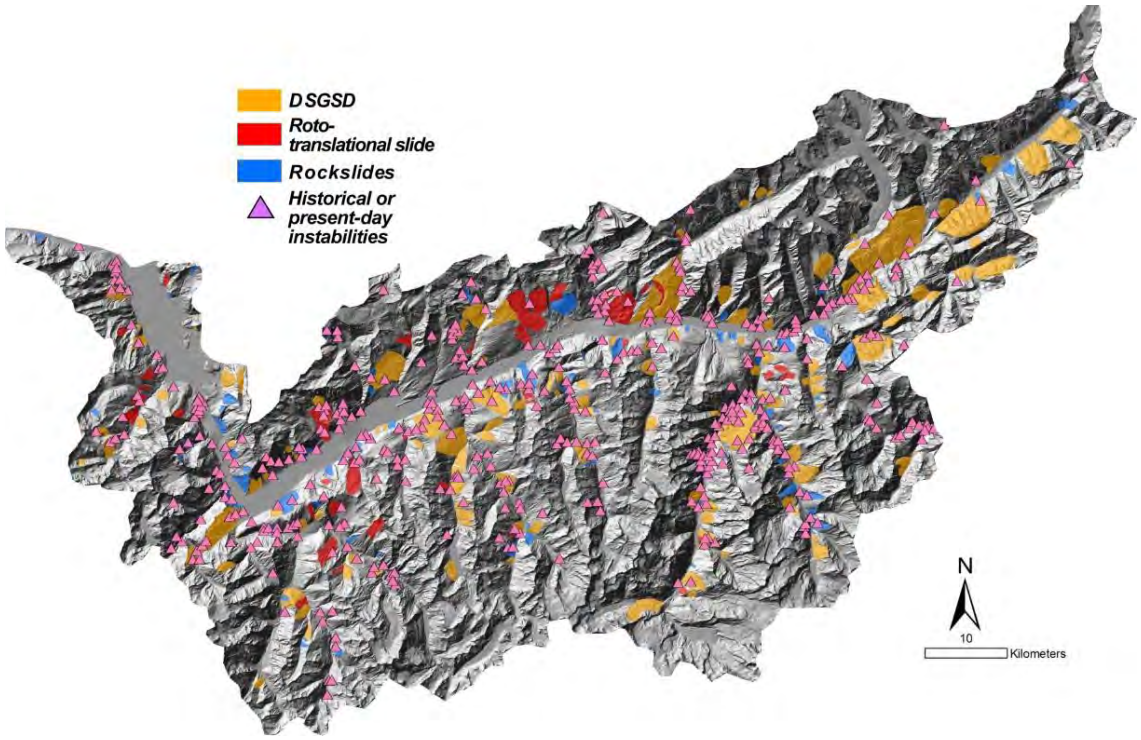

Figure 6.2-1: Comparison between the distribution of gravitational slope deformation and shallow/active instabilities within the Rhone catchment emphasising the important of multi scale approach to analyse the landslide hazard (Data CREALP and Bonnard pers. comm.).

Large gravitational slope deformations analysed in the first part of this thesis such as deep-seated gravitational slope deformations do not represent directly an important hazard. However, a better comprehension of these of phenomena has also important engineering implications. Actually, over long the long term, internal deformations affecting these phenomena can drastically increase to a rapid creep

failure and create destructive phenomenon such as rock-slides or rock avalanches. Moreover, the region interested by a DSGSD show frequently a lower rock mass strength promoting the local development of more superficial and active instabilities. The Rhone catchment represents an interesting study area where the control of large gravitational slope deformations on the development of active instabilities such as shallow landslides, rockfall or debris flow can be clearly highlighted. Figure 6.2-1 shows the spatial distribution of large scale gravitational slope deformations and superficial slope instabilities that are presently monitored or that provoked damage along road since the last century. Interesting, close to 50% of the instabilities are located within or close to the border of slope-scale gravitational slope deformations (Tonini et al., in prep). This highlights the importance to dispose of a comprehensive regional scale inventory of the gravitational slope not only for the characterization of long term landscape processes but also for a more accurate assessment of landslide hazards.

6.3 PERSPECTIVE FOR FUTURE WORKS

Achievements of this thesis, even if promising, require more detailed analyses and further improvement. According to the three aspects developed in this thesis several areas of research could be suggested for a better understanding of the slopes instabilities processes at different spatial scales:

- *Regional-scale analyses of gravitational slope deformations*

The gravitational slope deformations inventory on the Rhone catchment should be continued also in the north western zone of the study area (Préalpes Vaudoises) in other to dispose of a complete coverage of the upper Rhone catchment. The overall inventory can be substantially improved by coupling classical geomorphological mapping and regional-scale displacements data obtained by DInSAR or PSInSAR techniques. These techniques represent an important support to detect gravitational slope deformations which are not characterized by clear morphological features. Moreover, based on this data it will be possible to dispose of preliminary information concerning the state of activity of the detected instabilities. Preliminary results obtained in Saastal-Mattertal test area (Appendix B6) are encouraging suggesting the applicability of this coupled approached at the entire Rhone catchment.

Modelling the spatial distribution of the different parameters influencing the distribution of gravitational slope deformations such as uplift, main foliation orientation or seismic energy release represent an important step in the regional-scale analyses. Different interpolation techniques should be tested to avoid artefact that can potentially bias the interpretation of the results. Additionally, other geospatial analyses such as variography or three dimensional k-function calculations might be also tested to better characterize of the degree of spatial correlation of gravitational slope deformations with the different variables. The relation between high uplift gradient values and slope deformations distribution obtained for the Rhone valley is interesting but must be also tested in other similar catchment in European Alps and in more active mountain belts.

Presently, detailed pre-failure topography reconstruction and volume estimation were performed only for rockslide/rock-avalanches located along the main Rhone valley. To dispose of a more comprehensive view of the Lateglacial denudation rate, the detailed volumes reconstruction needs to be expanded to rockslide scars over the entire Rhone catchment. This should include the development of more accurate and

automatized procedure to calculate the rockslide volume. Moreover, the impact of DSGSD and largest landslides should be also integrated in the erosion rate calculation by estimating the material lost since the LGM and their connectivity to the river network.

Cosmogenic radionuclide dating of the rockslide scars and the surrounding areas will provide useful information concerning the relation between deglaciation, valley filling and rock slope failures development. Moreover, more precise estimation of the rockslide age will also provide a better estimation of the denudation rate associated to slope movements.

- *Influence of the inherited tectonic structures on the rock instabilities development*

Analyses performed at Turtle Mountain and on Sierre rock avalanche highlighted some interesting aspect of the potential interaction between tectonic structures and instabilities at both outcrops and slope scale. However, other case of large rock slopes instabilities located in area characterized by both thick and thin-skin tectonic including Rock Mountains or European Alps need to be analysed. At regional scale, analyses should be focused on the geometric characteristics of the anticline structures and thrusts and their relation with the topography and river/glacial erosion. At the local scale, detailed analyses should be focus on the variation in term of geometric and mechanical characteristics of fold-related fractures within the anticline structures. These analyses will be useful to identify the potential failure mechanisms within the different portion of the slope. An accurate description of the rock mass strength decrease associated to fold hinge or brittle regional-scale faults represent an important point for rock slope stability assessment. Rigorous field and numerical approaches need to be developed to obtain a better estimation of the potential extent of the rock mass damage associated to these structures.

- *Assessment of present-day instabilities based on multidisciplinary analyses*

As stated in the conclusion, the development of a reliable kinematic "conceptual" model represents a main issue to characterize the hazard posed by rock slope instabilities. More efforts should be made to better define the most representative 3D displacement patterns of the instability by integrating different remote sensing techniques and in-situ analyses. In particular, the integration of sequential TLS acquisitions and continuous GBInSAR will improve considerably the identification and the characterization of more active areas and should be widely adopted in early warning system.

In natural slopes, displacement analyses using TLS point clouds can detect displacements of few centimetres. Thanks to the large number of points that can be acquired in the same scan, displacements below 1 cm can potentially be detected. However, new methods for data treatment and more rigorous field acquisitions techniques should be consider.

Numerical models represent interesting tools to test and to improve the validity of "conceptual" slope instability model. However, for complex topography situations such natural slopes, numerical models are often performed in two dimensions only adopting a simplified topography. New developments are needed to include complex topography in 3D numerical models and to improve the development of more comprehensive conceptual instability models.